AD-A007 962

V/STOL AERODYNAMICS

Advisory Group for Aerospace Research and Development
Paris, France

October 1974

DISTRIBUTED BY:

NTIS
National Technical Information Service
U. S. DEPARTMENT OF COMMERCE

AD-A007 962

AGARD-CP-143

NORTH ATLANTIC TREATY ORGANIZATION

ADVISORY GROUP FOR AEROSPACE RESEARCH AND DEVELOPMENT

(ORGANISATION DU TRAITE DE L'ATLANTIQUE NORD)

AGARD Conference Proceedings No. 143

V/STOL AERODYNAMICS

Reproduced by
NATIONAL TECHNICAL
INFORMATION SERVICE
US Department of Commerce
Springfield, VA. 22151

Papers and Discussion of the Fluid Dynamics Panel Symposium
held in Delft, Netherlands, 24–26 April 1974.

THE MISSION OF AGARD

The mission of AGARD is to bring together the leading personalities of the NATO nations in the fields of science and technology relating to aerospace for the following purposes:

- Exchanging of scientific and technical information;
- Continuously stimulating advances in the aerospace sciences relevant to strengthening the common defence posture;
- Improving the co-operation among member nations in aerospace research and development;
- Providing scientific and technical advice and assistance to the North Atlantic Military Committee in the field of aerospace research and development;
- Rendering scientific and technical assistance, as requested, to other NATO bodies and to member nations in connection with research and development problems in the aerospace field;
- Providing assistance to member nations for the purpose of increasing their scientific and technical potential;
- Recommending effective ways for the member nations to use their research and development capabilities for the common benefit of the NATO community.

The highest authority within AGARD is the National Delegates Board consisting of officially appointed senior representatives from each member nation. The mission of AGARD is carried out through the Panels which are composed of experts appointed by the National Delegates, the Consultant and Exchange Program and the Aerospace Applications Studies Program. The results of AGARD work are reported to the member nations and the NATO Authorities through the AGARD series of publications of which this is one.

Participation in AGARD activities is by invitation only and is normally limited to citizens of the NATO nations.

A large part of the content of this publication has been reproduced
directly from material supplied by AGARD or the authors; the
remainder has been set by Technical Editing and Reproduction Ltd.

National Technical Information Service is authorized to
reproduce and sell this report.

Published October 1974

Copyright © AGARD 1974.

533.652.6:533.694:533.682

Printed by Technical Editing and Reproduction Ltd
Harford House, 7–9 Charlotte St, London. W1P 1HD

AGARD FLUID DYNAMICS PANEL OFFICERS

CHAIRMAN: Professor D.Küchemann
Royal Aircraft Establishment, Farnborough, Hampshire, UK

DEPUTY CHAIRMAN: Mr P.F.Yaggy
US Army Air Mobility R&D Laboratory, Ames Research Center
Moffett Field, California 94035, USA

PROGRAMME COMMITTEE MEMBERS

Mr J.P.Hartzuiker (Chairman)
NLR
Anthony Fokkerweg 2
Amsterdam-1017
Netherlands

Prof.Dr K.Gersten
Ruhr-Universität Bochum
463 Bochum-Querenburg
Postfach 2148
Germany

M. l'Ing. Principal C.J.Lievens
S.T.Aéronautique
4, Avenue de la Porte d'Issy
75996 Paris Armées
France

Dr R.C.Pankhurst
MOD – St. Giles Court
1–13 St. Giles High Street
London WC2 H8LD
United Kingdom

Dr U.Sacerdote
Aeritalia
Corso Marche 41
10100 Torino
Italy

Mr R.J.Templin
NAE
National Research Council
Ottawa 7,
Ontario
Canada

Mr P.F.Yaggy
US Army Air Mobility R&D Laboratory
Ames Research Center
Moffett Field
California 94035
United States of America

PANEL EXECUTIVE

Mr J.A.Lawford

FOREWORD

During the symposium reported in these Proceedings the themes of STOL and VTOL Aerodynamics were studied under headings of High-Lift Systems (Powered and Mechanical), Jet Lift, Ground Effect, and Aerodynamic Prediction Methods and Simulation Requirements. The symposium concluded with a general Round Table Discussion.

The symposium was held at the Technische Hogeschool, Delft, at the invitation of the Netherlands National Delegates to AGARD.

CONTENTS

Page

AGARD FLUID DYNAMICS PANEL OFFICERS, PROGRAMME COMMITTEE, AND MEETING THEME iii

Reference

INTRODUCTORY REVIEW

V/STOL AERODYNAMICS: A REVIEW OF THE TECHNOLOGY
by D.H.Hickey 1

SESSION I – POWERED HIGH-LIFT SYSTEMS

RESEARCH INTO POWERED HIGH-LIFT SYSTEMS FOR AIRCRAFT WITH TURBOFAN PROPULSION
by B.Eggleston 2

PREDICTING THE MAXIMUM LIFT OF JET-FLAPPED WINGS
by D.J.Moorhouse 3

WINDTUNNEL INVESTIGATION OF THREE POWERED-LIFT STOL CONCEPTS
by R.F.Osborn, and G.S.Oates 4

THE SPANWISE LIFT DISTRIBUTION AND TRAILING VORTEX WAKE DOWNWIND OF AN EXTERNALLY BLOWN JET-FLAP
by R.H.Wickens 5

THE FLOW AROUND A WING WITH AN EXTERNAL-FLOW JET-FLAP
by P.R.Ashill, and D.N.Foster 6

INVESTIGATION OF EXTERNALLY BLOWN FLAP AIRFOILS, WITH LEADING EDGE DEVICES AND SLOTTED FLAPS
by F.Mavriplis, and D.Gilmore 7

PRESENTATION DES RESULTATS AERODYNAMIQUES ET ACOUSTIQUES DES ESSAIS DE QUALIFICATION DU CONCEPT ALADIN II
par M.Collard, C.Doyotte, et M.Sagner 8

ETUDE THEORIQUE ET EXPERIMENTALE DU SOUFFLAGE DE COUCHE LIMITE A LA CHARNIERE D'UN VOLET HYPERSUSTENTATEUR
par B.Monnerie et G.Lovat 9

AERODYNAMICS OF JET FLAP AND ROTATING CYLINDER FLAP STOL CONCEPTS
by W.L.Cook, D.H.Hickey, and H.C.Quigley 10

SESSION II – MECHANICAL HIGH-LIFT SYSTEMS

PROGRES RECENTS EN HYPERSUSTENTATION MECANIQUE
par P.Perrier, et M.Lavenant 11

A METHOD FOR PREDICTION OF LIFT FOR MULTI-ELEMENT AIRFOIL SYSTEMS WITH SEPARATION
by K.Jacob, and D.Steinbach 12

EXPERIMENTAL HIGH-LIFT OPTIMIZATION FOR MULTI-ELEMENT AIRFOILS
by B.L.G.Ljungstrom 13

Reference

THE AERODYNAMICS OF TWO-DIMENSIONAL AIRFOILS WITH SPOILERS
by G.V.Parkinson, G.P.Brown, and T.Jandali 14

THE EFFECT OF VORTEX GENERATORS ON THE DEVELOPMENT OF A BOUNDARY LAYER
by S.de Ponte, and A.Baron 15

SESSION III – JET-LIFT

JET LIFT PROBLEMS OF V/STOL AIRCRAFT
by J.Barche 16

SIDESLIP IN VTOL-TRANSITION FLIGHT. A CRITICAL FLIGHT CONDITION AND ITS PREDICTION IN SIMPLE WINDTUNNEL TESTS
by B.Ewald 17

A METHOD FOR THE CALCULATION OF THE FLOW FIELD INDUCED BY A JET EXHAUSTING PERPENDICULARLY INTO A CROSS FLOW
by H.Snel 18

DESIGN AND TEST OF EJECTOR THRUST AUGMENTATION CONFIGURATIONS
by S.L.Brown, and R.D.Murphy 19

SESSION IV – GROUND EFFECT

GROUND EFFECT ON AIRFOILS WITH FLAPS OR JET-FLAPS
by K.Gersten, R.Löhr, and E.Beese 20

MEASUREMENT OF TILT-ROTOR VTOL ROTOR WAKE-AIRFRAME-GROUND INTERFERENCE FOR APPLICATION TO REAL TIME FLIGHT SIMULATION
by T.M.Gaffey, and M.D.Maisel 21

SESSION V – AERODYNAMIC PREDICTION METHODS AND SIMULATION REQUIREMENTS

US AIR FORCE V/STOL AIRCRAFT AERODYNAMIC PREDICTION METHODS
by H.W.Woolard 22

PREDICTION OF AERODYNAMIC INTERFERENCE EFFECTS WITH JET-LIFT AND FAN-LIFT VTOL AIRCRAFT
by D.Welte 23

A REVIEW OF THE LIFTING CHARACTERISTICS OF SOME JET LIFT V/STOL CONFIGURATIONS
by P.G.Knott, and J.J.Hargreaves 24

REQUIREMENTS FOR SIMULATION IN V/STOL RESEARCH AIRCRAFT PROGRAMS
by H.C.Quigley, and C.A.Holzhauser 25

ADDITIONAL PAPER IN SESSION III – JET LIFT

A LITERATURE SURVEY ON JETS IN CROSSFLOW
by E.C.P.Ransom, and P.M.Wood 26

APPENDIX A – ROUND TABLE DISCUSSION AT THE CONCLUSION OF THE SYMPOSIUM A-1

V/STOL AERODYNAMICS: A REVIEW OF THE TECHNOLOGY

David H. Hickey
Ames Research Center, NASA
Moffett Field, California 94035

SUMMARY

After 20 years of research, the western world has one operational V/STOL aircraft and that is a military aircraft. An examination of the technical reasons for this failure to convert research results to hardware indicates that the penalties for V/STOL capability are still too large for most applications. This cost may be reduced by improved efficiency of the propulsive lift components and use of the newly emerging augmentor technology. Payload-weight ratios of V/STOL aircraft are 10 to 20%; thus the productivity of the aircraft is very sensitive to small deficiencies or improvements in the various component efficiencies. The state of the art of some of these critical technological areas is reviewed. In particular, STOL augmentors, ground effects, and prediction methods are reviewed briefly. For VTOL, induced aerodynamics, vectoring devices, and modeling problems are reviewed. Research in these areas may significantly reduce the cost of V/STOL performance.

NOMENCLATURE

A	augmentation ratio
A_L	lifting element area, m^2 (ft^2)
A_T	wind-tunnel cross-sectional area, m^2 (ft^2)
Æ	aspect ratio, b^2/S
b	wing span, m (ft)
c	wing chord, m (ft)
C_j	jet momentum coefficient, T/qS
C_L	lift coefficient, L/qS
C_m	pitching moment coefficient, M/qSc
C_n	normal force coefficient, N/qS
C_p	pressure coefficient, $\Delta P/q$
D	diameter, m (ft)
DOC	direct operating cost
F_x	horizontal force, N (lb)
h	height from reference point to ground, m (ft)
ℓ	length from fan centerline to exhaust of hooded deflector, m (ft)
L	lift, N (lb)
m_s	augmentor secondary mass flow, kg/sec (lb/sec)
M	pitching moment, m-N (ft-lb)
M_{D_D}	drag divergence Mach number
N	force normal to the wing chord, N (lb)
P	pressure, N/m^2 (lb/ft^2)
PNdB	perceived noise level in decibels
q	dynamic pressure, N/m^2 (lb/ft^2)
r	distance from the engine axis, m (ft)
R	radius of hooded exhaust deflector centerline or jet exhaust, m (ft)
R_0	radius of engine exhaust, m (ft)

S	wing area, m^2 (ft^2)
t	time, sec
T	Thrust, N (lb)
u	velocity in jet exhaust, m/sec (ft/sec)
V	free-stream velocity, m/sec (ft/sec)
V_i	inlet velocity, m/sec (ft/sec)
V_j	jet velocity, m/sec (ft/sec)
W	gross weight, N (lb)
X	distance in the horizontal direction, m (ft)
α	angle of attack with respect to the free stream, deg
β_v	angle with respect to the fan axis, deg
δ_f	flap deflection, deg
δ_t	augmentor turning angle, deg
Δp	pressure difference, N/m^2 (lb/ft^2)
η_t	turning efficiency, %
θ_v	hooded deflector turning,angle, deg
λ	wing taper ratio
ϕ	augmentation ratio, T/T_N
Λ	wing sweep-back angle, deg

Subscripts

e	effective
max	maximum
N	nozzle
s	static
t	total pressure
TO	takeoff
1	ejector throat
2	ejector exit

1. INTRODUCTION

Research in V/STOL aerodynamics has spanned a period of at least 20 years, but only one production aircraft, the Hawker Harrier, has resulted. This paper discusses technology-oriented reasons for this failure to convert research into production hardware, and means to remedy that situation. While the discussion focuses on problems with civil applications, many of the comments also apply for military applications. First, the performance domain of V/STOL (powered lift) aircraft is defined by deriving the maximum field performance that can be expected from conventional aircraft. Then the causes for the poor economics of V/STOL aircraft based on present-day technology are reviewed and technological areas that may yield significant benefits are suggested. Finally, pertinent selected topics in STOL and VTOL aerodynamics are reviewed. These topics include prediction techniques, augmentor technology, induced aerodynamics, and ground effect.

2. PROBLEMS IN THE APPLICATION OF V/STOL TECHNOLOGY

The concepts considered here are, in most cases, those which have aerodynamic lift augmented by the propulsion system. However, before proceeding with a discussion of propulsive lift, it is advisable to define the performance requirements that lead to the utilization of powered lift.

2.1 Operational limits of conventional aircraft

Figure 1 shows the historical trend of maximum lift. Plain wing, trailing-edge flaps, and trailing- and leading-edge flap trends are shown. Progression in high lift capability was steady until the late 1960's. If the progression in this capability is to continue, either more complex conventional high lift systems or lift augmentation with the propulsion system must occur. If the former course is taken, the maximum lift coefficient capability in the near future could be about 3.5, and the lift coefficient in approach would be 2.1. The lift capability as a function of airspeed for these conditions and with a wing loading of 3.83 kN/m^2 (80 psf) is shown in Fig. 2. Also included in the figure is landing distance as a function of approach speed. With no lift augmentation, the landing distance is about 1160 m (3800 ft). For a field 610 m long (2000 ft), propulsive lift is required; including factors for engine out and thrust lapse, the thrust/weight ratio for an unaugmented system is approximately 0.7. In Fig. 3, typical takeoff aerodynamics are assumed. For a wing loading of 3.83 kN/m^2 (80 psf), a thrust/weight ratio of 0.36 is required to equal the landing field length capability of 1160 m (3800 ft). For a takeoff field 610 m long (2000 ft), the required thrust/weight ratio for an unaugmented system is C 6. Figure 4 compares an airplane planform for a 610 and 1220 m long (2000 and 4000 ft) field. The nacelles were sized to approximate the dimensions of a low noise engine. The 610 m (2000-ft) field length airplane may suffer in both low-speed and high-speed performance because of the large nacelle size. This, coupled with the high thrust/weight ratios required, makes this approach to short field lengths questionable. However, for field lengths in the 1220 m (4000 ft) category, this approach seems appropriate. It is realized, of course, that wing loading can be bartered for field length at the expense of complicated gust alleviation systems. This approach, however, complicates the aircraft and compromises cruise efficiency.

It is apparent that unpowered lift systems can provide a field length capability as low as 1200 m (4000 ft) with a reasonable wing loading, but for field lengths less than that, powered lift systems are required. This shorter field length capability offers a considerable advantage to a transportation system and deserves serious consideration. The remainder of this section deals with the penalties associated with the use of powered lift systems for VTOL or STOL performance.

2.2 Economic penalties of propulsive lift

Figure 5 (ref. 1) shows the direct operating cost associated with fields shorter than 1220 m (4000 ft). Designing an aircraft to operate with a 610 m long field (2000 ft) rather than 1220 m (4000 ft) increases the direct operating cost 20%. Figure 6 also shows the penalty to direct operating cost of noise reduction treatment as a function of field length. At all field lengths, the penalty for 95 PNdB at 152 m (500 ft) is large, and the penalty for a field length of 610 m (2000 ft) compared to 1220 m (4000 ft) is 20% higher. This would indicate that the increase in DOC as field length is shortened is caused by the additional noise treatment required by the larger powerplants. Removal of this effect would produce agreement with earlier studies, in which acoustics were ignored (ref. 2), which show DOC is not highly sensitive to field lengths above 610 m (2000 ft). Nevertheless, noise restrictions may become more severe rather than less severe. Therefore, propulsive lift technology must be examined to isolate areas where improvements can be made so that shorter field aircraft are more attractive in comparison with conventional aircraft.

The arguments thus far have been for STOL aircraft. For VTOL aircraft, the problem is much more severe. Figure 7 (ref. 3) shows the direct operating cost (in dollars) per aircraft mile as a function of stage length. Data from conventional two-, three-, and four-engine transport aircraft are shown along with the estimated operating cost of a 485-kN (109,000 lb), 100-passenger lift fan V/STOL transport aircraft. The operating cost of the V/STOL transport is comparable to the four-engine large aircraft and is approximately 60% higher than the two-engine aircraft with similar payload-range characteristics. Clearly, if V/STOL transport aircraft are to be made economically competitive, the number of engines must be reduced, the systems must be simplified, and the components must operate at top efficiency.

While the preceding arguments have concentrated on commercial applications of V/STOL technology, similar arguments hold for military applications. There maintenance costs, low payload to weight ratio, and restricted range and endurance have combined to handicap the utility of V/STOL aircraft for military missions. The result, of course, has been that only one military aircraft is in production.

2.3 Impact of a fuel shortage

The intuitive reaction to a shortage of aircraft fuel is that V/STOL aircraft would have a severe disadvantage because of the relatively large amount of propulsion required which increases aircraft weight and may produce lower propulsive efficiency in cruise. These factors, however, may be mitigated by other factors inherent in V/STOL operations. Reference 4 contains preliminary design information on several V/STOL aircraft and a conventional aircraft designed for a range of 556 km (300 n.m.) and a 120-passenger payload. These studies differ from more recent studies in that no effort was made to evaluate the penalties due to design for low noise.

The fuel load from some of these aircraft are tabulated below.

Aircraft	Fuel load, kN
Conventional	33
STOL	28.5
VTOL jet lift	28.8
VTOL tilt wing	29.9

All V/STOL aircraft in the study required less fuel than conventional aircraft. These surprising results stem from at least three factors. First, the short design range minimizes the effect of reduced cruise propulsive efficiency. Second, the calculations assume different maneuver times for the different aircraft (6 min for CTOL, 2.5 min for STOL, and 2 min for VTOL). Lastly, no penalty was included for quieting techniques. The first two items are valid for aircraft specifically designed for a mass short-haul transportation system, and the effect of the second item could be considerably larger because reduction of air congestion around airports could yield even larger differences in maneuver time and reductions in fuel for V/STOL aircraft. On the other hand, the study did not include penalties in operating efficiency from noise reduction hardware. As already pointed out, this penalty could reverse the trend.

The importance of minimizing fuel requirements further emphasizes the need to improve the lifting efficiency of V/STOL aircraft to improve the competitive position with all forms of transportation.

2.4 Advantages of propulsive lift

In spite of the economic penalties associated with powered lift aircraft, the ability to land and take off in field lengths under 1220 m (4000 ft) is very important in that it offers relief from air and ground congestion, it minimizes the impact of aircraft and ground equipment on the environment, it improves the service to the passenger, and it provides maximum flexibility in route structure. Because of these and other factors, V/STOL aircraft may require less fuel than other forms of transportation. For military applications, V/STOL aircraft offer dispersal of forces to minimize the effect of surprise attack, more direct supply and support of field forces, and freedom from large prepared airfields. With all these important advantages, every effort should be made to improve V/STOL technology so that practical and economical aircraft can fulfill these commercial and military needs.

3. POTENTIAL IMPROVEMENTS IN V/STOL AIRCRAFT

This section deals with V/STOL aerodynamic areas that appear to offer an opportunity for significant improvement and thus can enhance the possibility of the application of V/STOL technology to transportation system needs.

Figure 8 (ref. 1) shows the installed thrust/weight ratio required for 610 m (2000 ft) field length performance. Even the augmentor wing, the most efficient concept, requires substantially more thrust than a conventional aircraft; for VTOL aircraft, approximately four times more thrust is required. One obvious way to make the aircraft more viable economically is to increase the efficiency of the lifting system.

3.1 STOL

Static turning efficiency is one indicator of propulsive lift system efficiency. Figure 9 shows static turning efficiency in terms of lift vs. thrust referenced to the nozzle thrust for the externally blown flap (EBF), augmentor wing, and over-the-wing blowing concepts. For the externally blown flap (EBF) concept, the efficiency between deflections of 30° and 70° is about 80% (ref. 5). In view of the exhaustive research conducted on this concept, it is unlikely that this efficiency will be improved significantly. It may be that the concept is limited by the orientation of the flap with respect to the wing. Data from reference 6, with a canted variable camber exit louver cascade, are included to show what can be done by reorienting the flaps in cascade fashion. With this relatively efficient turning device, the efficiency was above 90% for angles from 0° to 90°. Turning for the over-the-wing STOL concept is substantially more efficient than for the EBF, at least between deflection angles of 30° to 50°.

For comparison, augmentor wing data are included in Fig. 9. Because of the augmentation ratio, efficiency referenced to nozzle thrust is greater than 100%. For these results, the lobe nozzle was canted 30° (fig. 10), so that the augmentation ratio is high over most of the usable flap angle range, but falls off somewhat above a flap deflection of 70°.

If it is assumed that static turning efficiency is not affected by airspeed (since these results give good agreement when incorporated in the theoretical prediction of the variation of C_L with C_j, this is a reasonable assumption), these results can be related to system performance. The effective C_j is that which provides the circulation, $C_L = f(C_{j_e})$, and

$$\frac{C_{j_e}}{C_j} = \eta_t A$$

where η_t is the turning efficiency and A is the augmentation ratio. From two-dimensional theory such as that of reference 8, C_L is proportional to $\sqrt{C_j}$: $C_L = K\sqrt{C_j \eta_t A}$ and for a given C_j

$$\frac{C_L}{C_{L(\eta_t A = 1)}} = \sqrt{\frac{C_{j_e}}{C_j}}$$

Figure 11 shows the dimensionless C_j and C_L as a function of $\eta_t A$, with the data from Fig. 9 spotted on the relative C_L curve. Over-the-wing blowing should be 7% more efficient in producing lift than the EBF, and the augmentor wing will be 31% more efficient. In addition, the augmentation ratio of the augmentor wing will provide more thrust at low flap deflection during takeoff.

For augmentor wing or other internally blown flap concepts, volume for ducting and nozzles in the wing is a very important parameter, and $\eta_t A$ bears directly on the duct area required. Figure 12 shows the relative duct area required for the same effective C_j as a function of $\eta_t A$. The augmentor wing requires 68% of the duct area required by an internally blown flap. Increasing augmentation ratio from the presently achievable 1.4 to 2.0 would lower the duct area required to 69% of that presently required. Installed thrust/weight ratio is also a function of $\eta_t A$ and this increase would reduce the thrust/weight ratio to 0.28 - 0.35, nearly that of conventional aircraft. Development of the ejector technology as described in reference 9 may provide such an increase in augmentation ratio.

Figure 13 (ref. 9) defines the ideal augmentation ratio as a function of augmentor geometry. In practice, losses occur and available installation volume is limited so that these values are not achieved. The inlet area ratio currently used falls between 10 and 15, and the exit diffuser area ratio falls between 1.5 and 2.0. The actual augmentation ratio realized is of the order of 1.5 compared to the value of greater than 2 for the ideal augmentor. To realize the theoretical potential, nozzles with rapid mixing rates must be developed so that mixing occurs within the augmentor. Further, separation on the augmentor diffuser must be avoided. Figure 14 shows conceptually how such an augmentor could be mechanized. Boundary-layer control is supplied on the diffuser walls to control airflow separation. Clearly, the additional capability would be achieved at the price of additional complexity.

3.2 VTOL

The means for improving the economics of VTOL aircraft and thus enhancing the acceptance of these concepts for short haul transportation is not as clear as for STOL aircraft. Concepts studied have used lightweight lift engines, or remotely driven fans or thrust augmenting ejectors to augment the thrust from the cruise propulsion system. In either case, the cost of the total propulsion system is about the same as that of a turbofan engine providing the same thrust. In addition, the installed thrust is 15 to 40% greater than takeoff weight to provide control forces, acceleration during hover, and survival of an engine failure. As a result, the propulsion system weight fraction is about double that for a 610 m (2000 ft) STOL aircraft. While it is unlikely that a thrust augmenting ejector would be significantly lighter than a lift fan or lift engine, it may be less costly. To avoid much oversized cruise engines, an augmentation ratio greater than 2 is required. With low-pressure augmentors, reference 10 has reported values approaching this magnitude with a reasonably compact augmentor. However, for a reasonable duct area, a high-pressure air supply will probably be required. As shown in Fig. 15 (ref. 11) the augmentation ratio will drop significantly as pressure ratio is increased. With current technology, this means that a longer (and less compact) augmentor is required. While there may be some promise in this approach, a great deal of effort is required on installation problems in order to provide a viable system. The previous discussion was slanted toward commercial applications. For aircraft that have high installed cruise thrust, the required augmentation is low and the augmentor can be more compact, thus installation problems are eased. Required ducting volume will, however, be relatively large (one such application is the Rockwell International XFV-12).

A weight breakdown for a typical V/STOL transport is shown below.

Component	Gross weight, %
Structure	23
Propulsion system	26
Subsystems	12
Usable Load	
Fuel load	20
Payload	19

The payload is 19% of the takeoff gross weight. A 5% improvement in vectoring efficiencies, ground effects, etc., will yield a 25% increase in payload capability. This high sensitivity of productivity to small losses in efficiency makes it imperative that the VTOL propulsion system components be optimized to a high degree. Furthermore, care must be taken to avoid adverse ground effects, reingestion, or other thrust-reducing effects. Clearly, research in these areas is important in establishing the competitiveness of VTOL systems.

4. STATUS OF V/STOL TECHNOLOGY

In this section, the state of the art of some areas of particular interest in V/STOL aerodynamics are discussed.

4.1 STOL

In the STOL aircraft area, the discussion includes recent advances in augmentor wing aerodynamics, comments on ground effects, and the state of the art of predictive techniques.

4.1.1 Augmentor wing technology. Figure 10 shows a perspective of one of the augmentors under consideration. Figure 16 shows conceptually the STOL augmentors currently being considered. The lobe augmentor was developed at Ames (ref. 11) and is characterized by a slot combined with the lobe nozzle. The cruise augmentor was developed by Boeing (ref. 12) under contract to Ames. In this example, the augmentor nozzle was moved to the upper surface of the wing and functions also as a cruise nozzle. This approach leaves more room in the wing for ducting and eliminates valves from the system. These two augmentor geometries are being examined for high wing flow (to reduce noise, 70 to 80% of the engine thrust appears at the augmentor nozzle so that the augmentor can be used to suppress noise). The cruciform augmentor nozzle is being developed by DeHavilland under contract to Ames. This nozzle is another answer to the problem of providing improved mixing, and the augmentor geometry is designed for a 40% wing flow. The "advanced augmentor" is to use the techniques described in reference 10 to obtain the highest augmentation ratio possible within the geometric confines of a large wing blowing augmentation system.

Although static augmentation ratio is a convenient measurement for comparing augmentors, consideration of this parameter only can lead to erroneous conclusions. An example of this is shown in Fig. 17 (ref. 11). Aerodynamic performance with a 60° flap is shown. The normal configuration has been optimized for static augmentation ratio. Lowering the shroud (moving it aft) improves the variation of lift with C_J at the expense of static augmentation ratio, and closing the lower flap gap further increases lift at a given C_J while reducing static augmentation ratio further. This improvement results from attaching the external flow on the shroud with better augmentor geometry and strengthening the boundary-layer control provided by the augmentor inlet. These results indicate that, for STOL applications, the augmentor should be optimized at forward speed.

This contention is further supported by the data in Fig. 18. Horizontal force, normalized by nozzle thrust, and augmentation ratio are presented as a function of velocity for a primary pressure ratio of 2.3. The horizontal force drops off with forward speed above 26 m/sec (50 knots). Also shown is the static augmentation ratio less the secondary ram drag for the same primary pressure ratio. The slope and magnitude of the two curves is approximately the same above 20 m/sec (50 knots), indicating that the secondary ram drag should be subtracted from the static augmentation ratio and, with 30° flap deflection, thrust recovery occurs above 50 knots. The thrust lapse for nozzle pressure ratios of 1.5 and 3.5, calculated in the same way as for the 2.3 pressure ratio case, are also shown in figure 18. Statically, the augmentation ratio at 3.5 nozzle pressure ratio is lowest. However, the thrust lapse with forward speed is less with the result that, above 40 knots, the augmentation ratio is higher than for the lower nozzle pressure ratios. It thus appears that, in optimizing the augmentor for takeoff, the augmentation ratio must be traded with mass-flow ratio to obtain the maximum thrust for best takeoff performance.

Similar results for the cruise augmentor are not available; however, some data at cruise Mach Numbers are available (ref. 13). These results were obtained with a 14% thick quasi-two-dimensional wing with propulsion nozzles as in the cruise augmentor. Figure 19 shows normal force coefficient as a function of drag divergence Mach number for several values of C_j. At cruise lift coefficients, the blowing increased the drag divergence Mach number slightly, and the actual value is sufficiently high to permit application to high subsonic cruise aircraft.

4.1.2 Ground effect. Ground effects are one of the least understood, yet potentially most important, problems in V/STOL aerodynamics. Special techniques such as the moving belt and jet blowing (ref. 14) have been developed to measure this effect at high lift. While these approaches may yield correct steady-state results, the question of dynamic effects still remains before the importance of ground effect can be accurately assessed.

Reference 15 describes these problems both aerodynamically and operationally and presents normalized curves of lift loss in ground effect for several concepts. Figure 20 contains data from reference 15, and data from a large-scale swept augmentor wing model (ref. 16). The large-scale results did not have the benefit of a moving ground plane; thus they should be considered conservative. Augmentor wing lift loss in ground effect is much less than represented by reference 15. In fact, for both flap deflections and over the major portion of the height range, ground effect is positive rather than negative. The reason for this discrepancy is not clear; however, the results illustrate that ground effects may differ between the various STOL concepts.

In terms of dynamic effects, little data with powered lift are available. One report (ref. 17) shows results using a moving model technique. The jet flap model was run at constant height over a ground plane to measure "steady-state" ground effect. To simulate the landing approach, a portion of the board was angled so that an approach at a constant angle was simulated. Data from reference 17 are shown in figure 21 for a 10° approach angle. Comparison of the dynamic and steady-state data shows that the dynamic lift loss lagged the steady-state lift loss by about four chord lengths.

Speculation about the scale factor that should be applied to these dynamic results can lead to surprising possibilities. For a given flight path, the time required to form the flow that produces the lift loss should be a function of the absolute distance from the ground, the true jet velocity, and the true airspeed. With these factors relative to the model in reference 17, for a low pressure blowing or augmentor wing aircraft, one obtains

	Scale factor
1/10 model scale	10
Low jet velocity	4
Low model velocity	2

If these factors are multiplicative, this leads to a time lag scale factor of 80. Figure 22 presents the derivative of the data in Fig. 21 with time, with 0 time corresponding to the onset of ground effect from the steady-state data in Fig. 23. The maximum change in lift with time occurred at 0.12 sec after entering steady-state ground effect. If the scale factor is applied for a full-scale, low-pressure jet flap model (or augmentor wing), the maximum change would occur 9.6 sec from the entry into ground effect. This would, of course, completely mask steady-state effects so far as aircraft operating problems are concerned. Although this scale factor is merely speculative, it illustrates that with dynamic effects included, ground effect may be substantially less severe than represented by steady state data. Further research on these effects is required.

4.1.3 Prediction of STOL aerodynamics. Recent developments in finite element, nonplanar lifting surface theory have led to the accurate prediction of lift from jet-flapped wings (refs. 18 and 19) and ground effect of conventional wings (ref. 20). These methods have also been applied to the externally blown flap STOL concept (ref. 21). The wing and flap are represented by a vortex-lattice arrangement (fig. 23), and the turbofan wake is represented by a series of ring vortices as shown in Fig. 24. The problem is solved iteratively by first calculating the upwash from the wing without the engine wake. The engine wake is then displaced according to the upwash from the power-off calculation, and the system of equations is solved with no flow allowed through the wing-flap control points. Figure 25 shows the results after one iteration. Agreement is good when the wake displacement is included in the calculation. These results may, however, be fortuitous because the theoretical C_j was not corrected for turning efficiency (see fig. 9).

4.2 VTOL aerodynamics

In the VTOL aerodynamics area, the discussion covers recent results on forces induced on the aircraft by propulsive flows, fan scale effects, and flow vectoring for thrust or lift.

4.2.1 Induced effects. Induced forces and moments from the interaction of the propulsive flow with the free stream is of interest from the standpoint of trim moments required, STOL overload capability, and power management. Reference 22 discussed lift, drag, and moment on VTOL lift-fan aircraft. Most designs studied were of the fan-in-wing variety. Since that time, design practice has been to place the fans external to the wing in order to keep the wing loading high for cruise efficiency. Figure 26 illustrates two such designs from references 3 and 23. In general, fans with vectoring devices to provide both lift and cruise functions are mounted on the aft fuselage and lift fans are mounted in wing pods or in the fuselage. These various locations offer the opportunity for both positive and negative lift to be induced by the flow from the fans.

Figure 27 presents the lift induced by fan flow as a function of forward speed for several forward-mounted fan locations (refs. 6 and 24). It is apparent that an outboard location of forward-mounted fans minimizes the down load on the airframe induced by the operation of forward-mounted fans.

Similar results (refs. 6 and 24) for aft-mounted fans are presented in Fig. 28. Even fans mounted aft on the fuselage provide some lift, but the largest lift is generated by fans inboard near the wing trailing edge. Figure 29 shows the induced lift for complete configurations. The configuration with outboard forward fans and inboard aft fans has as much induced lift as a fan-in-wing arrangement.

These results are for no thrust vectoring, which corresponds to a decelerating or descending transition. When the exit louvers are deflected to trim drag, the induced lift is sharply reduced. Figure 30 shows data from the model with outboard forward fans, inboard rear fans, and trailing-edge flaps up and down. For these data, drag is trimmed. The lift at 80 knots is approximately 15% greater than the lift at zero forward speed. The importance of this capability can be assessed by relating the overload capability to the increase in usable load. As mentioned before, the payload-weight fraction for a lift-fan transport design is 19%. The 15% overload capability with flaps down amounts to a 79% increase in payload capability when operating as a STOL aircraft; with flaps up, the corresponding value is 42%. If overload capability is important, this effect is well worth designing for.

The role of wall effects in producing induced lift is sometimes thought to be significant. Recent tests with a small-scale model have indicated that only a small amount of the total lift can be attributed to wall effects. A small-scale, fan-in-wing model (fig. 31) was tested both in the 7- by 10-Foot and the 40- by 80-Foot Wind Tunnels at Ames. The results are shown in Fig. 32. The lifting element area to tunnel cross-sectional area of the model in the 7- by 10-Foot Wind Tunnel was the same as that for the data in Figs. 29 and 30. Discrepancy in lift/static thrust ratio was at most 0.06 — substantially less than that produced by many of the configurations in Fig. 29. At 80 knots, a critical point in the transition maneuver, the discrepancy is approximately 0.03. These results were obtained with the model untrimmed in drag, which is comparable to the results presented in Fig. 29. When drag is trimmed, the discrepency would be even smaller. The approximate magnitude of induced lift has also been verified by comparing data from small-scale models (that approximate the large-scale models) tested in a large wind tunnel. Figure 33 (reproduced from ref. 25) shows a comparison of such results. The differences between the models are sufficient to account for the difference in induced lift.

While the operation of lift fans induces lift, it also induces pitching moment. Figure 34 shows the normalized moment variation with airspeed. For the fan-in-wing arrangement, the moment rapidly increases in a nose-up direction as airspeed is increased. This characteristic defined the longitudinal control power required for a fan-in-wing aircraft. On the other hand, the moment variation with airspeed for the podded configurations is much smaller than for the fan-in-wing configuration and, for the outboard forward fan and inboard aft fan, the induced lift is nearly the same.

Prediction of induced effects, especially moment, is desirable but difficult because separated flow is involved. Figure 35 illustrates the problem. The cause of the induced lift is the separated flow downstream from the fan. Reference 22 suggests a simplified semiempirical method for this caluclation which at least describes trends in induced effects for fan-in-wing configurations accurately. However, this method is not accurate with podded configurations because of overpredicting the forces on the surface aft of forward-mounted fans. A method has been developed recently for predicting the characteristics of two-dimensional lift-fan sections including separated flow (ref. 26). In this method, the airfoil and jet are represented by source or sink distributions. The static pressure in the separated area, the jet shape, and the free streamline shape are assumed. The solution is then developed through an iteration procedure that changes the shape of the jet sheet to balance pressure and centrifugal forces. Figure 36 describes the flow model and presents a sample of the data. Although limited to a thin jet, it is the only known solution to the induced effect problem that includes inlet flow, the separated flow area, and calculated jet sheet shape. This approach holds considerable promise for improving the calculation of induced effects.

4.2.2 Flow vectoring devices. The effectiveness of flow vectoring devices is critically important to the performance and installed thrust (and hence operating cost) of VTOL airplanes. The effect of vectoring efficiency on payload is as dramatic as the effect of induced lift. When deflectors are used to provide lift from lift/cruise fans, the deflectors tend to be both voluminous and heavy. It is thus necessary to develop deflectors that are both small (and lightweight) and efficient. Figure 37 (using data from ref. 6) illustrates the problem. A compact hooded flow vectoring device, with a radius/diameter ratio of 0.54 provides only 70% of the fan thrust for VTOL, while a similar device with a radius/diameter ratio of 0.78 provides greater than 90% of the fan thrust for VTOL. Although its performance is satisfactory, this latter device is quite large, and when scaled to aircraft size, it nearly impacts the ground in the VTOL operational mode. Clearly, this solution to the thrust vectoring problems for lift-cruise fans will not suffice. Figure 37 also shows the performance of a canted variable camber cascade. This device is more compact and turning is as efficient as for the large hooded device. However, if turning angles greater than 90° are required, another set of cascade vanes would probably be required. This approach would also suffer from thrust losses caused by the cascade remaining in the jet during cruise flight. None of the solutions shown in Fig. 37 is acceptable; research is required to produce a lift-cruise fan thrust vectoring device that will not seriously penalize an aircraft. This device will probably also be called on to provide hover control forces as well; thus the problem is a difficult and challenging one.

Lift fan vectoring effectiveness is shown in Fig. 38. The vectoring cascade at angles above 35° has both large losses and restricts the fan area, which causes a rapid loss in turning efficiency. Different vane aspect ratios, venting the fan hub (chevron-shaped louvers), and flapped louvers were studied to delay the rapid loss in efficiency. None of these approaches provided a significant increase in vectoring efficiency, although the flapped louvers could provide more negative vectoring capability. Where space is available, the combination of precambered louvers, canted cascade, and a rotating cascade may improve the turning efficiency while providing the capability of producing a side force. One approach using all these techniques was developed for the aircraft described in reference 3. Data for this arrangement (ref. 24) is also presented in Fig. 38. Referenced to the vertical lift, the vectoring to produce thrust increased efficiency with up to 40° turning. This, of course, indicates losses while vectoring for lift only were excessive. However, the results indicate that an improved lift-fan vectoring system of this type may be possible.

4.2.3 Modeling lift fans. The lift-fan aerodynamic results presented thus far were obtained with large-scale fans. This section discusses problems encountered when studying the aerodynamics of lift fan aircraft with nonscaled fans or small-scale fans.

Figure 39 shows the variation of fan thrust with forward speed for 0.91 m (3 ft) diameter fans with pressure ratios of 1.1 and 1.3 (ref. 6). The fans were tested in the same wing (ref. 27); however, inlets and internal flow paths as well as fan solidity, tip speed, and internal flow paths were different. Even so, the variation of fan thrust with forward speed was very similar. However, as shown in Fig. 40, the induced lift varied significantly. Furthermore, as shown in Fig. 41, the variation of moment with airspeed is different. The causes for these differences are unknown, but the results indicate that testing at full-scale size but subscale pressure ratios may not be sufficient: actual modeling of the flow path or absolute modeling of Reynolds number may be required.

Figure 42 shows the variation of fan thrust with forward speed for a 0.91-m (3 ft) diameter fan and a 0.38-m (15 in.) diameter fan. The data for the larger fan are the same as that in Fig. 41, while the data for the smaller fan are presented in reference 28. The larger fan was a tip-turbine-driven fan in a fairly thin installation. The smaller fan was a hub-driven fan in a thicker installation. Both fans were designed for the same pressure rise, but the aspect ratio of the blading was significantly different, the smaller fan having the lower aspect ratio. Considering these differences, the variation of thrust with airspeed for the two fans is remarkably similar. Figure 43 shows a different result. Small-scale fan data from reference 25 are compared with large-scale fan data from reference 6. Both fans were mounted in a fan-in-wing model. The large difference shown is opposite from what would be expected from Reynolds number effects.

The effects of Reynolds number on the turning effectiveness of cascades is shown in Fig. 44. The poor performance of the smaller cascade indicates that considerable care must be taken with vectoring devices to assure realistic performance data.

The foregoing results indicate that a great deal of care must be taken if small-scale testing is to yield accurate aerodynamic results. Extreme care must be taken with such details as inlets, fan flow paths, and vectoring devices. It may be that, rather than exact duplication of full-scale devices, Reynolds number sensitive devices must be designed to relieve that sensitivity. Finally, the performance of these devices must be measured so that, if the performance is substandard, the data can be corrected.

5. CONCLUDING REMARKS

The failure to use V/STOL technology in short-haul transportation system is disappointing, but not surprising because of the existing economic climate and poor operating economics of quiet V/STOL systems. However, the promise of V/STOL technology remains unblemished. This approach to short-haul transportation systems offers relief from airport congestion, minimum impact on the environment, maximum service to the passenger, maximum flexibility in route structure, and possibly a reduction in fuel usage compared to conventional aircraft operating in a congested environment.

Research must be directed to improve the operating economics by reducing thrust requirements and simplifying the aircraft systems. For STOL aircraft, these goals may be approached through improved lift system turning efficiency and improved augmentation systems. For VTOL aircraft, the goals may be approached through the development of small-volume, high augmentation ratio ejector systems and the invention of small, lightweight, thrust vectoring devices. While research in these areas is necessary for the economic acceptance of V/STOL aircraft, other research is needed to provide a technologically acceptable aircraft. Some of the more promising technological research areas are prediction methods, including V/STOL aerodynamics and augmentor characteristics, and ground effects, including dynamic characteristics.

REFERENCES

1. Galloway, Thomas L.: Future Short-Field Aircraft. NASA SP-320, Paper 2, 1972.
2. Holzhauser, C. A.; Deckert, W. H.; Quigley, H. C.; and Kelly, M. W.: Design and Operating Considerations of Commercial STOL Transports, J. Aircraft, Vol. 2 No. 2, March-April 1965, pp. 87-93.
3. V/STOL Aircraft Advanced Engineering Group: Conceptual Design of a V/STOL Lift Fan Transport – Summary. NASA CR-2184, July 1972.
4. The Boeing Co.: Study of Aircraft in Short Haul Transportation Systems. NASA CR-986, Jan. 1968.
5. Johnson, William G., Jr.: Aerodynamic and Performance Characteristics of Externally Blown Flap Configurations. NASA SP-320, Paper 5, 1972.
6. Kirk, Jerry V.; Hall, Leo P.; and Hodder, Brent K.: Aerodynamics of Lift Fan Aircraft. NASA TM X-62,086, Sept. 1971.
7. Aoyagi, Kiyoshi; Falarski, Michael D.; and Koenig, David G.: Wind-Tunnel Investigation of a Large-Scale Upper Surface Blown-Flap Transport Model Having Two Engines. NASA TM X-62,296, Aug. 1973.
8. Malavard, Lucien C.: Recent Developments in the Method of the Rheo-Electric Analogy Applied to Aerodynamics. J. Aero. Sci., Vol. 24, No. 5, May 1957, pp. 321-331.
9. Fancher, Richard B.: A Compact Thrust Augmenting Ejector Experiment. USAF ARL 70-0137, Aug. 1970

10. Quinn, B.: Recent Developments in Large Area Ratio Thrust Augmentors. AIAA Paper 72-1174, Nov. 1972.

11. Aiken, Thomas N.: Advanced Augmentor-Wing Research. NASA SP-320, Paper 8, Oct. 1972.

12. Roepcke, F. A.; and Nickson, T. B.: Design Integration and Noise Studies for Jet STOL Aircraft. NASA CR-114621, April 1973.

13. Mahal, A. S.; and Gilchrist, I. J.: Design Integration and Noise Studies for Jet STOL Aircraft; Augmentor Wing Cruise Blowing Valveless System. NASA CR-114560, Jan. 1973.

14. Hackett, J. E.; and Praytor, E. B.: Ground Effect for V/STOL Aircraft Configurations and its Simulation in the Wind Tunnel. NASA CR-114,495, Nov. 1972.

15. Hassell, James L., Jr.; and Judd, Joseph H.: Study of Ground Proximity Effects on Powered-Lift STOL Landing Performance. NASA SP-320, Paper 16, Oct. 1972.

16. Falarski, Michael D.; and Koenig, David G.: Longitudinal Aerodynamic Characteristics of a Large-Scale Model with a Swept Wing and Augmented Jet-Flap in Ground Effect. NASA TM X-62,174, Oct. 1972.

17. Turner, Thomas R.: Ground Influence on a Model Airfoil With a Jet Augmented Flap as Determined by Two Techniques. NASA TN D-658, Feb. 1961.

18. Lopez, M. L.; and Shen, C. C.: Recent Development in Jet Flap Theory and its Application to STOL Aerodynamic Analysis. AIAA Paper 71-578, June 1971.

19. Hackett, J. E.; and Lyman, V.: The Jet Flap in Three Dimensions: Theory and Experiment. AIAA Paper 73-653, July 1973.

20. Maskew, B.: On the Influence of Camber and Non-Planar Vortex Wake on Aerofoil Characteristics in Ground Effect. Loughborough Univ. of Technology, Oct. 1971.

21. Dillenius, M. F. E.; Mendenhall, M. R.; and Spangler, S. B.: Calculation of the Longitudinal Aerodynamic Characteristics of STOL Aircraft With Externally-Blown Jet-Augmented Flaps. NASA CR-2358, June 1973.

22. Hickey, David H.; and Cook, Woodrow L.: Aerodynamics of V/STOL Aircraft Powered by Lift Fans. AGARD CP 22, Paper 15, Sept. 1967.

23. Knight, Ronald G.; Powell, William V., Jr.; and Prizlow, Jerome A.: Conceptual Design Study of a V/STOL Lift Fan Commercial Short Haul Transport. NASA CR-2185, Nov. 1972.

24. Atencio, Adolph, Jr.; Hall, Leo P.; and Kirk, Jerry V.: Low-Speed Wind-Tunnel Investigation of a Large-Scale Lift Fan STOL Transport Model. NASA TM X-62,231, Feb. 1973.

25. Newsom, William A., Jr.; and Moore, Frederick L.: Wind-Tunnel Investigation of V/STOL Transport Model with Six Wing-Mounted Lift Fans. NASA TN D-5695, 1970.

26. Hu, Galen; Lotz-Flugge, I.; and Karamcheti, K.: An Analysis of a Two-Dimensional Propulsion Wing. Ph.D. Thesis, Stanford Univ., March 1971.

27. Kirk, Jerry V.; Hodder, Brent K.; and Hall, Leo P.: Large-Scale Wind-Tunnel Investigation of a V/STOL Transport Model with Wing-Mounted Lift Fans and Fuselage-Mounted Lift-Cruise Engines for Propulsion. NASA TN D-4233, Nov. 1967.

28. Lieblein, S.; Yuska, J. A.; and Diedrich, J. H.: Wind Tunnel Tests of a Wing-Installed Model VTOL Lift Fan with Coaxial Drive Turbine. NASA TM X-67854, June 1971.

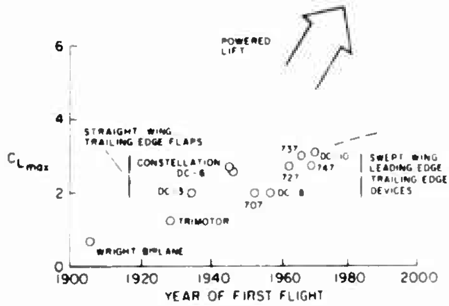

Fig. 1. Trend of maximum lift with time.

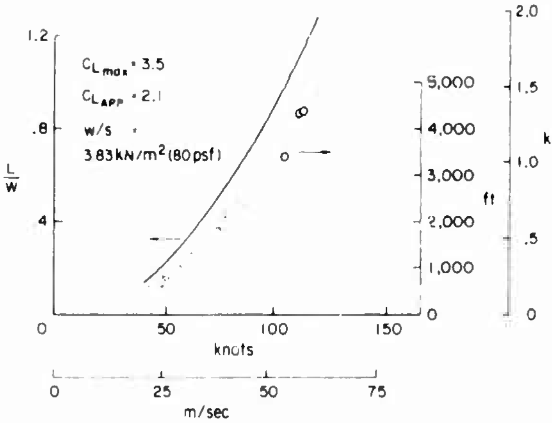

Fig. 2. Landing characteristics with mechanical flap systems.

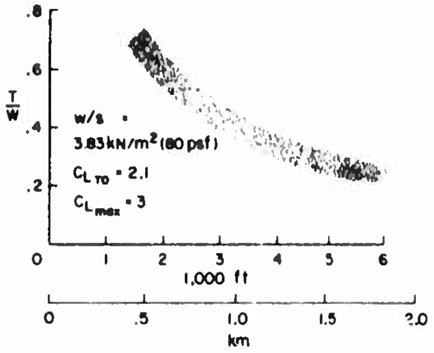

Fig. 3. Takeoff thrust required with mechanical flap systems.

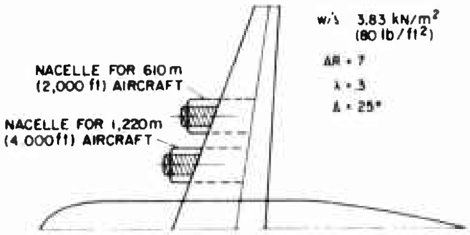
NACELLE FOR 610 m (2,000 ft) AIRCRAFT
NACELLE FOR 1,220m (4,000ft) AIRCRAFT
w/s 3.83 kN/m² (80 lb/ft²)
AR = 7
λ = .3
Λ = 25°

Fig. 4. Comparison of planforms for 610 m (2000 ft) and 1220 m (4000 ft) field length aircraft with mechanical flaps.

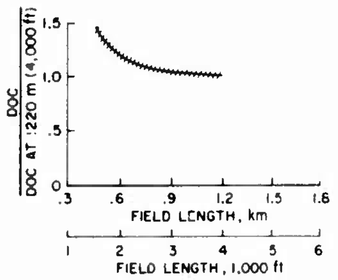

Fig. 5. Effect of field length on DOC.

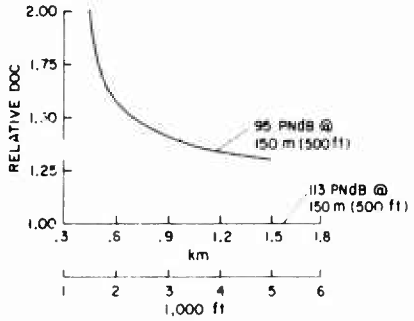

Fig. 6. Effect of noise reduction on direct operating costs.

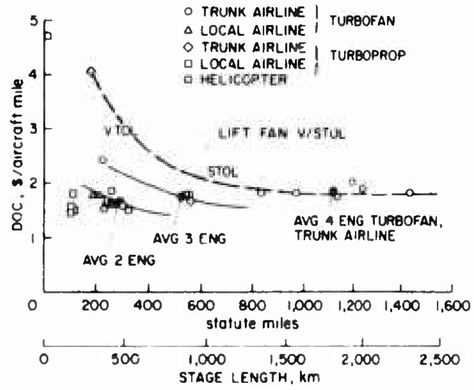

Fig. 7. Direct operating cost of commercial transport aircraft types.

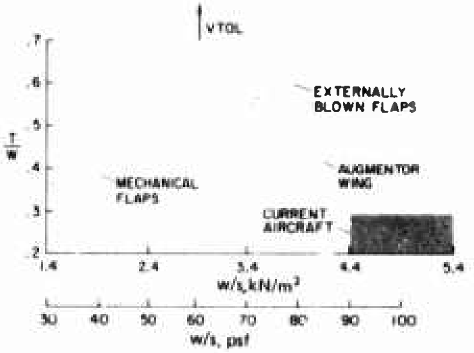

Fig. 8. Thrust required for 600 m (2000 ft) field length.

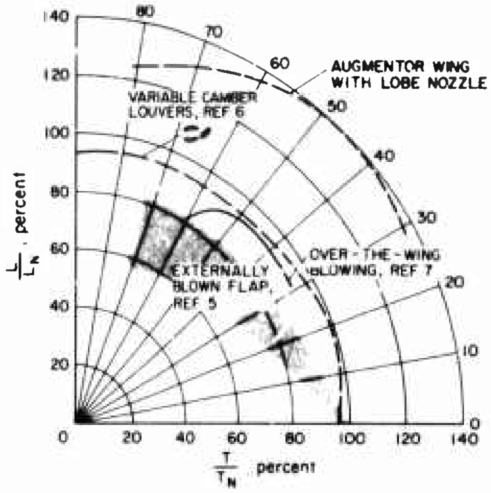

Fig. 9. Turning efficiency of various STOL concepts.

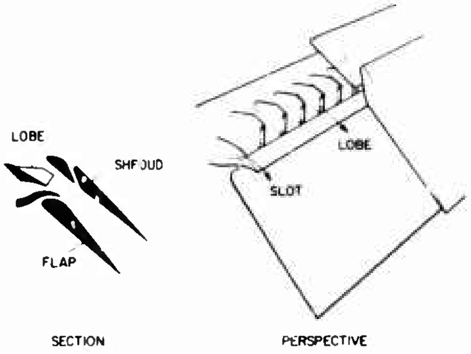
LOBE
SHROUD
FLAP
SECTION
LOBE
SLOT
PERSPECTIVE

Fig. 10. Perspective of lobe augmentor wing concept.

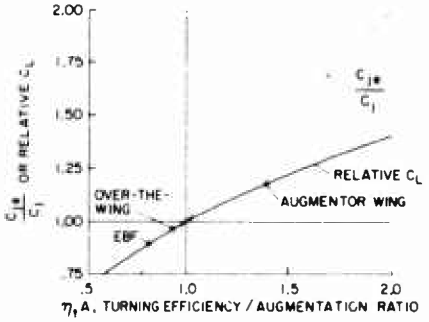

Fig. 11 Effect of lift system efficiency and augmentation ratio on C_{j_e} and C_L.

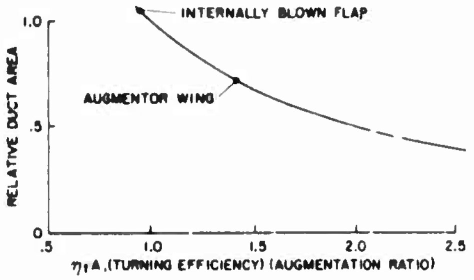

Fig. 12 Effect of turning efficiency and augmentation ratio on relative duct area.

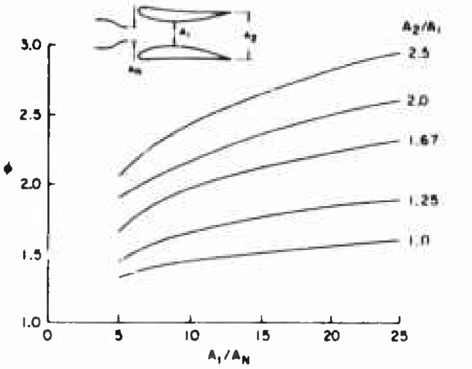

Fig. 13 Augmentation ratio of an ideal augmentor.

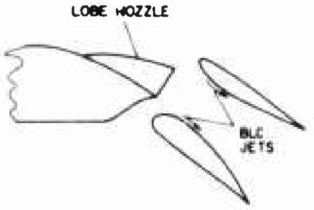
LOBE NOZZLE
BLC JETS

Fig. 14 Advanced augmentor concept.

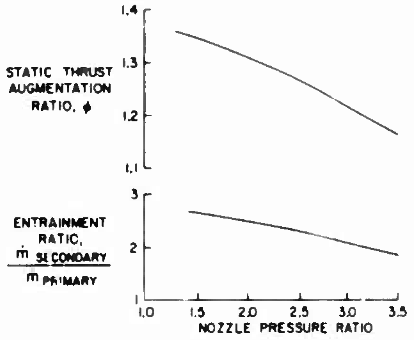

Fig 15 Effect of nozzle pressure ratio on augmentor characteristics, slot nozzle, δ_f = 30°.

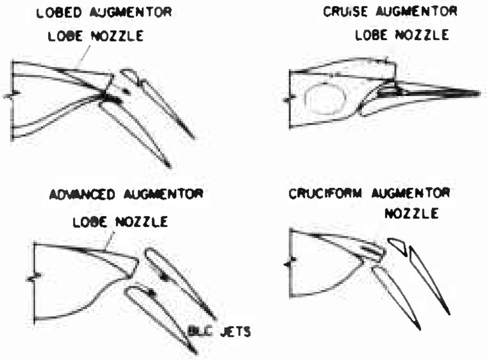
LOBED AUGMENTOR
LOBE NOZZLE
CRUISE AUGMENTOR
LOBE NOZZLE
ADVANCED AUGMENTOR
LOBE NOZZLE
BLC JETS
CRUCIFORM AUGMENTOR
NOZZLE

Fig. 16 Representative STOL augmentors being studied.

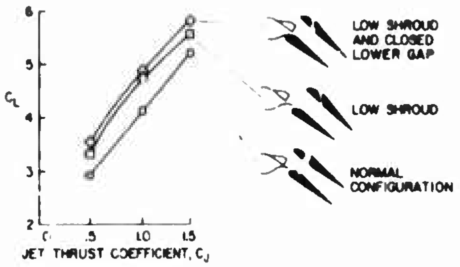

Fig. 17 Effect of augmentor geometry on augmentor wing lift; δ_f = 60°, α = 0°.

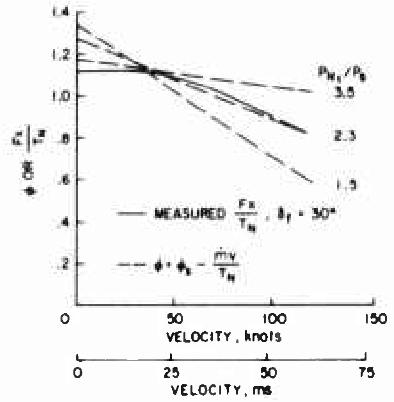

Fig. 18 Thrust velocity lapse with forward speed, primary nozzle pressure ratio of 2.3.

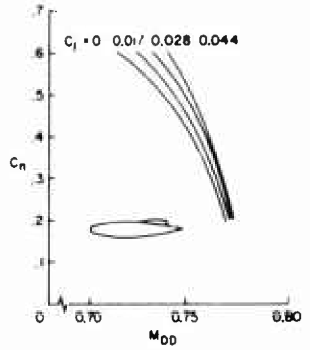

Fig. 19 Effect of nozzle thrust on drag divergence Mach number for cruise augmentor configuration.

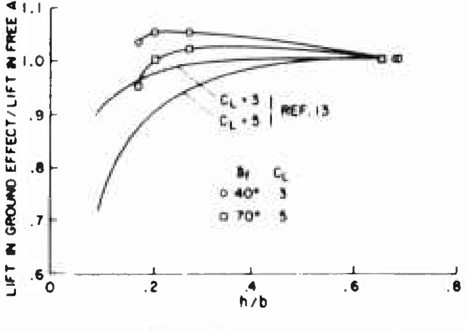

Fig. 20 Ground effect of a swept augmentor wing model.

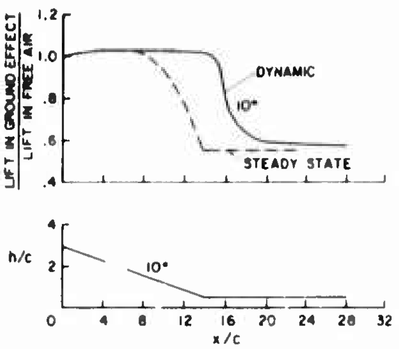

Fig. 21 Dynamic ground effect, jet flap model, $C_n = 3.5$, $\delta_f = 60°$.

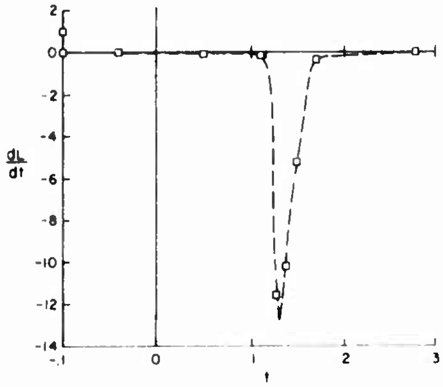

Fig. 22 Lift variation in ground effect for jet flap wing as a function of time; $\delta_f = 60$, $C_\mu = 3.5$.

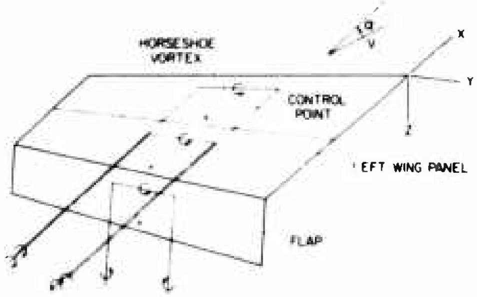
HORSESHOE VORTEX
CONTROL POINT
LEFT WING PANEL
FLAP
x
y
z
V

Fig. 23 Finite element representation of flapped wing.

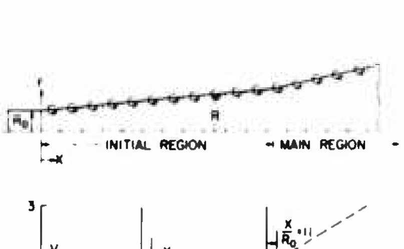
R₀
R
INITIAL REGION
MAIN REGION
x
3
2
1
r/R₀
V
x/R₀ = 1
x/R₀ = 5
x/R₀ = 11
0 2 4 6
0 2 4 6
0 2 4 6 8 10
u/V

Fig. 24 Finite element representation of engine exhaust.

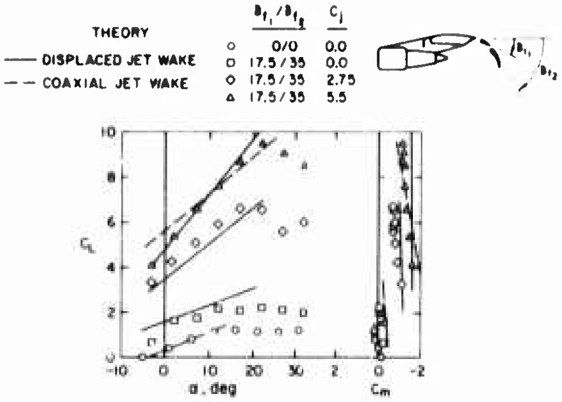

Fig. 25 Comparison of measured and predicted characteristics of an EBF configuration.

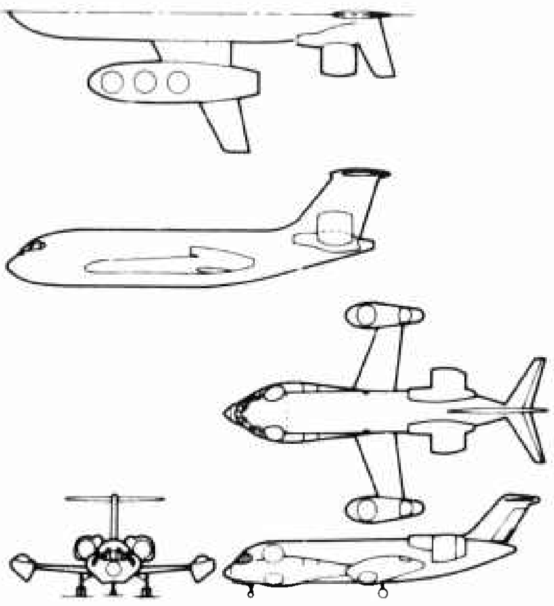

Fig. 26 Remote lift-fan VTOL transports.

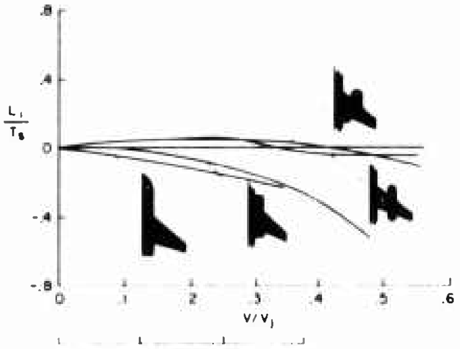

Fig. 27 Variation of induced lift with forward velocity for several forward fan locations; $\alpha = 0°$, $\delta_f = 0°$.

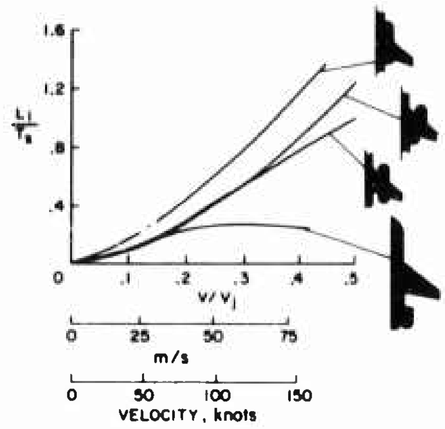

Fig. 28 Variation of induced lift with forward velocity for several aft fan locations; $\alpha = 0°$, $\delta_f = 0°$.

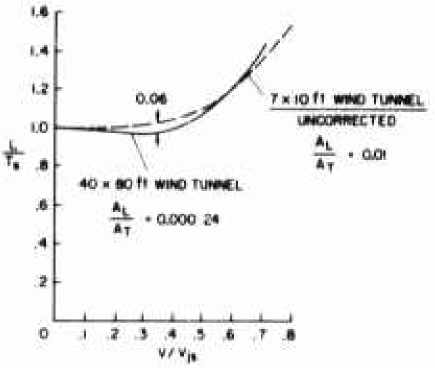

Fig. 32 Lift variation with forward speed for small-scale lift-fan model in two wind tunnels.

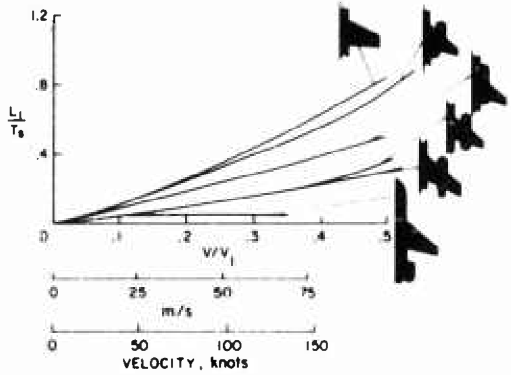

Fig. 29 Variation of induced lift with airspeed for several fan arrangements; $\alpha = 0°$, $\delta_f = 0°$.

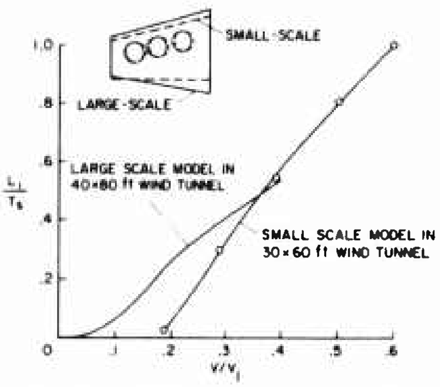

Fig. 33 Comparison of large- and small-scale fan-in-wing models, $\delta_f = 0$.

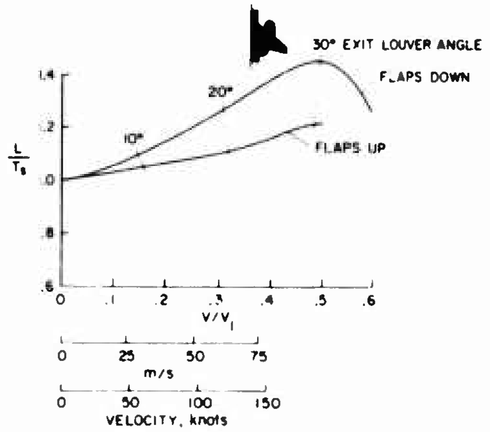

Fig. 30 Variation of lift with forward speed, drag = 0.

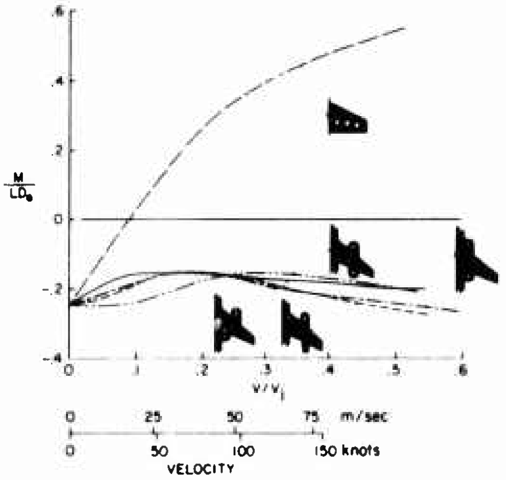

Fig. 34 Variation of moment with airspeed, $\delta_f = 0°$.

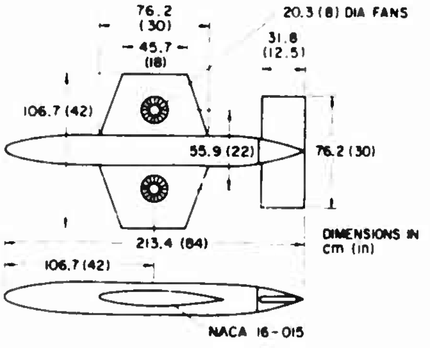
76.2 (30)
45.7 (18)
20.3 (8) DIA FANS
31.8 (12.5)
106.7 (42)
55.9 (22)
76.2 (30)
213.4 (84)
DIMENSIONS IN cm (in)
106.7 (42)
NACA 16-015

Fig. 31 Small-scale fan-in-wing model.

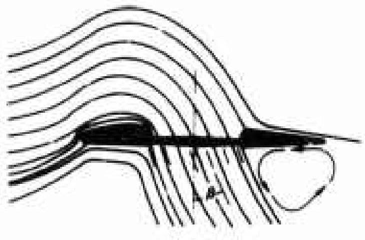

Fig. 35 Cross section of lift-fan flow field.

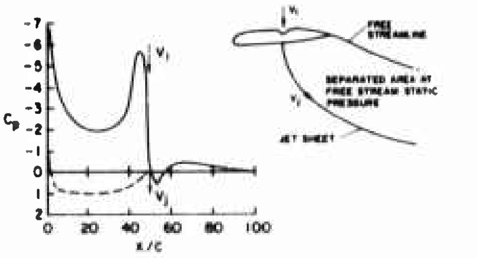

Fig. 36 Two-dimensional theoretical method for calculating fan-in-wing lift.

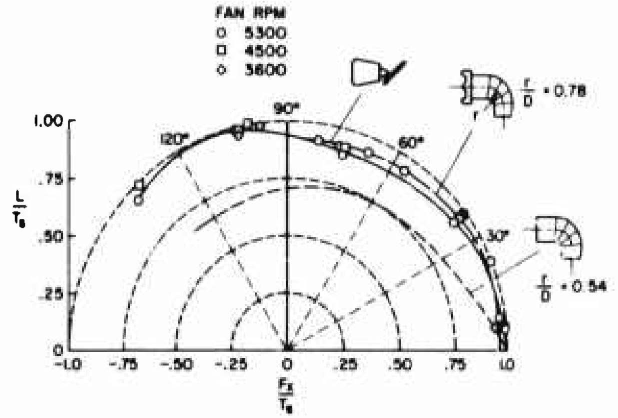

Fig. 37 Turning efficiency of hoods and cascades in lift-cruise fan vectoring applications.

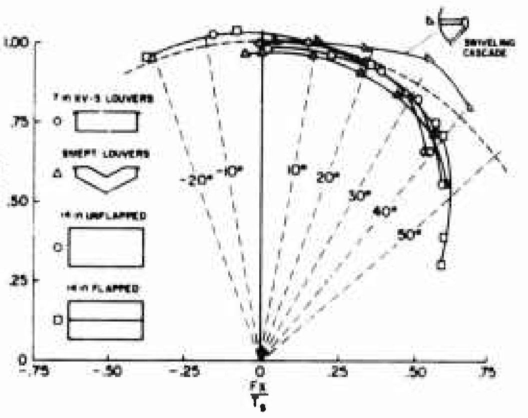

Fig. 38 Turning effectiveness of several exit louver systems.

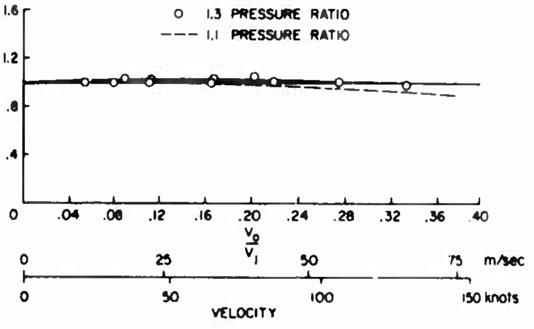

Fig. 39 Comparison of thrust variation with forward speed of 0.91 m (3 ft) diameter fans with different design pressure ratios.

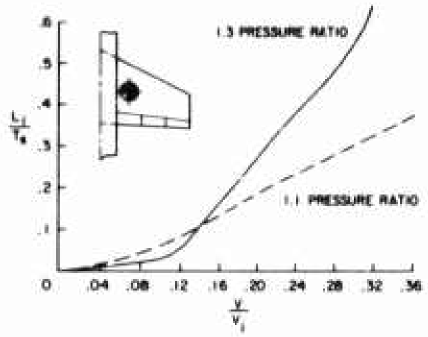

Fig. 40 Comparison of induced lift for the same model with different fans; $\delta_f = 0°$, $\alpha = 0°$.

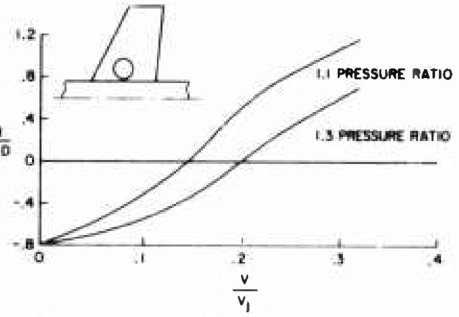

Fig. 41 Comparison of pitching moment for the same model, but different lift fans; $\delta_f = 0°$, $\alpha = 0°$.

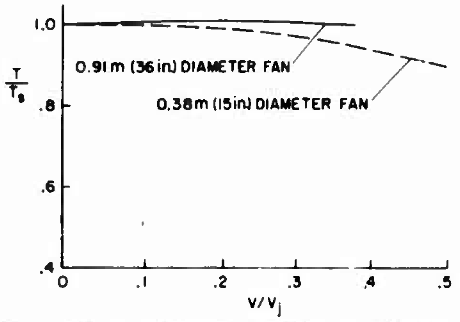

ig. 4 Effect of forward speed on the variation of thrust with forward speed for two high-pressure ratio fans.

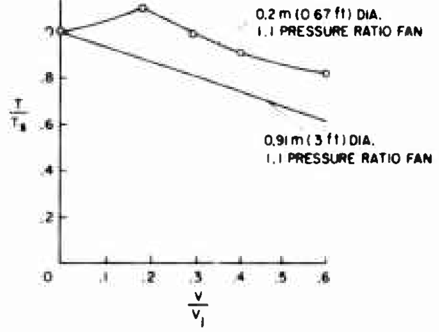

Fig. 43 Variation of fan thrust with forward speed for a small and a large lift-fan.

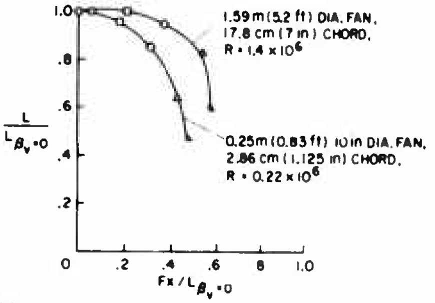

Fig. 44 Comparison of vectoring performance of large- and small-scale exit louver cascades.

RESEARCH INTO POWERED HIGH LIFT SYSTEMS
FOR AIRCRAFT WITH TURBOFAN PROPULSION

by

B. Eggleston
Advanced Projects Manager
The de Havilland Aircraft of Canada, Limited
Downsview, Ontario, Canada

SUMMARY

In the first part of the paper the characteristics and applications of powered high lift systems suitable for turbofan powered aircraft are reviewed.

The second part of the paper deals with aerodynamic research at de Havilland Aircraft of Canada upon high lift systems for use with high bypass ratio turbofan engines. The systems discussed include mechanical flaps, internally blown flaps, externally blown flaps and vectored thrust. Tests on two-dimensional and three-dimensional models are reviewed and the aerodynamics applied to design studies of a turbofan powered STOL transport aircraft.

The application of a computerized three-dimensional potential flow method to lift prediction for a wing with internally blown flaps is described.

INTRODUCTION

The objectives of this paper are twofold. The first is to provide an introduction to this session on research into the aerodynamics of powered high lift systems. This will be fulfilled by a general review of the characteristics and applications of those high lift concepts under study in NATO countries for application to transport aircraft.

The second and major objective of this paper is to describe some of the research at de Havilland Canada into the aerodynamics of STOL transport aircraft powered by turbofan engines. Our aerodynamic research is divided into two broad categories. One is the Augmentor-Wing while the other includes several high lift systems suitable for use with higher bypass ratio turbofan engines. It is the intention in this paper to concentrate on our research in the second category as Augmentor-Wing research has been well documented in recent papers by D.C. Whittley, references 1 and 2. Other research to be described includes parametric aircraft design studies using the alternative high lift systems and theoretical flow prediction methods for arbitrary configurations.

REVIEW OF POWERED HIGH LIFT SYSTEMS

- Background

Research into the aerodynamics of powered high lift systems has been intensified in recent years. This has occurred in response to near-term civil and military requirements for quiet, turbofan powered transport aircraft having either STOL performance or steep-gradient, RTOL capabilities. In the context of military operations the benefits of STOL which arise from increased mobility and reduced airfield construction time and costs, seem to be readily appreciated. In contrast there is still considerable debate about the merits, or otherwise, of powered lift STOL versus steep-gradient RTOL aircraft in civil applications. It is beyond the scope of this paper to become involved in such debates. Therefore, suffice it to say that beyond the immediate STOL application of aerodynamic research into powered high lift systems, a much wider variety of less exotic aircraft should eventually benefit from technological advances made in support of aircraft using powered high lift systems.

Before entering a more detailed review of the various powered high lift systems, mention should be made of the main factors influencing the designer's choice of a preferred system. These are summarized below and shown in Figure 1.

(a) design mission (field size, payload, cruise speed)

(b) wing loading (via comfort or cruise requirements)

(c) noise

(d) airworthiness requirements (safety margins, time delays, etc)

(e) powerplant requirements (new engines or modified existing engines)

(f) total system economics (cost penalties for STOL and noise, reduced airfield costs)

Of the above factors, field size has the greatest influence on the layout, choice of powerplant and selection of a high lift system. The influence of field size is illustrated in Figures 2 and 3 which show the trends of field size with installed thrust/weight ratio, wing loading and maximum lift coefficient for civil aircraft. The extent to which powered lift needs exploiting is seen to be strongly dependent on both wing loading and field size. For example operation from 2000 ft STOLports is feasible using advanced mechanical flap systems provided wing loadings about 55 lb/ft^2 are tolerable. Although the simplicity of this is appealing, considerations of comfort and cruise efficiency probably preclude such a solution for all but small, short-range aircraft.

Future turbofan powered transport will cruise at speeds in excess of 0.7 Mach number in which case the lowest wing loadings acceptable vary from 70 - 75 lb/ft^2 for small, short-range aircraft to 90 - 100 lb/ft^2 for large, long-range aircraft. In either case for STOL operation some form of powered lift is needed to supplement the power-off lift, however the degree of assistance required varies markedly, increasing rapidly with wing loading. This can have a strong influence on the severity of problems related directly to the magnitude of the powered lift increment such as noise, and control after an engine failure.

There are basically six powered high lift systems suitable for use with turbofan propulsion, plus various hybrids. The six basic concepts are illustrated in Figures 4a and 4b and listed below:

1) Internally blown flap (IBF)
2) Jet flap
3) Externally blown flap (EBF)
4) Upper surface blown flap (USB)
5) Augmentor-Wing
6) Mechanical flaps with vectored thrust (MF/VT)

Each of the above systems has different attributes in relation to the factors mentioned previously and no one system is likely to be pre-eminent in all applications. The following sections describe the characteristics and known applications of the above high lift systems.

- Aircraft Requirements, Flight Research Vehicles and Prototypes (Figure 5)

In terms of volume of research activity the United States is in a strong position relative to all the aforementioned powered high lift systems. This situation is not surprising as NASA funded research was intensified when pressure was felt from congestion and noise in civil operations. Simultaneously military funded research increased when a USAF requirement emerged for a turbofan powered STOL transport to replace the aging C-130 Hercules.

The military program for the C-130 replacement (designated AMST for Advanced Military STOL Transport) was at one time secure but recently it has been threatened by budget cuts, reference 3. The AMST research program is very broadly based. Extensive wind tunnel testing and comparative studies lead to the selection of two powered lift systems to be incorporated in separate flying prototypes. These will be matched in a competitive fly-off to establish the preferred high lift system for a production aircraft. The YC14 prototype under construction by the Boeing Company uses upper-surface-blowing, mechanical flaps and a blown cambered Kruger leading edge device. The YC15 under construction by the McDonnell Douglas Company uses externally blown flaps and part span, leading edge slats. Both aircraft are due to fly in 1975. NASA will be involved in this program to obtain information on operational requirements pertaining to civil STOL aircraft.

NASA has been active in research into Quiet Propulsive Lift Technology (QPLT) for civil applications since the early 1960's. The Augmentor-Wing concept is furthest advanced and a flight research vehicle has been developed in a joint U.S./Canadian program. During 1972 NASA was planning to follow up with a new flight research vehicle designated QUESTOL (Quiet Experimental STOL) which was to be an EBF aircraft capable of subsequent modification to Augmentor-Wing. This project was to have swept wings, high wing loadings and it was to demonstrate noise levels compatible with civil STOL operations. The program became defunct due to budgetary problems and overlap with the military AMST program. NASA is now considering yet another flight research vehicle, possibly based on the C-8 (Buffalo) airframe, using swept Augmentor-Wings or a hybrid upper-surface-blown, internally blown flap, reference 4.

In Canada our large aircraft requirements generally run parallel with U.S. developments. Due to the smaller size of the Canadian aircraft industry and our geographic situation there is also additional emphasis on smaller aircraft with STOL capabilities. This has lead to the recent development of the DHC-7 QSTOL civil airliner and the demonstrator STOL service between Ottawa and Montreal due to start in 1974. In the field of turbofan powered aircraft it was original Canadian research into the Augmentor-Wing concept which provided the basis for joint Canadian/U.S. development of a flight research vehicle. This aircraft is based on a modified de Havilland Buffalo airframe and Rolls-Royce Spey turbofan engines.

In Europe and the U.K. no definite requirements have emerged for STOL transport aircraft in either civil or military applications. No flight research vehicles of powered high lift systems are contemplated. Instead the emphasis is on quiet, steep gradient civil aircraft without powered lift and using purely mechanical flap systems. Examples of this are the Hawker Siddeley HS 146 and the Fokker F28 Series 5000 aircraft.

- Internally Blown Flap

The internally blown flap (IBF), also known as the BLC flap, has been widely used on various military aircraft. The IBF has tangential slots in the aerofoil upper surface from which blowing air issues to re-energize the boundary layer and prevent flow separation. The amount of blow used ($.02 < C_\mu < .08$) slightly exceeds the values needed for flow attachment to the trailing edge so that lift performance is insensitive to minor speed or attitude changes. With this level of blow, lift performance can be readily predicted using potential flow methods. The extension to finite aspect ratios can be made using span loading calculation methods such as Multhopp's.

In the early applications of IBF's, blowing air was tapped from the high pressure compressor stages and the high temperatures required the use of steel or titanium duct systems. As the engines were pure jets or low bypass ratio turbofans the losses in take-off thrust for IBF levels of bleed were large but tolerable. With modern high bypass ratio engines the situation is much worse as bleed flows represent larger proportions of core flows and typically the losses in take-off thrust can be 6 - 7 times the bleed thrust extracted for engines about six-to-one bypass ratio.

Simpler, lighter blowing systems become possible if lower blowing pressures are used and at pressure ratios about 2.5 aluminum systems become feasible. However the reduced specific thrust of low pressure bleed requires increased bleed flow which preclude its use on high bypass ratio turbofan engines. Alternative solutions available include the use of a separate blowing engine(s) or three-stream bleed/propulsion engines of the type in Figure 6. It seems that both the services and airlines are traditionally against mixed powerplant arrangements due to problems with spares logistics. As a consequence the separate blowing engine solution is not favoured despite its ability to use existing propulsion engines without modifications. The three-stream engine uses a conventional turbofan engine with an oversized intermediate compressor to provide permanent bleed and a variable pitch fan or thrust deflector is required to maintain high bleed at low net thrusts on the landing approach. An alternative arrangement used in a recent AMST study, reference 5, used turbofans of low bypass ratio (2.5) to give fan pressure ratios high enough to allow bleed extraction directly from the fan bypass flow. It was found in this study that relative to an EBF the weight savings of the simplified blowing system and smaller engines were entirely offset by the penalties in cruise fuel consumption due to the low bypass ratio of the powerplants.

The influence of permanent bleed extraction on take-off thrust and cruise s.f.c. is shown in Figure 7 for three-stream engines of constant core size and a fan pressure ratio about 1.3:1. An IBF typically requires about 8% of the total thrust as bleed and the corresponding penalties in take-off thrust and cruise s.f.c. are 6% and 3% respectively assuming bleed thrust recovery in both cases. The influence of bleed extraction on bypass ratio and uninstalled cruise s.f.c. is given in greater detail in Figure 8. Note that for IBF levels of bleed, high bypass ratios can be maintained with consequent benefits in fuel consumption at both cruise and off design conditions.

The IBF is a comparitively simple high lift system. Typically a single piece flap is used with a fixed offset hinge to give small chord extensions, Figure 9. As blowing quantities are low duct systems can be readily accommodated in the wing shroud region. However, unless the IBF is allied with a three-stream engine it loses much of its attraction and even then the penalties in cruise s.f.c. may be unacceptable for aircraft requiring long range operation.

- Jet Flap

The jet flap was conceived at NGTE in the U.K. in the early 1950's and subsequently developed into a flight research vehicle by Hunting Percival (H 126). The jet flap is similar to the IBF physically but uses much larger blowing thrust coefficients to increase lift above attachment levels by entering the supercirculation regime. The two-dimensional performance of the Jet Flap was formulated by Spence, reference 6 and extended to three dimensions by Maskell and Spence, reference 7, using linearized theory in both cases. More recently singularity methods have been used to study the influence of large deflections and finite thickness in the jet sheet, references 8 and 9.

The H 126 used the hot efflux of a pure jet engine to blow the jet flap. The lift performance of the aircraft proved inferior to small scale model tests and erratic, uncontrollable wing dropping at stall curtailed testing at high lift and blowing thrust coefficients. Subsequent model tests with leading edge slats showed improvements in stall behaviour, reference 10, but unfortunately these were never incorporated in the aircraft. The Jet Flap has difficulty generating steep approaches due to the good thrust recovery characteristics and further work was considered but not executed using in-flight thrust reversing for steep gradient studies. Following the generally bad experiences with the H 126 this concept has remained dormant until recently.

A new variant of the Jet Flap has been proposed by the Lockheed Company, reference 11. In this scheme deflection of the flap causes its cross-section to expand to form a spanwise duct of large proportions. The large cross-section of the duct permits low pressure fan air to be used for blowing, which allows conventional turbofan engines to be used for both blowing and propulsion. This concept has been combined with upper-surface-blowing in a hybrid system in recent NASA funded studies as a means of increasing lift and reducing noise, references 12 and 13. In this application a twin engined layout with a fan pressure ratio of 1.35 was used and the blowing system carried about 15% of the fan mass flow. The lateral/directional asymmetries after engine failure were compensated for by cross-ducting the bleed flows across the aircraft to maintain flap blowing after engine failure.

- Externally Blown Flap (EBF)

This concept was first explored by NASA in the mid 1950's. It did not find applications at that time as the only engines available were pure jets which would have required prohibitively heavy flap systems fabricated from steel. The development of the high bypass ratio turbofan engine with its comparitively cool and low velocity fan and core engine exhausts has rejuvenated this concept. It has been selected for the McDonnell Douglas YC15 prototype for the AMST fly-off competition. In addition it is under active consideration for civil STOL applications, figuring prominently in NASA aerodynamics and propulsive studies.

The externally blown flap uses direct impingement of the fan and core effluxes on a mechanical flap system to create lift by a combination of direct jet deflection and supercirculation effects as shown in Figure 10. The amount of lift generated can be directly controlled by the degree of flap immersion in the jets, reference 18, so that lift can be varied using either jet or flap deflection, thrust modulation or spoilers. It is an inherent characteristic of the EBF that engine failure causes large losses in lift and large lateral/directional moments. However, adequate lateral controls have been demonstrated for operation at very high lift coefficients ($C_L \approx 8$), reference 14. Longitudinal stability and control considerations require this concept to use horizontal tails with large volume coefficients, set well forward to operate in regions of favourable downwash.

The comparative simplicity of the EBF combined with its ability to use conventional turbofan engines make it very attractive for military applications. The application to large civil aircraft is not so straightforward due to noise considerations. The EBF generates additional noise due to jet impingement on the flaps and to achieve the noise goals for civil STOL (95 PNdB at 500 ft) requires compensation using lower jet velocities. This may be obtained using very high bypass ratios (≈ 17:1), or with mixer nozzles on lower bypass ratio engines to promote rapid decay of the exhaust velocity prior to impingement on the flaps. Both solutions can lead to large losses in cruise thrust due to excessive cowl drag in the former case and low nozzle efficiency in the latter, reference 15. Recent work using flaps with blowing and flaps with porous edges, reference 13, has shown substantial reductions in impingement noise but their integrated effect on performance and complexity has yet to be demonstrated.

The sheer compexity of the processes whereby the EBF generates lift is likely to defy analytic methods of performance prediction for some time yet. A procedure for a simplified two-dimensional inviscid case was presented in reference 16, while several researchers have developed semi-empirical methods for predicting EBF performance in three dimensions based on developments of jet-flap theory, references 17 and 18. The basic inputs to the semi-empirical methods are the static turning angle and thrust efficiency of the engine flap system. Hence predictions can only be made for engine/flap arrangements which have already been tested and as a result such methods will only be useful for minor perturbations about known geometries. The Quasi-2D technique discussed later may provide a simple, low-cost means of obtaining the additional data needed for new arrangements.

- Upper Surface Blown Flap

The upper surface blown flap (USB) was first tested by NASA about the same time as the externally blown flap and for similar reasons it found no applications at that time. The early tests established that its high lift and turning performance were similar to the EBF provided the jets were spread into thin sheets on the wing upper surface using flattened nozzles. It was also found that compared to the EBF there were large reductions in noise levels below the wing due to shielding effects. This latter characteristic has assumed particular significance for large, civil STOL aircraft as it will enable USB aircraft to use lower bypass ratios engines than EBF's with consequent improvements in propulsive efficiency, reference 4. The USB has been selected as the high lift system for the twin engined YC14 AMST prototype under construction by the Boeing Company.

There is little published data on USB research as interest in it is very recent and most of the work has been outside the public domain. Some recent Boeing data, reference 19, and NASA tests, references 20 and 21, show that good flow turning and high lift performance can be obtained even with large nozzles corresponding to high bypass ratio engines provided the nozzles are flattened to spread the flow. The Boeing work suggests that the exhaust nozzle geometries giving good high lift behaviour are in conflict with high speed requirements and difficult compromises may be involved. Based on these data USB aircraft may have difficulty generating steep descent gradients due to the good thrust recovery characteristics arising from jet flap effects. Shallow approaches at high incidence may be needed to obtain high lift coefficients which will degrade STOL performance and tend to increase the noise footprint area on the approach.

The USB is one of the few powered high lift systems which can be used on twin engines layouts. The lateral/directional moments due to engine failure can be made tolerable by mounting the engines well inboard and using two segment flaps which open up to form slots on the engine failed side to minimize lift loss. However, the thrust/weight ratios needed for twin-engined STOL are extremely high (≈.60) introducing significant mismatch between STOL and cruise thrust requirements with consequent weight and cost penalties. The USB has the advantage that existing high bypass ratio turbofan engines can be used in military applications but like the EBF new, very high bypass ratio engines will be needed for large civil STOL aircraft applications.

- Augmentor-Wing

The principle of the Augmentor-Wing was conceived independently in Canada and France. This high lift system is a derivative of the Jet Flap in which air bleed from the engines exhausts into a spanwise channel formed between upper and lower flap elements as shown schematically in Figure 4a. The inlet to the channel is on the wing upper surface which allows flow to be induced to mix with the jet flow and augment the thrust by ejector action. The Augmentor-Wing is used on the Buffalo/Spey flight research vehicle and the concept is prominent in NASA funded studies on aerodynamics, noise and propulsion, references 14 and 20. The blowing air is cross-ducted in the Augmentor-Wing which minimizes the lateral/directional moments after engine failure. As a result it is one of the few powered lift systems usable with safety on twin-engined layouts.

Recent research on the Augmentor-Wing has concerned improvements in thrust augmentation ratio using multi-lobe nozzles, evaluation of forward speed effects, a study of the noise reduction potential of lobe nozzles and lined flaps and development of layouts to reduce the complexity of blowing systems such as the "valveless" augmentor, reference 23. Other research includes studies of high speed cruise performance with the Augmentor open, with a view to improving cruise fuel consumption by airframe drag reduction and/or thrust augmentation. In addition, further tests have been undertaken at NASA Ames using a large swept wing model to explore noise, performance and stability and control characteristics.

The powerplant situation for the Augmentor-Wing is similar to the EBF. Comparisons of separate blowing compressors with two-stream or three-stream bleed/propulsion turbofan engines show the superiority of the bleed/propulsion arrangements. The two-stream engine is favoured for large civil aircraft with a thrust split of cold/hot flows of 80/20. The entire cold flow is ducted to the wing to maximize thrust augmentation and noise reduction potential. Very low bypass ratios (< 3:1) are needed to give fan pressure ratios high enough for compact blowing systems and this results in penalties to cruise specific fuel consumption about 30% relative to high bypass ratio turbofans as shown in Figure 8. On smaller civil aircraft, or large military aircraft where noise constraints will be less severe, three-stream bleed/propulsion engines of the kind shown in Figure 6 become feasible. It is considered that thrust splits of fan/blow/core flows of 40/40/20 are suitable which increase bypass ratios to approximately 5:1 and reduce the fuel consumption penalty to about 20%. The three-stream arrangement reduces the quantity of air to be ducted within the wing, simplifying the blowing system and problems of structural integration. The three-stream engines will require variable pitch fans or thrust deflectors to maintain bleed capability at approach conditions when thrust is low. The low bypass ratio engines used by the Augmentor-Wing have a low lapse rate of thrust with speed and altitude. As a result these aircraft will be capable of higher maximum cruise speeds than aircraft using the other powered high lift systems.

The Augmentor-Wing has been thoroughly investigated in both model and flight research programs, giving a high degree of confidence in its application to future aircraft. Its noise reduction potential is probably greater than any other powered lift system, so it is particularly competitive for large civil aircraft where noise goals are sufficiently stringent. The blowing system and double flap arrangement make it more complex and highly integrated than MF/VT or EBF. Combined with the requirement for a specialized bleed/propulsion engine having high fuel consumption this may defer the practical application of the concept until such time as advances in noise regulations preclude the use of other powered lift systems, Figure 11 and reference 14.

- Mechanical Flaps and Vectored Thrust

The Augmentor-Wing STOL flight research vehicle has very effectively demonstrated the use of propulsive thrust vectoring as a source of direct powered lift increments. Furthermore it has shown that varying the vector angle about the approach setting provides a powerful means of modulating drag and hence controlling flight path angle.

A combination of thrust vectoring and an efficient mechanical flap system (MF/VT) provides a comparitively simple powered high lift system. Research has shown that when a deflected jet operates in close proximity to a flap system beneficial lift interference occurs. The resulting rate of growth of lift with thrust is about half EBF values and the resulting increases in pitching moments are approximately equal to the moment of the gross thrust vector about the reference centre. Obviously this high lift concept requires higher thrust/weight ratios than an EBF to achieve a given lift coefficient and at very high values of lift the size of the pitching moments may preclude the use of aft nozzle locations with consequent loss of the induced lift component.

An MF/VT aircraft with high bypass ratio turbofan engines will use quite low deflection angles on the approach (60° - 70°) due to a combination of the large inlet momentum drag component and the large profile drag of mechanical flaps. This offers scope for the design of thrust deflectors which are simpler and lighter than the Pegasus type of nozzle used in the Augmentor-Wing application. Engine failure on the MF/VT introduces both large lateral/directional moments and lift losses which ultimately limit the usable vertical component of thrust on the approach. However, as the MF/VT has thrust deflection independent of flap deflection, unlike the EBF, it offers more scope for control procedures.

Recent military aircraft studies for the AMST have shown insignificant differences between the weights and wing loadings of aircraft with MF/VT and EBF powered high lift systems, reference 5. In contrast, in recent NASA civil STOL studies the MF/VT does not look attractive, reference 14, partially because the civil $C_{L_{max}}$ requirements are higher than the military case but also because the power-off aerodynamics used in these studies seem poor.

RESEARCH INTO THE AERODYNAMICS OF POWERED HIGH LIFT SYSTEMS

- Background

Throughout this section of the paper it will be evident that our research goals relate to future products which will be STOL, of relative' small capacity and designed for short haul operations. These aircraft could replace the Buffalo in military tactical supply roles or the DHC-7 in civil STOL roles. Such aircraft can tolerate lower wing loadings than the large, long range aircraft under consideration elsewhere and as a result lower maximum lift coefficients are needed. For cruise comfort it appears minimum wing loadings in the range of 70 - 75 lb/ft^2 are acceptable which correspond to maximum lift coefficients at landing of 4.5 - 5.0, as shown in Figure 3. These values are only slightly above levels obtainable from efficient mechanical flap systems on unswept wings, so that the lift increments required from power effects are quite small. It has been a primary objective of our research to achieve the highest power-off lift performance to minimize the additional lift needed from power effects as illustrated in Figure 12. This less extreme approach to powered lift STOL aircraft promises to alleviate the severe problems of noise, stability and control particularly evident with STOL aircraft using very high wing loadings.

High cruise speeds are not important for short range civil or military operations as their effects on block time are minimal as shown in Figure 13. In fact at short ranges the major time savings of STOL relative to CTOL arise from improved dispatch and ATC procedures. Cost studies show that once cruise speeds increase much beyond Mach 0.72 direct operating costs of STOL aircraft begin to rise rapidly as indicated in Figure 14. With these two considerations in mind it seems that cruise Mach numbers of 0.72 - 0.75 are most appropriate for the missions in view. At such cruise speeds the newly developed supercritical aerofoils will allow reasonably thick wings (about 13% t/c ratio) to be used with unswept wings. Furthermore the use of an unswept wing provides higher maximum lift coefficients as the lift penalties for sweep which follow a $\cos^N \Lambda_H$ (where $1 < N < 2$ and Λ_H is hinge line sweep angle) are avoided.

At the time this work commenced noise research was at an infant stage and the only sure way of reducing noise was by reduction of jet velocity. It appeared that fan pressure ratios about 1.25 ($V_J <$ 700 ft/sec) would be acceptable provided fans with low tip speed were used in conjunction with absorbers in the inlet and exit ducting. This order of fan pressure ratio corresponds to bypass ratios of 8 - 15 depending on the core engine cycle. These parameters were used in conjunction with an installed thrust/weight ratio of 0.45 and a wing loading of 75 lb/ft^2 to give the proportions of the research models used in our aerodynamic research programs.

As noted in the Introduction this review will be limited to those high lift systems which can use high bypass engines. The systems to be described include the Internally Blown Flap, Externally Blown Flap and Mechanical Flap combined with Thrust Vectoring.

- Two-Dimensional Testing

Our two-dimensional testing uses wings of two foot chord which completely span the six feet height of the NAE 6' x 9' low speed wind tunnel. The models are cantilevered from the tunnel balance at one end with end plates at the extremities. No form of wall treatment is used. The lift coefficients are based on the balance data which provides conservative estimates of sectional performance. Before using in spanwise loading calculations the drag is usually corrected for finite aspect ratio effects and end plate drag using corrections derived from previous drag measurements with wake traverse techniques. This procedure has provided estimates of wing lift and drag which agree closely with large-scale, complete model tests.

Recent work on the IBF studied blown, slotted flaps as a means of reducing the bleed levels required for a given lift coefficient. As noted in the REVIEW OF POWERED HIGH LIFT SYSTEMS under 'Internally Blown Flap', this can be very important when conventional engines are used as the source of blowing air for their thrust loss due to bleed is high. Typical slat, wing section, blowing nozzle locations and flap systems tested are shown in Figure 15. The model was blown from either a single slot or any two slots as desired.

Some results of tests without a slat are shown in Figure 16 which gives the variation of maximum lift coefficient with blowing coefficient and nozzle location. The flap deflection angle shown was beyond the value giving maximum lift with blowing-off, however, in the event of BLC failure sufficient lift remains for acceptable aircraft characteristics. The lift performance was found most responsive to blowing from the shroud tip or slightly ahead and at the levels of blow appropriate to conventional engines ($.02 < C_\mu < .04$) there was little to choose between nozzles B and D. The performance of a sealed flap is included for comparison and it is seen to be inferior at these low blowing coefficients. At the blowing coefficients achievable with high bypass ratio three-stream engines ($.08 < C_\mu < .12$) the blown, sealed, plain flap was found clearly superior.

Some results of tests on the same wing and flap system with slats are shown in Figure 17 which shows the variation of maximum lift with blowing coefficient. The figure also includes comparative data for blown single-slotted flaps, blown sealed flaps and a double-slotted flap with a moving vane which allowed very large flap deflections. At zero blowing the multi-slotted flaps were the most effective, with the moving vane type giving highest values ($C_{L_{max}} \approx 5.6$). To put these values in perspective we find aircraft maximum lift coefficients in 1g stall are usually at least 80% of the two-dimensional value, so that trimmed aircraft values of $C_{L_{max}} > 4.0$ should be achievable with such flap systems on unswept wings. Once blowing cleared up minor flow separations on the multi-slotted flaps their rate of growth of lift with thrust was quite low in comparison with the sealed and single-slotted flaps. Thus we found the blown slotted flaps were superior for $.02 < C_\mu < .04$, while once blowing exceeded about $C_\mu = .08$ the sealed flaps again had the highest performance.

Clearly the engine technology available will decide the preferred flap system. If only conventional engines are available for blowing, a highly developed mechanical flap system without any blowing could be preferable to a blown but simpler flap. If three-stream turbofan engines are available then the blown, sealed flap could be competitive.

- Quasi Two-Dimensional Testing

Quasi two-dimensional testing of powered lift configurations can provide a simple, low cost means of evaluating alternative nozzle locations, nozzle geometries and flap systems. It has been particularly popular in Canada and two other papers at this meeting will discuss Quasi-2D results obtained by other Canadian organizations. Furthermore if reliable methods can be developed for predicting aircraft aerodynamics from the Quasi-2D results, considerable savings in time and cost could be achieved as preliminary work could use Quasi-2D models.

The Quasi-2D model used in our tests comprised a two-dimensional wing and flap system with a single, centrally mounted fan jet nacelle, Figure 18. The vertical and chordwise location of the nozzle exit could be varied using offset and extension pieces. The nacelle could be fitted with plain circular nozzles or bifurcated Pegasus-type vectoring nozzles for investigations of EBF and MF/VT respectively. The highest nozzle locations tested placed the jet far enough below the wing to avoid scrubbing on the lower wing surface at cruise and also gave negligible impingement on the flaps at take-off deflections. Although this reduced the lift increments available from EBF effects it was felt acceptable due to the high power-off lift performance.

Typical lift results for the EBF with double-slotted flaps and a leading edge slat are summarized in Figure 19 for a representative landing configuration. All the high nozzle layouts tested had roughly similar lift performance, although the high/forward location was marginally better in terms of maximum lift coefficient. The lift with twin nozzles was not found significantly better than single nozzles which was unexpected as they impinged upon a greater spanwise extent of flap.

Typical Quasi-2D lift and pitching moment values for an MF/VT using vane double-slotted flaps and leading edge slat are shown in Figure 20. This figure shows the effect of vector angle on maximum lift coefficient and pitching moment at zero incidence for three nozzle locations at approximately equal gross thrust coefficients. At zero and negative jet deflections the model experienced strong EBF effects due to jet impingement of the flaps. As jet deflection was increased there was a minimum in lift and pitching moments at about thirty degrees deflection. Beyond this deflection angle lift increased due to beneficial interference and at about 90° deflection achieved a maximum value. At this point the lift increment due to vectored thrust was about 80% of the increment for an EBF at the same gross thrust. Typical deflection angles for an MF/VT STOL aircraft are about 60° - 70° and at these deflections the lift increment was from 50 - 70% of the EBF values, with the high-aft locations most effective.

As jet deflections were increased further lift collapsed suddenly at about 110° deflection. Flow visualization indicated that the jet had penetrated the stagnation streamline at the nose of the aerofoil at which point the jet began to break up intermittently with some chunks passing over the wing. Although these deflection angles were beyond STOL requirements, this problem could be of importance for VTOL aircraft using reversed jets for in-flight braking. In all cases tested the pitching moments of the MF/VT were close to the moment of the vector of the gross thrust about the moment centre. The pitching moments of the MF/VT with aft deflector locations were found no greater than the EBF for deflection angles suitable for STOL ($60^{\circ} < \delta_e < 70^{\circ}$) and if critical they could be reduced using more forward deflector locations.

A simple procedure was developed for predicting three-dimensional wing performance from the Quasi-2D aerodynamics. The Quasi-2D values were treated as sectional data and input into a spanwise loading calculation based on Multhopp's method. Although reservations were held about the theoretical grounds for such a method, it was simple to apply and capable of further elaboration if the general trends were found to be correct. Results of such calculations are shown in Figure 21 which compares the performance of EBF and MF/VT with a power-off case. It is of interest to note that when both high lift systems are constrained to the same approach angle and gross thrust coefficient the approach lift coefficients are almost identical. However the EBF has greater incidence and 'g' margins due to its increased maximum lift coefficient and higher stalling angle.

- Three-Dimensional Tests of IBF Models

Research into the aerodynamics of IBF aircraft used the model shown in Figure 22. This had an unswept wing of aspect ratio eight with full span blowing and a retractable leading edge slat. The wing was instrumented for measurements of spanwise and chordwise pressure distributions and the flap/aileron break could be placed at any of three spanwise locations.

During the course of flaps up tests it was found that 93% of the measured static thrust of the BLC was recovered while in addition, blowing tended to reduce the induced drag factor slightly, Figure 23. This appears to offer scope for blowing systems which are left on at cruise rather than exhausting through separate cruise propulsion nozzles. The resulting simplifications in valving and ducting could be a worthwhile trade for the slight loss in cruise thrust which is involved.

Typical lift data at normal IBF levels of blow ($C_\mu \approx .08$) and at a highly overblown condition ($C_\mu \approx .40$) are shown in Figure 24. The stall of the model at both levels of blow was characterized by a gentle lift break without large lift losses or indication of wing dropping. Tests on large scale models of the Augmentor-Wing with a leading edge slat have also shown similar stall behaviour to the IBF. In contrast data from RAE tests of the Jet Flap which did not have a leading edge slat, show evidence of a sharp lift break and large lift losses at stall. It seems that the slat is the controlling influence and provided it does not stall first it can maintain acceptable stall characteristics up to very high lift coefficients and in the post stall region.

- Three-Dimensional Tests of EBF and MF/VT

Three-dimensional testing of EBF and MF/VT concepts used the model shown in Figure 25. This had an unswept wing of aspect ratio eight, vane type double-slotted flaps and blown ailerons extending over the outboard 25% of span. The model had a retractable leading edge slat and it used an aerofoil suitable for cruise at 0.72 Mach number. Multi-tube ejectors were used to simulate the engine intake and exit flows, and the effective bypass ratio was about six to one. The nacelles could be fitted with various exit nozzles to simulate EBF, thrust vectoring and reverser arrangements. The nacelles had various chordwise and spanwise locations relative to the wing.

Typical results for an EBF with landing flap deflection ($\delta_F = 55^{\circ}$) and nacelles in a high-forward location are summarized in Figure 26. The values predicted from Quasi-2D tests are also shown for comparison. Generally agreement was found to be good on lift, although at low thrusts the 3D model appeared to suffer more from nacelle-wing interference than the Quasi-2D tests due to the relatively larger nacelle size. The axial force coefficients showed almost identical trends with thrust increase although there was a constant displacement of $\Delta C_D \approx .1$ between them. The discrepancies in axial force may be due to the half model test technique and the large model dimensions relative to the tunnel cross-section. Subsequent complete model tests in larger wind tunnels should clarify this problem. A comparison of pitching moments shows measured values to be substantially less than predictions, due in part to different locations of the moment reference centre.

The agreement between measured and predicted aerodynamics of the EBF was generally good. This indicates that for preliminary project evaluation purposes predictions based on Quasi-2D data appear adequate.

- Aerodynamic Comparisons of High Lift Systems

The influence of thrust (or blowing) coefficient on maximum lift coefficient is shown in Figure 27 for examples of IBF, EBF, MF/VT and slipstream deflection based on models tested by de Havilland Canada. All of these models had leading edge slats and they were tested at similar Reynolds numbers. The figure also contains values for the Jet Flap, reference 24, Augmentor-Wing, reference 14, USB, reference 19, and a more extreme form of EBF from reference 25. The achievement of 2000 ft STOL performance at wing loadings of 70 - 75 lb/ft^2 requires maximum lift coefficients of 4.5 - 5.0 and the following comments about the relative performance of the high lift systems are made with this target in mind.

The IBF has the highest performance at low levels of blowing, requiring only attachment blowing ($C_\mu \approx .07$) to achieve the target lift coefficients. At higher levels of blowing ($C_\mu > .4$) the IBF results fair into the Jet Flap values. Thereafter the Jet Flap has the highest lift performance although the lift coefficients are now beyond the range of our interest. The EBF and MF/VT layouts tested by de Havilland achieve the target maximum lift coefficients at thrust coefficients about 0.3 and 0.55 respectively, which are about half the thrust levels needed by more extreme EBF's using less sophisticated flaps.

The ability to generate drag restricts the amount of usable thrust in a landing approach. Hence a simple comparison of CL_{max} is insufficient to expose the merits of each high lift system and ultimately a full simulation of the landing is desirable. For present purposes the landing approach conditions will be used as a measure of the potential of each concept. Such a comparison is shown in Figure 28 which assumes an approach angle of 7 1/2° and a margin of 35% between maximum lift coefficients and usable values to allow for margins for gusts, trim and normal acceleration for flaring purposes. Our civil STOL studies in support of DHC-7 indicate that operation into 2000 ft STOLports is feasible at an approach speed of 80 kts provided advanced lift spoiling and braking systems are employed. The wing loading scale for 2000 ft STOLport operation shown on the right hand side of Figure 28 was constructed using this approach speed.

The EBF arrangements are capable of operating at wing loadings of 70 - 75 lb/ft^2, but to obtain higher values will require more powerful drag producing devices or the use of shallower approaches so that increased thrust can be used. The MF/VT's can operate at wing loadings of 75 - 80 lb/ft^2 with low deflection angles (60° - 70°) and low approach thrust/weight ratios ($.15 < T/W < .20$). Operation at higher wing loadings with MF/VT simply requires increased thrust and larger deflection angles; values of 90 lb/ft^2 can be obtained using 80° of deflection and an approach T/W of 0.25. This probably represents an upper limit on wing loading for the MF/VT as the approach T/W ratio becomes unduly high relative to total installed values and engine failure will become critical. The IBF blown to attachment levels achieves wing loadings of 75 lb/ft^2 without any supplement from thrust deflection. If thrust deflection is used, an angle about 85° is required due to the low drag of the IBF. With thrust deflection and attachment blowing the IBF can achieve wing loadings of 90 lb/ft^2 using approach T/W's about 0.22. Alternatively a highly overblown IBF ($C_\mu \approx .23$) could achieve wing loadings of 90 lb/ft^2 without needing any supplement from thrust vectoring.

Pitching moments are another critical aerodynamic consideration as they determine the trimming lift loss, tail area and tail lift coefficient requirements. The pitching moments at 5° incidence are shown as functions of blowing coefficients for the IBF, MF/VT and EBF in Figure 29. At thrust coefficients corresponding to a wing loading of 75 lb/ft^2 the differences between the pitching moments of each type are quite small, hence trim lift losses will be similar. A comparison with deflected slipstream shows generally similar values of pitching moments so that tail volumes and lift coefficient requirements should be similar to our existing propeller driven types. Downwash surveys at the tail location of the EBF indicate that a moving tailplane will be needed to encompass the large range of flow angles (see conference paper by R. H. Wickens).

- Design Study Comparisons

Aircraft design studies play an essential role in evaluating new high lift concepts. They are, nevertheless, no better than the quality of their basic assumptions, the uniformity of their aerodynamic data base and the degree of ingenuity and motivation used in solving critical problem areas. An interesting by-product of this situation are the weird designs which sometimes result when organizations promoting one type of high lift system do studies of competing concepts. Following that recital of reservations about design studies in general a brief review follows of our design studies of aircraft with EBF, MF/VT and IBF/VT high lift systems.

The application considered was for a STOL transport aircraft suitable as a turbofan powered follow-on to the DHC-7 and the Buffalo tactical transport. The design mission selected was to carry a payload equivalent to forty-eight passengers over a range of 300 nm cruising at 0.7 Mach number at 25,000 ft with full IFR reserves. The aircraft were sized to operate from 2000 ft STOLports on a 90°F day at sea level using civil operating rules. This corresponds approximately to a military STOL field size of 1300 ft in standard day sea level conditions and 1700 ft on a 90°F day at sea level conditions which is equivalent to the Buffalo performance.

The aerodynamics of the EBF were estimated from Quasi-2D data as discussed previously. The MF/VT values were based on the power-off values for the EBF. Subsequent 3-D tests showed the EBF aerodynamics satisfactory while the MF/VT values were conservative as no allowance was made for beneficial lift interference. The aerodynamics of the IBF/VT were derived from the 3-D model tests and no allowance was included for favourable interference between the wing and the deflected jets.

The powerplant performance of the EBF and MF/VT were based on turbofan engines of six-to-one bypass ratio with fans of 1.5 pressure ratio. The powerplant performance of the IBF/VT was based on the same core engine cycle and fan pressure ratio but bypass ratio was reduced to allow for permanent bleed extraction for IBF purposes. The engine weights and performance also included allowances for sound treatment to the intake and exit duct walls. Although this installation could meet FAR 36 noise levels with large margins, further silencing would be required to meet the civil STOL target noise level of 95 PNdB at 500 ft. Based on recent NASA funded studies, references 26 and 27, it appears this target noise level could be achieved with fans of pressure ratio about 1.25 with intake and exit treatment of the kind shown in Figure 30. A noise footprint for an EBF powered by such engines is compared with the DHC-7 estimates in Figure 31.

The results of the parametric studies are summarized in Figure 32. The spread of designs shown for the EBF and MF/VT were obtained by varying the sophistication of the flaps from vane-type double-slotted flaps to double-slotted flaps with large chord extension. The IBF/VT is a point design using attachment blowing levels. In all cases the engines were scaled and wing loadings selected to minimize take-off gross weight consistent with the mission and field performance requirements. A typical case is shown in Figure 33 for an EBF configuration with vane-double-slotted flaps and the corresponding aircraft layout is shown in Figure 34.

Each high lift system optimized at quite different wing loadings, although the spread of thrust/weight ratios was not large. The EBF with vane-double-slotted flaps had the lightest wing loading, 72 lb/ft^2, and the IBF/VT the highest at 92 lb/ft^2. The first costs of the aircraft showed little spread ($\pm$ 3% about the mean) as savings in structure weight and cost were usually offset by increases in engine related items. Direct operating costs for the IBF/VT and EBF show small differences (6%) in favour of the EBF which may be a significant factor for airline operations.

The design studies indicated that all the high lift systems were technically feasible for the mission considered and capable of exceeding the minimum levels of wing loading. The cost differences found are sufficiently small that external requirements are expected to play an important role in selecting a preferred high lift system. Such considerations could include the ability to use existing engines or the degree of modification required and the complexity and ease of maintenance of the high lift system. These remarks are probably only valid for civil STOL aircraft below about 70,000 lb maximum gross weight and military aircraft where noise is not a dominant consideration. In the case of larger, civil STOL aircraft noise has a much greater impact on engine choice and high lift system requirements and the options may not be so open.

- Research into Flow Prediction Methods

The objective of this research was to develop a method using digital computers to predict the flow about mutually interfering 3-dimensional bodies of arbitrary shape at subcritical speeds. The method is basically similar to that of Rubbert and Saaris, reference 29, using a combination of source panels and horseshoe vortices to represent the shape and lift effects.

The basis of the method is to find a solution to Laplace's equation in three dimensions which satisfies the boundary conditions that on the body the flow should be tangential to the surface and at large distances away it should tend to free stream velocity. The idealization used is illustrated in Figure 35. The body surface is broken into small quadrilateral panels each with uniform source density. In the wake behind the body there are trailing vortices whose direction is related empirically to the flap deflection. The vortex system is extended within the body with the chordwise gradation of strength prescribed. Application of the boundary conditions then leads to a system of integral equations which are solved numerically to give the strengths of the singularities. Once these are known it is a simple matter to calculate surface velocities and hence pressure coefficients and loads.

An interesting application of this method was the prediction of loads on a wing with internally blown flaps. When the IBF is blown to attachment levels boundary layer effects are suppressed and flow about the wing closely approaches the potential flow situation. During research into the IBF concept, pressure data were obtained for cases with the wing alone, flaps deflected and without the leading edge slat, so selected cases were modelled using the potential flow program. The wing was modelled using 320 panels and eight multi-horseshoe vortices per side, the flap deflection angle was 20°. Some experimentation was needed to define a suitable chordwise distribution of internal vorticity and the direction of the trailing vortices, although overall results were not found unduly sensitive to these parameters.

The spanwise loadings from experiment and calculations are compared in Figure 36 and typical chordwise loadings in Figure 37. The agreement between the measured and calculated values are generally good. The calculation took 20 minutes of C.P.U. time on an IBM 360, which compares favourably with values quoted elsewhere for problems of this size, see Figure 38 and reference 30.

CONCLUDING REMARKS

The research program described is very broadly based. Its general objectives are directed towards the development of powered high lift systems for future turbofan powered STOL transport aircraft suitable for operation into urban airports or for military tactical supply roles. These applications emphasize the need for quietness, moderately high subsonic cruise speeds, STOL performance and steep gradient capabilities.

It appears that these qualities can be provided without substantial penalties by several powered high lift systems including internally blown flaps, externally blown flaps and mechanical flaps combined with vectored thrust. In all applications high bypass ratio powerplants are needed to meet noise requirements, to give low fuel consumption and provide the high ratio of static to cruise thrust needed with STOL aircraft. Based on present aerodynamic data there is little to choose between the aforementioned high lift systems. Greater resolution may be possible using improved aerodynamics and research is continuing to establish a better base for each system. At this time it appears that external factors such as the availability of suitable engines and the complexity and maintainability of the high lift system will be powerful influences in selecting a preferred high lift system.

REFERENCES

1.	D.C. Whittley	The Aerodynamics of High Lift Illustrated by Augmentor-Wing Research. Paper 72/20, 12th Anglo American Aeronautical Conference - July 1971.
2.	D.C. Whittley	The Buffalo/Spey Jet-STOL Research Aircraft. AGARD/NATO Conference - October 1972.
3.		P23, Aviation Week - December 3, 1973.
4.		P179, 180, Aerospace Daily - December 4, 1973.
5.	J. Hebert	STOL Tactical Aircraft Investigation. SAE Paper 730913 - October 1973.
6.	D.A. Spence	A Treatment of the Jet Flap by Thin-Aerofoil Theory. RAE Report Aero 2568 - November 1955.
7.	E.C. Maskell D.A. Spence	A Theory of the Jet Flap in Three Dimensions. RAE Report Aero 2612 - September 1958.
8.	J.A. Albers M.C. Potter	Potential Flow Solution for a STOL Wing Propulsion System. NASA TND 6394. July 1971.
9.	A.C. Herold	A Two Dimensional,Iterative Solution for the Jet Flap. NASA CR 2190 - February 1973.
10.	K.D. Harris	The Hunting H 126 Jet-Flap Research Aircraft. AGARD-LS-43-71 - P14-1 April 1970.
11.		P61, Aviation Week - February 5, 1972.
12.	Lockheed Aircraft	Quiet Turbofan STOL Aircraft for Short Haul Transportation. Contract NAS 2-6995 - May 1973.
13.	R.E. Hayden	Fundamental Aspects of Noise Reduction from Powered-Lift Devices. SAE Paper 730376 - April 1973.
14.		STOL Technology. NASA SP-320 - October 1972.
15.	D.L. Maiden	Performance Comparison of a Lobed - Daisy Mixer Nozzle with a Convergent Nozzle at Subsonic Speeds. NASA TMX 2806 - September 1973.
16.	C.A. Shollenberger	Analysis of the Interaction of Jets and Airfoils in Two Dimensions. Journal of Aircraft, Vol. 10, No. 5 - May 1973.
17.	M.H. Roe	Air Force STOL Tactical Aircraft Investigation: Evaluation of Externally Blown Flaps. SAE Paper 730914 - October 1973.
18.	P.R. Ashill S.F. Mansfield	Note on Some Exploratory Tests on a Swept Wing with an External-Flow Jet Augmented-Flap. RAE TR 72192 - January 1973.
19.	J.K. Wimpress	Upper Surface Blowing Technology as Applied to the VC-14 Airplane. SAE Paper 730916 - October 1973.
20.	A.E. Phelps	Low Speed Wind-Tunnel Investigation of a Semispan STOL Jet Transport Wing-Body with an Upper Surface Blown Jet Flap. NASA TND 7183 - May 1973.
21.	A.E. Phelps	Wind-Tunnel Investigation of An Upper Surface Blown Jet-Flap Powered-Lift Configuration. NASA TND 7399 - December 1973.

22. Design Integration and Noise Studies for Jet STOL Aircraft, Volumes I to IV. NASA CR 114471-114474 - May 1972.

23. A.S. Mahal, I.J. Gilchrist — Design Integration and Noise Studies for Jet STOL Aircraft. Augmentor-Wing Cruise Blowing Valveless System. NASA CR 114560 - January 1973.

24. S.F.J. Butler, M.B. Guyett, B.A. Moy — Six Component Low Speed Tunnel Tests of Jet-Flap Complete Models with Variation of Aspect Ratio,Dihedral,and Sweepback, including the Influence of Ground Proximity. RAE REP AERO 2652 - June 1961.

25. R.D. Vogler — Wind Tunnel Investigation of a Four Engine Externally Blowing Jet Flap STOL Airplane Model. NASA TND 7034 - December 1970.

26. F.B. Metzger, D.B. Hanson, R.W. Menthe — Analytical Parametric Investigation of Low Pressure Ratio Fan Noise. NASA CR 2188 - March 1973.

27. D.P. Edkins, R. Hirschkron, R. Lee — TF 34 Turbofan Quiet Engine Study. NASA CR-120914.

28. Parametric Studies for Multi-Function Propulsion/Blowing Turbofan Engines. Rolls-Royce PS261 - April 1971.

29. P.E. Rubbert, G.R. Saaris — A General Three Dimensional Potential Flow-Method Applied to V/STOL Aerodynamics. SAE Paper 680304 - 1968.

30. Aerodynamic Interference. AGARD CP-71-71, Paper 11 - September 1971.

ACKNOWLEDGEMENTS

The author wishes to thank The De Havilland Aircraft Company of Canada and the Defence Research Board of Canada for permission to use results from DHC-DIR A-18 research program. The views expressed are those of the author and they do not necessarily reflect Company opinions. The author wishes to thank R.J.D. Poole, D.J. Barber and O.M.S. Colavincenzo for their valuable contributions to the experimental and theoretical work and to V.L. Gregg for his able assistance in producing this paper.

DH

FACTORS INFLUENCING CHOICE OF POWERED HIGH LIFT SYSTEM

- DESIGN MISSION
  - FIELD SIZE
  - RANGE, PAYLOAD
  - CRUISE SPEED
- WING LOADING
  - PASSENGER COMFORT
  - CRUISE EFFICIENCY
- NOISE
  - NOISE GOALS
  - POWERPLANT AND HIGH LIFT SYSTEM CONTRIBUTIONS
- AIRWORTHINESS
  - SAFETY MARGINS, SPEED, INCIDENCE, ACCELERATION
  - TIME DELAYS
  - ENGINE FAILURE
- POWERPLANT
  - ABILITY TO USE EXISTING ENGINES
  - CRUISE FUEL CONSUMPTION, BYPASS RATIO
  - INSTALLATION PENALTIES
- ECONOMIC PENALTIES
  - WEIGHT, COST INCREASE FOR STOL
  - WEIGHT, COST INCREASE FOR NOISE
  - OFFSETS
    - TIME AND COST SAVINGS
    - REDUCED CONGESTION
    - REDUCED AIRFIELD CONSTRUCTION COST

FIGURE 1

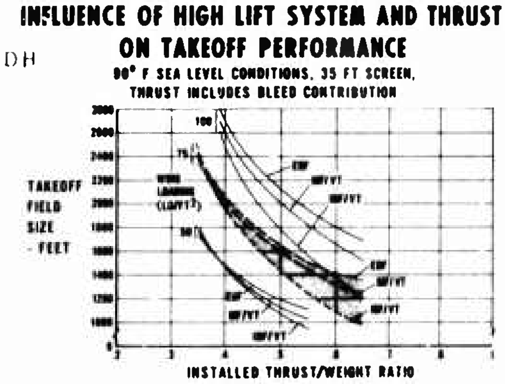
INFLUENCE OF HIGH LIFT SYSTEM AND THRUST ON TAKEOFF PERFORMANCE

90° F SEA LEVEL CONDITIONS, 35 FT SCREEN, THRUST INCLUDES BLEED CONTRIBUTION

FIGURE 2

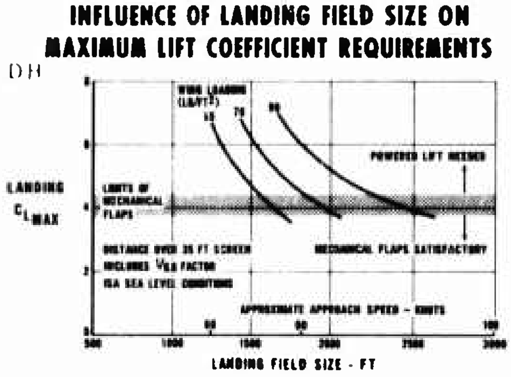
INFLUENCE OF LANDING FIELD SIZE ON MAXIMUM LIFT COEFFICIENT REQUIREMENTS

FIGURE 3

DH

SUMMARY OF CHARACTERISTICS OF POWERED HIGH LIFT SYSTEMS

TYPE OF POWERED LIFT SYSTEM		COMMENTS
INTERNALLY BLOWN FLAP	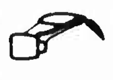	• TYPICAL LANDING $C_{L_{MAX}}$ ≈ 4.0 C_μ ≈ [illegible] • REQUIRES SPECIAL THREE STREAM ENGINE WITH V.P. FAN OR THRUST DEFLECTOR. CAN USE HIGH BYPASS RATIOS. LOW SFC • PROVEN TECHNOLOGY USED ON PRODUCTION AIRCRAFT • QUIET
JET FLAP	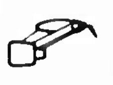	• TYPICAL LANDING $C_{L_{MAX}}$ ≈ 7 [illegible] • REQUIRES SPECIAL THREE STREAM ENGINE WITH V.P. FAN OR THRUST DEFLECTOR. LOW BYPASS RATIO. HIGH SFC • PROVEN TECHNOLOGY. RESEARCH VEHICLE FLOWN (H126) • REQUIRES LOW BLOWING PRESSURES (≈ 1.3) TO LIMIT NOISE
AUGMENTOR-WING	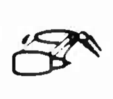	• TYPICAL LANDING $C_{L_{MAX}}$ ≈ 6 [illegible] • REQUIRES SPECIAL HIGH BLEED ENGINE. EITHER TWO STREAM (60/30) OR THREESTREAM WITH V.P. FAN (40/40/20). LOW BYPASS RATIO. HIGH SFC • POTENTIALLY VERY QUIET • EXTENSIVE AERODYNAMIC DATA BASE • BUFFALO/SPEY FLIGHT RESEARCH VEHICLE FLOWN

FIGURE 4a

DH

SUMMARY OF CHARACTERISTICS OF POWERED HIGH LIFT SYSTEMS

EXTERNALLY BLOWN FLAP	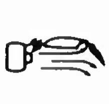	• TYPICAL LANDING $C_{L_{MAX}}$ ≈ 6.4 [illegible] C_μ < 1.4 • CAN USE EXISTING TURBOFANS FOR MILITARY APPLICATIONS. CIVIL APPLICATIONS REQUIRE VERY HIGH BYPASS RATIOS (8 TO 12). LOW SFC • NOISE PROBLEMS DUE TO JET IMPINGEMENT • CANNOT ACHIEVE HIGH DESCENT ANGLES • STABILITY AND CONTROL PROBLEMS RESOLVED • GOOD AERODYNAMIC DATA BASE. YC15 DEMONSTRATOR FLIES IN [illegible]
UPPER SURFACE BLOWN FLAP	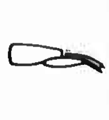	• TYPICAL LANDING $C_{L_{MAX}}$ ≈ 6.4 [illegible] C_μ < 1.2 • CAN USE EXISTING TURBOFANS FOR MILITARY APPLICATIONS. HIGHER BYPASS RATIOS NEEDED FOR CIVIL AIRCRAFT. LOW SFC • NOISE SHIELDING BY WING • REQUIRES FLATTENED EXHAUST NOZZLES FOR GOOD TURNING BY FLAP. IN CONFLICT WITH HIGH SPEED CRUISE REQUIREMENTS. SCRUBBING LOSS AT CRUISE • CANNOT ACHIEVE HIGH DESCENT ANGLES • LIMITED AERODYNAMIC DATA BASE. YC14 DEMONSTRATOR FLIES IN [illegible]
MECHANICAL FLAPS / VECTORED THRUST	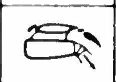	• TYPICAL LANDING $C_{L_{MAX}}$ ≈ 6.4 [illegible] C_μ < 1.5 • CAN USE EXISTING TURBOFANS FOR MILITARY APPLICATIONS. HIGHER BYPASS RATIOS FOR CIVIL AIRCRAFT. LOW SFC • DEFLECTOR NOISE UNCERTAIN • USES ELEMENTS OF PROVEN TECHNOLOGY • LIMITED AERODYNAMIC DATA BASE. NO DEMONSTRATOR

FIGURE 4b

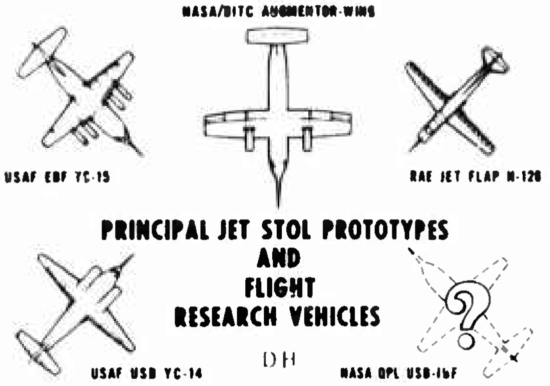

PRINCIPAL JET STOL PROTOTYPES AND FLIGHT RESEARCH VEHICLES

DH

FIGURE 5

THREE STREAM BLEED PROPULSION ENGINE

DH

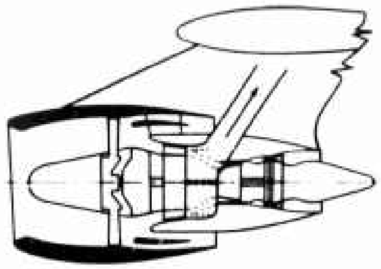

FIGURE 6

EFFECT OF BLOWING THRUST EXTRACTION AT CONSTANT CORE ENGINE SIZE

DH

(REF 20 ROLLS-ROYCE PS 701)

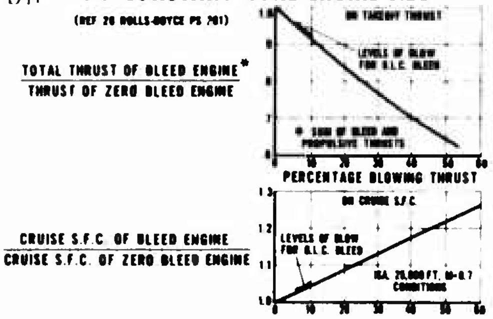

FIGURE 7

CRUISE SPECIFIC FUEL CONSUMPTION FOR A RANGE OF FIXED BLEED ENGINES

DH

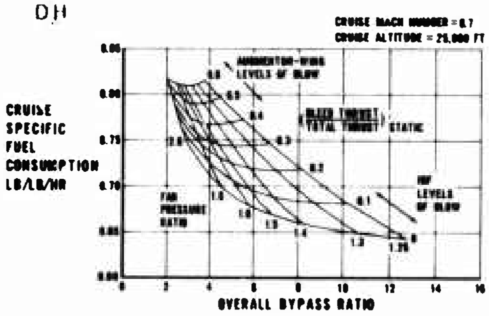

FIGURE 8

DH

TYPICAL IBF WITH LEADING EDGE SLAT

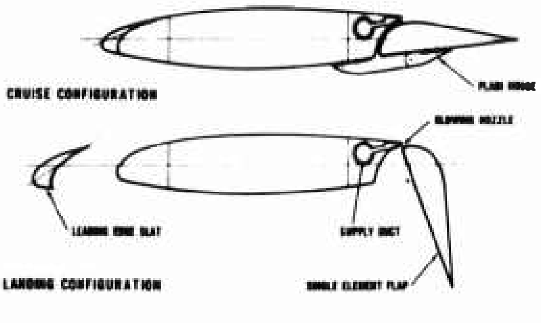

FIGURE 9

LIFT COMPONENTS FOR POWERED LIFT AIRCRAFT

DH

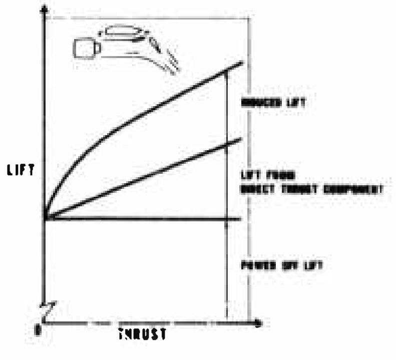

FIGURE 10

AIRCRAFT NOISE LEVEL GOALS

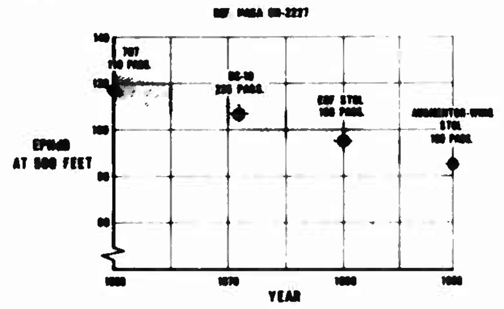

FIGURE 11

COMPARISON OF ADVANCED FLAP SYSTEMS WITH EXTREME EBF

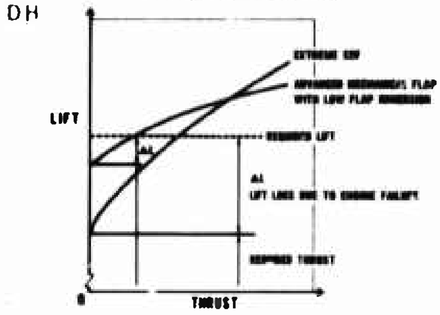

FIGURE 12

EFFECT OF CRUISE MACH NUMBER ON BLOCK TIME AND COMPARISON WITH N.E. CORRIDOR VALUES

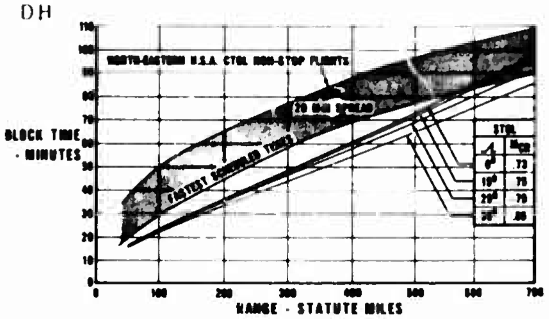

FIGURE 13

THE INFLUENCE OF CRUISE MACH NUMBER ON DIRECT OPERATING COSTS

2000 FT STOLPORT OPERATION

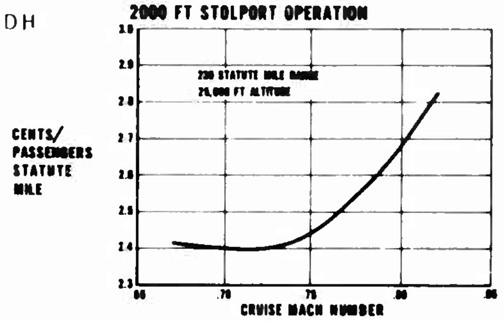

FIGURE 14

BLC NOZZLE LOCATION AND SUPPLY DUCTS

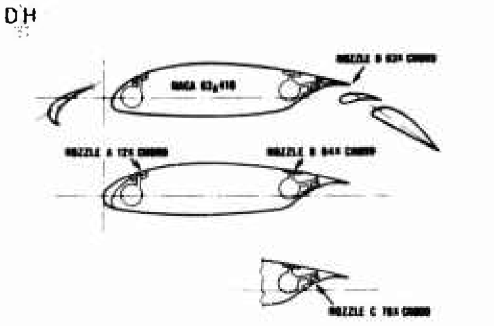

FIGURE 15

MODEL WITH VANE DOUBLE-SLOTTED FLAPS AND NO SLATS

EFFECT OF BLOWING LOCATION ON MAXIMUM LIFT

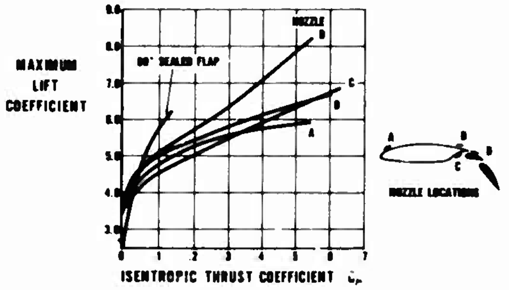

FIGURE 16

COMPARISON OF MAXIMUM LIFT FOR 2-D AEROFOILS

WITH IBF FLAPS AND SLATS

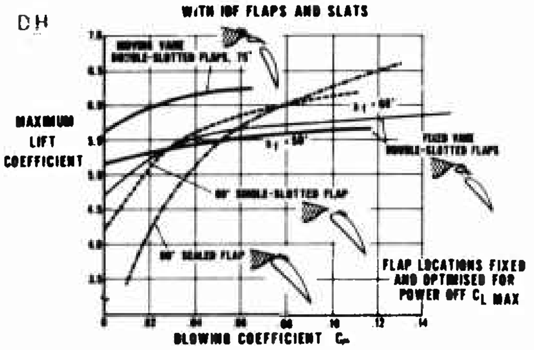

FIGURE 17

QUASI-2D WING CONFIGURATIONS AND STRAIGHT OFFSET NOZZLES LOCATIONS

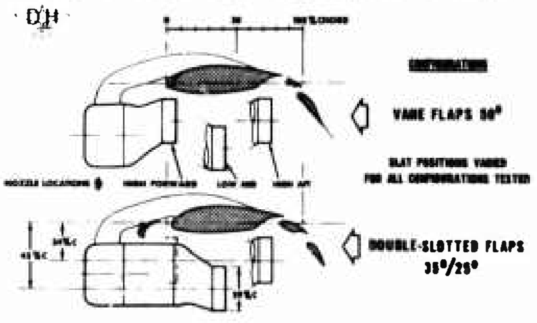

FIGURE 18

DH

SUMMARY OF QUASI-2D LIFT RESULTS FOR EBF CONFIGURATIONS

WITH DOUBLE-SLOTTED FLAPS

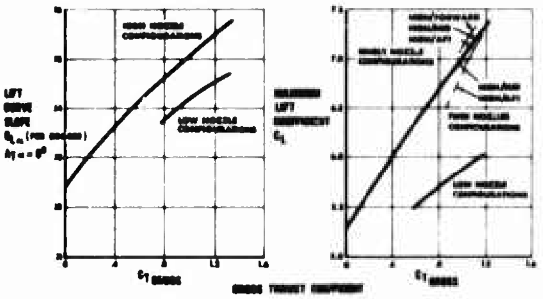

FIGURE 19

DH

QUASI-2D RESULTS FOR VECTORED THRUST

V.D.S. FLAPS 50° AND LEADING EDGE SLAT

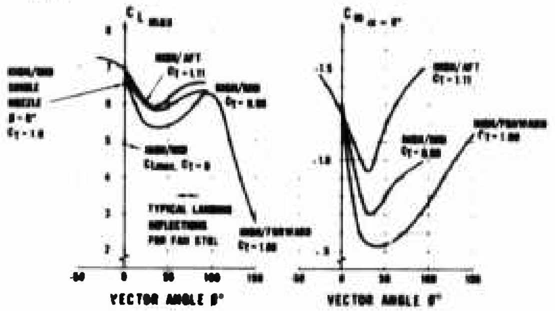

FIGURE 20

DH

PREDICTION OF LIFT, DRAG AND PITCHING MOMENTS

FOR EBF AND MF/VT AIRCRAFT

USING QUASI-2D DATA FOR DOUBLE-SLOTTED FLAPS

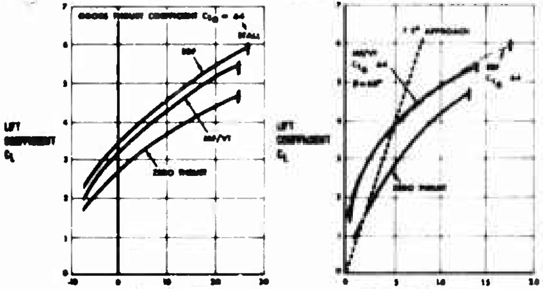

FIGURE 21

DH

THREE-DIMENSIONAL TEST OF IBF MODEL IN THE 6x9 FT WIND TUNNEL

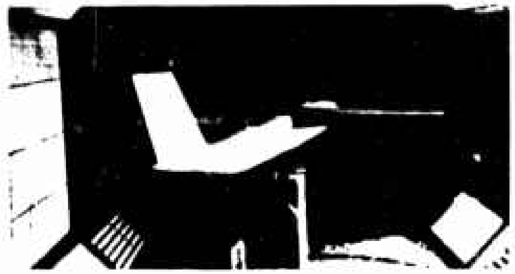

FIGURE 22

DH

DRAG DATA WITH FULL SPAN BLOWING FLAPS UP

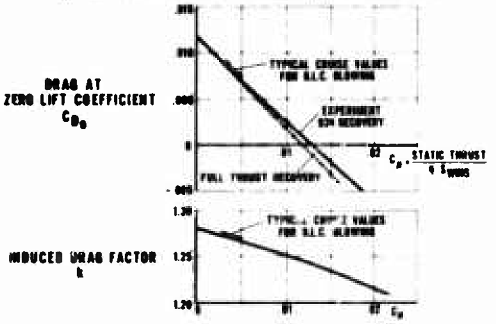

FIGURE 23

DH

HIGH LIFT COMPARISON OF IBF MODELS

LANDING FLAPS

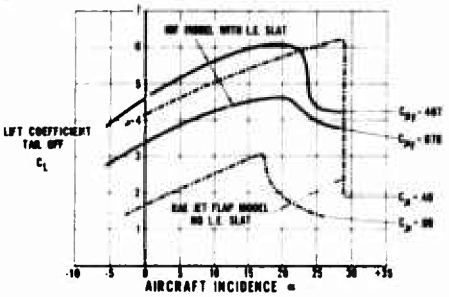

FIGURE 24

DH

EXTERNALLY BLOWN FLAP MODEL IN THE NAE 6x9 FT LOW SPEED TUNNEL

FIGURE 25

A COMPARISON OF EXPERIMENTAL RESULTS AND PREDICTIONS OF LIFT, DRAG AND PITCHING MOMENT FOR AN EBF CONFIGURATION

DH

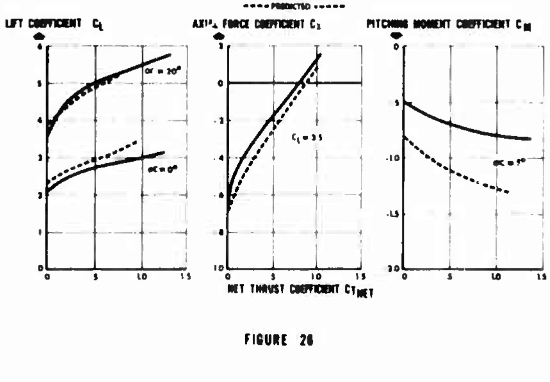

FIGURE 26

VARIATION OF MAXIMUM LIFT WITH THRUST FOR VARIOUS POWERED LIFT SYSTEMS

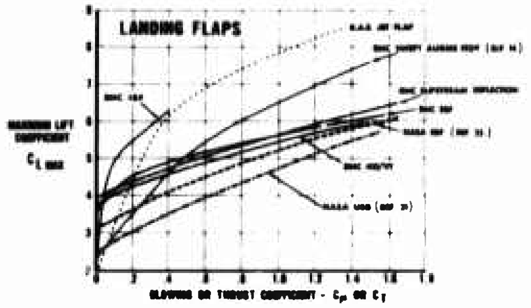

FIGURE 27

COMPARISON OF APPROACH CONDITIONS FOR VARIOUS HIGH LIFT SYSTEMS ON A WING OF ASPECT RATIO EIGHT AND AT A DESCENT GRADIENT OF 7.5°

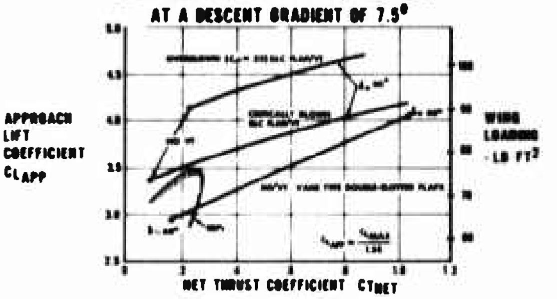

FIGURE 28

COMPARISON OF TYPICAL PITCHING MOMENTS FOR FAN STOL AIRCRAFT IN A LANDING CONFIGURATION

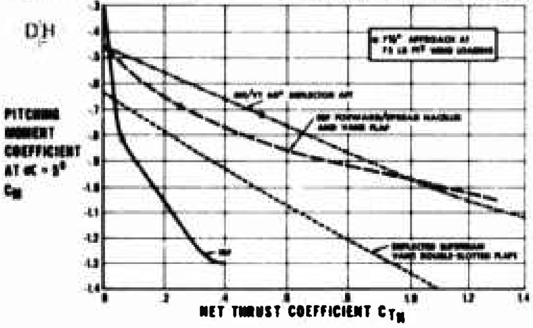

FIGURE 29

QUIET STOL TURBOFAN POWERPLANT FAN PRESSURE RATIO 1.25

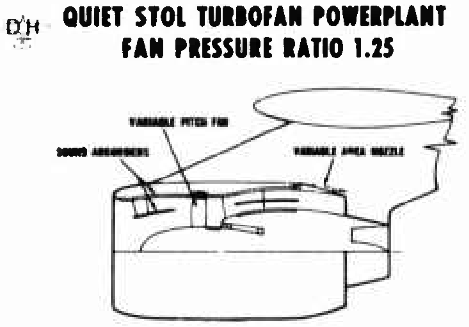

FIGURE 30

A COMPARISON OF STOL NOISE FOOTPRINTS FOR A QUIET FAN STOL* AND DHC-7 OPERATING FROM A 2000 FT STOLPORT

*(SOURCE OF NOISE DATA - NASA CR 114...)

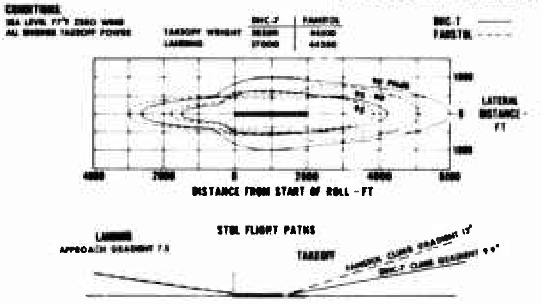

FIGURE 31

PARAMETRIC DESIGN STUDIES OF VARIOUS POWERED LIFT AIRCRAFT

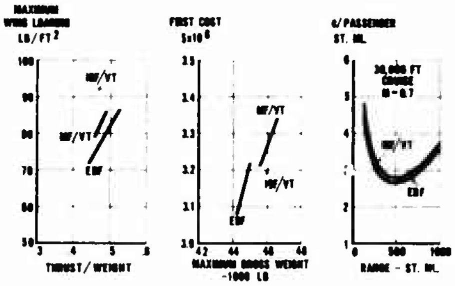

FIGURE 32

PARAMETRIC STUDY OF STOL AIRCRAFT WITH EXTERNALLY BLOWN VANE DOUBLE-SLOTTED FLAPS

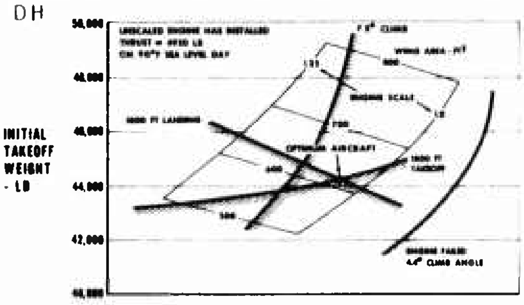

FIGURE 33

STOL TRANSPORT AIRCRAFT WITH EBF FLAPS AND BYPASS RATIO 6 TURBOFAN ENGINES

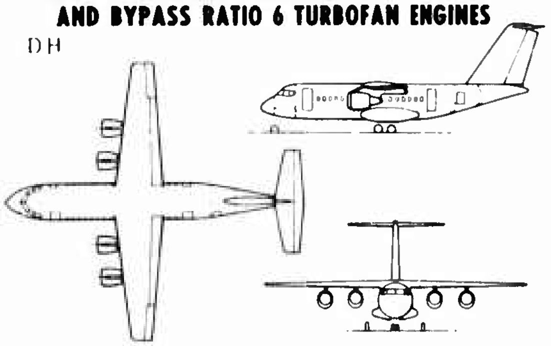

FIGURE 34

CONCEPTS EMPLOYED TO SOLVE FLOW PROBLEMS

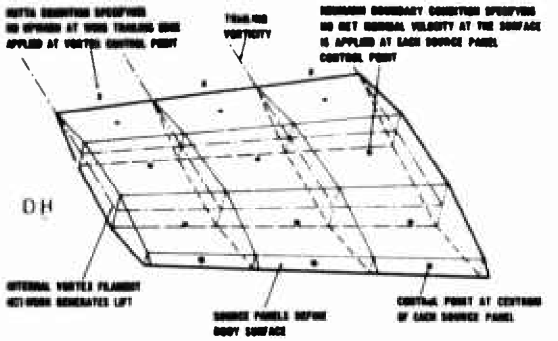
KUTTA CONDITION SPECIFYING NO UPWASH AT WING TRAILING EDGE APPLIED AT VORTEX CONTROL POINT
TRAILING VORTICITY
NEUMANN BOUNDARY CONDITION SPECIFYING NO NET NORMAL VELOCITY AT THE SURFACE IS APPLIED AT EACH SOURCE PANEL CONTROL POINT
DH
INTERNAL VORTEX FILAMENT NETWORK GENERATES LIFT
SOURCE PANELS DEFINE BODY SURFACE
CONTROL POINT AT CENTROID OF EACH SOURCE PANEL

FIGURE 35

NON-DIMENSIONAL SPANWISE LIFT DISTRIBUTION ON MODEL WING

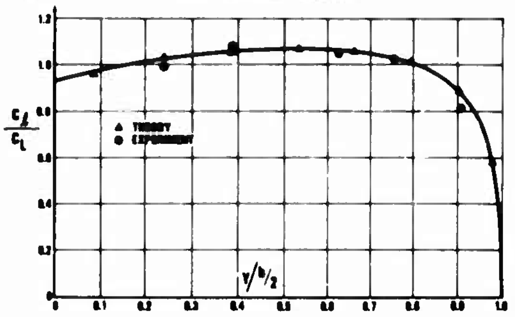

FIGURE 36

PRESSURE DISTRIBUTION ON MODEL WING

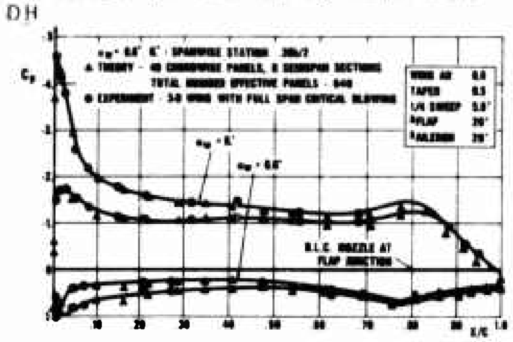

FIGURE 37

COMPARISON OF TIME REQUIRED TO SOLVE A THREE-DIMENSIONAL POTENTIAL FLOW PROBLEM ON A CDC 6600 FOR VARIOUS GROUPS

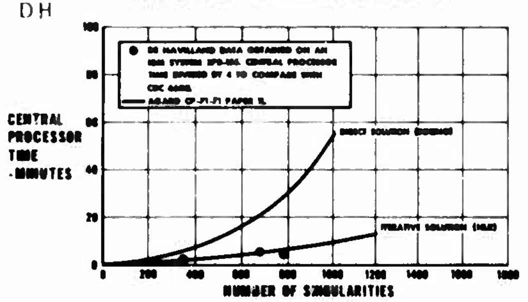

FIGURE 38

PREDICTING THE MAXIMUM LIFT OF JET-FLAPPED WINGS

David J. Moorhouse

Air Force Flight Dynamics Laboratory
Wright-Patterson AFB, Ohio 45433, USA

SUMMARY

The objective of this paper is to discuss the prediction of the maximum lift of jet-flap configurations. This objective is accomplished in three parts, as follows:

(i) Based on the assumption of a leading-edge stall, a theoretical expression is developed for the two-dimensional increment in maximum lift due to blowing. This extends previous work and includes additional terms compared to the previously published work.

(ii) The maximum lift of finite-aspect-ratio jet-flapped wings is shown to be a three-dimensional phenomenon. Corrections are applied to the two-dimensional theory to develop a procedure for predicting the increments in maximum lift due to blowing on finite-aspect-ratio wings with jet flaps. This procedure shows excellent agreement with measured results on various jet-flap concepts including pure jet flaps, internally blown flaps, externally blown flaps and upper surface blown flaps. More importantly, the results are independent of the actual presence of a leading-edge stall.

(iii) The effect of jet-flap blowing on boundary layer separation criteria is discussed. Preliminary results indicate that the well-known Stratford criterion is equally applicable to jet-flapped configurations.

LIST OF SYMBOLS

$\mathcal{AR}$	Aspect ratio
B_n	Coefficients in a Fourier series (Equation 1)
C_j	Momentum flux coefficient
C_l	Two-dimensional lift coefficient
C_L	Three-dimensional lift coefficient
C_p	Pressure coefficient
C_μ	Gross thrust coefficient
D_n	Coefficients in a Fourier series (Equation 1)
G	Leading-edge pressure gradient parameter
K_b	Part span flap factor
R_{e_o}	Reynolds number
x	Chordwise distance, fraction of chord
α	Angle of attack, rads.
α_{s_μ}	Power-on stall angle of attack, rads.
Δ	Denotes an incremental quantity
δ	Effective jet deflection angle, rads.
ε	Function of chordwise position, $x = \sin^2\varepsilon$
η	Efficiency factor
χ	Flap chord ratio

Subscripts:

max	Maximum
$C_\mu = 0$	Power-off conditions
μ	Power-on conditions

Special:

$\Delta C_{l_{max}}(C_\mu)$	Increment in two-dimensional maximum lift due to blowing
$\Delta C_{L_{max}}(C_\mu)$	Increment in three-dimensional maximum lift due to blowing
$\Delta C'_{L_{max}}(C_\mu)$	Increment in three-dimensional maximum lift due to blowing on full-span flaps

1. INTRODUCTION

In aircraft design determination of lift characteristics including maximum lift is required on different levels. For preliminary design a technique is desired which is simple to use. For detailed analysis more complexity can be accepted, usually computerized. In this paper both of these requirements are considered for jet-flap configurations. "Jet flap" is used as a generic term to cover various powered-lift concepts which use a jet of air to increase circulation lift. Some of these concepts are illustrated in Figure 1.

A theory of the "jet flap" was introduced many years ago and many attempts have been made to improve the details. This potential flow theory is unable to represent the maximum lift of jet flaps, however, for which no theory presently exists. Maximum lift is a viscous phenomenon, therefore calculation of the absolute level of lift requires consideration of boundary layer separation with the possible influences of jet-flap blowing. An accepted correlation technique is to assume that stall occurs at the leading edge. It is then possible to relate the power-on maximum lift to the power-off value. The technique used was first suggested by Foster (Reference 1) who compared the loading on the basic unflapped, unpowered airfoil with that on a jet-flapped airfoil. Methods are available to predict the unpowered lift characteristics of wings with leading-edge and trailing-edge flaps, it is felt, therefore, that the design requirement is for methods to predict the effects of power on a given configuration. That is the approach taken by the present author in this paper and also in Reference 2. The result given in Reference 2 for externally blown flap configurations is extended in this paper and it is also shown to apply to a variety of jet-flap concepts.

Spence's basic theory for jet flaps is a linear, small perturbation theory (Reference 3). It is found, however, that its range of applicability is greater than might be expected. In the present paper Spence's theory is assumed to apply to all "jet flap" concepts. The governing parameters are taken to be the effective trailing-edge momentum coefficient and the effective jet deflection angle. These parameters are defined by static power-on tests which give the direction of the resultant force and the efficiency factor (resultant force/unit thrust) as a function of flap deflection. The effective jet deflection angle is then given by the direction of the resultant force; the effective trailing-edge momentum coefficient is defined as the efficiency factor times the gross thrust coefficient. For design work these terms would not be known for a new configuration. Correlations of some typical results are given in an Appendix.

2. TWO-DIMENSIONAL THEORY

The development herein follows that of Foster (Reference 1) except that no initial approximations are made apart from the ones implicit in the basic jet-flap theory. Using linear theory the same result is obtained considering either the loading or the pressure gradient. In either case it is recognized that there are additional terms due to airfoil thickness, camber, etc. These terms are assumed to be independent of jet-flap blowing and do not affect the incremental values.

With the substitution $x = \sin^2\varepsilon$ Spence (Reference 3) gives the loading on a jet-flapped airfoil as

$$-\Delta C_p = \left(4\alpha + \frac{4\delta\chi}{\pi}\right)\cot\varepsilon + \frac{4\delta}{\pi}\log\left|\frac{\cos(\varepsilon + \chi/2)}{\cos(\varepsilon - \chi/2)}\right|$$

$$+ \frac{4}{\sin^3\varepsilon}\left[(\alpha B_o + \delta D_o)(1 - \cos\varepsilon) + \sum_{n=1}^{\infty}(\alpha B_n + \delta D_n)\left(\frac{1 - \cos\varepsilon}{1 + \cos\varepsilon}\right)^n\right] \qquad (1)$$

The first two terms represent the power-off loading. Differentiating these terms with respect to chordwise station, x, gives the power-off pressure gradient,

$$\left(\frac{\partial Cp}{\partial x}\right)_{C_\mu = o} = \frac{1}{\sin^3\varepsilon\cos\varepsilon}\left[\left(2\alpha + \frac{2\delta\chi}{\pi}\right) + \frac{4\delta\sin^2\varepsilon}{2\pi}\left(\frac{\sin(\varepsilon + \chi/2)}{\cos(\varepsilon + \chi/2)} - \frac{\sin(\varepsilon - \chi/2)}{\cos(\varepsilon - \chi/2)}\right)\right] \qquad (2)$$

Both the loading and the pressure gradient are infinite at the leading edge. In order to consider conditions in the vicinity of the leading edge, therefore, a parameter is required involving pressure gradient and chordwise distance to eliminate this singularity. This can be conveniently taken to be $\sin^3\varepsilon\cos\varepsilon\left(\frac{\partial Cp}{\partial x}\right)$ such that a leading-edge pressure gradient parameter, G, is defined as

$$G = \lim_{\varepsilon \to o}\left\{\sin^3\varepsilon\cos\varepsilon\left(\frac{\partial Cp}{\partial x}\right)\right\}$$

$$G_{C_\mu = o} = \lim_{\varepsilon \to o}\left\{2\alpha + \frac{2\delta\chi}{\pi} + \frac{2\delta\sin^3\varepsilon}{\pi}\left[\frac{\sin(\varepsilon + \chi/2)}{\cos(\varepsilon + \chi/2)} - \frac{\sin(\varepsilon - \chi/2)}{\cos(\varepsilon - \chi/2)}\right]\right\}$$

$$G_{C_\mu = o} = 2\alpha + \frac{2\delta\chi}{\pi} \qquad (3)$$

Substituting the expression $C_l = 2\pi\alpha + 4\delta\chi$ into Equation (3) yields

$$G_{C_\mu = o} = \frac{1}{\pi}\left(C_l - 2\delta\chi\right) \tag{4}$$

It is assumed that stall occurs at some particular value of G, i.e., G_{max}, such that

$$G_{\substack{max \\ C_\mu = o}} = \frac{1}{\pi}\left(C_{l_{\substack{max \\ C_\mu = o}}} - 2\delta\chi\right) \tag{5}$$

From Equation (1) the additional pressure gradient terms due to power are:

$$-\Delta C_p = \frac{4}{\sin^3\epsilon}\left[(\alpha B_o + \delta D_o)(1 - \cos\epsilon) + \sum_{n=1}^{\infty}(\alpha B_n + \delta D_n)\left(\frac{1 - \cos\epsilon}{1 + \cos\epsilon}\right)^n\right] \tag{6}$$

Differentiating term by term with respect to x, and evaluating the leading-edge pressure gradient parameter gives

$$\Delta G = (\alpha B_o + \delta D_o) + \left(\frac{\alpha B_1 + \delta D_1}{2}\right) \tag{7}$$

and all subsequent terms in the Fourier series tend to zero as ϵ tends to zero.

Adding Equations (4) and (7) the full leading-edge pressure gradient parameter is obtained for the power-on conditions in terms of the lift coefficient as

$$G_\mu = \frac{1}{\pi}\left[C_l - 2\chi\delta - 3\pi\,(\alpha B_o + \delta D_o) + \frac{\pi}{2}\,(\alpha B_1 + \delta D_1)\right]$$

Stall is again assumed to occur at a particular value of the pressure gradient parameter and at the power-on stall angle of attack, then

$$G_{\substack{max \\ \mu}} = \frac{1}{\pi}\left[C_{l_{\substack{max \\ \mu}}} - 2\chi\delta - 3\pi\,(\alpha_{S_\mu} B_o + \delta D_o) + \frac{\pi}{2}\,(\alpha_{S_\mu} B_1 + \delta D_1)\right] \tag{8}$$

Since it is assumed that power-on stall occurs at the same value of pressure gradient as power-off stall, then

$$G_{\substack{max \\ C_\mu = o}} = G_{\substack{max \\ \mu}}$$

and $C_{l_{\substack{max \\ C_\mu = o}}} - 2\chi\delta = C_{l_{\substack{max \\ \mu}}} - 2\chi\delta - 3\pi\,(\alpha_{S_\mu} B_o + \delta D_o) + \frac{\pi}{2}\,(\alpha_{S_\mu} B_1 + \delta D_1)$

Thus,

$$\Delta C_{l_{max}}(C_\mu) = 3\pi\,(\alpha_{S_\mu} B_o + \delta D_o) - \frac{\pi}{2}\,(\alpha_{S_\mu} B_1 + \delta D_1) \tag{9}$$

Equation (9) indicates that the increment in maximum lift due to blowing is a function of four Fourier coefficients, the effective jet flap deflection angle, and the power-on stall angle of attack. It is more useful, however, to relate this expression to the power-off stall angle of attack. The required relationship is obtained from the idealized stall characteristics shown in Figure 2. Thus

$$\alpha_{S_o} - \alpha_{S_\mu} = \frac{\Delta C_l(\alpha_{S_\mu}) - \Delta C_{l_{max}}(C_\mu)}{C_{l_{\alpha_{C_\mu = o}}}}$$

which gives

$$\alpha_{S_\mu} = \frac{\alpha_{S_o}}{1 + \frac{B_o}{2} + \frac{B_1}{4}} - \frac{(2D_o + D_1)\delta}{(4 + 2B_o + B_1)} \tag{10}$$

This result is now substituted into Equation (9) to give the final result

$$\Delta C_{l_{max}}(C_\mu) = \frac{3\pi}{1 + \frac{B_o}{2} + \frac{B_1}{4}}\left[\alpha_{S_o}\left(B_o - \frac{B_1}{6}\right) + \delta\left(D_o + \frac{D_o B_1}{3} - \frac{B_o D_1}{3} - \frac{D_1}{6}\right)\right] \tag{11}$$

This equation may be compared with previous work (References 1 and 2) which neglected all Fourier coefficients except B_o and D_o. Reference 2 gave the result:

$$\Delta C_{l_{max}}(C_\mu) = \frac{3\pi}{1 + \frac{B_o}{2}}\left[B_o\,\alpha_{S_o} + D_o\,\delta\right] \tag{12}$$

Thus, the exact theoretical expression contains two additional coefficients, the effect of which is to reduce the predicted value of the maximum lift increment.

Figure 3 shows a comparison of values predicted using the approximate Equation (12) with measured values from Reference 4. The agreement is poor and it can be seen that the theory considerably under-predicts the measured values. Qualitatively, the additional terms in Equation (11) reduce the predicted values by approximately 15% worsening the comparison shown in Figure 3. Thus, at this point there is a theoretical expression based on a leading-edge stall which shows poor agreement with experiment. In practice, also, leading-edge devices would probably be used to suppress leading-edge stall which tends to violate the basic assumption. Two alternatives are available - to attempt an empirical correlation or to examine different theoretical approaches. A correlation of three-dimensional results has been achieved based on the approximate Equation (12) (Section 3). Section 4 is a very preliminary consideration of a different theoretical approach.

3. THREE-DIMENSIONAL LIFT COEFFICIENT

The application of the two-dimensional theory to three-dimensional wings is subject to interpretation whether the full or the approximate expression is used. Reference 1 implied that the increment in three-dimensional maximum lift is equal to the increment in two-dimensional maximum lift, a result which assumes an elliptical lift distribution with the two-dimensional increment in maximum lift being achieved at each spanwise station, and

$$\Delta C'_{L_{max}}(C_\mu) = \Delta C_{l_{max}}(C_\mu) \qquad (13(a))$$

Reference 2 postulated that, at least for externally blown flaps, the effect of power is to cause a departure from an elliptical lift distribution. The result indicated by Equation (13(a)) therefore cannot be achieved; rather it requires a correction for three-dimensional effects - a premise now used for all jet-flap concepts. One approach could be an empirical correlation of experimental data using an assumed form of correction factor. Reference 5 developed a correction for three-dimensional effects using a lifting line theory which is not convenient for design work. Maskell and Spence (Reference 6) developed a factor to correct two-dimensional lift for finite aspect ratio, assuming an elliptical lift distribution. As a convenience, this factor was applied to the increment in lift at a particular power coefficient by the present author (Reference 2) and this approach is continued here. The three-dimensional increment in maximum lift is given by

$$\Delta C'_{L_{max}}(C_\mu) = \Delta C_{l_{max}}(C_\mu)\left[\frac{A\!\!\!/R + 0.637\,C_j}{A\!\!\!/R + 2 + 0.604\sqrt{C_j} + 0.876\,C_j}\right] \qquad (13(b))$$

Using Equation (12) increments in maximum lift coefficient predicted by both Equations (13(a) and 13(b) were compared with measured maximum lift increments for rectangular wings of different aspect ratios with full-span pure jet flaps (References 7 and 8). Figure 4 indicates that both approaches significantly underestimate the measured increments. There is an effect of aspect ratio on the measured increments in maximum lift, Equation 13(b) does indeed collapse values for different aspect ratios close to a straight line. This result is supported especially by the results for the configuration with endplates which change only the effective aspect ratio. The conclusion is that the increase in maximum lift due to blowing is a three-dimensional phenomenon and the semi-empirical correction factor of Equation 13(b) adequately represents this phenomenon - at least for aspect ratios greater than three.

Contrary to "normal" expectations the measured results show considerably higher increments in maximum lift due to blowing than are predicted. The results tend to collapse the total results to a single straight line, however, therefore a simple multiplier can thus be used to match the theoretical values to the measured results. With this multiplier the empirical expression for the increment in three-dimensional maximum lift coefficient due to blowing becomes

$$\Delta C'_{L_{max}}(C_\mu) = 5.5\pi\left[\frac{B_o\alpha_{S_\mu} + D_o\delta}{1 + \frac{B_o}{2}}\right]\left[\frac{A\!\!\!/R + 0.637C_j}{A\!\!\!/R + 2 + 0.604\sqrt{C_j} + 0.876\,C_j}\right] \qquad (14)$$

One more factor to be accounted for is the effect of part-span blowing, which includes configurations with discrete blowing such as externally blown flaps. It is assumed that the span of the physical flap is the governing parameter, which is accounted for using the unpowered part-span flap factor defined in Reference 9, and reproduced in Appendix A. This factor is further assumed to apply only to the circulation portion of the lift and not to the direct thrust component which is $C_j(\alpha + \delta)$ in Spence's theory. Thus Equation (14) defines the lift increment for a full-span flap, $\Delta C_{L_{max}}(C_\mu)$, and the increment in maximum lift for the part-span flap is defined by

$$\Delta C_{L_{max}}(C_\mu) = K_b\left[\Delta C'_{L_{max}}(C_\mu) - C_j(\alpha_{S_o} + \delta)\right] + C_j(\alpha_{S_o} + \delta) \qquad (15)$$

The effect of this part-span flap correction is illustrated in Figure 5 by comparing to test results from both externally blown flaps (Reference 10) and pure jet flaps (References 7 and 11). This figure demonstrates that Equation (15) provides excellent correlation of the part-span flap effects for two seemingly very different configurations. Also it shows excellent agreement with the magnitude of the maximum lift increments produced by the empirical factor introduced in Equation (14).

In Equation (15), the power-on stall angle of attack, α_{S_μ}, should be used and the last term should therefore be $C_j \sin(\alpha_{S_\mu} + \delta)$ to remove the small angle approximation. With the empiricism already introduced, however, the approximations used to develop Equation (15) are felt to be justified.

Equations (14) and (15) combine to form a unique prediction technique. Figure 6 shows the results of applying this technique to a variety of different jet-flap concepts (References 7,8, 10-16). Excellent agreement is shown between the predicted and measured values, demonstrating the effectiveness of the technique in predicting the increment in maximum lift coefficient developed by powered-lift systems. Although the theory is based on the assumption of a leading-edge stall, the final correlation does not depend on this and applies to configurations both with or without leading-edge devices. The final result is also independent of sweep angle.

4. INFLUENCE OF JET-FLAP BLOWING ON BOUNDARY LAYER SEPARATION

The correlation technique that has been presented is adequate for preliminary design analysis. A more rigorous analysis of jet-flap maximum lift characteristics will probably require consideration of boundary layer separation. A first question is whether the separation mechanism is affected by jet-flap blowing - addressed by considering separation criteria. One well-known criterion is the one by Stratford (Reference 17) which is expressed as

$$C_p \left(x \frac{\partial C_p}{\partial x} \right)^{1/2} \left(10^6 R_{e_0} \right)^{-1/10} \geq 0.39 \qquad (16)$$

i.e., separation is present when the left hand side of the above equation is equal to or exceeds 0.39.

Reference 4 presents measured pressure distributions at a particular angle of attack; Stratford's criterion has been assessed for these distributions. For the power-off data, the left hand side of Equation (16) is always less than 0.39 indicating that there should be no separation. This is confirmed by the lift data. For the power-on data, the angle of attack is very close to the stall angle of attack and the left hand side of Equation (16) exceeds 0.39 very close to the leading edge, thereby indicating separated flow. The existence of separation before maximum lift is reached is also in qualitative agreement with the description of stalling characteristics given in Reference 4. Thus, preliminary results indicate the possibility of using conventional separation criteria to predict the boundary layer separation of jet flap configurations.

5. CONCLUSIONS

A theoretical expression for the increment in maximum lift due to blowing on jet-flapped airfoils was obtained that was based on the assumption of a leading-edge stall. Comparisons with measured two-dimensional results show poor correlation. For practical application a three-dimensional theory is required, therefore with suitable corrections for finite-aspect-ratio and part-span flaps, an expression was developed for the three-dimensional maximum lift increment due to blowing at a constant flap deflection. This expression shows excellent agreement with measured results for pure jet flaps, internally blown flaps, externally blown flaps and upper surface blown flaps. The results are also independent of the actual presence of a leading-edge stall, independent of the sweep angle and applicable to aspect ratios greater than approximately three.

Preliminary results indicate that the Stratford criterion for boundary layer separation is also applicable to jet-flapped configurations. It is assumed that this approach would be combined with sophisticated techniques for computing the pressure distribution.

REFERENCES

1. Perry, D. H., "A Review of Some Published Data on the External-Flow Jet-Augmented Flap" (with Appendix by D. N. Foster), RAE TR 70240, 1970.

2. Moorhouse, D. J., "A Practical Look at the Stall and High Lift Operation of Externally Blown Flap STOL Transport Configurations", Conference on Fluid Dynamics of Aircraft Stalling, Lisbon, Portugal, April 1972.

3. Spence, D. A., "The Lift on a Thin Aerofoil with a Jet-Augmented Flap", Ae. Quart., Vol. 9, August 1958.

4. Hynes, C. S., "The Lift, Stalling and Wake Characteristics of a Jet-Flapped Airfoil in a Two-Dimensional Channel", Stanford University Report, SUDAAR No. 363, November 1968.

5. Hebert, J., Jr., et al, "STOL Tactical Aircraft Investigation", Vol. II, Design Compendium, AFFDL-TR-73-21-Vol II, May 1973.

6. Maskell, E. C., and Spence, D. A., "A Theory of the Jet-Flap in Three Dimensions", Proc. Roy. Soc., A, Vol. 251, pp 407-425, 1959.

7. Gainer, T. G., "Low-Speed Wind-Tunnel Investigation to Determine the Aerodynamic Characteristics of a Rectangular Wing Equipped with a Full-Span and an Inboard Half-Span Jet-Augmented Flap Deflected 55°", NASA Memo 1-27-59L, February 1959.

8. Lowry, J. G., and Vogler, R. D., "Wind Tunnel Investigation at Low Speeds to Determine the Effect of Aspect Ratio and End Plates on a Rectangular Wing with Jet Flaps Deflected 85°", NACA TN 3863.

9. Lowry, J. G., and Polhamus, E. C., "A Method for Predicting Lift Increment Due to Flap Deflection at Low Angles of Attack in Incompressible Flow", NACA TN 3911, 1957.

10. Fink, M. P., "Aerodynamic Characteristics, Temperature, and Noise Measurements of a Large-Scale External-Flow Jet-Augmented-Flap Model with Turbojet Engines Operating", NASA TN D-943, September 1961.

11. Otis, J. H., Jr., "Low-Speed Wind-Tunnel Investigation of a Reflection Plane Wing Model Equipped with Partial-Span Jet-Augmented Flaps", NASA TN D-815.

12. Parlett, L. P., and J. P. Shivers, "Wind Tunnel Investigation of a STOL Aircraft Configuration Equipped with an External-Flow Jet Flap", NASA TN D-5364, August 1969.

13. Freeman, D. C., Jr., Grafton, S. B., and D'Amato, R., "Static and Dynamic Stability Derivatives of a Model of a Jet Transport Equipped with External-Flow Jet-Augmented Flaps", NASA TN D-5408, September 1969.

14. Parlett, L. P., Freeman, D. C., Jr., and Smith, C. C., Jr., "Wind-Tunnel Investigation of a Jet Transport Airplane Configuration with High Thrust-Weight Ratio and an External-Flow Jet Flap", NASA TN D-6058, November 1970.

15. Vogler, R. D., "Wind-Tunnel Investigation of a Four Engine Externally-Blowing Jet-Flap STOL Airplane Model", NASA TN D-7034, December 1970.

16. Phelps, A. E., Letko, W., and Henderson, R. L., "Preliminary Low-Speed Wind-Tunnel Investigation of a Semispan STOL Jet Transport Wing with an Upper-Surface Blown Jet Flap", NASA TN D-7183, January 1972.

17. Stratford, B. S., "The Prediction of Separation of the Turbulent Boundary Layer", J. Fluid Mechanics, Vol. 5, pp 1-16, 1959.

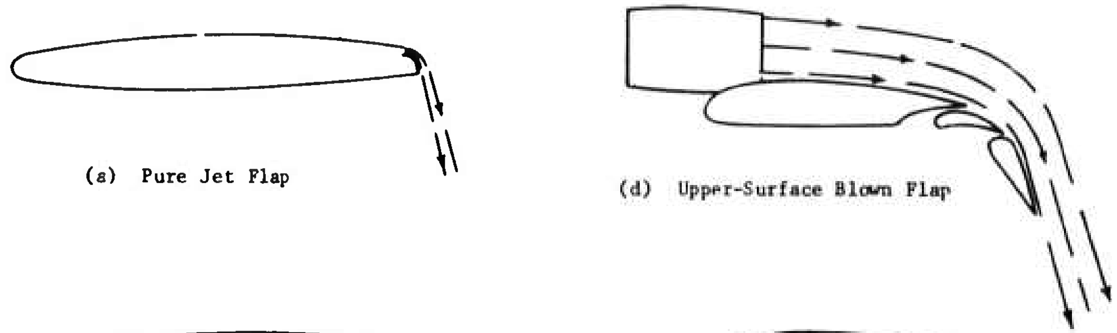

(a) Pure Jet Flap

(d) Upper-Surface Blown Flap

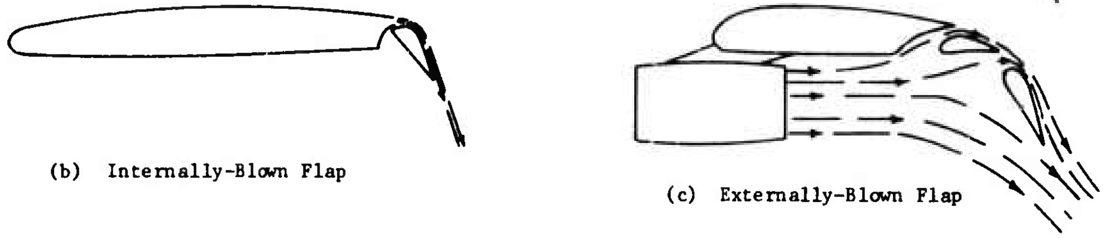

(b) Internally-Blown Flap

(c) Externally-Blown Flap

FIGURE 1 SKETCH OF JET FLAP CONCEPTS

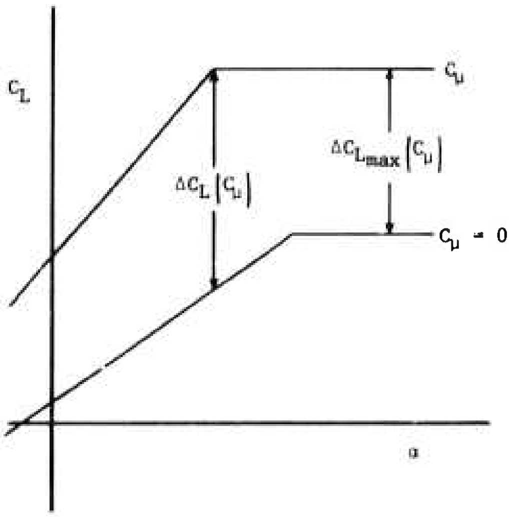

FIGURE 2 IDEALIZED SKETCH OF STALL CHARACTERISTICS

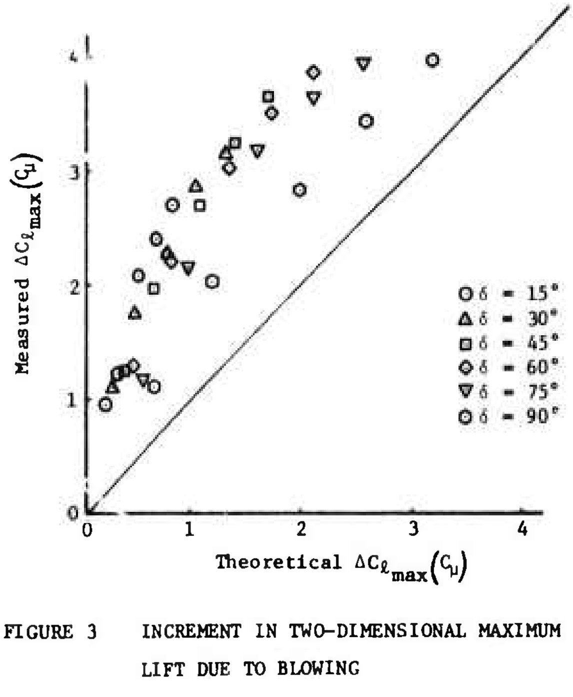

FIGURE 3 INCREMENT IN TWO-DIMENSIONAL MAXIMUM LIFT DUE TO BLOWING

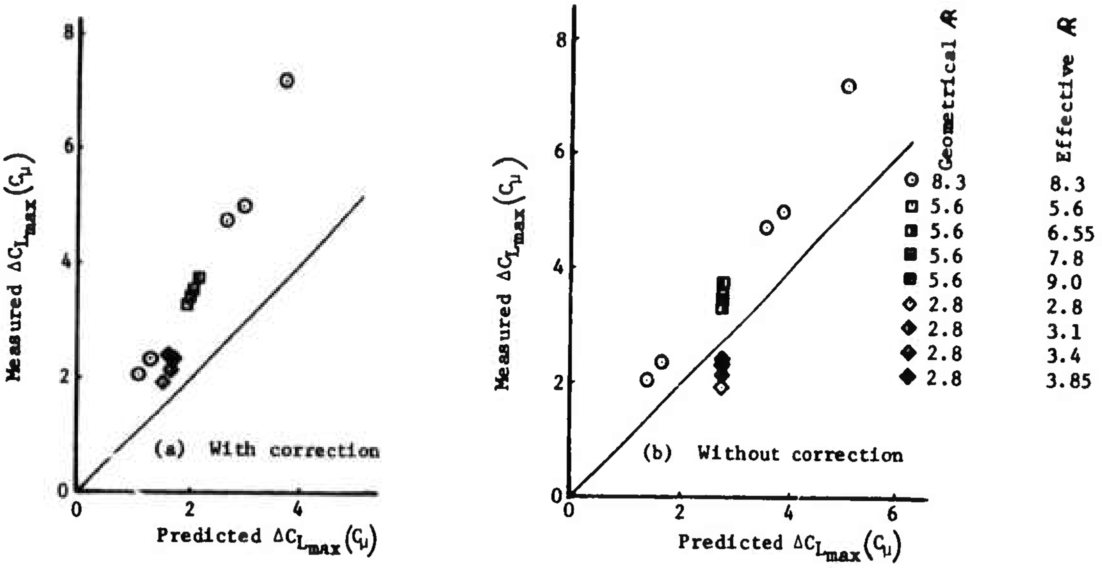

FIGURE 4 EFFECT OF ASPECT RATIO CORRECTION

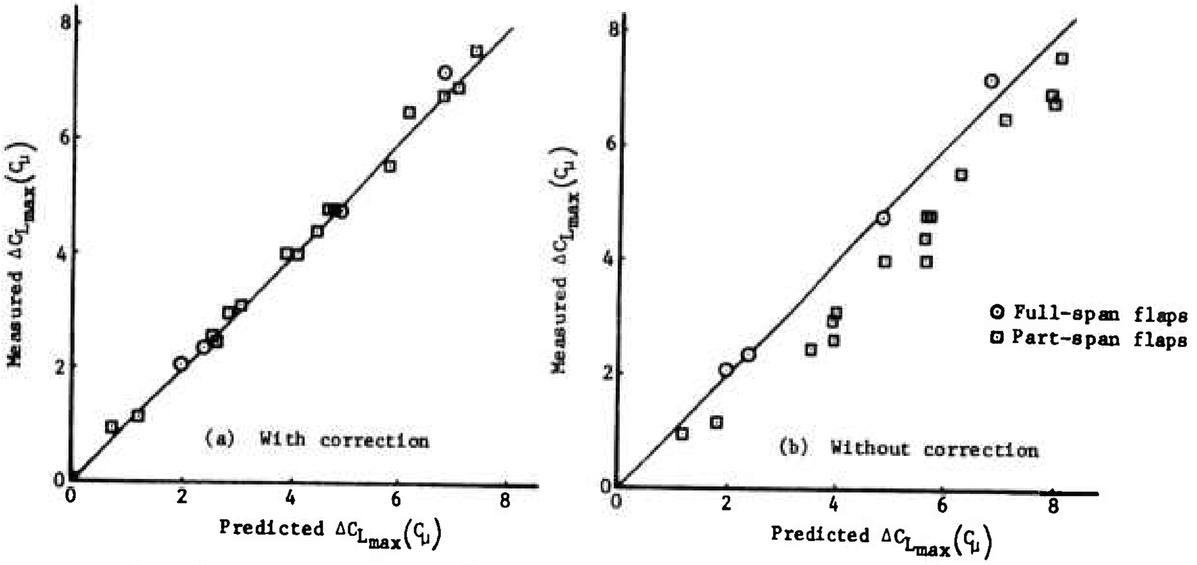

FIGURE 5 EFFECT OF PART-SPAN FLAP FACTOR

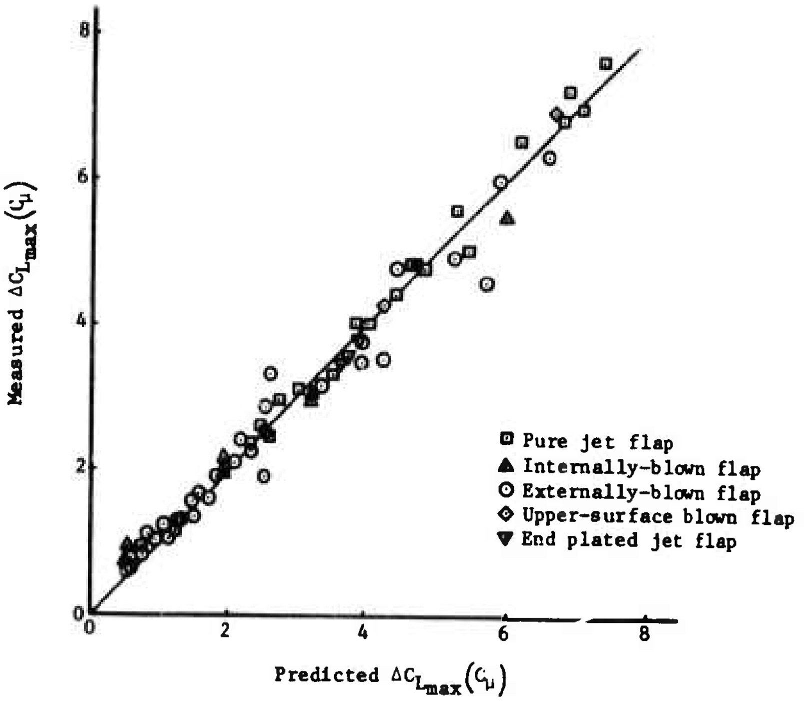

FIGURE 6 INCREMENT IN MAXIMUM LIFT DUE TO BLOWING

APPENDIX A

PARAMETERS REQUIRED TO CALCULATE MAXIMUM LIFT

The prediction method presented in this paper contains two parameters, the efficiency factor and the effective jet deflection angle, which are functions of the configuration. Values for these parameters would not be known for a new configuration. For completeness, this Appendix presents correlations of measured values of these parameters suitable for preliminary design work. Figure A.1 presents typical values of the efficiency factor for each of the powered lift concepts under consideration, taken from References A1, 7, 8 and 16. The efficiency factor of externally blown flap and upper-surface blown flap configurations is based on gross engine thrust. For pure jet flap and internally blown flap configurations the engine air is ducted through the wing, with resulting losses. The efficiency factor of the pure jet flap is unity based on the momentum flux coefficient available at the wing trailing edge. The efficiency factor of the internally blown flap is similarly based on the momentum flux coefficient at the knee of the flap. Figure A.2 presents a correlation of effective jet deflection angle for externally blown flap configurations (Reference A.1). For practical internally blown and upper surface blown flap configurations the effective jet deflection angle can be taken to be the angle of the upper surface of the flap.

Other required parameters are published in the literature but are reproduced here for convenience. Figure A.3 presents Spence's Fourier coefficients B_0 and D_0 (Reference 3). Figure A.4 presents the part span flap factor, K_b, Reference 9.

REFERENCE

A.1 May, F. and Widdison, C. A., "STOL High Lift Design Study", Volume 1, AFFDL-TR-71-26-Vol 1, April 1971.

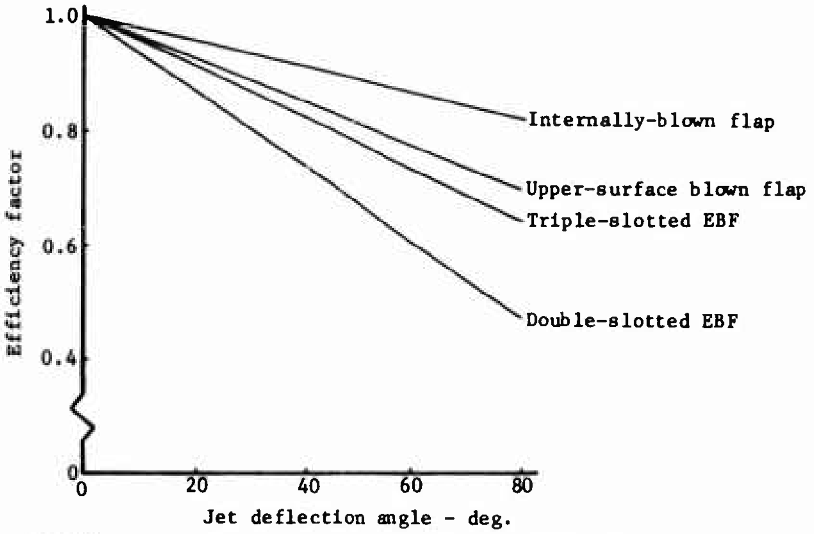

FIGURE A.1 CORRELATION OF JET FLAP EFFICIENCY FACTOR

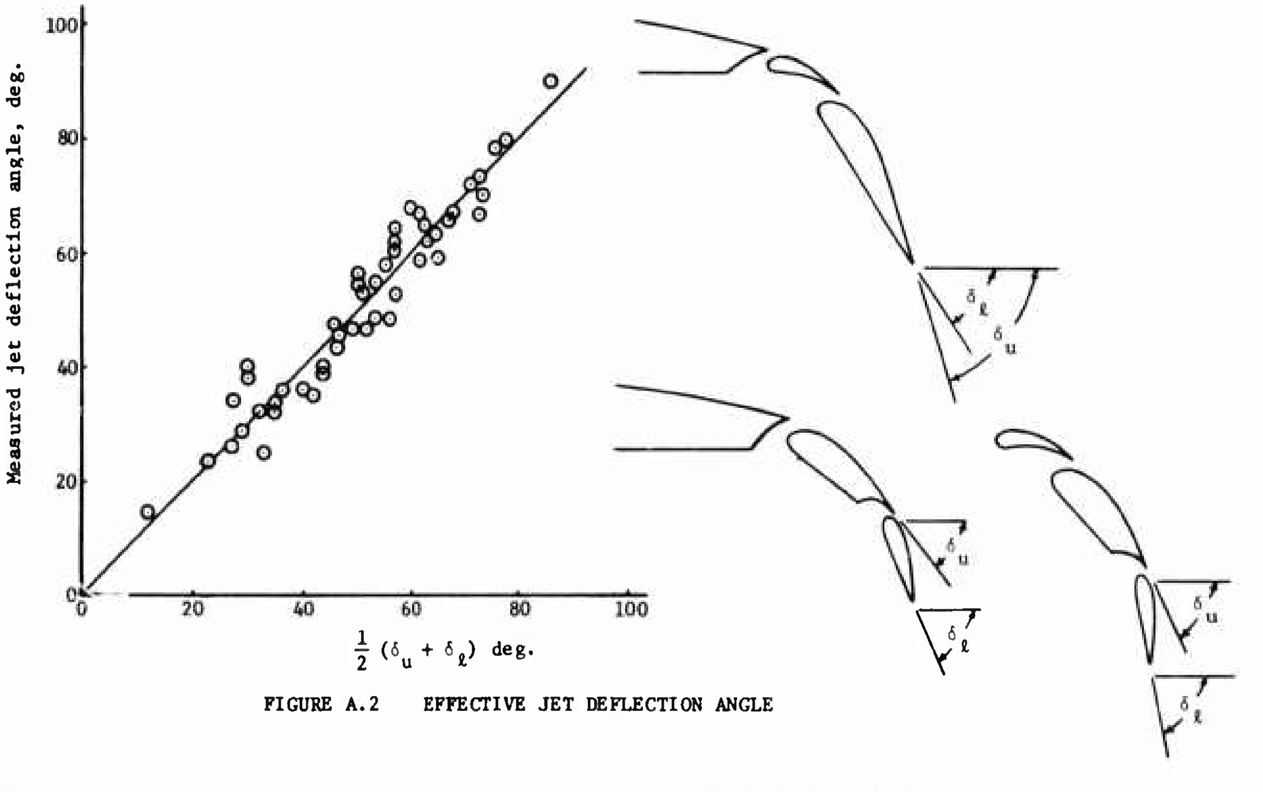

FIGURE A.2 EFFECTIVE JET DEFLECTION ANGLE

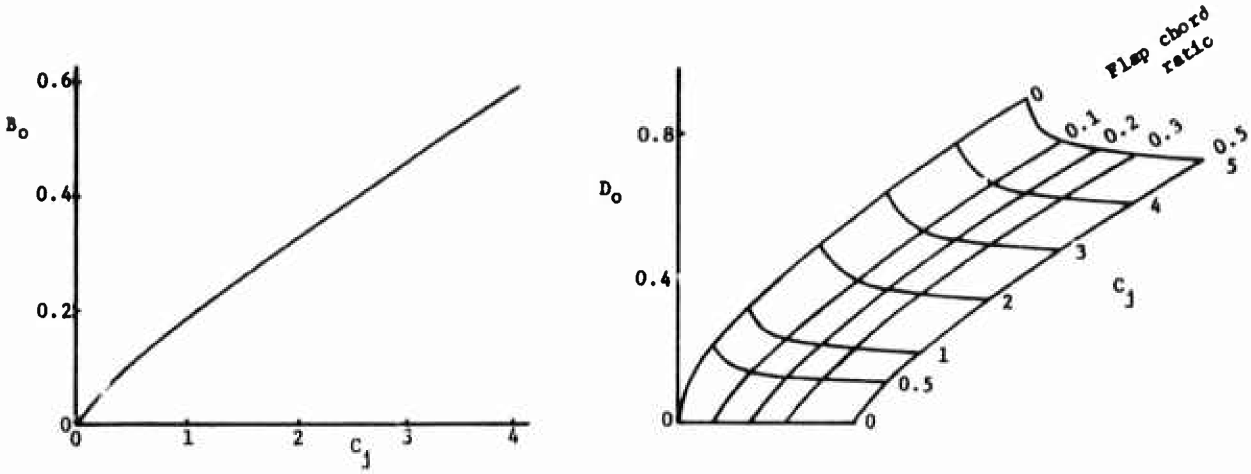

FIGURE A.3 FOURIER COEFFICIENTS

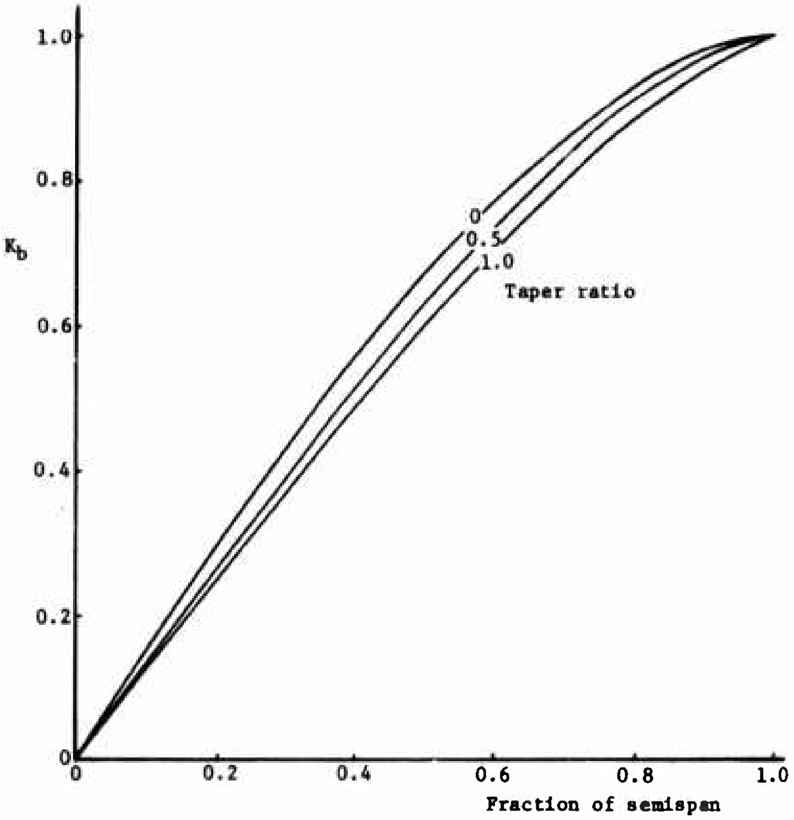

FIGURE A.4 PART SPAN FLAP FACTOR

WIND TUNNEL INVESTIGATION OF THREE POWERED-LIFT STOL CONCEPTS

R. F. Osborn
and
G. S. Oates
Air Force Flight Dynamics Laboratory
Wright-Patterson AFB, Ohio 45433, USA

SUMMARY

The results of a comprehensive, parametric wind tunnel investigation of three STOL concepts; the externally blown jet flap (EBF), internally blown jet flap (IBF) and the mechanical flap/vectored thrust (MF/VT) are presented. Wind tunnel model characteristics are shown along with details of the high lift devices tested.

The effect of engine location is discussed and is shown to be the dominant factor in EBF and MF/VT powered lift performance. Wing sweep and aspect ratio effects on lifting performance are also addressed.

Performance in ground effect is briefly discussed, utilizing the test data collected. Incremental changes in the lift, drag and pitching moment characteristics resulting from in-ground effect operation are explained.

Finally, a comparison of the aerodynamic performance of the three powered lift systems is made and future research topics suggested.

NOTATION

AR	Aspect ratio, b^2/s
b	Wing span
C	Wing chord
C_D	Drag coefficient
C_j	Thrust coefficient
C_L	Lift coefficient
C_μ	Boundary layer control momentum coefficient
C_m	Pitching moment coefficient
D_j	Jet engine nozzle diameter
DSF	Double slotted flap
h	Height of wing above ground plane
h/b	Wing height to span ratio
R	Radius of jet plume at flap trailing edge
S	Wing area
SSF	Single slotted flap
TSF	Triple slotted flap
Z_F	Distance flap trailing edge extends into jet plume perpendicular to engine centerline
α	Angle of attack
δ	Deflection angle
δ_{LE}	Leading edge deflection
δ_f	Flap deflection
δ_j	Jet deflection
ϕ	Effective jet turning angle
$\Lambda_{C/4}$	Quarter chord sweep

INTRODUCTION

In planning documents issued in late 1969 and early 1970 the United States Air Force (USAF) identified the mission area of tactical airlift as becoming increasingly critical. Largely due to the increased attrition rate of the USAF tactical transport inventory, Tactical Air Command (TAC) had substantiated requirements for new transport aircraft. A portion of these requirements was replacement of C-123 and C-7 aircraft that, for various reasons, were no longer available. Additionally, the workhorse C-130 fleet was becoming increasing aged, and a future replacement for this aircraft was required.

The principal need in accomplishing tactical airlift mission responsibilities is the capability to provide responsive and reliable airlift support during both assault and logistic operations. This can be accomplished under the widest possible set of conditions by having a tactical airlift capability with minimum dependence on prepared airfields. A short takeoff and landing (STOL) aircraft can provide this operational independence and, if turbofan-configured, can provide the rapid response (high subsonic cruise speed) desired.

With these requirements in mind, the Air Force Flight Dynamics Laboratory (AFFDL) began the formulation of a technology program with the objective of obtaining extensive parametric design data for the most promising STOL concepts. For many years, various schemes to obtain high lift coefficients for takeoff and landing operations have been pursued. The objectives of these programs, for the most part, have been to explore the general areas of performance and stability and control, with emphasis on finding solutions to configuration-oriented problems, with the result that the overall feasibility of the concept has proven difficult to assess.

By 1971 a number of high lift concepts had been proposed and investigated to some extent, as appropriate for incorporation on a Medium STOL Transport (MST). These included externally blown flaps (EBF), internally blown flaps (IBF), mechanical flaps (MF), mechanical flaps with vectored thrust (MF/VT), deflected slipstream, direct jet or fan lift, tilt wing and boundary layer control (BLC) devices. Of these concepts, the tilt wing and the deflected slipstream were configured with propellers and cross-shafting systems, examples being the Brequet 940 and 941, the Ling Temco Vought XC-142, the Canadair CX-84 and the Shin Meiwa PS-1 (not cross-shafted). Due to a preference for turbofan propulsion and the relatively low cruising speeds associated with propeller concepts, these were dropped from consideration as candidates for the future USAF MST. An analysis of the state-of-the-art and of the relative progress of technology in the area of purely mechanical high lift devices indicated that useable lift coefficients on the order of 2.5 (maximum lift coefficients of about 4.0) were the approximate limit of capability. However, if the mechanical flap is combined with vectored thrust, the useable lift can be approximately doubled. Investigation of the technological status of the IBF concept revealed that considerable effort was being expended on the augmentor wing (a very specific type of IBF system) and that in view of the limited funds, coupled with the National Aeronautic and Space Administration's (NASA) rather extensive augmentor wing program, the AFFDL would concentrate on non-augmentor wing IBF concepts. The three concepts that were finally selected for generalized analyses as having the highest potential for application to the MST were:

1. MF/VT - This system has normal force components due to conventional wing lift and engine thrust vectoring independent of the wing lifting system.

2. IBF - This system has normal force components due to conventional wing lift, vectored thrust and augmented wing lift via high energy blowing over the extended flap through a duct system internal to the wing.

3. EBF - This system has normal force components due to conventional wing lift, deflected thrust and augmented wing lift via high energy external blowing through the extended flap system.

It should also be pointed out that since this concept selection was made, another configuration holding high promise has surfaced, i.e., upper surface blowing (USB). This concept is actually another variation of the EBF concept, but it does possess significant differences which require separate investigation. In this concept, engine exhaust air travels over the upper surface of the wing until turned, in a Coanda fashion, over the deflected large radius flap. The concept is now being employed on one of the USAF Advanced Medium STOL Transport (AMST) prototypes, but it was not generally known in 1971 and was not investigated in the AFFDL STOL technology program.

The STOL Tactical Aircraft Investigation (STAI) program initiated by the AFFDL in mid-1971 consisted of configuration design [1,2,3], prediction technique development[4,5,6,7], establishment of STOL criteria, wind tunnel testing[8,9,10], ground-based flight simulation and flight control technology development.

The contracting plan for the program was that each of the three concepts would be investigated by two different contractors. This allowed for better coverage of each concept and assisted the AFFDL in tracking the overall program. The contract definition phase then resulted in an award to General Dynamics/Convair (San Diego) to investigate all three concepts; a contract to Boeing to investigate the MF/VT and IBF; and a contract to Rockwell International (Los Angeles Aircraft Division) to investigate the EBF. Since the purpose of this paper is to discuss the wind tunnel results only, further discussion will now be limited to that area of the AFFDL STOL technology program.

This portion of the overall effort involved extensive small scale wind tunnel tests of each selected high lift concept. Slightly over 2300 hours of testing was conducted in three facilities: 728 hours in the Boeing/Vertol 20 x 20 ft V/STOL wind tunnel, 509 hours in the Lockheed-Georgia 16 x 23 ft V/STOL wind tunnel and 1087 hours in the Convair/San Diego 8 x 12 ft low speed wind tunnel. The primary objective of this effort was to extend STOL wind tunnel testing into new areas and to close the gaps in existing test data for the three high lift concepts. Gaps in the existing data and areas requiring new testing were identified through development of the design compendium and the baseline configuration study which were other efforts within the STOL technology program. The models used in the wind tunnel tests possessed a high degree of parametric flexibility which allowed significant variations in their general characteristics. A typical model is shown in Figure 1. Parametric data was generated in sufficient detail to allow an accurate assessment of each concept to be made for a given mission. The principal parameters varied were:

1. Wing sweep
2. Aspect ratio
3. Trailing edge flaps (span, deflection, slots, etc.)
4. Leading edge devices and boundary layer control (BLC)
5. Nacelle location and multi-engine nacelles
6. Thrust coefficient
7. Asymmetric thrust and engine orientation
8. Tail surfaces or downwash rake location

An area which was considered to be important was the effect of close proximity to the ground on the aerodynamic coefficients. To ensure that these effects were accurately accounted for it was necessary to conduct a portion of the wind tunnel tests in ground effect. This testing was conducted in the presence of a moving belt ground plane (in the Convair and Boeing/Vertol tunnels).

The majority of the data presented in this paper was collected during the Convair contracted effort. This data was chosen for presentation since Convair investigated all three high lift concepts and hence collected the most consistent set of data. In cases where Boeing or Rockwell International data is presented it will be carefully noted.

MODEL CHARACTERISTICS

Figure 2 is a schematic of the model components used in the GD test program. The test article is a 1/20-scale model of a typical 150,000 lb gross weight medium STOL transport with a wing span of 70 inches. An air carry-through sting mounting fixture was used to support the model in the upright position for free air testing and inverted for ground effect studies; the latter being accomplished with a moving belt ground plane that was lowered from above.

Some difficulties were experienced in constructing a model to accommodate the wing sweep range (between 12.5 and 35 degrees), and retain a good wing/body fairing. Compromises were required in this area, although subsequent testing indicated the fairings used did not result in any significant regions of flow separation. For the purpose of data reduction, it was assumed the non-optimum design affected each swept wing configuration by approximately the same amount and no specific corrections were applied. However, construction of a model for testing at one sweep with an optimized wing/body joint should result in some improvement in lifting performance.

High lift devices typical of those tested in the Convair and Boeing programs are shown in Figure 3. The Convair test matrix was the most comprehensive, incorporating alternate single, double, and triple slotted flap designs with segments of different proportions, and unblown and blown leading edge devices of 15 and 25 percent chord. Geometric details of the Convair leading edge systems are illustrated in Figure 4.

The alternate Boeing flap system, used for MF/VT testing, was a 33 percent chord triple slotted arrangement similar to the one that appears on that Company's 727 commercial aircraft. The same leading edge blowing boundary layer control device was used in both IBF and MF/VT testing. It should be mentioned here that the use of identical leading edge equipment in conjunction with flap systems of greatly different performance potential is not a recommended practice. Normally leading edge systems are specifically tailored to match flap performance, however, the number of geometric test variables already included in the STAI program was of such magnitude that time did not permit a comprehensive leading edge study. For this reason, leading edge testing was limited to blowing rate and flap deflection variations in the Boeing program.

Engine simulation is a subject where individual test organizations differ in opinion. Convair and Rockwell International selected ejector type engine simulators whereas Boeing chose direct internal ducting of air to the jet nozzle as shown in Figure 5. Neither type accurately models full scale engine effects. Ejector engines do not model the inlet flow field properly, producing inaccuracies in ram drag and aerodynamic interference measurements. The closed inlet system also requires data correction for aerodynamic interference and an analytical estimation of ram drag. Accurate simulation of both the inlet and exit flows can be achieved with a model fan engine of correct bypass ratio, but such hardware is expensive and funds were not included in the program for the purchase of this equipment. Both systems have been used successfully in previous powered lift test programs and proved completely adequate for this parametric investigation.

The wind tunnel models were fitted with accurate flow measuring devices in the engines and in the boundary layer control devices of the leading and trailing edges. Provisions were made to cut the air supply to individual engines simulators for engine-out testing without model disassembly.

Because of the importance of tail sizing in powered-lift aircraft design, measurements were made in the vicinity of the horizontal tail using specially constructed wake rakes (Figure 1). Rakes on the Boeing and Convair models were adjustable in all three planes.

HIGH LIFT SYSTEM

Leading edge devices are an integral part of the overall high lift system selected for any aircraft. Ingenius aerodynamic/mechanical designs in this area have produced lift improvements of significant proportions in recent years. An example of this is the variable-camber leading edge device used on the Boeing 747 which increased the maximum lift coefficient an increment of 0.3 above more conventional shaped devices. Additional improvement in leading edge performance is promised with the implementation of blowing boundary layer control if mechanical and air delivery problems are successfully resolved.

Figure 6 illustrates the performance characteristics of a 15 percent chord leading edge device with and without blowing boundary layer control. In this particular case, the BLC system produces a 12 percent increase in maximum lift coefficient, and it occurs at a higher angle of attack than with the unpowered system. Perhaps more importantly, BLC smoothes the stalling characteristics, a significant factor in STOL operation. The test data shown were taken with the Convair model equipped with the leading edge devices of Figure 4. BLC slot width varied from .007 inches at the root to .003 inches at the wing tip. The slot was continuous with no spanwise interruptions. Figure 7 illustrates what happens when spanwise breaks are incorporated into the model to simulate actual full scale vehicle construction breaks. Slot breaks of .375 inches built into the Boeing model cause the degradation in lifting performance shown when compared with the .04 inch break test data acquired later in the program. These findings once again illustrate the importance of duplicating full scale aircraft characteristics during wind tunnel testing.

A comparison of single, double and triple slotted flap performance for the EBF configuration is shown in Figure 8. These data were obtained with engines located in the high forward position operating at a thrust coefficient of 2.0. Examination of the lift levels indicates the unsuitability of single slotted flaps for externally blown flap powered-lift applications. The triple slotted versus double slotted flap lift increment is due primarily to differences in extended chord length.

PLANFORM CHARACTERISTICS

Sweep, aspect ratio and flap span effects were the planform characteristics investigated which produced the most significant impact on aerodynamic performance. Of the three, wing sweep produces the most adverse effect on lifting performance. Figure 9 indicates a maximum lift decrement of approximately 10 percent is incurred by increasing the wing sweep from 12.5 to 35 degrees. Also affected is the lift curve slope which decreases with increasing sweep. Changes in aspect ratio do not produce the increment in lifting performance found with sweep variation either power-off or power-on. In fact, varying the aspect ratio 10 percent above or below a nominal value of eight shows only a minor impact on lifting performance.

The influence of flap span on lifting performance power-off is given in Figure 10. Lift loss due to aileron span varies between 5 and 10 percent depending on the overall lift level. Some STOL transport designs being studied incorporate ailerons with lengths greater than 25 percent of the wing span, which would result in further lift loss. To counteract these performance degradations, aircraft designers are attempting to incorporate slotted flaperon lateral control systems on the latest STOL aircraft designs. Implementation of this type of system does, however, require the solution of some rather complex mechanization problems.

Review of the planform data suggests that for good low speed performance a medium STOL transport should be configured with a straight wing and a full span flap system (flaperon lateral control). The effect of low sweep on cruise performance can be somewhat alleviated by the use of supercritical airfoil sections in the wing.

Having established basic lifting system performance levels and planform influences, attention will now be focused on pertinent aerodynamic test results related to powered-lift configuration selection.

EXTERNALLY BLOWN FLAP PERFORMANCE

The externally blown flap powered-lift concept has been the subject of many aerodynamic tests in recent years and is considered to be a prime candidate for use on future USAF transport aircraft. In fact, this concept is being applied on the McDonnell Douglas advanced medium STOL transport prototype presently being developed under Air Force sponsorship.

Aerodynamic performance of the EBF concept is a function of turning efficiency, which in turn is basically a function of flap geometry and engine location. Starting with a good flap design, configured to handle high velocity engine exhaust flows, the major parameter the designer is required to optimize is engine location. During the optimization process, cruise aerodynamics and thrust reverser operation must also receive attention. Before proceeding with the discussion on engine location and wing geometric effects, a brief comment on flap system development is necessary.

Flap development was not a primary subject of this test program. Participants were asked to select representative flap systems for use on their models based on the results of analysis and available test data. Both Convair and Rockwell International tested several flap designs with different gap/overlap geometry. The testing was accomplished during the first days of tunnel occupancy to determine performance levels, and could not be classified as optimization since flap segment geometries were not altered. This is not to say that future EBF flap research is unnecessary, in fact, quite the contrary is true; additional design and testing will result in better flow turning characteristics and improved efficiencies. It should be noted here that the Convair and Rockwell International designs have demonstrated turning efficiencies comparable to the better externally blown flap systems for which test data are available.

The primary engine location factor affecting EBF performance is position in the chordwise/vertical plane. Figure 11, a composite of Convair data, shows the effect of varying engine position in this plane. These data indicate fore and aft movement of the engine produces only minor changes in lifting performance, while vertical position dramatically impacts powered lift characteristics. From this it can be concluded that the effective jet turning angle is directly related to the portion of jet momentum intercepted by the flap. Rockwell International, in the course of their analysis development, arrived at an interesting scheme for showing this relationship (Figure 12).

The jet turning angle, ϕ, is the effective direction at which the jet leaves the trailing edge of the flap system, and defines the direction of the total reaction force vector. Using wind tunnel results, it is possible to correlate jet turning angle with the degree of flap penetration into the jet, and arrive at a useable engine positioning design tool. The geometry of jet impingement is shown in the aforementioned figure. In this particular development, the effective source length, $2.3D_j$, is based on a jet expansion envelope with zero velocity at the edge of the jet wake profile. Other definitions, such as, one percent or five percent of the maximum jet velocity could be used, if necessary, to improve data correlation. The design curves also shown in Figure 12 represent the better performance data reviewed by Rockwell International.

Nearly complete jet turning is accomplished with a flap immersion of $Z_F/R = 0.65$ except in cases where flow separation over the flap is present. An immersion factor of 0.65 requires either high forward placement of the engines or the use of nozzle deflectors. By the same token, increasing engine bypass ratio necessitates extending the deflected flap chord to retain the same immersion ratio.

Spanwise location of engines on an EBF design is considerably more simplified than chordwise positioning. Test data indicates the engines should be placed as close to the fuselage as is practical without neglecting the maintenance of good cruise performance. This produces the smallest rolling moment under engine-out operating conditions. A word of caution should be introduced here regarding the use of Siamese nacelle arrangements on an EBF configuration. The high inboard loading of the wing resulting from the close-to-fuselage installation of dual engines in a single nacelle produces a vortex flow pattern in the vicinity of the horizontal tail which severely limits its effectiveness. Additional testing is required to determine the feasibility of the Siamese configuration.

MECHANICAL FLAP/VECTORED THRUST

The mechanical flap/vectored thrust powered lift concept was the only system tested which did not show substantial lift augmentation due to supercirculation. Performance of this system is predicated on matching a good mechanical high lift design with an efficient thrust vectoring nozzle to produce a total system capable of efficient flow turning and rapid variation of lift and drag forces.

Figure 13 presents data showing the tail-off performance levels achieved with the Boeing MF/VT design. The data indicates little lift or drag variation with engine position, but a substantial change in pitching moment. A forward engine location results in a balance between aerodynamic and thrust forces producing a favorable longitudinal trim situation.

The major problem encountered with forward engine positioning was adverse aerodynamic interference. This interference was observed to decrease lift at all except the highest angles of attack, and in most instances increase drag. The probable explantion for the variation of interference with angle of attack is flow entrainment by the jet plumes. The entrained flow induces downwash at the trailing edge, which effectively reduces trailing edge flap angle, producing the observed loss in lift at low to moderate angles of attack. The jet flow also induces a downward velocity at the leading edge, which effectively reduces the local angle of attack felt by the leading edge flap, thereby aggravating the undersurface separation occurring behind the flap at low angles of attack. The net effect is a loss of lift and an increase in parasite drag. As the angle of attack increases, the jet effect tends to reduce the local angle of attack at the leading edge delaying separation on the upper surface permitting the flow to remain attached at a higher angle (and lift coefficient) than achieved power-off.

Test data collected show that optimum chordwise engine placement is not nearly as well defined as it was for EBF designs, suggesting the need for additional testing.

Engine-out problems encountered with this concept are similar to those for EBF systems. To minimize rolling moment difficulties, engines should be placed as close to the fuselage as other considerations allow. Siamese nacelles were found to aggravate adverse aerodynamic interference effects.

INTERNALLY BLOWN FLAP

The internally blown jet flap concept has been the subject of wind tunnel tests for many years. However, most of this testing was conducted on configurations where all of the engine air was ducted into the wing and used to power the jet flap. In a practical airplane application, such a configuration would probably be less efficient than a design where only bypass air was internally ducted, allowing the hot core jet to exhaust aft or be deflected for additional lift or glide path control. This latter configuration was investigated in the STAI program.

The low speed characteristics of a typical Convair IBF design are shown in Figure 14. These results identify the IBF as the superior lifting performer of the three lift concepts investigated. However, large pitching moments accompany this increased lift since it is produced well aft on the wing.

Since all the Convair powered lift systems were tested with the same leading edge device (which in this instance was designed for the EBF system), it can be realistically assumed that additional maximum lift performance should be obtainable with a leading edge system that is configured for the lift levels of the IBF system.

Traditionally the performance of an airplane with jet flaps has been computed discounting the residual thrust effects, if any, on the jet sheet. For engines mounted below the wing this consequence can result in serious errors in the calculation of performance. Residual engine exhaust will interact with the jet sheet and reduce its effective deflection or create a partial span cutout.

The level of these interference effects are a direct function of the engine thrust coefficient. Test results show overall lift being degraded as much as 10% at higher engine thrust levels. This effect on lifting performance is of sufficient magnitude to force the consideration of alternate IBF engine placement or nozzle deflection. A configuration under serious consideration at the present time, incorporates both an upper surface engine location and a deflector nozzle at the flap hinge line.

Engine-out performance of the IBF concept is very satisfactory if a cross-ducting system is utilized to uniformly distribute blowing air in the event of engine failure. The large engine-out rolling moments encountered with EBF and MF/VT configurations are not experienced by an IBF system designed in this fashion.

GROUND EFFECTS

The first indications that flight in close proximity to the ground could be a significant design consideration came in the early days of aviation where the main concern was with its positive effects. As time progressed and the study of vertical takeoff and landing aircraft became reality, attention was directed to the potentially adverse effect of operations near the ground. A great deal of testing and analysis was conducted to increase the understanding of ground effect, and such terms as "suckdown," "fountain effect," and entrainment became familiar to engineers working in the area. In the study of STOL aerodynamics, however, these phenomena are complicated by the fact that under different conditions, different effects result. Under one set of circumstances, such as takeoff flap settings, ground effect produces an increase in the lift coefficient and a decrease in drag, while in the landing configuration the same aircraft operating at higher lift levels experiences a loss in lift when operated near the ground. Configuration variables of the concepts being tested (engine location, flap setting, etc.) produce the multiplicity of problems that were encountered in VTOL ground effects experiments.

Figure 15 presents selected data on the Convair EBF configuration, both power-off and power-on. At lower angles of attack, the in-ground effect lift level is greater than that measured in free air, but the lift curve slope is decreased. As the aircraft angle of attack increases, the in-ground effect and free air lift curves cross, resulting in reduced lift in ground effect. Also, the in-ground effect maximum lift coefficient is a significant increment below the free air level and occurs at a lower angle of attack. An explanation of these ground effects can be given by considering the velocities induced by the images of a bound and trailing vortex system.

The image trailing vortices reduce the downwash, increasing angle of attack and lift coefficient while reducing drag coefficient. The image bound vortex induces a tailwind, reducing all forces. The latter effect is proportional to the lift coefficient squared, and is usually masked by the angle of attack change except at high lift coefficients. As the lift level is increased the tailwind effect becomes predominant, decreasing lift.

IBF in-ground effect data exhibits a trend similar to the EBF characteristics at comparable lift levels. MF/VT ground effect testing produced the most disconcerting results. At thrust deflections below 30 degrees, in-ground effect performance parallels that of an EBF configuration with the same geometric characteristics. However, at nozzle angles approaching 90 degrees, some of the engine exhaust, after impinging on the ground, is deflected forward of the aircraft and recirculated by the lifting system. At thrust deflection settings between these extremes, thrust level has a more dominant effect on ground effect aerodynamics than in the case of the EBF. Because of these jet entrainment and ground impingement effects, further ground effect testing of the MF/VT concept is warranted.

POWERED-LIFT PERFORMANCE COMPARISON

Untrimmed drag polars for the three powered-lift concepts studied are shown in Figure 16. These data were taken with the Convair STOL model in the indicated configuration.

The IBF design demonstrates the most substantial lift augmentation and is the most efficient system for thrust deflection. The MF/VT design, while not expected to produce the lift augmentation of the other concepts, had been expected to show superior climb capability (i.e., to have a more negative drag coefficient at a given lift coefficient) because of the potentially high turning efficiency of a vectored nozzle. This turned out not to be the case, and MF/VT results were quite disappointing due to the problem of jet induced adverse aerodynamic interference.

EBF designs produced performance levels lying in the middle range, with a triple slotted flap configuration showing a slight lift superiority at 60 degrees flap deflection.

EBF and MF/VT systems both generate large rolling moments in engine-out operation and require powerful roll control devices to maintain wings level flight. The IBF, with a good cross-ducting arrangement, does not experience this problem and for the same reason does not require as much directional control power.

Turning for a moment to the design studies, which were an important part of the overall program, additional points pertinent to the selection of a particular powered-lift system will be discussed. From a strictly aerodynamic point of view the characteristics having greatest influence on STOL transport design are:

-Useable maximum lift coefficient. This parameter determines minimum speed for a given wing loading.

-The range of the net force along the flight path. This determines the maximum climb and descent angles. The capability to modulate this force for path angle control is essential.

The first item can be somewhat misleading depending on mission requirements, and in particular the takeoff and landing ground rules that are specified. For example, the STAI takeoff specifications were predicated on an accelerate/stop distance of 2000 feet at an altitude of 2500 feet and a temperature of 93°F. Under these conditions the aircraft designs were takeoff critical and the driving aerodynamic parameter was low drag at takeoff flap settings. This led to designs incorporating double slotted flaps rather than the more complex triple slotted configuration. The final Convair EBF design had computed takeoff and landing performance respectively of 2000 feet and 1550 feet. Admittedly, the landing maneuver is the more difficult of the two to accomplish precisely, and future flight test programs may demonstrate the need for adding an additional distance penalty to account for flare and ground effect nonlinearities.

The internally blown jet flap design exhibited the best aerodynamic efficiency in the test program, but its incorporation resulted in heavier weight vehicles. There are several reasons for this occurrence, the most important of which is the additional weight embodied in the engine installation and internal/air ducting system.

The MF/VT and EBF airplanes had comparable gross weights depending on the thrust vectoring system used. A corollary study was conducted in this area (11, 12) and several interesting designs resulted. At the time the configuration studies were completed, it was recognized that thrust deflector nozzle weight estimates could be questioned, and as a result the weight of the MF/VT propulsion package could vary over a wide range.

CONCLUSIONS

It is reasonable to conclude that acceptable military STOL transports could be developed using any one of the subject powered-lift systems. However, there are several areas where additional research and development would produce more efficient powered-lift performance.

- Mechanical Flap/Vectored Thrust
  - Further definition of aerodynamic interference effects (wind tunnel)
  - Deflected thrust nozzle development
- Externally Blown Flap
  - Development of flap shapes with increased turning efficiencies
- Internally Blown Jet Flap
  - Internal ducting technology development
  - Air distribution system configuration research
    - External ducting
    - Engine/flap integration

Additional ground effect testing is needed on all designs, particularly the MF/VT. Special emphasis should be placed on dynamic testing where the model is flown into the ground plane simulating actual approach conditions.

Finally, since the upper surface blowing powered-lift concept is receiving both commercial and military support, a basic study to define the aerodynamic mechanism responsible for the turning of thick jets over large radius convex surfaces is needed.

REFFRENCES

1. Carroll, R H, Tants, J W and Milns, P, STOL Tactical Aircraft Investigation Configuration Definition: Medium STOL Transport with Vectored Thrust/Mechanical Flaps, AFFDL-TR-73-19, Vol I, May 1973.

2. Owens, H G, Renselaer, D J, Kaneshiro, R S, Schlundt, D W, et al, STOL Tactical Aircraft Investigation - Externally Blown Flap, Configuration Definition, AFFDL-TR-73-20, Vol I, April 1973.

3. Hebert, J, et al, STOL Tactical Aircraft Investigation, Configuration Definition, AFFDL-TR-73-21, Vol I, May 1973.

4. Runciman, W J, Letsinger, G R, Ray, B F, and May F W, STOL Tactical Aircraft Investigation Aerodynamic Technology Design Compendium, Vectored Thrust/Mechanical Flaps, AFFDL-TR-73-19, Vol II, Part I, May 1973.

5. Davenport, F J, STOL Tactical Aircraft Investigation, A Lifting Line Analysis Method for Jet-Flapped Wings, AFFDL-TR-73-19, Vol II, Part II, May 1973.

6. Roe, M H, Renselaer, D J, Quam, R A, et al, STOL Tactical Aircraft Investigation - Externally Blown Flap Design Compendium, AFFDL-TR-73-20, Vol II, April 1973.

7. Hebert, J, Levinsky, E S, Ramsey, J C, Laudeman, E C, Altman, H G, and Barbee, L G, STOL Tactical Aircraft Investigation, Design Compendium, AFFDL-TR-73-21, Vol II, May 1973.

8. Monk, J R, Lee, J L, and Palmer, J P, STOL Tactical Aircraft Investigation Analysis of Wind Tunnell Data: Vectored Thrust/Mechanical Flaps and Internally Blown Jet Flaps, AFFDL-TR-73-19, Vol IV, May 1973.

9. Papp, P A, Quam, R A, and Freeman, G A, STOL Tactical Aircraft Investigation - Externally Blown Flap, Analysis of Wind Tunnel Data, AFFDL-TR-73-20, Vol IV, April 1973.

10. Hebert, J, Ramsey, J C, Laudeman, E C, Ponomareff, N A, and Altman, H G, STOL Tactical Aircraft Investigation, Wind Tunnel Data Analysis, AFFDL-TR-73-21, Vol IV, May 1973.

11. Petit, J E, Scholey, M B, STOL Transport Thrust Reverser/Vectoring Program, AFAPL-TR-72-109, Vol I, February 1973.

12. Petit, J E, Scholey, M B, STOL Transport Thrust Reverser/Vectoring Program, AFAPL-TR-72-109, Vol II, February 1973.

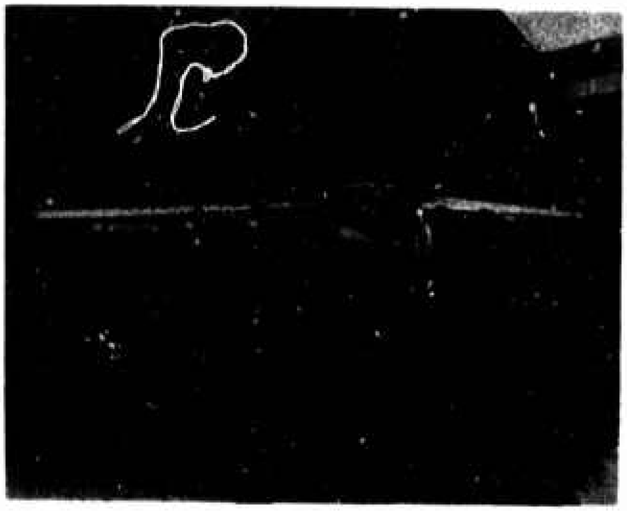

Figure 1 - Convair 1/20 Scale Medium STOL Transport Model Installed in the General Dynamics 8 foot x 12 foot wind tunnel.

Figure 2 - Convair Wind Tunnel Test Variables.

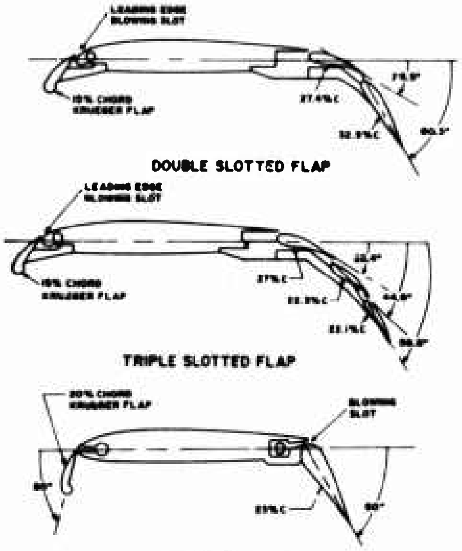
LEADING EDGE BLOWING SLOT
15% CHORD KRUEGER FLAP
27.4%C
52.9%C
DOUBLE SLOTTED FLAP
LEADING EDGE BLOWING SLOT
15% CHORD KRUEGER FLAP
27%C
TRIPLE SLOTTED FLAP
20% CHORD KRUEGER FLAP
BLOWING SLOT
60°
25%C
60°
PLAIN BLOWN FLAP

Figure 3 - Typical Convair and Boeing High Lift Devices.

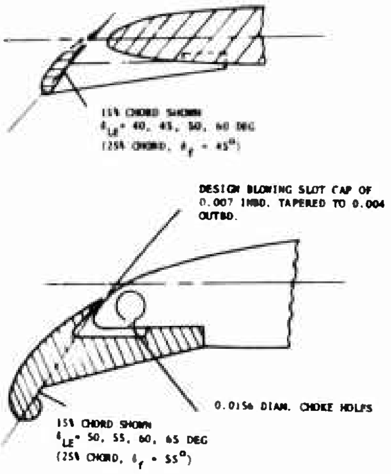
15% CHORD SHOWN
δ_{LE} = 40, 45, 50, 60 DEG
(25% CHORD, δ_f = 45°)
DESIGN BLOWING SLOT CAP OF 0.007 INBD. TAPERED TO 0.004 OUTBD.
0.0156 DIAM. CHOKE HOLES
15% CHORD SHOWN
δ_{LE} = 50, 55, 60, 65 DEG
(25% CHORD, δ_f = 55°)

Figure 4 - Convair Leading Edge Test Articles.

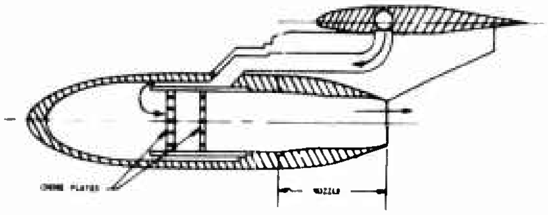
CHOKE PLATES
NOZZLE

Figure 5 - Boeing Model Engine Simulator

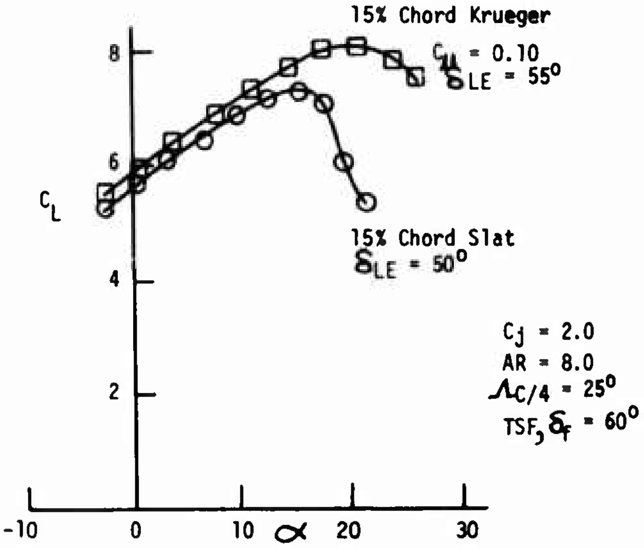

Figure 6 - Leading Edge Performance EBF Test Data, AR = 8, $\Lambda c/4$ = 25 Degrees, Triple Slotted Flap (δ_f = 60 Degrees)

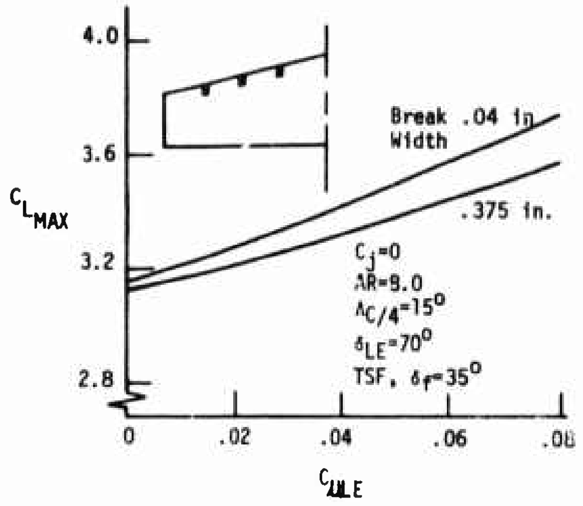

Figure 7 – Effect of Spanwise Breaks on the Performance of Leading Edge Boundary Layer Control Slots

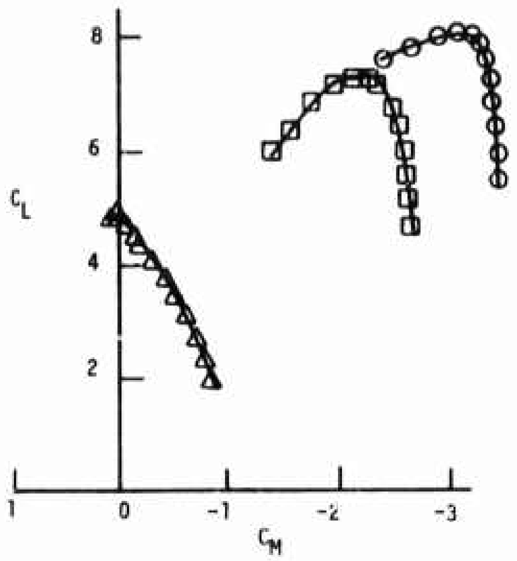

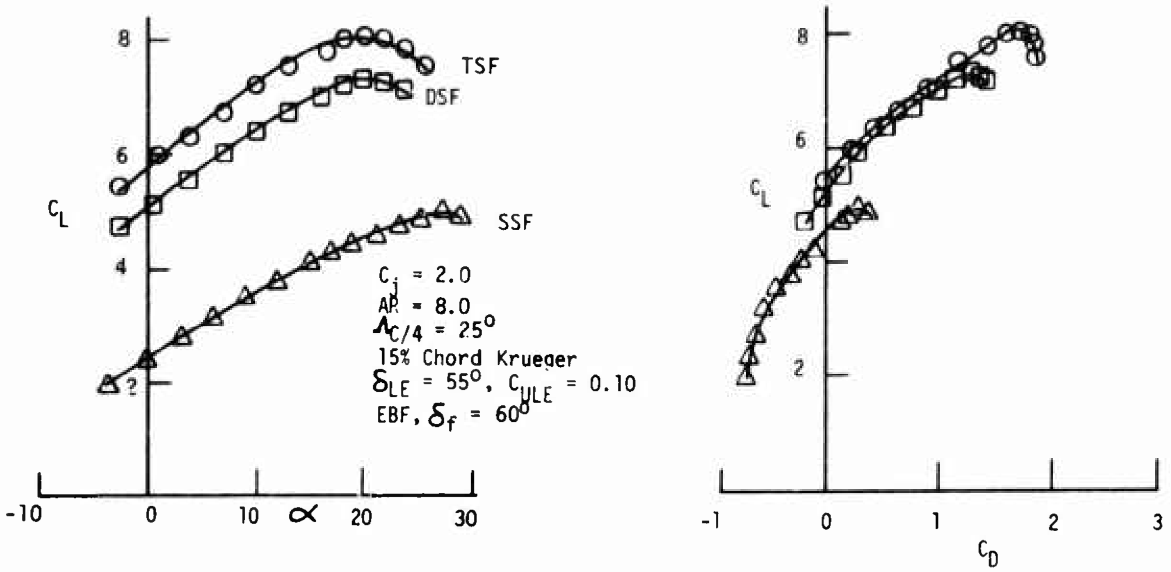

Figure 8 – Convair Flap Performance Comparisons, EBF Test Data, AR = 8, $\Lambda_{c/4}$ = 25 Degrees, Thrust Coefficient = 2.0

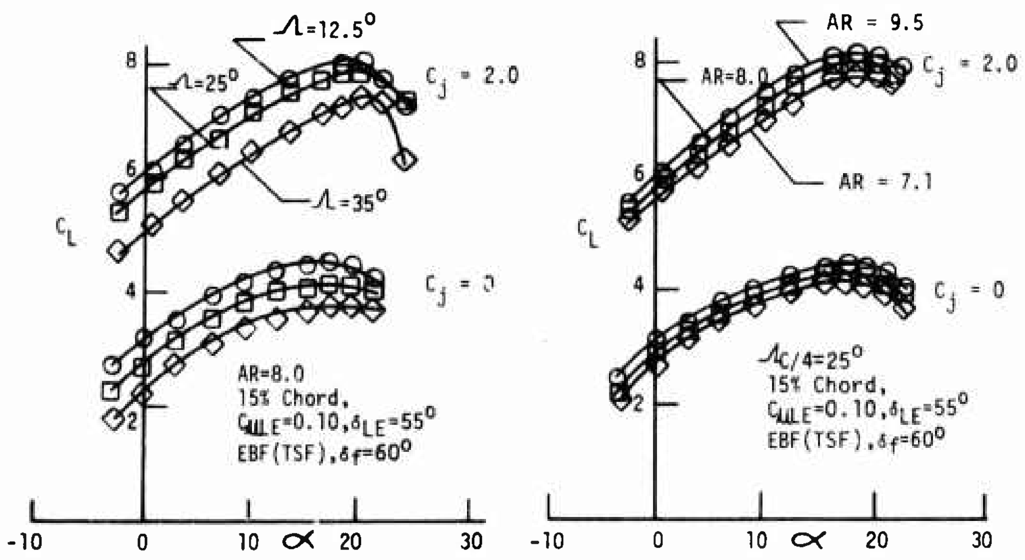

Figure 9 – Convair EBF Data Showing the Effect of Aspect Ratio and Sweep

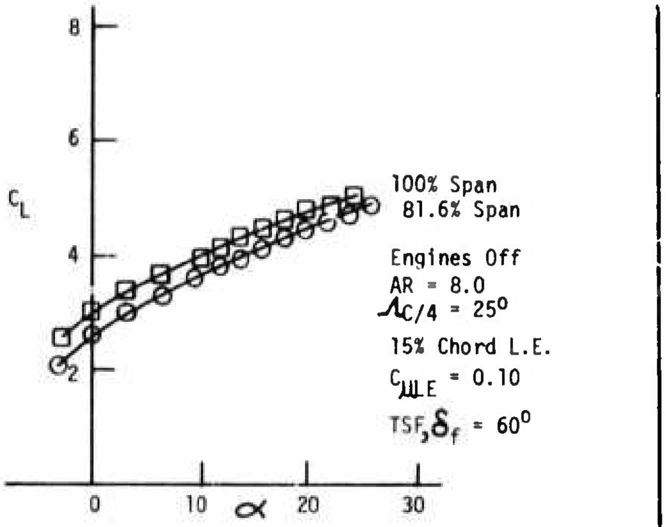

Figure 10 - Influence of Trailing Edge Flap Span on Unpowered Lifting System Performance

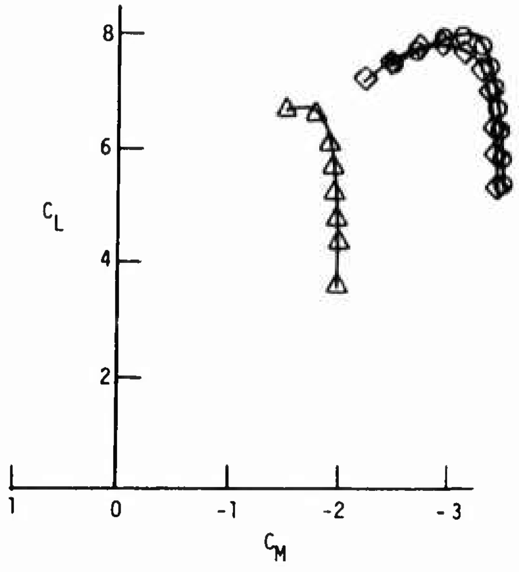

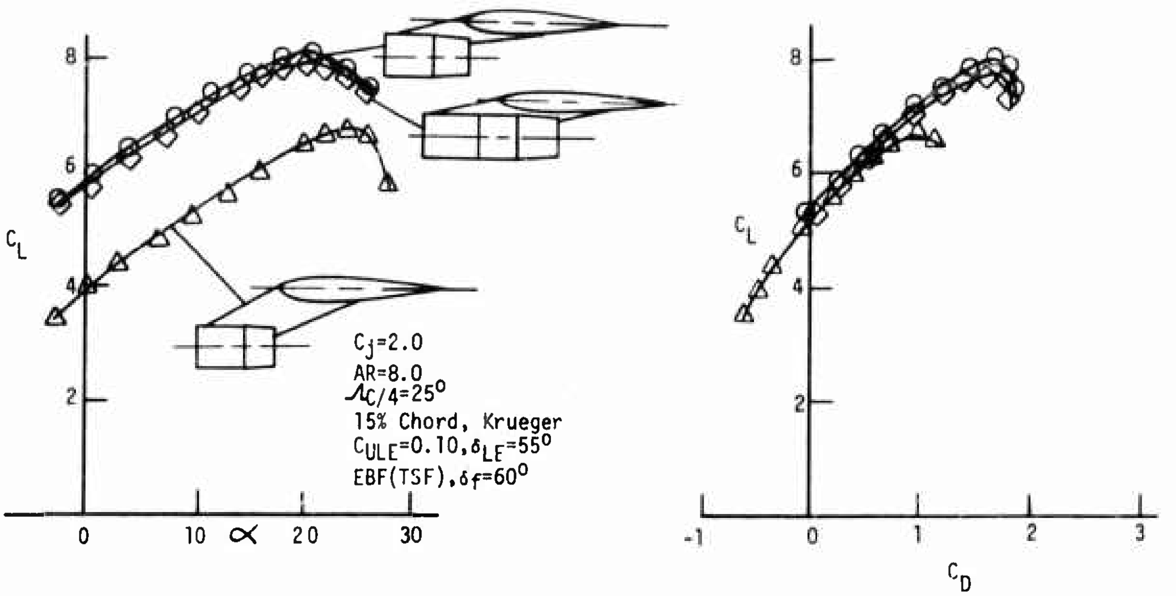

Figure 11 - Chordwise and Vertical Engine Location Effect, Convair EBF Test Data, AR = 9, $\Lambda_{c/4}$ = 25 Degrees, Triple Slotted Flap (δ_f = 60 Degrees)

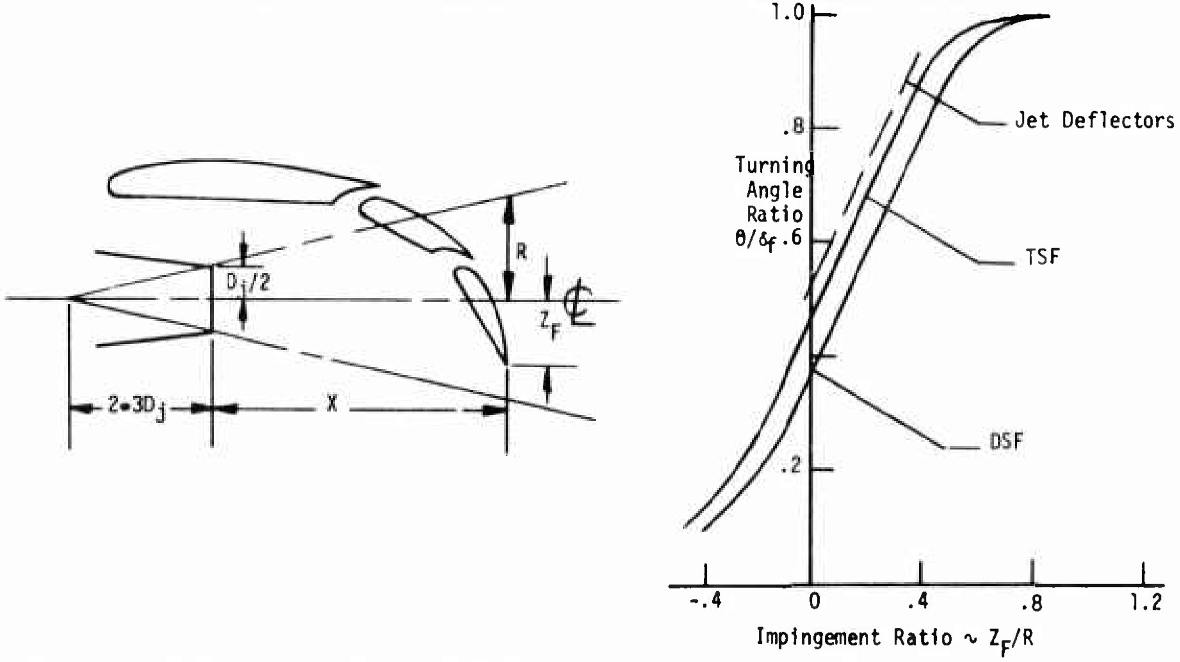

Figure 12 - Rockwell International EBF Engine Location Versus Turning Efficiency Correlation

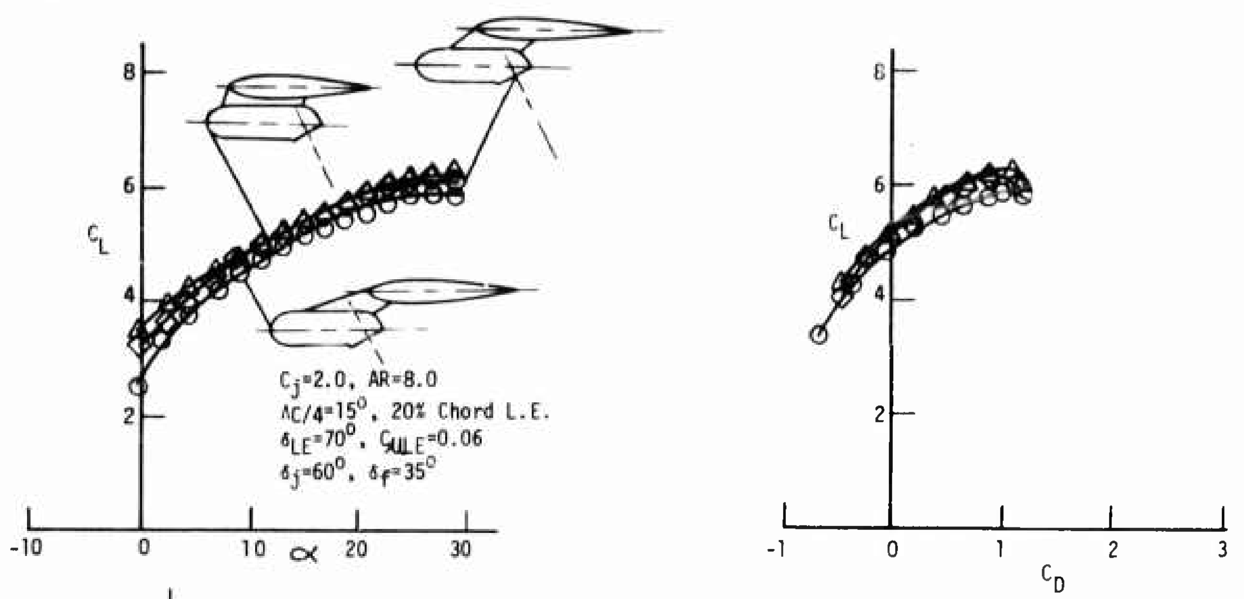

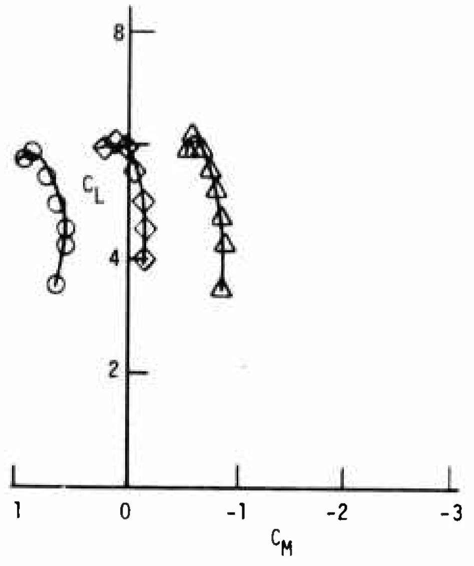

Figure 13 - Chordwise and Vertical Engine Location Effects, Boeing MFVT Data, AR = 8, $\Lambda_{c/4}$ = 15 Degrees, Triple Slotted Flap (δ_f = 35 Degrees), Jet Deflection (δ_j = 60 Degrees)

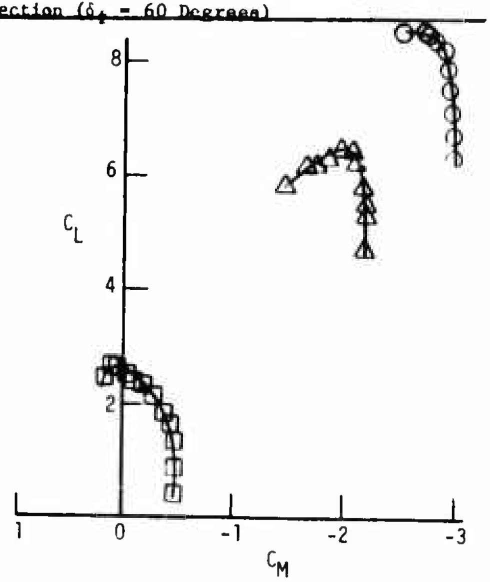

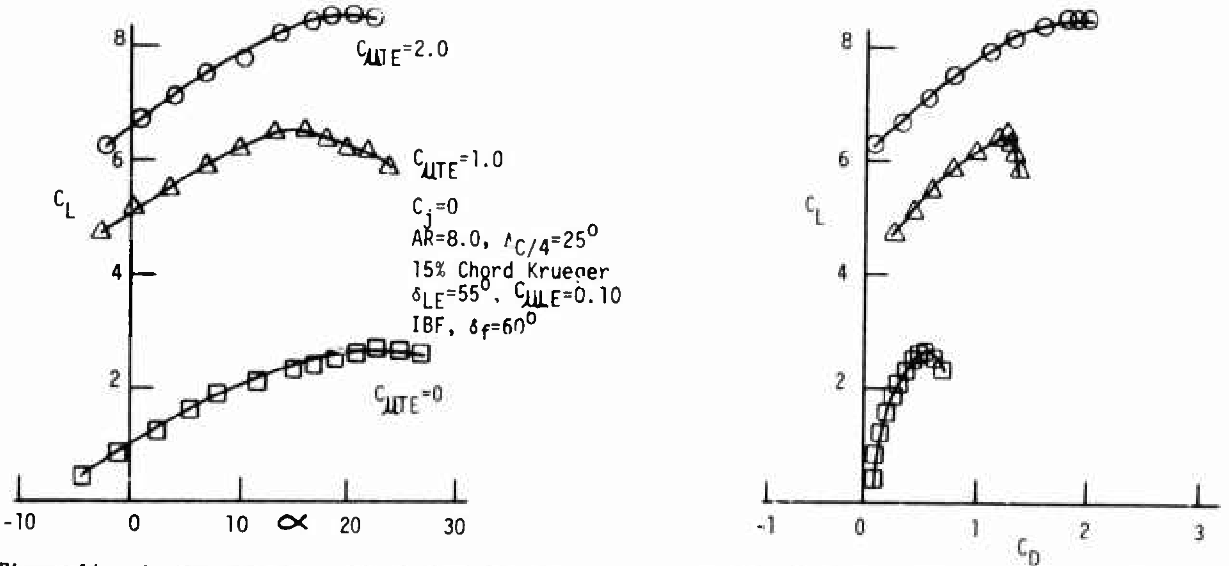

Figure 14 - Convair IBF Performance Data, AR = 8.0, $\Lambda_{c/4}$ = 25 Degrees, Plain Blown Flap (δ_f = 60 Degrees)

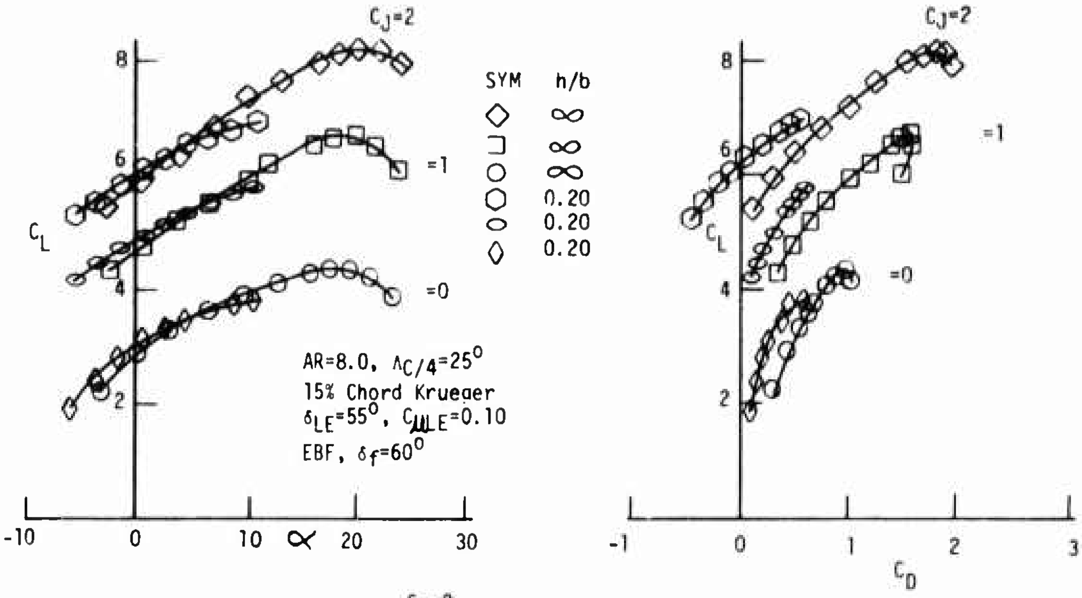

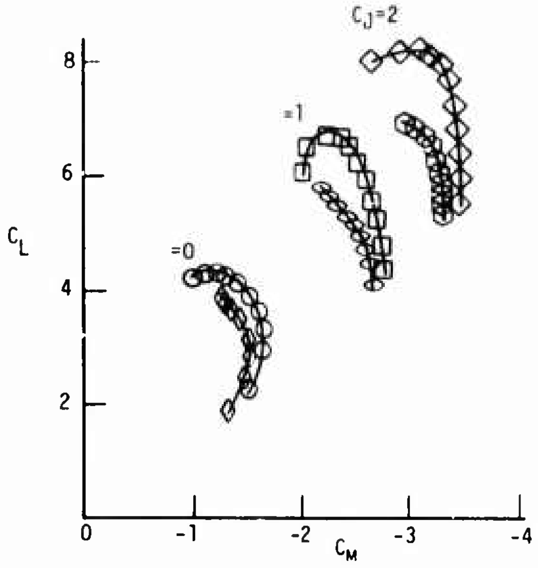

Figure 15 - Convair EBF Performance Data in Ground Effect, AR = 8, $\Lambda_{c/4}$ = 25 Degrees, Triple Slotted Flap (δ_f = 60 Degrees)

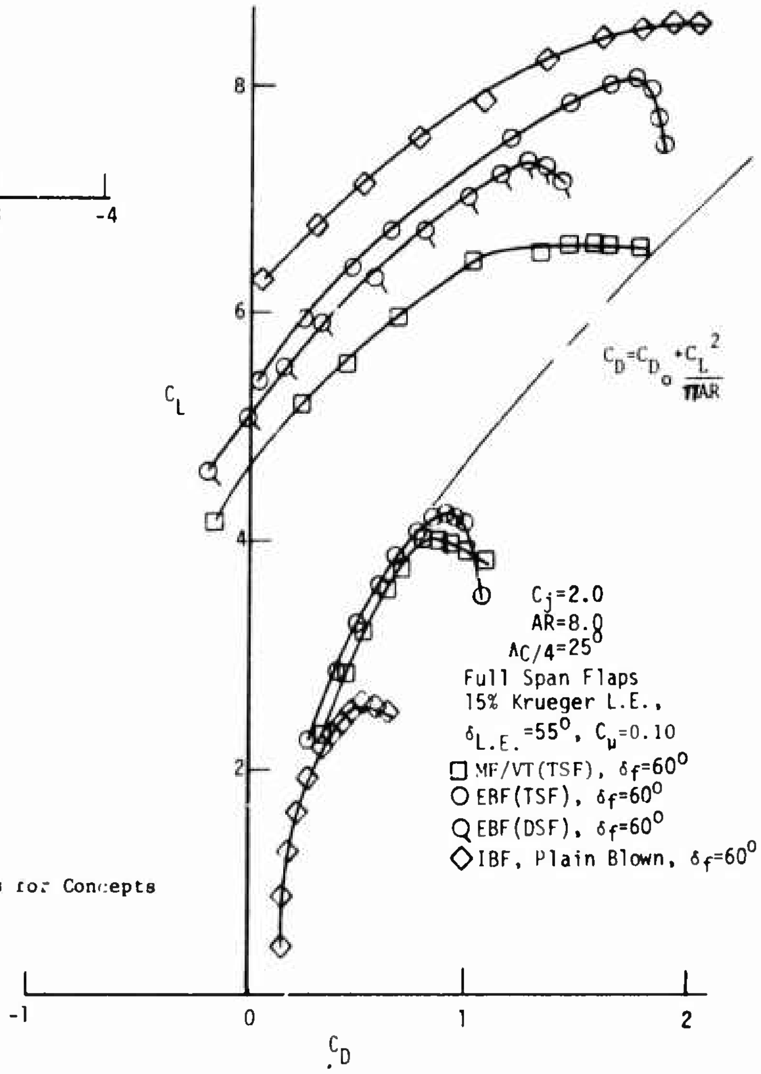

Figure 16 - Convair Untrimmed Drag Polars for Concepts Studied

THE SPANWISE LIFT DISTRIBUTION AND TRAILING VORTEX WAKE DOWNWIND OF AN EXTERNALLY-BLOWN JET FLAP

R. H. Wickens
Associate Research Officer
Low Speed Aerodynamics Laboratory
National Aeronautical Establishment
National Research Council of Canada
Ottawa, Ontario, Canada
K1A 0R6

SUMMARY

The aerodynamic characteristics of the Externally-Blown Jet Flap (EBF) are presented for configurations of the quasi-2-D and reflection-plane type respectively.

Force and surface pressure measurements have shown that significant lift increments can be realized by external blowing, and that the spanwise effect of this increase extends outward from the nacelle location. The effective stream tube dimension of the additional lift can be a significant fraction of the wing span.

The relationship between the quasi-2-D and 3-D polars has been shown to result from a rearward rotation of these forces through an induced incidence $\Delta\alpha_i$, which is due to the decrease in effective aspect ratio.

Downstream flow surveys have shown that the presence of mixed regions of propulsive and vortex flows is typical of the EBF, particularly for multi-engined finite wing configurations.

Wake measurements downwind of a half-model of a multi-engined aircraft of the EBF type have shown that behind each half-wing, there are two trailing vortices, one from the wing tip, and one from the flap tip. The propulsive jet sheet rolls up around the vortex from the flap tip.

LIST OF SYMBOLS

A	wing aspect ratio, b^2/S
b	wing span
b'	span of the powered lift stream tube
c	chord, ft.
C_μ	thrust coefficient, T/q_tS
C_L	lift coefficient, L/q_tS
C_D	drag coefficient, D/q_tS
C_{N_i}	sectional normal force coefficient, N_i/q_tC, $i = 1, 2, 3, 4$
C_ℓ	sectional lift coefficient, ℓ/q_tC
C_p	pressure coefficient, $p-p_o/q_t$
D	drag
e	wing efficiency factor
H	wake total pressure
K	powered-lift stream tube parameter
L	lift
p	static or surface pressure
p_o	tunnel reference static pressure
q_t	tunnel dynamic pressure
r	thrust recovery factor
S	wing reference area
T	thrust
V	tunnel velocity
w	wake downwash velocity (positive in positive lift direction)
v	wake sidewash velocity (positive when directed along port sem-span, looking upstream)
x, y, z	wing reference dimensions
α_w	angle of attack
ψ	wake sidewash angle, measured at flap trailing edge (but in a plane parallel to deflected flap element)

δ_f	flap angle
ϵ	wake downwash angle
θ	jet downwash angle

SUBSCRIPTS

w	refers to wing forces only
T	refers to total forces
2D, 3D	refers to quasi-2-D and half-model configurations respectively

1.0 INTRODUCTION

Current generations of jet transport aircraft operate on the approach at speeds in the range of 130 - 150 knots, and use airfields of 8 - 12,000 feet in length. The proposed development of STOL transports assumes landing fields 2000 - 3000 feet in length, and approach speeds of about half the above figure. In order to achieve comparable ride comfort, the wing loading, and hence $C_{L_{app.}}$ and $C_{L_{max}}$ must be higher than is currently possible with conventional passive high lift systems(1).

It is clear that some form of powered lift must be used to achieve this performance, and current interest at the N.A.E. centres on the turbo-fan powered transport using the externally-blown jet flap (EBF). In this concept, the entire engine and fan flow impinges onto highly deflected, slotted flaps. This flow, at a total head higher than the ambient fluid, is directed downward, and spreads in a spanwise manner, thus generating supercirculation and increased lift.

The EBF is one of the major classifications of blown flaps, and its relatively simple external configuration is considered to be an alternative to the complexities and weight penalties which may characterize jet flap or augmentor wing concepts. The most serious disadvantage of the EBF, however, is its low thrust recovery, a factor crucial in determining engine-out climb performance, and also the rolling moments induced by an asymmetric loss of lift caused by an engine failure.

Much work has been done on complete aircraft configurations (Ref. (2) to (5)); however, it was the aim of the experimental program at the N.A.E. to explore the effects of a single jet impinging onto a two-dimensional wing with slotted flaps, in isolation from the fuselage or other airframe components. It was also hoped by testing in the half-model configuration, to be able to assess the effects of a change of aspect ratio.

It is commonly known that the wake downwind of an EBF is characterized by concentrations of trailing vorticity, caused by non-uniform span loading, and rolling-up of the jet sheet. The downwash induced at a tailplane location will have a serious effect on its design and ultimate location, and under asymmetric flight conditions, these flows may seriously affect the aircraft stability and control.

Flow surveys, made downwind of the N.A.E. model and also behind a multi-engined EBF transport model, have shown that the wake flow has both propulsive and vortical components, and that downwash and sidewash velocities of considerable magnitude exist.

2.0 DESCRIPTION OF MODELS AND TEST

The wind tunnel model, a quasi-two-dimensional configuration, was mounted in the 6 ft. × 9 ft. horizontal tunnel, as shown in Figure 1. The basic wing profile was the NACA 63A418 with a vane and slotted flap assembly fitted. The flap could be positioned to either 30° or 68°, with the vane location set to give the highest $C_{L_{max}}$. The basic wing span was 73.88 in. (1.877 m) and the chord was 25 in. (.635 m).

The simulated jet engine was of the ejector type in which a primary flow issues from nozzles placed internally. The nacelle exit diameter was 5 in., and the average jet velocity was about 600 ft/sec.

The nacelle, inclined 10° downward relative to the wing chord line, was not on the balance, but rotated with the wing. Thrust was measured from a prior calibration and was maintained constant during the test. C_μ was varied by changing tunnel flow so that wing Reynolds number also varied ($.87 \times 10^6$ to 1.74×10^6). The greatest lift was obtained with the nacelle positioned near the leading edge, and with a flow deflector installed. This device, indicated schematically in Figure 1 enabled the engine exhaust to be directed more effectively onto the wing and flap under-surface, and provided a definite improvement in lifting performance.

The wing was also tested in the half-model configuration in the 30 ft. × 30 ft. V/STOL wind tunnel. In this installation the wing and end plate were raised above the floor boundary layer to minimize flow disturbances, and a simple wing tip was fitted (Figure 1). The aspect ratio of the half-wing was 5.91.

The wind tunnel investigation included force and surface pressure measurements (quasi-2-D only) and also wake flow surveys at a downstream location 3 chords behind the wing.

Flow surveys were also made, jointly with DeHavilland of Canada, in the flow at the tailplane location of a multi-engined EBF transport model. Reference 6 describes the wind tunnel installation of this model, and the traversing rake of five-hole probes which is located downwind.

The flow probes were of a standard design, constructed of small-bore stainless tubing, with heads machined to an included angle of 90°. The calibration and data reduction procedure is similar to that of reference 7 and enables the determination of induced velocities, total head, and flow direction, relative to the probe axis.

3.0 WIND TUNNEL FORCE MEASUREMENTS

The data presented in this section were taken from both the 6 ft. × 9 ft. and 30 ft. × 30 ft. wind tunnels, so that it will be possible to compare and analyze the quasi-2-D data with half-model data respectively.

Since the powered nacelle was not on the balance, the basic model reactions were "wing forces", i.e. L_w, D_w, M_w. "Total forces", i.e. L_T, D_T and M_T were computed by adding on the appropriate nacelle force increments which had been determined in a separate test. The data were uncorrected.

3.1 EBF Lift Coefficients

The lifting characteristics of the externally blown flap model in both the 2-D and half-model configurations are shown in Figures 2 and 3 for $\delta_F = 30°$ and 68° respectively (Total forces, C_{L_T} vs. α_w), and for different values of C_μ.

The main effect of external blowing was to increase lift and $C_{L_{max}}$ significantly while producing minor changes in lift slope.

The lift increments produced were found to be quite sensitive to nacelle location, and the largest increment was obtained with the nacelle positioned near the leading edge and with a flow deflector installed. This device, indicated schematically in Figure 1 enables the engine exhaust to be directed more effectively onto the wing and flap undersurfaces, and provided a definite improvement in lifting performance.

The effects of the finite wing span of the half-model configuration are evident, from a comparison of the 2-D and half-model lift curves. The lift curve slope has decreased for the 3-D model and corresponds approximately to a rotation of the lift curve about α_{zL}. The lift increment ΔC_{L_T} is also significantly reduced (about 20%).

Total force polars, C_{D_T} vs. C_{L_T} are presented in Figure 4 to $\delta_F = 68°$. These demonstrate the effects of blowing and finite span upon EBF characteristics. Thrust recovery, an important factor in the comparison of the various powered-lift schemes, is estimated to be about 0.65. The increased curvature of the 3-D force polars are due to the three-dimensional effects of the finite span half-model with its smaller effective aspect ratio.

3.2 Wing Force Polars

Drag polars, composed of wing forces only, (i.e. C_{L_w} vs. C_{D_w}) are plotted in Figures 5 and 6 for the two flap angles, and for both 2-D and half-model configurations.

It seems fairly clear from these graphs that the data for all C_μ's tends to collapse upon a single polar curve. This is particularly true for the 30° flap case (3-D) in the range $2 < C_{L_w} < 4$. In the 68° case (3-D) the data tend to collapse at small blowing values, although individual values of C_μ are identifiable, and the collapse is less perfect. The 2-D data behave in a similar way except that the polar curve is less steep.

It appears, then, that the EBF wing forces behave in a manner similar to an unpowered finite wing in that the drag polar is represented approximately by the relation

$$C_{D_w} = C_{D_o} + \frac{C_{L_w}^{\,2}}{\pi e A} \qquad (1)$$

and it is possible to fit such a curve through the data in all four cases shown here. The value of e, or eAR varies, but can be inferred from the slopes of the $((dC_{D_w})/(dC_{L_w}^{\,2}))$ relationship for the various model flow conditions. Quantities e_{3D} and $(eA)_{2D}$ so determined are plotted in Figure 7 where it can be seen that the effect of blowing (and hence spanwise non-uniformity of load) changes the effective aspect ratio of the 2-D wing greatly, but that of the 3-D wing very little. Polar curves calculated from eq (1), and using values of e or eA in Figure 7 are noted in Figures 5 and 6.

3.3 Aspect Ratio Correction to Drag Polars

The experimental data has suggested that in terms of wing forces, the EBF drag polars can be represented by the unpowered drag polar of a wing having a certain effective aspect ratio.

It should therefore also be possible, when considering the observed differences between two- and three-dimensional polars, to apply the same rules to the powered lift system as to the unpowered system. Thus the drag polars of Figures 5 and 6 (C_{L_w} vs. C_{D_w}) can be considered, in the three-dimensional case, to have been affected by an induced incidence $\Delta\alpha_i$ which is due to the change in effective aspect ratio from quasi 2D to 3D.

i.e.

$$\frac{\Delta\alpha_i}{C_{L_w}} = \frac{57.3}{\pi}\left[\frac{1}{eA_3} - \frac{1}{eA_2}\right] \tag{2}$$

This quantity has been determined from the values of equivalent aspect ratio shown in Figure 7, and was found to have a value of approximately 3.0 for both the 30° and 68° flap settings. This value was confirmed by observations of the shift in the C_{L_T} vs. α_w curves, although the agreement was not good for the higher blowing coefficients at $\delta_F = 68°$. The transformation of total force data from quasi 2D to 3D is as follows:

$$C_{L_{T_3}} = C_{L_{T_2}}\cos\Delta\alpha_i - C_{D_{T_2}}\sin\Delta\alpha_i \tag{3}$$

$$C_{D_{T_3}} = C_{D_{T_2}}\cos\Delta\alpha_i + C_{L_{T_2}}\sin\Delta\alpha_i \tag{4}$$

Graphs showing a comparison of experimental and transferred data are shown in Figure 8 for $\delta_F = 30°$ and 68°. For the higher flap angle case, a value of $(\Delta\alpha_i)/(C_{L_w}) = 2.3$, taken from the shift in the C_L vs. α_w curves, was found to give the correct transformation.

3.4 An Analogy with the Jet Flap

It would be worthwhile, at this point, to introduce a momentum model for powered lift which, in its simplest form, is identical to the jet flap equation of Spence and Markell.

The vector diagram of this model is illustrated in Sketch 1 below.

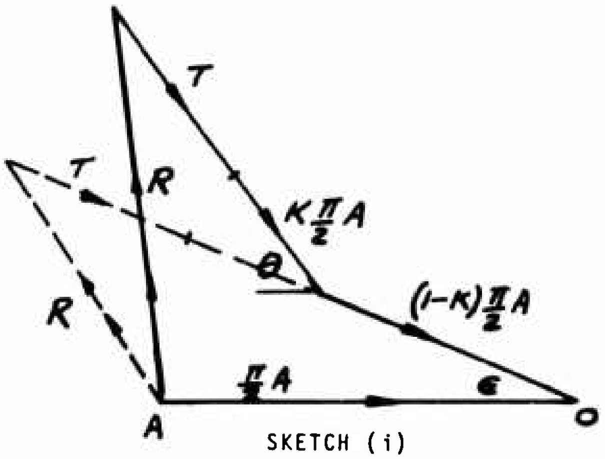

SKETCH (i)

The vector OA is the dimensionless approaching stream tube momentum of magnitude $\frac{\pi}{2}A$, having a flow area of $\frac{\pi b^2}{4}$. If the wing is unpowered, then the departing momentum is also $\frac{\pi}{2}A$, but leaves the wing at downwash angle ϵ. When power is applied uniformly over the full span as in the jet flap or augmentor-wing, then the thrust vector T is simply added to the departing wing momentum and it is assumed that the wing downwash angle ϵ is the same as the thrust deflection angle θ.

If power is applied over part of the wing span only, (and thus at a different local downwash angle) it is assumed that a certain fraction of the departing momentum $K\frac{\pi}{2}A$ leaves the wing at the jet downwash angle θ, while the remainder, $(1-K)\frac{\pi}{2}A$, leaves at the angle ϵ. The effective span of the powered lift stream tube is thus proportional to the factor K.

R is the resultant total force, having wind axis components C_{L_T} and C_{D_T}. These components may be obtained from the vector diagram as follows

$$C_{L_T} = (1-K)\frac{\pi A}{2}\sin\epsilon + \left(C_\mu + \frac{\pi A}{2}\right)\sin\theta \tag{5}$$

$$C_{D_T} = C_{D_o} - \left(C_\mu + \frac{K\pi A}{2}\right)\cos\theta + \frac{\pi A}{2}[1-(1-K)\cos\varepsilon] \qquad (6)$$

If the reactive components are subtracted from the total force, then expressions for wing forces are:

$$C_{L_w} = \frac{\pi A}{2}[(1-K)\sin\varepsilon + K\sin\theta] \qquad (7)$$

$$C_{D_w} = C_{D_o} + \frac{\pi A}{2}[1-(1-K)\cos\varepsilon - K\cos\theta] \qquad (8)$$

If we consider the unpowered wing ($K = 0$, $\varepsilon = \theta$) and full span power effects ($K = 1$, $\varepsilon = \theta$), respectively, then it can be shown that eqs (7) and (8) will, for each case, reduce to the simple polar equation for induced drag as given by eq (1).

i.e. $$C_{D_w} = C_{D_o} + \frac{{C_{L_w}}^2}{\pi A} \qquad (9)$$

Thus it seems, that in terms of wing forces even a complex device such as a jet flap behaves in a manner similar to an unpowered wing of the same aspect ratio except that, due to supercirculation effects, it is now capable of achieving much higher levels of lift and drag than its unpowered counterpart.

3.5 Wing Efficiency Factor

For values of K between 0 and 1, to which the EBF or any part-span blowing concept is assumed to be appropriate, the relationship between C_{L_T} and C_{D_T} or C_{L_w} and C_{D_w} will be different. In fact the distance OD in the sketch will have a shorter radius as compared with the unbent vector OD'. That is, the effective aspect ratio will decrease when K lies between 0 and 1, and if we assume that the EBF wing polar can be represented by:

$$C_{D_w} = C_{D_o} + \frac{{C_{L_w}}^2}{\pi e A} \qquad (10)$$

as the experimental data seems to indicate, then the wing efficiency factor e can be related in some way to the effective powered-lift stream tube b'/b and the ratio of the two downwash angles θ/ε by the use of eqs (7), (8) and (10). Figure 9 shows wing efficiency factor e calculated in this way plotted against ε/θ for increasing fractions of the wing span affected by power. As the powered lift downwash angle Θ increases relative to the unpowered portion ϵ, then the wing efficiency factor e decreases, since the non-uniformity of lift will also increase. The loss of wing efficiency, however, is tempered by the amount of span which is assumed to be active; minimum values of e evidently occur for a span ratio of b'/b about .4. The calculated factors of Figure 9 may be compared with those inferred from the force data.

3.6 Thrust Recovery Factor

One way of comparing various powered-lift concepts is by the Thrust Recovery Factor r which may be determined from total force polar curves such as those of Figure 4 (r is defined in Figure 10). Values of r determined from force data are shown in Figure 10. Also shown are typical values for the augmentor wing, and a complete aircraft configuration using the EBF concept. The low values of thrust recovery achieved by the various EBF types are evident in this graph, particularly for larger flap angles. This contrasts with the quite high values of r achieved by the augmentor wing, which has a more uniformly distributed jet flow.

The diagram of Sketch (i) suggests that there is an inevitable loss of thrust recovery for systems in which only part of the span is active, and that r is probably related to wing efficiency factor e. Thus the full-span jet flap or augmentor wing configurations will always have a superior performance in this respect.

4.0 AERODYNAMIC LOAD DISTRIBUTION

It is evident from the force measurements, that external blowing has a dominant effect on the wing aerodynamic characteristics. The jet flow impinges initially on the main aerofoil, and spreads rapidly, flowing outwards and along the flap elements. This added flow induces a supercirculation, and increased lift which affects a significant portion of the wing span. A simple analysis of the force data has suggested that the powered-lift stream tube size can cover half the effective wing span.

Chordwise and spanwise load distributions were obtained on the quasi-2-D model from surface pressure measurements at the 30 and 68 degree flap positions, and for several values of C_μ. Normal and chord force values were obtained for each of the aerofoil components at various spanwise locations by integration of C_p vs. x/c and y/c respectively.

Chordwise pressure distributions at the jet centreline are shown in Figure 11 and 12 for the 30 and 68 degree flap settings. It is evident from these results that the jet flow induces some very large changes in the local aerodynamic loading, particularly on the flap components, and the impingement region of the main aerofoil lower surface.

A comparison of centreline pressures of the 30 and 68 degree flap angles (Figures 11 and 12), shows that the lower surface pressures due to jet impingement are approximately the same, for the same value of C_μ. On the main wing upper surface, for $\delta_F = 68°$, increases of C_μ result in increasing negative pressures, due, probably, to supercirculation. The upper surface pressures for the 30 degree flap setting do not change with C_μ.

The high pressures induced by the impinging jet are carried over onto the vane and flap elements, with resulting high local loads. This is particularly true for the 68 degree flap setting, where the vane experiences very high positive and negative pressures, and carries a significant proportion of the total aerofoil load. For the 30 degree flap setting, the positive and negative pressures on the vane are also high, but since the local vane incidence is negative, the net load is quite low. Very high pressures are also present on the leading edges of the flap elements (Figure 11).

The distribution of local normal force C_N along a semi-span of the quasi-2D model is shown in Figures 13 and 14 for each component and different amounts of jet blowing. These figures show that the aerodynamic loading, particularly on the flap elements, extends well beyond the original dimensions of the jet. On the main wing, the local loading is high, but drops off rapidly from the jet centreline, and becomes approximately constant at the outboard stations. At $(y)/(b/2) = .1$ there is a minimum in the curve followed by a gradual rise of C_N; this behaviour is attributed to the effects of jet impingement, and three-dimensional separation of the main wing lower surface boundary layer.

Some details of the jet impingement are shown in Figure 15. The photograph, for $\delta_F = 68°$, $C_\mu = 0.5$, shows this flow made visible by a mixture of French chalk and oil. The main characteristics of the flow appear to be a separation of the wing boundary layer along the curved boundary, and a source-type flow within the jet impingement area itself. The flow on the flap elements is not too clearly shown, but it is evident that the local flow velocities are directed outboard on either side of the jet centreline. A schematic representation of the jet impingement flow on the wing lower surface, with surface pressure distributions through the point of impingement are also shown in Figure 15.

The distribution of local lift coefficient C_ℓ is shown in Figure 16 for the 30 and 68 degree flap setting. For $C_\mu = 1.5$, the lift distribution is very non-uniform, and is concentrated near the centreline of the jet. At lower C_μ's the load distribution tends to be more uniform. The loading on the flap elements is also high, particularly for $\delta_F = 68°$, and extends well outboard, due to the spreading of the jet sheet.

5.0 WAKE FLOW CHARACTERISTICS

In the external flow jet flap concept, the entire engine and fan flow impinges onto highly deflected, slotted flaps. This flow, at a higher total head than that of the ambient fluid, is directed downward, and spreads in a spanwise direction, thus generating a supercirculation, and increased lift.

Observation has shown that under high lift conditions the engine exhaust, initially circular, is quickly transformed into a thin sheet which leaves the flap trailing edge and subsequently deforms into a U-shaped pattern downstream. Vorticity was also observed along the edges of the spreading jet on the wing lower surface (Figure 15);

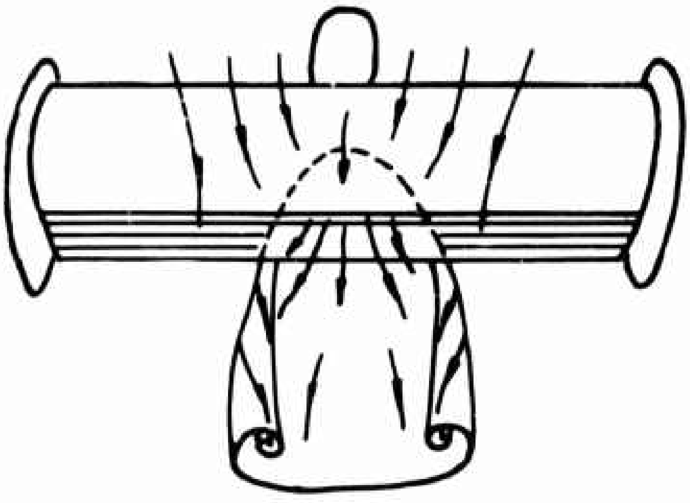

SKETCH (ii)

however, the flow in the wake is characterized mainly by the behaviour of the entire jet sheet, which rolls up into two well-defined trailing vortices. Sketch ii shows schematically, the essential features of the flow downwind of a quasi-2-D model. The amount of jet spreading, and hence the effective span of the trailing jet sheet, is related to the distribution of additional lift on the wing. Flow visualization, and an analysis of the force data seemed to indicate that the size of the powered lift stream tube would be a significant fraction of the wing span. Since it was also evident that the flow behind the wing contained both propulsive and vortical components, traverses were made using five-hole probes in order to achieve as complete a description as possible of the physical nature of the trailing wake.

5.1 Quasi-2-D and Half-Model Wakes

Flow surveys were made downwind of the 2-D model and also the half-model for flap settings of 30° and 68°. The model incidence and C_μ were those for which pressure and load distribution data were obtained (see Figure 16). The half-model incidence (30' × 30' tunnel) was set so as to give the same value of C_{L_w} as the 2-D model, for a given δ_F and C_μ. The downstream location of the traverse was 3 chords (75 in.) behind the wing quarter-chord point. For the quasi-2-D model only, a flow survey was also made at the trailing edge. Table I, below, lists model and flow parameters for which wake data were obtained.

TABLE I

Model Config.	δ_F	C_μ	C_{L_w}	α_w	x_w/c
2-D	30	.76	3.17	0	3.0
2-D	30	.76	3.17	0	T.E.
3-D	30	.76	3.17	11.6	3.0
2-D	68°	.50	4.40	-7.0	3.0
2-D	68°	.50	4.40	-7.0	T.E.
3-D	68°	.50	4.40	3.2	3.0

The flow at the flap trailing edge is depicted in Figures 17 and 18 by contours of dynamic pressure ratio q/q_t and sidewash angle ψ, for flap angles of 30° and 68°, and flow conditions noted in Table I. These contours show that the jet has elongated in a spanwise direction, and leaves the trailing edge as a flattened sheet. The spanwise distribution of dynamic pressure is also plotted, at locations below the wing approximately in the centre of the deforming jet, and close to the flap trailing edge.

Figures 17 and 18 also show the spanwise variation of sidewash angle ψ at locations above the wing and along the flap surface close to the trailing edge. These results, confirmed by flow visualization, indicate that fluid above the wing is directed inward toward the jet centreline as a result of the low pressures there. This is in contrast to the vigorous expanding jet sheet which flows around and outward along the flap components (Sketch ii). The sudden change in the direction and magnitude of the velocities near the flap surface suggests strong vorticity, which has both spanwise and streamwise components.

The main characteristics of the fully developed wake flow ($\frac{x_w}{c} = 3$) are illustrated in Figures 19 and 20 for the 30° and 68° flap settings. Presented in these figures are contours of sidewash $\frac{v}{V}$, downwash $\frac{w}{V}$ and total head, $\frac{H - P_o}{q_t}$, for both the quasi-2-D and half-model configurations. The sidewash and downwash contours are presented as a composite, in the downwind plane. The rolled-up vortices which characterize the trailing jet sheet were observed by smoke flow visualization, but a concentration of vorticity is also suggested by the relative orientation of the downwash and sidewash contours in these figures. Contours of $\frac{H - P_o}{q_t}$ confirm the presence of a propulsive stream tube which is deforming and rolling up with the vortices emanating from the wing. The propulsive flow is also indicated by the shaded contour on the sidewash and downwash graph.

In Figure 19 ($\delta_F = 30°$, $C_\mu = .76$, $C_{L_w} = 3.18$) the vortex span of the quasi-2-D model is approximately 0.6 × (model span) and lies 0.1 × (model span) below the wing. The propulsive wake extends further outboard, and lies below the trailing vortices.

Interpretation of the induced velocity patterns downwind of the half-model is complicated by the existence of a wing tip vortex and also the presence of separated flow from the wing-groundboard junction. The flow contours are difficult to interpret, but the sidewash patterns seem to place the vortex at roughly the same span as for the 2-D configuration. Its location underneath the wing, however, is nearly three times that of the quasi-2-D model which was tested at the same lift coefficient. The propulsive wake also lies further below the wing than was originally anticipated.

It will be recalled from section (3.3) that an analysis of the force data (i.e. C_{L_w} vs. C_{D_w}) showed that the half-model forces were related to the quasi-2-D forces by a rotation of the wind vector through an angle which depended on lift, and the aspect ratio of the half model. Thus models tested at the same lift should have the same average downwash in the wake, and the same general location of the trailing vortices. The fact that from the wake flow measurements, this does not appear to be so, may cast some doubt on this hypothesis, but it should be recalled that the floor, which was present for the quasi-2-D test, but not for the 3-D test, would to some extent, prevent the downward movement of the wake vortices and propulsive jet.

Flow patterns for the 68° flap setting ($C_\mu = 0.5$, $C_{L_W} = 4.4$) are shown in Figure 20. The trailing vortex flow is evident from the induced velocity patterns of both the quasi-2-D and 3-D configurations; the propulsive flow is located about a semi-span below the wing, and has deformed laterally almost the entire semi-span. From the induced velocity contours of the half-model flow, it is possible to identify not only the powered-lift vortices but the wing-tip vortex as well. Their estimated location is marked on Figure 20, and it appears that the mutual effect of the induced velocities is causing the vortices to move relative to one another as they trail downstream. Thus the vortices, V_2 and V_3 in Figure 20 will tend to rotate about one another, with the wing tip vortex tending to rise above the wing plane.

5.2 The Flow Downwind of a Multi-Engined EBF Configuration

The flow downwind of a complete aircraft, such as a multi-engined EBF transport during a STOL approach under powered lift, will, naturally, be more complex than that of the simple configurations discussed in the preceding sections. The performance of the horizontal tailplane is crucial under these conditions, and a knowledge of the downwash velocities would be considered useful for preliminary design studies. Flow traverses were made, therefore, using 5-hole probes, at the tailplane location of a reflection-plane model of a four-engined transport, employing the EBF concept. A general view of this model with the wake traverse gear positioned, is described in Reference (6).

The model configuration and tunnel flow were appropriate to a landing approach under powered lift ($\delta_F = 55°$, $C_L = 3.5$, $C_\mu = 0.75$, $\alpha_W = 0°$).

Figures 21 and 22 describe the wake flow behind this model for $C_\mu = .75$, and for nacelle locations in the spread and coupled configuration respectively.

It was evident from the measurements that the trailing wake of this model contained the propulsive and vortical flows which are characteristic of the EBF, and which were described in the preceding sections. These flows are depicted in Figure 21 (nacelles spread) by contours of sidewash v/V and downwash w/V, and also total head $\frac{H - p_o}{q_t}$. The relative orientation of w/V and v/V suggests the presence of at least two strong vortices, V_1 and V_2 shed from the flap/aileron junction, and wing tip respectively. There is also some evidence of a third vortex on the inboard side, due, possibly, to a wing/fuselage separation, or the rolling up of the inboard portion of the jet sheet.

The location of the propulsive stream tube in the wake is given by the contours $\frac{H - p_o}{q_t}$ shown on the same graph. Although it is not possible to identify the details of each engine flow, it can be seen that the maximum values of total head occur well below and slightly outboard of the engine locations, thus emphasizing the outward lateral drift of the jet exhaust. The total efflux, having left the wing as a flattened sheet, has subsequently deformed into a U-shaped mass as it is drawn toward and rolls up with the vortex emanating from the flap/aileron junction. This efflux is indicated schematically as a shaded overlay on the induced velocity contours.

The flow in the wake of this configuration is therefore characterized by the behaviour and mutual interaction of the deforming jet and the streamwise vortices emanating from the flap/aileron junction and wing tip. A result of this interaction is the unusual location of the outer vortex: this vortex is positioned above the wing plane and inboard of the wing tip. It is evident that the upper and lower vortices have rotated about one another since leaving the wing trailing edge, and will continue to do so at locations further downstream.

The propulsive stream tube will also continue to deform since it is the more passive of the two wake components and will be dominated by the trailing vorticity. Local regions of quite low total head $\left(\frac{H - p_o}{q_t} < 0\right)$ were observed at the centres of the vortices V_1 and V_2; this is consistent with the flow in a vortex core, which is typified by intense rotation, low pressures and viscous diffusion.

Figure 22 which shows a similar presentation for the coupled engine nacelles ($C_\mu = 0.75$) exhibits the same general properties as for the spread nacelles. The only noticeable difference in the wake is that of the propulsive flow, which appears to be thinner, and slightly less deformed compared to the spread nacelle configuration.

6.0 CONCLUSIONS

The following conclusions can be drawn from the investigations of the External Blowing Concept for powered lift.

1) External Blowing has a dominant effect on the wing aerodynamic characteristics such as lift and $C_{L_{max}}$. In this regard, the EBF is comparable to other forms of powered lift, such as the jet flap or augmentor wing.

2) The analysis of the "wing only" drag polars of the EBF models have shown that they can be regarded as a form of jet flap, having a polar equation of the form: $C_{D_W} = C_{D_O} + (C_{L_W}{}^2)/(\pi eA)$. The wing efficiency factor e and thrust recovery factor r were found to be related to the amount of part-span blowing. Low values of e and r are, therefore, an inherent characteristic of the EBF, or any other powered lift system in which only part of the span is active.

3) The relationship between the quasi-2D and half-model configurations is that lift and drag forces can be considered, in the half-model case, to have been rotated through an induced incidence $\Delta\alpha_i$, which is the result of a change in effective aspect ratio from approximately 30 to about 5.

4) The jet flow induces some very large changes in the local aerodynamic loading, particularly on the flap components, and the impingement region of the main aerofoil lower surface. Although the loading is localized mainly at the centre of the wing, it extends well beyond the original dimensions of the jet, particularly on the flap elements.

5) The flow in the wake of the EBF is characterized by the existence of trailing vortices, which have resulted from the non-uniform span loading, and which induce downwash and sidewash velocities of considerable magnitude. The propulsive jet, which leaves the flap trailing edge as a flattened sheet, deforms and rolls up with the trailing vortices into a U-shaped pattern.

6) The wake behind a multi-engined transport configuration also contains both propulsive and vortical components. Measurements downwind of a half-model have shown that behind each half-wing, there are two trailing vortices, one from the wing tip and one from the flap/aileron junction. The propulsive jet flow rolls up behind the vortex from the flap tip. The interaction of the two vortices causes the wing tip vortex to lie above the wing plane.

7.0 REFERENCES

1. Wick, B.H. and Kuhn, R.E. Turbo Fan STOL Research at NASA, Astronautics and Aeronautics, Vol. 9, No. 5, May 1971.

2. Vogler, R.D. Wind Tunnel Investigation of a Four-Engined Externally Blowing Jet-Flap STOL Airplane Model. NASA TN D-7034, Dec. 1970.

3. Freeman, D.C. and Parlett, O.P. et al. Wind Tunnel Investigation of a Jet Transport Airplane Configuration with an External-Flow Jet-Flap and Inboard Rod-Mounted Engines. NASA TN D-7004, Dec. 1970.

4. Parlett, O.P. and Shivers, J.P. Wind Tunnel Investigation of a STOL Aircraft Configuration Equipped with an External-Flow Jet-Flap. NASA TN D-5364, Aug. 1969.

5. Perry, D.H. A Review of Some Published Data on the External-Flow Jet-Flap. ARC CP 1194.

6. Wickens, R.H. DHC WTBJ II Reflection Plane Model - Wake Flow Components. NRC, NAE Wind Tunnel Data Report 6×9/0196, Dec. 1972.

7. Wickens, R.H. Experimental Developments in V/STOL Wind Tunnel Testing at the National Aeronautical Establishment. Canadian Aeronautics and Space Institute, Annual General Meeting, May 1972.

8.0 ACKNOWLEDGEMENTS

The author wishes to acknowledge the cooperation of DeHavilland Aircraft of Canada, Limited, who supplied the flap components, and also the EBF half-model. Acknowledgements are also due to R.J. Templin and Y. Nishimura who contributed to the analysis and reduction of data respectively.

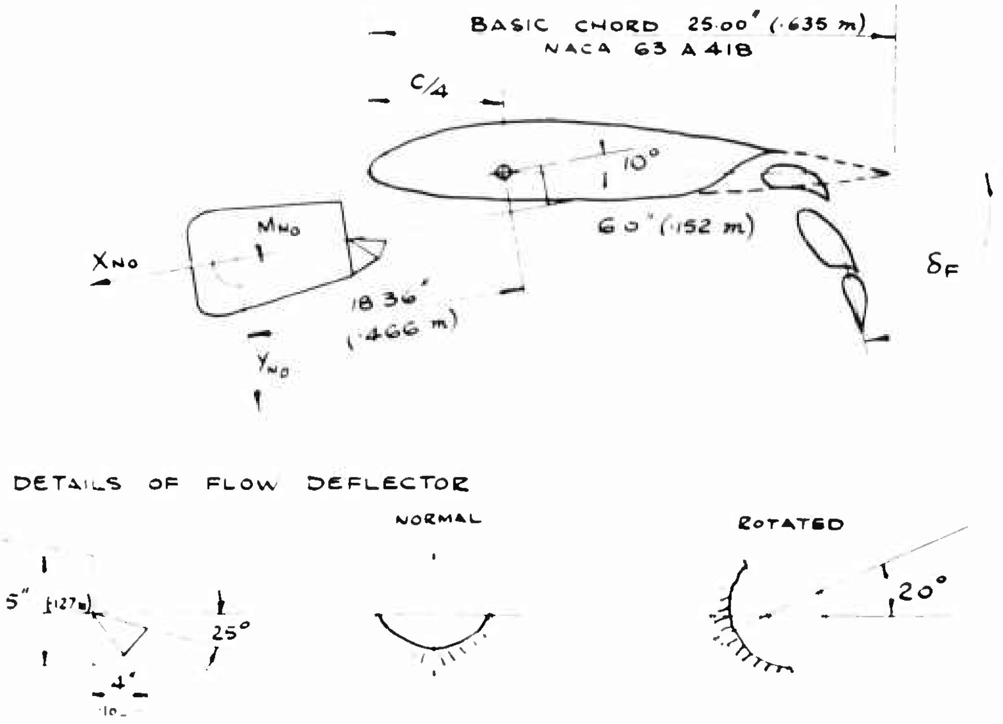
BASIC CHORD 25.00" (.635 m)
NACA 63 A418
C/4
10°
6.0" (.152 m)
M_NO
X_NO
Y_NO
18.36" (.466 m)
δ_F
DETAILS OF FLOW DEFLECTOR
NORMAL
ROTATED
5" (.127 m)
25°
4" (.10)
20°

GENERAL ARRANGEMENT OF MODEL, NACELLE & FLOW DEFLECTOR.

QUASI-2D CONFIGURATION

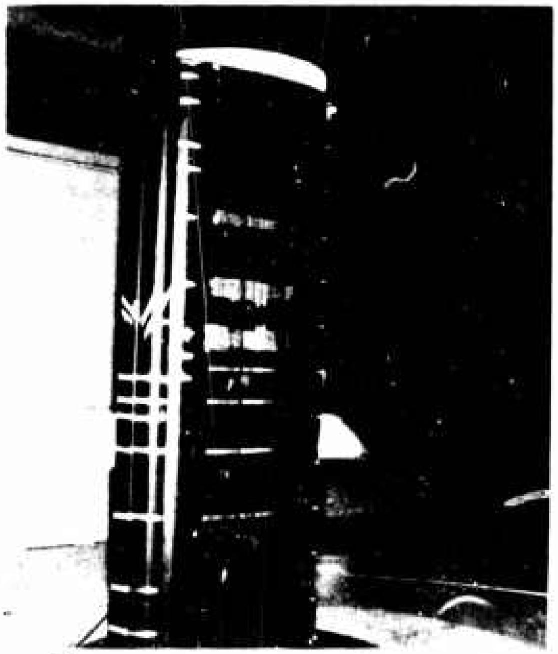
HALF-MODEL CONFIGURATION

FIGURE 1 GENERAL ARRANGEMENT OF WING SECTION AND WIND TUNNEL MODELS

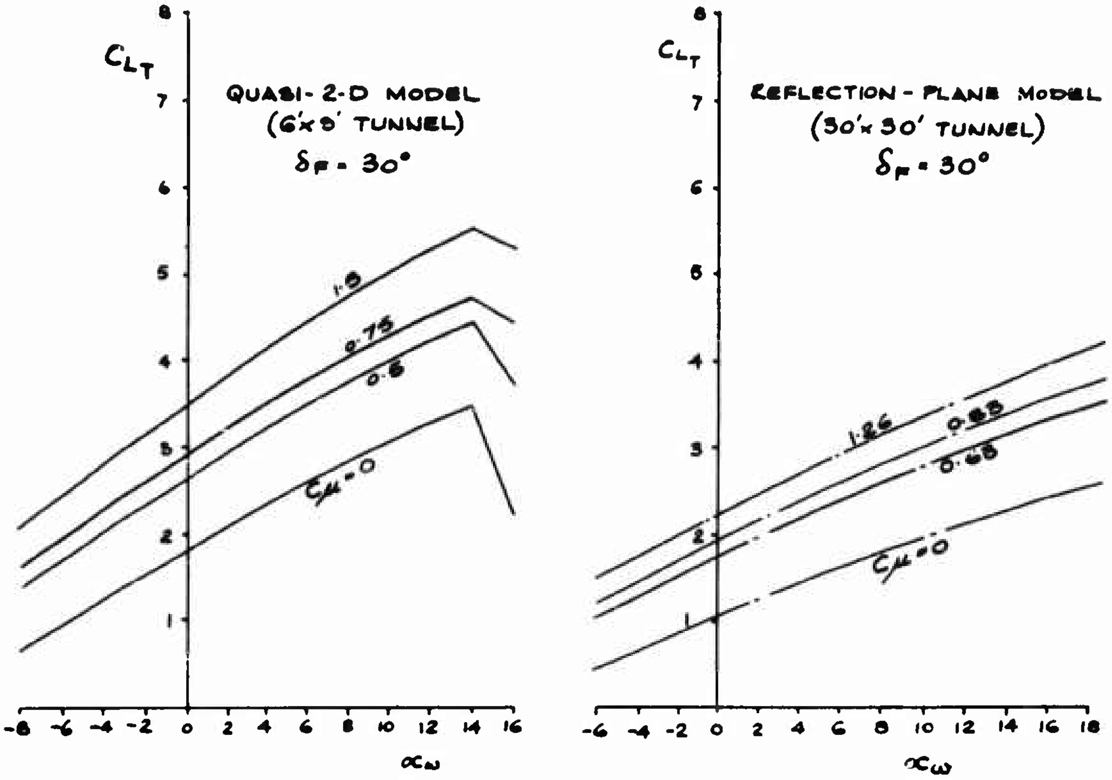

FIGURE 2 TOTAL LIFT COEFFICIENT C_{L_T}, $\delta_F = 30°$

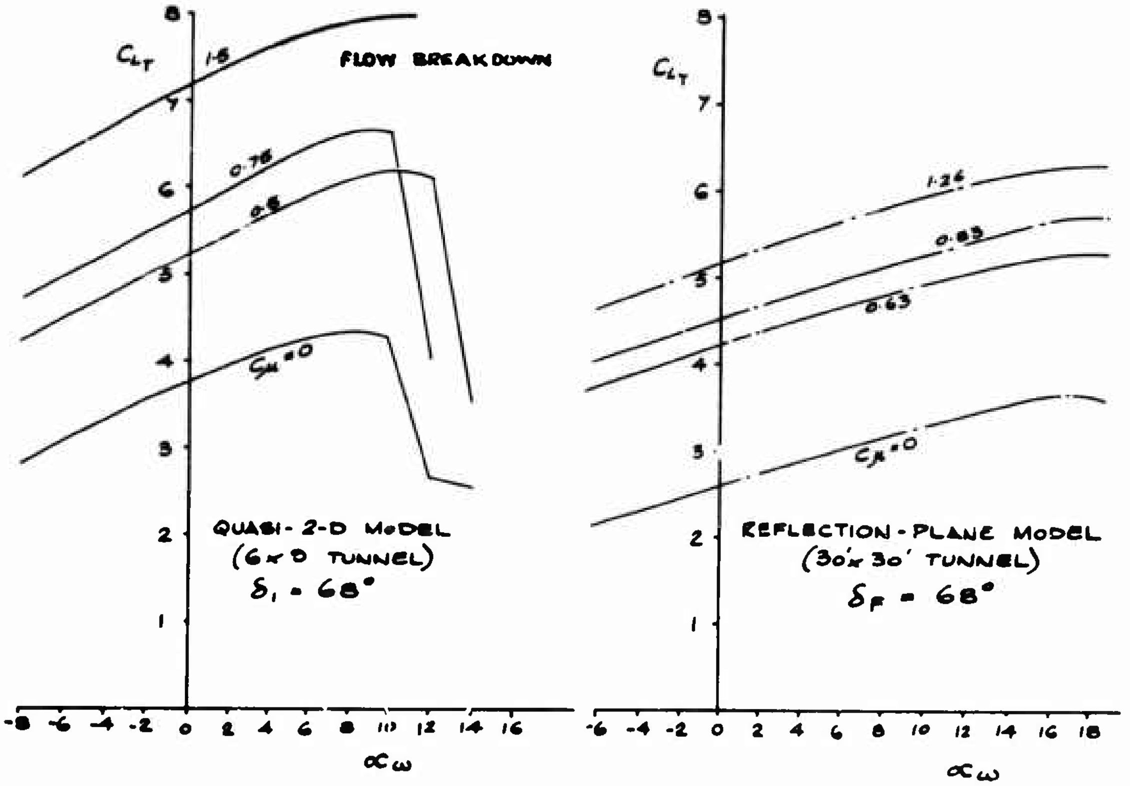

FIGURE 3 TOTAL LIFT COEFFICIENT C_{L_T}, $\delta_F = 68°$

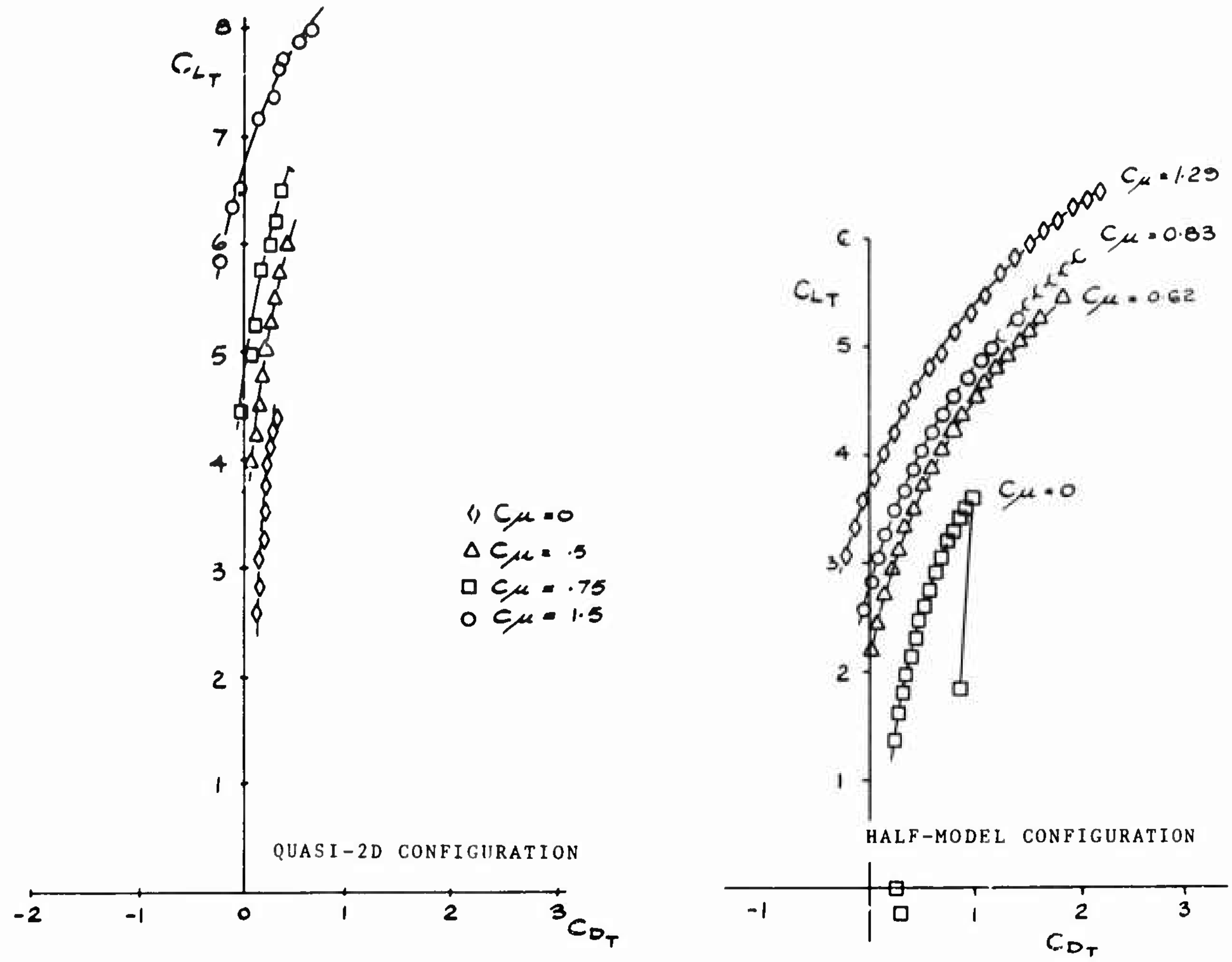

FIGURE 4 TOTAL FORCE POLARS, δ_F = 68°

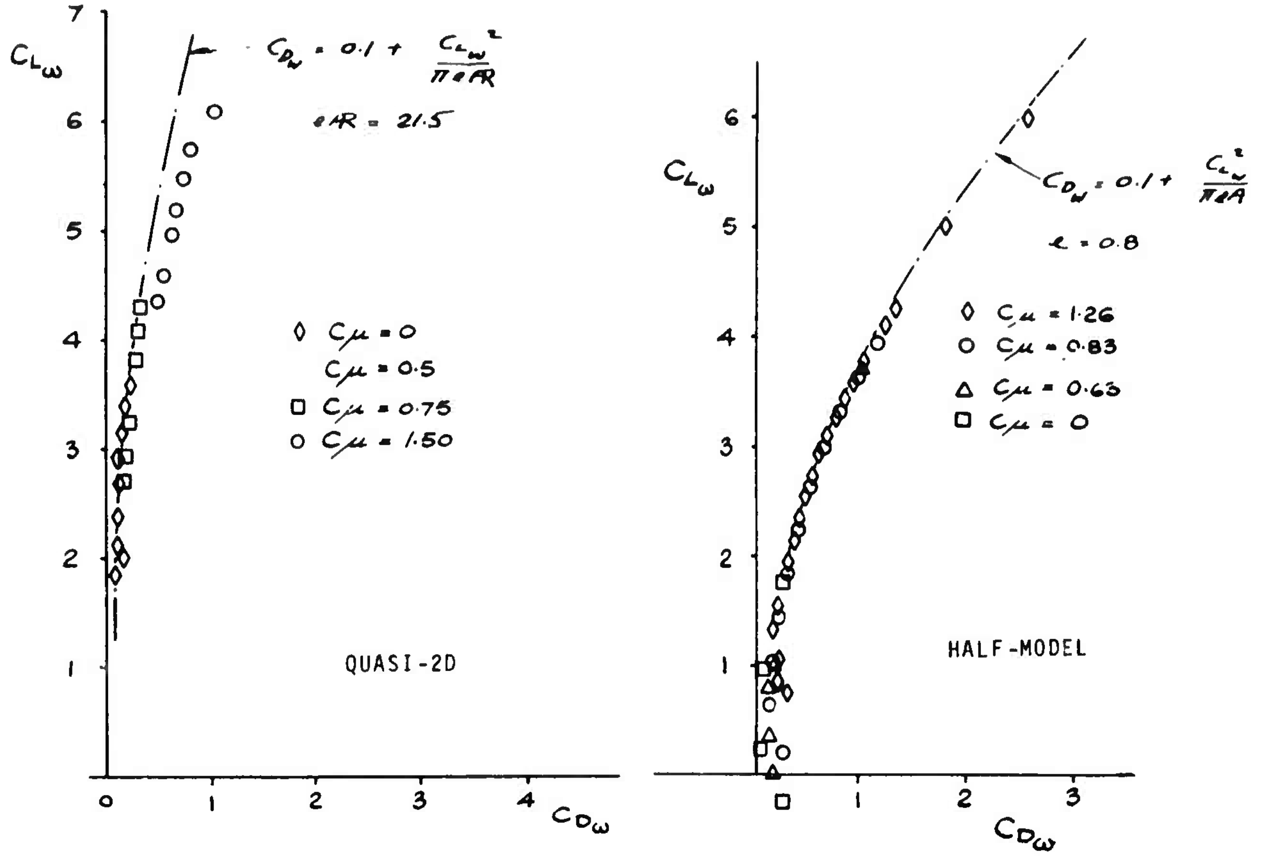

FIGURE 5 WING FORCE POLARS, δ_F = 30°

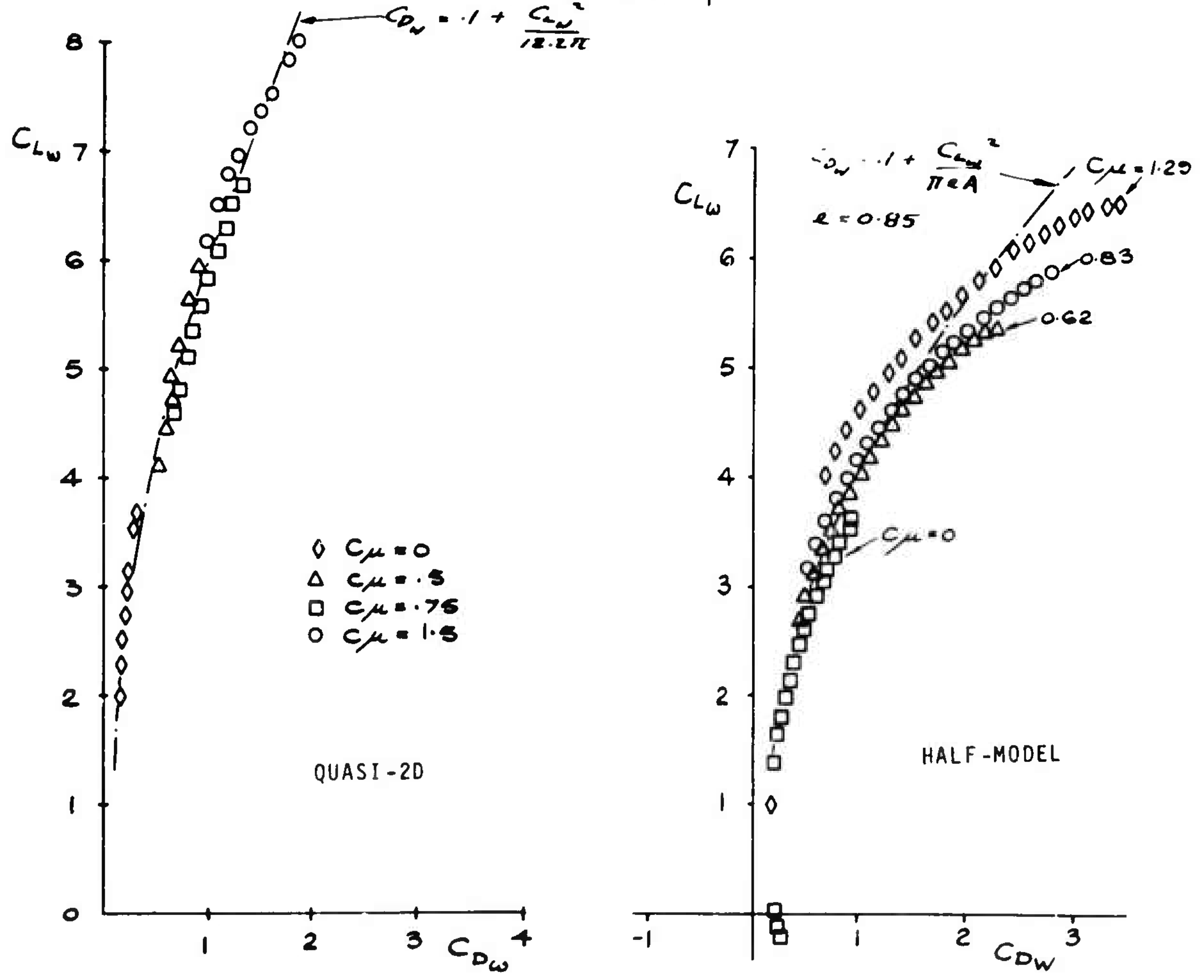

FIGURE 6 WING FORCE POLARS, δ_F = 68°

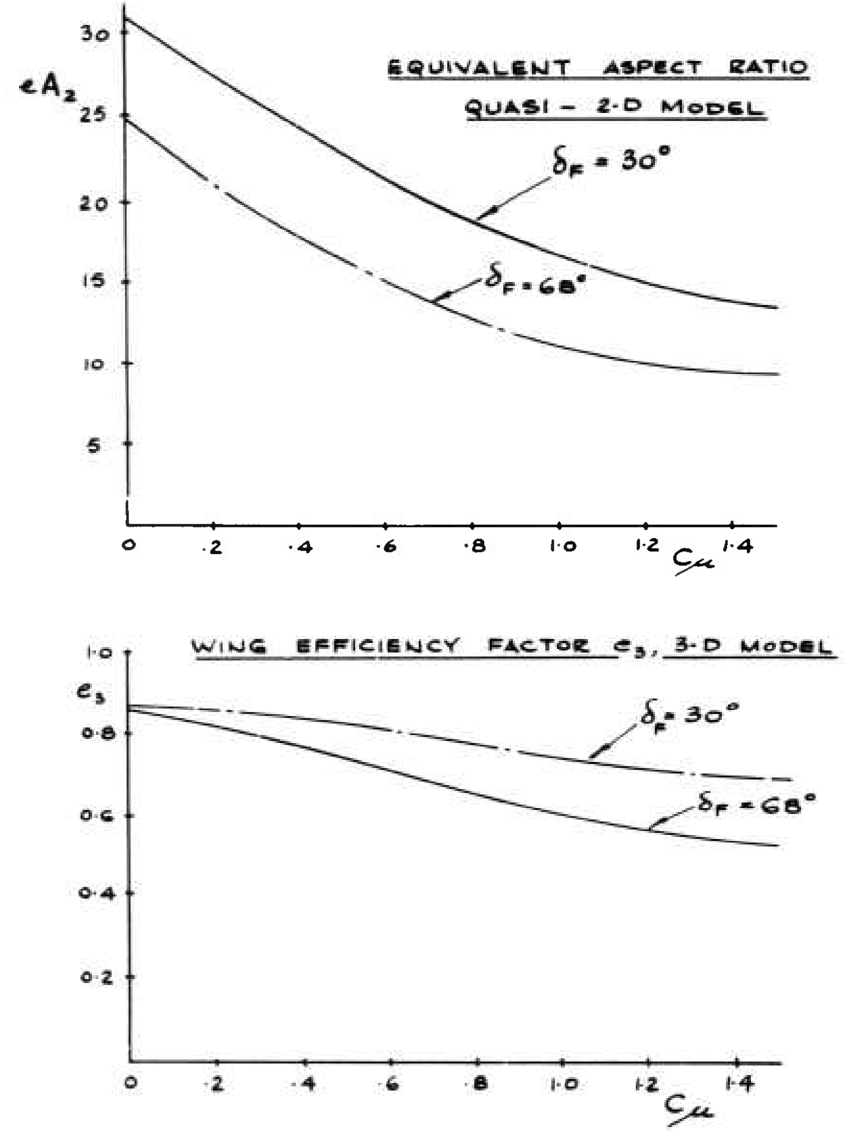

FIGURE 7 EQUIVALENT ASPECT RATIO AND WING EFFICIENCY FACTOR, QUASI-2D AND HALF-MODEL CONFIGURATIONS

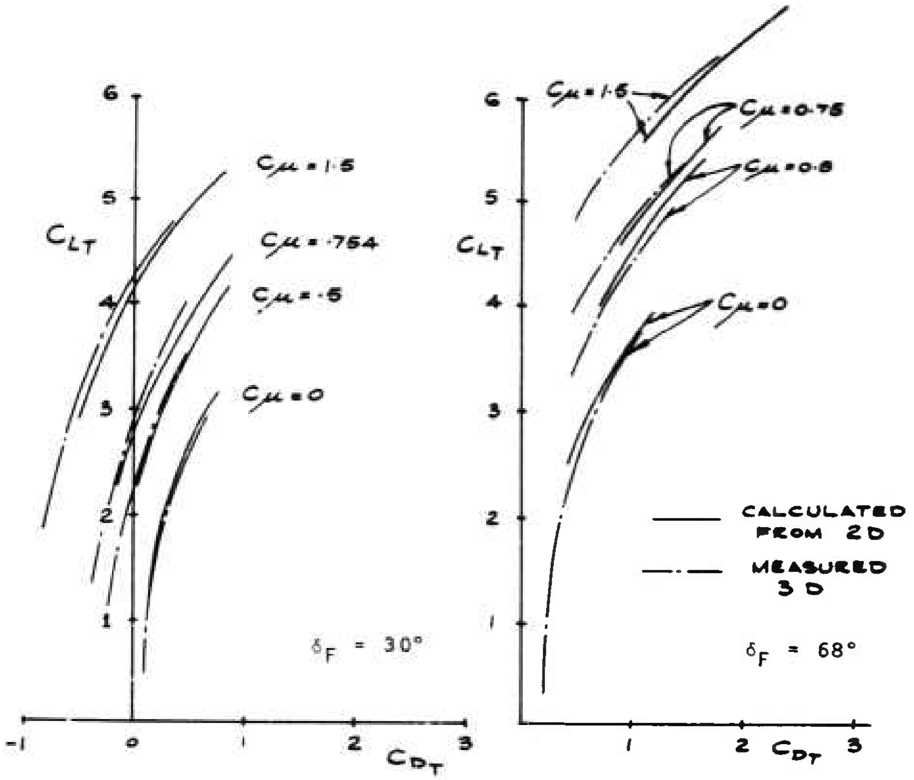

FIGURE 8 COMPARISON OF MEASURED AND TRANSFERRED FORCE POLARS,

δ_F = 30° AND 68°

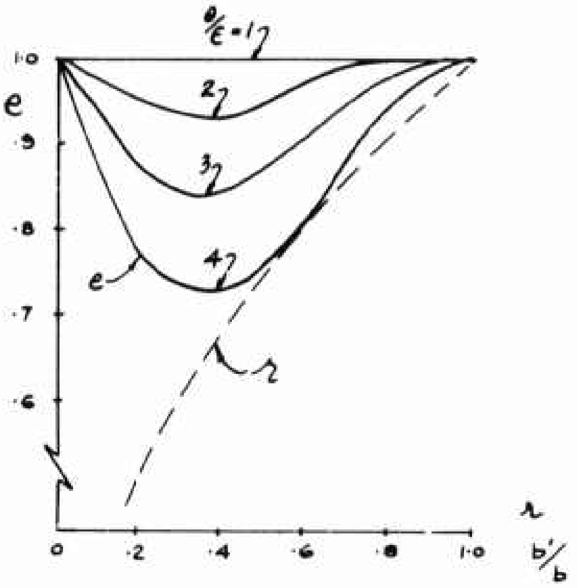

FIGURE 9 WING EFFICIENCY FACTOR

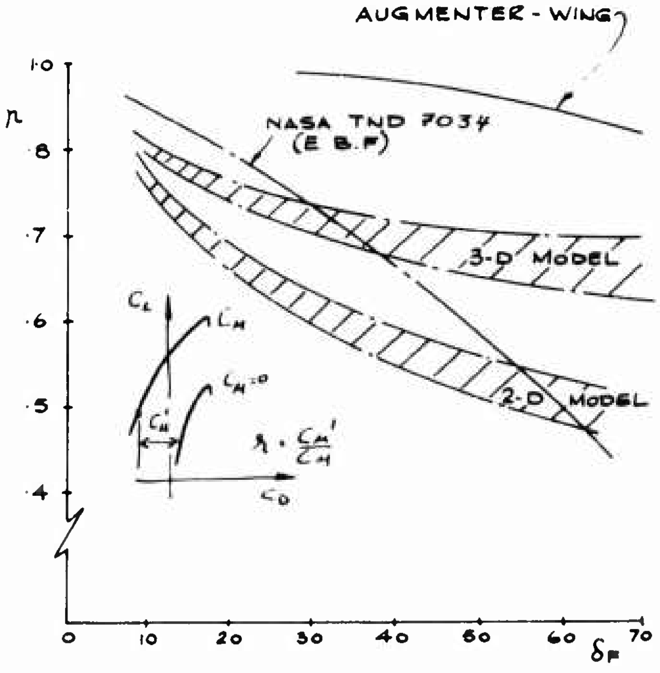

FIGURE 10 THRUST RECOVERY FACTORS

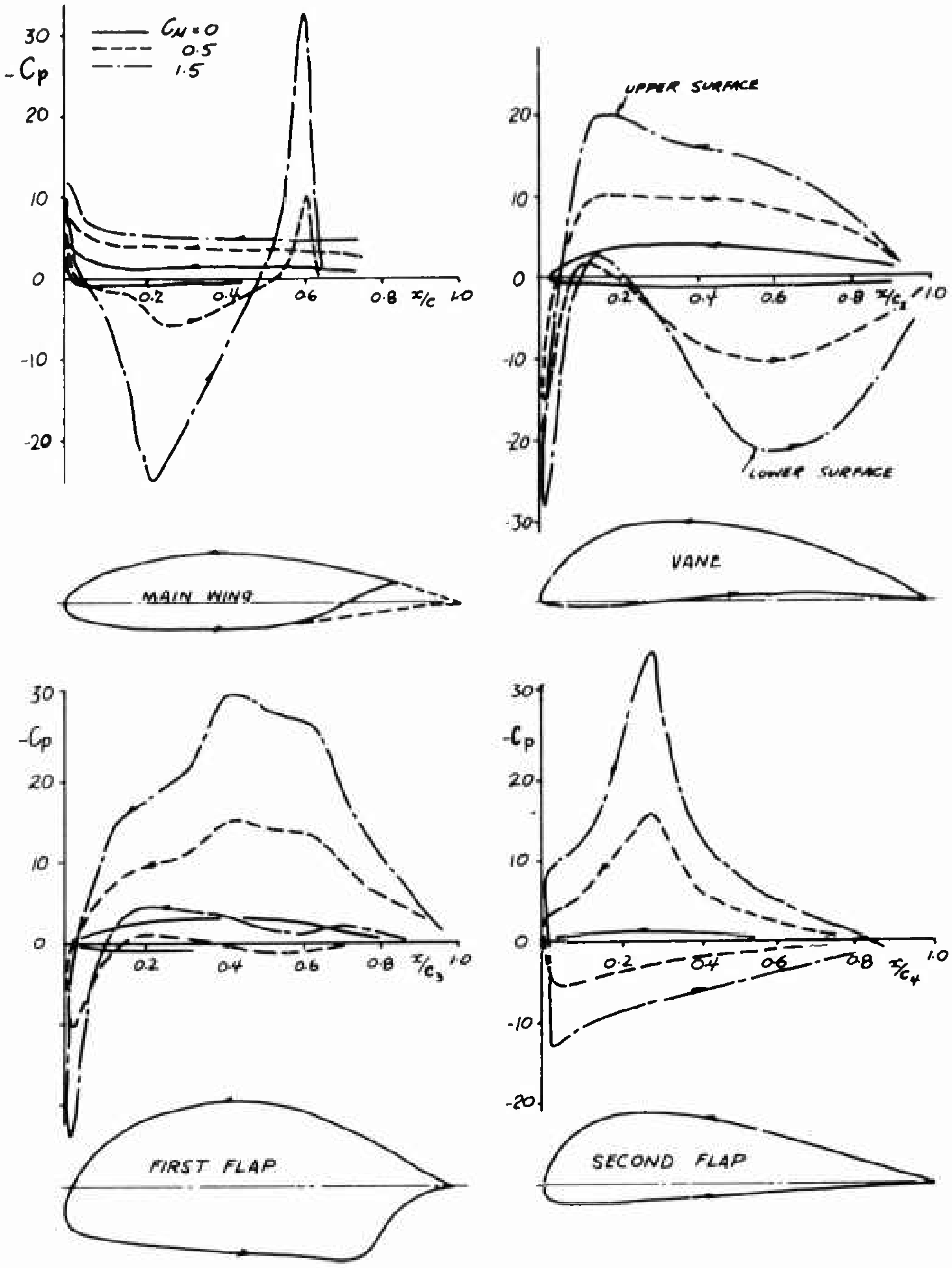

FIGURE 11 CENTRELINE PRESSURE DISTRIBUTION ON THE MAIN AEROFOIL AND FLAPS,
δ_F = 68°, α = -7.0° QUASI-2D CONFIGURATION

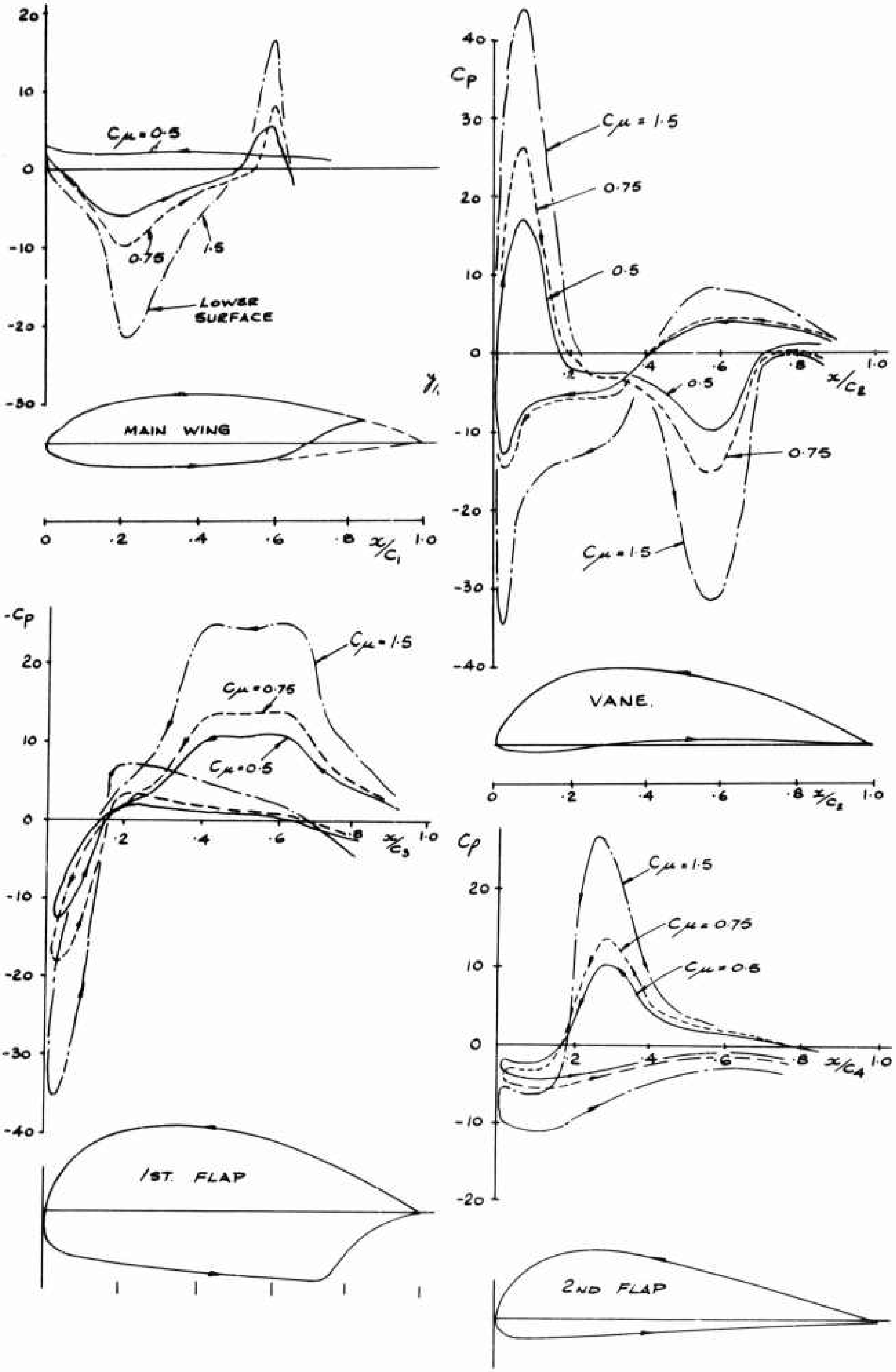

FIGURE 12 CENTRELINE PRESSURE DISTRIBUTION ON THE MAIN AEROFIL AND FLAPS, $\delta_F = 30°$, $\alpha = 0°$ QUASI-2D CONFIGURATION

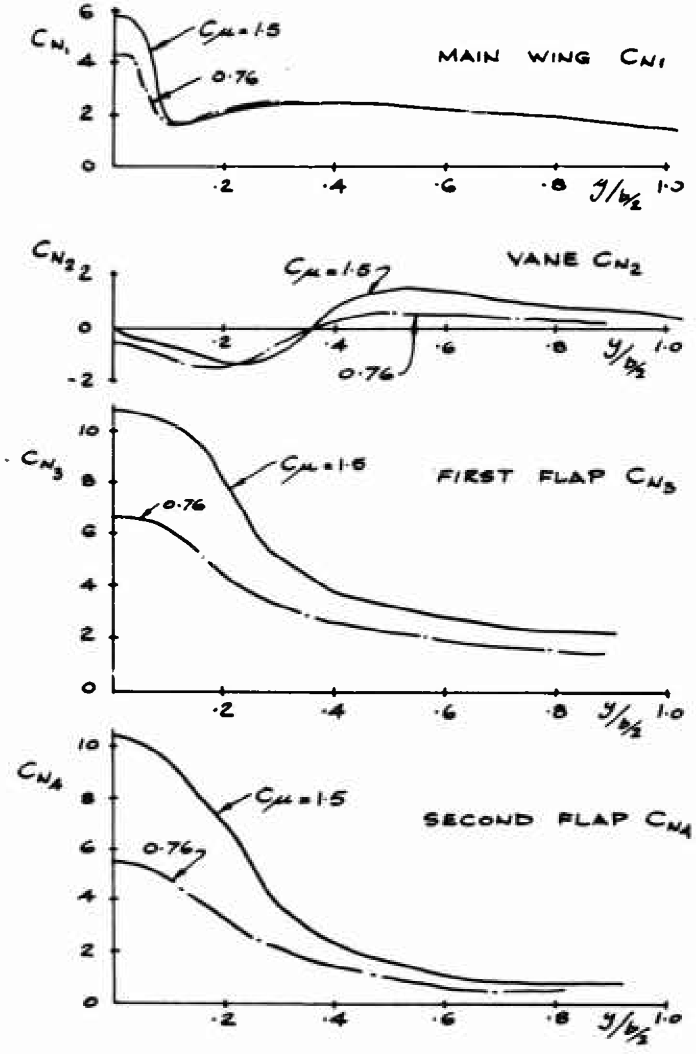

FIGURE 13 DISTRIBUTION OF NORMAL FORCE COEFFICIENT C_N

QUASI-2D CONFIGURATION $\delta_F = 30°$, $\alpha_W = 0°$

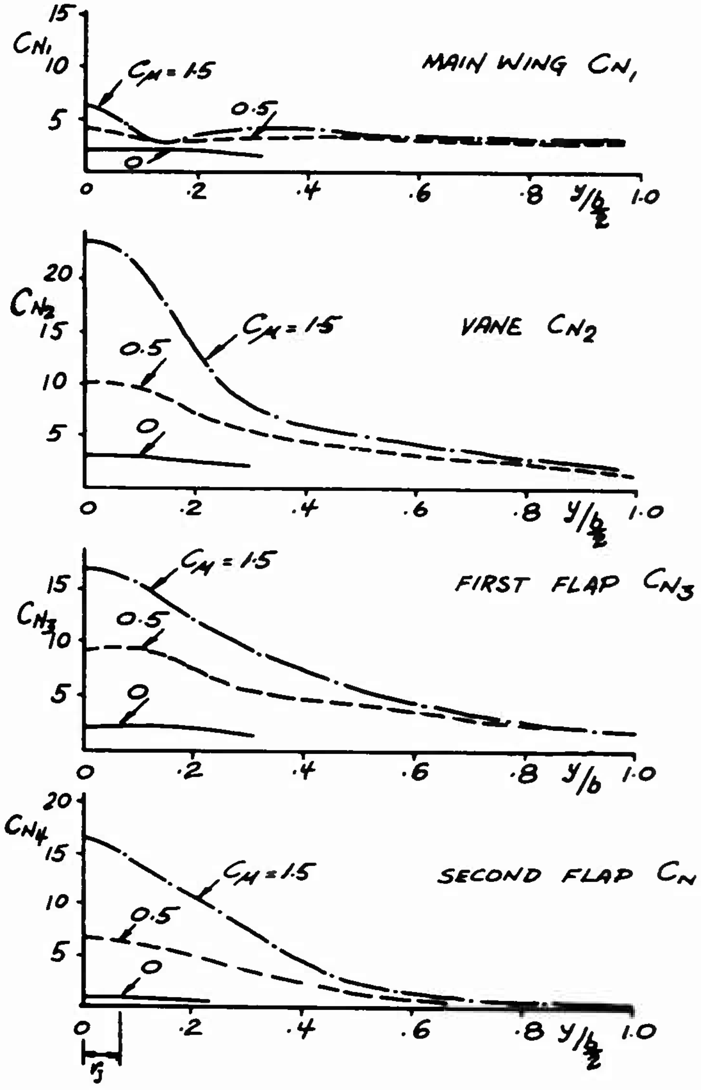

FIGURE 14 DISTRIBUTION OF NORMAL FORCE COEFFICIENT C_N

QUASI-2D CONFIGURATION $\delta_F = 68°$, $\alpha_W = -7.0°$

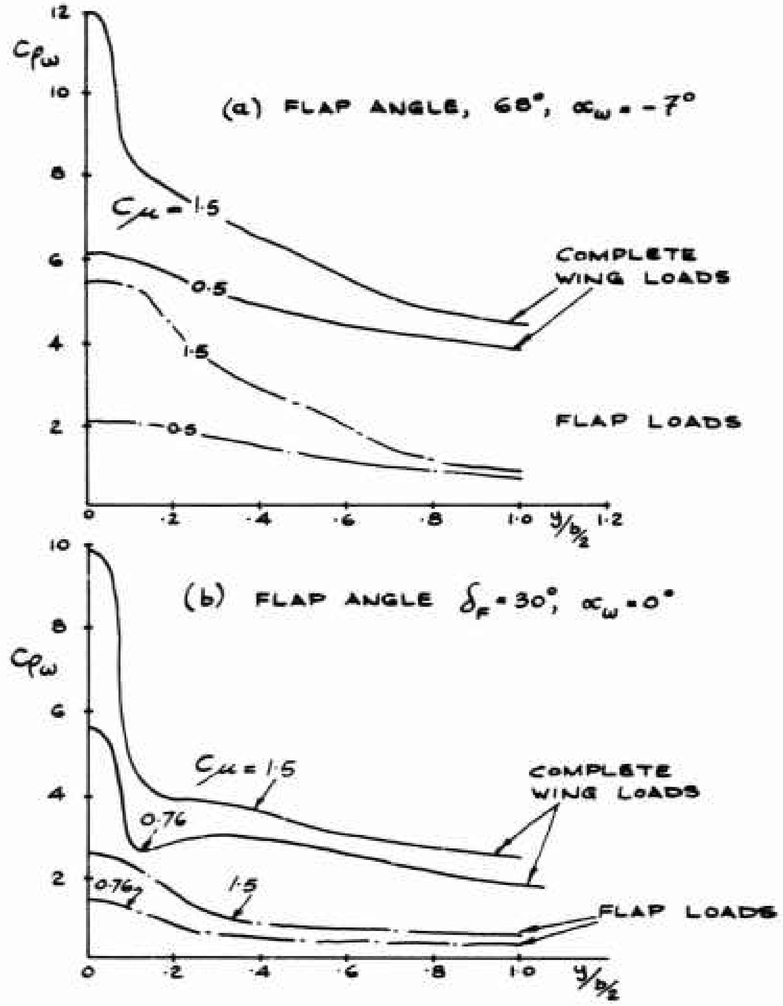

FIGURE 16 SPANWISE DISTRIBUTION OF LOCAL LIFT COEFFICIENT C_ℓ, FOR δ_F = 30° AND 68° QUASI-2D CONFIGURATION

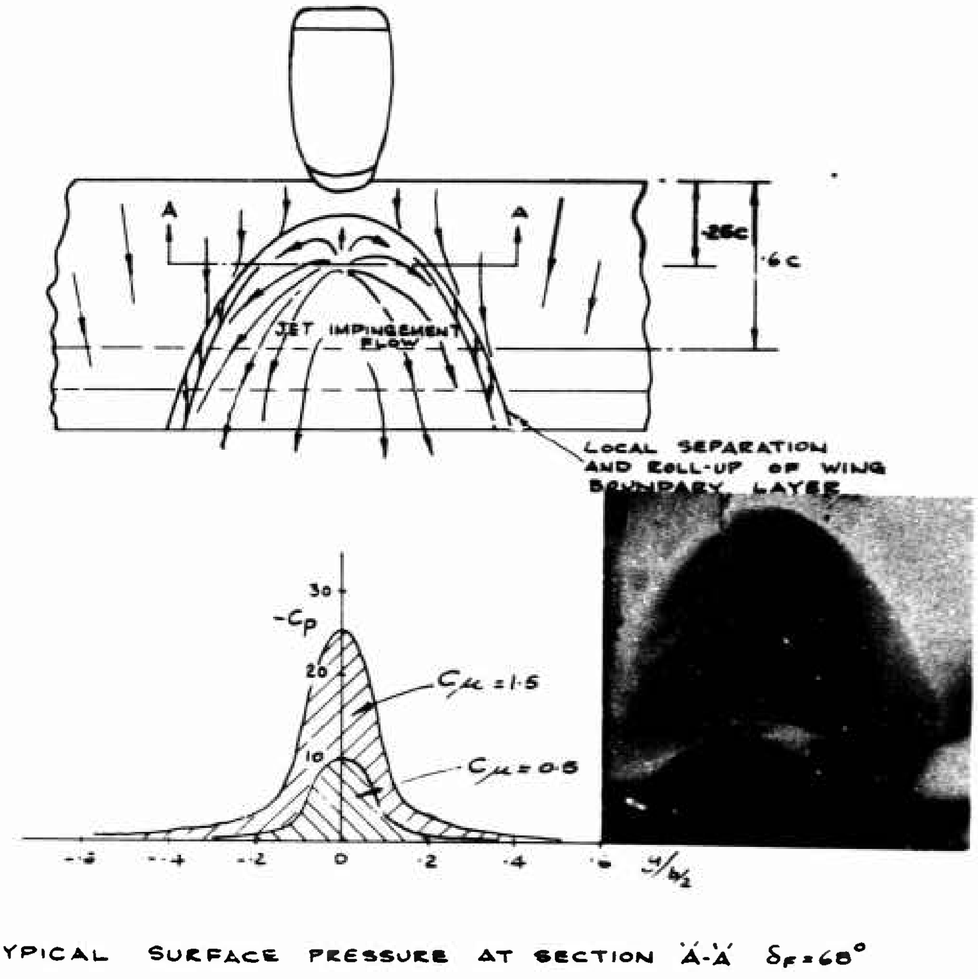
A
A
·25c
·6c
JET IMPINGEMENT FLOW
LOCAL SEPARATION AND ROLL-UP OF WING BOUNDARY LAYER
$-C_p$
30
20
10
$C_\mu = 1.5$
$C_\mu = 0.5$
-·6
-·4
-·2
0
·2
·4
·6
$y/_{b/2}$
TYPICAL SURFACE PRESSURE AT SECTION A'-A' $\delta_F = 68°$

FIGURE 15 JET IMPINGEMENT FLOW ON THE MAIN AEROFOIL LOWER SURFACE QUASI-2D CONFIGURATION

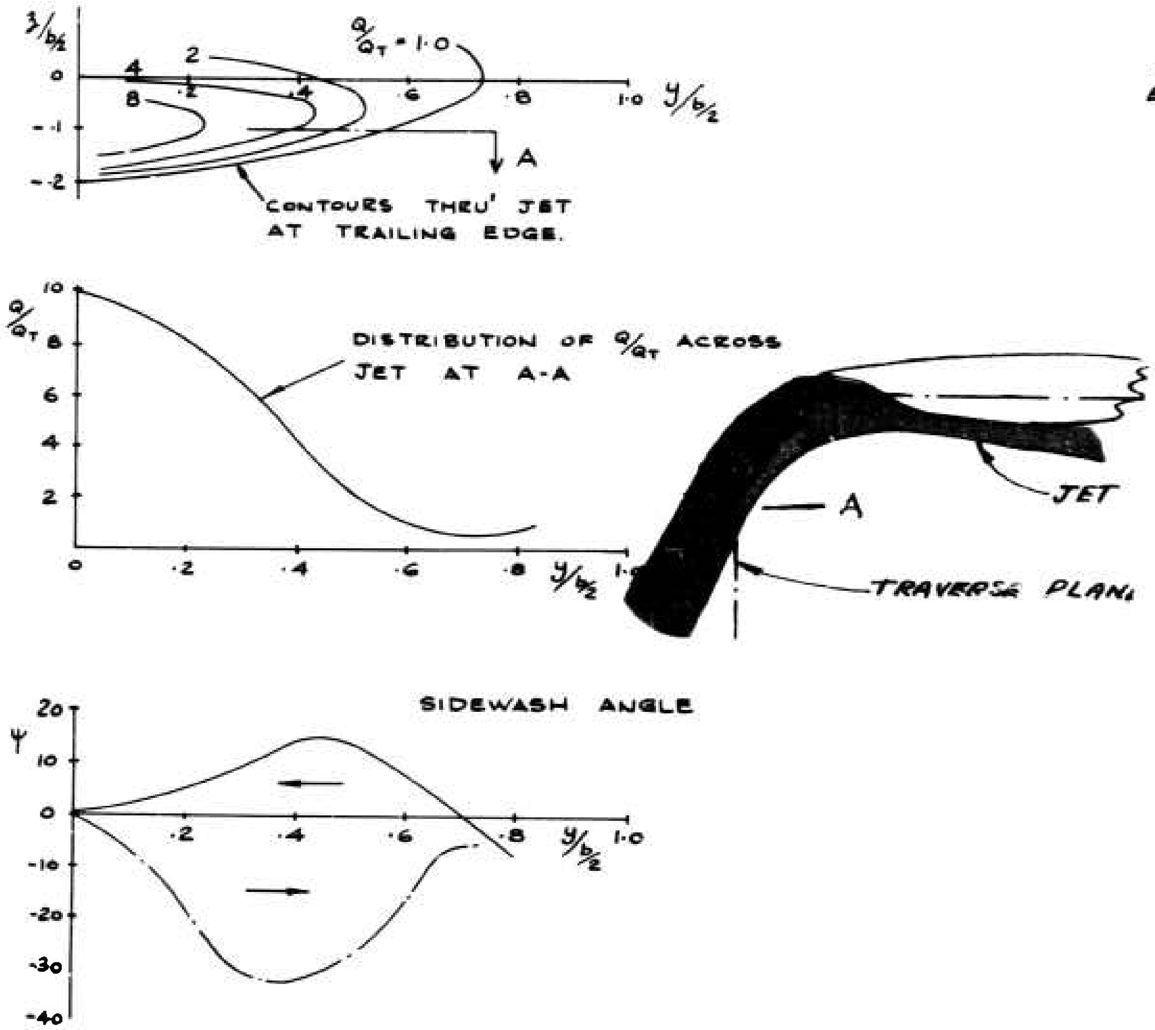

FIGURE 17 DYNAMIC PRESSURE AND FLOW DIRECTION AT THE TRAILING EDGE, δ_F = 30° QUASI-2D CONFIGURATION

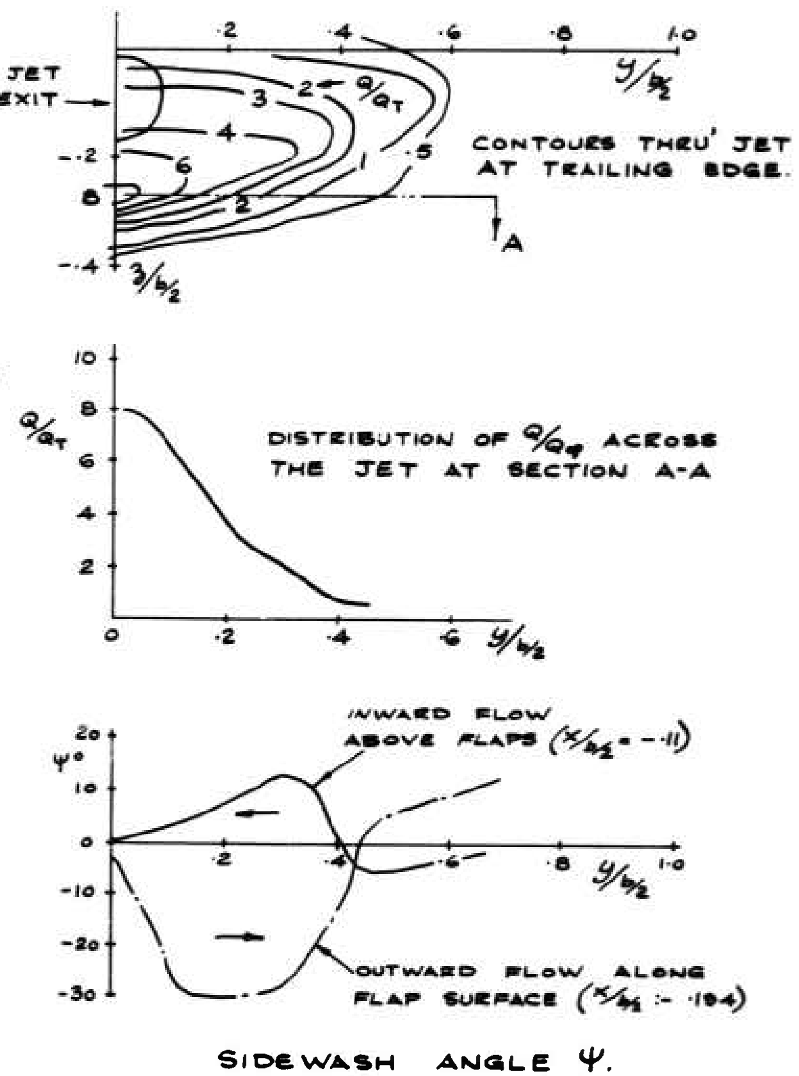

FIGURE 18 DYNAMIC PRESSURE AND FLOW DIRECTION AT THE TRAILING EDGE, δ_F = 68° QUASI-2D CONFIGURATION

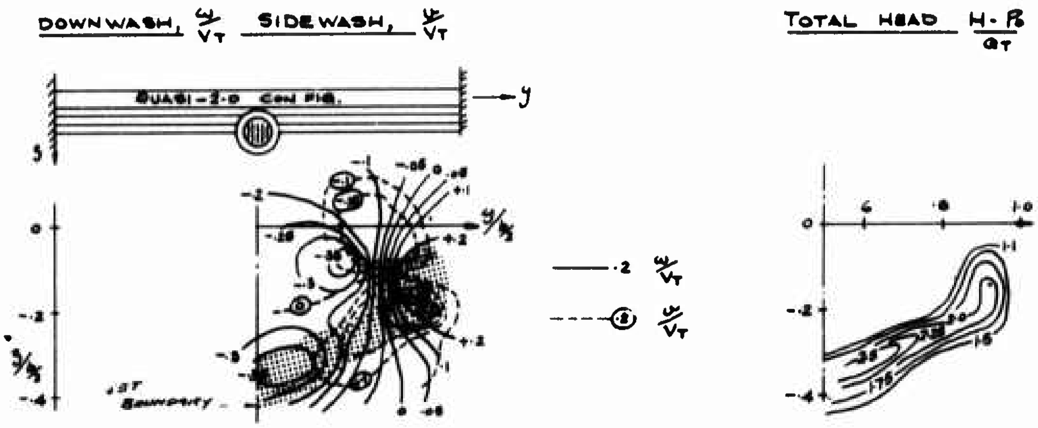

δ_F = 30°

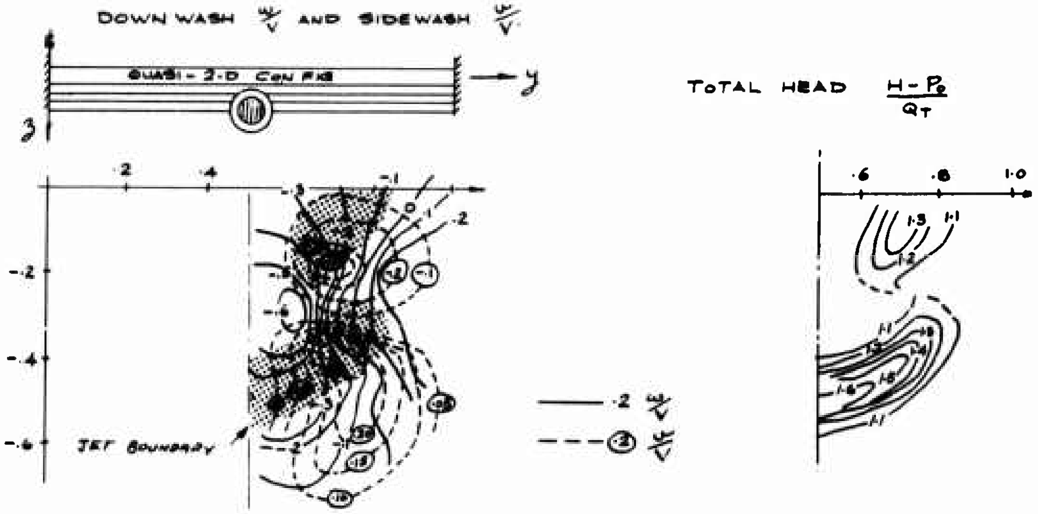

, δ_F = 68°

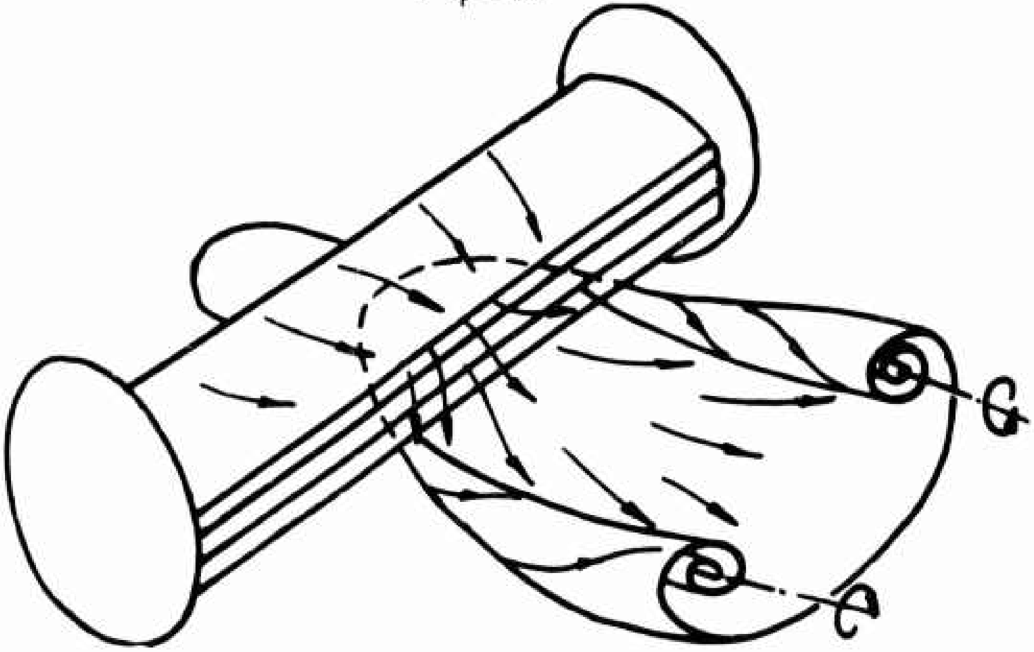

FIGURE 19 FLOW IN THE TRAILING WAKE, QUASI-2D CONFIGURATION

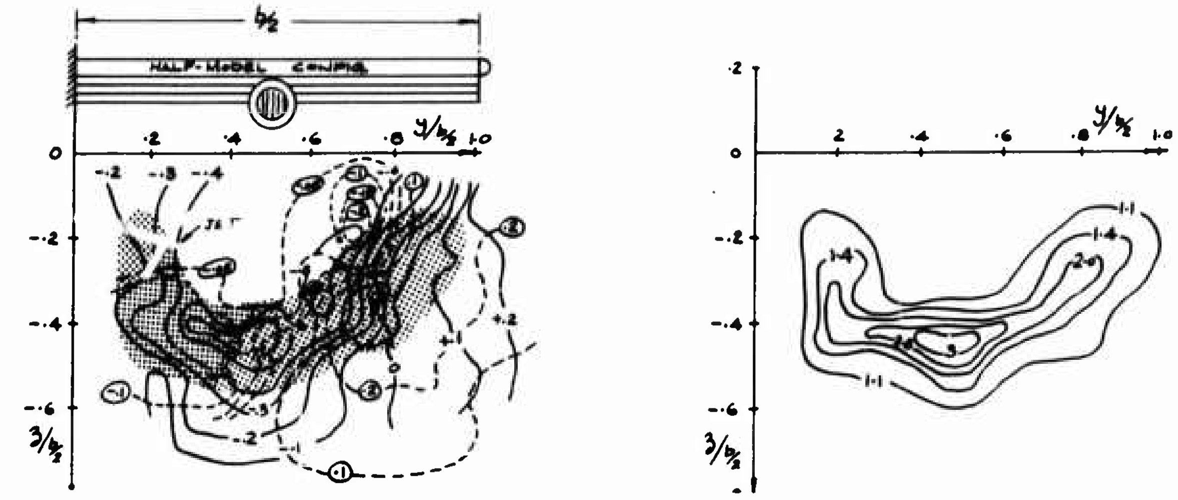

DOWN WASH $\frac{w}{V}$ AND SIDEWASH $\frac{v}{V}$

δ_F = 30°

TOTAL HEAD $\frac{H-P_0}{Q_T}$

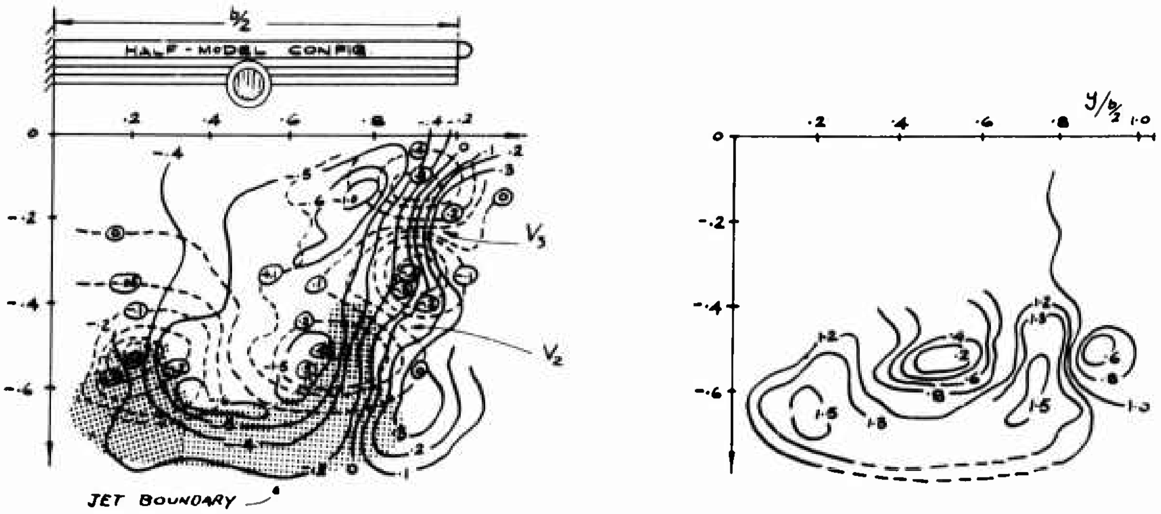

δ_F = 68°

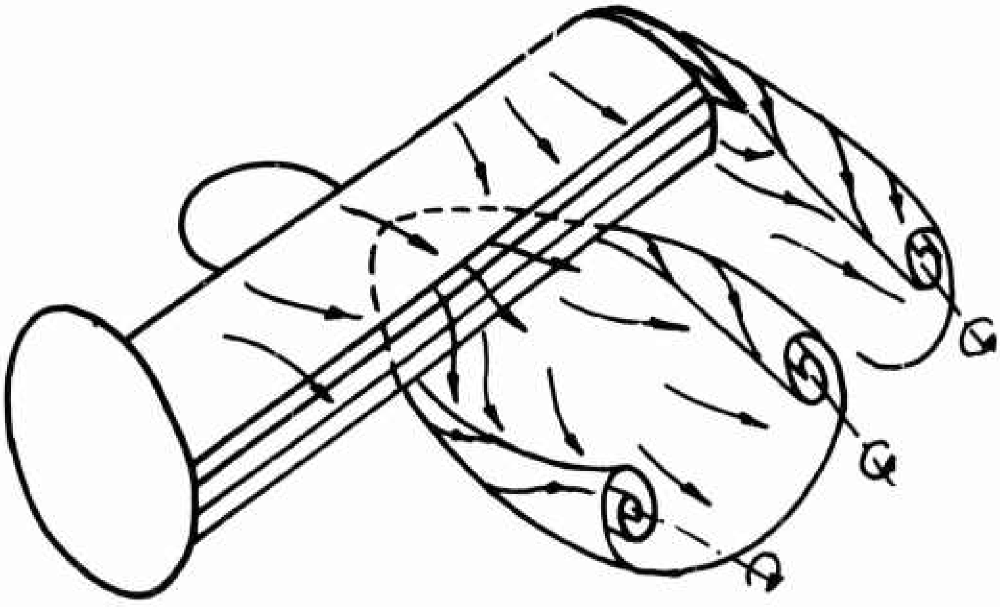

FIGURE 20 FLOW IN THE TRAILING WAKE HALF-MODEL CONFIGURATION

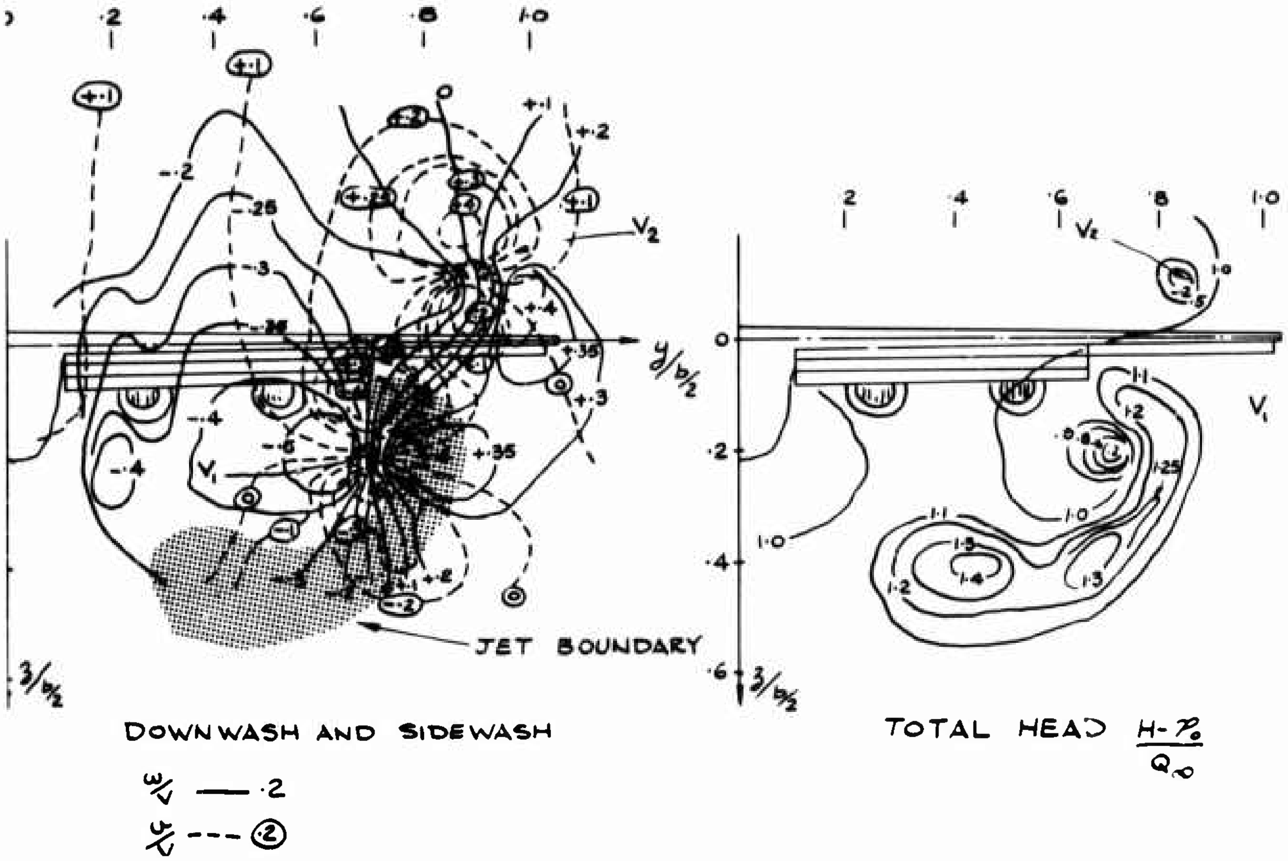

FIGURE 21 THE FLOW DOWNWIND OF A MULTI-ENGINED EBF TRANSPORT, NACELLES SPREAD, C_μ = 0.75, α_W = 0°

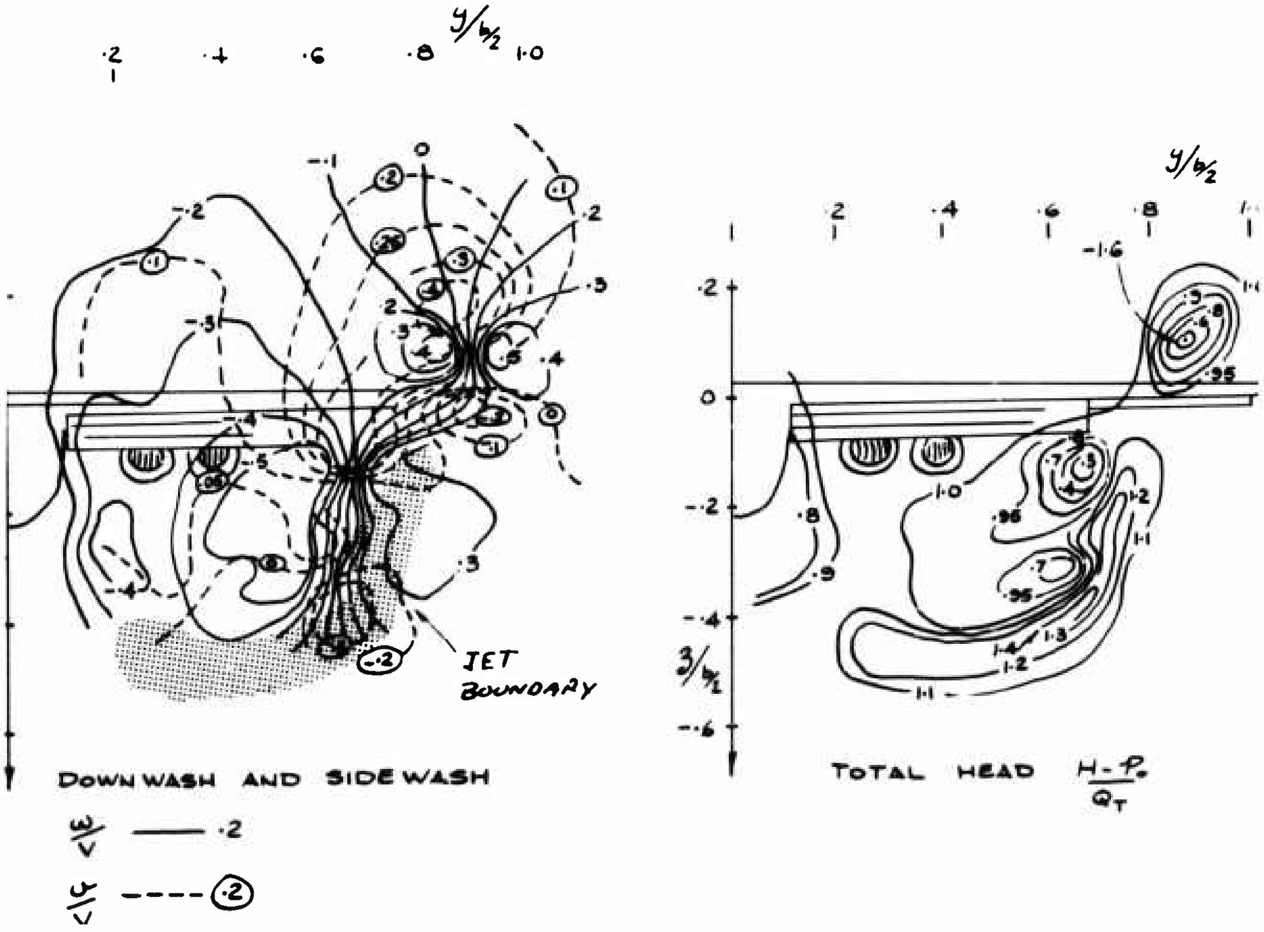

FIGURE 22 THE FLOW DOWNWIND OF A MULTI-ENGINED EBF TRANSPORT, NACELLES COUPLED, C_μ = 0.75, α_W = 0°

THE FLOW AROUND A WING WITH AN EXTERNAL-FLOW JET FLAP

P R ASHILL and D N FOSTER

ROYAL AIRCRAFT ESTABLISHMENT, BEDFORD, ENGLAND

SUMMARY

The aim of this paper is to identify and to interpret the main features of the flow around a wing with an external-flow jet flap. Measurements were made, under wind-on and wind-off conditions, on a half model of a wing-fuselage with an injector-powered nacelle mounted beneath the wing, the wind-on tests being performed at 30 m/s. The wing was tested at two angles of sweepback; 0° and 20°.

Analysis of the velocity distributions measured in the jet at the trailing edge of the flap suggests that the turning and spreading process is sensibly independent of forward speed. As might be expected, sweepback has the effect of biasing the spanwise distribution of momentum towards the wing tip.

The spanwise distributions of lift and pressure drag, derived from static pressure measurements made under wind-on conditions, exhibit a pronounced non-uniformity in the neighbourhood of the nacelle. However the residual load, defined as the wind-on load minus the wind-off load, is distributed in a relatively uniform manner across the span, supporting the view that the distribution of the direct jet reaction under wind-on conditions is similar to that under wind-off conditions. Analysis of the spanwise distributions of residual loading and jet momentum suggests that the contribution of the jet-flap effect to the total lift is small.

LIST OF SYMBOLS

$b_{\nu\mu}$ $b_{\nu\nu}$	influence coefficients in Multhopp's method of calculating spanwise load distribution(13)
C_D	drag coefficient
$\bar{C}_{Di}$	induced drag coefficient
$\bar{C}_{DJ}$	jet-reaction drag coefficient
$\bar{C}_{DM}$	measured overall-drag coefficient
C_{Dp}	pressure drag coefficient
$\bar{C}_{D\Gamma}$	circulation drag coefficient
C_L	lift coefficient
$\bar{C}_{LJ}$	jet-reaction lift coefficient
$C_{L\Gamma_J}$	circulation lift coefficient of jet
$C_{L\Gamma_W}$	circulation lift coefficient of wing
$\hat{C}_{L\Gamma}$	equivalent two-dimensional circulation lift coefficient
C_p	pressure coefficient
C_T	net thrust coefficient of isolated nacelle
C_{TG}	excess gross-thrust coefficient
C_X	$= (X - X_m)/qc$
C_Y	$= (Y - Y_m)/qc$
C_Z	$= (Z - Z_m)/qc$
C_μ	excess momentum coefficient, $= (J - J_m)/qc$
$\hat{C}_\mu$	effective two-dimensional excess momentum coefficient
c	reference chord of unswept wing (Fig 2)
f_2	downwash angle induced at jet by unblown flat wing at unit angle of incidence in reverse flow
g'	non-dimensional, vortex strength for a two-dimensional, jet-augmented flap(17)

H	total pressure in jet
J	jet momentum in streamwise plane
N	number of terms in Multhopp spanwise load calculation
n	distance measured normal to the local surface of deflected flap
p_r	reference static pressure in undisturbed main flow
q	dynamic pressure of undisturbed main flow
S	wing area
s	wing semi-span
T_s	static thrust
U_∞	undisturbed main flow velocity
X,Y,Z	local contributions to force on wing in x,y,z directions
x,y,z	left-handed Cartesian co-ordinates with origin on the fuselage centre-line at the leading edge of the unswept wing
α	angle of incidence
Γ	circulation
γ	local strength of spanwise vortices
η	non-dimensional spanwise distance, $= y/s$
η_J	thrust recovery factor
θ_J	local jet deflection angle

PREFIX

Δ	incremental part of

SUPERSCRIPT

—	overall value

SUFFIXES

e	effective conditions at wing section
i	conditions induced by vortex distributions on wing and jet
J	terms appertaining to jet
m	terms appertaining to mainstream flow
o	conditions of zero static thrust
R	terms derived as difference between wind-on and wind-off terms, ie residual terms
T	conditions at wing trailing edge
w	terms appertaining to wing
Γ	terms due to circulation
∞	conditions at infinity downstream
1	terms appertaining to forward motion
2	terms appertaining to reverse motion

1 INTRODUCTION

The external-flow jet flap is perhaps the simplest concept, structurally and mechanically, of all the powered-lift systems. Two basic configurations have been proposed, one with the engines mounted just beneath the wing and the other with the engines installed on the upper surface of the wing, with trailing-edge flaps being deflected at moderate to large angles in both cases. In the former scheme, the efflux from each engine impinges on the flaps, is deflected downwards and is spread spanwise, thereby converting the efflux into a jet sheet having a span that is greater than the diameter of the nacelle. In the latter scheme, on the other hand, the turning process is achieved through the Coanda effect, whereby the flow remains attached to the knee of the flaps, and there is little or no spanwise spreading, so that a compact jet-sheet results. This paper is concerned with the first of these schemes.

Notwithstanding the fact that the flow around the wing is of extreme complexity, various attempts have been made to model the flow[1,2,3], but none of these is entirely satisfactory. As a consequence, heavy reliance has had to be placed on the results of overall-force tests on particular configurations[4,5,6]. The methods that are generally used to analyse the forces may be summarized with the aid of Fig 1. This figure is based on experimental data obtained from tests performed, at low Mach number, on a model representing an aircraft with an external-flow jet flap of the type under consideration. In particular, Fig 1a indicates a breakdown of the overall lift, $\bar{C}_L$. The contribution from the component of the jet-reaction force, $\bar{C}_{LJ}$, is derived from wind-off tests. The analysis is therefore based on the assumption that the main flow (ie the flow external to the efflux) does not influence the development of the jet, with the consequence that forward speed is assumed to have no effect on the jet-reaction force. Hence the residual lift $\bar{C}_{LR} = \bar{C}_L - \bar{C}_{LJ}$ is assumed to arise solely from the circulation of the main flow around the wing. The residual lift may be thought to comprise a contribution corresponding to zero static thrust, $\bar{C}_{Lo}$, and an increment $\Delta\bar{C}_{LR}$ which is usually attributed to two effects. Firstly, a portion of the efflux passes through the slots of the trailing-edge flap and, after turning around the noses of the flap elements, energizes the boundary layer on the flap upper surface (the boundary-layer-control effect). Secondly, the efflux situated downstream of the trailing edge is considered to have an effect that is similar to that of the jet sheet of the classical jet flap (the jet-flap effect).

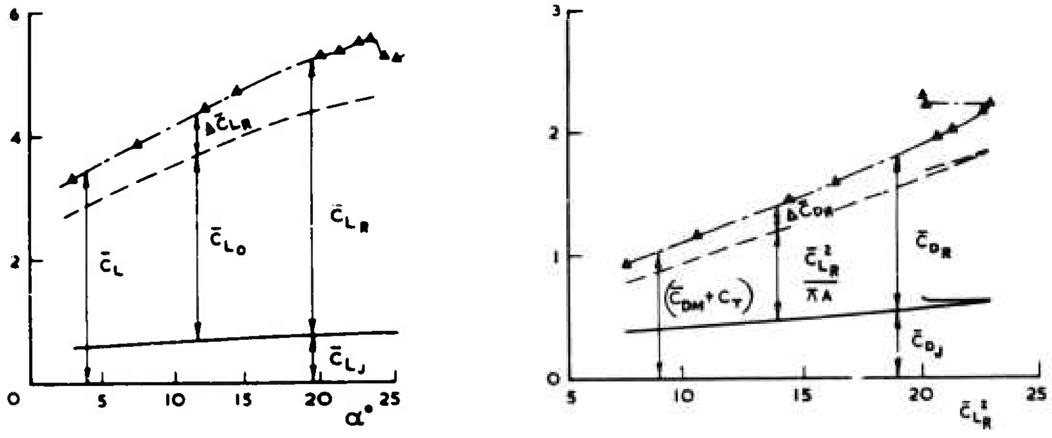

a LIFT b DRAG

FIG.1 ANALYSIS OF LIFT AND DRAG OF EXTERNAL-FLOW, JET FLAP

Fig 1b shows a similar analysis performed for drag. The term resulting from the algebraic addition of the measured overall drag C_{DM} and the net thrust of the isolated powerplant, C_T, is broken down into a jet-reaction drag, $\bar{C}_{DJ}$, and a residual drag $\bar{C}_{DR}$. As with the lift, the jet-reaction drag, which is due to the impingement of the efflux on the flap system, is derived from wind-off tests. Perry[2] suggested that the residual drag could best be analysed by ignoring the jet-flap effect. This implies that the residual drag is analysed into a vortex drag $\bar{C}_{LR}^2/\pi A$ and a remainder, $\Delta\bar{C}_{DR}$, that is usually attributed to the boundary layer on the parts of the model that are not immersed in the jet.

These analyses, whilst they are useful tools for interpreting the data, pose more questions than they answer. For example, it is questionable whether or not the jet-reaction forces are independent of forward speed. In addition, the apparent success of Perry's analysis of drag points to the possibility that the jet-flap effect is relatively small, with its implications on the origin of the increment $\Delta\bar{C}_{LR}$. The aim of this paper is to examine these questions with the aid of some measurements made on a constant-chord wing. The measurements comprised surveys of flow velocity at the trailing edge of the flap, static pressures at various positions on the wing, and overall-force measurements. Two wing sweeps, 0° and 20°, have been examined with the aim of understanding the influence of sweep on, for example, the spread of the jet across the span after impingement on the flap. The majority of tests were performed at a gross-thrust coefficient of approximately 1.0, this being considered to be a typical value for a civil STOL aircraft.

2 MODELS AND INSTRUMENTATION

2.1 Wing and nacelle

The model, which simulated the port half of a wing-fuselage combination with a single turbofan engine mounted beneath each wing, is shown in Fig 2. Mounted vertically on a half-model balance the model was assembled either as an unswept or swept wing (Fig 2), the unswept wing being rectangular in planform. The swept configuration was derived by rotating the wing through 20°, a fairing being added to the tip to preserve the span of 2.06m (81 in). Consequently the chord was increased by the factor sec 20°, and as shown in Fig 2, the deflection angles of the three elements of the high-lift system were reduced slightly. For both configurations the flap brackets were in a streamwise direction; the slat brackets were, however, maintained normal to the leading edge, and thus were not changed when the angle of sweep was altered.

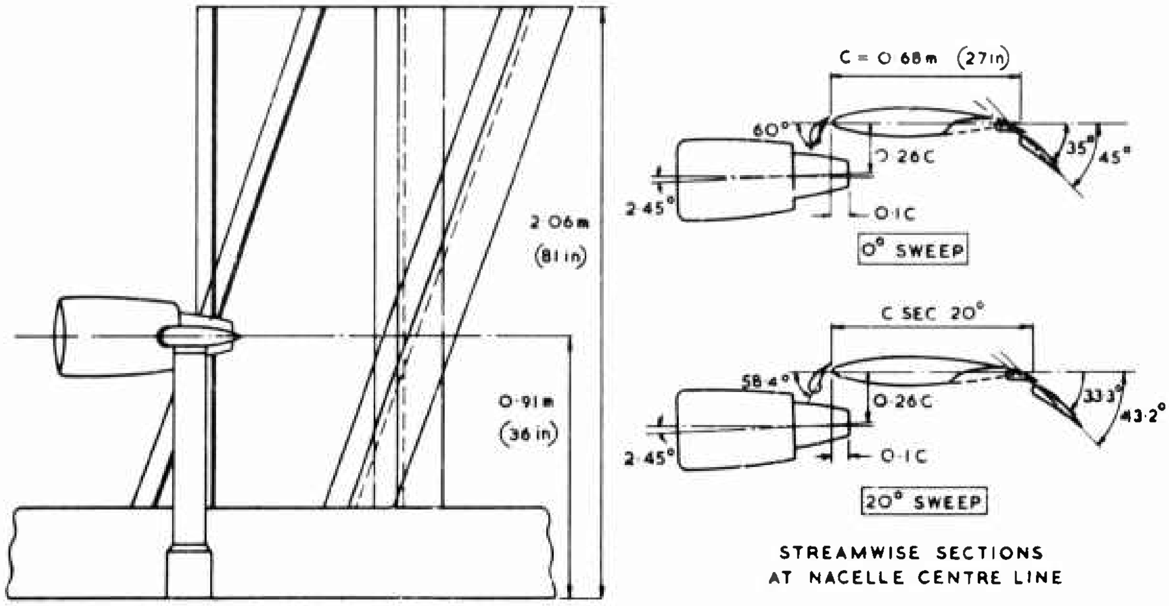

FIG.2 GEOMETRY OF UNSWEPT AND SWEPT VERSIONS OF MODEL

An injector-powered nacelle, which has been described elsewhere[7], simulated a turbofan engine possessing a bypass ratio of the order of 3. The nacelle was mounted independently of the wing, so that its position relative to the wing and its inclination could be varied over a wide range. For the tests to be discussed in this paper the position of the nacelle relative to the leading edge of the main wing at the spanwise station of the nacelle axis and the inclination of the nacelle were fixed at the position shown in Fig 2. This geometry was considered to be a reasonable compromise between the achievement, on the one hand, of low cruise drag, and on the other of high lift-augmentation. That this geometry was suitable from the lift-augmentation standpoint was subsequently proved by overall-force measurements. An overall-force calibration of the isolated nacelle under wind-off conditions indicated that the nose-down inclination of the nacelle was effectively 1.2° ± 0.1° greater than the nominal inclination owing to an asymmetry in the flow of the efflux.

2.2 Pressure measurement system

Pressure transducers and scanivalves were used to measure the static pressures on the wing at a total of 1320 tappings which were divided equally between 12 spanwise stations. The choice of the range of the transducers was influenced by the expectation that, as a result of direct jet impingement, pressures in excess of $20\mathrm{kNm}^{-2}$ ($3\ \mathrm{lbf/in}^2$), would occur on parts of the lower surface of the wing. Since there was no prior knowledge of where these pressures might occur it was decided that all the transducers would have a range of ± $34\mathrm{kNm}^{-2}$ ($5\ \mathrm{lbf/in}^2$). However, to ensure an adequate resolution for the measurement of pressures on the remainder of the wing it was arranged that the signals from the transducers would be amplified before they were coded onto paper tape.

2.3 Wake-survey rig

Velocity distributions at the trailing edge of the flap were measured with a non-nulling, five-tube probe. This comprised a centre tube and four outside tubes which were placed at equal angular intervals around the centre tube All the tubes were of internal diameter 0.85mm (0.033 in) and the distance between the centres of each pair of opposite tubes was 2.6mm (0.102 in). The outside tubes were chamfered to an angle of 45° to the axis of the probe. The probe was mounted from the lower surface of the flap for surveys above the flap, and from the upper surface for surveys below the flap. Provision was made for surveys at up to six spanwise stations below the flap and for up to eight spanwise stations above the flap. A traverse of the probe across the jet, in the direction normal to the adjacent surface of the flap at the trailing edge, was accomplished by means of a small motor mounted in the probe support, the position of the probe being defined by the count of electrical pulses transmitted by a micro-switch activated by the rotation of the motor shaft.

A non-nulling probe is limited to a certain range of pitch angle and yaw angle, depending on the type of calibration used. It was considered that yaw angles exceeding the working range of the probe might be found in the jet; therefore provision was made for setting the probe at two angles of yaw other than 0°, namely ± 20°.

3 TEST TECHNIQUE AND DATA REDUCTION

3.1 General considerations

The wind-on tests were performed in the 13ft x 9ft wind tunnel at RAE, Bedford at a wind speed of 30 m/s (100 ft/s). Tests were performed for a range of nacelle thrusts, but most emphasis was placed on the two cases $T_s = 0$, $T_s = 857.6$N (192.8 lbf), hereafter referred to as the 'thrust-off' and 'thrust-on' cases, respectively. Here T_s is the static thrust of the isolated nacelle, obtained from a static calibration.

To avoid problems due to the recirculation of the flow in the wind tunnel, wind-off tests were conducted in a large room beneath the tunnel working section. The thrust setting for these tests was the same as for the thrust-on case above. This thrust could be controlled to an accuracy better than ± 0.2% which is comparable with the precision of control of the dynamic pressure of the tunnel airstream.

3.2 Pressure distributions

Pressure distributions were generally measured in the wind-on tests at intervals of angle of incidence of 4° between 0° and 20°. The dynamic pressure used in the reduction of the pressures to coefficient form was that calculated for the wind-tunnel speed and was given to the computer as a 'constant'. A similar process was used to determine notional pressure-coefficients, for the wind-off tests, based on the wind speed of the wind-on tests.

Integrations to obtain the components of the pressure-force coefficients acting on each element were based on the assumption of a linear variation between the tappings. Resolution of these components relative to the stream direction led to the pressure-lift and pressure-drag coefficients for each complete section.

No wind-tunnel corrections were applied to the wind-on results, because the aim of this study was to derive a basic understanding of the flow rather than to provide data. However, to gain some indication of the magnitude of the wall effect, these corrections were calculated. The increment in angle of incidence due to tunnel-wall, lift constraint was obtained by assuming that the wing could be considered equivalent to an 'unblown' wing of the same geometry and at the same overall, residual-lift coefficient, $\bar{C}_{LR}$, as the model. By using this assumption in conjunction with theoretical results given by Acum[8] it was found that the incremental angle of incidence is 1.08 $\bar{C}_{LR}$ degrees for the unswept wing and 1.16 $\bar{C}_{LR}$ degrees for the swept wing. Theoretical blockage increments to the dynamic pressure of the tunnel airstream, q, were found to be 0.0317 q for the thrust-off case and 0.0087 q for the thrust-on case, the difference between the two values being attributable to the sink effect of the intake and also the entrainment of flow into the efflux[9].

3.3 Wake surveys

The velocities at the trailing edge of the unswept wing were measured wind on and wind off, but, for the swept wing, measurements were only made with the wind on. For the wind-on tests, surveys were made at all the spanwise stations at an angle of incidence of 4°. Surveys at two other incidences, 0° and 8°, were also made at the station closest to the nacelle axis. The tests were, in the main, with thrust on.

The pressures in the tubes were measured by five pressure transducers each of range ± $17\mathrm{kNm}^{-2}$ ($2\frac{1}{2}$ $\mathrm{lbf/in}^2$). The signals from the transducers were amplified and subsequently coded onto paper tape prior to reduction, by computer, into dynamic head, static pressure, yaw angle and pitch angle. The computer program, which was written at BAC, Weybridge, uses a form of the calibration described by Bryer and Pankhurst[10].

The interval between each point in the survey varied between 0.05mm (0.002 in) and 2.5mm (0.1 in) depending on the gradients of the five pressures across the jet.

3.4 Presentation of data

Unless otherwise stated the data presented in this paper corresponds to an angle of incidence of 4° for both the unswept wing and sweptback wing. In general, the coefficients are non-dimensionalised using the length of the streamwise chord of the basic wing (Fig 2).

4 DISTRIBUTION OF JET MOMENTUM ACROSS THE SPAN

This section deals with the interpretation of the results of the surveys at the trailing edge of the flap. An illustration of the way the jet is distributed across the span is provided by Fig 3 which shows the variation of the total-pressure coefficient, $C_{p_t} = (H - p_r)/q$, normal to the upper and lower surfaces of the flap at the trailing edge. Here H is the jet total pressure and p_r is the static pressure of the undisturbed main flow. It can be seen that the jet is mainly concentrated below the flap in the immediate vicinity of the axis of the nacelle. However, sufficient flow passes through the slots of the flap system to give a propulsive contribution from the upper-surface flow. In addition, the total pressure of this flow seems to decay less rapidly across the span than for the flow below the flap.

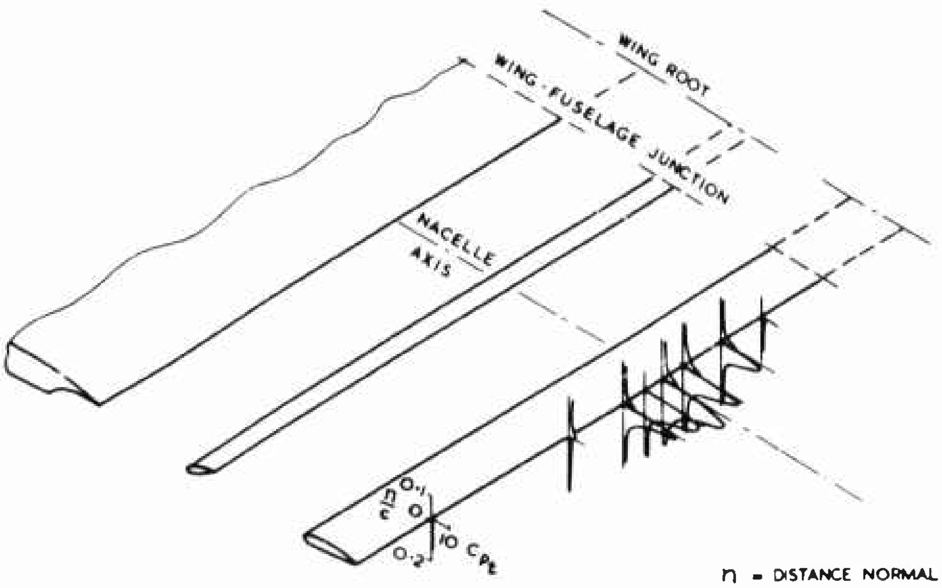

η = DISTANCE NORMAL TO LOCAL SURFACE OF FLAP

FIG.3 DISTRIBUTION OF TOTAL PRESSURE AT VARIOUS STATIONS ACROSS THE SPAN OF UNSWEPT WING, WIND ON, THRUST ON.

4.1 Local integrated jet momentum

Although the distributions of Fig 3 are interesting, more useful information can be obtained by considering integrated properties of the jet. The direct jet-reaction can be most conveniently analysed by considering the momentum flux passing across, and the normal pressure forces acting on, the traverse planes. Consideration is therefore given to the force coefficients:

$$C_X = (X - X_m)/qc \ ; \quad C_Y = (Y - Y_m)/qc \ ; \quad C_Z = (Z - Z_m)/qc \ ,$$

where X, Y and Z are the local contributions to the forces on the wing in the x, y, z directions (Fig 4) due to the momentum and static pressure in the jet, suffix m denotes the corresponding values for the main flow, and c is the chord of the basic, unswept wing as defined in Fig 2. The integrations to obtain these coefficients were performed numerically, and the main flow was assumed to be characterised by the flow measured at the edge of the jet. Fig 4 shows the spanwise distribution of the three coefficients for three cases, the two wing sweeps under wind-on conditions, and the unswept wing under wind-off conditions, the coefficients for the last case being based on the dynamic pressure of the forward speed tests. The figure indicates that the main flow has a minimal effect on the force coefficients. In particular, the force coefficient C_Y, which is a measure of the spread of the jet across the span of the flap, is hardly affected by the main flow, a result of some significance. As might be expected the effect of sweep is to bias the coefficients C_X and C_Z towards the tip and to give rise to a nonzero, overall force in the spanwise direction.

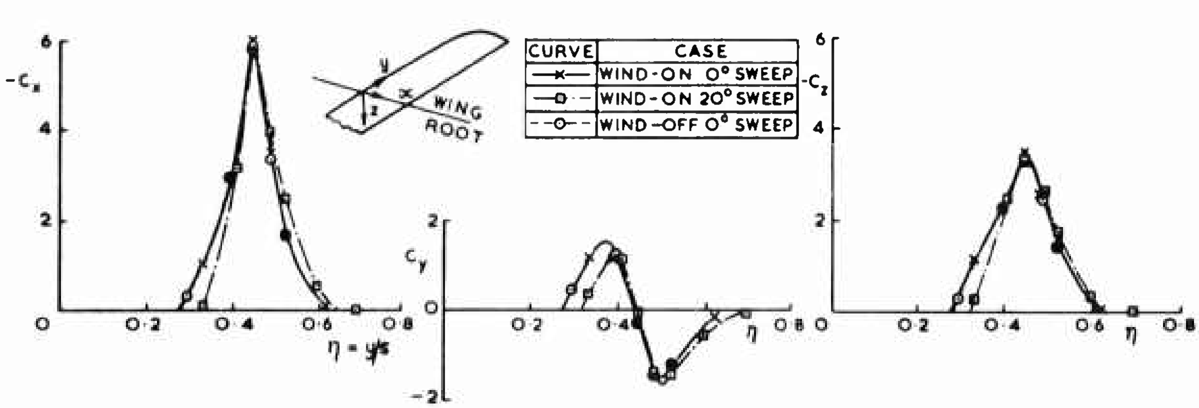

FIG. 4 DISTRIBUTION OF JET-REACTION COEFFICIENTS ACROSS THE SPAN

4.2 Overall integrated jet momentum

Integration of the distributions of force coefficients across the span allows the determination of the overall jet-deflection angle

$$\bar{\delta}_J = \tan^{-1}(\bar{C}_Z/\bar{C}_X) ,$$

and the overall thrust-recovery factor

$$\bar{\eta}_J = (\bar{C}_Z{}^2 + \bar{C}_X{}^2)^{\frac{1}{2}}/C_{TG} ,$$

where bars denote overall forces and C_{TG} is the gross-thrust coefficient of the nacelle minus the gross thrust corresponding to a jet dynamic pressure equal to free-stream dynamic pressure.

TABLE 1

Case	Wing Sweep	$\bar{\eta}_J$	$\bar{\delta}_J$
Wind off	0°	0.811	37.2°
Wind on	0°	0.831	37.4°
Wind on	20°	0.839	35.2°

The results, which are shown in Table 1, confirm that the wind-off characteristics substantially define the direct jet reaction under wind-on conditions. In addition, they show that sweep has little effect on the turning characteristics of the flap system, the small reduction in overall, jet-deflection angle with sweep being consistent with the fact that flap deflection was reduced in the process used to sweep the wing.

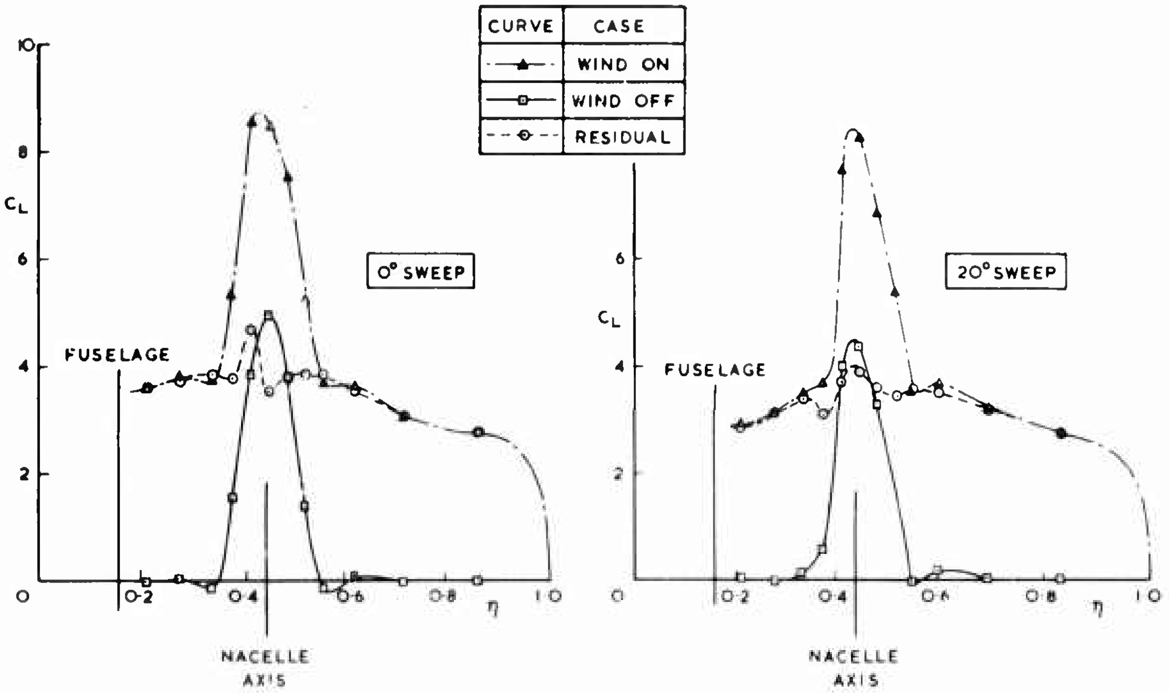

FIG 5 ANALYSIS OF DISTRIBUTION OF LIFT ACROSS THE SPAN

5 DISTRIBUTION OF PRESSURE OVER THE WING

5.1 Synthesis of spanwise distributions of lift and pressure drag

Distributions of pressure lift, or simply lift, across the span of the wing are shown in Fig 5. It is seen that, for both wing sweeps, the wind-on distribution displays a pronounced peak in the vicinity of the nacelle axis. By contrast, the residual distributions, which are derived by subtracting the wind-off distributions from the wind-on distributions, are much more uniform, although undulations in the residual curves are in evidence close to the axis of the nacelle. Comparable distributions of pressure drag C_{D_p} are shown in Fig 6, and again the residual distributions are more even than the corresponding wind-on distributions. The fact that the peaks in the wind-on loads are largely accounted for by the wind-off loads supports the conclusion of section 4 that the distribution of the direct jet-reaction under wind-on conditions is similar to that under wind-off conditions. Consequently, the residual lift may be considered to be substantially equal to the lift associated with the circulation of the main flow around the wing section, or the circulation lift. Similarly, it seems reasonable to expect that the residual pressure drag does not differ greatly from the 'circulation drag', that is the drag resulting from the pressures induced at the wing by the vortex distributions which may be used to represent the wing and the jet. Alternatively, by analogy with the classical jet flap[11], the circulation drag may be defined as the induced drag minus the reduction in jet-reaction thrust due to the deflection of the efflux. Here the term induced drag means the loss of thrust due to the existence of trailing vortices in the main flow. The magnitude of the circulation drag is discussed in section 6.

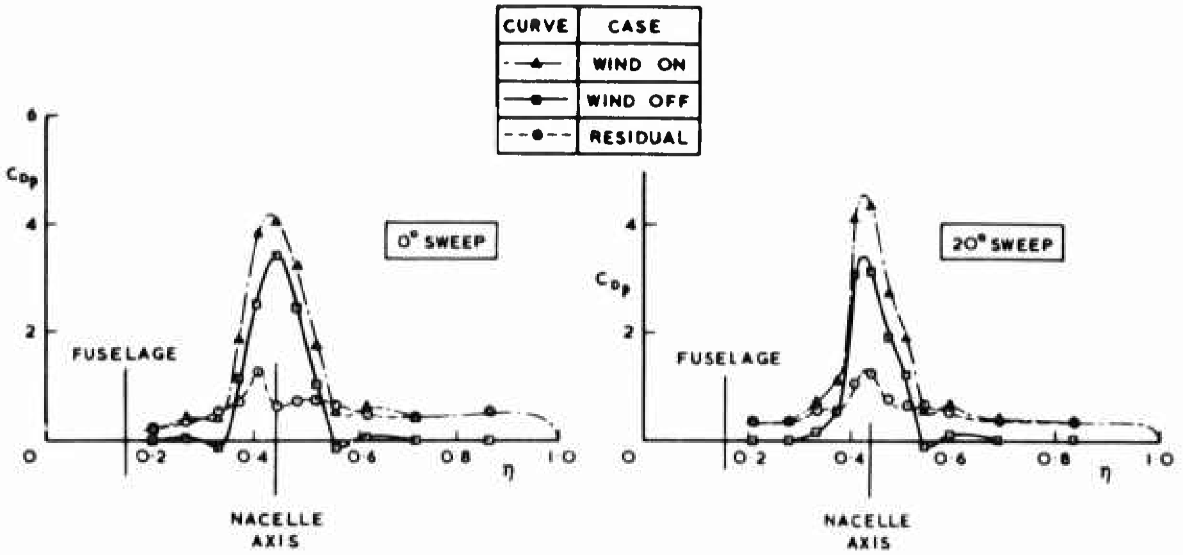

FIG.6 ANALYSIS OF DISTRIBUTION OF DRAG ACROSS THE SPAN

5.2 Residual-lift distributions: effect of thrust and incidence

The effect of thrust on the residual-lift distributions is clearly demonstrated in Fig 7 which shows a significant increase in residual lift due to thrust for both wing sweeps. The residual lift for the thrust-off case is, of course, equal to the measured lift. Not surprisingly, perhaps, the increase is greatest in the region of the wing corresponding to the span of the jet at the flap trailing edge. Presumably, the increase inboard and outboard of this region is due to a combination of the favourable effects associated with the increase in circulation lift in the region spanned by the jet, and the circulation around the jet downstream of the flap trailing edge,ie the jet-flap effect.

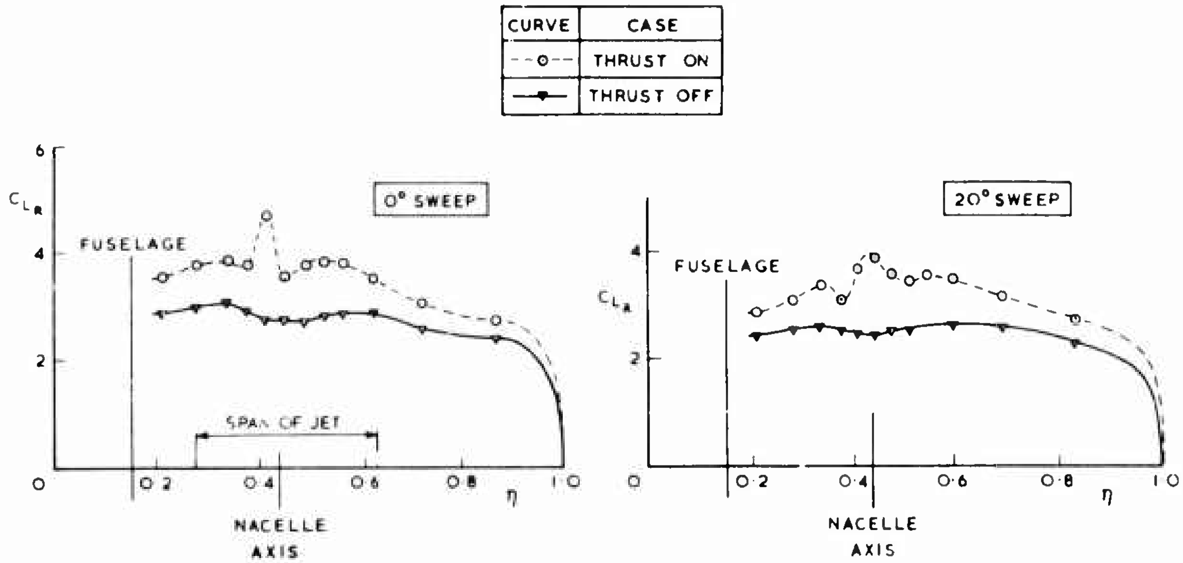

FIG.7 DISTRIBUTION OF RESIDUAL LIFT ACROSS THE SPAN, THRUST ON AND THRUST OFF

The increment in residual lift due to thrust, ΔC_{LR}, is shown in Fig 8 for angles of incidence of 0^o, 4^o and 8^o. The interesting feature of these results is that, with the exception of a narrow strip on the unswept wing adjacent to $\eta = 0.4$, incidence appears to have only a marginal influence on the magnitude of the increment. To some extent this result is consistent with observations made by Foster, Irwin and Williams[12] of the flow over an aerofoil with a slotted flap but without jet augmentation. They found that incidence does not affect the nature of either the inviscid or the viscous flow over the flap. Consequently, it seems unlikely that an increment in residual lift, due only to the boundary-layer-control effect, would be sensitive to incidence. It would, however, be difficult to reconcile the insensitivity of the residual-lift increment to changes in incidence with the existence of a powerful, jet-flap effect. The question of the magnitude of any jet-flap effect is considered in section 6.

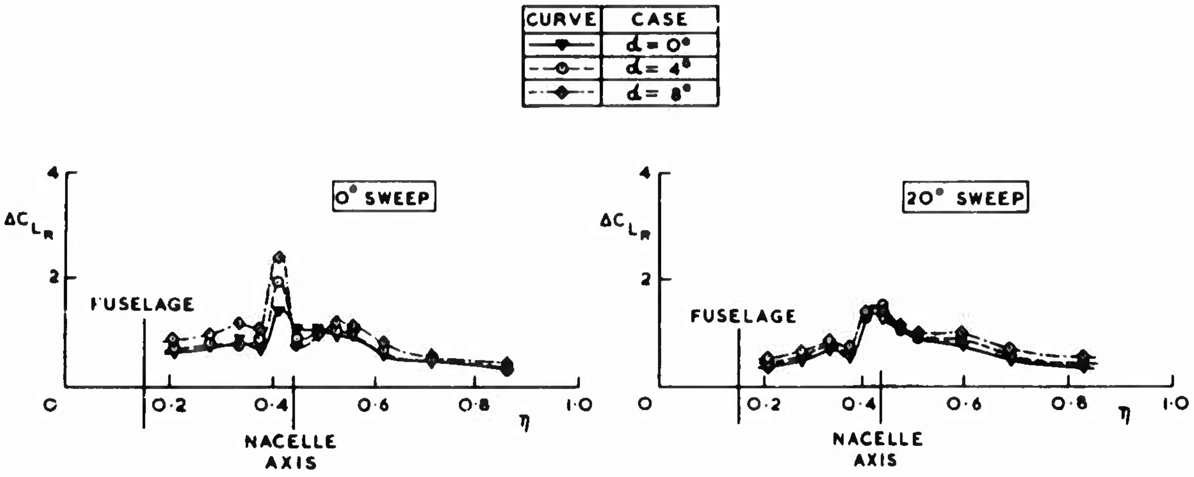

FIG. 8 INCREMENTS IN RESIDUAL LIFT DUE TO THRUST FOR VARIOUS INCIDENCES

5.3 Analysis of pressure distributions

The method of analysing the load distributions into a wind-on distribution and a residual distribution can be applied to the pressure distributions. Fig 9 illustrates such a breakdown for the unswept wing, the distributions of pressure along the chord line of each element being plotted on staggered axes to facilitate the comparison of the pressure distributions at various spanwise stations. The figure reflects, to a large extent, the results of Figs 5 and 6 by revealing that the residual pressures are, on the whole, much more uniform across the span than the wind-on pressures, particularly on the parts of the wing that are spanned by the jet. With the exception of one of the spanwise stations the residual-pressure coefficients are nowhere greater, algebraically, than unity, lending further support to the notion that the residual lift is essentially equal to the circulation lift.

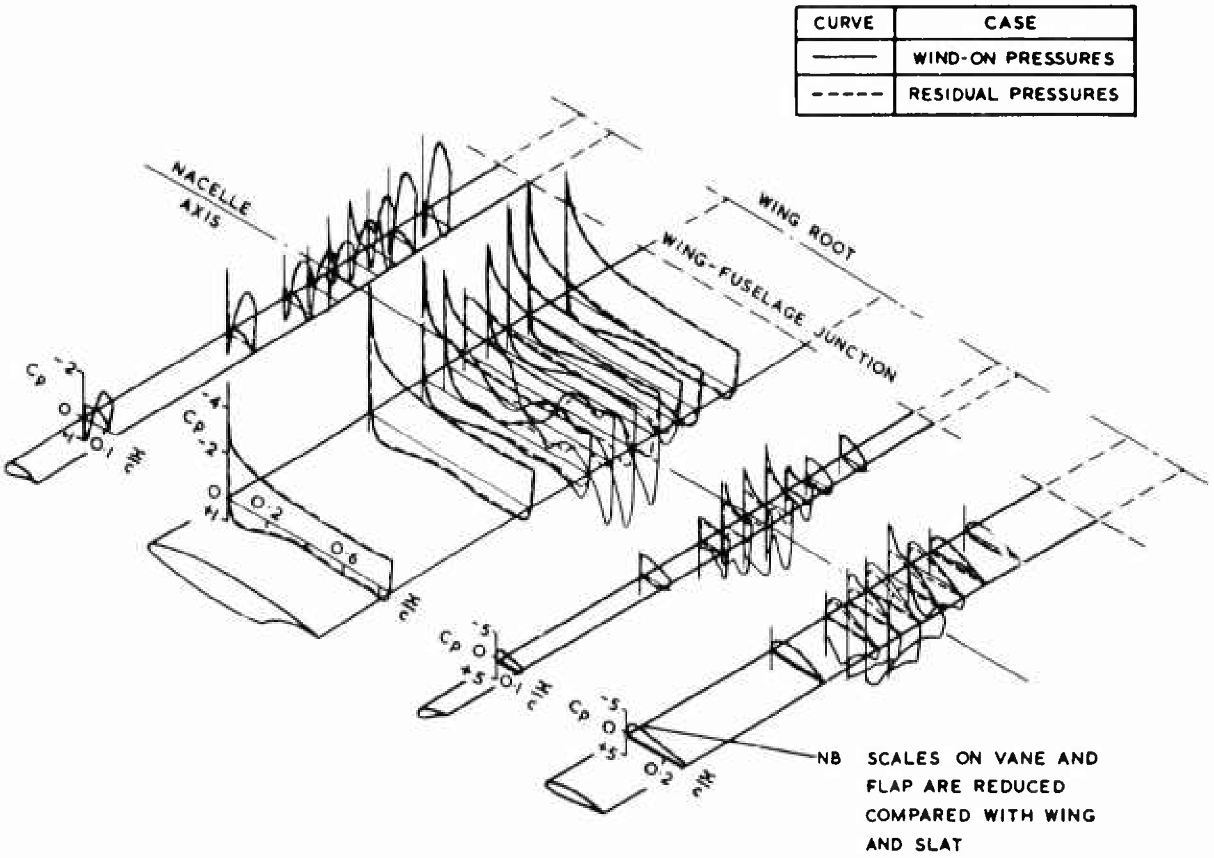
CURVE
CASE
WIND-ON PRESSURES
RESIDUAL PRESSURES
NACELLE AXIS
WING ROOT
WING-FUSELAGE JUNCTION
Cp
-2
0
+1
0·1
x/c
-4
Cp -2
0
+1
0·2
0·6
x/c
-5
Cp 0
+5
0·1
x/c
-5
Cp 0
+5
0·2
x/c

NB SCALES ON VANE AND FLAP ARE REDUCED COMPARED WITH WING AND SLAT

FIG. 9 PRESSURE DISTRIBUTIONS OVER UNSWEPT WING AND ITS HIGH-LIFT DEVICES

6 ANALYSIS

In this section consideration is given to the origins of the increment in residual lift due to thrust.

As noted in the Introduction, this increment is generally attributed to two effects, namely the jet-flap effect and the boundary-layer-control effect. Section 6.1 deals with an examination of the former effect whilst an assessment of the latter effect is made in section 6.2 where the equivalent, two-dimensional lift due to circulation is discussed. Allied with the study of the jet-flap effect is an investigation of the circulation drag, described in section 6.3, the aim of which is to indicate the relationship between the drag derived from the classical jet-flap theory and that given by the simpler, thrust-deflector theory. The analyses were performed for the unswept wing with the angle of incidence 4° and, unless otherwise stated, for the thrust-on case.

6.1 Jet-flap effect

The jet-flap effect is related to the spanwise distribution of circulation around each streamwise section of the jet, Γ_J. Appendix A contains the method used to estimate this quantity which can be expressed conveniently as a coefficient of 'circulation lift' acting on the jet $C_{L\Gamma_J} = 2\Gamma_J/U_\infty c$, with U_∞ the undisturbed, mainstream speed. The spanwise distribution of $C_{L\Gamma_J}$ is shown in Fig 10. It is seen, by comparing this figure with Fig 5, that, typically, this coefficient is small compared with the residual-lift coefficient in the region of the jet. This suggests that the increment in overall circulation-lift due to the jet-flap effect, $\Delta\bar{C}_{L\Gamma_W}$, is small compared with the overall circulation lift. This view is supported by calculations that are based on a method described in Appendix A. These calculations yield the result $\Delta\bar{C}_{L\Gamma_W} = 0.18$, which should be compared with (a) the overall, residual-lift coefficient, $\bar{C}_{LR} \simeq 3.5$, (b) the increment in the overall-lift coefficient due to thrust $\Delta\bar{C}_L \simeq 1.2$ and (c) the increment in the overall, residual-lift coefficient due to thrust $\Delta\bar{C}_{LR} \simeq 0.6$. Thus the jet-flap effect accounts for only a small proportion of both the residual lift and the incremental lift due to thrust, and, consequently, it would appear that the majority of the increment in residual lift can be attributed to the boundary-layer-control effect.

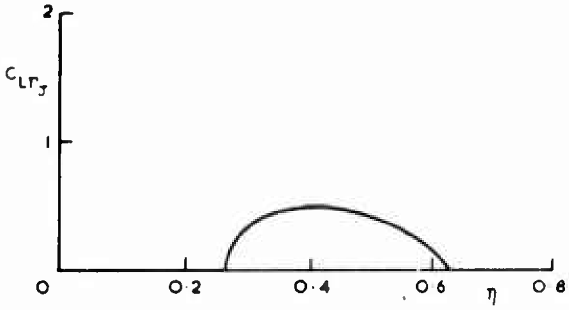

FIG.10 CALCULATED SPANWISE DISTRIBUTION OF 'CIRCULATION LIFT' ACTING ON JET DOWNSTREAM OF FLAP

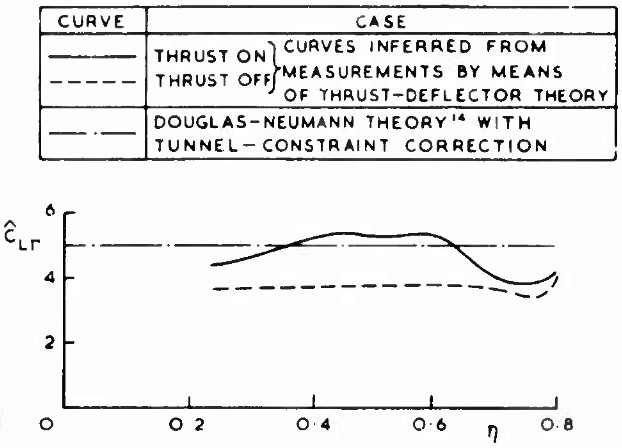

FIG.11 SPANWISE DISTRIBUTION OF EQUIVALENT TWO-DIMENSIONAL LIFT, DUE TO CIRCULATION, ACTING ON WING

6.2 Equivalent, two-dimensional lift due to circulation

Since the jet-flap effect appears to exert only a small influence on the circulation lift it seems reasonable to analyse the circulation lift by using the thrust-deflector hypothesis, that is by disregarding the jet-flap effect altogether. The circulation lift may then be analysed by supposing that the excess momentum in the jet at the flap trailing edge is zero but that the spanwise distribution of circulation lift is unchanged. Standard, lifting-surface theories, such as that due to Prandtl[13], may be used to determine the equivalent, two-dimensional lift due to circulation, $\hat{C}_{L\Gamma}$, at the same geometric incidence as the wing. The advantage of considering the sectional circulation lift is that it is possible, in principle, to isolate the direct effect of boundary-layer control from the indirect effect of the spanwise lift distribution.

Since Prandtl's theory is standard it will be sufficient to state here that the coefficient $\hat{C}_{L\Gamma}$ follows readily from this method given the sectional, lift-curve slope and the downwash angle induced at the wing by the trailing vortices shed from the wing. The first of these parameters was derived from the Douglas-Neumann solution[14] of the potential flow about the aerofoil section, whilst the second was found by using Prandtl's assumption[13] that the downwash angle induced at the wing by the trailing vortices is one half of the downwash angle induced by them far downstream. In the calculations of the induced downwash angle the spanwise distribution of circulation lift was taken to be the residual-lift distribution with some modifications. The modifications involved, firstly, an arbitrary smoothing of the residual-lift distribution in the vicinity of the axis of the nacelle in order to remove the undulations which were considered to have resulted from effects extraneous to that of the wing-induced circulation, eg that associated with the presence of the nacelle. Secondly, the residual-lift distribution was extrapolated in a reasonable manner to the fuselage axis. Allowance for the influence of the body on the effective incidence of the wing was made by assuming that the body may be represented by an infinite cylinder. The angle of incidence of the cylinder was taken to be the geometric incidence of the body minus the downwash angle induced at the wing-body junction by the trailing vortices associated with the modified distribution of residual lift. This correction to the effective incidence of the wing is, in fact, very small.

The results thus obtained for $\hat{C}_{L\Gamma}$ are illustrated in Fig 11 for the thrust-off case as well as the thrust-on case. There they are compared with the value calculated by using the Douglas-Neumann method[14], referred to above, suitably corrected to allow for the effect of blockage constraint on the tunnel dynamic pressure and the influence of the tunnel walls on the effective incidence of the wing (section 3.2), both assumed to be uniform across the span of the wing. This comparison shows that, in the region of the wing spanned by the jet, the theory and the thrust-on curve are in reasonable agreement. Inboard and outboard of this region, however, the thrust-on curve lies noticeably below the theoretical value and is quite close to the thrust-off curve, which, as expected, is reasonably uniform across the span. This is consistent with the suggestion that, where the jet exists, it energizes the boundary layer on the flap upper surface and thereby increases the effectiveness of the flap. Elsewhere, the flap would be expected to be less effective and to exhibit sectional characteristics similar to those achieved in the thrust-off case.

6.3 Circulation drag

Two expressions are derived in Appendix B for the circulation drag coefficient, $\bar{C}_{D\Gamma}$, firstly by using the jet-flap theory and secondly by employing the thrust-deflector hypothesis. The results, which are inferred from the modified distribution of residual lift and the wake-survey data, are summarized in the table below.

$\bar{C}_{D\Gamma}$	
Jet-Flap Theory	Thrust-Deflector Hypothesis
0.595	0.625

It is seen that the jet-flap theory predicts a circulation drag that is slightly lower than that given by the thrust-deflector hypothesis. If it is supposed that, to a first approximation, the jet-flap effect is equivalent to an increase in the effective incidence of the wing, it is clear that the reduction in circulation drag due to the jet-flap effect is consistent with the conclusion that the jet-flap effect is responsible for a small increment in circulation lift. The results also bear the expected relationship to the residual, pressure-drag coefficient, which has a value of 0.64.

7 CONCLUSIONS

From the experimental results and theoretical analyses presented in this paper, the following conclusions have been drawn:

1) The presence of an external airflow does not affect the turning and spreading process of the efflux of the engine. Static tests may therefore be used to define the direct effect of the efflux on the loading on the wing for a wide range of forward speeds.

2) The effect of changing from an unswept wing to a sweptback wing is to bias towards the wing tip the spanwise distribution of the jet flow leaving the wing trailing edge, and to give a non-zero force in the spanwise direction.

3) The jet-flap effect accounts for only a small proportion of the overall lift increment due to the engine efflux.

4) The jet exerts a boundary-layer-control effect on wing sections within that part of the wing spanned by the jet, so that they generate a lift coefficient of the order of that predicted by inviscid theory. Spanwise carry-over of lift leads to wing sections outboard of the jet span experiencing lift coefficients greater than those generated in the thrust-off case.

5) Jet-flap theory predicts a slightly lower circulation drag than the thrust-deflector hypothesis, and this is consistent with the observation that the increment in circulation lift due to the jet-flap effect is small.

These conclusions do, of course, strictly apply only to an aircraft configuration having one engine mounted beneath each wing, a moderate flap deflection angle, a gross thrust coefficient of approximately one, and no artificial spreading of the jet ahead of the flap. It is, however, of interest to consider how the last three conclusions might change if the thrust coefficient were increased. As the turning and spreading process is the same for static conditions, which correspond to a thrust coefficient of infinity, and for a thrust coefficient of one, it is likely to be the same for intermediate values of the thrust coefficient. Inviscid jet-flap theory[11] suggests that for a wing with a jet-augmented flap, having the low value of aspect ratio which would correspond to the span of the wing affected by the jet, the contribution to the lift due to the jet-flap effect increases only slowly with increasing jet momentum, once a certain minimum value of the jet momentum has been achieved. As the span of the wing affected by the jet will not change with increasing thrust coefficient, and the lift coefficient generated by the action of boundary-layer control cannot exceed the lift coefficient corresponding to inviscid flow, it would seem that the circulation lift will not increase markedly with increase of thrust coefficient. It follows that the changes in lift which do occur will result mainly from the increase in the direct thrust component. Since the circulation lift will then become a decreasing proportion of the total lift increment, the thrust-deflector hypothesis for the analysis of drag should become progressively more valid. Thus, to end on a slightly controversial note, it might be concluded that, if the term 'external-flow, jet flap' is meant to imply the existence of a significant jet-flap effect, the term is a misnomer.

APPENDIX A

EVALUATION OF MAGNITUDE OF JET-FLAP EFFECT

The aim of this appendix is to describe the method used to evaluate the approximate magnitude of the jet-flap effect for the unswept wing. Because of the complexity of the flow it is necessary to make some radical simplifications. For the present purpose a suitable framework appears to be the 'thin-jet' method of Maskell and Spence[11], which is based on the linearised, lifting-surface theory.

The jet is assumed to have negligible spanwise component of velocity. Strictly, this is known to be untrue but, as Fig 4 implies, the spanwise spread is least where the jet-reaction forces in the x and z directions are greatest. Thus it would seem reasonable to expect that the errors caused by this assumption are not serious.

Since it is assumed that there is zero transport of momentum in the jet in the spanwise direction the strength of the spanwise vortices simulating the jet, γ_J, depends only on the excess momentum flux, $J - J_m$, and the curvature of the jet, respectively in streamwise planes. Hence use may be made of a result given by Spence[15] for a two-dimensional, jet flap, which in the present notation becomes

$$\gamma_J = -\tfrac{1}{2} U_\infty C_\mu c \, d^2 z_J/dx^2 ,$$

where z_J is the downward displacement of the jet relative to the plane $z = 0$, and $C_\mu = (J - J_m)/\tfrac{1}{2}\rho U_\infty^2 c$. Thus the total vortex strength or circulation around each streamwise section of the jet is given by

$$\Gamma_J = \int_{x_T}^{\infty} \gamma_J \, dx = \tfrac{1}{2} U_\infty C_\mu c \left(\theta_J + \alpha - \alpha_{i\infty}\right) , \qquad (A.1)$$

with $\theta_J = dz_J/dx \,\big|_{x_T}$ the local jet-deflection angle at the wing trailing edge, α the angle of incidence of the wing and $\alpha_{i\infty}$ the induced downwash angle of the vortex sheet far downstream.

In order to make an estimate of the induced downwash angle at infinity the following assumptions are made; first, the influences of both the fuselage and nacelle on the velocity field are neglected; second, the tunnel-wall, lift effect is ignored. Consequently it is found that[11]

$$\alpha_{i\infty} = \frac{1}{2\pi U_\infty} \frac{\partial}{\partial y} \int_{-s}^{s} \frac{\Gamma_\infty}{y - y'} \, dy' , \qquad (A.2)$$

with

$$\Gamma_\infty = \Gamma_W + \Gamma_J , \qquad (A.3)$$

Γ_W the circulation of the main flow around each section of the wing and s the semispan of the wing.

The indications of sections 4 and 5 are that the residual lift is approximately equal to the circulation lift; in other words, it is reasonable to write

$$C_{LR} = C_{L\Gamma_W} = 2\Gamma_W/U_\infty c . \qquad (A.4)$$

Therefore, equations (A.1), (A.3) and (A.4) may be used to replace equation (A.2) by the expression

$$\alpha_{i\infty} = \alpha_{i\infty_W} + \frac{1}{4\pi} \frac{\partial}{\partial y} \int_{-s}^{s} \frac{C_\mu c(\theta_J + \alpha - \alpha_{i\infty})}{y - y'} \, dy' , \qquad (A.5)$$

with

$$\alpha_{i\infty_W} = \frac{1}{4\pi} \frac{\partial}{\partial y} \int_{-s}^{s} \frac{C_{LR} \, c}{y - y'} \, dy' .$$

Equation (A.5) is an integral equation for $\alpha_{i\infty}$, the terms $C_\mu \simeq (C_X^2 + C_Z^2)^{\frac{1}{2}}$ and $\theta_J \simeq \tan^{-1}(C_Z/C_X)$ being determined from the wake surveys, and C_{LR} being deduced from the residual-pressure distributions in the manner outlined in section 6.2.

The solution of equation (A.5) is facilitated by replacing the integral term with a Multhopp sum[13], so that

$$\alpha_{i\infty}(y_\nu) = \alpha_{i\infty_W}(y_\nu) + \frac{1}{2s}\left(b_{\nu\nu}\left[C_\mu c\left(\theta_J + \alpha - \alpha_{i\infty}\right)\right]_\nu - \sum_{\substack{\mu=1 \\ \mu\neq\nu}}^{N-1} b_{\nu\mu}\left[C_\mu c\left(\theta_J + \alpha - \alpha_{i\infty}\right)\right]_\mu\right) ,$$

where $b_{\nu\nu}$ and $b_{\nu\mu}$ are Multhopp coefficients[13]. This expression is solved by an iteration scheme which is started by assuming that the summation term is zero. Satisfactory convergence appears to be obtained after a small number of iterations.

By using the spanwise distribution of $\alpha_{i\infty}$ thus derived it is straightforward to obtain the 'circulation-lift coefficient' of the jet, $C_{L\Gamma_J} = 2\Gamma_J/U_\infty c$, a typical distribution being shown in Fig 10. This result does not lead directly to the circulation lift induced by the jet sheet. However, to obtain an estimate of this lift, use is made of 'the second interpolation of downwash' due to Maskell and Spence[11], in which the jet is assumed to have the same streamwise distribution of spanwise vortices as a two-dimensional wing of the same section and jet deflection angle, at the incidence $(\alpha - \alpha_i)$ and with the jet-momentum coefficient

$$\hat{C}_\mu = C_{L\Gamma_J}/(\theta_J + \alpha - \alpha_i) ,$$

where $\alpha_i \simeq \alpha_{i\infty}/2$ is the angle of incidence induced at the wing by the trailing vortices. Additionally, it is assumed that the flap system can be replaced by a plain flap which (a) is of the same chord length as the combined chord length of the vane-flap and (b) is deflected through the angle $\theta_J(y)$ in the part of the wing spanned by the jet.

The vortex distribution of the jet having been defined use may be made of the reverse-flow theorem of Ursell and Ward[16], which, with γ the strength of the spanwise vortices and w the induced downwash, may be expressed as

$$\int_\Sigma \gamma_1 w_2 \, dx \, dy = \int_\Sigma \gamma_2 w_1 \, dx \, dy , \qquad (A.6)$$

Σ denoting integration over all vortex elements. Here the forward motion (suffix 1) is identified with the vortex distribution required on Σ by the presence of the jet, and, for the reverse motion (suffix 2), the wing is supposed flat, unblown and at unit incidence, the free-stream speed being supposed the same for the two cases. Upon substituting the appropriate values of γ and w in equation (A.6) it is found that the increment in circulation lift due to the jet-flap effect is given by

$$\Delta\bar{C}_{L\Gamma_w} = 2 \Big(\iint\limits_{\text{wing}} (\gamma_1/U_\infty) \, dx \, dy\Big)/S, = 2 \Big(\int_J \int_{x_T}^{\infty} f_2 \,(x,y)\; g' \,(x;\, C_\mu, \theta_J, \alpha - \alpha_i) \, dx \, dy\Big)/S , \qquad (A.7)$$

where use is made of the requirement that w_1 is zero at the wing, in order to ensure that the wing is a streamsurface. Additionally, g' is the non-dimensional vortex strength derived by Spence[17] for a two-dimensional, jet-augmented flap, $-U_\infty f_2$ is the downwash velocity induced in $x > x_T$, suffix J denotes integration across the span of the jet and S is the reference planform-area of the wing.

An examination of the various terms in equation (A.7) shows that the integrand is heavily weighted towards $x = x_T$. According to Prandtl's aerofoil theory[13] the flow induced by the reverse motion in this region comprises the two-dimensional, flow field of a flat plate at an angle of incidence equal to the effective incidence $\alpha_e = C_{L2}/2\pi$, where C_{L2} is the local lift coefficient of the wing in reverse motion, superposed on the near-field flow of the trailing vortices. Thus by referring to tables of complex-velocity functions[16] for two-dimensional flows it is found that, with $x = 0$ the leading edge of the wing,

$$f_2 = \alpha_e \left[\left(\frac{x}{x - x_T}\right)^{\frac{1}{2}} - 1 \right] + (\alpha_e - 1) ,$$

where the last term is the contribution of the trailing vortices in the near field of the wing. Upon substituting this expression for f_2 in equation (A.7) the integral with respect to x is recognised as an integral already evaluated by Spence[15,17], and the y integration is readily performed numerically or graphically. The result thus obtained for the incremental circulation lift, $\Delta\bar{C}_{L\Gamma_w}$, due to the jet-flap effect is 0.18.

APPENDIX B

EVALUATION OF CIRCULATION DRAG

B.1 JET-FLAP THEORY

The analysis of this appendix is based on the assumptions which were used in Appendix A to determine the induced downwash angle far downstream. Thus, upon referring to the analogy[11] between the wing, with a jet sheet downstream of the flap trailing edge, and the wing alone but with the same spanwise distribution of the circulation Γ_∞, it is readily found that the induced drag coefficient is given by

$$\bar{C}_{Di} = \frac{1}{2S} \int_{-s}^{s} c \, C_{L\infty} \, \alpha_{i\infty} \, dy , \qquad (B.1)$$

where

$$C_{L\infty} = C_{L\Gamma_\infty} + C_\mu \, \alpha_{i\infty} , \qquad (B.2)$$

and

$$C_{L\Gamma_\infty} = 2\Gamma_\infty/U_\infty c . \qquad (B.3)$$

Alternatively, by reference to equations (A.1), (A.3), (A.4), (B.2) and (B.3), equation (B.1) may be rewritten as

$$\bar{C}_{Di} = \frac{1}{2S} \int_{-s}^{s} c \left[C_{L\Gamma} + C_\mu \,(\theta_J + \alpha)\right] \alpha_{i\infty} \, dy .$$

It will be recalled that the circulation drag is defined as the induced drag minus the increment in jet-reaction drag due to the deflection of the efflux. This increment is readily found from momentum considerations to be given, in coefficient form, by

$$\Delta\bar{C}_{DJ} = \frac{1}{S} \int_{-s}^{s} c \, C_\mu \left[1 - \cos\,(\theta_J + \alpha) \right] dy \;\simeq \frac{1}{2S} \int_{-s}^{s} c \, C_\mu \,(\theta_J + \alpha)^2 \, dy$$

to the order of approximation of the present analysis which is based upon the linearised, lifting-surface theory. Therefore the circulation drag coefficient may be written as

$$\bar{C}_{DT} = \frac{1}{2S} \int_{-s}^{s} c\left(\left[C_{LR} + C_\mu (\theta_J + \alpha)\right]\alpha_{i\infty} - C_\mu (\theta_J + \alpha)^2\right) dy \, . \qquad (B.4)$$

Equation (B.4) is evaluated by using Multhopp's method of integration[13], and the terms under the integral sign are either those used in or those derived from the analysis of Appendix A.

B.2 THRUST-DEFLECTOR THEORY

According to the thrust-deflector hypothesis the circulation around each streamwise section of the jet is zero. Hence it may be inferred from equations (A.1) and (A.2) that, where $C_\mu c$ is nonzero, this hypothesis requires that

$$\theta_J + \alpha - \alpha_{i\infty} = 0 \, , \qquad (B.5)$$

and

$$\alpha_{i\infty} = \alpha_{i\infty}(\Gamma_J = 0) \, . \qquad (B.6)$$

Therefore, by combining equations (B.4), (B.5) and (B.6), it is found that the thrust-deflector hypothesis leads to the result

$$\bar{C}_{DT} = \frac{1}{2S} \int_{-s}^{s} c \, C_{LR} \, \alpha_{i\infty}(\Gamma_J = 0) \, dy \, .$$

The method used to evaluate this expression follows that employed to derive the circulation drag from the jet-flap theory.

REFERENCES

1 P R Ashill. A theoretical and experimental investigation of the external-flow, jet-augmented flap. Paper 6 AGARD CP 135 (1973).

2 D H Perry. A review of some published data on the external-flow jet-augmented flap. (Appendix by D N Foster) RAE TR 70240 (1970).

3 C A Schollenberger. A three-dimensional wing/jet interaction analysis including jet distortion influences. AIAA Paper 73-655 (1973).

4 L P Parlett, M P Fink, D C Freeman. Wind tunnel investigation of a large jet transport model equipped with an external-flow, jet flap. NASA TN D-4928 (1968).

5 L P Parlett, J P Shivers. Wind tunnel investigation of an STOL aircraft configuration equipped with an external-flow jet flap. NASA TN D-5368 (1969).

6 D C Freeman, L P Parlett, R L Henderson. Wind tunnel investigation of a jet transport configuration with an external-flow jet flap and inboard pod-mounted engines. NASA TN D-7004 (1970).

7 P R Ashill, S F Mansfield. Note on some exploratory tests on a swept wing with an external-flow jet-augmented flap. RAE TR 72192 (1973).

8 W E Acum. Corrections for symmetrical swept and tapered wings in rectangular wind tunnels. R&M 2777 (1950).

9 P R Ashill. On the blockage interference of a powered model in a wind tunnel of closed working section. RAE report in preparation.

10 D W Bryer, R C Pankhurst. Pressure-probe methods for determining wind speed and flow direction. HMSO, London. (1971).

11 E C Maskell, D A Spence. A theory of the jet flap in three dimensions. Proc. Roy. Soc. A, 251, 407 (1959).

12 D N Foster, H P A H Irwin, B R Williams. The two-dimensional flow around a slotted flap. R&M 3681 (1971).

13 B Thwaites (Ed). Incompressible aerodynamics. Claredon Press, Oxford. (1960).

14 J L Hess, A M O Smith. Calculation of potential flow about arbitrary bodies. Progress in Aeronautical Sciences, Vol 8, 1, 138. Pergamon Press, London. (1966).

15 D A Spence. A treatment of the jet flap by thin-aerofoil theory. RAE Report Aero 2568 (1955).

16 R T Jones, D Cohen. High speed wing theory. Princeton University Press, Princeton. (1960).

17 D A Spence. The lift on a thin aerofoil with a jet-augmented flap. Aero. Quart. 9, pp 287-299 (1958).

ACKNOWLEDGEMENTS

The Commercial Aircraft Division of The British Aircraft Corporation constructed the high-lift devices of the model, and provided staff for the testing and initial reduction of the data. The paper is reproduced by permission of Her Britannic Majesty's Stationery Office, and is British Crown Copyright.

INVESTIGATION OF EXTERNALLY BLOWN FLAP AIRFOILS WITH LEADING EDGE DEVICES AND SLOTTED FLAPS

by

Fotis Mavriplis * and David Gilmore **
Canadair Limited,
P.O. Box 6087,
Montreal, Canada
H3C 3G9

SUMMARY

An investigation was conducted to provide detailed information on the aerodynamics of externally blown flap systems, and to establish the correspondence of such systems, in which the flap is blown by a jet of circular cross-section, with two-dimensional jet flaps. Wind tunnel tests were conducted with a two-dimensional high-lift wing model and a tip-turbine fan having a diameter-to-wing chord ratio of 0.365. A semi-empirical 2D method is described which enables the application of Spence's theoretical relationships for jet flaps to multi-element airfoils. A theoretical 2D method is also presented which is an extension of Spence's theory to thin multi-element airfoils of arbitrary camber and a non-linear jet geometry. Good agreement was obtained between calculations with these methods of C_L versus α and experimental data for the externally blown flap configuration of this investigation. The measured data yielded useful empirical relationships for estimating the two-dimensional $C_{L_{max}}$ and C_D. These relationships together with the above agreement between theory and experiment suggest that an externally blown flap can be represented by an equivalent two-dimensional jet flap system.

NOTATION

A	Constant	
C,c	Wing chord	ft.
C_A	Axial force coefficient	
C_D	Drag coefficient	
ΔC_D	Increment in drag coefficient due to jet	
C_f	Flap chord projection on wing chord	
$C_{i,j}$	Influence coefficient for total velocity induced at i^{th} control point by j^{th} vortex element	
C_j	Jet momentum coefficient at the trailing edge	
C_L	Lift coefficient	
$C_{L_{C_T=0}}$	Lift coefficient at zero thrust	
C_{L_Γ}	Jet circulation lift coefficient	
$C_{L_{max}}$	Maximum lift coefficient	
C_{L_j}	Direct jet reaction lift component	
$\Delta C_{L_{C_j}}$	Increment in lift coefficient due to jet	
ΔC_{L_V}	Difference between potential flow and viscous flow	
$\Delta C_{L_{\delta,C_j}}$	Increment in lift coefficient due to flap deflection δ_j and C_j	
C_M	Pitching moment coefficient (Reference 0.[illegible]C)	
C_N	Influence coefficient for normal velocity induced at an element	
C_p	Surface pressure coefficient	
C_T	Jet thrust coefficient near wing leading edge	
$C_{T_{C_j=0}}$	Thrust coefficient at which circulation lift equals potential flow lift	
C_x	Influence coefficient for velocity in x-direction at an element	
C_y	Influence coefficient for velocity in y-direction at an element	
D	Drag Force	lb.
E	Ratio of projected flap chord to wing chord	
F_A	Axial force T_A-T_D	lb.
F_N	Normal force $L-T_N$	lb.
L	Lift force	lb.
M	Number of vortices representing airfoil	
N	Number of vortices representing jet	
Q,q	Dynamic pressure	lb./ft.^{2}
$r_{i,j}$	Separation distance between elements i and j	%c
R	Resultant force, $\sqrt{F_N{}^2+F_A{}^2}$	lb.
R	Right-hand side of matrix equation (15)	
R	Local radius of curvature of jet	%c
s	Distance along airfoil surface	%c
T	Jet thrust	lb.
T_A	Axial component of jet thrust	lb.
T_N	Normal component of jet thrust	lb.
t	Wing thickness	ft.
U_x,U_i	Total velocity in x-direction	ft./sec.
U_y	Total velocity in y-direction	ft./sec.
V,U_∞	Freestream velocity	ft./sec.
V_T	Total tangential velocity at an element	ft./sec.
x,y	Control point coordinates	%c
x_j,y_j	Jet origin at flap trailing edge	%c
x_v,y_v	Vortex point coordinates	%c
α	Angle of incidence	degrees or radians
Γ	Circulation strength	ft.^{2}/sec.
δ_f	Flap deflection angle	degrees or radians
δ_j	Jet deflection angle (angle between wing chord and direction of jet at trailing edge)	
ϵ	Element slope in x-y coordinate system	
η	Jet turning efficiency, R/T	
η'	Jet momemtum loss factor due to friction	
θ	Body angle relative to main airfoil chord	degrees
λ_a	Airfoil vorticity density	$d\Gamma_a/d_s$
λ_j	Jet vorticity density	$d\Gamma_j/d_s$
τ	Angle between final flap segment chord and direction of jet at the trailing edge	degrees or radians

---

* Senior Staff, Aerodynamic Technology Development
** Staff Aerodynamics Engineer.

1. INTRODUCTION

Recent interest in a turbofan STOL aircraft for commercial and military applications has put emphasis on the development of various powered lift concepts. In such concepts turbofan engine power is used to augment the lift normally achieved by the wing and flap system alone. Two of the most promising powered lift concepts for turbofan STOL applications are the internally blown flap (IBF) and the externally blown flap (EBF).

In the internally blown flap system, air from the engines is ducted through the wing and ejected from slots along the wing span to blow over the trailing edge flaps. The jet leaving the trailing edge with a finite momentum induces additional circulation lift over the wing.

In the externally blown flap system, use is made of the efflux of a very high bypass ratio engine by simply deflecting a slotted flap into the engine stream. The engine air in interaction with the flap spreads spanwise, flows through slots and leaves the trailing edge with excess energy to induce additional circulation lift over the wing.

Each system has its own problems, noise being a major problem common to both. However, the externally blown flap is the simpler of the two systems since it eliminates the need for complicated internal ducting.

The present investigation was undertaken with the aim of providing detailed information for externally blown flap systems which could be used both for the design of optimum high-lift configurations and the prediction of their aerodynamic characteristics.

One of the objectives of this investigation was to establish whether or not the externally blown flap can be represented by an equivalent jet-flap system. Moreover, whether two-dimensional jet-flap theory can be applied to such a system where the flap is blown by a jet of a circular cross-section.

For this purpose wind-tunnel tests were conducted with a two-dimensional wing model and a relatively large engine diameter to span ratio aiming at a reasonable jet momentum distribution at the trailing edge. In addition analytical work was carried out which included the development of methods, based on two-dimensional jet-flap theory, for predicting the aerodynamics of EBF multi-element airfoils, application of these methods to the configurations used in this test, and correlations with the experimental results.

This paper presents a description and the main results of this investigation.

2. WIND-TUNNEL TEST

For the wind-tunnel investigation, a 2-foot chord by 3-foot span high-lift wing model (NACA 64A211) was used in interaction with a jet from an 8-inch diameter tip-turbine fan engine. The engine produced 180 pounds of static thrust at a fan pressure ratio of 1.2 corresponding to a high bypass ratio turbofan jet engine. The tests were conducted at the NAE 6 by 9-foot Low-Speed Wind Tunnel in Ottawa using the Canadair 2D blowing walls which provide wall boundary layer control. A description of the 2D blowing wall facility and its operation is given in Reference 1. Figure 1 shows the test installation.

The test configurations included a Kruger flap, a Kruger slat, a slat and a droop in conjunction with single-slotted, double-slotted and triple-slotted flaps. The gap sizes and deflection angles of each leading edge device and flap segment were optimized to produce the highest lift coefficient in an earlier investigation without the engine reported in Reference 1.

In the present tests, the engine model was isolated from the wing force balance and could be adjusted to either a *high* or a *low* position and one of three tilt angles, 0°, −3° and −6°. Figure 2 shows the relative engine position for each particular leading edge configuration. Figure 3 shows details of a typical configuration of the wing model fitted with the Kruger slat (L5) and double-slotted flap (TA235), with the engine in the *low* position and tilted −6° (Position 2A).

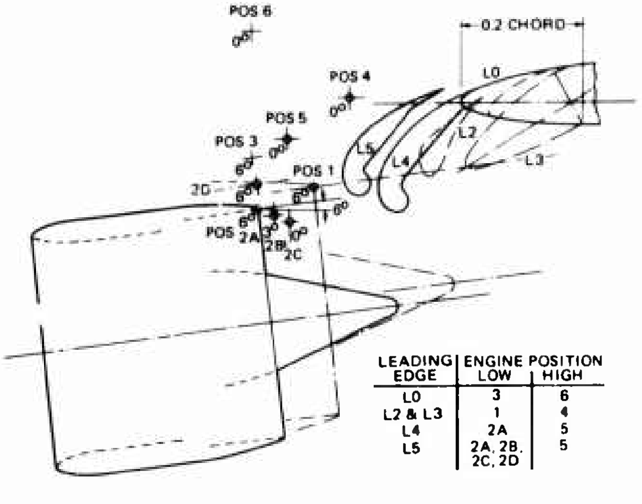

LEADING EDGE	ENGINE POSITION LOW	HIGH
L0	3	6
L2 & L3	1	4
L4	2A	5
L5	2A, 2B, 2C, 2D	5

Figure 2 Position of engine nacelle relative to the various leading edges of externally blown flap wing model

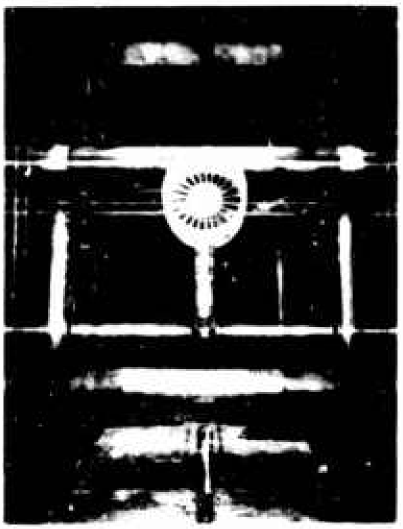

Figure 1 Installation of high-lift wing model and turbine fan between 2D blowing walls

The engine was calibrated to determine the jet thrust as a function of engine rotational speed. For this purpose measurements were made both with strain gauges on the engine supports and with wake rakes at three locations downstream of the engine. The thrust measured by strain gauges was found to be about equal to that obtained by integration of the wake rake measurements of the jet flow near the wing leading edge and was used to determine jet-thrust coefficients.

The effects of wall blowing on the tunnel dynamic pressure in the working section were investigated and found to be negligible. The optimum wall blowing rate was determined prior to the test on the basis of minimum drag for each particular configuration.

Static tests were made to determine the optimum engine position in terms of jet deflection angle and turning efficiency, and the jet reaction forces on the wing. The wind-on tests were made at a tunnel free stream dynamic pressure of 11 lb./ft.^{2} corresponding to a velocity of 97 ft./sec. and a Reynolds number of 1.22 x 10^6 per wing chord. Each configuration was tested at various values of thrust coefficient C_T ranging from 0 to 2.1. In the zero thrust condition the fan was driven to produce an average jet dynamic pressure equal to that of the tunnel free stream.

Standard corrections were applied to the power-off data according to Reference 2 and only to the part of the power-on data due to circulation (excluding the direct jet effect) according to Reference 3.

3. EFFECT OF WALL BLOWING ON EXPERIMENTAL DATA

Figure 4 shows the importance of the wall blowing technique used in these tests for obtaining good quality data. Wall blowing appears to reduce the drag and increase the lift, $C_{L_{max}}$ and lift-curve slope. This of course is the result of eliminating induced drag due to wall flow separation and its detrimental effect on lift. At 70° flap deflection, floor flow breakdown was observed to be caused by jet impingement on the floor. Wall blowing improved the data considerably but could not eliminate the effect of floor flow breakdown.

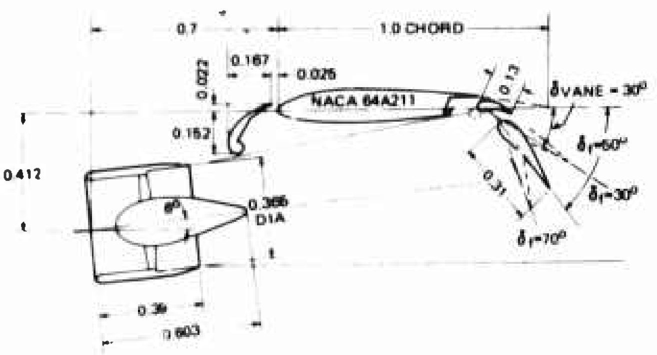

Figure 3 Details of EBF model wing with Krüger slat (L5) and double-slotted flap (TA235) and tip-turbine fan position 2A.

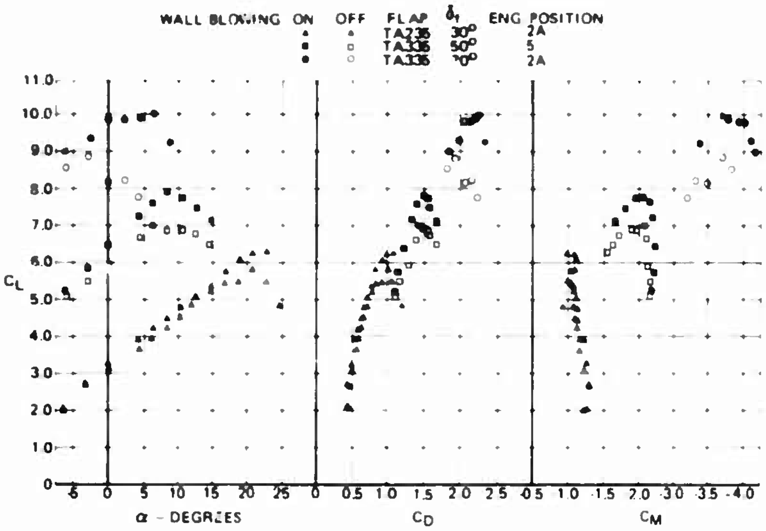

Figure 4 Effect of wall blowing on aerodynamic characteristics of EBF wing with slat L5 and various flap configurations.

4. EFFECT OF CONFIGURATION DESIGN ON AERODYNAMIC CHARACTERISTICS

In general, the flap designs with the best performance at zero thrust were also the best with jet blowing for a given engine position. Triple-slotted flaps achieved the highest lift increments due to jet blowing and the lowest drag coefficients. The double-slotted flap with a small vane and a large chord rear flap (TA235) was only slightly lower in high-lift performance than the triple-slotted flaps. Lower pitching moments were achieved for the same total flap deflection with double-slotted flaps than with triple-slotted flaps. And for flaps with the same number of segments, pitching moments were lower when the rear segment was the smallest rather than the largest.

Leading edge devices with the best performance at zero thrust were also the best with jet blowing for a given engine position. It appears that large chord leading edge devices that also extend the basic wing chord like the L4 and L5 will be needed to relieve the high pitching moment of EBF wings. In addition, better high-lift performance may be achieved when the lower surface of such leading edge devices is smooth. The best performance in this test was achieved with the Kruger slat (L5).

5. EFFECT OF ENGINE POSITION

Figure 5 shows the effect of engine position on the aerodynamic characteristics of the EBF wing with Kruger slat (L5) and double-slotted flap (TA235) at 50° flap deflection. It can be seen that the highest lift was obtained with the engine tilted -6° in a *low* position (2D) which permitted a small amount of the jet flow to pass over the top of the wing. Without tilting the engine and allowing about a third of the engine air to pass over the top of the wing (Position 5), the lift increment due to the jet was only 60 percent of that in Position 2D. The second best appears to be again a *low* position (2A) with the engine tilted -6° at which the entire jet flow is passing (theoretically) under the wing.

The lowest lift increment was obtained with the engine axis parallel to the wing chord in a *low* position (2C). This is an interesting case where the lift increment due to the jet compensates the difference between the experimental and potential flow C_L values of this configuration. An estimate based on static jet turning efficiency and jet deflection angle values indicates that this lift increment is due entirely to the direct jet reaction force and therefore does not include any increments due to the removal of the viscous effects and to supercirculation. In this position the jet impacted below the leading edge of the rear flap so that there was no jet flow through the slots for boundary layer control. In addition about two-thirds of the jet flow was passing directly under the flap trailing edge resulting in a jet angle of 21° as compared with 50° flap angle.

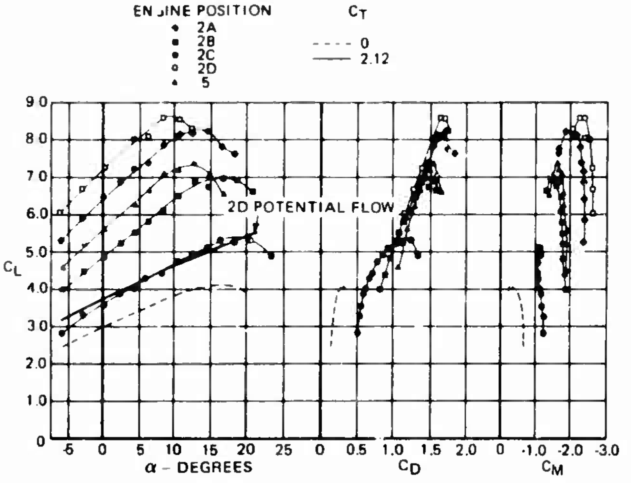

Figure 5 Effect of engine position on aerodynamic characteristics of EBF wing with slat L5 and double-slotted flap TA235 at $\delta_f = 50°$.

Figure 5 shows that with the engine in position 2C the drag was lowest and varied in a more non-linear fashion with lift than with the other engine positions where supercirculation occurred. The drag was highest with the engine in the *high* position.

Pitching moments were lowest for engine position 2C and highest for position 2D where the highest lift increment was achieved.

6. EFFECT OF JET BLOWING ON LIFT

Figure 6 shows lift, drag and pitching moment characteristics obtained in the tunnel for the configuration of Figure 3 at 0° and 50° flap angles at thrust coefficients C_T ranging from 0 to 2.12. In addition, calculated two-dimensional potential flow C_L versus α curves are shown for the same configurations including nacelle interference. The calculations were performed with the surface vorticity computer method described in Reference 1 by using an exact airfoil geometry and an equivalent system of two-dimensional bodies representing the axisymmetric nacelle. The latter were obtained by transformation of coordinates using the hydraulic analogy as in Reference 4.

It can be seen that, for the flaps-up configuration (δ_f=0°), where the viscous effects are comparatively small, there is little difference between potential flow theory and experiment. At 50° flap deflection at zero thrust, the viscous effects are large as indicated by the difference between potential flow and experimental data.

Figure 7 shows how the experimental lift coefficient varied with thrust coefficient at constant angle of attack for the configuration of Figure 3 at 50° flap deflection. Also shown is the two-dimensional potential flow value of this configuration with nacelle interference.

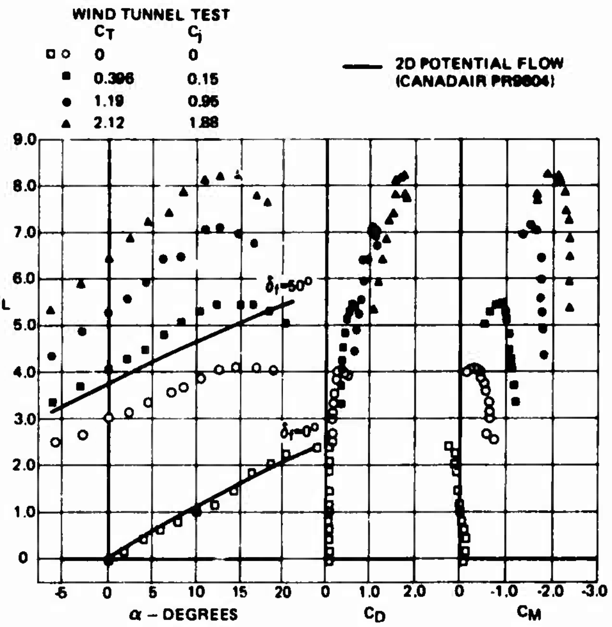

Figure 6 Experimental data showing aerodynamic characteristics of EBF wing configuration of Figure 3, δ_f = 50°, at various values of C_T, and comparison with potential flow lift coefficients

In Figure 7 we see first a region in which viscous effects are gradually reduced with increasing C_T until at C_T=0.24 the circulation lift of this configuration reaches its potential flow value. The total C_L at this point is higher by the amount of $\eta C_T \sin(\delta_j+\alpha)$ representing the direct jet reaction lift. The average jet momentum coefficient at the trailing edge C_j is assumed to be zero at C_T=0.24 for this configuration. An increase of C_T beyond this value would then result in the jet leaving the trailing edge with momentum $C_j=C_T-C_{T(C_j=0)}$ and acting as a jet flap. As C_j increases, there are additional losses ΔC_j caused by friction due to scrubbing of the jet over the flap surfaces. These losses are proportional to the C_T increment and amount to 2–3 percent of C_j. They can be accounted for by a factor $\eta' = (C_j - \Delta C_j) / C_j$.

In the jet-flap region we may consider the experimental lift coefficient as consisting of the following four components:

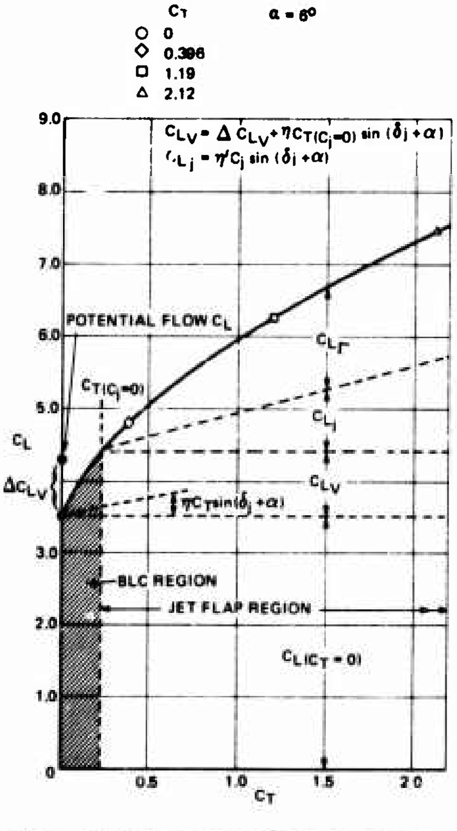

Figure 7 Resolution of external flow jet-flap lift into components. Configuration of Figure 3 δ_f = 50°.

(a) a basic lift coefficient at zero thrust $C_{L(C_T=0)}$

(b) a component of lift due to the function of the jet in eliminating viscous effects

$$C_{L_V} = \eta\, C_{T(C_j=0)} \sin(\delta_f + \alpha) + C_{L_{P.F.}} - C_{L(C_T=0)}$$

(c) a direct jet reaction component $C_{L_j} = \eta' C_j \sin(\delta_j+\alpha)$

(d) a component due to supercirculation induced by a jet with an average momentum coefficient $\eta' C_j = \eta' \left[C_T - C_{T(C_j=0)}\right]$ and deflection angle δ_j at the trailing edge.

Figure 8 shows the variation of thrust coefficient $C_{T(C_j=0)}$ at which potential flow lift was achieved with the configuration of Figure 3 at various flap deflections and constant angle of attack. These thrust coefficients were used to determine the values of jet momentum coefficient at the trailing edge C_j for the wind-on condition. The latter were subsequently used in conjunction with values of δ_j from static tests for the prediction of the lift coefficients of the test configurations.

7. MAXIMUM LIFT COEFFICIENTS

Correlations of the experimental maximum lift coefficients were based on the relationships developed for flapped airfoils by McRae (Reference 5) and for jet-flapped airfoils by Foster (Reference 6). Reference 5 shows that, for airfoils having a leading edge type of stall, the increments in $C_{L_{max}}$ due to flap deflection in two-dimensional flow are approximately one-half of the increments in C_L (due to flap deflection) at α=0°. By applying the same hypothesis to Spence's jet-flap theory, Reference 6 derived the following analogous relationship for jet-flapped airfoils in two-dimensional flow:

$$C_{L_{max}} = C_{L_{max,\substack{\delta=0\\C_j=0}}} + \tfrac{1}{2}\left(\Delta C_{L_{\delta,C_j}} + \tfrac{1}{2}\Delta C_{L_{C_j}}\right)_{\alpha_s} \tag{1}$$

where $\Delta C_{L_{\delta,C_j}}$ is the lift increment due to both flap deflection and jet momentum and $\Delta C_{L_{C_j}}$ the increment in C_L due to jet momentum for the deflected flap configuration, with both ΔC_L terms evaluated at the stalling incidence α_s.

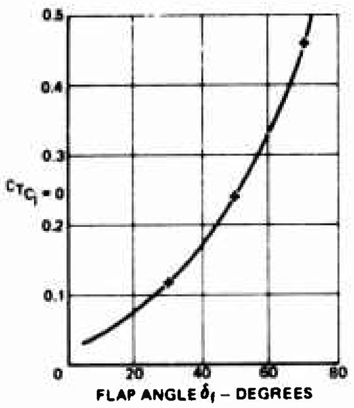

Figure 8 Thrust coefficient at which potential flow lift was achieved for configuration of Figure 3 at various flap angles and $\alpha = 6°$.

A more convenient and perhaps more accurate theoretical expression for $C_{L_{max}}$ may be obtained by considering Equation (1) in terms of $\Delta C_{L_{\delta,C_j}}$ and $\Delta C_{L_{C_j}}$ at $\alpha=0°$. The resulting expression using terms from Spence (Reference 7) is:

$$C_{L_{max}} = C_{L_{max,\delta=0,\,C_j=0}} \left(1+\tfrac{3}{2}B_0\right) + \tfrac{1}{2}\left(\Delta C_{L_{\delta,C_j}} + \tfrac{1}{2}\Delta C_{L_{C_j}}\right)_{\alpha=0°} \qquad (2)$$

where $\frac{3}{2}Bo = \frac{3C_j^{1/2}}{8\pi}\,(1.152 + 1.106\,C_j^{1/2} + 0.051\,C_j)$

which for $0.5 \leq C_j \leqq 5.0$ may be replaced by $\frac{3}{2}Bo \cong 0.276\,C_j^{0.826}$

Figure 9 shows a plot of $C_{L_{max}}$ versus the expression within brackets of Equation 2 using the experimental data of Figure 6 and values of the ΔC_L terms at $\alpha = 0°$. Where necessary the experimental data were adjusted to correspond exactly to C_j values of 0, 1.0 and 2.0. It can be seen that the experimental data form separate curves of constant C_j which have a common origin at $\delta_f = 0°$ and $C_j = 0$, and a distinct bend between 0° and 30° flap angle. The first part of the curves may have a slope of 1.0 or higher indicating a trailing edge type of stall (Reference 5). The second part has a slope of 1/2 as predicted by Equation 2 for a leading-edge type of stall in two-dimensional flow. The vertical spacing of the experimental C_j lines is of the order of $0.276\,C_j^{0.826}\,C_{L_{max\,\delta=0,\,C_j=0}}$ as indicated by theory in Equation (2). It should be pointed out that $C_{L_{max\,\delta=0,\,C_j=0}}$ is the *leading edge stall* $C_{L_{max}}$ which in this case is hypothetical and can be found by extending the $C_j = 0$ line with slope 1/2 to the zero flap case (Reference 5).

The slightly lower $C_{L_{max}}$ values at 70° flap deflection are believed to be due to the effect of jet impingement on the floor at the higher values of C_T combined with a high angle of incidence. At zero thrust coefficient, $C_{L_{max}}$ appears to collapse just below 50° flap indicating that the maximum flap angle (with which highest C_L is achieved at $\alpha = 0°$) has been exceeded. However, flap effectiveness at 50° and 70° is restored by applying sufficient blowing for boundary layer control ($C_T > 0$, $C_j = 0$) as shown in Figure 9.

8. DRAG INCREMENT DUE TO EXTERNAL BLOWING OF THE FLAP

The results of this investigation show that the drag increment due to external jet blowing correlates well with the following empirical relationship

$$\Delta C_D = C_D - C_{D_{C_T=0}} = K\,C_T\left[\sin^2(\delta_f + \alpha) \pm \sin^2(\tau)\right] \quad (3)$$

where $\tau = |\delta_j - \delta_f|$ with $+\sin^2\tau$ used when $\delta_j > \delta_f$ and $-\sin^2\tau$ when $\delta_j < \delta_f$. K is an empirical factor which was found to vary with engine position approximately as shown in Table 1.

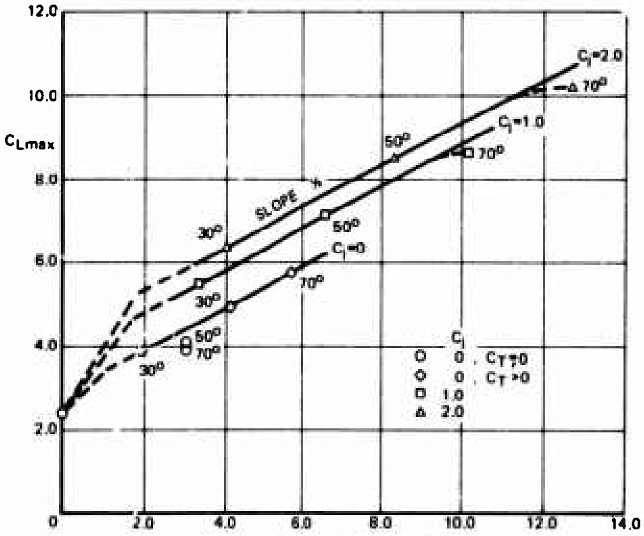

Figure 9 Maximum lift coefficients versus lift increments at $\alpha = 0°$ of externally blown flaps of Figure 3.

TABLE 1

ENGINE POSITION	ENGINE TILT ANGLE	K
2A LOW	-6°	1.0
2B LOW	-3°	0.82
2C LOW	0°	0.56
2D LOW but higher than 2A	-6°	1.0
5 HIGH	0°	0.91

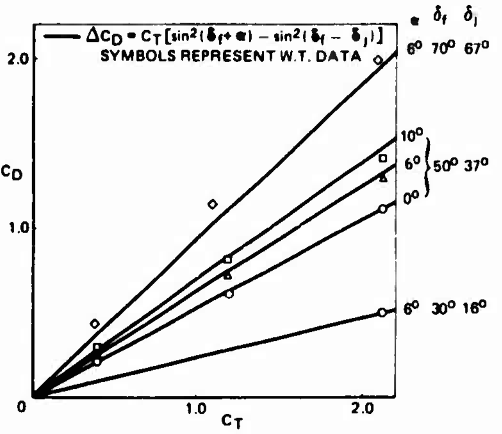

Figure 10 Total drag increment due to jet blowing EBF configuration of Figure 3. Correlation of experimental data.

It appears that K represents the fraction of jet flow that is in direct interaction with the flap and may therefore depend on such parameters as jet-diameter-to-flap-chord ratio and relative engine position and inclination to the wing chord, as well as the number of slots in the flap.

Figure 10 shows good agreement between the experimental data with the engine-airfoil configuration of Figure 3 and calculations using K = 1.0 with Equation (3). The experimental data at 70° flap angle are believed to include a vortex drag component (not accounted for by Equation (3)) due to flow separations from the tips of the rear flap segment observed during the test. Figures 11 to 15 are photographs of flow visualizations made during the test with the configuration of Figure 3 at 50° and 70° flap deflection. Figure 14 shows for the 70° flap at $C_T = 0.387$ large areas of flow separation (dark areas adjacent to the walls). At $C_T = 2.08$ (Figure 15) the flow over the flap improved considerably but flow separation was not completely eliminated. At 50° flap angle, flow separations from the flap were observed at low C_T and high α (Figure 12) but at $C_T = 1.0$ (Figure 13) there was already no separation visible.

An empirical relationship for the axial force derived from Equation (3) is

$$C_A = C_T - C_D = (1 - K)C_T + K\,C_T\left[\cos^2(\delta_f + \alpha) \mp \sin^2\tau\right] - C_{D_{C_T=0}} \quad (4)$$

where $-\sin^2\tau$ is used when $\delta_j > \delta_f$, and $+\sin^2\tau$ when $\delta_j < \delta_f$.

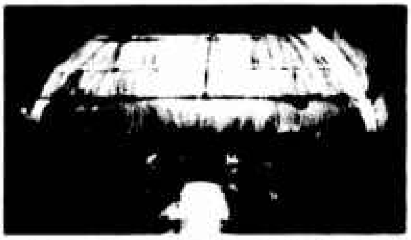

Figure 11 Flow visualization, leading edge EBF wing of Figure 3, $\delta_f = 50°$, $\alpha = 12°$ and $C_T = 0.396$.

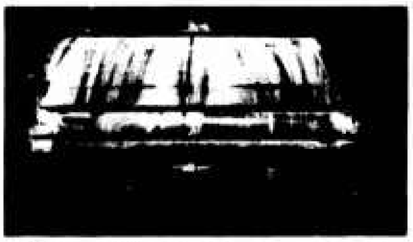

Figure 12 Flow visualization, flaps EBF wing of Figure 3, $\delta_f = 50°$, $\alpha = 12°$ and $C_T = 0.396$

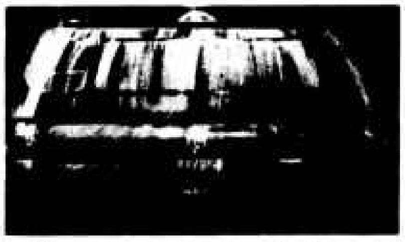

Figure 13 Flow visualization, flaps EBF wing of Figure 3, $\delta_f = 50°$, $\alpha = 12°$ and $C_T = 1.0$

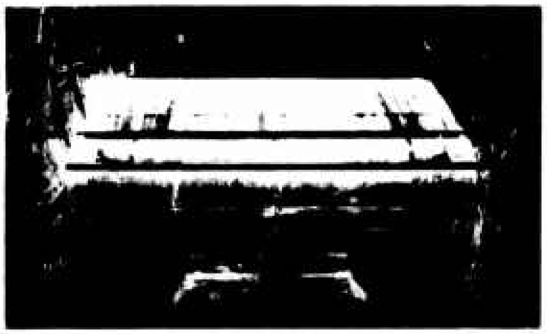

Figure 14 Flow visualization, flaps EBF wing of Figure 3, $\delta_f = 70°$, $\alpha = 10°$ and $C_T = 0.387$.

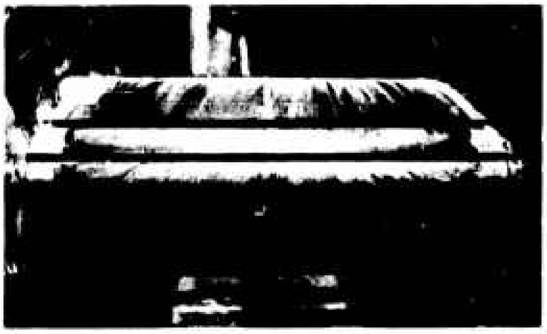

Figure 15 Flow visualization, flaps EBF wing of Figure 3, $\delta_f = 70°$, $\alpha = 10°$ and $C_T = 2.08$.

9. EFFECT OF NACELLE AND JET ON CHORDWISE PRESSURE DISTRIBUTION

Figure 16 shows potential flow pressure distributions for the configuration of Figure 3 at 50° flap with and without nacelle interference. Also shown for comparison are experimental surface pressures at mid-span of the wing with nacelle at zero thrust coefficient. At the bottom surfaces, positive C_p values higher than 1.0 are caused by velocity peaks in the jet flow exceeding the average jet velocity which was set to be equal to the tunnel free-stream velocity. The theoretical method appears to predict well the effect of nacelle interference which alters the slat pressure distribution considerably. The remaining differences between theory and experiment may be attributed to viscous effects.

It was stated before that the viscous effects were reduced with increasing C_T until at $C_T = 0.24$ the circulation lift of this configuration equaled its potential flow value. To check the validity of this statement a comparison of potential flow pressure distribution with experimental data at C_T of 0 and $C_T = 0.396$ (closest to $C_T = 0.24$ available data) is presented in Figure 17. At $C_T = 0.396$ the jet is supposed to leave the trailing edge with jet momentum $C_j = 0.15$ which induces a small amount of lift due to supercirculation ($C_{L_\Gamma} = 0.34$). The experimental C_p s are therefore expected to be slightly higher in absolute values than the potential flow ones. In effect the experimental data at $C_T = 0.396$ are almost identical to the potential flow ones at the main airfoil. At the upper slat and flap surfaces, the experimental data show higher suction and at the lower flap surfaces they show high positive pressures due to jet impact.

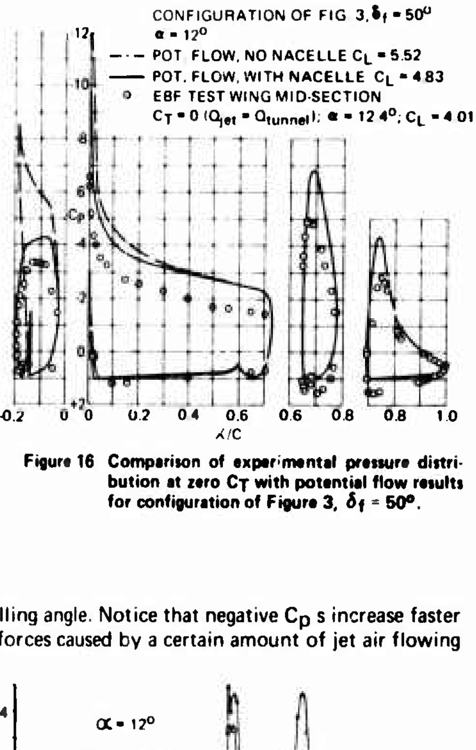

Figure 16 Comparison of experimental pressure distribution at zero C_T with potential flow results for configuration of Figure 3, $\delta_f = 50°$.

Similar results are shown in Figure 18 for the same configuration just before the stalling angle. Notice that negative C_p s increase faster with C_T at the flaps than the rest of the wing. This is probably due to centrifugal forces caused by a certain amount of jet air flowing over the upper flap surfaces.

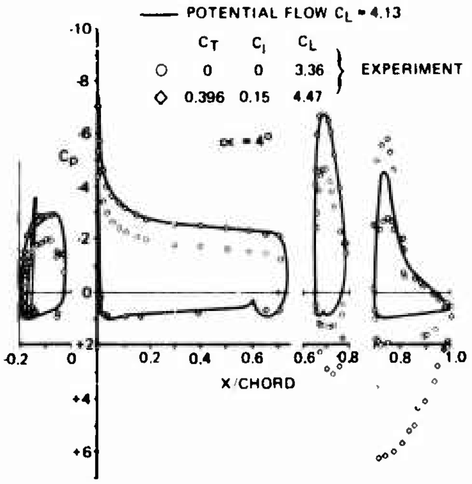

Figure 17 Comparison of potential flow pressure distribution with experimental data at zero and low C_T for configuration of Figure 3, $\delta_f = 50°$.

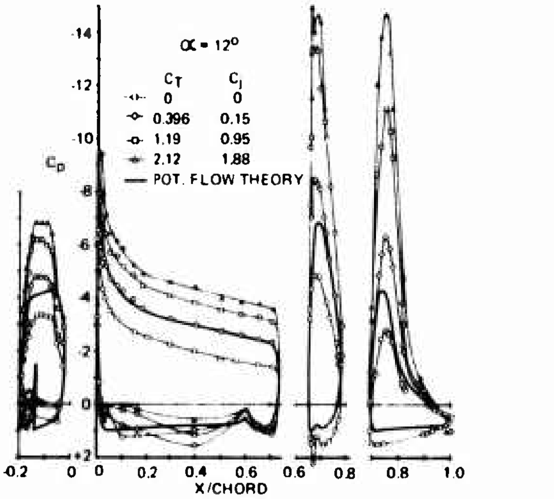

Figure 18 Experimental pressure distributions at various values of C_T in comparison with potential flow results for configuration of Figure 3, $\delta_f = 50°$.

The positive surface pressures of the flaps corresponding to the results of Figures 17 and 18 are shown separately in Figure 19.

Figures 17, 18 and 19 show that with increasing C_T the load increases faster at the flaps than the rest of the wing. The effect is a shift of the center of pressure towards the trailing edge associated with large negative pitching moments (See Figure 6.)

10. EFFECT OF NACELLE AND JET ON SPANWISE PRESSURE DISTRIBUTION

Figure 20 shows the spanwise distribution of surface pressures corresponding to those of Figures 18 and 19. They were obtained at C_T of 2.12 for selected chordwise locations representing pressure peaks, and one at 0.4 c representing the average over the main section. Figure 21 gives an approximate picture of the spanwise load distribution based on ΔC_p of upper and lower surface at the selected chordwise locations. These distributions are shown to be symmetrical about the wing-nacelle axis on the basis of flow visualizations (see Figures 11 to 15).

The results of Figures 20 and 21 may be summarized as follows:

Just above the jet there is a region of strong interference due to the nacelle and the jet which extends spanwise a little more than one jet diameter. Within this region the nacelle and the jet appear to reduce the local angle of incidence at the leading edge while the jet appears to increase it at the flaps. These effects decay spanwise, first rapidly and then (outside this region) more gradually until they become negligible at two jet diameters from the jet axis.

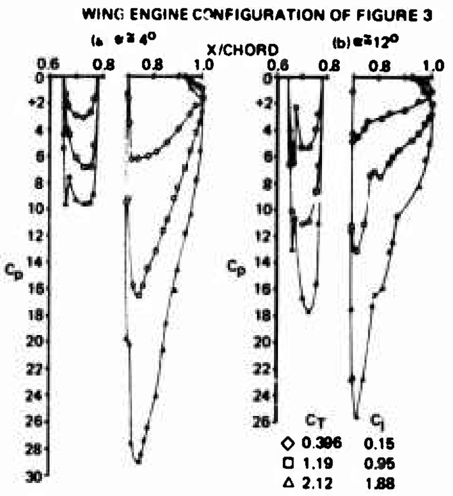

Figure 19 Experimental pressure distributions over lower surfaces of vane and flap at various values of C_T for configuration of Figure 3, $\delta_f = 50°$

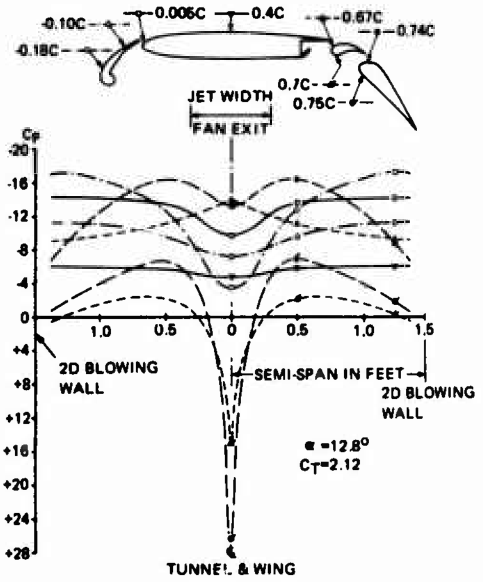

Figure 20 Spanwise distributions of experimental surface pressures for selected chordwise locations of EBF wing, configuration of Figure 3, $\delta_f = 50°$

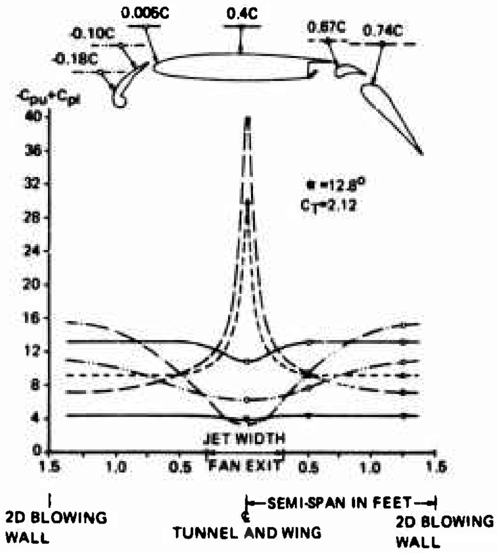

Figure 21 Spanwise load distributions for selected chordwise locations of EBF wing, configuration of Figure 3, $\delta_f = 50°$

The interaction of the jet with the flaps results in very high positive pressures due to jet impact at the lower flap surfaces and additional suction at the upper flap surfaces due to jet air flowing through the slots. At the bottom surface the jet flow accelerates spanwise quickly, resulting in high negative C_p's just outside the region of direct impact. The spanwise load distribution on the flaps has a peak value at the jet axis and decreases to a lower, almost uniform loading at about one jet diameter on each side of the jet axis.

11. PREDICTION METHODS FOR MULTI-ELEMENT AIRFOILS WITH JET-BLOWN FLAPS

For the comparison of the experimental results of this investigation with theory, a method was first needed for multi-element airfoils with a jet flap. An obvious choice for a simple method was Spence's two-dimensional jet-flap theory (References 7, 8 and 9). An investigation of the applicability of Spence's method revealed that a simplified representation of a multi-slotted flap by a single plate flap element cannot give reasonable results. For example, the lift coefficient for a given total flap deflection may vary between two double-slotted flaps with a different vane-to-flap-chord ratio while with Spence's method only one value can be obtained. Spence's method gives also one value of lift-curve slope for all airfoil configurations at $C_j = 0$ while potential flow theory shows a decreasing value of lift-curve slope with increasing flap deflection.

One approach, therefore, was to find a more reasonable representation of the airfoil geometry so that the results of Spence's theory would still be applicable. Another approach was to develop a two-dimensional non-linear jet-flap method for thin cambered multi-element airfoils with correct jet shape representation. These two methods are described below.

11.1 Semi-Empirical Method

For two-dimensional inviscid flow, the theory of References 7, 8 and 9 gives the following expression for the lift coefficient of a thick jet-flapped airfoil of t/c thickness ratio.

$$C_L = \left(1 + \frac{t}{c}\right)\left[\delta_f \frac{\partial C_L}{\partial \delta_f} + \tau \frac{\partial C_L}{\partial \tau} + \alpha \frac{\partial C_L}{\partial \alpha}\right] - \frac{t}{c} C_j (\delta_j + \alpha) \tag{5}$$

The derivative $\partial C_L/\partial \delta_f$ is a function of flap-chord ratio E and jet momentum coefficient C_j while $\partial C_L/\partial \tau$ and $\partial C_L/\partial \alpha$ are functions of jet momentum coefficient only. Theoretical values of these derivatives are given in Reference 7 where $\partial C_L/\partial \tau$ is the same as $\partial C_L/\partial \delta_f$ for E = 0 (pure jet flap) and $\partial C_L/\partial \alpha$ the same as $\partial C_L/\partial \delta_f$ for E = 1.0. Following the same approach of linear superposition as in Equation (5), it seems reasonable to assume that for a slotted flap with up to three elements the following expression would apply if a representative flap-chord ratio could be defined for each flap element.

$$\delta_f \frac{\partial C_L}{\partial \delta_f} = \delta_{f_1} \frac{\partial C_L}{\partial \delta_{f_1}} + \delta_{f_2} \frac{\partial C_L}{\partial \delta_{f_2}} + \delta_{f_3} \frac{\partial C_L}{\partial \delta_{f_3}} \tag{6}$$

It was found empirically that representative flap-chord ratios could be defined by taking the projected chord of each flap element separately in proportion to the wing chord ahead of the flap element. For example, a representative jet flap model for the double-slotted flap configuration of Figure 3 is shown in Figure 22.

On the basis of this model, the individual flap element-to-wing chord ratios are $E_1 = c_{f_1}/c_1$ and $E_2 = c_{f_2}/c$. For these values of E_1 and E_2 one may obtain the corresponding values of $\partial C_L/\partial \delta_f$, and for E = 0 the value of $\partial C_L/\partial \tau$. For δ_{f_1} and δ_{f_2} one must use the true-chord deflection angle of each flap element. The jet-flap angle in this case $\tau = \delta_j - \delta_{f_2}$ with δ_j being the value of jet deflection angle as determined from static tests. Since in this case $\delta_j < \delta_{f_2}, \tau$ is negative.

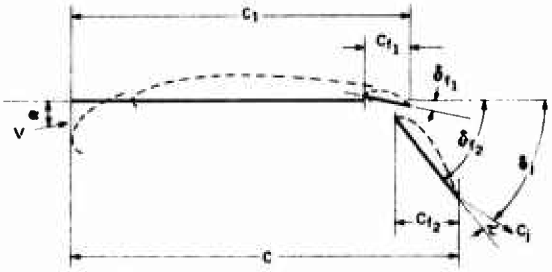

Figure 22 Flat-plate airfoil jet-flap model for configuration of Figure 3

In addition it was found empirically that a better value for the term $\left(1 + \frac{t}{c}\right)\frac{\partial C_L}{\partial \alpha}$ in Equation (5) could be obtained by using the potential flow lift-curve slope of the exact configuration without jet and the increment $\Delta\left(\frac{\partial C_L}{\partial \alpha}\right)$ due to jet as calculated by Spence, i.e.,

$$\left(1 + \frac{t}{c}\right)\frac{\partial C_L}{\partial \alpha} = \left(\frac{\partial C_L}{\partial \alpha}\right)_t = \left(\frac{\partial C_L}{\partial \alpha}\right)_{P.F.} + \left[\left(\frac{\partial C_L}{\partial \alpha}\right)_{C_j} - \left(\frac{\partial C_L}{\partial \alpha}\right)_{C_j=0}\right]_{\text{Spence}} \tag{7}$$

Therefore the new expression for the lift coefficient corresponding to that of Equation (5) for the case of a double slotted flap is

$$C_L = \left(1 + \frac{t}{c}\right)\left[\delta_{f_1} \frac{\partial C_L}{\partial \delta_{f_1}} + \delta_{f_2} \frac{\partial C_L}{\partial \delta_{f_2}} + \tau \frac{\partial C_L}{\partial \tau}\right] + \alpha \left(\frac{\partial C_L}{\partial \alpha}\right)_t - \frac{t}{c} C_j (\delta_j + \alpha) \tag{8}$$

with $\left(\frac{\partial C_L}{\partial \alpha}\right)_t$ given by Equation (7).

11.2 Theoretical Method

A two-dimensional incompressible, inviscid flow, thin-airfoil method has also been developed to calculate the aerodynamic characteristics of multi-element jet flapped airfoils. The method is an extension of Spence's theory (Reference 7) satisfying the Laplace equation while retaining the non-linear character of the governing equations.

There are at least two known methods which are extensions of Spence's theory. Reference 10 uses a distribution of discrete vortices on the camberline and describes the non-linear jet geometry by closed form expressions. Only single flat-plate airfoils have been treated with this method (Reference 10). Reference 11 treats the problem of multi-element airfoils interacting with thick two-dimensional jets. Linear distributed singularities are placed on airfoil camberlines and jet boundaries. Jet geometry is determined iteratively by satisfying the exact boundary conditions. Again only examples of flat-plate airfoils are shown in Reference 11.

The present method is based on a discrete vortex representation of a continuous vorticity over the actual airfoil camberline and jet centerline. These lines are divided into small elements each having a discrete vortex at the element 1/4 chord representing the average load over the element, and a control point at the 3/4 chord.

Figure 23 shows the vortex-element representation of a single-slotted flag airfoil with a slat and a jet issuing from the trailing edge. All coordinates are referenced to an x-y system whose x-axis is aligned with the freestream. The unknown airfoil vortex strengths, and therefore the loading, are determined by requiring the sum of the normal velocities induced by all the airfoil and jet vortices, and that of the freestream at each control point of the airfoil and the jet to be equal to zero. Since the jet shape is unknown, an iterative scheme is used to obtain the jet geometry and loading. The iterations begin by assuming an initial jet geometry in the form of a curvature distribution which directly determines the jet loading, and the calculations procedure can then start. During the iterations, the jet elements are adjusted to align themselves with the local total induced velocity vector.

The basic equation to be solved is

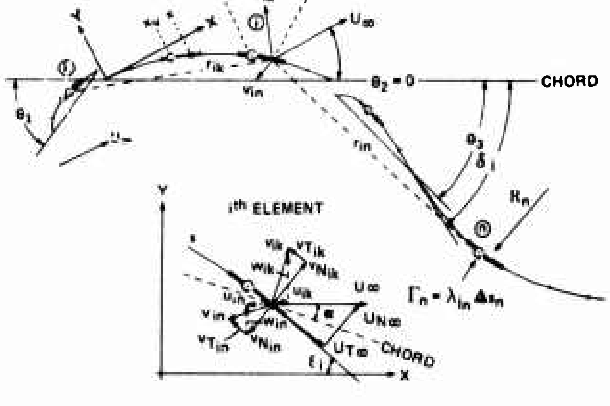

Figure 23 Vortex-element representation of a three-segment airfoil with a jet flap and induced velocities.

$$\int_0^c \lambda_a C_N \, dx + \int_c^\infty \lambda_j C_N \, dx = -U_\infty \sin(\epsilon - \alpha) \tag{9}$$

where λ_a, λ_j are the airfoil and jet vortex loading densities ($d\Gamma/ds$) respectively, C_N is the influence coefficient of the normal induced velocities on the airfoil surface, ϵ the local airfoil surface slope angle and α the angle of attack.

For the representation of Figure 23, Equation (9) is transformed into a system of linear equations which after separating the known and unknown parts is

$$\sum_{i=1}^{M} \sum_{k=1}^{M} \lambda_{a_k} C_{N_{i,k}} \Delta s_k = -\sum_{i=1}^{M} [U_\infty \sin(\epsilon - \alpha)_i + \sum_{n=M+1}^{M+N} \lambda_{j_n} C_{N_{i,n}} \Delta s_n] \tag{10}$$

where
$$\lambda_{j_n} = U_\infty C_j \frac{c}{2R_n} \tag{11}$$

and
$$C_{N_{i,j}} = C_{y_{i,j}} \cos(\epsilon - \alpha)_i + C_{x_{i,j}} \sin(\epsilon - \alpha)_i \tag{12}$$
$$(j = k \text{ or } n)$$

C_x and C_y are the x- and y- components of the total velocity v induced by vortex k or n of unit strength at the i^{th} element, i.e.

$$C_{i,j} = \frac{\Delta s_j}{2\pi} \frac{1}{r_{i,j}} \tag{13}$$

where
$$r_{i,j} = \sqrt{(x_i - x_{v_j})^2 + (y_i - y_{v_j})^2}$$

$$C_{x_{i,j}} = C_{i,j} \frac{y_i - y_{v_j}}{r_{i,j}} \quad \text{and} \quad C_{y_{i,j}} = C_{i,j} \frac{x_i - x_{v_j}}{r_{i,j}} \tag{14}$$

Equation (10) re-written in a matrix notation is

$$[C_N] [\lambda_a] = [R] \tag{15}$$

from which λ_a can be solved by inverting $[C_N]$. Solution of Equation (15) ensures that the boundary condition of zero normal velocity is satisfied on the airfoil and that the Kutta condition is also met at the trailing edge of each body, except that shedding the jet.

To start the calculation procedure, an initial shape for the jet is formulated from the following function

$$\frac{d^2y}{dx^2} = A [\log(x - x_j) - \log(x)] \tag{16}$$

where
$$A = -(\tan\alpha + \tan\delta_j) / 2{\cdot}45$$

The iterations proceed with calculation of airfoil loading corresponding to a given jet geometry and subsequent determination of the velocity slope at each jet control point. The current jet shape is than adjusted to the local velocity by using

$$\Delta\left(\frac{d^2y}{dx^2}\right) = f_c \left(\frac{d^2U_y}{dU_x^2} - \frac{d^2y}{dx^2} \right) \tag{17}$$

where f_c is a relaxation factor ($0 < f_c < 0.5$) which is varied during iterations to keep the evolving jet geometry smooth. Typical jet wakes extend to four chords downstream of the trailing edge to where the loading is reduced to less than 2% of that on the first jet element.

Convergence is achieved when one of two criteria is met. The first is based on the difference in curvature at each element between previous and current jet. The second is based on the current total jet strength which is compared with its theoretical value as given by Reference 7.

The method calculates $\Delta C_p = C_p$ *upper* $- C_p$ *lower* from the Kutta-Joukowski rule. The pressure distribution C_p and the coefficients C_L, C_D and C_M are then obtained from the following relations:

$$C_{p_{lower_i}} = 1. - (1 - \tfrac{1}{2}\lambda_{a_i})^2 \tag{18}$$

$$C_{p_{upper_i}} = C_{p_{lower_i}} + \frac{2 \lambda_{a_i} \Delta s_i}{c} \frac{V_{T_i}}{U_\infty^2} \tag{19}$$

$$C_L = 2 \sum_{i=1}^{M} \lambda_{a_i} \Delta s_i \frac{U_i}{U_\infty^2} + C_j \sin(\delta_j + \alpha) \tag{20}$$

or
$$C_L = \sum_{i=1}^{M} \Delta C_{p_i} \cos(\tan^{-1} \epsilon_i) \Delta s_i + C_j \sin(\delta_j + \alpha) \tag{21}$$

$$C_M = -2 \sum_{i=1}^{M} \lambda_{a_i} x_i \Delta s_i \frac{V_{T_i}}{U_\infty^2} - C_j \sin\delta_j \tag{22}$$

Both Equations (20) and (21) are used to obtain C_L. Equation (20) gives C_L from integration of vortices while Equation (21) from integration of pressures. Good agreement between these two values (within 0.5%) verifies the integration procedure.

The method can handle up to eight interfering airfoils of arbitrary camber for a specified jet momentum and jet angle at the trailing edge. It uses only a minimum of information describing the geometry of the airfoil and jet to construct the detailed arrangement of lifting elements. A cosine rule is used to divide each chordline into elements. The jet element length is varied parabolically in order to satisfy the condition of constant loading along the jet. Continuity of loading between jet and airfoil is achieved by making the first jet element nearly equal in length to the airfoil trailing edge element shedding the jet.

12. COMPARISON OF PRESENT METHODS WITH THEORY AND EXPERIMENT

A comparison of the present theoretical jet flap method with Spence (Reference 7) and that of Reference 10 is shown in Figure 24 for a 2D flat-plate airfoil with a jet flap. C_L and C_M values are shown as a function of jet angle at a relatively high jet momentum coefficient, $C_j = 4.0$. The results of the other two methods were taken from Reference 10.

As can be seen, all three methods agree very well up to 30° jet angle. At higher jet angles, the non-linear methods (present and Reference 10) deviate from the results of Spence showing, as expected, lower C_L and C_M values. At 70° jet angle the C_L and C_M values of the present method are 15 percent lower than these of Spence.

Figure 25 shows a comparison between the semi-empirical and the theoretical jet flap method of this paper for a 2D single-slotted flap airfoil with a Kruger and a jet flap. The thick airfoil and the representative flat-plate and camberline geometries used in the methods are also shown in Figure 25. Calculated C_L versus α curves are shown for 30° flap deflection, 43.9° jet angle and C_js ranging from 0 to 2.89. Thickness corrections were applied also to the theoretical jet-flap method by multiplying the pressure lift coefficient by the factor $(1 + t/c)$.

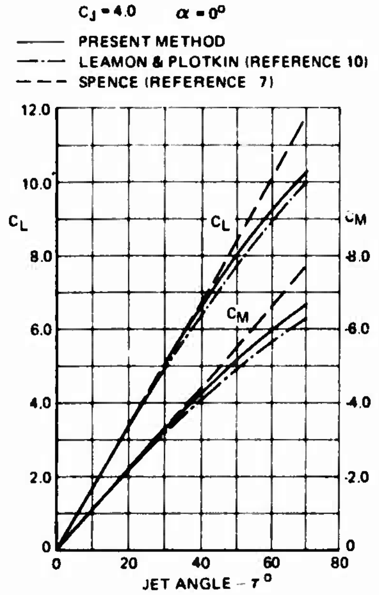

Figure 24 **Comparison between present and other theoretical jet-flap methods**

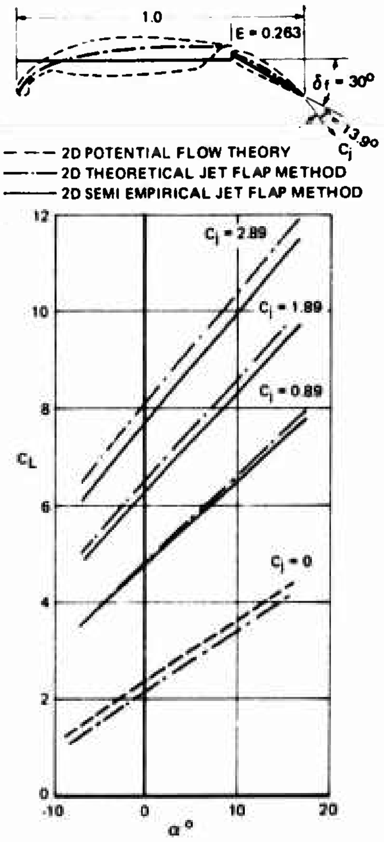

Figure 25 **Comparison between semi-empirical and theoretical jet-flap method**

At $C_j = 0$ the comparison is made with 2D potential flow calculations of the exact airfoil geometry (dotted line). The results of the semi-empirical method at $C_j = 0$ agree well with potential flow theory and have been omitted for clarity. The theoretical jet flap method closely predicts the lift curve slope at slightly lower than potential flow C_L value.

For the jet-flap cases there is good agreement between the two methods both in C_L and $C_{L\alpha}$ at the lower C_j values. As C_j increases, the results of the two methods deviate from each other with the theoretical method showing higher C_L values (up to 5% at $C_j = 2.89$) than the semi-empirical method. In view of the simplifications made to represent such an arbitrary airfoil geometry, the agreement between the two methods is surprisingly good.

The present methods were finally applied to the externally blown flap configurations of this investigation in order to establish on the basis of comparisons with experiment the correspondance of such systems with 2D jet flaps. The calculations were carried out for the engine-wing-flap configuration of Figure 3. The camberline representation of this configuration used for the 2D theoretical jet flap method is shown in Figure 26. The representative model for the semi-empirical method is shown in Figure 22.

The required jet momentum coefficient at the trailing edge, C_j for these calculations was determined from experimental data as described in Section 6. The average jet deflection angle was assumed to have the value of δ_j determined from static tests.

Comparisons between calculated and experimental lift coefficients versus angle of attack are shown in Figure 27 for 0° and 30° flap deflections, and in Figure 28 for 0° and 50° flap deflections. The calculated data include the 2D potential flow C_L versus α of the exact airfoil geometry with an analogous 2D nacelle obtained with the vorticity method of Reference 1 for the zero and deflected flap cases. Thickness correction have been applied to the results for the jet flap cases as described before. In addition, the calculated results include the direct jet reaction lift component $\eta C_{T(C_j=0)}\sin(\delta_j+\alpha)$ which applies to externally blown flaps and exists in the test data (see Section 6).

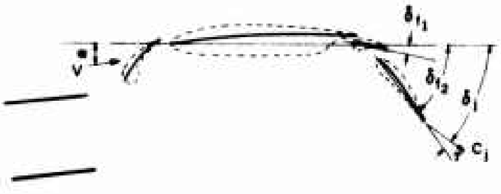

Figure 26 **Camberline representation of configuration of Figure 3**

It can be seen that 2D potential flow theory predicts very well C_L and C_{L_α} for the zero and 30° flap cases where the viscous effects are relatively small. At 50° flap deflection, it predicts C_{L_α} reasonably well but theoretical C_L values are higher than experimental by a $\Delta C_L = 0.8$ indicating the presence of large viscous effects.

The present jet-flap methods compare well with 2D potential flow at $C_j=0$. For clarity, the semi-empirical method at $C_j=0$ has not been plotted in Figure 28.

The calculated data for the jet blowing cases agree well with the experimental ones both in C_L and C_{L_α} except for the 50° flap at $C_T=2.12$ where the semi-empirical method overpredicts C_L by 6%. The theoretical jet flap method appears to show again slightly higher C_L and C_{L_α} than the semi-empirical method.

While the camberline representation of an airfoil predicts C_L reasonably, it does not, in general, give good prediction of ΔC_p with x, since it contains nose pressure peaks which do not exist on the real airfoil. An improvement in this direction may be achieved by correcting for thickness using a procedure similar to that given by Küchemann (Reference 12) which considers the thickness distribution along the camberline.

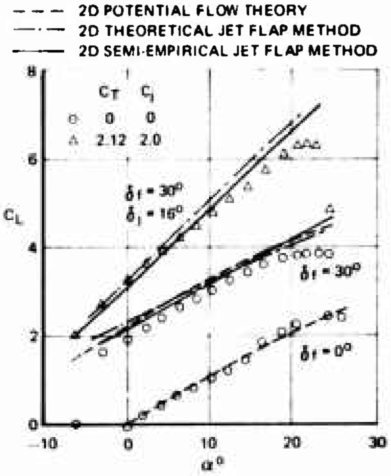

Figure 27 Comparison of calculated lift coefficients versus α with experimental results for configuration of Figure 3, $\delta_f = 30°$

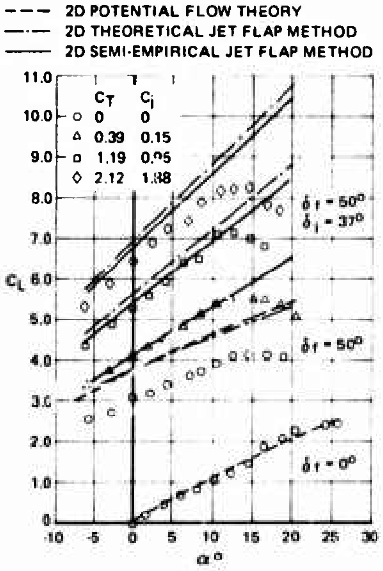

Figure 28 Comparison of calculated lift coefficients versus α with experimental results for configuration of Figure 3, $\delta_f = 50°$

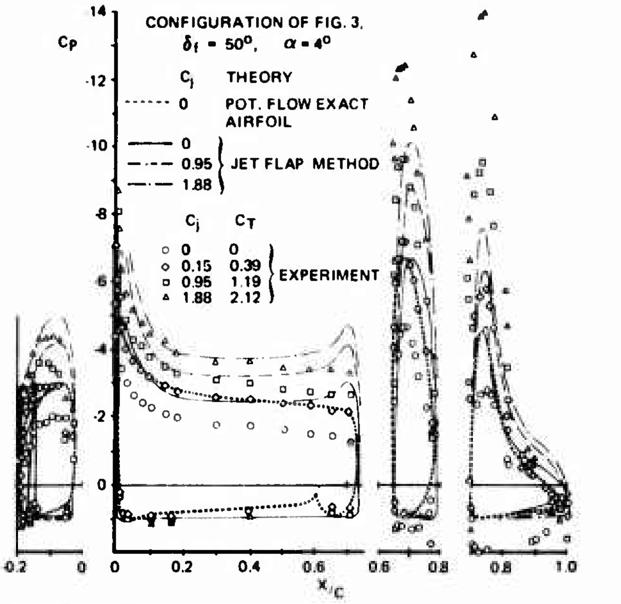

Figure 29 Comparison between computed and experimental pressure distributions for configuration of Figure 3, $\delta_f = 50°$ at various values of C_T

Another approach for obtaining reasonable pressure distributions with the thin-airfoil jet-flap method is to use an upper surface representation of the airfoil. Figure 29 shows the results of such a model in comparison with experimental data for the configuration of Figure 3 at 50° flap deflection. The total C_L values corresponding to these pressure distributions were about 10% higher than those shown in Figure 28. Figure 29 shows reasonable agreement with potential flow and experimental data except at the flaps with jet blowing where the experimental data show higher negative pressures.

The difference between the calculated and experimental C_ps may be attributed to centrifugal effects of jet air flowing through the slots and over the flap upper surfaces. Based on this assumption, it is possible to estimate approximately the percentage of total C_j due to jet flow over the flap upper surfaces. Such estimates show that at $C_j=0.95$, the share in total C_j due to jet flow over the vane upper surface is 5%, over the rear flap 29%, and under the flaps 71% of C_j. At $C_j=1.88$, the corresponding values are 6.5%, 34.5% and 65.5% of C_j.

13. CONCLUSIONS

The results of this investigation show that externally blown flap systems using a jet of circular cross-section can be tested in the tunnel as other two-dimensional airfoil systems. This may be achieved by choosing a relatively large jet diameter-to-span ratio and by using wall boundary layer control.

The aerodynamic characteristics obtained in this manner in the tunnel appear to be like two-dimensional ones. This conclusion is based on the agreement obtained between experimental data and calculations of C_L versus α for the test configurations based on two-dimensional jet-flap theory and an analogous jet-flap system.

The measured $C_{L_{max}}$ values correlate well with a theoretical relationship [Equation (2)] based on the pressure loading near the airfoil leading edge and on two-dimensional jet-flap theory. This relationship may be used to predict the two-dimensional $C_{L_{max}}$ for various C_j from known values of $C_{L_{max}}$ of the unblown, unflapped configuration and ΔC_L increments due to jet and flap deflection at zero angle of incidence.

A semi-empirical and a theoretical method have been presented in this paper for calculating the two-dimensional aerodynamic characteristics of multi-element airfoils with a jet flap. These methods can be used for externally blown flaps provided that the average jet deflection angle and jet mementum coefficient at the trailing edge are known for the forward airspeed condition. At the present, the latter can only be determined on the basis of experiment and potential flow theory as shown in this paper.

For the prediction of pressure distributions of multi-element jet flaps it is necessary to extend the thin airfoil method to include a thickness distribution.

Further testing with a semi-span model is essential for extending the 2D methods and relationships of this investigation to 3D EBF configurations.

REFERENCES

(1) Mavriplis, F. – *Aerodynamic Research on High Lift Systems*, Canadian Aeronautics and Space Journal, Vol. 17, No. 4, May 1971.

(2) Pankhurst, R.C. and Holder, D.W. – *Wing Tunnel Technique*, Sir Isaac Pitman and Sons Ltd., London.

(3) Kuhn, R. and Naeseth, R. – *Tunnel-Wall Effects Associated with VTOL-STOL Model Testing*, AGARD Report 303, March 1959.

(4) Gay, A. – *Wing-Nacelle Interaction Investigation*, General Dynamics Convair GCD-ERR-1474, December 1969.

(5) McRae, D.M. – *Aerodynamics of Mechanical High Lift Devices*, AGARD Lecture Series No. 43 on "Assessment of Lift Augmentation Devices", AGARD-LS-43-71.

(6) Perry, D.H. (Appendix by Foster, D.N.) – *A Review of Some Published Data on the External-Flow Jet-Augmented Flap*, ARC CP NO 1194, December 1970.

(7) Spence, D.A. – *The Lift on a Thin Aerofoil with a Jet-Augmented Flap*, The Aeronautical Quarterly, Volume IX, August 1958, pp. 287-299.

(8) Spence, D.A. – *Some Simple Results for Two-Dimensional Jet-Flap Aerofoils*, The Aeronautical Quarterly, Volume IX, November 1958, pp. 395-406.

(9) Williams, J., Butler, S.F.J., and Wood, M.N. – *The Aerodynamics of Jet-Flaps*, Great Britain MOA, RAE Report Aero 2646, January 1961.

(10) Leamon, R.G. and Plotkin, A. – *An Improved Solution of the Two-Dimensional Jet-Flapped Airfoil Problem*, Journal of Aircraft, Vol. 9, No. 9, September 1972.

(11) Shollenberger, C.A. – *Analysis of the Interaction of Jets and Airfoils in Two Dimensions*, Journal of Aircraft, Vol. 10, No. 5, May 1973.

(12) Küchemann, D., – *A Method for Calculating the Pressure Distribution over Jet-Flapped Wings*, RAE, Report No. Aero 2573, May 1956.

ACKNOWLEDGEMENT

The authors would like to acknowledge permission of Canadair Ltd. for publication of this work. The work was accomplished under DIR Programs A-11 and A-21 on High-Lift Systems R&D and Aerodynamic Methods which are jointly funded by the Defence Research Board of Canada and Canadair Ltd.

PRESENTATION DES RESULTATS AERODYNAMIQUES ET ACOUSTIQUES DES ESSAIS DE QUALIFICATION DU CONCEPT ALADIN II

par

Maurice COLLARD, Ingénieur
Claude DOYOTTE, Ingénieur
Max SAGNER , Ingénieur

Société BERTIN & Cie
B.P. 3
78370 - PLAISIR
France

1 - INTRODUCTION

Le concept ALADIN II est une proposition visant à réaliser des avions à décollage court, en n'utilisant que des moteurs disponibles à dilution modérée et pouvant par conséquent être réalisés dans des délais relativement brefs.

Le schéma de l'ensemble propulseur est représenté en figure 1.

Le jet d'un réacteur à dilution modérée est divisé et étalé latéralement par une tuyère dite "queue de carpe" dont on voit la géométrie en figure 5.

Ce jet alimente un éjecteur rectangulaire où il est dilué pour augmenter sa quantité de mouvement.

Cet ensemble est situé sous une aile et souffle les volets de bord de fuite.

Ce système vise l'obtention d'une atténuation importante des bruits du jet par sa division en un certain nombre de jets élémentaires et par sa dilution dans une trompe traitée acoustiquement. Nous avons pu aussi constater que la remontée du bruit due à l'impact d'un jet cylindrique sur des volets hypersustentateurs épargnait presque complètement le jet rectangulaire.

Comme moyen d'arriver aux hautes portances, ce système se présente comme une variante des systèmes d'ailes soufflées par dessous. La quantité de mouvement du jet soufflé obtenue avec un grand débit et une vitesse modérée et sa forme rectangulaire permet d'espérer a priori une efficacité importante.

Pour juger de l'intérêt du concept et concrétiser un exemple d'utilisation possible, nous avons esquissé un avant-projet d'appareil quadri-réacteur de masse totale 30 tonnes utilisant les réacteurs RR SNECMA M 45 H.

La figure 2 représente le plan 3 vues et la figure 3 une maquette de présentation de l'avant-projet. Nous noterons seulement l'aile droite épaisse comportant une importante partie rectangulaire, solutions dictées par le souci de simplicité, la facilité de conception aérodynamique et l'interaction aile - propulseur et la gamme de vitesses modérées visées par le concept (Mach 0,5).

Cette vitesse est l'optimum pour un avion destiné à transporter 60 à 100 passagers ou 6 à 8 tonnes de cargo sur des étapes courtes (500 km. maxi.).

A partir de cet avant-projet, un programme d'étude et d'essais a été réalisé. Il comportait d'abord une campagne d'essais aérodynamiques sur une maquette à l'échelle 1/12.

Ces essais aérodynamiques avaient pour but d'explorer le domaine des performances d'hypersustentation possible, de vérifier les méthodes de calculs mises en oeuvre pour établir l'avant-projet, de s'assurer de la possibilité de contrôle latéral par des méthodes aérodynamiques classiques, et d'explorer en première approximation les possibilités d'équilibrage longitudinal.

La figure 4 représente la maquette installée dans la Soufflerie de Cannes.

Le programme comportait aussi des essais de maquettes de propulseur destinés à dégrossir les problèmes du bruit et à optimiser le dessin des éléments du système propulsif.

Des essais à l'échelle approximative 1/2 utilisant l'Aérotrain haute vitesse et son moteur JT 12, destinés à l'étude du bruit au point fixe et en translation ont été effectués.

Cette communication présente rapidement les résultats aérodynamiques et acoustiques obtenus au cours de ces essais et insiste sur les points présentant un intérêt général :

- les méthodes de prévision des performances du système éjecteur - aile
- les méthodes de calcul de dimensionnement des éléments.

2 - ETUDE AERODYNAMIQUE

Le projet ALADIN a fait l'objet d'une étude aérodynamique préalable de façon à réduire les tâtonnements empiriques et limiter les essais. Les travaux décrits ci-dessous constituent un exemple des possibilités pratiques offertes par le calcul pour étudier une formule aérodynamique nouvelle sans nécessairement mettre en oeuvre des moyens très importants.

2.1. - Estimation des performances aérodynamiquesde l'aile

Le but de cette première étude est de fournir une estimation des caractéristiques de l'aile soufflée (portance, traînée) en fonction des paramètres suivants : allongement, proportion d'envergure équipée de volet, profondeur et braquage de volet, coefficient de soufflage, caractéristiques de la trompe - ce qui permet de définir le dimensionnement général de la maquette pour remplir les objectifs de performances visés. Ultérieurement et après ajustement de certains coefficients, la méthode peut être utilisée pour interpoler les résultats d'essais ou pour les étendre à d'autres configurations.

Il s'agit d'une méthode de calcul semi-empirique et simple faisant appel à des données classiques.

La portance est exprimée sous la forme d'une somme de différents termes :

- la portance de l'aile nue
- un supplément de portance due aux volets sans effet de soufflage, fonction de la profondeur du volet, de leur envergure et du braquage (réf. 1)
- un supplément de portance due à l'hypercirculation induite par le soufflage, fonction du coefficient de soufflage de l'angle du jet, les valeurs sont déduites des calculs de SPENCE (réf. 2)
- la portance due au jet en tenant compte de la poussée réelle et de l'angle effectif de déviation $\Delta Cz = \eta \varnothing C\mu \sin(\theta_{j} + L)$

La traînée est également décomposée de la façon suivante :

- la traînée de frottement et de forme Cx_o
- un supplément de traînée de forme due au volet (réf.1)
- une traînée induite relative aux seuls effets de portance liés à la circulation autour de l'aile
- la composante horizontale de la poussée du jet $Cx = - \eta \varnothing C\mu \cos(\theta_{j} + \dot{L})$
- la traînée de captation de la trompe.

On remarquera que certaines de ces estimations sont pessimistes, par exemple le supplément de portance des volets est probablement sous-estimé. D'autres, par contre, sont optimistes, par exemple l'effet d'hypercirculation est probablement surestimé par les théories linéarisées aux grands braquages.

On notera également une différence importante de ce modèle avec la théorie du jet flap en ce qui concerne la traînée, d'une part on ne considère que la composante horizontale de la poussée du jet défléchi au lieu de la poussée totale, d'autre part la traînée induite n'est relative qu'à la part de portance liée à la circulation. Cette hypothèse purement empirique est justifiée par les comparaisons avec les résultats expérimentaux ; elle donne des valeurs plus réalistes pour un fort $C\mu$ et un grand braquage.

Les résultats obtenus avec ce modèle très simple sont satisfaisants à condition d'introduire les particularités suivantes :

- le carénage inférieur de la trompe muni de son bec de bord d'attaque fortement courbé vers le bas constitue une surface portante non négligeable calée négativement par rapport à l'aile, il en résulte une valeur assez élevée de l'incidence de portance nulle ($L \sim 5°$).

- l'angle de déviation effectif du jet pour un braquage donné des volets est plus faible que pour les systèmes classiques de soufflage externe ainsi que l'ont montré les essais au point fixe.

On a représenté planche 6 les coefficients de portance et de traînée pour différents braquages des volets en fonction du $C\mu$. On constate que l'accord entre le calcul et l'essai est relativement bon dans l'ensemble.

On note que le calcul est assez pessimiste pour $C\mu > 2$ et pour les Cz aux faibles braquages. Il serait certainement possible d'obtenir un meilleur accord en ajustant les différents coefficients du modèle. On observe également la perte d'efficacité des volets pour un braquage de 70° et une incidence de 20°.

Le modèle a permis de définir le dimensionnement général de la maquette :

- Allongement : 5
- Proportion d'envergure occupée par les volets 60 %

- Profondeur relative des volets 30 % (20 % + 10 %)
- Braquage approximatif des volets :

	Premier volet	Deuxième volet
Décollage	15	30
Approche	30	60

REMARQUE - L'évaluation de la portance maximale est très difficile avant les essais. Une estimation grossière peut en être faite en fixant l'incidence de portance maximale entre 20 et 25° pour des hypersustentateurs de bord d'attaque efficaces.

2.2. - Etude en courant plan

Elle a pour objet principal de définir les formes et les positions des différents profils (profil principal, bec de bord d'attaque, carénage de trompe, profil de la tuyère motrice, volets de bord de fuite) dans la partie centrale de l'aile rectangulaire.

On a utilisé une méthode de singularité pour calculer l'écoulement en fluide parfait autour des divers profils. L'effet d'aspiration de la trompe est simulé au moyen d'un artifice (planche 7) qui consiste à prolonger le profil du carénage inférieur de la trompe par un divergent fictif de façon à obtenir au col de celle-ci le débit induit évalué par ailleurs (calcul monodimensionnel de trompe). Les répartitions de vitesses ainsi calculées ne sont significatives que sur la partie amont de l'écoulement, cette limitation est sans conséquence pour l'étude des contournements des bords d'attaque. Les formes et les positions des différents éléments ont été modifiées jusqu'à l'obtention de survitesses raisonnables et bien réparties dans les différentes zones de façon à limiter les risques de décollement. La déterminatior des lignes de courant permet également de guider le tracé des formes. Selon les problèmes étudiés on peut considérer 2, 3 ou 4 profils ; selon la précision recherchée sur la répartition de vitesse, chaque profil sera défini par un nombre de points plus ou moins élevé (de 12 à 96).

Après un examen préliminaire qui a conduit à un principe de trompe intégrée dans lequel le profil principal constitue le carénage supérieur de la trompe, l'étude a porté sur les paramètres suivants :

- position longitudinale de la trompe : une position avancée favorise l'écoulement au bord d'attaque du profil, une position reculée favorise le contournement du carénage inférieur.

- forme du carénage inférieur : il a été nécessaire de munir le bord d'attaque d'un bec basculant

- volet de bord d'attaque : la forme, la position et l'incidence du volet ont été choisies pour minimiser les survitesses. Deux volets ont été étudiés, l'un de 20 % de la corde, l'autre de 15 %. Le dernier a été retenu pour limiter les interactions avec les fuseaux moteurs, il s'est révélé suffisamment efficace.

- tuyère évolutive : bien qu'elle ne soit pas strictement bidimensionnelle, la position et l'incidence d'un profil "moyen" ont été déterminées pour minimiser les perturbations de l'alimentation de la trompe.

La planche 8 représente les répartitions de vitesse obtenues sur les différents bords d'attaque, on constate que les survitesses sur les différents profils porteurs sont relativement modérées et à peu près équilibrées. Les essais ont montré qu'effectivement il n'y a pas d'anomalies d'écoulement dans ce domaine, il n'a pas été nécessaire d'ajuster au cours des essais le calage du bec de bord d'attaque.

Etude des volets de bord de fuite

Le système de bord de fuite doit remplir deux conditions :

- dévier efficacement le flux du soufflage,
- éviter le décollement à l'extrados des volets.

En l'absence de méthode directement utilisable pour calculer l'écoulement non isentropique autour des volets (calcul d'écoulement visqueux ou de jet en fluide parfait) l'étude a été limitée à quelques essais simples de déviation d'un jet de trompe du type ALADIN par un volet plein au point fixe, en utilisant le montage conçu pour les essais acoustiques. La figure 9 représente les sondages de vitesses dans le plan de symétrie pour différentes configurations.

On constate qualitativement que l'angle de déviation du jet est inférieur à l'angle du volet, d'autant plus que l'angle du volet est grand et que sa corde est petite, c'est une des particularités de la formule de soufflage par trompe qui conduit à un jet d'épaisseur supérieure à celui du soufflage externe classique, les volets devraient être étudiés spécialement pour ce cas.

Les sondages dans un plan latéral ont montré que le jet présente un angle de diffusion initial faible (de l'ordre de 7°) qui augmente brusquement à la rencontre des volets (de l'ordre de 25°). Des mesures de pression à l'intrados du volet ont permis d'évaluer très approximativement le débit de soufflage des fentes.

Il est intéressant de noter que les défauts les plus importants de la maquette résident dans le dessin des volets de bord de fuite pour lesquels les moyens de calcul faisaient défaut.

2.3. - Etude tridimensionnelle

L'étude de la répartition de portance en envergure et des différents effets tridimensionnels a été effectuée au moyen d'un calcul de fluide parfait non linéarisé. La méthode mise au point au Centre de Calcul Analogique du Professeur MALAVARD (réf. 7) utilise une répartition de singularité à la surface de l'aile. Elle reste valable aux incidences et braquages élevés permis par le soufflage contrairement aux méthodes habituelles de surface portante linéarisées.

L'aile schématisée dans le calcul comprend une partie centrale rectangulaire munie d'un volet simple, et d'une extrémité trapézoïdale vrillée et munie d'ailerons.

La trompe, le soufflage et le bec de bord d'attaque ne sont pas représentés, on admet que l'effet du volet en fluide parfait est équivalent à celui du volet soufflé en fluide réel. L'étude a été limitée aux paramètres suivants :

- braquage des volets,
- braquage des ailerons,
- vrillage de l'extrémité.

La répartition de Cz en envergure (planche 10) met en évidence un creux de portance très important dans la zone immédiatement à l'extérieur des volets. Cette diminution de Cz correspond à une dépression à intrados près du bord de fuite induite par le tourbillon marginal issu du volet. L'examen des survitesses au bord d'attaque montre qu'il n'y a pas de risque de décrochage prématuré de la partie munie d'ailerons pour un vrillage modéré de - 5° de la corde d'extrémité, un vrillage supérieur (- 8°) a été néanmoins adopté pour améliorer l'efficacité maximale des ailerons, il en résulte une perte de 2 % de Cz total et un gain de 3 % sur la traînée induite.

L'étude tridimensionnelle fournit quelques indications relatives au contrôle latéral en cas de panne d'un moteur : l'efficacité des ailerons peut être estimée par le calcul. L'effet d'interaction avec le tourbillon marginal du volet se traduit par une amélioration de l'efficacité d'ailerons du côté de l'aileron baissé. Par ailleurs, le moment lié à la panne de moteur peut être décomposé en une composante du jet facile à estimer et un effet d'hypercirculation; pour l'estimation de ce dernier terme deux hypothèses extrêmes peuvent être proposées :

- hypothèse optimiste - le soufflage du moteur restant se répartit sur l'ensemble du volet
- hypothèse pessimiste - la totalité de l'effet de soufflage est perdue dans la zone intéressée par le moteur en panne.

Les essais ont donné des résultats intermédiaires qui pourraient être introduits dans une méthode de prévision plus perfectionnée.

3 - ESSAIS

Les essais ont été effectués à la soufflerie S_1 Ca de l'ONERA à Cannes, diamètre de la veine 3 m. La majorité des essais ont été affectés à 22 m/s, le C_μ maximum à cette vitesse est de 2,7.

Ils ont permis, d'une part de mesurer les performances aérodynamiques, d'autre part d'étudier le contrôle latéral en cas de panne d'un moteur.

La maquette est constituée d'une demi-maquette non empennée et montée à la paroi. Les moteurs alimentant les tuyères en forme de "queue de carpe" des trompes sont eux-mêmes simulés par des trompes alimentées en air comprimé ; leurs dimensions s'inscrivent dans des fuseaux de proportion voisine de ceux des moteurs réels munis de silencieux d'entrée. Le mât support a été cependant grossi pour permettre un débit d'air suffisant. Les trompes de soufflage sont réalisées de façon plus simple que les trompes réelles, leurs coefficients de poussée au point fixe est de 1,12.

Les mesures comportent la portance, la traînée, le moment de tangage et le moment de roulis de la demi-voilure. Les C_μ sont rapportés à la quantité de mouvement de la tuyère queue de carpe cornus grâce à un tarage préalable en fonction de la pression génératrice. Les visualisations aux fils de laine permettent de détecter les défauts d'écoulement.

Les paramètres variables sont les suivants :

- coefficient de soufflage C_μ avec simulation de la panne du moteur extérieur,
- le braquage θ_1 et θ_2 des volets de bord de fuite,
- le calage des becs de bord d'attaque (en fait il n'a pas été nécessaire de les modifier)
- les ailerons de 25 % de profondeur.

RESULTATS

Visualisation

Qualitativement les visualisations montrent que l'écoulement est sain dans son ensemble jusqu'à des incidences élevées d'autant plus grandes que le C_μ est grand (20° pour $C_\mu > 1$). Le décrochage se manifeste par un tourbillon au niveau de l'emplanture de l'aile. Pour le braquage le plus élevé ($\theta_1 = 40° - \theta_2 = 70°$) l'extrados du deuxième volet est mal alimenté, ce défaut provient certainement d'un mauvais dessin de la fente de soufflage, prévue pour un braquage moindre.

Essais au point fixe

La mesure du vecteur poussée en fonction du braquage fait apparaître :

- un coefficient d'augmentation de poussée de la trompe (à braquage nul) de 1,12.
- un rendement de déviation (poussée/poussée à braquage nul) qui décroît assez fortement avec le braquage selon une loi voisine de celle obtenue dans d'autres essais de soufflage externes (réf. 3 - 6)
- un angle de déviation plus faible que dans les références ci-dessus (planche 11).

Cet écart peut être attribué au fait que le jet, issu de la trompe, est beaucoup plus épais que le jet produit par l'aplatissement du jet sonique. Les essais de déviation (planche 9) ont montré en effet que le rapport de la corde du volet à la hauteur du jet est un paramètre important. Des calculs de fluide parfait le confirme (réf. 8). Il semble qu'une amélioration significative pourrait être obtenue sur l'efficacité des volets en jouant sur la profondeur, la largeur des fentes et le dessin des fentes, on peut estimer qu'un gain de 10° sur l'angle de déviation effectif donnerait un $\Delta Cz \sim 0,5$ à $C_\mu = 1$.

Essais de performances

Les courbes de portance (planche 12) indiquent une bonne linéarité jusqu'à 20° environ pour $C_\mu > 1$. Pour le braquage $\theta_1 = 15°$, $\theta_2 = 30°$ l'incidence de Cz maximum n'a pu être atteinte et est voisine de 32°, pour un braquage plus élevé, un Cz maximum de 7,3 a été mesuré à $C_\mu = 2,7$.

Les polaires (planche 13) ont des allures voisines de celles obtenues dans d'autres essais de soufflage externe. Elles mettent en évidence la bonne efficacité des becs de bord d'attaque, l'effet de la trompe qui augmente la poussée brute du jet et introduit par contre une traînée de captation, la limitation de la déviation aux grands braquages.

Equilibre transversal en cas de panne

Le problème consiste à équilibrer la portance des deux côtés, la panne du moteur extérieur étant a priori la plus critique.

Les moyens de contrôle expérimentés sont les suivants :

- braquage différentiel des ailerons ± 25°
- braquage d'un spoiler
  braquage différentiel du deuxième volet de bord de fuite.

Les essais montrent que l'arrêt du moteur externe se traduit par une perte de portance légèrement supérieure à la diminution liée à la seule réduction du C_μ (les deux moteurs en service) mais cependant inférieure à la moitié de l'effet de soufflage total. Le moteur restant souffle donc probablement en partie la zone de volet correspondant au moteur en panne. Ceci est confirmé par la position du point d'application de cette force. Le braquage des ailerons ± 25° donne une efficacité (ΔCz ± 0,3) sensiblement égale à celle trouvée par le calcul tridimensionnel de fluide parfait pour un braquage moindre (20°).

L'effet d'interaction de l'aileron avec le tourbillon marginal du volet semble se retrouver, en effet la portance de l'aileron baissé est supérieure à celle de l'aileron levé, par contre, le point d'application est plus proche du volet ce qui indique que le gain de portance se situe dans une zone proche du volet.

Le braquage du spoiler a une influence très modeste (ΔCz - 0,15) quelle que soit la configuration.

Par contre le braquage différentiel du deuxième volet est très efficace.

Au total l'utilisation des ailerons seuls permet d'équilibrer la panne d'un moteur externe pour C_μ voisin de 1. L'adjonction d'un braquage différentiel de ± 10° du deuxième volet assure une marge d'au moins 30 % sur l'ensemble des configurations du projet (planche 14).

En cas de panne, les polaires équilibrées en latéral sont sensiblement les mêmes que celles sans panne à même C_μ total. Il reste à ajouter l'effet de l'équilibrage en tangage et en lacet. En ce qui concerne le tangage, les mesures de Cm et de la déflexion au niveau de l'empennage ont montré qu'une surface d'empennage horizontal de 40 % permet d'assurer une marge de centrage confortable.

CONCLUSIONS SUR L'ETUDE AERODYNAMIQUE

La définition de la maquette résultant de l'étude préalable s'est révélée presque entièrement satisfaisante ce qui permet de limiter les essais. La principale correction apportée a consisté à augmenter le braquage des volets pour compenser leur manque d'efficacité de déviation. Les performances seraient certainement améliorées par un meilleur dessin des volets ; leur étude serait facilitée par une méthode de calcul qu'il semble possible de mettre au point rapidement. Les performances peuvent être prévues avec une précision acceptable au stade de l'avant-projet et peut-être même l'efficacité du contrôle latéral en cas de panne pourrait être également estimée.

La prédiction précise de la portance maximale est certainement plus difficile et exige des calculs de couche limite et de décollement délicats. On remarquera que les valeurs obtenues en soufflerie à un bas nombre de Reynolds ($0,5\ 10^6$) sont probablement pessimistes.

4 - MISE AU POINT ACOUSTIQUE ET PROPULSIVE DU SYSTEME D'EJECTION

Le groupe moto-propulseur composé du moteur M 45 H, des traitements acoustiques, des parties tournantes et du système d'éjection (queue de carpe et trompe) constitue un tout dont l'optimisation conditionne les performances globales de l'avion.

Le traitement acoustique des parties tournantes se compose d'une tranche d'entrée d'air traitée permettant une réduction de 12 PNdB du bruit rayonné vers l'amont et d'un traitement du canal du flux secondaire jusqu'au raccordement avec le flux chaud donnant une atténuation vers le bruit rayonné vers l'aval de 20 PNdB.

Pour réduire les niveaux de bruit dus à l'éjection du moteur, la solution étudiée consiste d'abord à mélanger les deux flux pour abaisser la température et la vitesse d'éjection des gaz, le jet est ensuite divisé au moyen de la tuyère en forme de queue de carpe, la trompe réalisant en dernière étape une dilution importante. La trompe est traitée acoustiquement afin de réduire le bruit provenant du mélange des flux moteur et induit.

La mise au point acoustique est propulsive du dispositif d'éjection a été menée parallèlement aux études et essais aérodynamiques de l'avion sur des petites maquettes (échelle 1/10) et en dernière étape sur des moteurs de la gamme des 1200 daN de poussée au décollage.

Ces travaux concernant essentiellement des configurations de point fixe, des essais prévus prochainement en translation sur Aérotrain avec moteur GE J85 permettront de confirmer sur un ensemble de synthèse les performances acoustiques et propulsives du dispositif jusqu'à un Mach voisin de 0,25.

4.1. - Etapes successives des travaux de mise au point - maquettes

Sur le plan propulsif, la mise au point du dispositif a permis de minimiser les pertes internes de la tuyère aux formes relativement complexes tout en conservant ses performances acoustiques. On a par ailleurs étudié l'influence des paramètres géométriques des trompes utilisées aux différents stades du perfectionnement de la tuyère et de la modification de ses formes externes.

Les moyens d'essai dont nous disposons conditionnent les dimensions générales de nos tuyères. L'échelle adoptée était voisine de 1/10. Les performances propulsives ont été mesurées sur notre banc de poussée du Quai de la Gare à Paris et dans les installations du Centre d'Essai des Propulseurs à Saclay, les mêmes maquettes ont servi également au contrôle des performances acoustiques en gaz chaud au CEPr et en gaz froid dans nos installations.

Ce programme d'évaluation sur petites maquettes a été mené sur trois tuyères chaudronnées du type de celle présentée figure 16, correspondant aux différents stades de la mise au point.

Une maquette d'un quart de tuyère en plastique moulé nous a permis par visualisation sur un banc hydraulique, d'améliorer les formes internes et de répartir les aubages nécessaires à une bonne distribution de l'écculement dans toute la zone d'éjection.

Du fait des incertitudes concernant les transpositions des résultats acoustiques à l'échelle du M 45 H un programme complémentaire a été lancé ayant pour but d'étudier le dispositif d'éjection sur un moteur réel (JT 12 A6 de Pratt et Whitney) dont l'échelle est moitié par rapport au M 45 H. La maquette de la tuyère (figure 5) réalisée pour ce moteur plus chaud que le M 45 H nous a permis également d'aborder le problème technologique lié à la réalisation d'un tel ensemble et de trouver des solutions satisfaisantes.

Concernant les trompes, l'étude paramétrique (acoustique et propulsive) a porté essentiellement sur l'influence du σ_c de la présence ou non d'un diffuseur et du traitement acoustique.

4.2. - Résultats des essais

4.2.1. - Performances propulsives

Par rapport à la première tuyère utilisée pour dégrossir les performances du dispositif, un gain de 4 % sur le coefficient de poussée a été obtenu au cours des essais successifs de mise au point. Cette amélioration a été réalisée en optimisant les formes internes de façon à supprimer les décollements, en réduisant la surface des aubages internes pour limiter les pertes par frottement et en ajustant les lois de section de façon à réduire les vitesses dans les zones les plus critiques.

Les courbes (planche 15) du coefficient de poussée montrent que pour la tuyère seule, les pertes diminuent lorsque le rapport de détente du jet augmente; en fait les pertes demeurent sensiblement les mêmes mais l'induction qui s'établit au niveau des injecteurs les compensent d'autant plus que la vitesse d'éjection augmente. Globalement, dans les conditions du M 45 H pour un rapport de détente du jet mélangé voisin de 1,56, les pertes de l'injecteur par rapport à une tuyère convergente de référence seront de l'ordre de 3 à 4 %.

Les essais avec trompe ont permis de chiffrer l'influence des paramètres géométriques σ_c, σ_d en particulier sur les performances propulsives et pour les configurations avec traitement acoustique, d'estimer les pertes de poussée correspondantes. Nous avons résumé ces principaux résultats dans le tableau ci-dessous, les gains de la trompe étant exprimés en pourcentage par rapport à la tuyère de référence.

Gain de poussée au point fixe de la trompe par rapport à la tuyère de référence $\frac{P_j}{P_a} = 1,6$

	σ_c	$\sigma_d = 1$	$\sigma_d = 1,17$
Trompe lisse	4	14,5 %	20 %
	4,5	16,5 %	22 %
	5	20,5 %	25 %
Trompe traitée	4	12,5 %	17,5 %
	4,5	14 %	19 %
	5	18 % %	21 %

L'effet de diffuseur est assez conséquent au point fixe, toutéfois en vitesse son influence devenant moins bénéfique, une optimisation sera nécessaire. L'estimation des pertes de poussée dues au traitement acoustique pour le projet est fonction de la valeur du coefficient de frottement à la paroi que l'on adopte. Les essais sur maquette comparés à nos calculs de prévision nous ont permis d'évaluer ce coefficient de frottement. La valeur adoptée correspond à environ 2,5 fois celle du coefficient de frottement sur la plaque plane lisse, valeur qui par ailleurs semble se recouper avec des mesures de frottement en tunnel hydrodynamique sur tôle perforée.

Du point de vue de l'interprétation de ces résultats, en tenant compte de l'effet d'échelle et en particulier des culots dont on ne peut s'affranchir pour la réalisation des tuyères, nous estimons que le gain au point fixe du dispositif au régime de décollage est d'au moins 15 %.

4.2.2. - Performances acoustiques

La mise au point acoustique du dispositif est intimement liée aux performances propulsives. La division du jet implique une augmentation importante du périmètre de tuyère donc des surfaces de frottement. D'une manière générale le meilleur compromis est atteint lorsque l'atténuation complémentaire due à une modification par rapport à la solution optimisée est équivalente à ce que l'on aurait eu si on avait opéré une réduction de la poussée égale à celle créée par le complément de pertes.

Les étapes successives de l'optimisation tant acoustique que propulsive nous ont permis d'obtenir au stade actuel sur maquette une atténuation du bruit de jet latéralement à 150 m au groupe moto-propulseur de 13 PNdB. En survol la forme bidimensionnelle du jet de soufflage est favorable à une diminution du bruit d'interaction avec les volets par rapport à un jet cylindrique ayant même rapport de pression. Sur maquette l'atténuation correspondante obtenue a atteint 10 PNdB. Les diagrammes de directivité présentés sur la planche 5 donnent une estimation de la forme des champs sonores linéaires transposés à partir des essais sur maquette au point fixe.

Les essais effectués sur le moteur JT 12 A6 (dispositif seul sans voilure) ont confirmé les résultats obtenus sur maquette.

CONCLUSION ET POURSUITE DES MISES AU POINT DU DISPOSITIF D'EJECTION

Les essais sur maquette nous ont montré que ce type de groupe moto-propulseur présentait l'intérêt de disposer au décollage d'un apport de poussée par rapport au moteur de référence de l'ordre de 15 % tout en limitant les nuisances acoustiques à des niveaux acceptables.

La poursuite de ces travaux dans le sens de l'optimisation aux différentes phases de vol devra nous permettre de présenter un projet de GMP aux performances très homogènes. Du point de vue acoustique, l'effort doit se centrer sur l'efficacité du traitement de trompe et sur l'influence de la vitesse de vol sur les performances effectives du dispositif, nos prochains essais en translation nous fourniront un enseignement précieux à ce sujet.

CONCLUSIONS GENERALES

Les essais résumés ci-dessus ont permis d'affronter la faisabilité du concept "ALADIN II" comme propulseur silencieux. L'application à un projet d'avion STOL est possible au prix d'un taux de motorisation limité à 0,4 et le contrôle transversal et longitudinal de l'appareil aux basses vitesses apparait possible au moyen de gouvernes classiques.

NOTATIONS

C_μ	coefficient de soufflage apporté à la quantité de mouvement de la tuyère motrice
Cx	coefficient de traînée
Cz	coefficient de portance
Cm	coefficient de moment de tangage
C_I	coefficient de moment de roulis de la demi-voilure
η	rendement de déviation $\dfrac{\text{Poussée déviée}}{\text{Poussée sans déviation}}$
Ø	coefficient d'augmentation de poussée de la trompe $= \dfrac{\text{Poussée brute trompe}}{\text{Poussée tuyère}}$
θ_1	angle de braquage du 1er volet
θ_2	angle de braquage du 2ème volet
θ_j	angle du jet
i	angle d'incidence
σ_C	$= \dfrac{\text{section du mélangeur de la trompe}}{\text{section efficace de la tuyère}}$
σ_D	$= \dfrac{\text{section de sortie du divergent de la trompe}}{\text{section du mélangeur}}$
C''_T	coefficient de poussée rapporté à la poussée isentropique du flux moteur.

REFERENCES

1 - A.D. YOUND
The aerodynamic characteritics of flap
ARC. n° 2622

2 - E.C. MASKELL et SPENCE
A theory of the jet flap on three dimensions
Proc. Roy. So. vol. 251 1959

3 - NASA TN. D 4928

4 - NASA TN. D 5364

5 - NASA TN. D 943

6 - P. KUELL - D. WELTE
Basic investigation on an unswept rectangular wing with an externally blown flap

7 - T.S. LUU - G. COULMY - J. SAGNARD
Calcul non linéaire de l'écoulement à potentiel autour d'une aile d'envergure finie de forme arbitraire.
Association Technique Maritime et Aéronautique - Session 1971

8 - R.Y. CHANG et J.F. CONLY
Potential flow of segmental jet deflectors
J. Fl. Mech. vol. 46 - p. 3

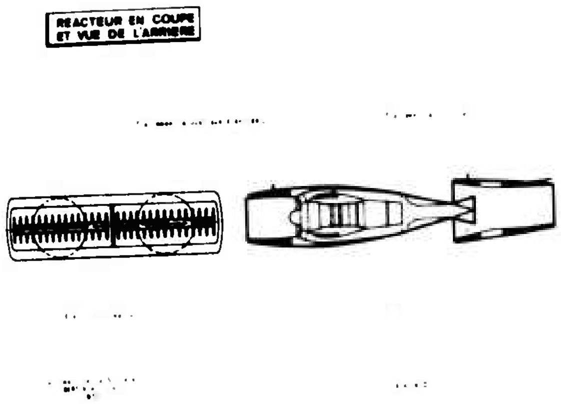
REACTEUR EN COUPE
ET VUE DE L'ARRIERE

Figure 1

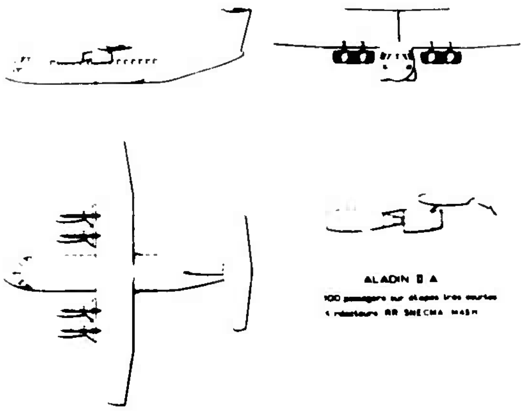
ALADIN II A
100 passagers sur étapes très courtes
4 réacteurs RR SNECMA M45H

Figure 2

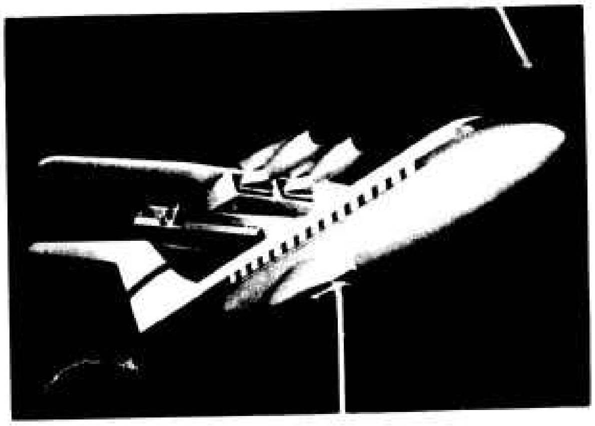

Figure 3

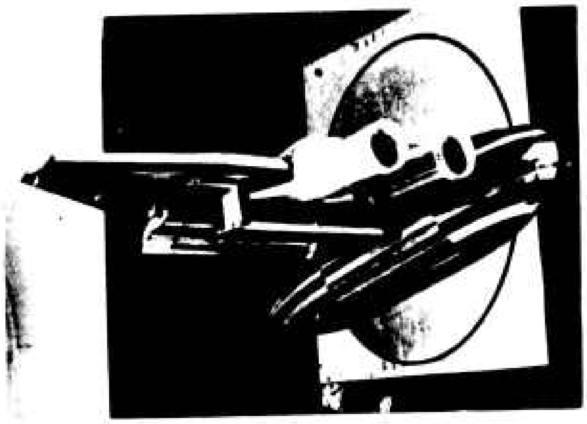

Figure 4

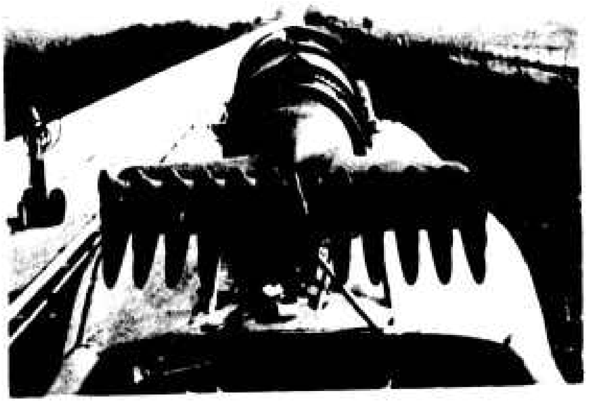

Figure 5

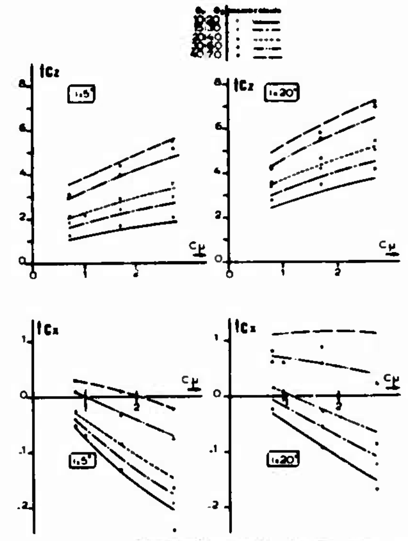

- COMPARAISON CALCULS ESSAIS - Planche 6

Planche 6

- CALCUL BIDIMENSIONNEL DE FLUIDE PARFAIT - Planche 7

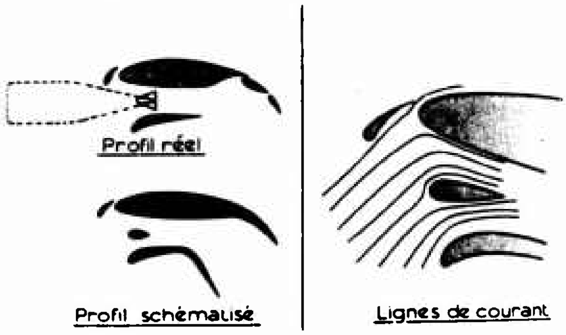
Profil réel
Profil schématisé
Lignes de courant

Planche 7

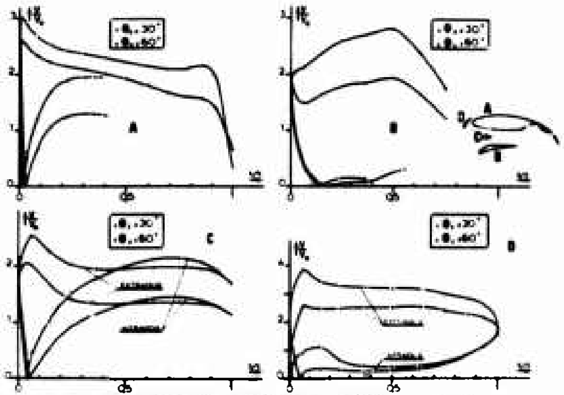

- REPARTITION DES VITESSES SUR LES PROFILS - Planche 8

Planche 8

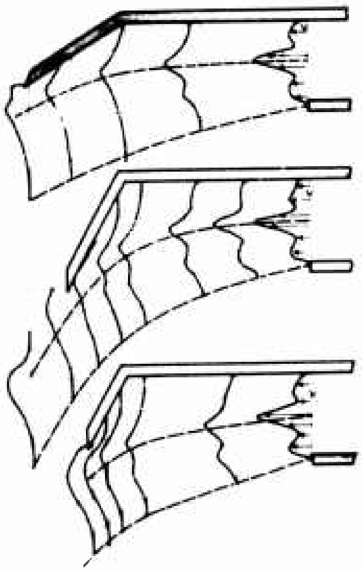

ESSAI DE DEFLEXION DU JET V∞=0 - Planche 9

Planche 9

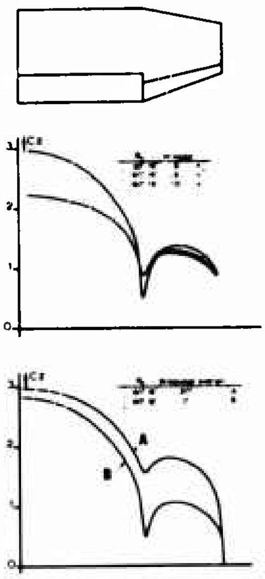

- CALCUL TRIDIMENSIONNEL - Planche 10

Planche 10

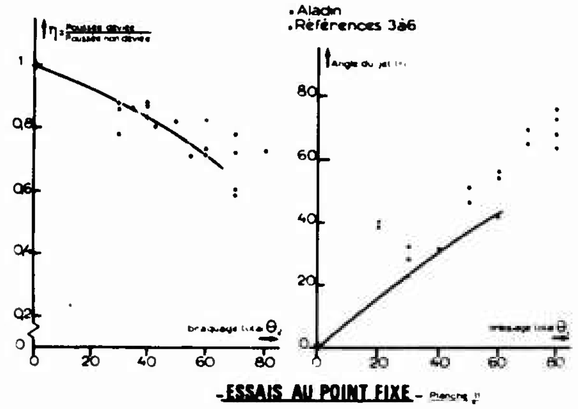

Planche 11

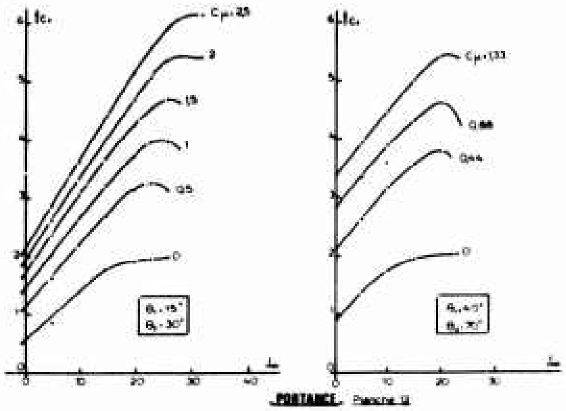

Planche 12

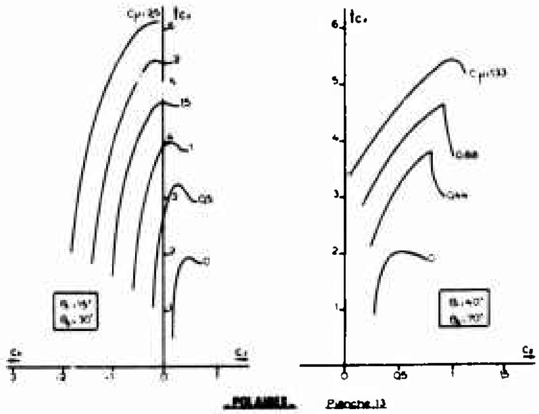

Planche 13

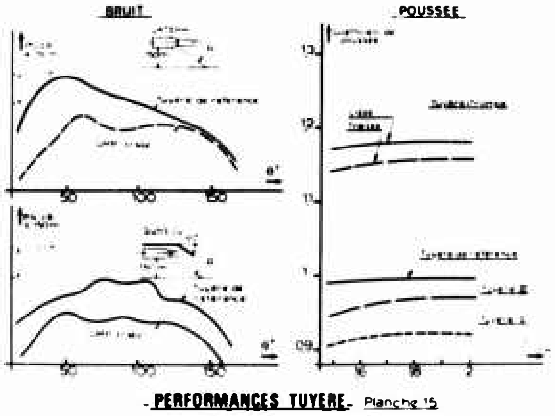

Planche 15

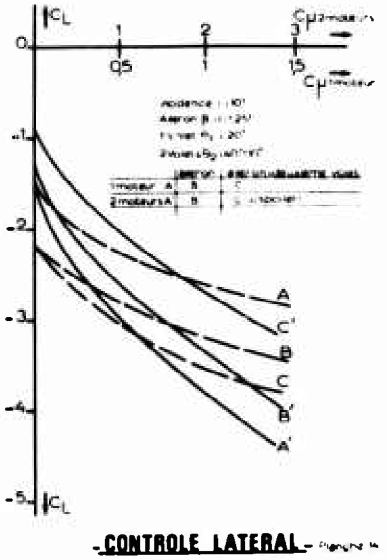

Planche 14

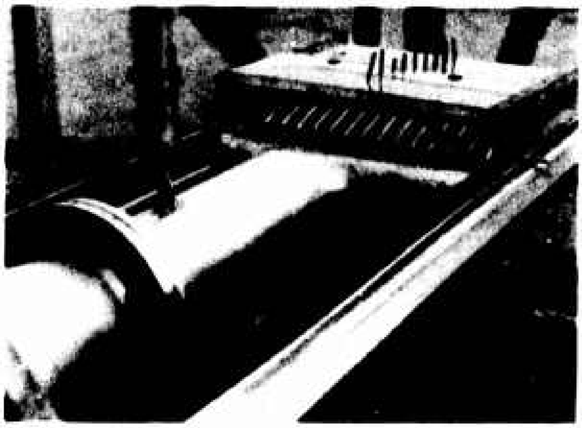

Figure 16

ETUDE THEORIQUE ET EXPERIMENTALE DU SOUFFLAGE DE COUCHE LIMITE A LA CHARNIERE D'UN VOLET HYPERSUSTENTATEUR

par Bernard MONNERIE et Guy LOVAT
Office National d'Etudes et de Recherches Aérospatiales (ONERA)
92320 CHATILLON (France)

RESUME

Dans le but d'approfondir les connaissances sur l'hypersustentation par soufflage de la couche limite, un montage à grande échelle permettant l'étude détaillée des couches limites bidimensionnelles soufflées a été mis au point pour une soufflerie basse vitesse de trois mètres de diamètre.

Les étapes marquantes de la mise au point et en particulier les mesures qu'il a fallu prendre pour obtenir un écoulement suffisamment bidimensionnel sont exposées.

Les résultats de l'exploration de la zone de mélange entre jet et couche limite sont présentés et confrontés aux résultats de calculs effectués en utilisant un modèle de turbulence reposant sur l'emploi de l'équation de Nee-Kovasznay pour le coefficient de viscosité.

THEORETICAL AND EXPERIMENTAL STUDY OF BOUNDARY LAYER CONTROL BY BLOWING AT THE KNEE OF A FLAP

SUMMARY

To increase the knowing on lift augmentation by boundary layer blowing, a large scale mounting for detailed study of two-dimensional boundary layers has been set up in a low speed, three meters in diameter, wind tunnel.

The important phases to work it and particularly the means required to get a two-dimensional flow are explained.

The experimental results obtained by probing the jet - boundary layer mixing zone are presented and compared with computed results using a turbulence model based on the Nee-Kovasznay equation for the viscosity coefficient.

NOTATIONS

A	constante de production de viscosité effective.
b	envergure de la tranche centrale de la maquette.
B	constante de dissipation de viscosité effective.
C_μ	coefficient de débit de quantité de mouvement : $q_m V_j / q_0 \, b . \ell$
e	largeur de fente.
K	constante de von Karman.
K_p	coefficient de pression statique $(p - p_0)/q_0$
K_{p_a}	coefficient de pression d'arrêt $(p_a - p_0)/q_0$
ℓ	corde du profil.
L_d	longueur de dissipation.
p	pression statique locale.
p_a	pression d'arrêt locale.
p_{iAV}	pression d'alimentation de la fente située à l'avant des panneaux.
p_{iAR}	pression d'alimentation de la fente située à l'arrière des panneaux.
p_{ic}	pression d'alimentation de la partie centrale du canal de soufflage.
p_{im}	pression d'alimentation des parties marginales du canal de soufflage.
p_0	pression statique de veine.
q	pression cinétique locale $\frac{1}{2} \rho u^2$
q_m	débit masse de soufflage.
q_0	pression cinétique à l'infini amont $\frac{1}{2} \rho V_0^2$
R	rayon de courbure du volet.
s	abscisse curviligne comptée à partir de la fente.
u	composante moyenne de la vitesse dans la direction principale de l'écoulement.
u'	composante fluctuante de la vitesse dans la direction principale de l'écoulement.
u_τ	vitesse de frottement $= \sqrt{\tau_0/\rho}$
v	composante moyenne de la vitesse sur l'axe perpendiculaire à la maquette.
v'	composante fluctuante de la vitesse sur l'axe perpendiculaire à la maquette.
V_0	vitesse à l'infini amont.
V_j	vitesse conventionnelle du jet en sortie de fente.
x	coordonnée dans la direction principale de l'écoulement.
y	coordonnée suivant l'envergure de la maquette.
X	coordonnée dans la direction principale de l'écoulement.
Y	coordonnée perpendiculaire à la paroi de la maquette.
Z	coordonnée perpendiculaire à la paroi de la maquette.
δ	angle de braquage du volet.
$\Delta p_{ic} = p_{ic} - p_0 \qquad \Delta p_{im} = p_{im} - p_0$	
Φ	fonction pouvant représenter u ou ν_e
ψ	fonction de courant locale.
ψ_i	fonction de courant à la frontière intérieure de l'écoulement.
ψ_e	fonction de courant à la frontière extérieure de l'écoulement.
ν	coefficient de viscosité cinématique.
ν_T	coefficient de Boussinesq de viscosité $\tau / \rho \frac{\partial u}{\partial y}$ turbulente
ν_e	coefficient de viscosité turbulente effective $= \nu + \nu_T$
ρ	masse volumique de l'air.
τ	frottement turbulent. $= - \rho \overline{u'v'}$
ω	fonction de courant réduite.

1 - INTRODUCTION -

L'intérêt du contrôle de couche limite par soufflage pour augmenter les coefficients maxima de portance des ailes est bien connu.

Pour se remémorer le bénéfice qui peut en être tiré on pourra se reporter par exemple à la figure 1.

La réduction des distances d'atterrissage et de décollage qui en résulte peut être sensible, ce qui a fait adopter le procédé sur quelques avions, en particulier sur les avions de l'Aéronavale qui ne disposent que d'un espace très restreint pour atterrir et décoller [F8, F4, BUCCANEER par exemple]. Evidemment l'utilisation de ce procédé entraîne l'installation dans l'avion d'un canal de soufflage et de tuyauteries pour y amener l'air comprimé et cela se traduit par une augmentation du coût et de la masse de l'avion.

Pour savoir si cette pénalisation est rentable et s'il faut adopter cette méthode d'hypersustentation plutôt qu'une autre il faut d'abord bien connaître les phénomènes physiques sur lesquels elle repose et batir un modèle mathématique permettant de les décrire avec précision.

Alors seulement on peut envisager d'optimiser le procédé (c'est-à-dire de déterminer où, comment et combien il faut souffler) et d'évaluer ce qu'il coûte.

Si l'on dispose à l'heure actuelle de nombreux résultats globaux sur l'utilisation du soufflage de couche limite sur volet [1], les analyses expérimentales détaillées sont peu nombreuses ou effectuées dans des cas encore assez éloignés du cas réel des applications.

Encouragé et soutenu financièrement par les services officiels français (Service Technique de l'Aéronautique de la Délégation Ministérielle à l'Armement) l'ONERA a lancé la mise au point d'un dispositif expérimental permettant l'analyse détaillée des couches limites soufflées sur volet hypersustentateur dans des conditions de nombre de Reynolds aussi réalistes que possible, l'objectif étant triple :

- améliorer la compréhension des phénomènes,
- obtenir des informations précises sur l'effet des divers paramètres vitesse de jet, rayon de courbure du volet, nombre de Reynolds,
- fournir des résultats expérimentaux de référence pour la mise au point des méthodes de calculs.

L'objet de cette communication est de présenter le montage, les étapes de sa mise au point et les premiers résultats obtenus.

2 - CHOIX DE LA MAQUETTE -

Compte tenu des objectifs que nous nous étions fixés : possibilité d'études détaillées, obtention de grands nombres de Reynolds, comparaison des résultats expérimentaux à des résultats de calculs, il était tout indiqué d'effectuer une étude en courant plan. En effet, l'utilisation d'une maquette tridimensionnelle, même d'allongement relativement faible, nous aurait conduits à des longueurs de corde petites (inférieures à 50 cm dans une soufflerie de trois mètres), et par ailleurs, les méthodes disponibles actuellement pour le calcul du mélange turbulent ne concernent que des écoulements bidimensionnels.

Il a donc été décidé de mener une étude en bidimensionnel dans la soufflerie S1 de l'établissement ONERA de Cannes*, soufflerie de type Eiffel à veine circulaire de 3 m de diamètre où sont habituellement effectuées les études de profils aux basses vitesses ($V_o < 40$ m/s) pour l'ONERA.

Pour ce genre d'essai, deux panneaux verticaux distants de 1 m sont placés dans la soufflerie et la longueur de la corde des profils qui sont essayés, est généralement de 0,750 m.

Pour l'étude dont il est question, il fallait reconstituer une couche limite au niveau du volet qui soit très épaisse de façon à être dans des conditions aussi réalistes que possible par rapport au cas du vol et pour pouvoir mener sans risque de perturbation importante toutes les investigations expérimentales nécessaires, en particulier, l'exploration de la couche visqueuse au moyen de sondes à fil chaud en x dont on sait qu'elles ne peuvent être très petites ($\emptyset \simeq 3$ mm).

Il a donc été décidé d'utiliser une maquette très longue constituée pour l'essentiel par un plancher de 1,6 m de long équipé d'une partie avant de 0,5 m, cambrée, et ayant un grand rayon de courbure au bord d'attaque pour éviter le décollement prématuré de l'écoulement dans cette région [figure 2]. A l'extrémité du plancher, peuvent être montés divers volets fixes, caractérisés par leur braquage et le rayon de la portion de cylindre circulaire qui raccorde au plancher leur partie plane braquée.

La fente de soufflage, d'épaisseur variable, est située à l'extrémité aval du plancher, c'est-à-dire à l'amont du volet.

---

* L'étude du montage, la surveillance de sa réalisation, ainsi que la conduite des essais ont été assurées par Monsieur A. BEVERT, Chef de l'établissement de Cannes.

3 - MISE AU POINT DU MONTAGE -

3.1 - Généralités -

La maquette qui vient d'être sommairement décrite est susceptible de donner pleine satisfaction à tous les objectifs que l'on s'est fixés pour l'étude dans la mesure où l'on est capable de réaliser effectivement un écoulement bidimensionnel autour de celle-ci et ceci, on s'en doute, demande quelques précautions compte tenu de sa grande taille et de son faible allongement.

3.2 - Moyens de contrôle de la bidimensionnalité -

L'uniformité transversale a été contrôlée au moyen des techniques suivantes dont certaines se sont révélées extrêmement sensibles :

- utilisation de brins de laine : ce procédé met bien en évidence l'apparition des décollements mais ne peut fournir d'indication très précise sur l'uniformité transversale de la couche visqueuse,
- utilisation de plusieurs prises de pression statique réparties en envergure à une même abscisse.

  La figure 3 donne un exemple typique d'équipement de volet en prises de pression dans ce but.

  L'expérience a montré que ce test était relativement peu sensible et que, sauf pour des configurations très dissymétriques avec décollement localisé au voisinage d'un seul panneau, la répartition des pressions statiques en envergure reste assez uniforme même si la couche visqueuse est assez sensiblement non bidimensionnelle.
- utilisation des prises de pression précédentes en prises de Stanton pour juger de l'évolution en envergure du coefficient de frottement à la paroi,
- utilisation d'une rangée de prises de pression d'arrêt sur une ligne parallèle au bord de fuite à une altitude de 15 mm. Ce test permet réellement d'avoir une idée précise de la bidimensionnalité de la couche visqueuse et c'est celui qui a été le plus utile dans toute la phase de mise au point,
- enfin, comme test ultime, des sondages de pression d'arrêt ont été effectués en plusieurs positions en envergure au voisinage du bord de fuite au moyen d'un peigne de pression d'arrêt,
- aux techniques utilisées dans les conditions normales de fonctionnement du montage, il faut ajouter le contrôle de l'épaisseur de fente au moyen de jauges d'épaisseurs calibrées et un dispositif pour l'exploration hors veine de l'écoulement en sortie de fente.

Avant d'obtenir les résultats satisfaisants auxquels nous sommes arrivés en ce qui concerne la qualité de la bidimensionnalité, toute une mise au point a été nécessaire dont les diverses étapes vont être rapidement évoquées.

3.3 - Problèmes liés à la présence des panneaux -

Bien évidemment si aucune précaution n'est prise, un décollement s'installe au voisinage des panneaux latéraux, soit des deux côtés, soit, plus fréquemment, d'un seul côté et l'écoulement dans ce cas est extrêmement tridimensionnel.

La première idée a été de contrôler la couche limite des panneaux latéraux (voir, figure 4, les mesures adoptées à Cannes) ; en fait, sauf pour des volets faiblement braqués, cette mesure est insuffisante et il faut simultanément augmenter la quantité de mouvement injectée à la charnière du volet au voisinage des panneaux.

Ceci peut être effectué de deux façons, en augmentant soit la largeur de la fente au voisinage immédiat des panneaux, soit, dans le cas où le canal de soufflage est fractionné en plusieurs chambres le long de l'envergure, en augmentant la pression génératrice dans les chambres situées au voisinage des panneaux.

Les avantages de la première solution sont de permettre une évolution de l'accroissement du soufflage fonction de la proximité du panneau et d'être facilement mise en oeuvre : avec notre maquette, il suffisait de retirer un peu de la matière du volet au droit de la fente, près des panneaux ; cependant, la manoeuvre inverse est nettement plus compliquée et, de plus, on ne peut effectuer de réglage en marche.

La seconde solution nécessite un canal de soufflage spécialement conçu pour alimenter indépendamment les parties marginales de la fente et elle conduit, sauf dispositions particulières, à un accroissement de la quantité de mouvement soufflée constant en envergure sur la largeur des parties marginales ce qui constitue deux inconvénients ; en revanche, elle permet un réglage en marche ce qui est très pratique.

Compte tenu de ce bilan, nous avons finalement utilisé simultanément les deux méthodes et les figures 5 et 6 donnent la configuration des chanfreins qui a été adoptée et le schéma du canal de soufflage et de ses canalisations d'alimentation.

3.4 - Problèmes liés à la fente de soufflage -

Un autre problème à résoudre est celui de l'uniformité en envergure de l'épaisseur de fente et de la pression d'alimentation. La constance de l'épaisseur de fente en envergure ne peut être assurée qu'en utilisant des entretoises pour empêcher la lèvre de fente de se déformer.

Des irrégularités dans la répartition en envergure de la pression d'arrêt et de la turbulence du jet en sortie de fente apparaissent alors, provoquées par les sillages des entretoises.

Pour y remédier, il a été nécessaire de placer un tamis un peu en aval des entretoises et juste avant la sortie de fente (figure 7).

4 - PRESENTATION DU MONTAGE, DE L'EQUIPEMENT DE MESURES ET DE LA TECHNIQUE EXPERIMENTALE -

Compte tenu des étapes successives de la mise au point, la maquette et la technique expérimentale ont subi une évolution et c'est uniquement la phase finale qui est ici présentée.

4.1 - La maquette -

La forme générale de la maquette est celle décrite au chapitre 2.

Jusqu'à présent quatre configurations de volet ont été essayées (voir figure 8) :

- **une configuration non braquée qui fournit un cas de référence simple et donc particulièrement intéressant pour tester la validité des modèles de turbulence,**
- **deux configurations de volets de 20 % environ de profondeur relative, braqués à 40° avec des rayons de courbure de 120 et 240 mm (∿ 4,5 et 9 % de la corde) et déterminés de façon à ce que leurs efficacités soient sensiblement les mêmes,**
- **une configuration de volet braqué à 65° avec un rayon de courbure de 120 mm.**

La maquette est montée entre panneaux au centre de la veine, à incidence nulle.

Compte tenu des efforts importants qui sont susceptibles de s'exercer sur elle, elle ne peut être montée sur les balances de la soufflerie ; elle est tenue par trois mâts inertes venant du plafond de la soufflerie et, pour que ceux-ci soient chargés en traction, la maquette est retournée, l'extrados étant donc en bas et l'intrados en haut (figure 9).

4.2 - Les panneaux -

Les panneaux sont équipés de deux fentes de soufflage dont les pressions d'alimentation peuvent être établies à des niveaux différents (la figure 4 en présente les principales caractéristiques).

Le réglage est effectué soufflerie en marche, en présence de la maquette équipée de la configuration à étudier et alimentée à un $C\mu$ supérieur au $C\mu$ de recollement : Un peigne fournissant en lecture directe sur un multimanomètre à alcool le profil des pressions d'arrêt de la couche limite sur le panneau au droit de la fente de soufflage du volet, les diverses pressions de chambre sont ajustées de façon à obtenir le profil le plus plat possible.

Des exemples sont présentés sur la figure 10.

Pour des essais à une autre vitesse, on conserve sensiblement constant le coefficient de quantité de mouvement correspondant c'est-à-dire qu'en pratique on fait évoluer la surpression $(P_i - P_o)$ comme le carré de la vitesse d'essai.

4.3 - Le canal de soufflage -

Le canal de soufflage est conçu de façon à ce que les parties marginales de la fente, sur 150 mm d'envergure au voisinage des panneaux puissent être alimentées si nécessaire à une pression différente de celle qui est utilisée pour la partie centrale.

Le débit masse alimentant la partie centrale de 700 mm d'envergure est mesuré par un débitmètre AFNOR à diaphragme, ce qui permet de déterminer le coefficient de quantité de mouvement conventionnel de l'essai :

$$C\mu = \frac{q_m \; V_j}{q_o \; \ell \; b}$$ avec :

q_m	débit masse mesuré,
q_o	pression cinétique de l'écoulement extérieur,
ℓ	longueur du plancher 2,1 m
b	envergure de la partie centrale 0,7 m
V_j	déterminé par détente isentropique entre la pression de chambre et la pression statique de veine.

L'écoulement en sortie de fente doit être le plus uniforme possible c'est pourquoi le dispositif d'alimentation comporte :

- une chambre d'alimentation et une chambre de distribution en amont de la chambre de tranquillisation qui conduit à la fente (figure 11]
- deux tamis, l'un de 41 % de perméabilité géométrique dans la chambre d'alimentation et l'autre de 29 % à l'aval des entretoises.

Les volets sont fixés sur la base du canal de soufflage par l'intermédiaire d'un talon d'assemblage.

Des cales insérées entre la base du canal et le talon permettent de faire varier l'épaisseur de fente.

4.4 - Détermination de la vitesse d'essai -

Etant donné la faible longueur de la veine d'essai par rapport à la longueur de la maquette, la vitesse d'essai doit être déterminée par intégration des indications d'une série de sondes de pression statique placées en amont de la maquette un peu en aval du bord d'attaque des panneaux.

4.5 - Equipement de mesure -

Outre l'équipement déjà signalé pour le contrôle de la bidimensionnalité (voir § 3), la maquette est équipée à l'extrados d'une rangée de prises de pression statique permettant de reconstituer toute l'histoire de la couche limite depuis sa naissance au bord d'attaque jusqu'au bord de fuite.

Pour effectuer les sondages de la couche visqueuse, on utilise un explorateur dissimulé dans un carénage d'intrados qui porte soit une bisonde pour la mesure de la pression d'arrêt et de la pression statique (figure 12) soit une sonde à fils chauds croisés pour la détermination du frottement turbulent τ. On vérifie sur les répartitions de pression statique longitudinale que le dispositif de sondage ne perturbe pas de façon sensible l'écoulement.

4.6 - Chaines de mesures -

Les chaines de mesures sont de type classique, TRANCHANT pour les mesures de pression et DISA pour les mesures de turbulence.

L'acquisition des résultats est effectuée grâce à un ensemble HEWLETT PACKARD qui permet notamment la conduite automatique des explorations.

Il faut signaler enfin, qu'à cause de la présence d'un niveau de turbulence important dans la zone de mélange, il est nécessaire de filtrer les hautes fréquences lors des mesures de pressions d'arrêt si l'on veut limiter la dispersion des mesures. Des filtres passe-bas ayant une fréquence de coupure à 0,1 Hertz ont été utilisés pour les essais.

4.7 - Mode opératoire -

Le soufflage des panneaux étant réglé comme indiqué au § 4.2, on procède au réglage du soufflage de l'alimentation des fentes marginales en observant la répartition des pressions d'arrêt et des pressions statiques en envergure au voisinage du bord de fuite.

Il faut remarquer que ce réglage n'a pas une importance critique, l'écoulement dans la partie centrale de la maquette étant relativement peu dépendant de ce qui se passe au voisinage des panneaux dès lors qu'un décollement ne s'y produit pas (figure 13).

Le relevé de la répartition longitudinale des pressions est ensuite effectué puis on passe au sondage de la couche visqueuse.

5 - PRESENTATION DES RESULTATS EXPERIMENTAUX -

5.1 - Volet non braqué -

La répartition de pression longitudinale sur la maquette qui, dans ce cas, est pratiquement une plaque plane est donnée figure 14 avec les répartitions de la pression statique et de la pression d'arrêt en envergure au voisinage du bord de fuite pour 2 valeurs du coefficient $C\mu$ de débit de quantité de mouvement.

Ces éléments permettent de voir que la qualité de la bidimensionnalité obtenue pour l'écoulement est assez bonne à faible $C\mu$ et qu'elle se détériore légèrement lorsque le $C\mu$ augmentant, les coefficients de frottement pariétaux deviennent plus élevés. La figure 15 montre par ailleurs les écarts maxima trouvés entre six sondages effectués à la même abscisse ($s = 642$) à des positions différentes en envergure $[200 < Y_{mm} < 800]$.

Les profils de pression statique $[Kp]$ et de pression d'arrêt $[Kp_1]$ dans la couche de mélange à diverses stations en aval de la fente de soufflage et pour 2 valeurs du coefficient $C\mu$ sont présentés figures 16_{ABCD} tandis que le profil de la couche limite initiale au droit de la fente est donné figure 17.

Les figures 18 et 19 montrent l'évolution des profils de vitesse correspondant à ces mesures lorsque l'on s'éloigne de la sortie du jet.

Enfin on trouvera figure 20 les profils de frottement turbulent réduit $-\overline{u'v'}/V_0^2$.

5.2 - Volet braqué à 40° -

5.2.1 - La caractérisation complète de l'écoulement sur le volet ayant un rayon de courbure de 240 mm (volet 240/40°) a été effectuée comme précédemment pour un cas d'essai. Sont présentés pour une vitesse d'essai de 20 m/s, une épaisseur de fente de 2 mm et un $C\mu$ de 0,02 :

- Figure 21, la répartition de pression statique longitudinale et les répartitions de pression statique et de pression d'arrêt en envergure au voisinage du bord de fuite,
- Figures 22 $_{ABC}$, les profils de pression statique et de pression d'arrêt dans la couche de mélange aux stations s = 140, 280 et 580 mm,
- Figure 23, les profils de vitesse correspondants,
- Figure 24, les profils de frottement turbulent réduit,
- Figure 25, le profil de couche limite sur la maquette au droit de la fente.

5.2.2 - L'effet d'une variation de l'épaisseur de fente c'est-à-dire, à coefficient $C\mu$ constant, d'une variation de la vitesse de jet peut être apprécié d'après les sondages effectués à la station 580 et présentés figure 26. On constate un effet favorable de la diminution de l'épaisseur de fente conformément à ce que de nombreux auteurs ont déjà fait ressortir.

L'effet d'une variation du nombre de Reynolds, obtenue en augmentant la vitesse d'essai, a été examiné de la même façon pour l'épaisseur de fente la plus petite.

Les résultats présentés figure 27 montrent un effet favorable de l'augmentation du nombre de Reynolds qui se traduit par une diminution du $C\mu$ de recollement, valeur du coefficient de quantité de mouvement minimale nécessaire à l'obtention d'un régime sans décollement sur le volet.

On peut l'entrevoir sur la figure 28 qui donne l'évolution de la pression cinétique réduite q/q_o à 15 mm d'altitude au voisinage du bord de fuite en fonction du $C\mu$.

Bien qu'aucune recherche systématique n'ait encore été effectuée pour déterminer de façon très précise les valeurs des $C\mu$ de recollement, les essais effectués à ce jour, ayant montré qu'au $C\mu$ de 0,01 il y a décollement dans tous les cas on peut avancer avec une marge d'incertitude de l'ordre de 0,002 les évaluations suivantes pour les $C\mu$ de recollement :

0,0150 à 20 m/s pour la fente de 2 mm

0,0125 à 20 m/s pour la fente de 1 mm

0,0105 à 30 m/s pour la fente de 1 cm.

5.2.3 - L'effet d'une variation du rayon courbure du volet est donné figure 29.

On constate un effet favorable de la diminution du rayon de courbure qui conduit à un $C\mu$ de recollement pour le volet 120/40° avec fente de 2 mm égal sensiblement à celui obtenu pour le volet 240/40° avec fente de 1 mm.

Les répartitions de pression longitudinales et transversales correspondant à ce volet sont portées figure 30.

5.3 - Volet braqué à 65° -

Les résultats concernant ce volet sont présentés :

- Figure 31 pour la répartition de pression statique longitudinale et les répartitions de pression statique et de pression d'arrêt en envergure,
- Figure 32 pour le profil de pression statique et de pression d'arrêt au bord de fuite.

L'évaluation du $C\mu$ de recollement comme précédemment donne une valeur de l'ordre de 0,035.

6 - EXPOSE DE LA METHODE DE CALCUL.- COMPARAISON DES RESULTATS AVEC L'EXPERIENCE -

6.1 - Généralités -

La méthode de calcul que nous avons utilisée dans le but de prévoir l'évolution d'un profil de couche limite soufflée est une méthode aux différences finies préférable aux méthodes intégrales qui nécessitent la connaissance de la forme du profil.

Parmi les divers modèles de turbulence existants, on a choisi un modèle utilisant le coefficient de Boussinesq ν_T qui en dépit de certaines imperfections, (caractère local, isotropie des échanges turbulents, incompatibilité avec le cas du jet pariétal pour lequel $\overline{u'v'}$ ne s'annule pas au maximum du profil des vitesses) donne dans bien des cas des résultats acceptables.

Le problème de l'élimination du caractère local de ce coefficient de viscosité turbulente est résolu par l'utilisation de l'équation de Nee-Kovasznay [2] qui a de plus l'avantage d'avoir une forme analogue à celle de l'équation de quantité de mouvement, et donc de permettre un traitement numérique identique à celui utilisé pour la résolution de cette équation.

Le programme utilisé a été mis en oeuvre par D. Jeandel [3] pour la couche limite puis adapté au cas du jet pariétal et de la couche limite soufflée par P.M. Riboud [4].

6.2 - Equation de Nee-Kovasznay -

C'est une équation de comportement de la viscosité turbulente effective ν_e $(\nu_e = \nu + \nu_T)$ constituée :

- d'un terme de convection $u \frac{\partial \nu_e}{\partial x} + v \frac{\partial \nu_e}{\partial y}$
- d'un terme de diffusion $\frac{\partial}{\partial y}\left(\nu_e \frac{\partial \nu_e}{\partial y}\right)$
- d'un terme de production $A\left[\nu_e - \nu\right] \frac{\partial u}{\partial y}$
- d'un terme de dissipation $B\left[\nu_e - \nu\right] \nu_e / L^2 d$

Elle s'écrit :

$$u \frac{\partial \nu_e}{\partial x} + v \frac{\partial \nu_e}{\partial y} = \frac{\partial}{\partial y}\left(\nu_e \frac{\partial \nu_e}{\partial y}\right) + A\left(\nu_e - \nu\right) \frac{\partial u}{\partial y} - B \frac{\left[\nu_e - \nu\right] \nu_e}{L^2 d}$$

L'utilisation de cette équation impose le choix d'un modèle de longueur de dissipation L_d ainsi que des deux constantes A et B. Celles-ci ne sont pas indépendantes puisque près de la paroi, à la frontière de la sous couche laminaire $[Y u_\tau / \nu > 30]$ dans une zone où convection et dissipation sont négligeables on doit avoir l'égalité entre production et dissipation ce qui conduit à : $A = K^2 B$ K étant la constante de la loi de longueur de mélange dans la zone de paroi (constante de Von Karman).

Dans la zone de paroi, les dimensions caractéristiques des structures fines dissipatives suivent celle des structures à plus grande échelle ce qui conduit à poser $L_d = Y$.

L'hypothese suivant laquelle la dissipation de la viscosité turbulente est commandée par les structures du jet conduit à poser $L_d = Y_{1/2}$ à l'extérieur de cette zone, $Y_{1/2}$ étant défini comme l'ordonnée du point, situé dans la partie supérieure du jet, où la vitesse est égale à la demi-somme de la vitesse extérieure et de la vitesse maximale du jet. En définitive pour $0 < Y < Y_{1/2}$ on a $L_d = Y$

et pour $Y > Y_{1/2}$ on a $L_d = Y_{1/2}$

Ce modèle étant adopté pour la longueur de dissipation, les constantes A et B ont été choisies égales à celles définies par P.M. Riboud pour le cas du jet pariétal ($A = 0{,}133$; $B = 1{,}05$).

En effet, un examen comparatif des profils de vitesse et de turbulence sous forme réduite pour le jet pariétal et pour la couche limite soufflée justifie ce choix.

6.3 - Méthode de résolution -

La méthode utilisée pour résoudre le système des trois équations de base (équation de continuité, équation de quantité de mouvement, équation de Nee-Kovasznay) est celle de Patankar et Spalding [5].

Elle consiste à utiliser non pas un système de coordonnées (X, Y) mais un système (x, ω) qui a l'avantage de suivre l'évolution transversale du profil. On satisfait à l'équation de continuité en introduisant la fonction de courant Ψ telle que :

$$\frac{\partial \Psi}{\partial x} = -\rho v$$

$$\text{et} \quad \frac{\partial \Psi}{\partial Y} = -\rho u$$

La fonction de courant sans dimension ω est alors définie par : $\omega = \dfrac{\Psi - \Psi_I(x)}{\Psi_E(x) - \Psi_I(x)}$

où Ψ_E et Ψ_I sont les valeurs de la fonction de courant aux frontières.

Les deux équations se ramènent alors à la forme commune :

$$\frac{\partial \phi}{\partial x} + (a_\phi + b\omega)\frac{\partial \phi}{\partial \omega} = \frac{\partial}{\partial \omega}\left(c\,\frac{\partial \phi}{\partial \omega}\right) + d\phi$$

ϕ pouvant représenter la vitesse u ou la viscosité turbulente effective ν_E .

Par la linéarisation de ces équations on obtient deux relations implicites indépendantes relatives à la vitesse et à la viscosité.

Les données nécessaires à la résolution numérique de ces équations sont les valeurs $\phi(x)$ aux frontières I et E ainsi que les profils initiaux $\phi(\omega)$.

6.4 - Cas d'une couche limite soufflée se développant en l'absence de gradient de pression -

Ce cas est pratiquement réalisé lors de l'étude du volet à braquage nul.

L'utilisation du programme de calcul nécessite des données qui sont les profils de vitesse et de viscosité dans la section initiale, ainsi que l'évolution longitudinale de la vitesse et de la viscosité turbulente à la frontière extérieure.

Les données dans la section de sortie du jet sont mal connues, les dimensions de la fente ne permettant pas des explorations précises, notamment en ce qui concerne la viscosité turbulente, par suite des dimensions des sondes à fils croisés. Pour cette raison, les calculs ont d'abord été effectués à partir d'une station en aval de la fente (s = 140 mm), station où les sondages de vitesse et de contraintes turbulentes deviennent possibles et permettent de préciser les conditions initiales du calcul.

Le bon accord des résultats de calculs avec l'expérience, obtenu au cours de l'évolution de la couche limite soufflée jusqu'au bord de fuite du volet, aussi bien pour des profils de vitesse que pour les profils des contraintes turbulentes, a justifié à posteriori les divers choix effectués et permis d'envisager les calculs à partir de la fente.

Pour ceux-ci on a considéré le jet comme constitué de deux couches limites se raccordant à une zone où la vitesse reste constante. La viscosité initiale a été obtenue en utilisant une loi de longueur de mélange pour l'ensemble du profil.

Les résultats obtenus pour $C\mu = 0{,}01$ ainsi que leur comparaison aux résultats expérimentaux sont présentés figure 33 au niveau des profils de vitesse et des profils de contrainte tangentielle turbulente réduite.

Le bon accord observé entre l'expérience et les résultats de calcul est remarquable compte tenu des légères incertitudes expérimentales et de la façon relativement schématique de représenter le profil initial du jet.

Pour un volet à braquage nul, il apparait donc que, le fait d'avoir choisi un modèle de turbulence faisant coïncider le point de contrainte turbulente nulle avec l'extrêmum des vitesses, n'est pas rédhibitoire et que l'emploi des constantes A et B déterminées pour un jet pariétal, convient au calcul d'une couche limite soufflée jusqu'à un moment assez tardif de son évolution.

6.5 - Cas d'une couche limite soufflée se développant en présence de gradients de pression -

Dans le cas d'un volet braqué, le calcul doit tenir compte non seulement d'un gradient de pression longitudinal mais aussi d'un gradient de pression transversal par suite de la courbure du volet.

La prise en compte de l'effet de courbure introduit une équation supplémentaire et modifie les équations de départ ce qui empêche leur résolution par la méthode de calcul utilisée ici.

Plutôt que de négliger purement et simplement cet effet nous avons introduit en données un champ de pression $P(x,y) = P(x,0) + y\frac{\partial P}{\partial y}(x)$; $\frac{\partial P}{\partial y}(x)$ étant obtenu soit par l'expérience soit au moyen d'un calcul en fluide parfait.

Un seul calcul a été pour l'instant effectué. La confrontation des résultats avec les résultats expérimentaux présentée figure 34 montre un accord assez satisfaisant dans l'ensemble ce qui laisse bien augurer de l'utilisation de cette méthode dans l'avenir.

Il est certain cependant qu'une amélioration est souhaitable pour la définition du profil de départ du jet et pour la prise en compte de l'effet de courbure.

7 - CONCLUSIONS -

Un montage à grande échelle permettant l'étude détaillée des couches limites bidimensionnelles soufflées sur volet hypersustentateur, dans des conditions réalistes de nombre de Reynolds, a été mis au point.

Le problème posé par l'obtention d'une bidimensionnalité effective de la couche visqueuse sur le volet a été résolu en effectuant le contrôle de la couche limite des panneaux latéraux par soufflage, en augmentant le débit de quantité de mouvement injecté sur le volet au voisinage immédiat des panneaux et en veillant à ce que la bidimensionnalité du jet à la sortie du canal de soufflage soit elle-même irréprochable.

L'utilisation du montage a permis d'obtenir un ensemble complet de résultats expérimentaux sur le développement du mélange entre le jet et la couche limite de la maquette.

Ceux-ci, qui comprennent des données sur le frottement turbulent doivent permettre de choisir parmi les modèles de turbulence existants ceux qui permettent de prévoir par le calcul le développement de mélange observé.

Un modèle relativement simple mais prometteur a été mis en oeuvre. Il utilise le concept de viscosité turbulente et repose sur l'utilisation de l'équation de Nee Kovasznay.

Les premières comparaisons effectuées entre résultats expérimentaux et résultats de calcul sont en effet très encourageantes. Il apparait toutefois souhaitable d'affiner la modélisation du jet pour un calcul partant de la sortie de fente et d'améliorer la prise en compte de l'effet de courbure.

- REFERENCES -

[1] Lachmann G.V. -
Boundary layer and Flow control.
PERGAMON PRESS.

[2] Nee V. et Kovasznay L.S.G. -
Simple phenomenological Theory of Turbulent shear flows. The Physics of Fluid - vol. 12, number 3 (1968).

[3] Jeandel D. -
Méthode de calcul de la couche limite turbulente utilisant une équation de comportement du coefficient de Boussinesq. (Thèse de Docteur-Ingénieur soutenue devant l'Université Claude Bernard de Lyon - 1972).

[4] Riboud P.M. -
Thèse de Docteur-Ingénieur (à paraître).

[5] Patankar S.V. et Spalding D.B. -
A finite difference Procedure. Heat and Mass Transfer in Boundary Layers. Int. J. Heat Mass Transfer n° 10 pp 1389 - 1411 (1967).

D'après SCHWIER AVA GOTTINGEN

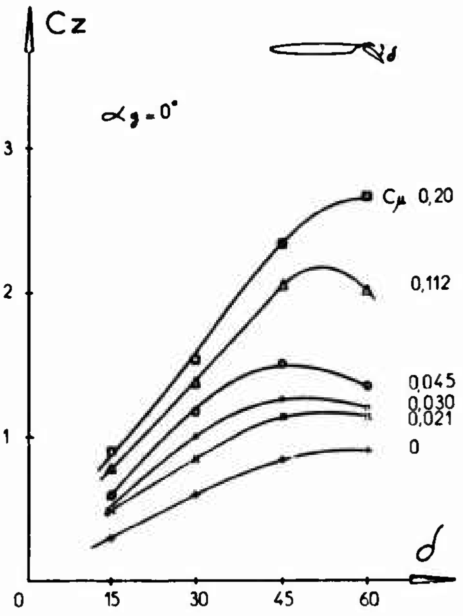

Figure 1 - Amélioration des qualités d'hypersustentation d'un profil par soufflage.

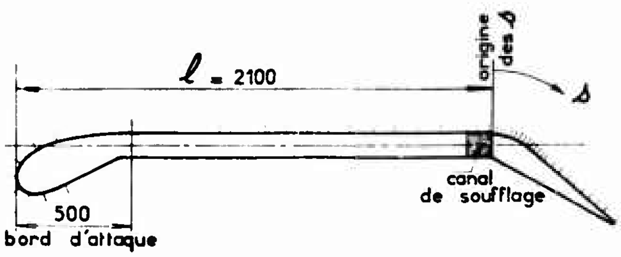
ℓ = 2100
origine des δ
δ
canal de soufflage
500
bord d'attaque

Figure 2 - Maquette pour l'étude du soufflage interne.

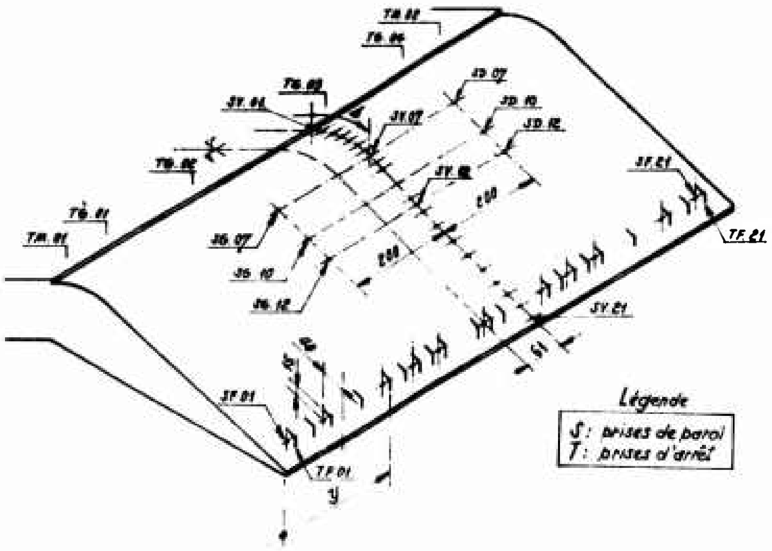
TR 01
TG 01
TF 21
SV 21
SF 01
TF 01
y
Légende
S : prises de paroi
T : prises d'arrêt

Figure 3 - Equipement des volets en prises de pression.

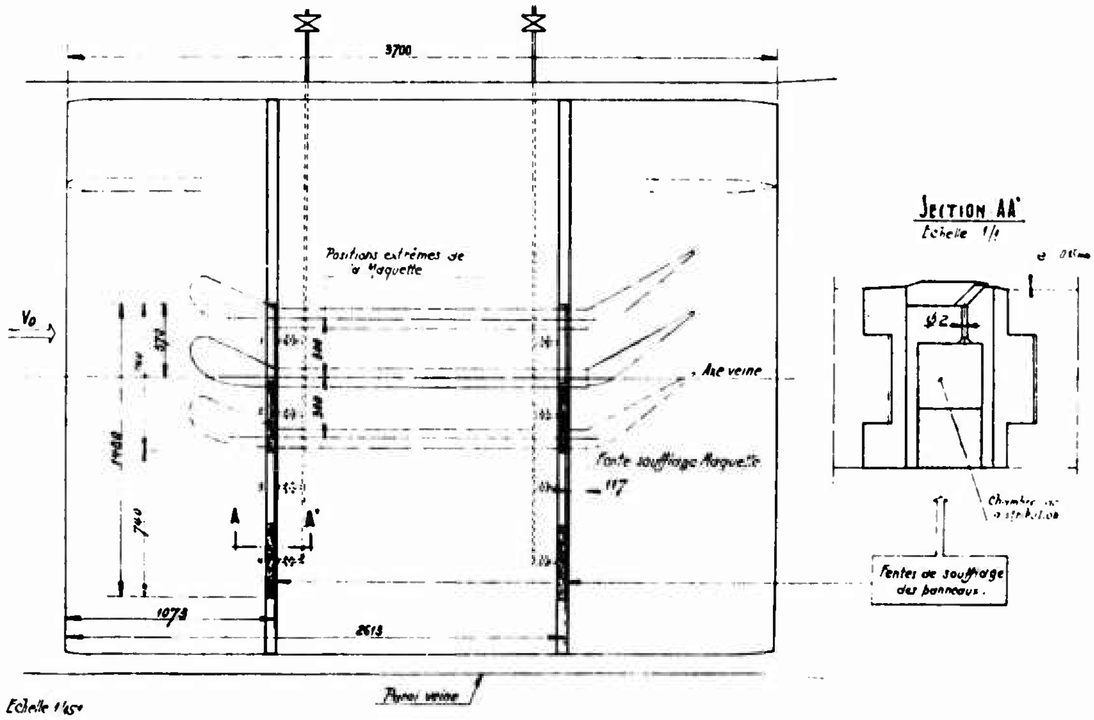
3700
Positions extrêmes de la Maquette
V0
Axe veine
Fente soufflage Maquette
A
A'
1073
2613
Paroi veine
Echelle 1/50
SECTION AA'
Echelle 1/1
ø2
Chambre de distribution
Fentes de soufflage des panneaux.

Figure 4 - Equipement pour le soufflage des panneaux.

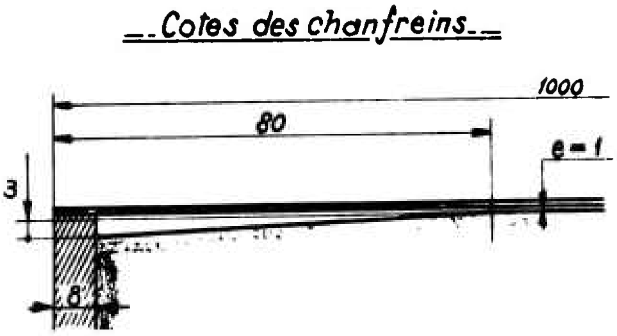
Cotes des chanfreins.
1000
80
e = 1
3
8

Figure 5 - Dessin des chanfreins.

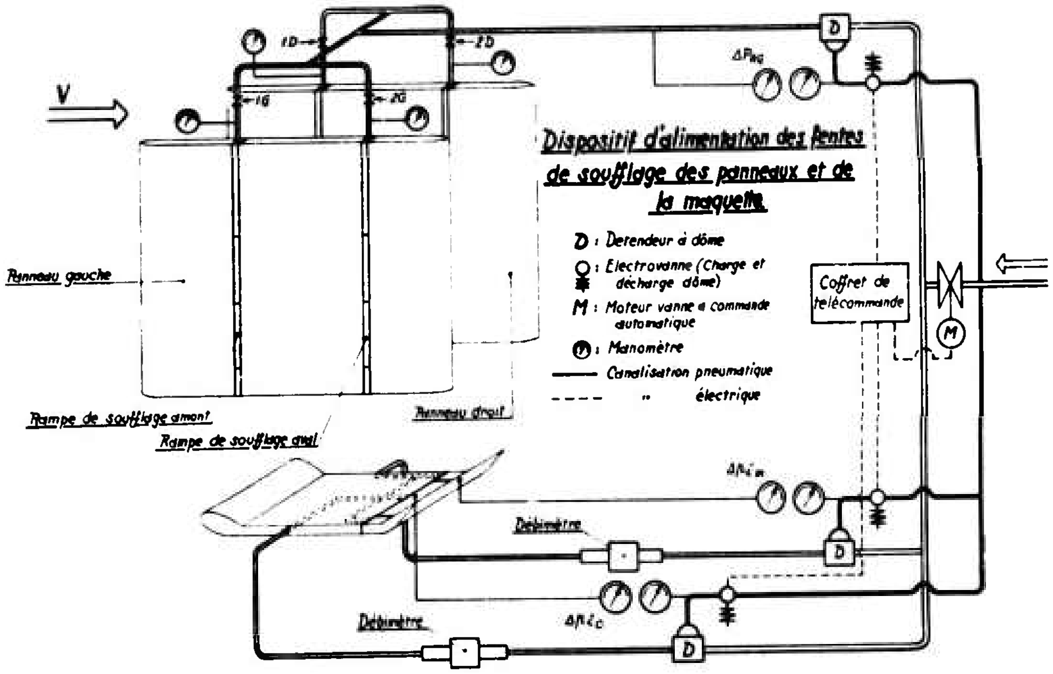
V
1D
2D
1G
2G
ΔP_{aG}
Dispositif d'alimentation des fentes de soufflage des panneaux et de la maquette
D : Detendeur à dôme
: Electrovanne (Charge et décharge dôme)
M : Moteur vanne à commande automatique
: Manomètre
Canalisation pneumatique
" électrique
Coffret de télécommande
M
Panneau gauche
Rampe de soufflage amont
Rampe de soufflage aval
Panneau droit
ΔP_{im}
Débimètre
D
ΔP_{ic}
Débimètre
D

Figure 6 - Schéma d'alimentation de la maquette.

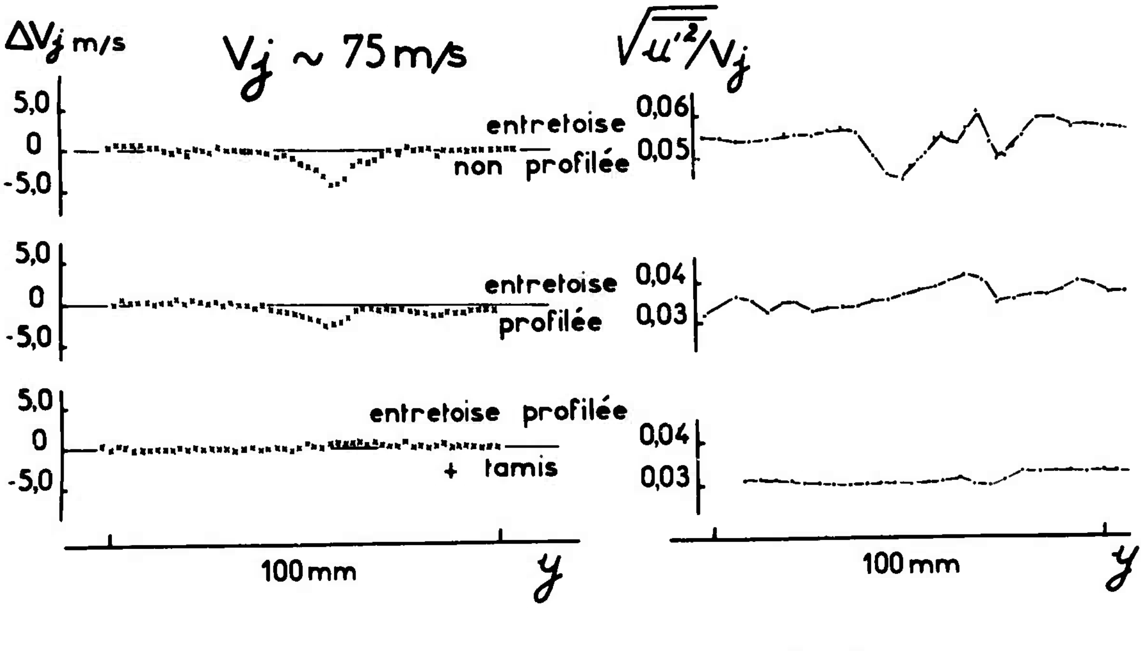

Figure 7 - Effet de l'interposition d'un tamis sur les distributions de vitesse et de turbulence en sortie de fente.

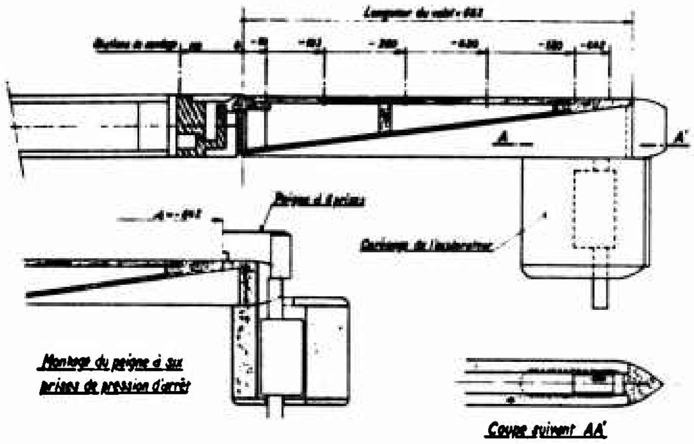
A
A'
Montage du peigne à six prises de pression d'arrêt
Coupe suivant AA'

Figure 8_A - Géométrie du volet non braqué.

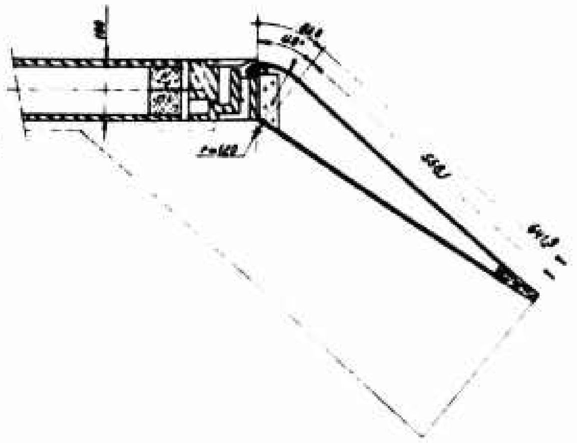

Figure 8C - Géométrie du volet
δ = 40° R = 120

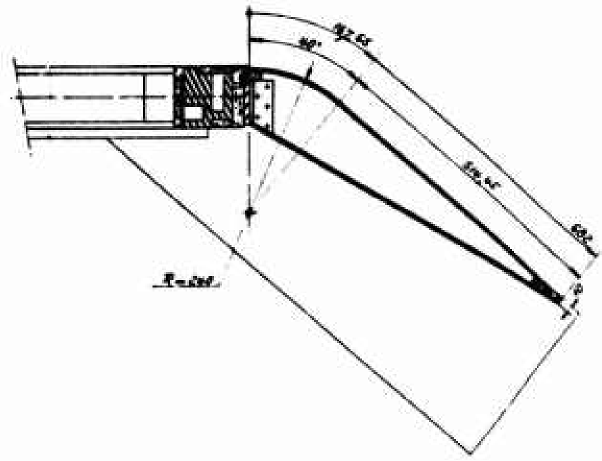

Figure 8_B - Géométrie du volet
δ = 40° R = 240

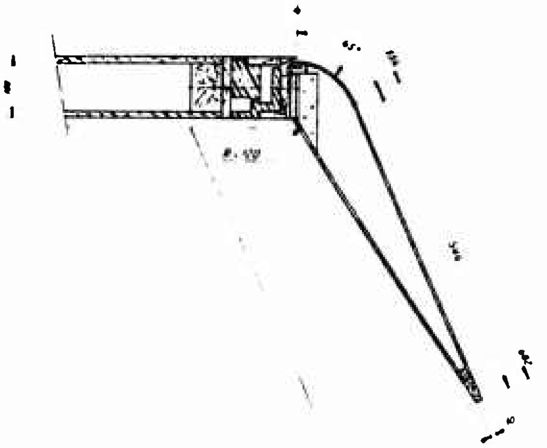

Figure 8_D - Géométrie du volet
δ = 65° R = 120

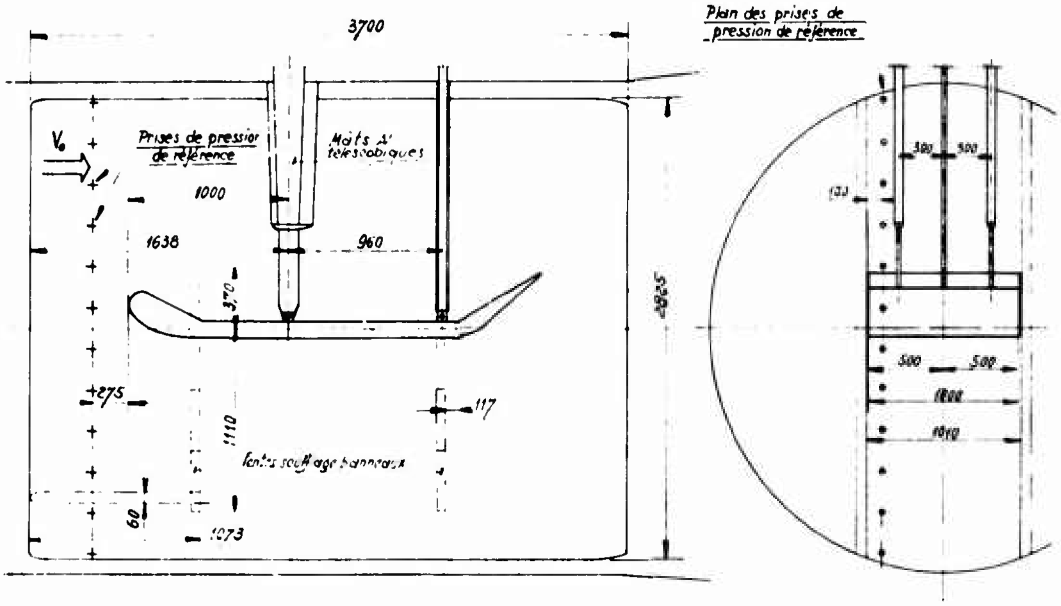
3700
V_0
Prises de pression de référence
Mâts A' télescopiques
1000
1638
960
370
2825
275
117
1110
Fentes soufflage bandeaux
60
1073
Plan des prises de pression de référence
300
300
133
500
500
1800
1010

Figure 9 - Schéma du montage de la maquette en veine.

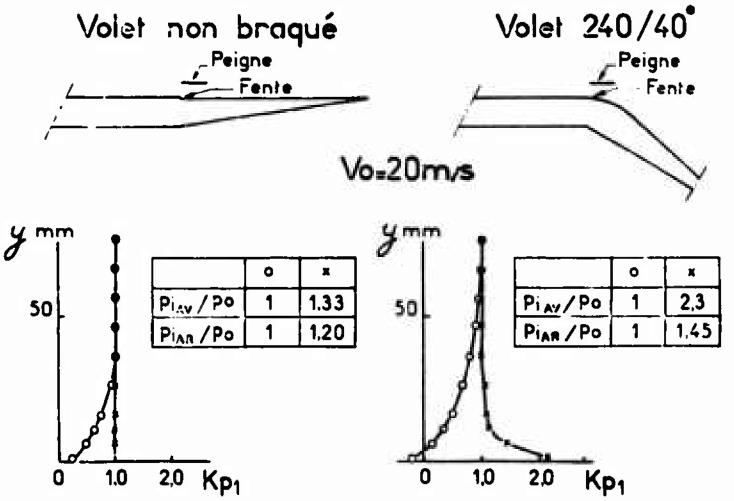

	o	x
Pi$_{AV}$/Po	1	1.33
Pi$_{AR}$/Po	1	1.20

	o	x
Pi$_{AV}$/Po	1	2.3
Pi$_{AR}$/Po	1	1.45

Figure 10 - Effet du soufflage des panneaux sur l'épaisseur de leur couche limite.

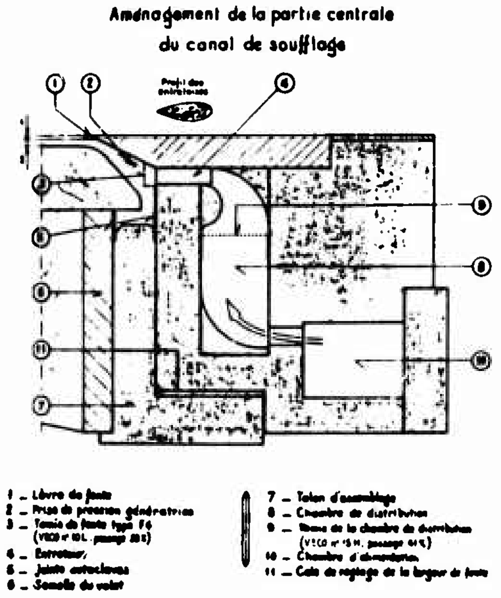
Aménagement de la partie centrale du canal de soufflage
①
②
Profil des entretoises
④
③
⑤
⑥
⑨
⑧
⑩
⑪
⑦
1 – Lèvre de fente
2 – Prise de pression génératrice
3 – Tamis de fente type F6 (VECO n° 10 L. passage 20%)
4 – Entretoise
5 – Joints autoclaves
6 – Semelle de volet
7 – Talon d'assemblage
8 – Chambre de distribution
9 – Tamis de la chambre de distribution (VECO n° 15 H. passage 41%)
10 – Chambre d'alimentation
11 – Cale de réglage de la largeur de fente

Figure 11 - Schéma du canal de soufflage.

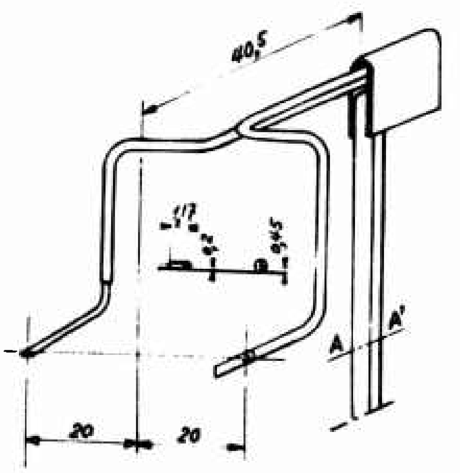
40,5
1,7
0,2
0,45
A
A'
20
20

Figure 12 - Schéma de la bisonde utilisée pour les sondages de couche limite.

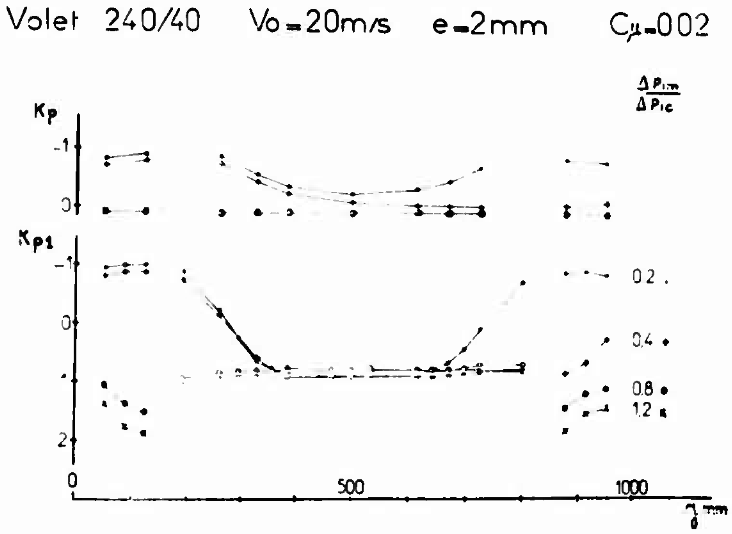

Figure 13 - Réglage du soufflage des fentes marginales.

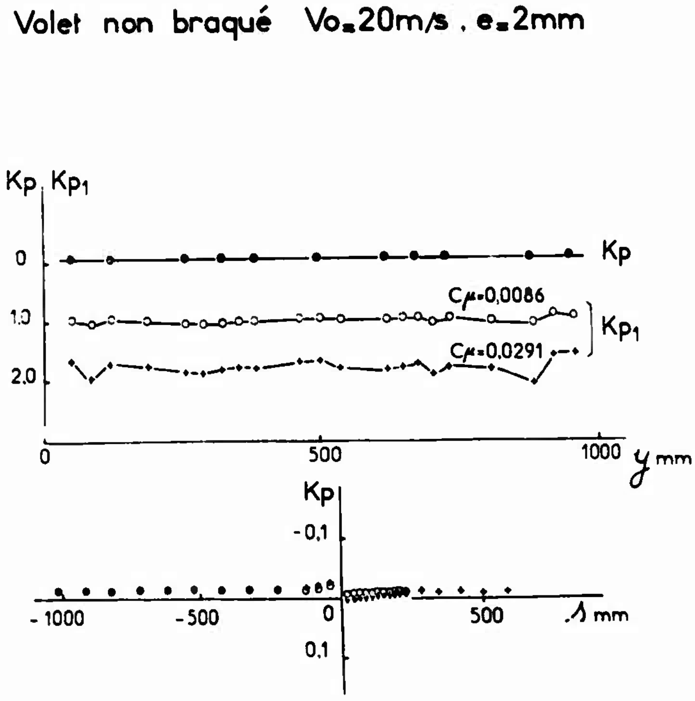

Figure 14 - Répartitions de pression mesurées sur le volet non braqué.

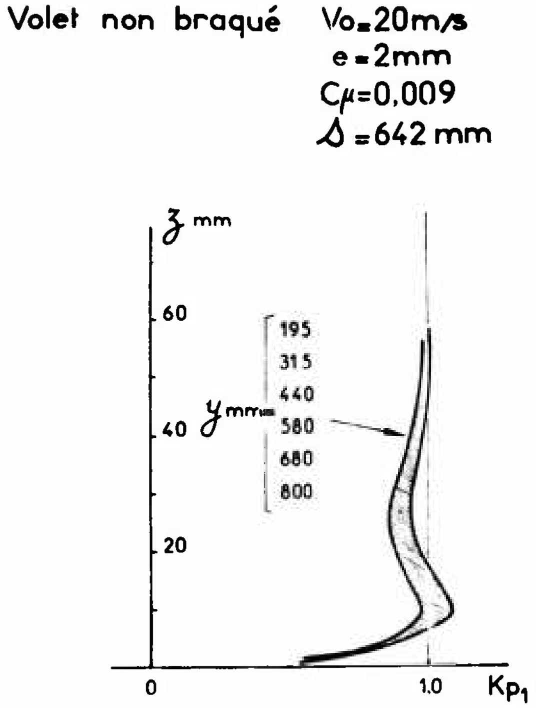

Figure 15 - Ecarts observés entre les profils de Kp_1 mesurés à diverses positions en envergure.

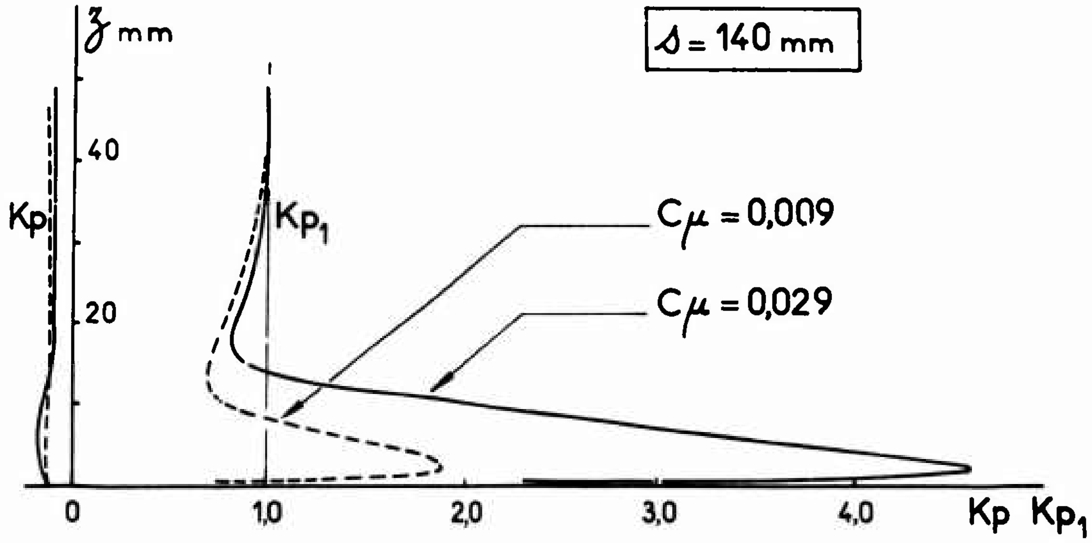

Figure 16_A - Profils de pression d'arrêt et de pression statique mesurés dans la couche limite soufflée sur le volet non braqué à l'abscisse 140 mm.

Volet non braqué Vo=20m/s e=2mm

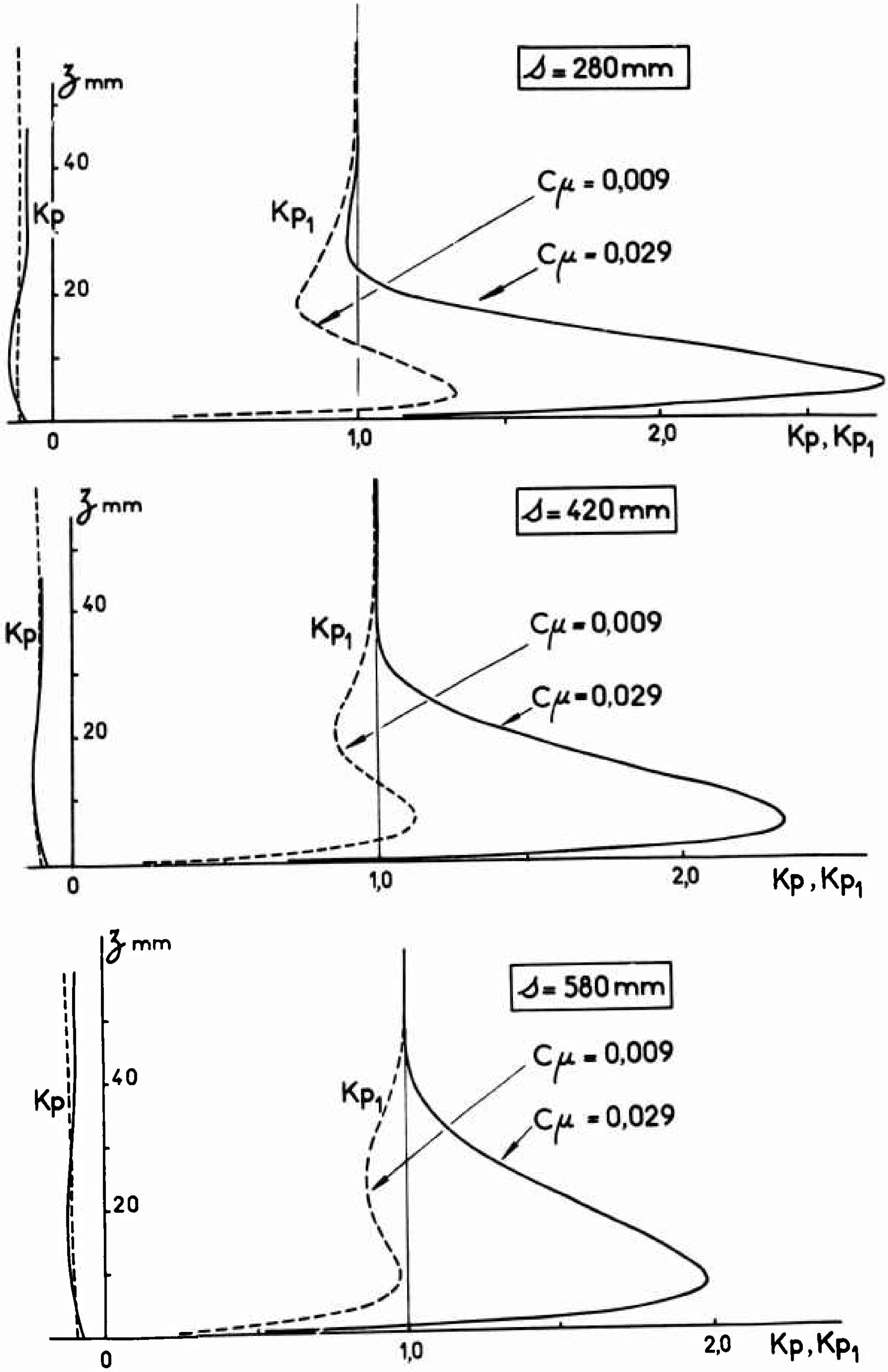

Figures $16_{B.C.D.}$ – Profils de pression d'arrêt et de pression statique mesurés dans la couche limite soufflée sur le volet non braqué aux abscisses 280,420,580 mm

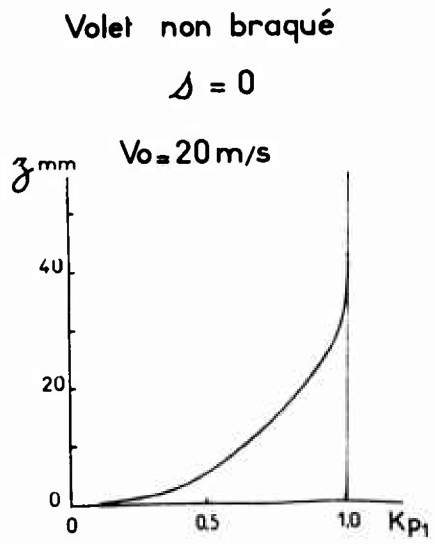

Figure 17
Profil de pression d'arrêt mesuré dans la couche limite sur la maquette au droit de la fente de soufflage (volet non braqué).

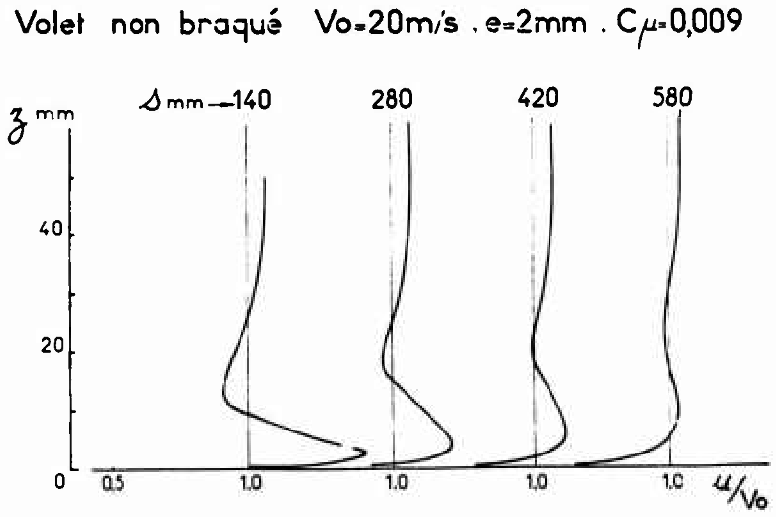

Figure 18 - Evolution du profil de vitesse mesuré dans une couche limite soufflée lorsque la distance à la sortie de jet croît (volet non braqué, C_μ = 0,009).

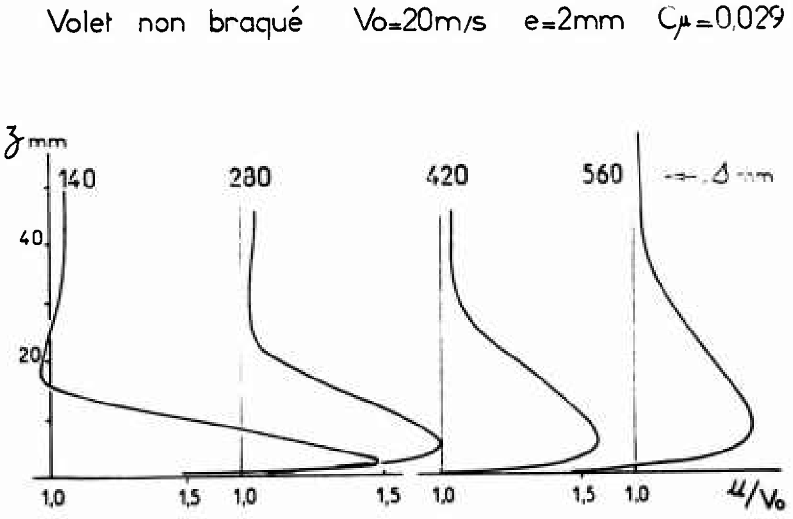

Figure 19
Evolution du profil de vitesse mesuré dans une couche limite soufflée lorsque la distance à la sortie de jet croît (volet non braqué, C_μ = 0,029).

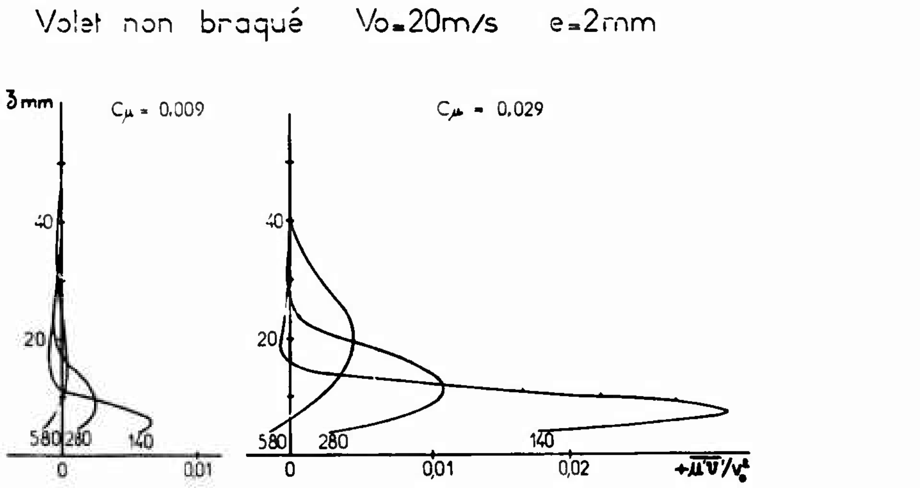

Figure 20
Profils de frottement turbulent réduit mesurés dans une couche limite soufflée sur volet non braqué.

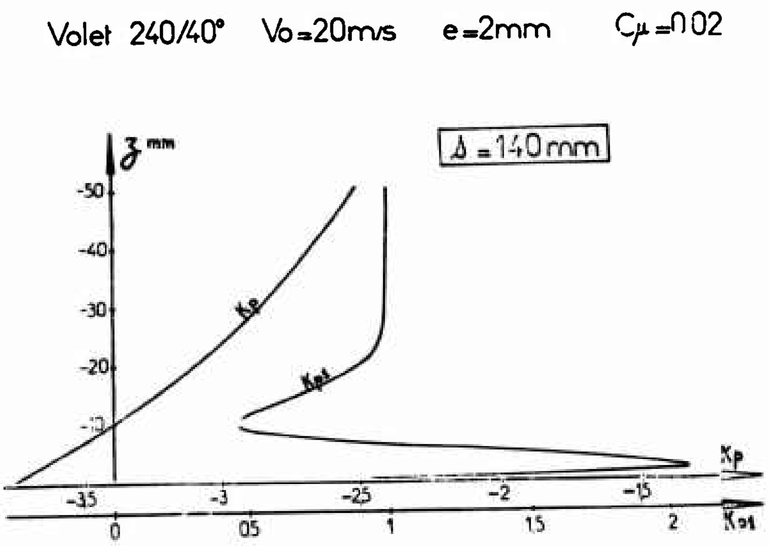

Figure 22$_A$

Profils de pression d'arrêt et de pression statique mesurés dans la couche limite soufflée sur le volet 240/40, à l'abscisse 140 mm.

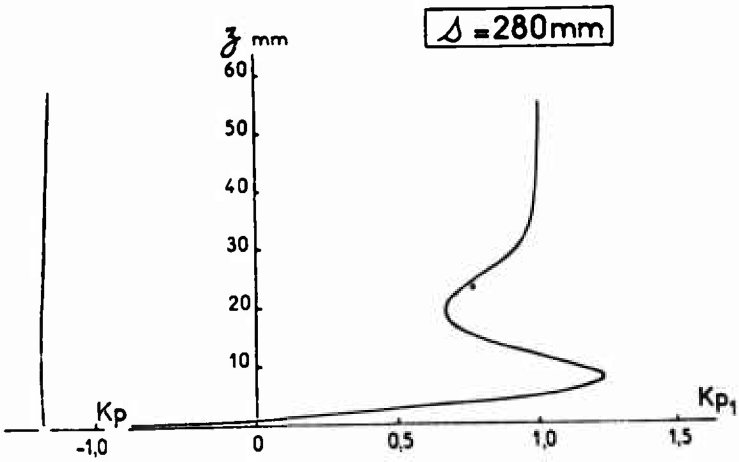

Figure 22$_B$

Profils de pression d'arrêt et de pression statique mesurés dans la couche limite soufflée sur le volet 240/40, à l'abscisse 280 mm.

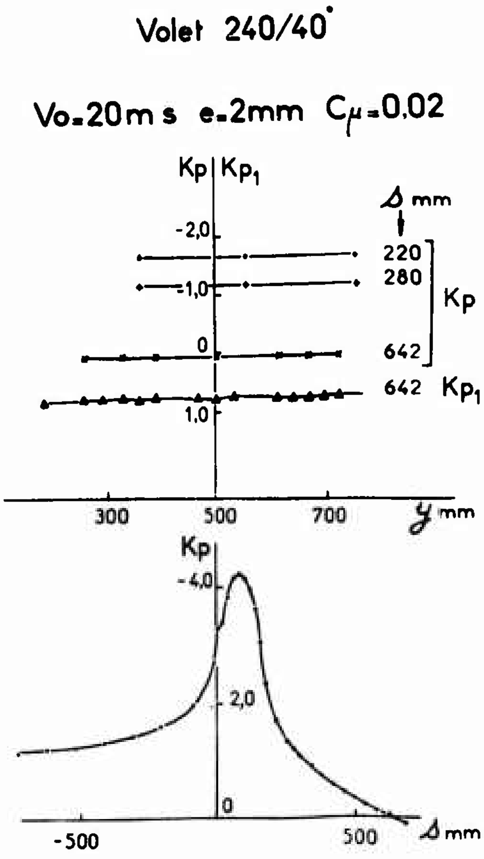

Figure 21

Répartitions de pression mesurées sur le volet 240/40°.

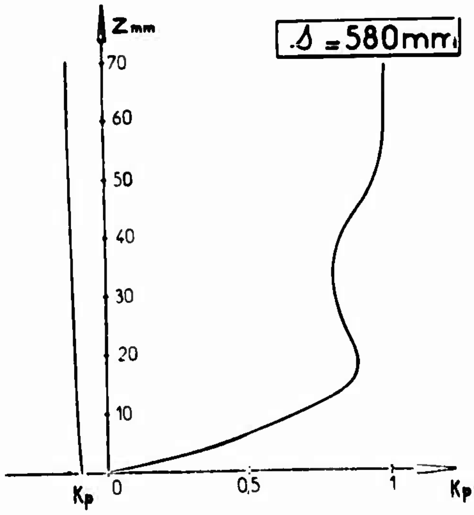

Figure 22$_C$ - Profils de pression d'arrêt et de pression statique mesurés dans la couche limite soufflée sur le volet 240/40, à l'abscisse 580 mm.

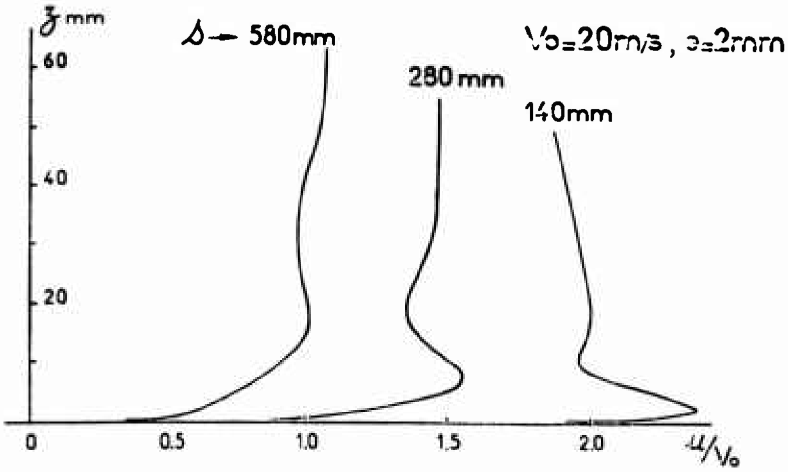

Figure 23

Evolution du profil de vitesse mesuré dans une couche limite soufflée lorsque la distance à la sortie de jet croît (volet 240/40°, C_μ = 0,020).

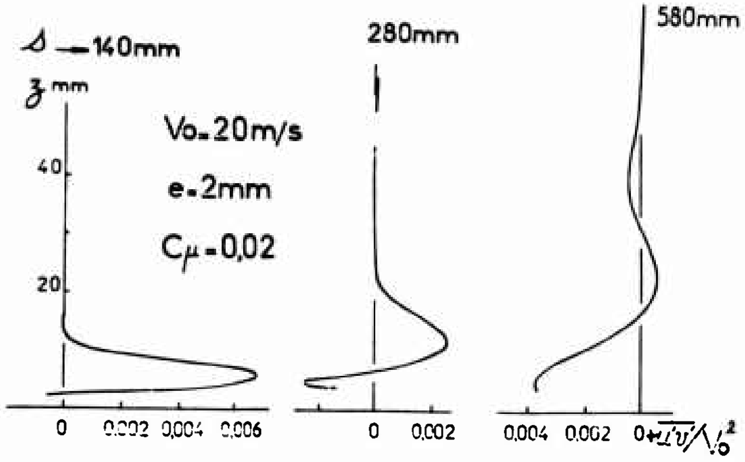

Figure 24

Profils de frottement turbulent réduit mesurés dans la couche limite soufflée sur le volet 240/40°.

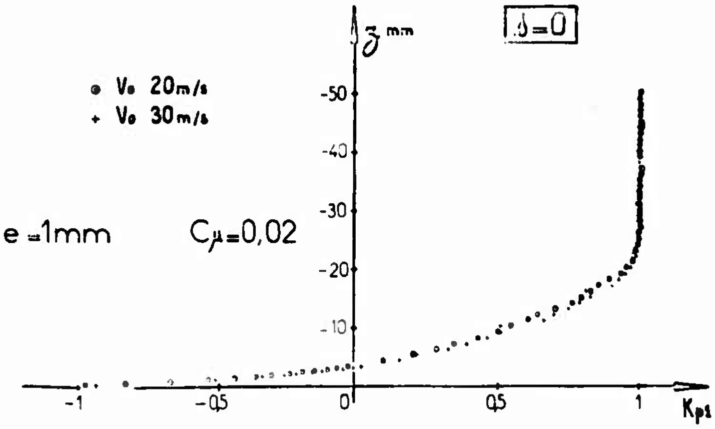

Figure 25

Profil de pression d'arrêt mesuré dans la couche limite sur la maquette au droit de la fente de soufflage (volet 240/40°).

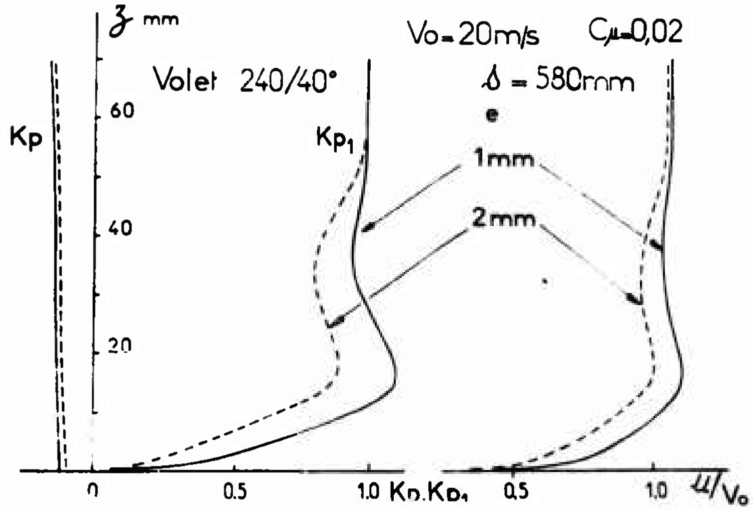

Figure 26

Effet d'une variation de l'épaisseur de fente sur les profils de pression mesurés dans la couche visqueuse au voisinage du bord de fuite.

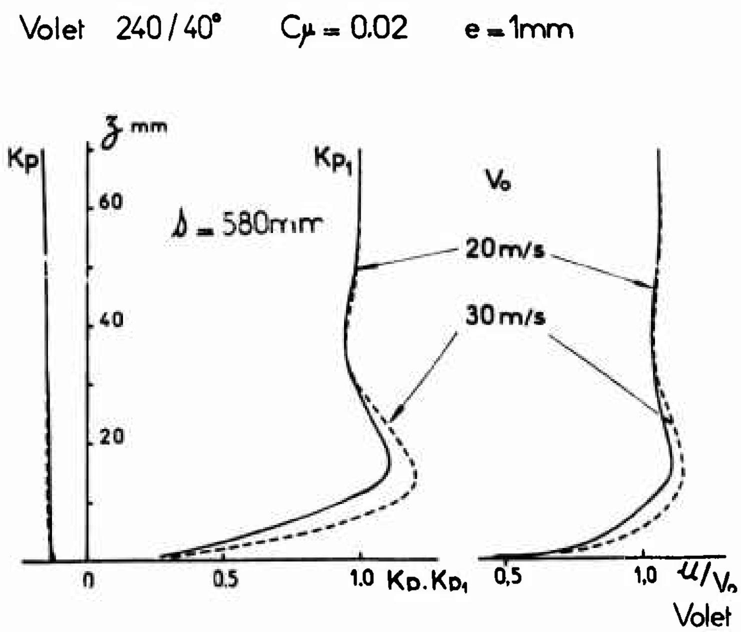

Figure 27

Effet d'une variation du nombre de Reynolds sur les profils de pression mesurés dans la couche visqueuse au voisinage du bord de fuite.

Figure 30

Répartitions de pression mesurées sur le volet 120/40°.

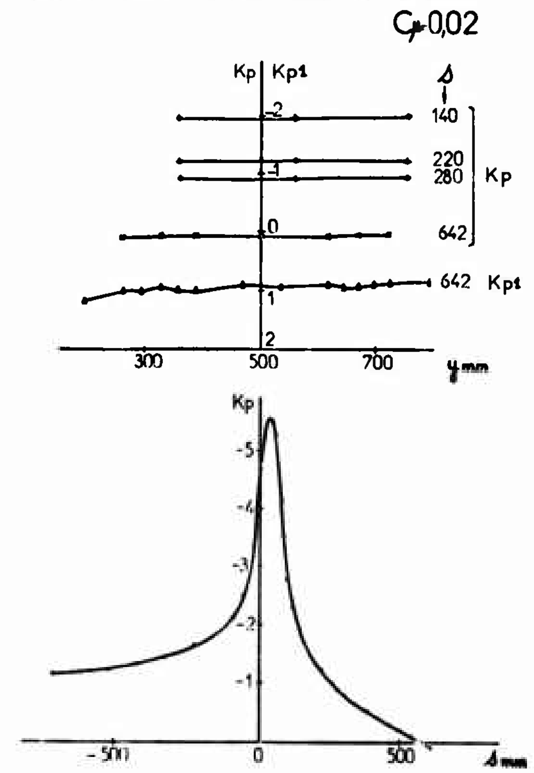

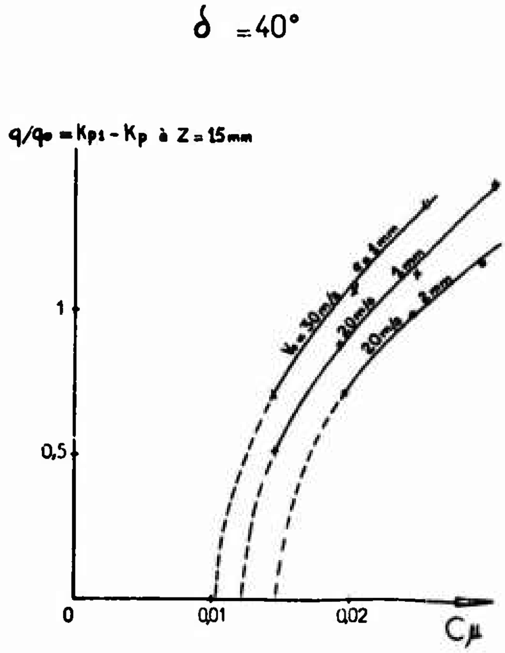

Figure 28

Evolution en fonction du $C\mu$ de la pression dynamique en un point situé à 15 mm d'altitude au niveau du bord de fuite.

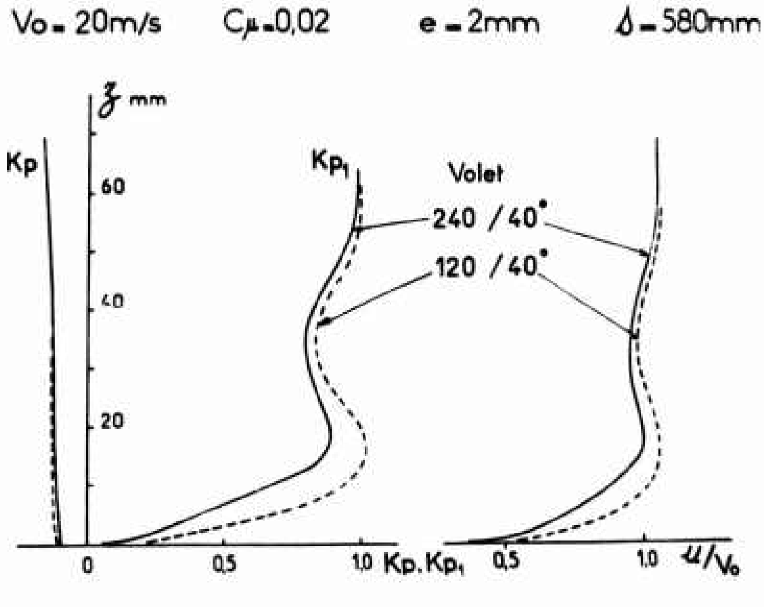

Figure 29

Effet du rayon de courbure du volet sur les profils de pression mesurés dans la couche visqueuse au voisinage du bord de fuite.

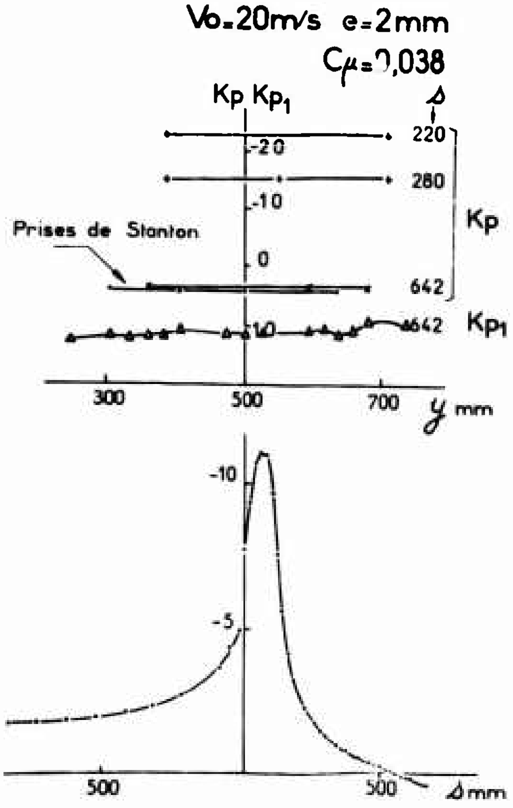

Figure 31 - Répartitions de pression mesurées sur le volet 120/65°.

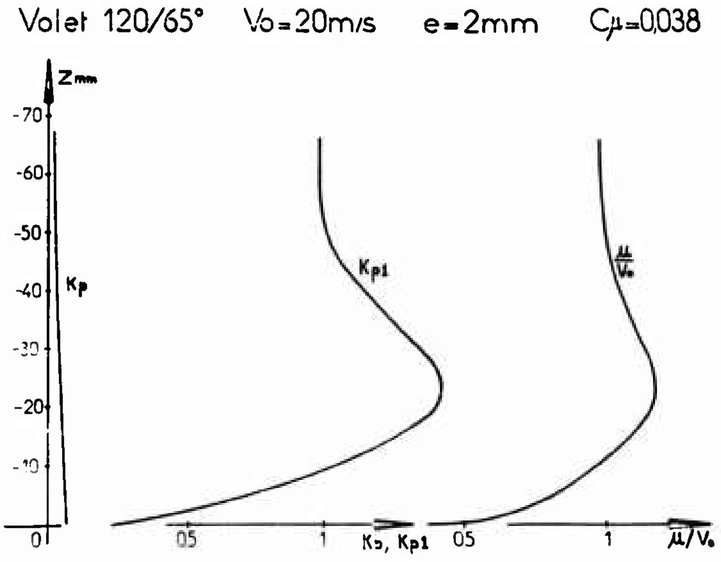

Figure 32 - Profils de pression d'arrêt et de pression statique mesurés dans la couche visqueuse sur le volet 120/65° à l'abscisse 580 mm.

Figure 33 - Voir page suivante.

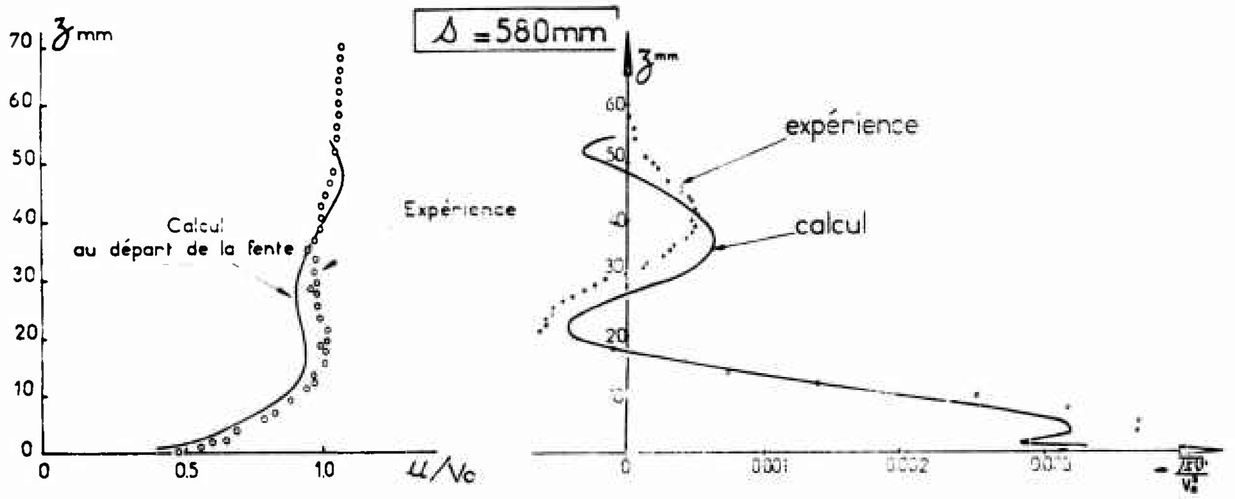

Figure 34 - Profils de vitesse et de frottement dans la couche limite soufflée sur le volet 240/40°: comparaison calcul-expérience (V_0 = 20 m/s e = 2 mm C_μ = 0,02).

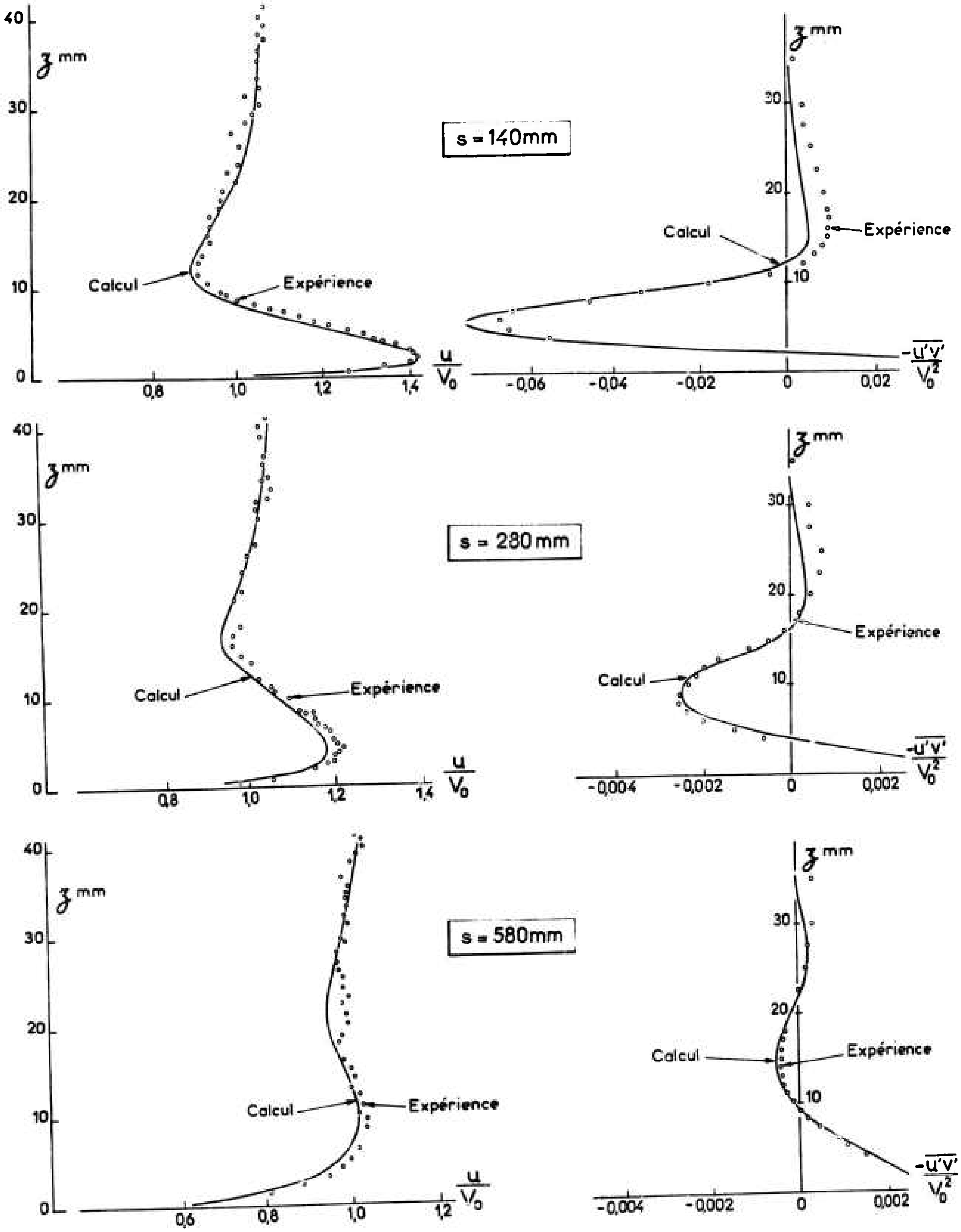

Figure 33 - Profils de vitesse et de frottement dans la couche limite soufflée sur le volet non braqué : comparaison calcul - expérience (V_0 = 20 m/s e = 2 mm C_μ = 0,009).

Figure 34 - Voir page précédente.

AERODYNAMICS OF JET FLAP AND ROTATING CYLINDER FLAP STOL CONCEPTS

Woodrow L. Cook, David H. Hickey, and Hervey C. Quigley
Ames Research Center, NASA
Moffett Field, California 94035

SUMMARY

The aerodynamic effectiveness of various propulsive lift concepts to provide for the low-speed performance and control required of short takeoff and landing (STOL) aircraft depends on a close interrelationship between the propulsion system and aerodynamic components of the aircraft. The relative effectiveness of different lift concepts has been evaluated through static and wind tunnel testing of various aerodynamic models and propulsion components, simulations of aircraft, and, in some cases, flight testing of research aircraft incorporating the concepts under study.

The concepts tested were augmented and internally blown jet flaps, upper-surface blown flaps, and externally blown flaps. Results of testing with large-scale models are presented, which show the aerodynamic effectiveness for the various concepts. Advanced augmented jet flaps were tested for improvements of the static augmentation ratio, effects of forward velocity on augmentation ratio lapse rate, and for potential reductions in noise. The results of flight tests of STOL research aircraft incorporating augmented jet flaps and rotating cylinder flaps are presented and indicate the relative effectiveness of these aircraft in providing steeper approach flight paths at low forward speeds as well as the effect of ground on their aerodynamics.

NOMENCLATURE

A	landing approach flight condition
AAR	nozzle array area ratio, nozzle height/nozzle area
AERO	aerodynamic lift coefficient
AR	aspect ratio, b^2/S
b	wing span, ft (m)
$\bar{c}$	mean aerodynamic chord
C_D	drag coefficient, drag/qS
C_L	lift coefficient, lift/qS
e	elevator control deflection
G	in ground effect
h	aircraft wing height above ground, ft (m)
h_E	equivalent lobed nozzle height, nozzle area/nozzle span
L	augmented jet flap chord length, ft (m)
m	meter
NPR	nozzle pressure ratio
o	out of ground effect
PNdB	perceived noise level (PNL) in decibels
q	dynamic pressure, lb/ft^2
S	wing area, ft^2 (m^2)
T	thrust, lb (kg)
V	flight speed, ft/sec (m/sec)
w	aircraft weight, lb (kg)
α	angle of attack, deg
δ	control surface deflection, deg
$\ddot{\phi}$	lateral control, rad/sec^2
ϕ	augmentation ratio, total thrust/nozzle thrust
γ	aircraft flight path angle, deg

1. INTRODUCTION

A number of propulsive lift concepts for providing STOL aerodynamics have been investigated in wind tunnels at the NASA–Ames Research Center.

Figure 1 shows the concepts studied: the augmented jet flap (AJF), the externally blown flap (EBF), the upper-surface blown flap (USB), and an internally blown flap (IBF). Test data were obtained on large-scale models of similar geometry in the Ames 40- by 80-Foot Wind Tunnel. The IBF is blown at the main flap radius of curvature and also at the auxiliary trailing edge flap at the upper and lower surface; blowing at the upper surface increases as the auxiliary flap is deflected downward. The EBF and USB flaps also have auxiliary trailing edge flaps for maximum deflection.

Table 1 compares the geometries of the wind tunnel models in terms of aspect ratio, sweep, taper ratio, and airfoil thickness. For purposes of comparing their aerodynamics, the four concepts are seen to be roughly equivalent, with small differences in geometry tending to offset one another.

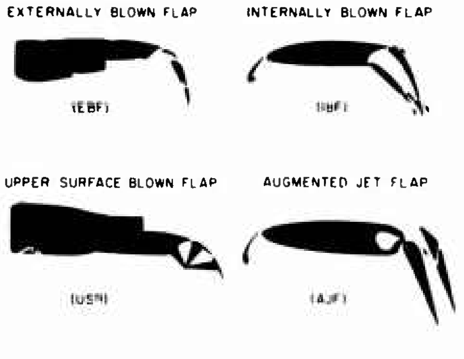

Fig. 1 Propulsive lift concepts tested

Table 1 Geometry Comparison of Four Large-Scale Propulsive Lift Models

	ASPECT RATIO	SWEEP OF QUARTERCHORD, deg	TAPER RATIO	AIRFOIL THICKNESS RATIO ROOT/TIP
EBF	7.28	25.0	0.4	0.14/0.11
USB	7.28	25.0	0.4	0.14/0.11
IBF	8.0	27.5	0.3	0.125/0.105
AJF	8.0	27.5	0.3	0.125/0.105

Only the augmented jet flap and rotating cylinder flap concepts have been flight tested in research aircraft; of the two, the augmented jet flap aircraft provided the majority of the flight testing results discussed here. These aircraft, shown in Figs. 2 and 3, are intended primarily as aircraft flight facilities for advanced STOL low-speed research in general and were not designed specifically for development tests of any particular concept. Specific areas of flight investigation during STOL low-speed takeoff, landing, and terminal operations with the propulsive lift concepts under study are the aerodynamics, power management, ground effects, handling qualities, control and stability augmentation requirements, engine-out characteristics and requirements, noise footprints, certification considerations, and guidance, navigation, and information display requirements for piloted curvilinear approaches to landing.

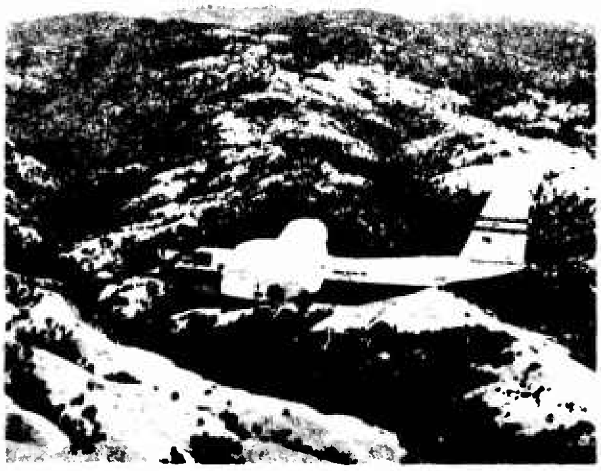

Fig. 2 Augmented Jet Flap STOL Research Aircraft

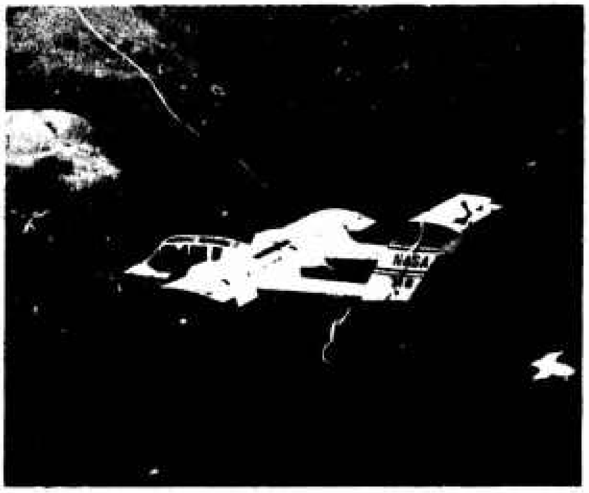

Fig. 3 Rotating Cylinder Flap YOV-10A Research Aircraft

2. PROPULSIVE LIFT CONCEPT AERODYNAMIC COMPARISONS

A nominal takeoff flap configuration was used in testing the four propulsive lift concepts for lift coefficient (C_L) as a function of aircraft angle of attack (α) and the thrust minus drag coefficient (C_D).

The points on the curve in Fig. 4 indicate the typical lift coefficient for STOL aircraft at climb speed with a wing landing of 400 kg/m² (80 pounds per square foot). The thrust required to provide the propulsive lift in terms of thrust-to-weight ratio (T/W) and the climb gradient (γ) for each concept indicates its relative aerodynamic efficiency for takeoff. The upper-surface-blown flap and the augmented jet flap have about a 6° climb gradient with required thrust-to-weight ratios of 0.29 and 0.20, respectively; the IBF and EBF have climb gradients of 3.8° to 4.5°, respectively, with corresponding T/W ratios of 0.235 and 0.30. In general, the one-engine-out climb gradient determines the engine size requirements for propulsive lift aircraft, which for comparable swept-back wing aircraft and equivalent four-engine climb gradient of 13°, results in the EBF requiring a T/W = 0.58; the USB a T/W = 0.50; the IBF a T/W = 0.45; and the AJF a T/W = 0.38.

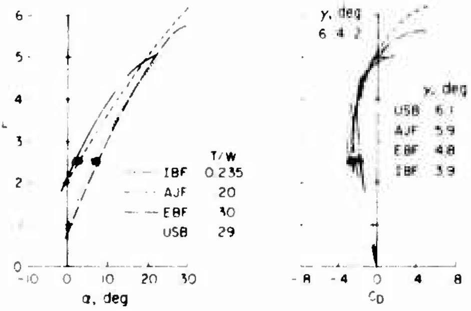

Fig. 4 Comparison of propulsive lift concept aerodynamics

3. AUGMENTED JET FLAP PERFORMANCE AND NOISE

Slotted nozzles were used on the augmented jet flap STOL research aircraft and the large-scale wind tunnel models with straight and swept-back wings. NASA and The Boeing Airplane Company have tested slotted nozzles and a number of variations of multi-element lobed nozzles on the same model. A typical lobed nozzle, augmented jet flap configuration is shown in Fig. 5. The multi-element lobed nozzle provides greater mixing of the primary nozzle air and secondary air, thus improving static performance and reducing noise levels due to entrainment of ambient air between nozzle elements. This nozzle also shifts the blowing jet peak noise to a higher frequency than conventional nozzles, and the augmented flaps and acoustic lining absorb and contain the higher frequency noise levels.

The data in Fig. 6 show the effect of nozzle array area ratio and flap length on the static augmentation ratio, the ratio of total augmented thrust to primary nozzle thrust. The augmentor mixing lengths were derived by varying the ratio of flap mixing length to equivalent nozzle height for a slotted nozzle and a multi-element lobed nozzle (L/h_E). The array area ratio (AAR) is the total nozzle height divided by the equivalent slotted nozzle height. Results for the multi-element lobed nozzle indicate that the greater the AAR, the greater the augmentation ratio up to the limits of the particular test variables. The augmentation ratio for the Buffalo STOL research

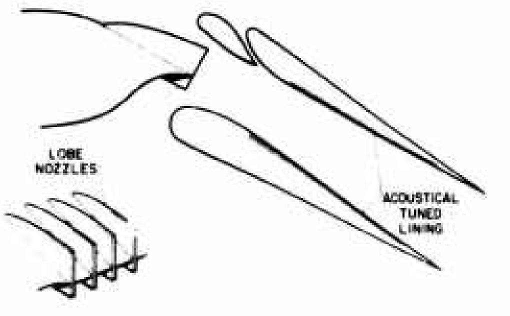

Fig. 5 Typical augmented jet flap with lobed nozzles and acoustic treatment

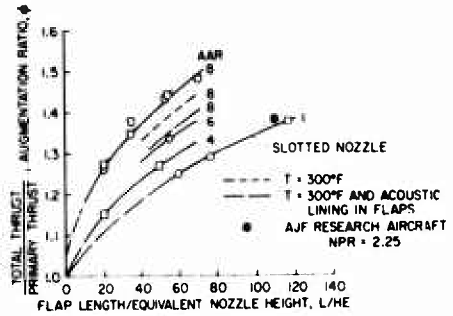

Fig. 6 Effect of nozzle array area ratio and flap length on static augmentation ratio. NPR = 2.6

aircraft with the slotted augmented jet flap was 1.38 at a L/h_E ratio of about 110 as shown. These tests were performed on a 0.7 scale model of the research aircraft augmented jet flap with a pressure ratio of 2.6; the same model was used for design verification testing of the research aircraft. Figure 6 also shows the effects of cold air versus an air temperature of 300°F and acoustic lining in the flaps on the augmentation ratio for the same multi-element nozzle configuration. The reduction of augmentation ratio from 1.44 to 1.35 at a L/h_E ratio of 55 was approximately equally divided between the effect of temperature of 300°F and the effect of rougher acoustically treated surfaces. At an AAR of 8, the number of nozzle lobes per unit length had little or no effect on the augmentation ratio. The flagged symbols denote 172 lobes per unit length and the unflagged symbols, 20 lobes per unit length.

The data in Fig. 7 indicate the effect of forward velocity on the thrust augmentation lapse rate for the augmented jet flap having a nozzle pressure ratio of 2.6. These results were obtained with a small-scale two-dimensional model tested in a wind tunnel. The data show a significant lapse rate of net thrust with speed at a climbout speed of about 50 m/sec (96 knots), resulting in a thrust augmentation ratio of approximately 1.2. A comparison of these data with those for a turbo-fan engine having similar fan characteristics, whose net thrust is approximately 0.9 of the static thrust at 96 knots, yields an effective augmentation ratio for the augmented jet flap of about 1.3. At nozzle pressure ratios lower than 2.6, the lapse rate increases significantly, resulting in very low values of effective thrust augmentation at climb speeds greater than 50 m/sec (ref. 1).

The data in Fig. 8 show the effectiveness of acoustically treated augmented jet flaps having multi-element lobed nozzles for reduction of relatively high pressure ratio jet noise. The figure also includes the augmented jet flap noise level for the research aircraft with no acoustic treatment as measured at the takeoff nozzle pressure ratio of 2.25. For a 21,800 kg (48,000-lb) aircraft at a pressure ratio of 2.6 for takeoff, the total noise at 152.5 m (500-foot) sideline is 23 PNdB less than that with a normal circular nozzle. The lobed nozzle with AAR = 8 reduced the noise by about 12 PNdB, the unlined ejector flaps reduced the noise by an additional 4 PNdB, and the acoustic treatment with tuned lining reduced the noise level still further, by 7 PNdB. Curves are given for two different acoustic linings; the lower values of noise level at takeoff nozzle pressure ratios were obtained with a lining more closely tuned to the higher frequency noise at these pressure ratios and nozzle configuration. Further reduction in noise level results from tuning for the landing lower nozzle pressure ratio conditions. The potential noise level for a 21,800 kg (48,000-lb) aircraft is 92 PNdB during takeoff and 90 PNdB at 152.5 m (500 foot) sideline distance during a −7-1/2 degree landing approach.

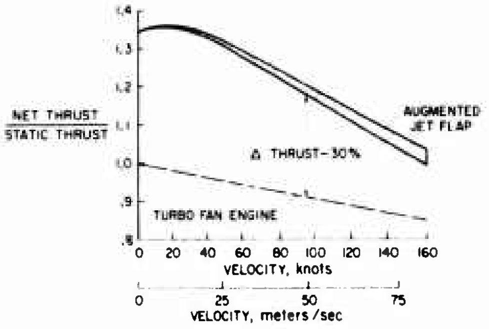

Fig. 7 Effect of velocity on augmentation ratio lapse rate

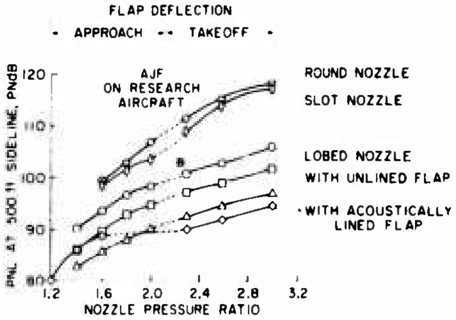

Fig. 8 Effect of augmented jet flap components on noise reduction for range of nozzle pressure ratio

4. FLIGHT TEST RESULTS

Two STOL research aircraft have been in flight testing at Ames Research Center for the past 2-1/2 years. The augmented jet flap STOL research C-8A aircraft (Fig. 2) is a modified deHaviliand Buffalo aircraft having two modified Rolls Royce Spey jet engines instead of propellers, a shortened 23.8 m (78-foot) span wing (compared to the original 28.1 m), an augmented jet flap, and a new lateral control system composed of blown ailerons, spoilers, and outboard augmentor choke. The rotating cylinder flap STOL aircraft (Fig. 3) is a modified North American YOV-10A aircraft having rotating cylinder two-segment flaps, reduced diameter Canadian CL-84 VTOL aircraft propellers, cross-shafting and gear boxes from the CL-84, and two T-53 free turbine engines operated at reduced power. The rotating cylinder is 0.305 m (12 inches) in diameter and driven by hydraulic motors at a rotational speed of 7500 rpm for the flight tests. Both aircraft have fixed landing gear and are design-speed limited to about 82.5 m/sec (160 knots) for cost-saving purposes as the objective of the flight program is the low-speed regime of takeoff and landing. Table 2 compares the pertinent characteristics of the two research aircraft with the Breguet-941; all three have been flown by Robert Innis, the Ames project pilot.

The objective of the augmented jet flap aircraft was to achieve a fan jet aircraft with the STOL takeoff and landing performance of the Breguet-941 propeller-driven aircraft, while retaining good control and one-engine-out characteristics. As can be seen, the geometric characteristics of the aircraft are quite similar, except that the augmented jet flap aircraft has 16 percent higher wing loading. The objective of the rotating cylinder flap aircraft program was to assess handling qualities problems with a propeller-powered STOL aircraft at higher lift coefficients, thus at lower speeds at comparable wing loadings than with Breguet-941.

Table 2 STOL Aircraft Characteristics

CHARACTERISTICS	BREGUET-941	AUGMENTED JET FLAP BUFFALO C-8A	ROTATING CYLINDER FLAP YOV-10A
AIRCRAFT WEIGHT, lb (kg)	38,500 (17,500)	45,000 (20,450)	11,700 (5320)
WING AREA, ft^2 (m^2)	889 (82.5)	865 (80.3)	244 (22.7)
WING ASPECT RATIO	6.52	7.2	4.72
HORIZONTAL TAIL VOLUME	1.1	1.0	0.78
VERTICAL TAIL VOLUME	0.126	0.097	0.153
T/W, (UNINSTALLED)	0.48	0.45	0.45
ENGINE	—	ROLLS ROYCE SPEY 801-SF	LYCOMING T-53-L11

Table 3 Landing Approach Characteristics

	W/S lb/ft^2 (kg/m^2)	V_A knots (m/s)	γ, deg	C_L APPROACH	LIMITING CONDITION
BREGUET-941	43 (215)	60 (30.9)	-7 1/2	3.5	PROXIMITY TO V_{min}
*AUGMENTED JET FLAP AIRCRAFT, BUFFALO	50 (250)	63 (32.4)	-7 1/2	3.7	ABILITY TO FLARE AT TOUCHDOWN AND SINK RATE
ROTATING CYLINDER	47 (235)	57 (29.3)	-8	4.3	LATERAL-DIRECTIONAL CHARACTERISTICS AND α

*STABILITY AUGMENTATION IN THE LATERAL DIRECTIONAL AXIS ONLY

Table 3 shows the landing approach characteristics and reasons for limiting flight speed. The augmented jet flap aircraft was flown between 31 and 34 m/sec (60 and 65 knots) in approach at −7-1/2° descent angle at a lift coefficient of 3.7, equal to that of the Breguet-941, but at a slightly higher wing loading. During these flights, the lateral-directional stability augmentation system reduced the pilot workload considerably, and the ability to flare at touchdown and touchdown sink rate were considered the limiting conditions for further reduction in approach speed. The existing unmodified C-8A Buffalo longitudinal control system was considered inadequate during the initial tests at low forward speeds; as a result, a fully powered elevator with greater control authority and improved control response has recently been installed in the aircraft. The powered elevator improved the ability to flare at touchdown. The rotating cylinder flap aircraft was flown at speeds of 29 to 31 m/sec (55 to 60 knots) up to −8° approaches, which corresponded to a lift coefficient of about 4.3 compared to 3.5 for the Breguet-941. In the pilot's opinion, any further reductions in approach speed for the YOV-10A RCF aircraft were limited by the lateral-directional stability and control characteristics, as well as the aircraft angle of attack.

Figure 9 is a schematic of the lateral control system which is comprised of three elements to provide the rolling moments. These are the drooped blown aileron, upper surface spoiler forward of the aileron, and augmentor choke in the outboard spanwise section of the augmented jet flap. The gearing and magnitude of deflection of the three control surfaces can be varied to provide the desired level of control power and sensitivity. The data in Fig. 10 show lateral control performance (in radians per second squared) of the augmented jet flap aircraft as a function of pilot control wheel angle. Initial control is obtained by blown aileron deflection about a nominal flap angle of 30° and spoiler deflection on the downgoing wing. At 17° of wheel angle, the augmentor choke in the flaps outboard of the engine nacelles is activated to provide a maximum control power of about 0.7 radians/sec². The effectiveness of the control surfaces is about equal. The design objectives of 0.5 radians/sec² and a sensitivity of 0.1 radians/sec²/inch were exceeded. These control characteristics can be modified on the aircraft for research purposes. The maximum utilization of control used by the pilots to date during landing approach and low-speed flight has been a control wheel angle deflection of about 25°.

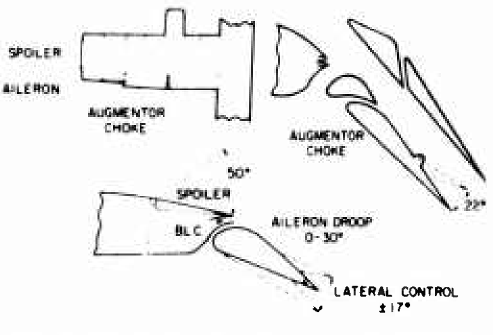

Fig. 9 AJF research aircraft lateral control system

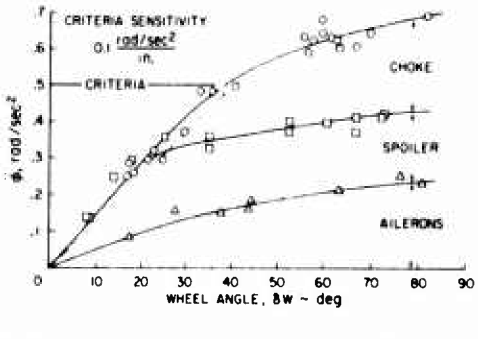

Fig. 10 Lateral control effectiveness at landing approach

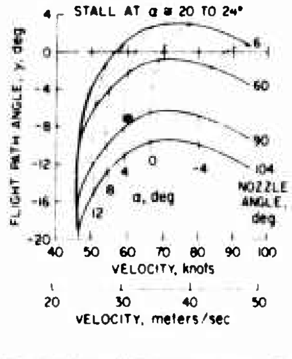

Fig. 11 Low speed descent capability. Gross weight = 40,000 lb. Flap deflection = 65°.

The data in Fig. 11 show flight path descent angle capability of the augmented jet flap aircraft for a range of landing approach forward speeds at 65° flap deflection and fixed throttle setting of 94 percent engine rpm, which corresponds to about 60 percent of maximum thrust. To give greater research flexibility, Pegasus nozzles were installed on the Rolls Royce Spey engines to deflect all the hot thrust, which at landing approach is approximately 60 percent of the total thrust. All the fan air, approximately 40 percent of the thrust, is directed into the wing to the augmented jet flaps and the blown ailerons. The single point on the figure indicates the nominal approach speed of 60 knots and flap angle of 65°, a Pegasus nozzle deflection of 85°, and an angle of attack of 3°, which results in a −7-1/2° approach flight path angle. The margins to stall are greater than 5 m/sec in velocity and nearly 20° in angle of attack as the maximum angle of attack varies from 20° to 24°, depending on the power condition. The pilot also has two variables to control flight path angle, (1) the throttle for small changes once flight path angle is established, and (2) the Pegasus nozzle angle for larger changes, which gives at least a 4° greater descent angle at this approach condition, if desired.

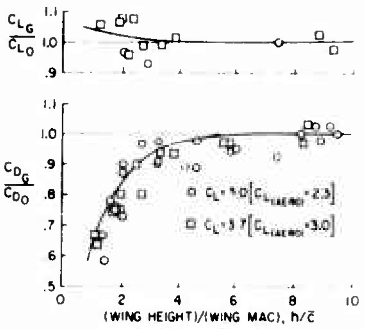

Fig. 12 Effect of ground on AJF research aircraft aerodynamics

The data in Fig. 12 show the effect of ground on the augmented jet flap aircraft as measured in level flight flyovers during the flight test program. In landings, particularly at the lower flight path descent rates of less than 1 m/sec (3 feet per second), there is an increase in lift and a reduction in drag resulting in a definite floating tendency. At −7-1/2° descent angle at higher sink rates, however, the floating tendency was not as apparent, and if floating did occur, power could be cut during the flare to obtain a positive touchdown. The typical nose-down pitching moment was also encountered, requiring significant elevator control of about 8° for trimmed flight. Although the maximum lift coefficient during these close-to-ground flights was about 3.7, the aerodynamic lift coefficient was about 3.0 due to the vectored thrust component in lift from the Pegasus nozzles. The faired curves shown in Fig. 12 are based on a least-squares fit to the data from four test runs using a regression parameter identification technique. With the augmented jet flap at the maximum lift coefficient of 3.7, there was no evidence of a suckdown effect due to ground proximity.

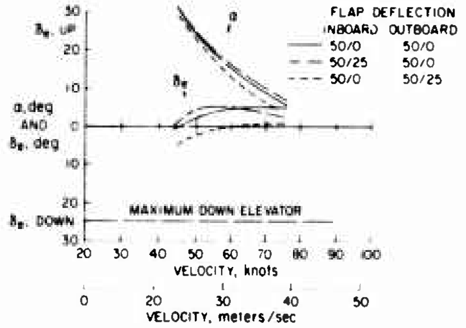

Fig. 13 Effect of spanwise RCF flap deflection on longitudinal characteristics

The data in Fig. 13 show the effect of spanwise variation of rotating cylinder flap deflection on the longitudinal trim and stability of the aircraft. The aircraft has a strong pitch-up characteristic at speeds below about 31 m/sec (60 knots) with flap deflection held at constant angles of 50/0 degrees, on each side of the tail booms, inboard and outboard as shown. With reduced total flap deflection, 30/0 inboard of the tail boom, less elevator control in the nose-down direction was required and the static longitudinal stability was improved, whereas with reduced total flap deflection inboard rather than outboard of boom, the static longitudinal stability was lower at all speeds below 34 m/sec (65 knots).

5. CONCLUDING REMARKS

The oral version of the paper concludes with a short film of the augmented jet flap STOL research aircraft "Buffalo" during short takeoffs and landings with −7-1/2° approaches; a flight in-ground effect at 31 to 36 m/sec (60 to 70 knots) also is shown. The film includes −8° landing approaches performed by the rotating cylinder flap research aircraft (YOV-10A RCF), and indicates the difference in flare compared to the Buffalo. The Buffalo is flared consistently whereas the YOV-10A RCF is flared very little and has solid contact with the ground. Some of this difference in operation of the two aircraft during flare may be due to the difference in landing gear characteristics. The Buffalo has a stiff conventional type landing gear, while the YOV-10A has a softer rough terrain type landing gear similar to that used on the Breguet-941.

The Augmented Jet Flap STOL Research Aircraft "Buffalo" has been flown by 10 pilots (2 NASA, a Boeing Airplane Co., a de Havilland Aircraft Ltd., a Canadian MOT, a Canadian Air Force, a Canadian NAE, a U.S. Air Force, an FAA, and one pilot from the RAE of England). These pilots have evaluated the low-speed flight characteristics during STOL operations for normal two-engine conditions and with one engine out. The advanced flight research and experimental tests with STOLAND installed in the aircraft are scheduled to start during the fall of this year.

REFERENCES

1. Hickey, David H.: V/STOL Aerodynamics: A Review of the Technology. AGARD Paper 1, April 24, 1973.

2. Falarski, Michael D. and Koenig, David G.: Aerodynamic Characteristics of a Large-Scale Model with a Swept Wing and Augmented Jet Flap. NASA TM X-62,029, July 1971.

3. Aoyagi, Kiyoshi; Falarski, Michael D.; And Koenig, David G.: Wind Tunnel Investigation of a Large-Scale Upper Surface Blown-Flap Transport Model having Two Engines. NASA TM X-62,296, August 1973.

4. Aiken, Thomas N.; Aoyagi, Kiyoshi; and Falarski, Michael D.: Aerodynamic Characteristics of a Large-Scale Model with a Swept Wing and a Jet Flap having an Expandable Duct. NASA TM S-62,281, September 1973.

5. Aoyagi, Kiyoshi; Falarski, Michael D., and Koenig, David G.: Wind Tunnel Investigation of a Large-Scale 25° Swept-Wing Jet Transport Model with an External Blowing Triple-Slotted Flap. NASA TM X-62,197, Nov. 1973.

6. Phelps, Arthur E.: Aerodynamics of Upper Surface Blown Flap STOL Technology. NASA SP-320, October 1972.

7. O'Keefe, J. F., and Kelley, G. S.: Design Integration and Noise Studies for Jet STOL Aircraft. Vol. I – Program Summary. NASA CR-114471, May 1972.

8. Roepcke, F. A., and Kelley, G. S.: Design Integration and Noise Studies for Jet STOL Aircraft – System Design and Evaluation Studies – Volume II. NASA CR-114472, May 1972.

9. Campbell, J. M.; Lawrence, R. L.; and O'Keefe, J. V.: Design Integration and Noise Studies for Jet STOL Aircraft – Static Test Program – Volume III. NASA CR-114473, May 1972.

10. Wang, T.; Wright, F.; and Mahal, A.: Design Integration and Noise Studies for Jet STOL Aircraft – Wind Tunnel Test Program – Volume IV. NASA CR-114474, May 1972.

11. Campbell, J. M., Harkonen, D. L., Lawrence, R. L., and O'Keefe, J. V.: Noise Suppression of Improved Augmentors for Jet STOL Aircraft – Task V. NASA CR 114534, January 1973.

12. Bosch, J. C.: Noise Estimates for a Family of Four-Engine Augmentor Wing STOL Aircraft. NASA CR-114633, October 1973.

13. O'Keefe, J. V.; Nickson, T. B.; and True, H. C.: A Comparative Study of Augmentor Wing, Ejector Nozzle and Powered Jet Flap Low Noise STOL Concepts. The Boeing Company, November 1972 (Presented at the 84th Meeting of the Acoustical Society of America).

14. Ashleman, R. H. and Skavdahl, H.: The Development of an Augmentor Wing Jet STOL Research Airplane (Modified C-8A) Volume I – Summary NASA CR-114503, August 1972.

15. Quigley, Hervey C. and Vomaske, Richard F.: Preliminary Results of Flight Tests of the Augmentor-Wing Jet STOL Research Aircraft STOL Technology. NASA SP-320, October 1972.

16. Cichy, D. R.; Harris, J. W.; and MacKay, J. K.: Flight Tests of a Rotating Cylinder Flap on a North American Rockwell YOV-10A Aircraft. NASA CR-2135, November 1972.

17. Weiberg, James A.; Giulianetti, Demo; Gambucci, Bruno; and Innis, Robert C.: Takeoff and Landing Performance and Noise Characteristics of a Deflected STOL Airplane with Interconnected Propellers and Rotating Cylinder Flaps. NASA TM X-62,320, December 1973.

18. Innis Robert C.; Holzhauser, Curt A.; and Quigley, Hervey C.: Airworthiness Considerations for STOL Aircraft. NASA TN D-5594, January 1970.

PROGRESS REPORT ON MECHANICAL FLAPS

PROGRES RECENTS EN HYPERSUSTENTATION MECANIQUE

par

P. PERRIER*, M. LAVENANT**
Avions Marcel Dassault-Breguet Aviation
78, Quai Carnot
92214 SAINT CLOUD

RESUME

Le développement des avions R/STOL nécessite un développement simultané de l'hypersustentation des ailes. Les limitations et les problèmes posés par les hypersustentations motorisées ont incité AMD-BA à tenter la conception d'une hypersustentation mécanique ayant un coefficient de portance supérieur à 4.

Cet objectif n'a pu être atteint qu'en faisant appel à des méthodes de calcul aérodynamique élaborées, dont on expose la méthodologie et les objectifs. Des comparaisons entre le calcul et l'expérience permettent d'apprécier la validité de ces méthodes dans des cas aussi complexes que les écoulements tridimensionnels décollés.

Une voilure à forte hypersustentation mécanique a été définie en associant ces méthodes de calcul et l'expérience acquise par AMD-BA dans la mise au point de systèmes mécaniques avancés. Les résultats acquis en soufflerie sur une maquette complète ont confirmé que ce type d'hypersustentation, est un candidat sérieux pour l'équipement des avions R/STOL.

SUMMARY

Development of R/STOL aircraft implies simultaneous development of wing lift augmentation. Limitations and problems associated with powered lift have convinced AMD-BA of the interest of designing mechanical high lift devices capable of lift coefficient greater than 4.

To obtain such a high figure, full use of advanced computerized aerodynamics has been necessary. Methodology and objectives are described. Comparisons between estimated and test results are given permitting to appreciate the validity of the procedure in complex cases with tridimensional and separated flow.

A wing with powerful mechanical high lift devices has been designed with a combined use of theoretical aerodynamic methods and practical experience gained by AMD-BA in the development of advanced mechanical systems. Wind tunnel tests, on a complete model, have confirmed that this type of high lift schemes is a serious candidate for R/STOL aircraft applications.

AVANT PROPOS

La conférence qui va suivre résume certains résultats obtenus en hypersustentation par la Société DASSAULT-BREGUET (AMD-BA) dans le cadre d'études préliminaires concernant les avions à décollage et atterrissage courts. Ces études, effectuées en 1971, 1972 et 1973, ont été partiellement financées par un contrat du Ministère des Transports Français.

Nous remercions la Société DASSAULT-BREGUET d'avoir bien voulu nous permettre de publier les résultats essentiels de ces études.

1. INTRODUCTION

1.1. Les besoins :

La nécessité de développer l'hypersustentation des ailes apparaît lorsqu'on veut faire atterrir sur des pistes courtes des avions de transport civils capables d'une grande vitesse de croisière.

On peut voir en effet, sur la figure 1, que pour utiliser des pistes de l'ordre de 600 à 1200 m il faut pratiquer des vitesses d'approche (V_{REF}) de l'ordre de 80 à 110 noeuds. Cela entraîne, pour des avions ayant une charge alaire comprise entre 400 et 600 kg/m^2, des coefficients de portance en approche (C_{ZREF}) de l'ordre de 2 à 6. Les avions classiques actuels utilisant des C_{ZREF} d'environ 1,6 il est nécessaire de faire un effort important sur l'hypersustentation.

1.2. Les hypersustentations motorisées :

Devant l'ampleur de l'effort à entreprendre la plupart des constructeurs d'avions ou organismes de recherche se sont tournés vers le développement des hypersustentations motorisées, la puissance des moteurs venant suppléer l'insuffisance de l'hypersustentation mécanique classique.

---

* Division des Etudes Avancées, Aérodynamique Théorique
** Division des Avions STOL.

Les possibilités des hypersustentations motorisées sont bien connues (réf. 1 à 26) et les très forts coefficients de portance maximaux obtenus, 6 à 10, ont souvent impressionné les non-spécialistes. Malheureusement, lorsqu'on tient compte des réalités opérationnelles, les pannes possibles, par exemple, on est bien obligé de constater que le coefficient de portance utilisable en approche, C_{ZREF}, est d'environ 3,5 à 4. C'est cependant un progrès considérable par rapport au $C_{ZREF} = 1,6$ d'aujourd'hui, et on peut constater, sur la figure 1, que cela est suffisant pour atterrir en 2 000 pieds.

Mais les hypersustentations motorisées souffrent de graves limitations qui peuvent condamner leur avenir. En effet, on peut dire, sans entrer dans les détails, que pour toutes les formules, il est difficile de justifier le comportement après panne d'un moteur, ou après éclatement d'une tuyauterie pour les solutions à soufflage interne (réf. 13 à 26). L'expérimentation en vol des prototypes AMST BOEING et MAC DONNELL-DOUGLAS apportera sur ce point des précisions importantes. D'autre part, d'après les connaissances actuelles (réf. 27 à 43), toute augmentation importante de portance due à la motorisation augmente inéluctablement plus ou moins le bruit généré par les moteurs eux-mêmes.

1.3. L'hypersustentation mécanique :

Le niveau de bruit paraissant être un élément critique du système de transport civil R/STOL, notre Société a préféré poursuivre le développement de l'hypersustentation mécanique, car ses caractéristiques de bruit se présentent de façon plus favorable.

Nous avons été encouragés dans ce choix par l'examen du développement historique de l'hypersustentation mécanique. On peut voir, sur la figure 2, qu'il n'est pas utopique d'envisager des coefficients de portance maximaux supérieurs à 4 dans les années 1980 à 1990. Or, en tenant compte de la composante de la poussée, normale à la vitesse, qui est importante dans le cas d'un avion très motorisé, cela veut dire qu'on peut espérer pratiquer en approche un C_{ZREF} de l'ordre de 3. D'après la figure 1, cela entraînerait une charge alaire d'environ 600 kg/m^2 pour un RTOL atterrissant en 4000 pieds, et d'environ 300 kg/m^2 pour un STOL atterrissant en 2000 pieds.

Pour réussir la conception d'une hypersustentation mécanique ayant un coefficient de portance maximal supérieur à 4, nous avons choisi la politique de développement suivante :

- Utilisation de méthodes de calculs aérodynamiques sophistiquées capables de simuler des écoulements tridimensionnels avec décollement
- Utilisation de l'expérience acquise par AMD-BA dans la mise au point de systèmes mécaniques avancés (avion à flèche variable en particulier).
- Itérations fréquentes entre les aérodynamiciens et les mécaniciens pour que le produit final ressemble plus à une voilure d'avion qu'à un gadget de laboratoire.

2. METHODOLOGIE DE RECONSTITUTION PAR LE CALCUL

2.1. Les limites des méthodes de corrélation.

Nous allons montrer que les méthodes basées sur la corrélation de résultats globaux sont inadéquates si on veut tenir compte de l'ensemble des éléments d'un système d'hypersustentation.

En effet, ces éléments ne sont pas liés seulement à la forme en plan, à la flèche, à l'allongement et au braquage des becs et des volets, sinon on aurait réussi depuis longtemps à corréler l'ensemble des résultats de soufflerie disponibles en gradient de portance ou de stabilité, en fonction de paramètres en nombre limité. Il n'est bien entendu pas question de tenir compte des formes exactes sans entrer dans une augmentation exagérée du nombre des paramètres. On pourrait aussi tenir compte des résultats d'essais en vol qui sont malheureusement en nombre beaucoup plus restreint, ce qui limiterait encore le nombre des paramètres significatifs contrôlés par des essais.

En fait, cette méthode de corrélation reviendrait à améliorer à l'aide de l'ensemble de tous les résultats didponibles les schémas simplifiés (fig. 3) qui avaient été utilisés par LOWRY (réf. 44) dans un rapport déjà ancien pour donner une méthode d'évaluation rapide de volets. Si on utilise ce rapport sur un grand nombre de cas, tous les bureaux d'études savent que l'on obtient souvent un ordre de grandeur approximativement correct du Cz_0 voire du Cz_α à portance nulle mais qu'on est incapable de faire une quantification à grand Cz de différentes hypersustentations.

En faisant une corrélation du type qui vient d'être décrit, on ne peut faire apparaître en principe que l'aspect de dégradation par rapport à une valeur "théorique" de référence.

Les valeurs "théoriques" de référence utilisées consistent essentiellement en résultats de calculs préalables en fluides parfaits qui donneraient pour une configuration partielle ou complète, une valeur du gradient de portance (Cz_α) ou de la stabilité et, vu l'imprécision des corrélations possibles on arrive malheureusement rapidement à la conclusion suivante : il est illusoire d'augmenter la précision de calcul des Cz_α ou des pentes de portance, et il est souhaitable au contraire de garder un schéma suffisamment simple, par exemple celui décrit dans la méthode de LOWRY ou bien d'autres méthodes simplifiées basées uniquement sur l'effet de la surface, de la forme en plan, de l'allongement et de la flèche à 25 % par exemple, pour obtenir une valeur approchée du Cz_α qui ne nuit pas à la précision ultérieure des résultats. On ne sait plus alors d'où viennent les erreurs ou les efficacités.

Cependant on saura ainsi rapidement si le résultat à atteindre est ambitieux ou conservatif par rapport à l'ensemble des résultats disponibles,se rappelant que plus un projet est ambitieux, plus la corrélation est douteuse.

Nous ne rejetons cependant pas la méthode des corrélations mais la renvoyons à un stade très préliminaire ou global de la conception de l'hypersustentation. Elle corrèle suffisamment de vérités de bon sens pour garder une utilité au niveau d'un jugement global.

2.2. La nécessité d'éviter une simplification excessive des équations

2.2.1. Problèmes de géométrie :

Entre une méthode de corrélation simplifiée qui vient d'être décrite (qui nécessite auparavant un travail de dépouillement d'essais très important) et la méthode qu'il est souhaitable de réaliser pour savoir déterminer d'une façon scientifique sinon optimale le dessin complet d'un avion hypersustenté, il est intéressant de savoir qu'il y a un pas technique très important. Le saut à faire, pour passer de cette représentation sommaire de corrélation traditionnelle aux présentations valables permettant de concevoir complètement une hypersustentation, doit prendre en compte une représentation géométrique très complète des corps : non seulement le positionnement après braquage par une cinématique complexe, mais la totalité des formes, la totalité des effets d'envergure, sauf les modifications très locales qui seront réservées aux essais en soufflerie.

2.2.2. Problèmes de fluide parfait :

Il faut absolument que la méthode de calcul utilisée permette de faire une comparaison rigoureuse et sans aucune correction, avec des essais de soufflerie. Certaines parties du programme de calcul utilisant des théories qui ont une importance plus faible que d'autres, il n'est pas souhaitable de faire systématiquement le calcul avec une méthode extrêmement compliquée faisant intervenir l'aspect complet des phénomènes, car le prix de l'étude risquerait d'être trop élevé. Cependant, on ne pourra justifier les résultats qu'avec le programme le plus complet de calculs pour évaluer les limites de certaines simplifications. Par exemple, il est nécessaire de faire un calcul tridimensionnel complet d'une voilure hypersustentée. Or, ce calcul est naturellement très coûteux si on prend en compte d'un seul coup la totalité d'une voilure, et une méthode approchée assez efficace consiste à calculer le champ induit local dans une section sous l'effet des vitesses induites non seulement verticales mais transversales et longitudinales et à introduire ce champ induit dans un calcul simplifié. Ce résultat est rarement suffisant dans la majorité des cas d'hypersustentation. Il doit être abandonné complètement quand on traite le voisinage d'un fuselage ou d'un fuseau réacteur. Mais il permet de faire une économie notable.

2.2.3. Problème de fluide visqueux.

Il est encore plus dangereux de simplifier les équations relatives aux fluides visqueux. En effet, une hypothèse sur les équations de fluides parfaits, peut être facilement vérifiable car l'on dispose de programmes de calcul capables de prendre en compte des configurations complexes. Ce n'est pas le cas avec des fluides visqueux car une solution numérique exacte n'est pratiquement jamais disponible, étant donné qu'on est très loin d'appréhender de façon correcte la structure même des écoulements turbulents. Ce n'est pas une question de discrétisation mais d'impossibilité de calcul. On rappelle qu'il est actuellement possible de faire des calculs en résolvant les équations de NAVIER STOKES sur des configurations simples à des Reynolds relativement limités, mais c'est à la limite de ce qui est acceptable comme temps de calcul sur les ordinateurs actuels. Un progrès peut être espéré dans l'avenir ; malheureusement le but est trop lointain. Il est certain que les validations ne pourront pas être faites par comparaison théorie-théorie, mais par comparaison théorie-expérience. Ceci veut dire que l'on doit nécessairement faire une programmation qui soit capable de reconstituer les schématisations fondamentales ou les expériences fondamentales disponibles, sinon il sera impossible de faire un contrôle, avec le même programme de calcul, des simplifications obligatoires introduites.

Rappelons que, si l'on admet de faire une simplification excessive au niveau du calcul, on restreint automatiquement la gamme possible de paramètres de conception. Par exemple, si l'on renonce à faire une certaine évaluation correcte de la transition de la couche limite, on renonce automatiquement à la possibilité de faire un contrôle précis de résultats de soufflerie où la transition apparaît toujours comme un paramètre très important, d'où une difficulté de corréler la soufflerie et le vol par le calcul.

Autre exemple : on sait que les problèmes de mélange jouent un rôle fondamental dans les systèmes hypersustentateurs. Or, ce problème de mélange fait intervenir une schématisation qui rappelle le problème du jet pariétal et le problème du mélange sillage/couche limite. Ces deux problèmes ne sont pas justifiables des modèles simples de turbulence : longueur de mélange, énergie turbulente moyenne, etc... En effet la contrainte de cisaillement turbulente maximum n'est pas reliée de façon directe avec le gradient de vitesse locale. Les effets de restructuration de la turbulence moyenne y jouent un rôle fondamental, l'effet des turbulences extérieures et des transitions y est également fondamental ; enfin on peut rappeler que des modèles améliorés dans une hypothèse "couche limite" sont insuffisants dans la mesure où les dimensions des zones de mélange sont d'ordre de grandeur comparable aux rayons de courbure locaux des profils. La possibilité ou l'impossibilité d'optimiser des fentes de soufflage minces sur des profils courbes à grande incidence résultera de la validité des méthodes retenues.

2.3. Conclusion : quelle est la schématisation souhaitable ?

En résumé. le calcul de l'hypersustentation doit constituer en une reconstitution tridimensionnelle des écoulements avec zones turbulentes collées et avec décollement, y compris leur aspect instationnaire. Ce but peut paraître hors de portée. En fait, si l'on admet de limiter un certain nombre de calculs à l'état où sont parvenues les techniques de calcul actuelles, c'est déjà une "somme" de toutes les meilleures méthodes de calcul élémentaires disponibles actuellement, intégrées dans un ensemble complet.

On doit insister sur le fait que cette reconstitution doit être faite à l'aide d'éléments tous validés et tous contrôlés étant donné qu'on arrive à une dimension de programme telle qu'il est hors de question d'obtenir par une vérification globale, le contrôle du programme. On tombe dans le cadre des travaux sur les gros systèmes informatiques avec la nécessité de fonctionnement systématique prolongé pour déterminer l'ensemble des erreurs de programmation, d'un entretien suivi du programme par une équipe d'ingénieurs de façon à continuellement mettre à jour le programme. Enfin, une équipe de scientifiques doit être capable de tester les sous-programmes en vue de les critiquer et de les améliorer sur toute nouvelle expérience disponible.

3. MOYENS DE CALCULS DISPONIBLES

3.1. Calculs en fluide parfait

Ces calculs tridimensionnels peuvent être considérés comme de la routine tant que l'écoulement, bien que localement supersonique, n'a pas de chocs. Nous utilisons soit la méthode intégrale, soit la méthode des éléments finis.

3.1.1. Méthode intégrale :

Dans la méthode intégrale, nous schématisons la surface du corps par un ensemble de quadrilatères portant des répartitions uniformes surfaciques de sources et de tourbillons, l'espace étant également dans les zones compressibles à fort gradient ou rotationnel rempli d'hexaèdres de densité uniforme volumique de sources et de tourbillons pour résoudre l'équation de POISSON :

$$\Delta\phi = - M^2 \frac{dv}{ds} + \frac{1}{C_p}\frac{d}{ds}\,\vec{V}.\overrightarrow{\text{grad } s}$$

Cette équation est rigoureuse pour les fluides non visqueux compressibles et nous la résolvons par itération de résolution des systèmes linéaires correspondant aux conditions linéaires de contact ($\overrightarrow{\text{grad}}\ \phi\ .\ \vec{n} = 0$ sur le corps) et non linéaires de JOUKOWSKI traitée par la méthode de NEWTON à chaque pas. Cette méthode est le développement ultime de la méthode de singularité initiée par FUHRMANN (réf. 45) et que A.M.O. SMITH a le premier généralisée au calcul non portant tridimensionnel (réf. 46). Nous utilisons depuis de nombreuses années sa généralisation au cas portant (réf. 47) en tenant compte des effets non linéaires attachés aux conditions de JOUKOWSKI, à l'enroulement de la nappe des tourbillons avals (réf.48) et à la compressibilité dont une présentation claire est donnée réf. 49.

Pour résoudre des problèmes très précis d'hypersustentation, la dimension des matrices à laquelle nous limitent nos ordinateurs actuels (de l'ordre de 1500) ne nous permet pas une précision suffisante localement. Ceci nous a conduit à résoudre approximativement des tailles de matrices nettement plus grandes (de l'ordre de dix fois la précédente) en approchant le champ de vitesse créé en un point par le champ lointain approché créé par la discrétisation légère, et en ne résolvant que le système local des facettes serrées voisines de taille plus restreinte (fig.4). On dispose ainsi toujours d'au moins 250 facettes par section caractéristique de profils hypersustentés, ce qui donne une précision suffisante pour le calcul ultérieur des couches limites et zones visqueuses. De même, on ne réitère qu'au stade des discrétisations légères les interactions avec l'empennage pour l'évaluation des moments globaux.

3.1.2. Méthode des éléments finis :

Quand des problèmes de mauvais conditonnement de la matrice liés à des conditions aux limites trop contraignantes (élargissant la largeur des termes forts d'influences réciproques) se posent, nous utilisons une méthode beaucoup plus tolérante qui est la méthode des éléments finis (réf. 50). Nous avons développé (réf. 51) cette méthode en tridimensionnel compressible avec beaucoup de succès. Elle présente par rapport à la méthode intégrale l'inconvénient de nécessiter le maillage (fig. 5) de tout l'espace autour du corps (du moins jusqu'à une certaine distance de l'ordre de l'envergure), mais présente toujours des matrices bien conditionnées, en bandes étroites.

Les conditions aux limites finies sont plus facilement prises en compte que les infinies. Ceci est un avantage pour la reconstitution d'essais en soufflerie.

3.2. Calculs de couplage fluide visqueux-fluide parfait.

Connaissant les couches limites et zones visqueuses, il est nécessaire de reprendre les calculs de fluide parfait de façon à prendre en compte les couplages. Deux voies sont possibles : soit la méthode des couplages faibles, soit la méthode d'interaction complète.

Dans la méthode des couplages faibles, nous engraissons les corps des épaisseurs de déplacement des couches limites et mettons dans l'espace l'équivalent des sillages en écoulement de puits et rotationnel. Ce processus n'est théoriquement pas convergent si l'on itère sans précaution (réf. 52). Il est nécessaire de partir d'une solution initiale réaliste, et de se limiter à 2 itérations en excluant les zones de couplage singulier (bord de fuite essentiellement) qu'on peut considérer comme des zones de couplage fort.

Pour les couplages forts (ou singuliers) nous faisons une prévision a priori des zones décollées pour avoir leur forme à partir de 2 ou 3 positions du point de décollement, données a priori - ou bien nous nous servons de solutions de NAVIER STOKES. C'est par itération et interpolation entre ces différentes solutions complètes que nous reconstituons directement un cas de couplage fort, toute tentative de solution directe (en dehors des solutions exactes de NAVIER STOKES, mais à des Reynolds trop faibles) se révélant extrêmement instable (fig 6). De toute façon, on peut considérer ce point comme important mais non critique par rapport à la méconnaissance des structures turbulentes des écoulements - excepté pour les modèles trop complexes de zones décollées tridimensionnelles qui doivent être nettement améliorés.

3.3. Calculs de fluides visqueux.

3.3.1. Fluides visqueux laminaires :

Les calculs laminaires tridimensionnels ne présentent pas de difficultés particulières dans le cadre des hypothèses de couches limites où ils sont maintenant classiques (réf. 53 et 54). Les calculs hors hypothèse de couche limite peuvent, à faible nombre de Reynolds, être effectués maintenant directement à l'aide de la résolution des équations de NAVIER STOKES. Nous utilisons de plus en plus cette voie à l'aide de la méthode des éléments finis qui est bien adaptée à ce traitement d'équations non linéaires par une suite de minimisations garantissant une distance à la solution exacte suffisamment faible (réf. 55). Les limitations dues au nombre de Reynolds n'empêchent pas un réalisme de la représentation des zones visqueuses décollées complexes dont on est loin de disposer en turbulent et qui, par conséquent, fournit des modèles souvent très valables dès que Re > 500.

3.3.2. Fluides visqueux turbulents :

Les méthodes de traitement de la turbulence font appel soit à un traitement local où le tenseur de frottement visqueux est relié à une donnée locale (en général le gradient de vitesse local) généralisé par l'emploi d'une longueur intégrale faisant intervenir la dimension de la zone visqueuse, soit à un traitement Lagrangien qui suit le développement des cisaillements dans le fluide. Seule la deuxième méthode est théoriquement exacte (réf. 56) mais le délai d'aboutissement des recherches théoriques correspondantes le réserve à un futur qu'on espère rapproché. Nous utilisons systématiquement par conséquent le calcul par la méthode des différences finies du traitement local de la turbulence. Nous avons renoncé cependant aux modèles de longueur de mélange pour des modèles de longueur de dissipation et l'utilisation de l'énergie cinétique moyenne suivant la méthode aux différences finies de SPALDING (réf. 57). Si les résultats sont équivalents aux méthodes plus classiques telles que celles de CEBECI et SMITH (réf. 58) on peut seules les utiliser dans les cas complexes (fig. 7) de mélanges de sillages et de couches limites (réf. 59).

On peut considérer que le traitement jusqu'au décollement des couches limites turbulentes tridimensionnelles est ainsi très suffisamment obtenu mais qu'il n'en est pas de même du traitement des zones de jet pariétal, à forte courbure où des progrès énormes restent à faire ainsi qu'au voisinage des éclatements de sillages. De plus, on rappelle la méconnaissance relative des phénomènes de transition très importants pour la transposition au vol et la validité des essais de soufflerie.

Une revue détaillée des problèmes correspondants est donnée dans la référence 60. On retiendra que c'est surtout dans ce domaine que l'amélioration des méthodes de calcul aux différences finies actuelles risque d'améliorer le plus nos moyens de calcul, et par conséquent la qualité des hypersustentations conçues à l'aide de ces calculs. On insiste à nouveau sur le fait que, désormais, c'est seulement par des expériences et théories fondamentales que se fera une amélioration de ce calcul des zones turbulentes.

4. RESULTATS DE CALCUL - COMPARAISONS

4.1. Calculs avec et sans décollements.

La comparaison des résultats expérimentaux aux résultats théoriques ne sera significative qu'avec décollements. On peut considérer en effet que sans décollement, un écart ne peut venir que d'une mauvaise discrétisation de calcul. Sur la figure 8, une comparaison portant sur une maquette en flèche de 4 m d'envergure en 5 corps montre le type de recoupement qu'il est possible d'effectuer. Figure 9 des tracés ordinateur montrent la présentation des résultats de calcul en Cp, H de couche limite et en structure et profil de vitesses qui servent de base aux comparaisons fines de compréhension. Sur la figure 9, des comparaisons à $\alpha = 30°$ montrent qu'il est possible d'obtenir de bons recoupements en pression sur des écoulements très décollés sur l'aile en flèche précédente ; une prise en compte de l'aérodistorsion de la maquette a été nécessaire, comme pour un avion réel.

Le calcul des sillages ne présente pas de difficultés, mais des configurations complexes d'interruption de volets introduisent des sillages compliqués, tels ceux que l'on donne figure 10 et dont la partie interne a été bien reconstituée en soufflerie.

4.2. Influence du nombre de Reynolds

Dans les résultats présentés ci-dessus, l'effet du nombre de Reynolds est prépondérant. On donne sur la figure 11 l'influence du Reynolds sur la portance de la configuration 3 corps présentée en haut de la figure 9, où l'effet de l'établissement d'une bulle de décollement est très important. On voit que les courbes de portance sont très différentes, et ceci revêt une grande importance pour la transposition au vol des résultats de soufflerie après décrochage. Un des mérites non négligeables des calculs préalables de comparaison soufflerie-vol sera de pouvoir éliminer les choix de maquettes ou de souffleries inadéquats à l'aide de diagrammes analogues à ceux de la figure 12 : celui-ci donne pour le MERCURE les zones possibles de fonctionnement en fonction du nombre de Reynolds unitaire de la corde.

4.3. Comparaisons détaillées des zones visqueuses.

On donne figure 13 deux exemples de comparaison de résultats de mesure et de méthodes de calcul par différences finies sur les profils de vitesse en aval d'une fente. La réorganisation des structures turbulentes se traduit par une dissipation plus ou moins rapide des creux de vitesse amont. Cette réorganisation prend place le plus souvent sur toute la longueur du profil hypersustenté mettant en évidence l'importance de ce phénomène qui gouverne les possibilités de récupération de pression des couches visqueuses malgré les gradients de pression défavorables. Figure 14, le résultat présenté est relatif à des mesures effectuées en vol au bord de fuite de l'aile hypersustentée du MIRAGE G-01. Des comparaisons sur les effets globaux instationnaires semblent également encourageants ; là aussi, l'intérêt fondamental d'une meilleure compréhension de la structure de la turbulence est évident.

4.4. Conclusions.

Les quelques comparaisons que nous avons présentées ci-dessus (et un ensemble plus complet donné dans la référence 52) permettent d'avancer les conclusions suivantes que nous donnons en guise de bilan de la validité de notre système de calcul théorique :

- l'état actuel des méthodes de calculs tridimensionnels compressibles sans décollements importants est assez satisfaisant,
- la prévision des effets du nombre de Reynolds est correcte, excepté pour les effets liés à la transition (maquettes de soufflerie)
- un perfectionnement du traitement des zones visqueuses turbulentes complexes est souhaitable.

Bien que notre connaissance actuelle d'un certain nombre de modèles simples de simulation des écoulements turbulents permette déjà des calculs globalement valables, les progrès évidents restant à faire laissent entrevoir des gains ultérieurs. Ces progrès devront porter au stade de la recherche fondamentale sur la mise en évidence de modèles turbulents plus universels (pour des calculs globaux) - ou à défaut d'être universels, plus sophistiqués pour être à même de suivre la restructuration des zones turbulentes et leur mélange ou leur dissipation dans des processus tridimensionnels et instationnaires de confluence ou de dissipation (éclatement de vortex, ou sillages, par exemple).

Avec les limitations évoquées ci-dessus, on peut maintenant utiliser l'outil informatique pour concevoir complètement les formes et positions relatives des éléments d'un dispositif hypersustentateur complet. Ce travail peut être considéré d'abord comme un moyen de travail précis de routine grâce à la comparaison globale des portance, traînée et stabilité calculées des différentes configurations à l'étude : on peut souvent effectuer ainsi des comparaisons portant sur des dizaines de configurations, chacune avec sa recherche propre de positions optimales en fente et surplomb (exemple de recherche d'optimum fig. 15) des différents corps. Mais ce travail apporte aussi la possibilité de comprendre le "pourquoi" de chaque résultat, sa sensibilité aux hypothèses ou théories, et de voir quelles sont les possibilités d'une amélioration et ses limites.

On retiendra également que les calculs sophistiqués qui sont présentés ici ne diminuent pas les besoins en essais de soufflerie. Ils conduisent par contre à les repenser : les essais sommaires sont maintenant à compléter par des essais mieux préparés où tout est en place pour essayer de comprendre un écart théorie-expérience : la maquette est équipée de mesures spécialisées d'exploration de sillages, de couches limites, etc... pour détecter ce qui n'est pas conforme au modèle mathématique et n'a pu être utilisé à fond dans l'optimisation théorique préalable.

5. CONCEPTION D'UNE VOILURE A FORTE HYPERSUSTENTATION MECANIQUE

Il convient maintenant de voir comment on peut utiliser les moyens de calcul précédents pour la conception d'une voilure à forte hypersustentation mécanique.

Le premier travail a consisté à définir un profil de base aussi bien lisse qu'hypersustenté. Une épaisseur relative de 12,3 % a été choisie afin de ne pas trop compromettre les performances de croisière, le profil étant d'un type avancé mais non supercritique. Le bec de bord d'attaque et les volets ont été définis après de nombreuses itérations entre les désirs des aérodynamiciens et ceux des responsables de la structure, comme si on allait construire rapidement un avion et non pas seulement une maquette de soufflerie. Cela est très important pour apprécier la crédibilité des résultats obtenus.

La forme en plan de la voilure est caractérisée par une flèche à 25 % de l'ordre de 25°, et un allongement d'environ 10, les volets s'étendent sur toute l'envergure. Les profils de définition de la voilure ont été obtenus par évolution progressive à partir du profil de base. Les critères retenus pour la définition de ces profils étaient, bien entendu, l'importance du coefficient de portance, mais aussi la qualité de l'évolution du coefficient de moment de tangage, aussi bien en configuration lisse qu'hypersustentée, et jusqu'aux très grandes incidences.

Pour bien mesurer l'importance du travail effectué, il ne faut pas perdre de vue que la voilure hypersustentée est obtenue après déplacement des becs et des volets suivant leurs cinématiques respectives et que, par conséquent, toute modification de forme ou de réglage ne peut être définie et évaluée qu'après un grand nombre d'itérations mettant simultanément en jeu les programmes de calcul géométriques et aérodynamiques. Les contraintes géométriques peuvent parfois empêcher d'avoir localement le réglage ou la forme que l'on souhaiterait.

Pour compléter la démonstration de la crédibilité de l'hypersustentation mécanique proposée, nous avons entrepris la construction d'une maquette structurale. Cette maquette représente la moitié de la voilure interne d'un avion de transport civil, à l'échelle 1/2. La conception de la cinématique de volets a pu être vérifiée sur ce banc d'essai ainsi que celle des commandes de vol. La figure 16 montre une photographie de cette maquette, en configuration d'atterrissage.

6. ESSAIS EN SOUFFLERIE D'UNE MAQUETTE COMPLETE

Pour aller plus loin qu'avec un simple essai de principe, nous avons construit une maquette complète d'un avion de transport civil R/STOL équipée de l'hypersustentation mécanique étudiée précédemment.

La maquette aérodynamique que l'on peut voir sur la photographie de la figure 17 est en particulier équipée de gouvernes sur les trois axes. Les essais ont été effectués avec et sans nacelles motrices.

Après résolution de quelques problèmes de mise au point, nous avons obtenu les résultats globaux exposés sur la figure 18. On peut constater que le coefficient de portance maximal dépasse nettement 4, ce qui nous récompense des efforts entrepris. D'autre part, la stabilité obtenue est bonne, avec seulement une petite instabilité observée quelques degrés après le décrochage, précédant l'hyperstabilité définitive. On peut donc dire que la configuration retenue est particulièrement saine, malgré ses hautes performances.

Les résultats obtenus dépendent étroitement du nombre de Reynolds, comme prévu par le calcul, car la maquette aérodynamique fonctionne avec des décollements laminaires, contrairement à l'avion réel qui fonctionnera avec des décollements turbulents. On a pu ainsi constater que l'ensemble de la courbe "portance/incidence" se décalait vers le haut, comme prévu par le calcul, à mesure que la vitesse de la soufflerie augmentait. Cela pose quelques problèmes d'extrapolation.

L'ensemble des résultats obtenus en soufflerie a permis de fabriquer un jeu complet de données pour constituer un modèle de simulation. On a pu ainsi évaluer, sur simulateur, les qualités de vol en approche finale, avec ou sans aides au pilotage.

7. CONCLUSION

Grâce aux progrès réalisés en aérodynamique théorique, on peut dire que les résultats acquis au cours de cette étude dans les domaines suivants :

- aérodynamique
- performances
- qualités de vol
- structure
- coûts,

montrent que ce type d'hypersustentation mécanique est un candidat sérieux pour l'équipement des avions R/STOL.

REFERENCES

Cette liste contient seulement un nombre limité de références (44 à 60) pour les problèmes spécifiques de mécanique des fluides pour lesquels une bibliographie plus complète est donnée dans la référence 60.

1 - CARRIERE, EICHELBRENNER, POISSON-QUINTON : Contribution théorique et expérimentale à l'étude du contrôle de couche limite par soufflage ONERA RAPPORT 1/2261 A, 1958.

2 - POISSON-QUINTON, LEPAGE : Synthèse des recherches françaises sur les contrôles de couche limite et de circulation. ONERA RAPPORT 3/1727 A, 1959.

3 - M. P. FINK : Aerodynamic characteristics, temperature, and noise measurements of a large-scale external-flow jet-augmented-flap model with turbojet engines operating. NASA TN D-943, 1961.

4 - J. WILLIAMS, S.F.J. BUTLER : Aerodynamic aspects of boundary layer control for high lift at low speeds. AGARD REPORT 414, 1963.

5 - R. LÖHR : Erhöhung des Maximalauftriebes eines Rechteckflügels in Bodennähe durch kombiniertes Ausblasen an der Flügelnase und an der Hinterkantenklappe. DLR FB 64-02, 1964.

6 - L.P. PARLETT, M.P. FINK, D.C. FREEMAN : Wind tunnel investigation of a large jet transport model equipped with an external-flow jet flap. NASA TN D-4928, 1968.

7 - L.S. ROLLS, A.M. COOK, R.C. INNIS : Flight-determined aerodynamic properties of a jet-augmented, auxiliary-flap, direct lift control system including correlation with wind-tunnel results. NASA TN D-5128, 1969.

8 - K. AOYAGI, S.O. DICKINSON : Investigation of a 0.3 scale jet-transport model having a jet-augmented boundary-layer-control flap with direct-lift control capability. NASA TN D-5129, 1969.

9 - L.P. PARLETT, J.P. SHIVERS : Wind tunnel investigation of a STOL aircraft configuration equipped with an external-flow jet flap. NASA TN D-5364, 1969.

10 - D.C. FREEMAN, S.B. GRAFTON, R. d'AMATO : Static and dynamic stability derivatives of a model of a jet transport equipped with external-flow jet-augmented flaps. NASA TN D-5408, 1969.

11 - C.R. TAYLOR : Flight test results of a trailing edge flap designed for direct-lift control. BOEING NASA CR-1426, 1969.

12 - L.P. PARLETT, D.C. FREEMAN, C.C. SMITH : Wind tunnel investigation of a jet transport airplane configuration with high thrust-weight ratio and external-flow jet flap. NASA TN D-6058, 1970.

13 - R.D. VOGLER : Wind tunnel investigation of a four-engine externally blowing jet-flap STOL airplane model. NASA TN D-7034, 1970.

14 - D.C. FREEMAN, L.P. PARLETT, R.L. HENDERSON : Wind tunnel investigation of a jet transport airplane configuration with an external-flow jet flap and inboard pod-mounted engines. NASA TN D-7004, 1970.

15 - C.C. SMITH : Effect of engine position and high lift devices on aerodynamic characteristics of an external-flow jet-flap STOL model. NASA TN D-6222, 1971.

16 - A.M. COOK, T.N. AIKEN : Low-speed aerodynamic characteristics of a large scale STOL transport model with an augmented jet flap. NASA TM X-62017, 1971.

17 - M.D. FALARSKI, K.W. MORT : Large-scale wind-tunnel investigation of a ducted-fan deflected slipstream model with an auxiliary wing. NASA TN D-6223, 1971.

18 - R.L. HENDERSON : Low speed wind tunnel investigation of a semi-span STOL jet transport wing with deflected thrust and blowing boundary layer control. NASA TN D-6256, 1971.

19 - L.P. PARLETT, C.R. CARTER : Wind tunnel investigation of an external-flow jet-flap transport configuration having full-span triple-slotted flaps. NASA TN D-6391, 1971.

20 - A.E. PHELPS, W. LETKO, R.L. HENDERSON : Low speed wind-tunnel investigation of a semi-span STOL jet transport wing-body with an upper-surface blown jet flap. NASA TN D-7183, 1973.

21 - H.C. QUIGLEY, T.C. NARK : A progress report on the development of an augmentor wing jet STOL research aircraft. SAE 710757, 1971.

22 - F. MAY, C.A. WIDDISON : STOL high-lift design study. Volume I : State-of-the-art review of STOL aerodynamic technology. AFFDL-TR-71-26, 1971.

23 - R.L. GIELOW : Performance prediction and evaluation of propulsion-augmented high lift systems for STOL aircraft. AIAA Paper n° 71-990, 1971.

24 - H.S. SWEET, H.R. LESLIE, J.A. BENNETT : Design studies of low-noise propulsive-lift airplanes. SAE 730 378, 1973.

25 - R.E. HAGE, M.D. MARKS : The future for STOL. DOUGLAS PAPER 6103, 1973.

26 - M.L. LOPEZ : Aerodynamics and performance characteristics of wing lift augmentation schemes. VKI Lecture series 60, 1973.

27 - J.A. HOOPER : Engine integration and noise considerations for STOL aircraft. VKI Lecture series 60, 1973.

28 - J.V. O'KEEFE, G.S. KELLEY : Design integration and noise studies for jet STOL aircraft. NASA CR-114 283, 1972.

29 - R.G. DORSCH, E.A. KREJSA, W.A. OLSEN : Blown flap noise research. SAE 71-745, 1971.

30 - R.G. DORSCH, W.J. KREIM, W.A. OLSEN : Externally-blown-flap noise. AIAA Paper n° 71-129, 1972.

31 - W.A. OLSEN, R.G. DORSCH, J.H. MILES : Noise produced by a small-scale externally blown flap. NASA TN D-6636, 1972.

32 - R.J. RULIS : Status of current development activity related to STOL propulsion noise reduction. SAE 730 377, 1972.

33 - M. RESHOTKO, R. FRIEDMAN : Acoustic investigation of the engine-over-the-wing concept using a D-shaped nozzle. AIAA Paper n° 73-1030, 1973.

34 - W.L. JONES, L.J. HEIDELGERG, R.G. GOLDMAN : highly noise suppressed bypass 6 engine for STOL application. AIAA Paper n° 73-1031, 1973.

35 - M.R. FINK : Mechanisms of externally blown flap noise. AIAA Paper n° 73-1029, 1973.

36 - B.J. CLARK, R.G. DORSCH, M. RESHOTKO : Flap noise prediction method for a powered lift system. AIAA Paper n° 73-1028, 1973.

37 - J.H. GOODYKOONTZ, R.G. DORSCH, D.E. GROESBECK : Noise tests of a mixer nozzle externally blown flap system. NASA TN D-7236, 1973.

38 - R. G. DORSCH, M. RESHOTKO, W.A. OLSEN : Flap noise measurements for STOL configurations using external upper surface blowing. AIAA Paper n° 72-1203, 1972.

39 - M. HAAS : Blown flap noise. MIT, FTL Report 72-5, 1972.

40 - H.H. HUBBARD, D. CHESNUTT, D.J. MAGLIERI : Noise control technology for jet-powered STOL vehicles. ICAS Paper n° 72-50, 1972.

41 - F.W. GIBSON : Noise measurements of model jet-augmented lift systems : NASA TN-D 6710, 1972.

42 - J.H. GOODYKOONTZ, R.G. DORSCH, D.E. GROESBECK : Mixer nozzle-externally blown flap noise tests. NASA TMX - 68021, 1972.

43 - J.F. GROENEWEG, G.L. MINNER : Measured noise of model fan-under-wing and fan-on-flap jet flap configurations.NASA TN D-6781, 1972.

44 - LOWRY : NACA TN 3911.

45 - FUHRMANN : Etude des carènes de dirigeable par une méthode théorique - Congrès Volta 1912.

46 - J.L. MESS et A.M.O. SMITH : Calculation of potential flow about arbitrary bodies. Progress in Aeronautical Sciences vol.8, 1967.

47 -G. HECKMANN & W. VITTE : Ecoulement à potentiel tridimensionnel portant - Colloque d'Aérodynamique appliquée, AFITAé (AAAF) 1971.

48 - P. PERRIER & W. VITTE : Elements d'aérodynamique tridimensionnelle en fluide parfait - enroulement de la nappe tourbillonnaire. Colloque d'aérodynamique appliquée. AFITAé (AAAF) 1970.

49 - T.S. LUU, G. COULMY & A. DULIEU : Calcul de l'écoulement transsonique autour d'un profil en admettant la loi de compressibilité exacte (A.T.M.A. 1972).

50 - J.H. ARGYRIS, etc.. : Two and three dimensional flow using finite elements, Aero. J.R.Aé.S.73 (1969).

51 - J. PERIAUX : Three dimensional analysis of compressible potential flows with the finite element methods. Symposium on finite element methods. University of Swansea (janv. 1974).

52 - M.D. VAN DYKE : Perturbation method in fluid mechanics. Academic Press 1964.

53 - EICHELBRENNER & OUDART : Calculs de couche limite laminaire tridimensionnelle sur un ellipsoïde de révolution en incidence. La Recherche Aéronautique (ONERA 1958).

54 - SHANEBROOK : Three dimensional boundary layer. ARC. 1965.

55 - Intégration des équations de NAVIER-STOKES par la méthode des éléments finis. Note AMD-BA/DEA 5459 (1974).

56 - LUMLEY : Toward a turbulent constitutive relation. J. Fluid Mech. Vol. 41, part 2, 1970.

57 - PATANKAR S.V. et SPALDING D.B. : A finite difference procedure for heat and mass transfer in boundary layer (Int. J. HMT n° 10 - 1967). Voir B.E. LAUNDER et D.B. SPALDING : Mathematical models of turbulence. Academic Press (1972).

58 - T. CEBECI, A.M.O. SMITH & L.C. WANG : A finite difference method for calculating compressible laminar and turbulent boundary layers. McDonnel Douglas DAC 67131 (1969).

59 - D. JEANDEL & J. MATHIEU : Méthode de calcul de la couche limite turbulente utilisant une équation de comportement du coefficient de Boussinesq. Journal de Mécanique - vol. 12 n° 4 1973.

60 - P. PERRIER et J.J. DEVIERS : Calculs tridimensionnels d'hypersuctentation. Colloque d'aérodynamique appliquée de l'AFITAé (AAAF), 1972.

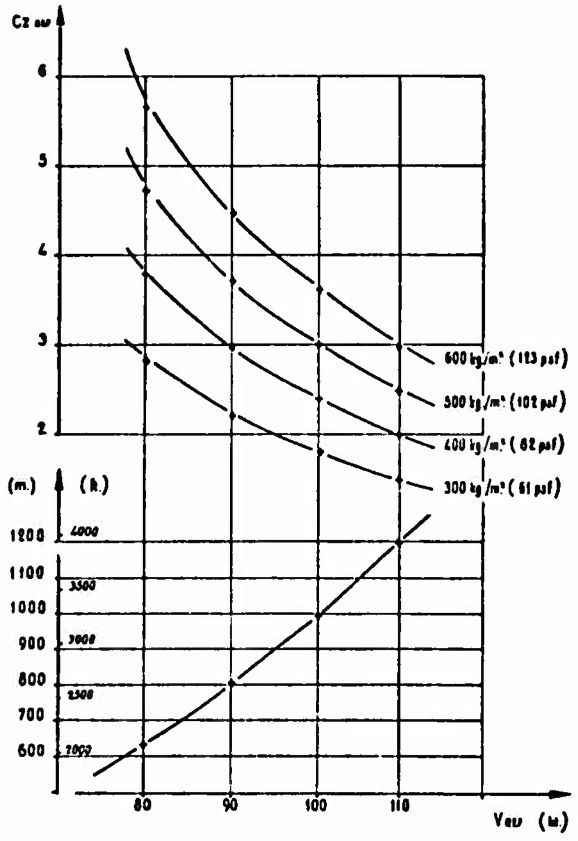

FIG. 1 _ ATTERRISSAGE (Piste mouillée)
LANDING (Wet runway)

NACA TN 2278

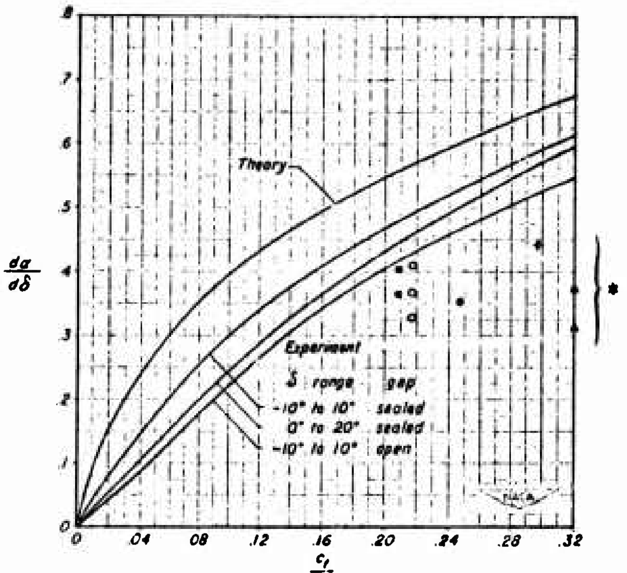

* *Flight test results of typical aircraft*

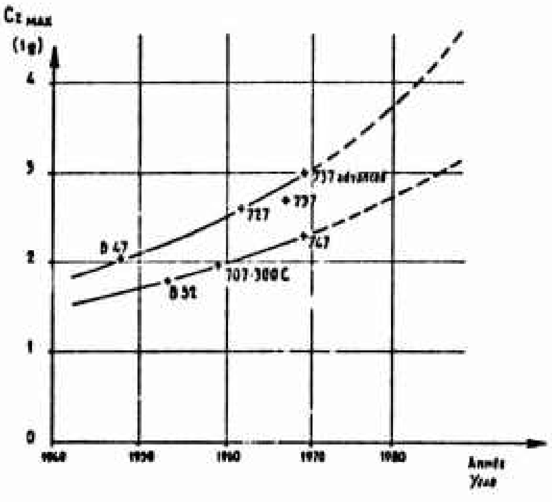

FIG. 2 _ HYPERSUSTENTATION MECANIQUE
MECHANICAL FLAPS

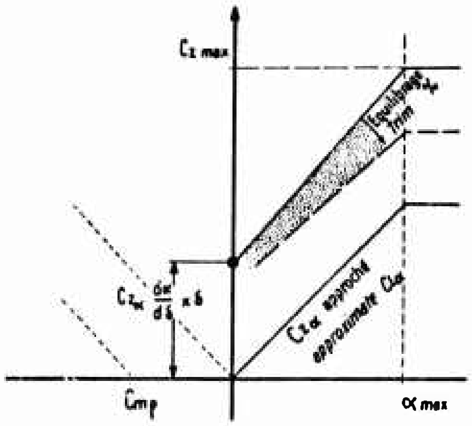
Cz max
Equilibrage trim
$Cz_{\alpha} \frac{d\alpha}{d\delta} \times \delta$
Czα approché approximate CLα
Cmp
α max

FIG. 3 _ PRINCIPE DE CORRELATION
CORRELATION PRINCIPLE

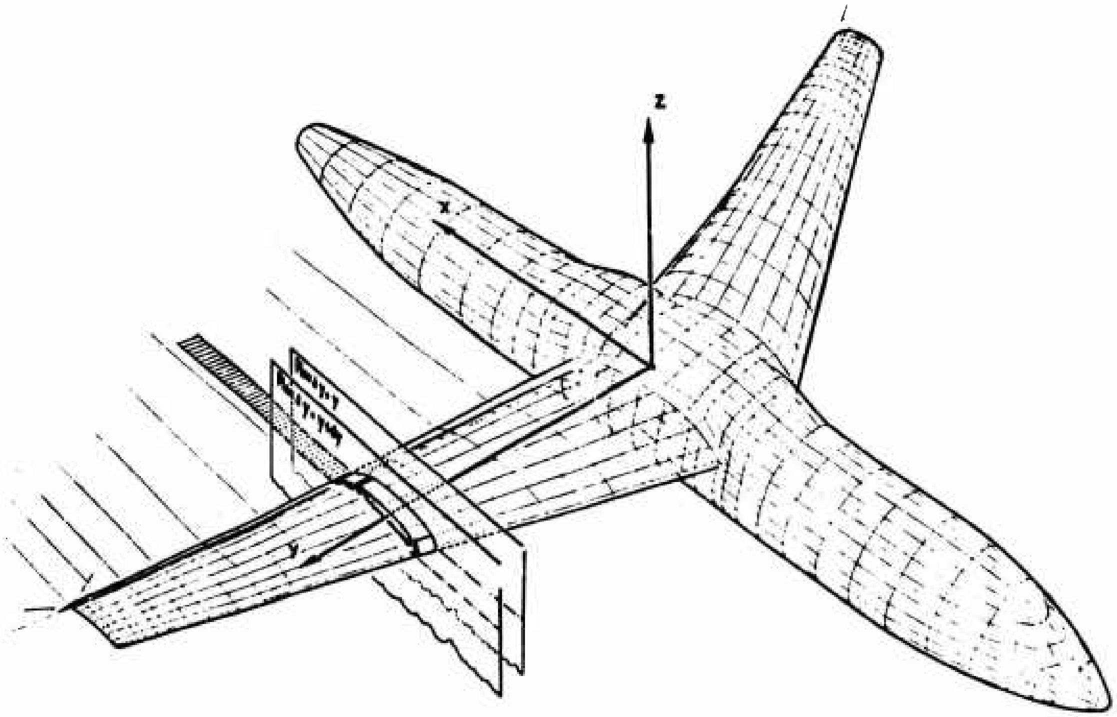

FIG. 4 - DISCRETISATION LEGERE SUR AVION HYPERSUSTENTE
SURFACE PANEL REPRESENTATION ON HIGH LIFT AIRCRAFT

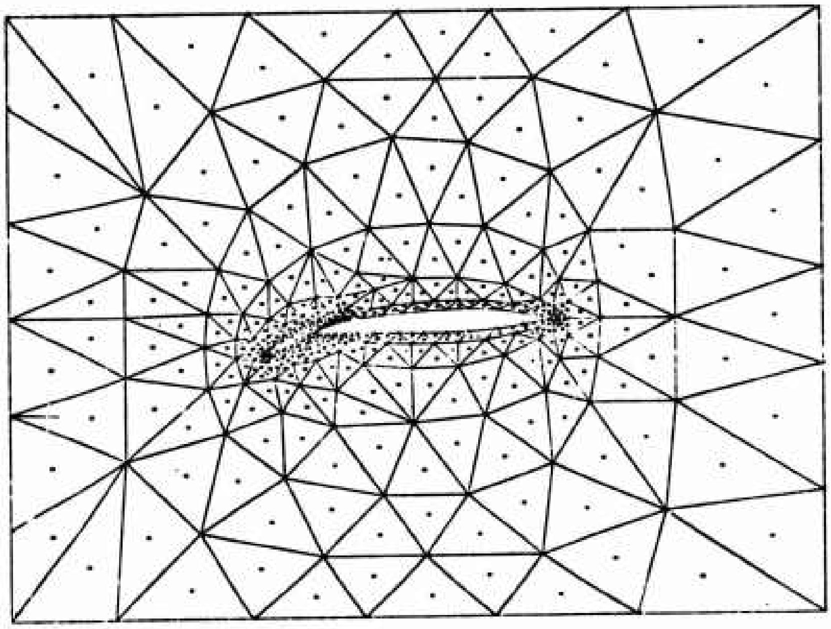

FIG. 5 - TRIANGULATION D'UN DOMAINE MULTI-CONNEXE
TRIANGULATION OF A MULTIPLY-CONNECTED DOMAIN (F.E.M.)

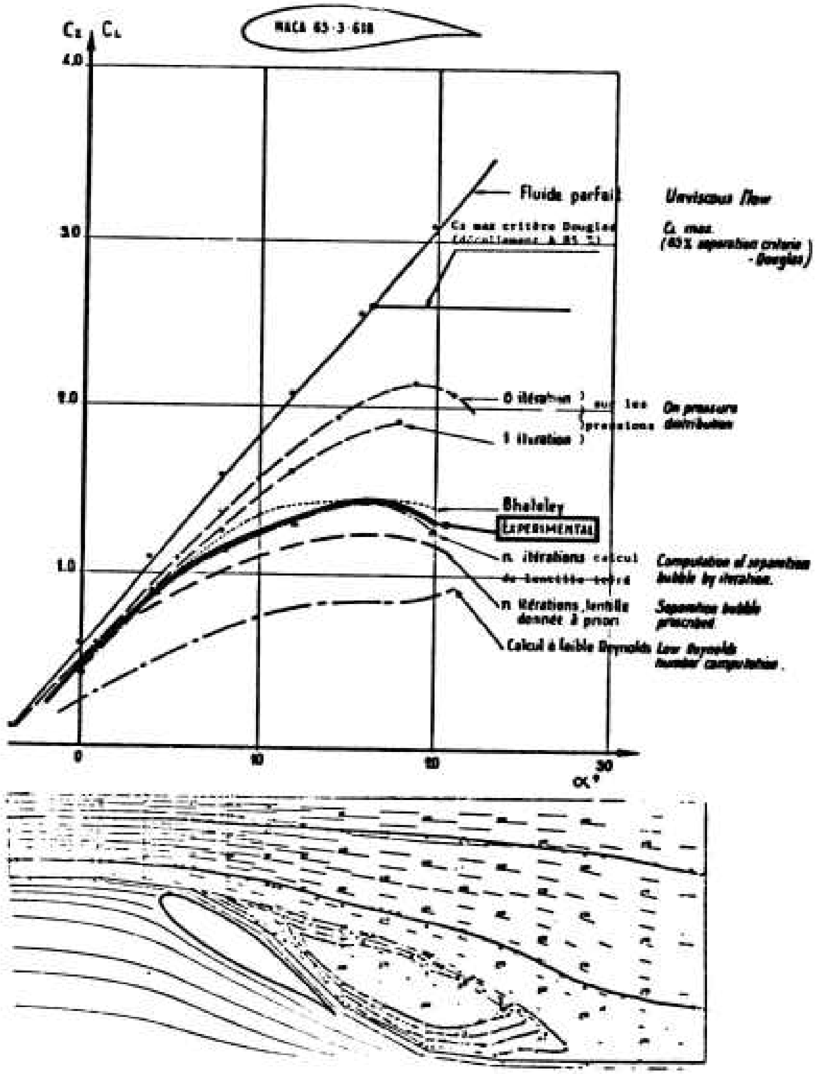

FIG. 6 _ INFLUENCE DU COUPLAGE SUR LA PORTANCE
COUPLING PROCEDURES INFLUENCE ON Cʟ

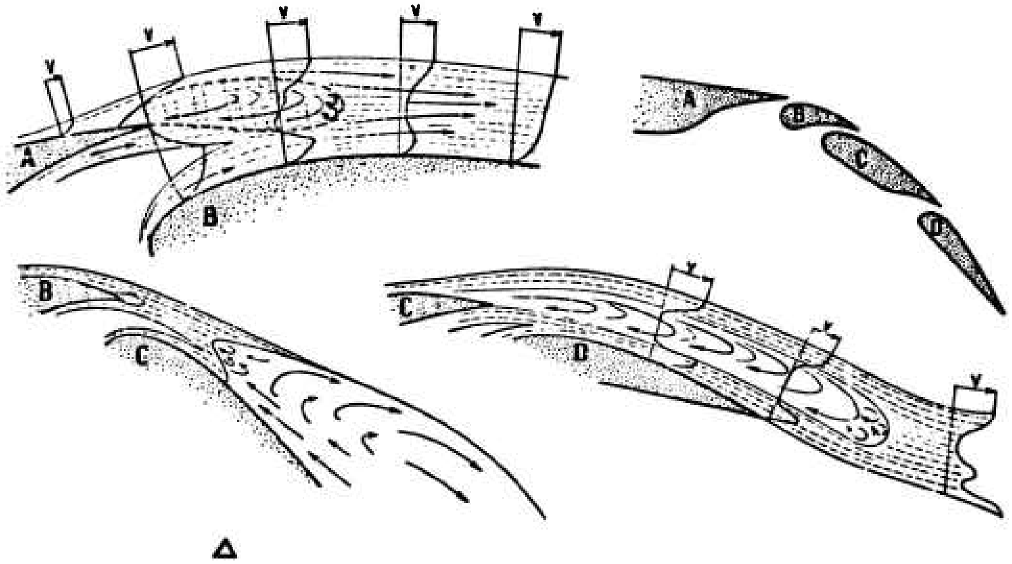

FIG. 7 _ CAS COMPLEXE DE ZONE VISQUEUSE.
COMPLEX VISCOUS FLOW.

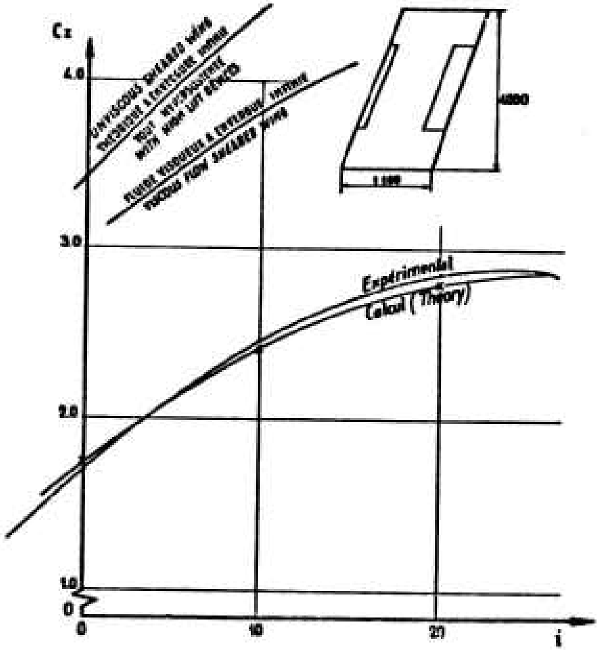

FIG. 8 _ COMPARAISON GLOBALE TRIDIMENSIONNELLE.
TRIDIMENSIONAL LIFT COMPARISON.

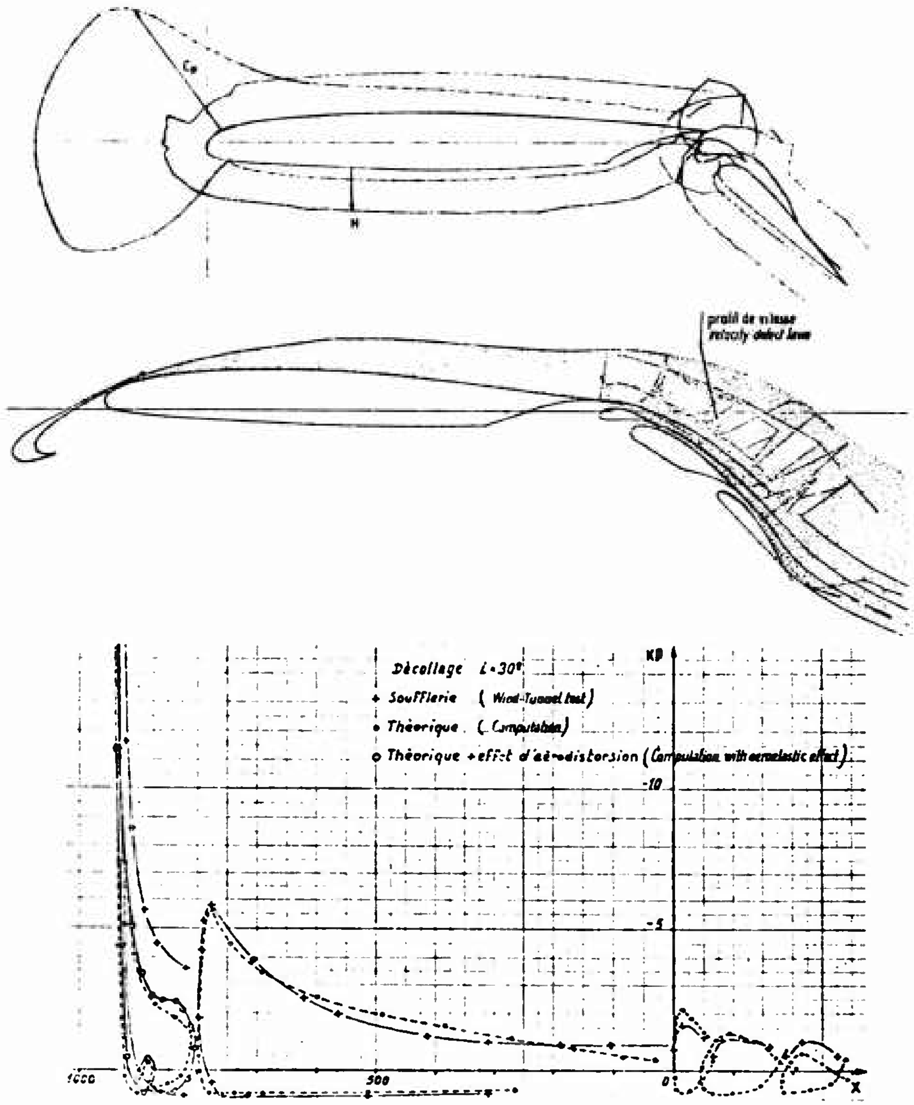

FIG. 9 - ECOULEMENTS AVEC DECOLLEMENT SUR UNE AILE HYPERSUSTENTEE (Eléments de comparaison).
SEPARATED FLOWS ON HIGH LIFT WING (data comparisons).

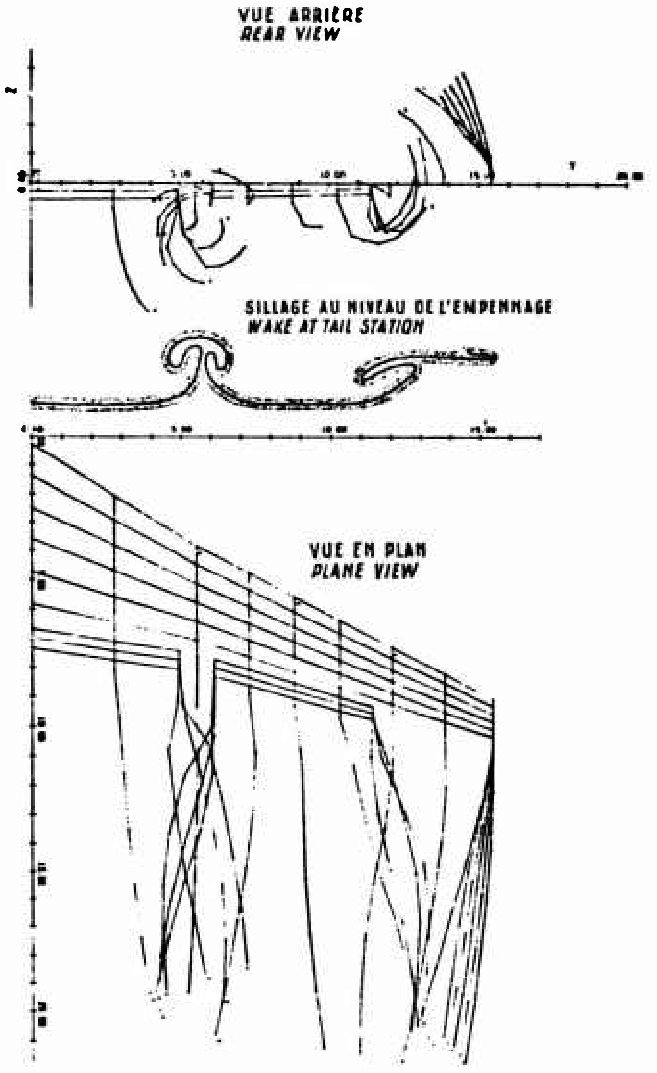
VUE ARRIERE
REAR VIEW
Z
Y
0
5 m
10 m
15 m
20 m
SILLAGE AU NIVEAU DE L'EMPENNAGE
WAKE AT TAIL STATION
VUE EN PLAN
PLANE VIEW

FIG. 10 - SILLAGES D'UNE CONFIGURATION COMPLEXE
INTERRUPTED FLAPS WAKES

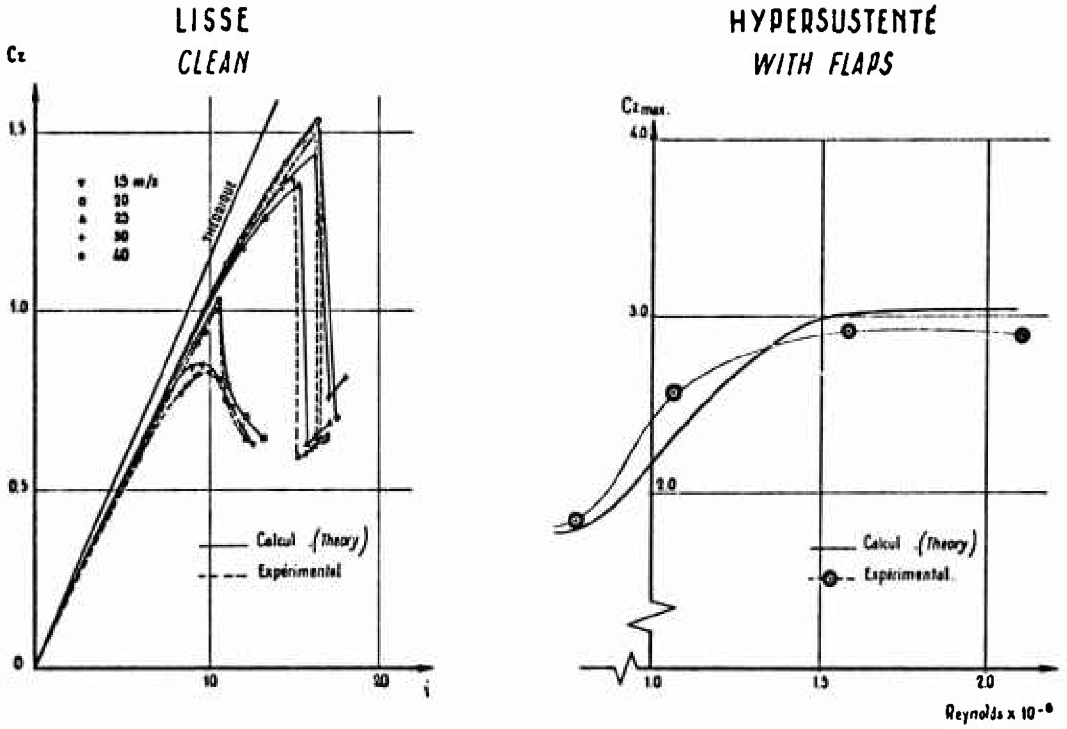
LISSE
CLEAN

HYPERSUSTENTÉ
WITH FLAPS

FIG. 11 _ EFFET DU NOMBRE DE REYNOLDS
REYNOLDS NUMBER INFLUENCE.

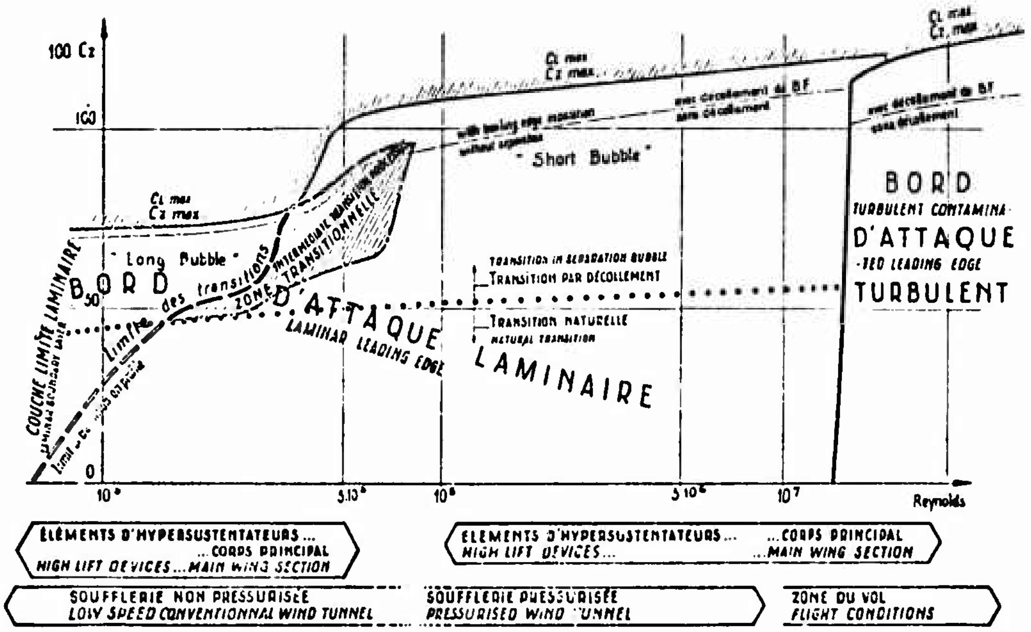
100 Cz
100
50
0
Cl max
Cz max
Cl max
Cz max
Cl max
Cz max
with trailing edge separation
without separation
avec décollement du B.F.
sans décollement
avec décollement du B.F.
sans décollement
" Short Bubble "
" Long Bubble "
COUCHE LIMITE LAMINAIRE
LAMINAR BOUNDARY LAYER
BORD D'ATTAQUE LAMINAIRE
LAMINAR LEADING EDGE
Limite des transitions
ZONE TRANSITIONNELLE
INTERMEDIATE TRANSITION
Limit of transitions
TRANSITION IN SEPARATION BUBBLE
TRANSITION PAR DÉCOLLEMENT
TRANSITION NATURELLE
NATURAL TRANSITION
BORD D'ATTAQUE TURBULENT
TURBULENT CONTAMINATED LEADING EDGE
10⁵
5.10⁵
10⁶
5 10⁶
10⁷
Reynolds
ÉLÉMENTS D'HYPERSUSTENTATEURS ... ... CORPS PRINCIPAL
HIGH LIFT DEVICES ... MAIN WING SECTION
ELEMENTS D'HYPERSUSTENTATEURS ... ... CORPS PRINCIPAL
HIGH LIFT DEVICES ... ... MAIN WING SECTION
SOUFFLERIE NON PRESSURISÉE
LOW SPEED CONVENTIONNAL WIND TUNNEL
SOUFFLERIE PRESSURISÉE
PRESSURISED WIND TUNNEL
ZONE DU VOL
FLIGHT CONDITIONS

FIG. 12 _ ZONE DE FONCTIONNEMENT TRIDIMENSIONNEL
TRIDIMENSIONNAL BOUNDARY LAYER PATTERN.

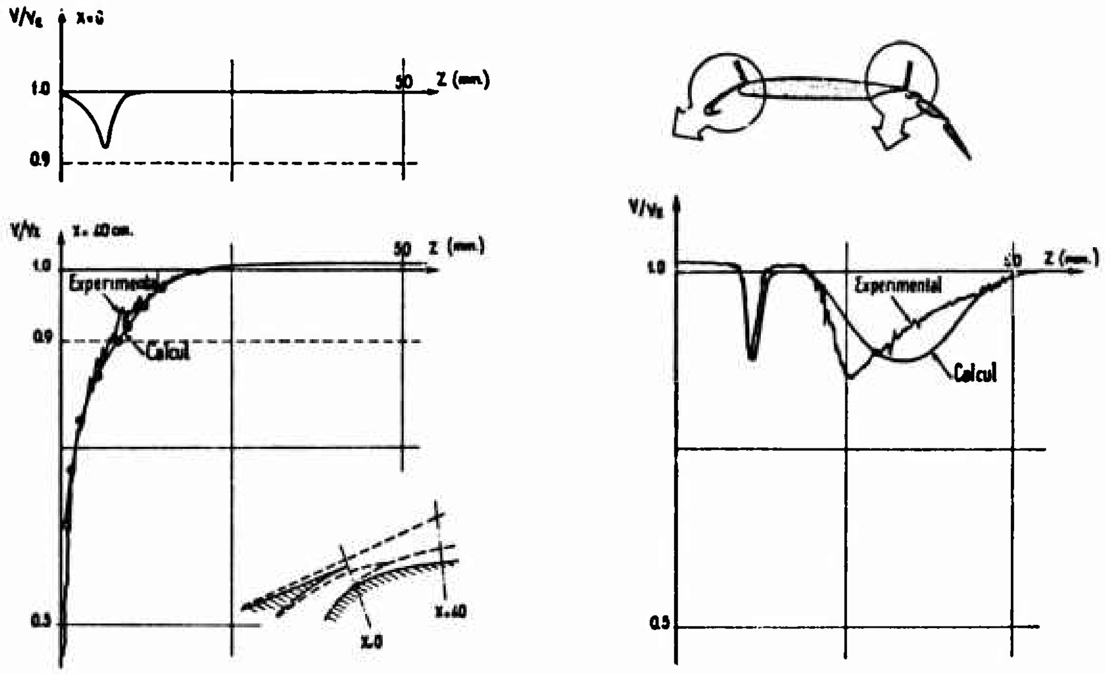

FIG. 13 _ COMPARAISONS CALCUL-SOUFFLERIE
EN ZONES VISQUEUSES COMPLEXES

THEORITICAL-WT TESTING COMPARISONS
INSIDE COMPLEX VISCOUS AREAS.

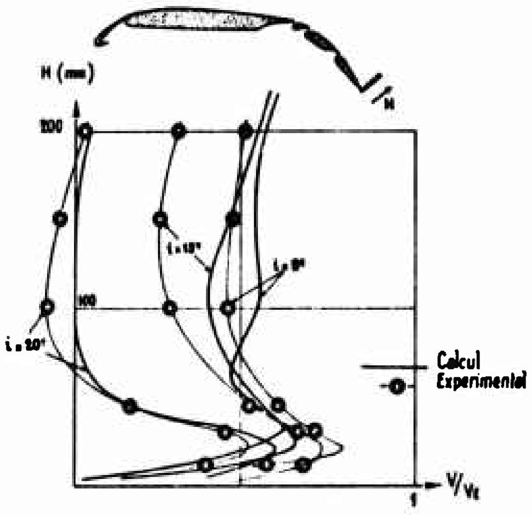

FIG.14 _ COMPARAISON CALCUL-VOL AU BORD DE FUITE

THEORITICAL-FLIGHT TESTING COMPARISONS
AT THE TRAILING EDGE.

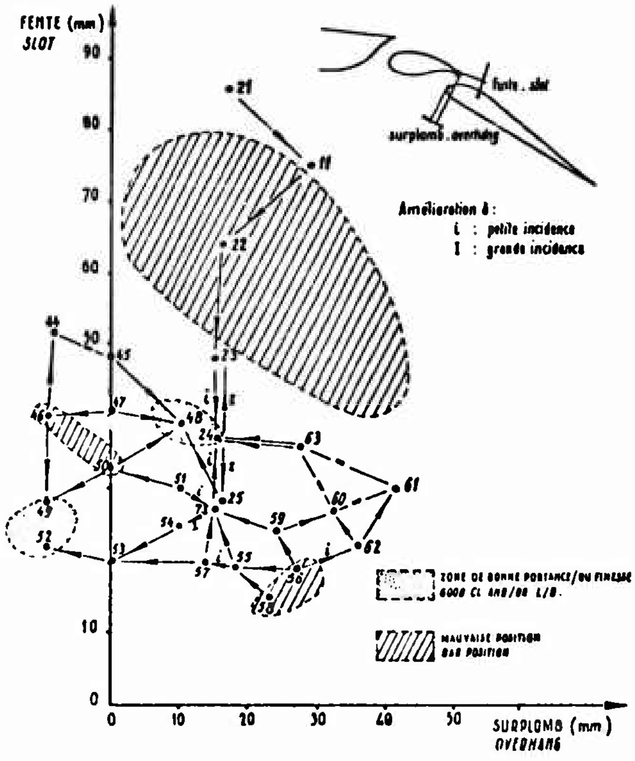

FIG. 15 _ RECHERCHE DE POSITION OPTIMALE
SEEK FOR THE OPTIMUM POSITION.

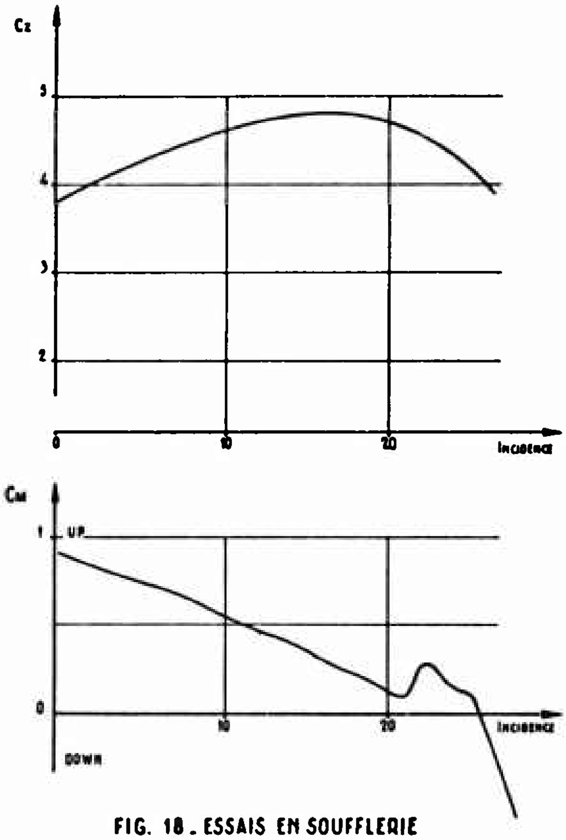

FIG. 18 _ ESSAIS EN SOUFFLERIE
WIND TUNNEL TESTS

FIG. 16 _ MAQUETTE STRUCTURALE
STRUCTURAL MOCK-UP

FIG. 17 _ MAQUETTE DE SOUFFLERIE
WIND TUNNEL MODEL

A METHOD FOR PREDICTION OF LIFT FOR MULTI-ELEMENT AIRFOIL SYSTEMS WITH SEPARATION

by

K. Jacob[1], D. Steinbach[2]

Deutsche Forschungs- und Versuchsanstalt für Luft- und Raumfahrt
Aerodynamische Versuchsanstalt Göttingen, Bunsenstr. 10

SUMMARY

For the analysis of high lift devices, such as leading edge slats and slotted flaps, a numerical method is presented, which allows to predict pressure distributions and lift for almost arbitrary airfoil combinations in incompressible flow. The method not only takes care of the boundary layer displacement effect but also allows for rear separation with a dead air region. The maximum lift can be predicted in dependence of the geometry of the system and the Reynolds number of the flow. By the principle of reflection also the ground effect can be taken into account.

The method is a combination of potential flow- and boundary layer calculations. The potential flow calculation is based on singularity distributions (vortices and sources) on the surface of the airfoils. A dead air region is simulated by an outflow region, produced by a proper source distribution on the rear part of the upper surface of the airfoil. The point of separation is found by iteration postulating that the foremost point of the dead air region has to coincide with the point of separation of the boundary layer, as calculated for the attached part of the flow.

This method has been programmed in FORTRAN for an IBM 360-65 computer and it was applied to several airfoil combinations. Comparisons of theoretical and experimental results yield good agreement.

NOTATION

a_1, a_2, b, d	weight factors for basic flows (a_1), (a_2), (b), (d)
α	angle of attack
c	chord of main airfoil (Fig. 12)
c_p	pressure coefficient
c_f	local skin friction coefficient
$c_d = \frac{2}{\rho v_t^3} \int_0^\infty \tau \frac{\partial u}{\partial \eta} d\eta$	dissipation coefficient
c_L	lift coefficient
$\delta_1 = \int_0^\infty \left(1 - \frac{u}{v_t}\right) d\eta$	displacement thickness of the boundary layer
$\delta_2 = \int_0^\infty \frac{u}{v_t}\left(1 - \frac{u}{v_t}\right) d\eta$	momentum thickness of the boundary layer
$\delta_3 = \int_0^\infty \frac{u}{v_t}\left[1 - \left(\frac{u}{v_t}\right)^2\right] d\eta$	energy thickness of the boundary layer
h	ground distance from x-axis of the common coordinate system, Fig. 7
γ	transformed local vortex strength, Eq. (8b)
Γ_i	total circulation around airfoil No. i
i, j, k	airfoil numbers
I	total number of airfoils in the airfoil system
μ, ν	surface point numbers
M	total number of surface points
M_k	total number of surface points at airfoil No. k
p	static pressure
Ψ	stream function
q	transformed local source strength, Eq. (8a)
$Re = \frac{V_\infty \cdot c}{\nu}$	Reynolds number, based on chord of main airfoil and free stream velocity
s, σ	distance, measured along surface of an airfoil
S	foremost point of the dead air region on upper surface, Fig. 2b
T	foremost point of the dead air region on lower surface, Fig. 2b
TE	trailing edge
τ_k	angle between trailing edge tangent (perpendicular to the mean line of the airfoil) and x-axis, Fig. 2a
u	local velocity within the boundary layer
U	point on the upper separating streamline, above trailing edge, Fig. 2b
V_∞	free stream velocity
v_t	tangential velocity (of potential flow) at the airfoil's surface
v_n	normal velocity (of potential flow) at the airfoils' surface (identical with local source strength)
x, y	common coordinate system for all airfoils, Fig. 2a
$x_{k\mu}, y_{k\mu}$	coordinates of surface point $P_{k\mu}$, Fig. 2a
η	coordinate, normal to the surface

---

[1] Dr.-Ing., [2] Dipl.-Phys.

1. INTRODUCTION

Airplanes for short take off and landing (STOL) need wings with high lift at low speed. For that many means have been invented: Multi-element airfoils with slats and different kinds of flaps, and several ways of boundary layer control by blowing and suction (see Fig. 1a). For survey and further references in this field see G. V. Lachmann (Ref. 1). H. Schlichting and E. Truckenbrodt (Ref. 2) and AGARD. CP (Ref. 3).

The maximum lift of an airfoil always occurs with separation of the boundary layer. All the means shown in Fig. 1a aim at postponing strong separation (breakdown of lift) to higher angles of attack and to higher lift coefficients (see Fig. 1b). This is achieved either by direct action on the boundary layer (cases A 1 and B 1 in Fig. 1a) or indirectly by producing "favourable" pressure distributions, using mechanical high lift devices (cases A 2, B 2 in Fig. 1a). For avoiding separation it is favourable to reduce positive pressure gradients. Slats do this by reducing negative pressure peaks near the leading edge (case A 2), and deflected flaps increase the negative pressure on the rear part of the main airfoil's upper surface (case B 2). By combining both and even using double slotted flaps (case C) the resulting gain in lift can be very considerable (see Fig. 1b). For further understanding of the aerodynamics of multi-element airfoils see A. M. O. Smith (paper No. 10 in Ref. 3).

There have been many experimental investigations on multi-element wings, but no general theoretical method exists which allows to predict the maximum lift for such complicated configurations. Maximum lift is often found, when there exists already a separated region of moderate size. Thus a prediction method for lift, including the maximum lift, has to take into account the influence of a dead air region. The most general case of three-dimensional compressible flow with interaction and separation is extremely difficult. But for the analysis and optimisation of high lift devices it may be already helpful to have a method for the two-dimensional incompressible flow with separation.

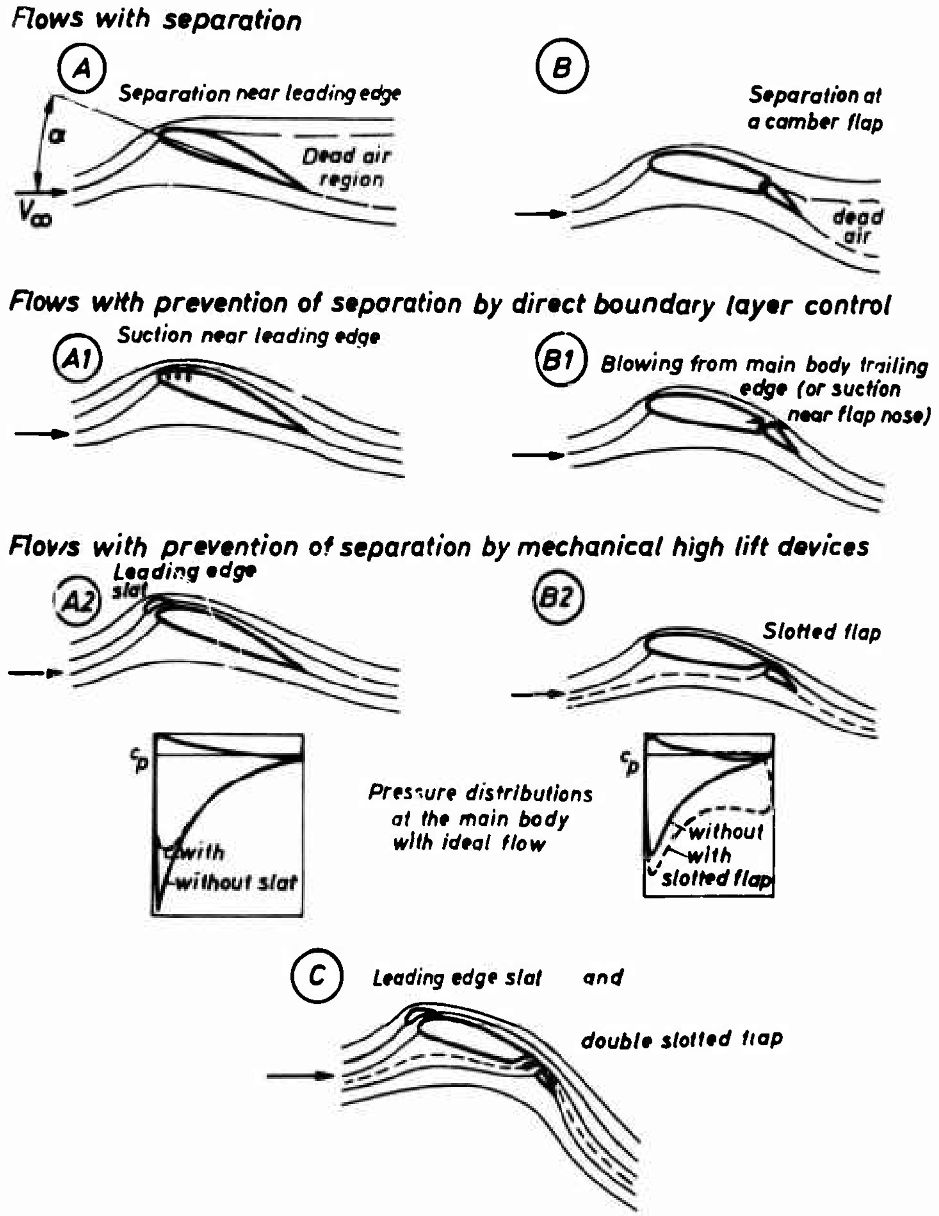
Flows with separation
A
Separation near leading edge
α
Dead air region
V_∞
B
Separation at a camber flap
dead air
Flows with prevention of separation by direct boundary layer control
A1
Suction near leading edge
B1
Blowing from main body trailing edge (or suction near flap nose)
Flows with prevention of separation by mechanical high lift devices
A2
Leading edge slat
B2
Slotted flap
c_p
with
without slat
Pressure distributions at the main body with ideal flow
c_p
without
with
slotted flap
C
Leading edge slat and
double slotted flap

Fig. 1a Various means for gaining high lift

For single airfoils such a method has already been published in 1969 by the first author (Ref. 4). Since then various reseachers, as Bateley and Bradley (paper No. 12 in Ref. 3) and the authors, have been working on similar methods for multi-element airfoil systems. In this paper the authors' present state-of-the-art is presented. This paper is an abbreviated version of a recent report, (Ref. 5), supplemented by the latest improvements and results.

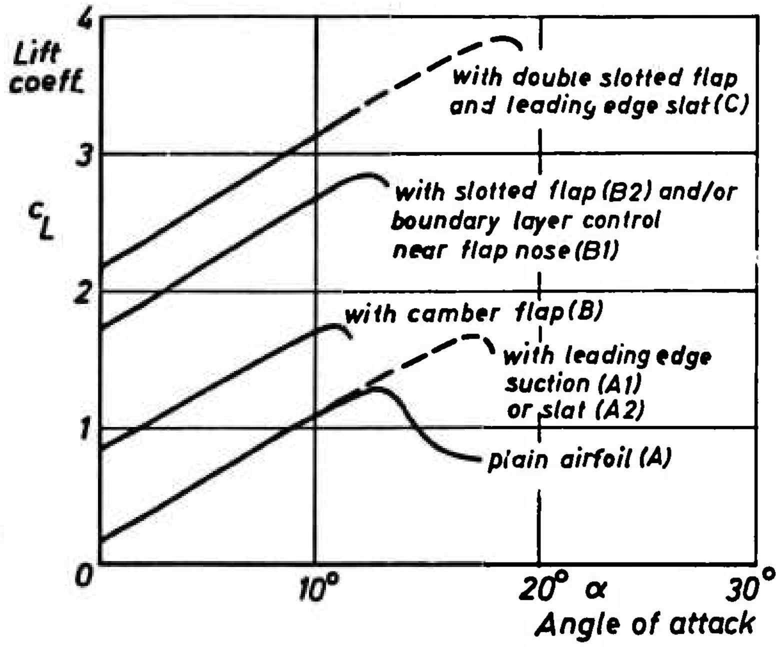

Fig. 1b Scetch of $c_L(\alpha)$-curves for an airfoil with various high lift devices

2. BASIC IDEAS OF THE METHOD

In order to calculate the incompressible flow for a multi-element airfoil system (Fig. 2a) first of all one needs a powerful potential flow method, including the interaction of all parts of the system. To calculate the flow up to and beyond maximum lift, one also has to account for viscous effects, especially for separation and the displacement effect of a separated wake (dead air region). The flow outside of a dead air region can be considered as inviscid, but, compared to the fully attached flow, the streamlines of this flow are displaced by the presence of the dead air region. The corresponding change in the pressure distribution on the airfoils' surfaces influences the forces and also the position of the separation point.

A. Walz (Ref. 6) has already shown in 1940 that a dead air region can be simulated in potential flow theory by an appropriate extension of the rear part of the airfoil. In our potential flow model we will use a source distribution on the rear part of the airfoil surface to produce an outflow region (Fig. 2b), which will serve for simulation of a dead air region. For a given angle of attack and with a fixed formost point S of the simulated dead air region and with certain conditions to fix its shape a potential flow with dead air simulation can be calculated, as shown later on in some detail.

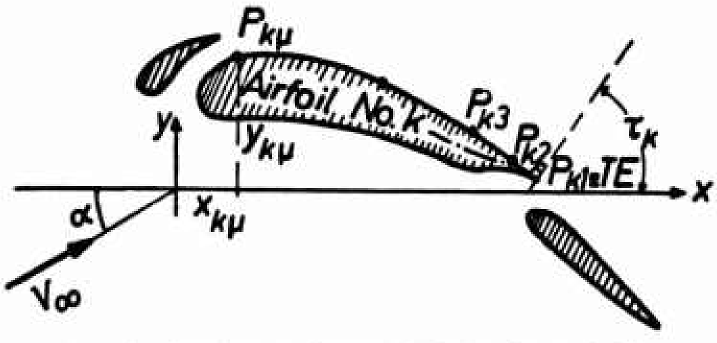

Fig. 2a Geometry of a multi-element airfoil system

However, with different positions of point S the potential flow theory gives different possible solutions. But only one of those can be physically possible for a given Reynolds number. This must obviously be the one flow for which point S coincides with the point of separation of the boundary layer, calculated with the pressure distribution in front of point S.

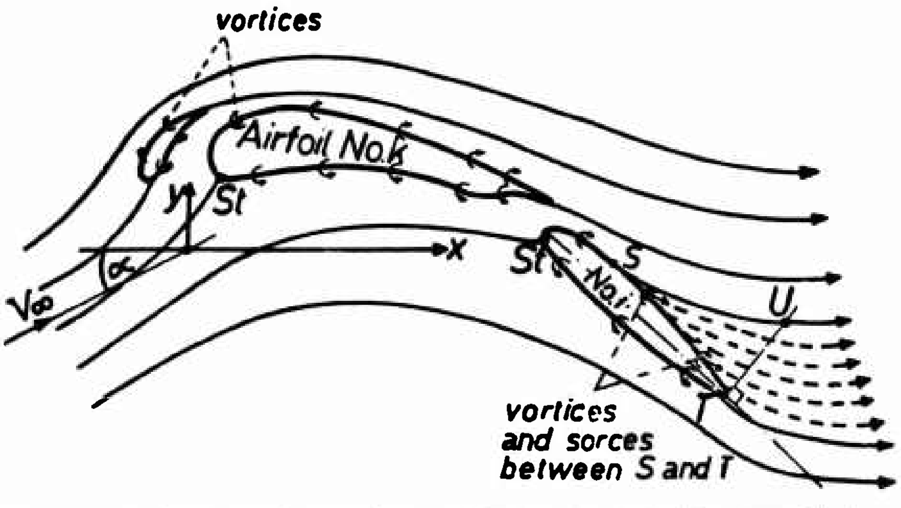

Fig. 2b Potential flow around a multi-element airfoil system with dead air simulation at the rearmost element

Now we can see that each part of the calculation, potential flow with dead air simulation on one hand and boundary layer calculation on the other hand, requires certain results from the other part. Consequently the total calculation procedure can only be some iterative combination of the two parts. We will now deal in some more detail with each of the two parts of the calculation, and in section 3

Basic flow (a_1): Uniform approach flow in x-direction

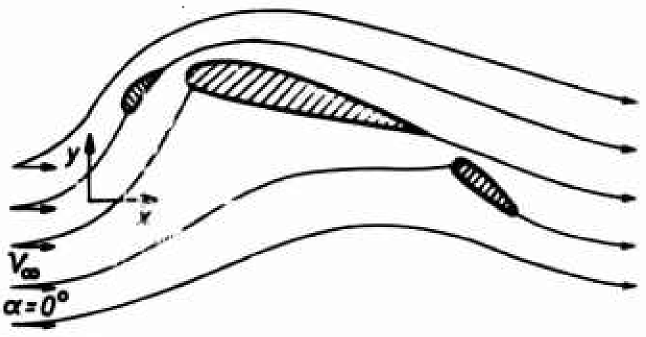

Basic flow (a_2): Uniform approach flow in y-direction

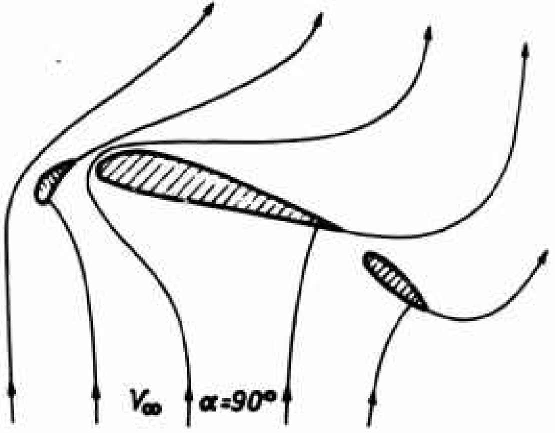

Basic flow (b): Circulatory flow around one of the airfoils

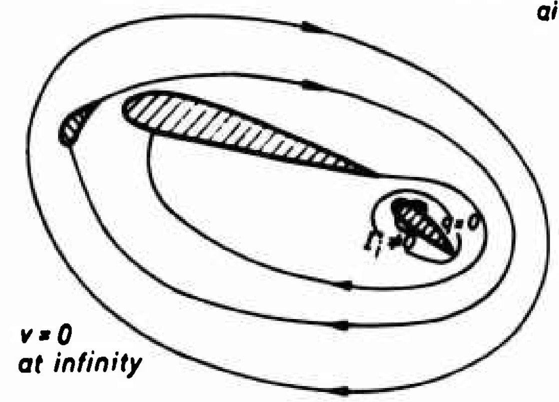

Basic flow (d): Outflow from one of the airfoils

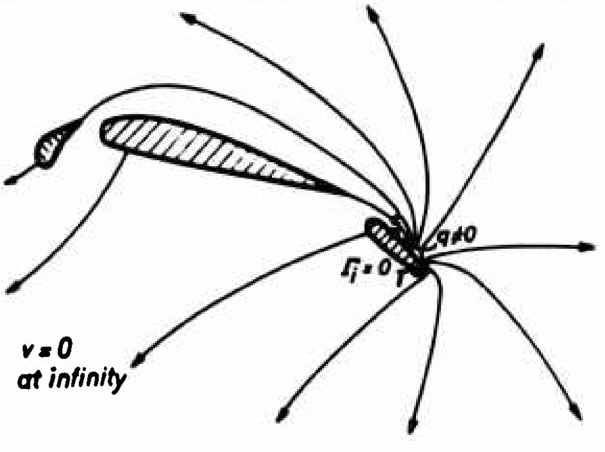

Fig. 3 Scetches of the four basic flows

we will see how to combine them.

For the potential flow calculation we will use a surface singularity method, based on the integral equation of E. Martensen (Ref. 7). That leads to a large system of linear equations for the unknown tangential velocities at a finite number of points on the airfoils' surface (see section 4). In that system of equations the flow conditions at infinity as well as some given source distribution on the surface go only into the right hand sides. Thus certain different "basic flows" (see Fig. 3) can be computed independently. These basic flows shall be:

(a_1) a uniform approach flow in x-direction,

(a_2) a uniform approach flow in y-direction,

(b) a circulatory flow around one of the airfoils, and

(d) an outflow, produced by a source distribution on part of the surface of that same airfoil.

Then for a given angle of attack and fixed positions of the points S and T , a flow as shown in Figure 2b can be obtained by superposition of these basic flows.

But we are still left with the problem, what conditions we shall pose on the simulated dead air region to get a physically realistic flow outside of that region. Now, with regard to experimental observations, we introduce the following conditions:

(1) The separating streamline shall take off tangentially from the surface (no corner flow), because observed pressures correspond to a smooth non-zero velocity distribution around the separation point (see Fig. 4).

(2) The separating streamline shall have an approximately constant pressure distribution near the airfoil, because of observed approximately constant pressure in a real dead air region.

More precisely we demand that the pressure is equal at three special points of the separating streamlines, namely at the foremost points S and T and at point U above the trailing edge (Fig. 4). This gives two conditions

(2a) $c_{pS} = c_{pT}$ and

(2b) $c_{pT} = c_{pU}$.

Moreover we want

(2c) the pressure to vary very little between points S and U .

Conditions (1) and (2c) can be satisfied by using our "standard source distribution" of Fig. 5 for the basic flow (d). Then the two conditions (2a) and (2b) can be met by proper choice of the two weight factors b and d of the circulatory flow and the outflow. That is

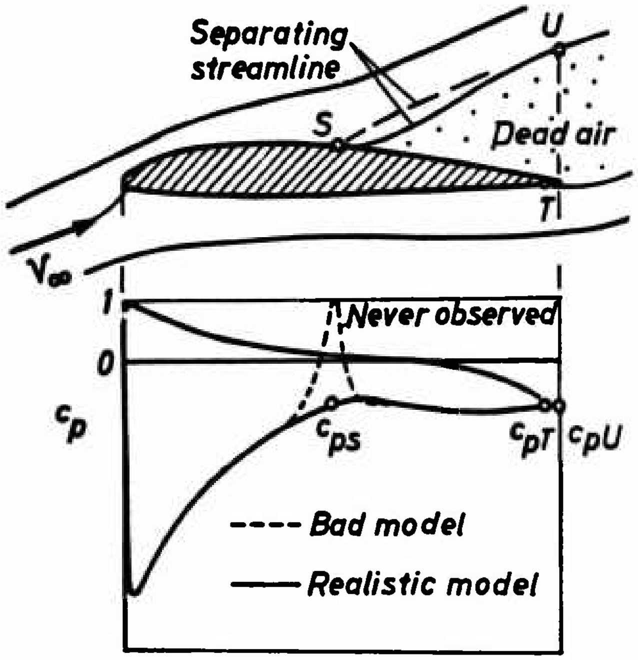

Fig. 4 Pressure distribution for flow with separated wake

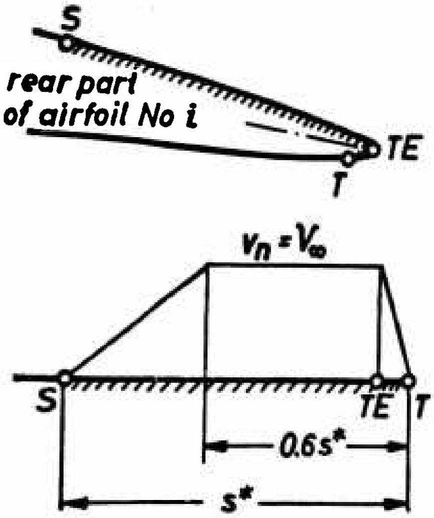

Fig. 5 The standard source distribution

so because the strength of the basic flows (b) and (d) influence the shape (direction and size) of the simulated dead air region in the resulting flow and thus the pressure at the points S, T, and U.

Now we can see: If we only decide for a certain standard source distribution, our potential flow model is unique for a fixed angle of attack α and given points S and T. It is the potential flow which results from superposition of the four basic flows (a_1), (a_2), (b), and (d) with the weight factors a_1 and a_2 being determined by α and the weight factors b and d being fixed according to conditions (2a) and (2b). The resulting flow looks like the one in Figure 2b, with an outflow region having important characteristics of a separated wake near the airfoil and going continuously to infinity with the pressure p going finally to p_∞.

From the mathematical point of view we have an elliptical problem with the following boundary conditions:

$v = (V_\infty \cos\alpha, V_\infty \sin\alpha)$ at infinity,

$v_n = d \cdot f(s)$ with given $f(s)$ between points S and T on the surface of one airfoil (No. i),

$v_n = 0$ everywhere else on the surfaces of the airfoils,

$v_t = 0$ at the trailing edges of all airfoils No. $k \neq i$ (Kutta condition).

Furthermore we have the two conditions (2a) and (2b) for fixing d and the circulation for airfoil No. i.

Now, having calculated such a potential flow with a simulated dead air region, we have to investigate by a boundary layer calculation, if, for a given Reynolds number, the chosen point S coincides with the separation point.

For the boundary layer calculation we will use the method of J. Rotta (Ref. 8) which is an approximate method based on the integration of momentum and energy equation. We always start the calculation near the leading edge stagnation point with a laminar boundary layer. As to separation and transition our program provides the following choice:

(1) For low Reynolds numbers (say $Re < 5 \cdot 10^4$):
The calculated separation point of the laminar boundary layer is used.
No transition and no reattachment takes place.

(2) For high Reynolds numbers (say $Re > 10^5$):
The separation point of the turbulent boundary layer is used
with (a) a given transition point (for instance from experiment)
or (b) a transition point which is identical with the calculated laminar separation point.

By not considering the possibility of formation and sudden bursting of separation bubbles we in effect always assume "rear stall" by so far.

Other kinds of stall (long bubble and leading edge stall) may occur at rather thin airfoils and low or moderate Reynolds numbers. Moreover merging and interaction of the boundary layers of the various airfoil elements may influence transition and separation. As D.N. Foster (paper No. 11 in Ref. 3) pointed out, these phenomena may in certain cases influence the flow noticably. Therefore some extensions of our method may be desirable.

3. SHORT DISCRIPTION OF THE PROCEDURE

The practical computation of the flow for an airfoil system with given geometry, angle of attack α, and Reynolds number Re is done by the following steps:

(1) Computation of the attached potential flow and the boundary layers for all the airfoils.

This step serves to get the displacement thickness of the boundary layers and to see whether there is separation at all and if so, at which airfoil.

Necessary substeps:

(1. 1) Calculation of basic flows (a_1) and (a_2) by setting up and solving the system of linear equations.

(1. 2) Superposition of these flows with proper weight factors a and b for the given angle of attack.

(1. 3) Boundary layer calculation for all airfoils for the given Reynolds number.

If multiple separation at more than one airfoil) is indicated, our program gives notice and then stops.

(2) Calculation of a basic flow (b) (circulatory flow around the airfoil with separation) and of a series of basic flows (d_ω) with standard source distributions for different points S_ω on the upper surface of the airfoil with separation. The points S_ω, $\omega = 1, 2, \ldots, \Omega$ shall be arranged such that S_1 is nearest to the trailing edge and with increasing ω the distance grows in small steps.

In addition a special basic solution (e) shall be calculated for simulation of the displacement thickness. This is done by using source distributions on all airfoils, with the local source strength being proportional to the local increase of displacement thickness and velocity (see section 4. 4).

Step (2) is a necessary preparation for the intended construction of a flow with a "dead air region" by superposition of all the basic flows.

Necessary substeps:

(2. 1) Preparation of all the source distributions.

(2. 2) Calculation of the basic flows (b), (d_ω), and (e) by setting up and solving a system of linear equations with several different right hand sides.

(3) Construction of a flow with a simulated dead air region by superposition of the basic flows (a_1), (a_2), (b), (d_ω). The resulting flow shall satisfy the condition of equal pressure at the points S_ω, T, and U. This has to be achieved by proper choice (iterativ calculation) of the weight factors b and d_ω for the corresponding basic flows, with the weight factors a_1 and a_2 being fixed by the given angle of attack (see section 5).

Necessary substeps:

(3. 1) Calculation of first approximations for the weight factors b, d_ω.

(3. 2) Calculation of the resulting flow by superposition.

(3. 3) Locating the point U on the upper separating streamline and calculating the pressures at S_ω, T, and U.

(3. 4) If there is no equal pressure at S_ω, T, and U improve the weight factors and return to (3. 2),

otherwise:

(3. 5) Boundary layer calculation for the resulting flow with the given Reynolds number, to check if separation is indicated in front of the foremost point S_ω of the dead air region. If so, return to (3. 1) using now the next basic flow $(d_{\omega+1})$ with a foremost point $S_{\omega+1}$ lying a bit ahead of S_ω.

If for the first time the boundary layer calculation indicates no separation ahead of the foremost point, the calculated flow is taken as the final result. Notice is given if multiple separation is indicated for this flow.

4. CALCULATION OF THE BASIC FLOWS

4.1 The fundamental integral equation

For the tangential velocity v_t on the surface Su of a closed body in two-dimensional incompressible potential flow, with the velocities $v = (V_\infty \cos\alpha,\ V_\infty \sin\alpha)$ at infinity and $v = 0$ inside of the body, the following integral equation is given in Ref. 7:

$$v_t(s) + \frac{1}{\pi}\frac{\partial}{\partial n}\int_{Su} v_t(\sigma)\ln\frac{1}{r(s,\sigma)}\,d\sigma = 2\left[\frac{dx}{ds}(s)\,V_\infty\cos\alpha + \frac{dy}{ds}(s)\,V_\infty\sin\alpha\right] - k_n(s) \qquad (1)$$

with s and σ meaning the distance, measured along the surface of the body,

$r(s,\sigma)$ meaning the straight distance between two points of the surface,

$\frac{\partial}{\partial n}$ meaning differentiation in the direction of the outer normal to the surface,

and

$$k_n(s) = \frac{1}{\pi}\frac{\partial}{\partial t}\int_{Su} v_n(\sigma)\ln\frac{1}{r(s,\sigma)}\,d\sigma \qquad (2)$$

being an integral containing given normal (blowing) velocities v_n on the surface.

Notice: Because the velocity inside of the airfoil is identical zero the tangential velocity at the surface v_t is identical with a surface vortex distribution and the normal velocity v_n with a surface source distribution.

4.2 System of linear equations for a single airfoil

It is shown in Refs. 5 and 7 that by

(1) introduction of a parameter presentation of the surface

$$x = x(\varphi),\quad y = y(\varphi),\quad \varphi = 0,\dots,2\pi \qquad (3)$$

with the airfoil being surrounded once counterclockwise with growing φ,

(2) introduction of some auxiliary variables,

(3) carrying out the differentiations, and

(4) discrete approximation of the resulting Fredholm integral equation by unsing M surface points $P_\mu(x_\mu, y_\mu)$, equidistant in φ,

one can finally arrive at a system of linear equations. This system has the following form:

$$\frac{1}{M}\sum_{\substack{\nu=1\\ \nu\neq\mu}}^{M}\left(K_{\nu\mu}\gamma_\mu - K_{\mu\nu}\gamma_\nu\right) = V_\infty(\dot{x}_\mu\cos\alpha + \dot{y}_\mu\sin\alpha) - \kappa_\mu \qquad (4)$$

for $\mu = 1, 2, \dots, M$

with

$$K_{\mu\nu} = \frac{\dot{y}_\mu(x_\mu - x_\nu) - \dot{x}_\mu(y_\mu - y_\nu)}{(x_\mu - x_\nu)^2 + (y_\mu - y_\nu)^2} \qquad (5)$$

$$x_\mu = \frac{\dot{q}_\mu}{M} + \frac{1}{M} \sum_{\substack{\nu=1 \\ \nu \neq \mu}}^{M} (L_{\nu\mu} q_\mu - L_{\mu\nu} q_\nu) \tag{6}$$

$$L_{\mu\nu} = \frac{\dot{x}_\mu (x_\mu - x_\nu) + \dot{y}_\mu (y_\mu - y_\nu)}{(x_\mu - x_\nu)^2 + (y_\mu - y_\nu)^2} \tag{7}$$

and

$$q_\mu = v_{n\mu} \cdot \dot{s}_\mu \quad \text{("transformed local source strength")} \tag{8a}$$

$$\gamma_\mu = v_{t\mu} \cdot \dot{s}_\mu \quad \text{("transformed local vortex strength")} \tag{8b}$$

with

$$\dot{s}_\mu = \sqrt{\dot{x}_\mu^2 + \dot{y}_\mu^2} \quad . \tag{9}$$

The dot always means the derivative with respect to the parameter φ. As to the derivatives of the coordinates $\dot{x}_\mu$, $\dot{y}_\mu$ it is recommended to calculate them with some good numerical method but finally introduce the angle of the tangent at the trailing edge into the calculation by recalculating $\dot{x}_{TE}$ from

$$\dot{x}_{TE} = \dot{y}_{TE} \cdot \operatorname{ctg} \tau \quad . \tag{10}$$

Due to the fact that the circulation of the flow is not yet fixed, the system of equation (4) is linear dependent and has to be supplemented by an additional condition, for instance the Kutta condition at the trailing edge

$$v_{tTE} = 0 \tag{11a}$$

or a prescribed total circulation

$$\Gamma = \int_{Su} v_t \, ds \approx \sum_{\mu=1}^{M} \gamma_\mu \Delta_\varphi = \text{const} \quad . \tag{11b}$$

4. 3 System of linear equations for a multi-element airfoil system

So far we dealt with a single airfoil. We now have to extend the system of equations to an airfoil system, consisting of I airfoils with interaction.

If for each airfoil No. k , we write down Eqs. (4) , supplemented by terms which express the influence of all other airfoils (nos. j ≠ k), we arrive at a system of I systems of linear equations:

$$\sum_{j=1}^{I} \mathfrak{A}^{(kj)} \bar{\gamma}^{(j)} = \bar{r}^{(k)} \quad , \quad k = 1, 2, \ldots, I \quad . \tag{12}$$

Here the vector components $\gamma_\nu^{(j)}$, $\nu = 1 \ldots M_j$, $j = 1 \ldots I$ are the $M = \Sigma M_j$ unknown values of the "transformed vortex distribution" at the given surface points. After solving the system the wanted velocities at the surface can easily be obtained, according to equation (8b), from

$$v_{t\nu}^{(j)} = \gamma_\nu^{(j)} / \dot{s}_\nu^{(j)} \tag{13}$$

with

$$\dot{s}_\nu^{(j)} = \sqrt{\dot{x}_{j\nu}^2 + \dot{y}_{j\nu}^2} \quad . \tag{13a}$$

For the matrix elements we get the following formulas:

$$A_{\mu\nu}^{(kj)} = K_{\mu\nu}^{(kj)} / M_j \quad \text{for} \quad j \neq k \quad \text{and/or} \quad \nu \neq \mu \tag{14}$$

and

$$A^{(kk)}_{\mu\mu} = -\sum_{\substack{\nu=1\\ \nu\neq\mu}}^{M_k} A^{(kk)}_{\nu\mu} \tag{15}$$

with

$$K^{(kj)}_{\mu\nu} = \frac{\dot{y}_{k\mu}(x_{k\mu} - x_{j\nu}) - \dot{x}_{k\mu}(y_{k\mu} - y_{j\nu})}{(x_{k\mu} - x_{j\nu})^2 + (y_{k\mu} - y_{j\nu})^2} \quad . \tag{16}$$

Notice: As shown in Ref. 9 for a very similar method it is better, especially for rather thin airfoils, to calculate the main diagonal elements of $\mathfrak{A}^{(kk)}$ by interpolation

$$A^{(kk)}_{\mu\mu} = \frac{1}{12}\left[4\left(A^{(kk)}_{\mu,\,\mu-1} + A^{(kk)}_{\mu,\,\mu+1} + A^{(kk)}_{\mu-1,\,\mu} + A^{(kk)}_{\mu+1,\,\mu}\right) - A^{(kk)}_{\mu,\,\mu-2} - A^{(kk)}_{\mu,\,\mu+2} - A^{(kk)}_{\mu-2,\,\mu} - A^{(kk)}_{\mu+2,\,\mu}\right] - \frac{1}{2} \tag{17}$$

and the elements below the other diagonal from Eq. (15)

$$A^{(kk)}_{\mu,\,M_k-\mu+2} = -\sum_{\substack{\omega=1\\ \omega\neq\mu}}^{M_k} A^{(kk)}_{\omega,\,M_k-\mu+2} \quad . \tag{18}$$

The components of the vectors $\bar{r}^{(k)}$ in Eq. (12) are

$$r^{(k)}_{\mu} = -V_{\infty}(\dot{x}_{k\mu}\cos\alpha + \dot{y}_{k\mu}\sin\alpha) + x^{(ki)}_{\mu} \quad . \tag{19}$$

If airfoil No. i is the one, on which a source distribution

$$v^{(i)}_{n\nu} = q^{(i)}_{\nu}/\dot{s}^{(i)}_{\nu} \quad , \quad \nu = \nu_T, \dots, \nu_S \tag{20}$$

for dead air simulation is arranged, we have according to Eq. (6) for $k = i$

$$x^{(ii)}_{\mu} = \frac{\dot{q}^{(i)}_{\mu}}{M_i} + \frac{1}{M_i}\sum_{\substack{\nu=1\\ \nu\neq\mu}}^{M_i}\left(L^{(ii)}_{\nu\mu}\, q^{(i)}_{\mu} - L^{(ii)}_{\mu\nu}\, q^{(i)}_{\nu}\right) \tag{21}$$

and for $k \neq i$ simply

$$x^{(ki)}_{\mu} = -\frac{1}{M_i}\sum_{\nu=1}^{M_i} L^{(ki)}_{\mu\nu}\, q^{(i)}_{\nu} \tag{22}$$

with

$$L^{(ki)}_{\mu\nu} = \frac{\dot{x}_{k\mu}(x_{k\mu} - x_{i\nu}) + \dot{y}_{k\mu}(y_{k\mu} - y_{i\nu})}{(x_{k\mu} - x_{i\nu})^2 + (y_{k\mu} - y_{i\nu})^2} \quad . \tag{23}$$

Now we have to fix the right hand sides of Eqs. (12), using Eq. (19) for the different basic solutions:

Basic flow (a_1):

Uniform approach flow in x-direction with $\alpha = 0^{\circ}$ and $v = V_{\infty}$ at infinity and no source distribution on any of the airfoils $(q^{(i)}_{\nu} = 0)$ leads to

$$r^{(k)}_{\mu} = -V_{\infty}(\dot{x}_{k\mu} + 0) + 0 = -\dot{x}_{k\mu}\cdot V_{\infty} \quad . \tag{24a}$$

The Kutta condition for all the airfoils gives the additional conditions for this flow

$$\gamma^{(k)}_{1} = 0 \quad , \quad k = 1 \dots I \tag{25}$$

with Index 1 from now on always marking the trailing edge. In a corresponding way we get for

Basic flow (a_2):

$$r_\mu^{(k)} = - \dot{y}_{k\mu} \cdot V_\infty \tag{24b}$$

and again the additional conditions (25).

Basic flow (b):

Pure circulatory flow around airfoil No. i with total circulation $\Gamma_i = 2\pi \, c \cdot V_\infty$, Kutta condition for all the other airfoils, no flow at infinity and no source distribution anywhere leads to

$$r_\mu^{(k)} = 0 \tag{24c}$$

and the additional conditions

$$\sum_{\nu=1}^{M_i} \gamma_\nu^{(i)} = M_i \cdot c \cdot V_\infty \quad \text{for airfoil No. } i \tag{26}$$

and Eq. (25) for all other airfoils No. $k \neq i$.

Basic flow (d):

Outflow produced by a given source distribution at the surface of airfoil No. i between points T and S

$$v_{n\nu}^{(i)} \neq 0 \quad \text{for} \quad \nu = \nu_T \ldots \nu_S \quad . \tag{27}$$

Further conditions for this flow are

no flow at infinity,

$\Gamma_i = 0$ (no circulation around airfoil No. i), and

$v_{t1}^{(k)} = 0$ for $k \neq i$ (Kutta condition for the other airfoils).

With that we get

$$r_\mu^{(k)} = \varkappa_\mu^{(ki)} \quad , \tag{28}$$

with $\varkappa_\mu^{(ki)}$ from Eqs. (21) and (22) and $q_\nu^{(i)}$ from Eq. (20), and the additional conditions

$$\sum_{\nu=1}^{M_i} \gamma_\nu^{(i)} = 0 \quad \text{for} \quad k = i \tag{29}$$

and Eq. (25) for all other airfoils $(k \neq i)$.

Notice: As to the choice of the source distribution $v_n^{(i)}$ we can, on the basis of some experience, recommend the one shown in Fig. 5. Point T should be chosen at about 99 % chord at the lower surface.

For all basic flows certain additional conditions have somehow to be included in the system of systems of Eqs. (12). It is recommended to add in each partial system the corresponding condition, divided by M_k, to each equation.

4. 4. Effect of the boundary layer displacement thickness

In order to take into account the displacement effect of the attached boundary layer we calculate an additional basic flow (e):

This shall be an outflow which, after superpostion with the basic flows (a) and (b), shall give a little outflow region all around each airfoil which corresponds to the displacement thickness $\delta(s)$ of the boundary layer (see Fig. 6).

We will use a source distribution on the surface, corresponding to the local increase of the displacement thickness δ and the velocity v_t

$$v_n = d(\delta \cdot v_t)/ds \quad .$$

Thus we get approximately for airfoil No. j

$$q_\nu^{(j)} = v_{n\nu}^{(j)} \cdot \left(\frac{ds}{d\varphi}\right)_\nu^{(j)} =$$

$$= \frac{M_j}{4\pi}\left[\left(\delta_{\nu+1}^{(j)} - \delta_{\nu-1}^{(j)}\right) \cdot v_{t\nu}^{(j)} + \right.$$

$$\left. + \left(v_{t\nu+1}^{(j)} - v_{t\nu-1}^{(j)}\right) \cdot \delta_\nu^{(j)}\right] \quad . \tag{30}$$

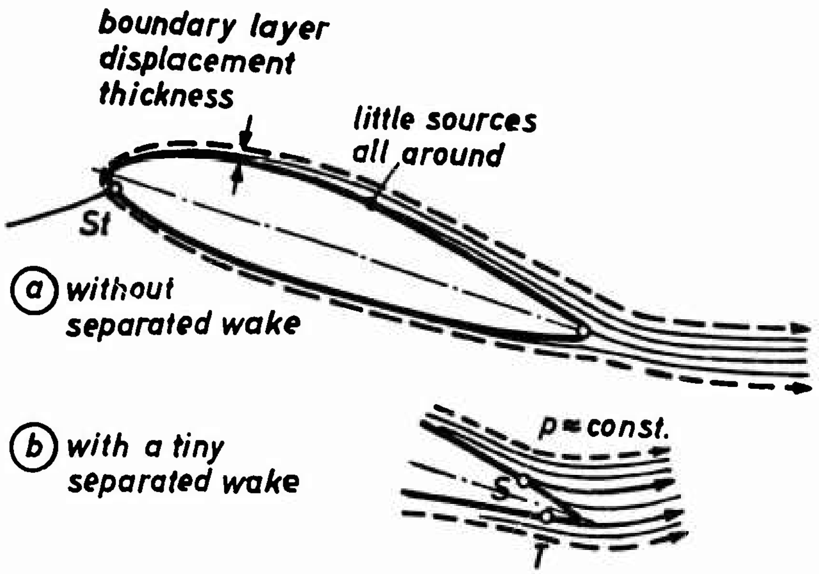
boundary layer displacement thickness
little sources all around
St
(a) without separated wake
(b) with a tiny separated wake
p=const.
S
T

Fig. 6 Simulation of boundary layer displacement thickness

Further conditions for this basic flow shall be $v = 0$ at infinity and $v_{t1}^{(k)} = 0$ at the trailing edge (which makes sure that after superposition we still get no flow around the trailing edges). So we finally get

$$r_\mu^{(k)} = \sum_{j=1}^{I} x_\mu^{(kj)} \tag{31}$$

with $x_\mu^{(ki)}$ from Eqs. (21) and (22) with $q_\nu^{(j)}$ from Eq. (30) and again Eq. (25) as the additional conditions.

Notice: The boundary layer calculation gives the displacement thickness only up to the calculated separation point. From there on or at the latest from about 96 % chord on we chose v_n going linearly down to zero at the trailing edge. Thus we get a simulated displacement thickness which still grows a bit near the trailing edge. Finally, even for the fully attached flow, we add a little "dead air region" (from 96 % chord on) to make the wake flow off like a tiny separated wake with constant pressure near the airfoil (see Fig. 6).

4. 5. Ground effect

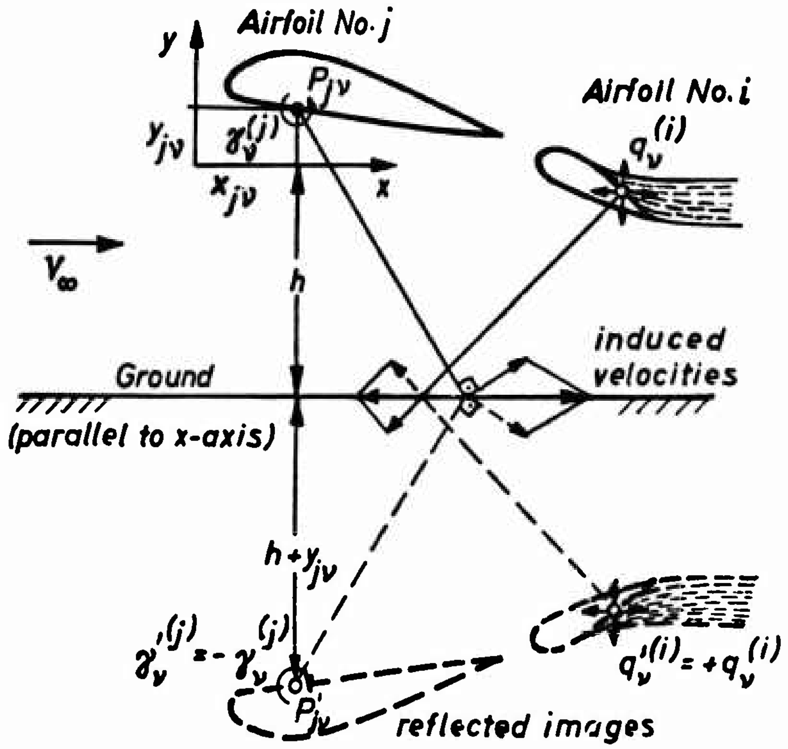
Airfoil No. j
y
$P_{j\nu}$
$y_{j\nu}$
$\gamma_\nu^{(j)}$
$x_{j\nu}$
x
Airfoil No. i
$q_\nu^{(i)}$
V_∞
h
induced velocities
Ground
(parallel to x-axis)
$h+y_{j\nu}$
$\gamma_\nu'^{(j)} = -\gamma_\nu^{(j)}$
$q_\nu'^{(i)} = +q_\nu^{(i)}$
$P'_{j\nu}$
reflected images

Fig. 7 Model of simulating ground effect

Now we want to incorporate the ground effect into our potential flow method. This can be done by reflecting the total airfoil system at the ground (see Fig. 7). Then each pair of elementary singularities induces only tangential (no normal) velocities at the ground. Thus, with the onset flow parallel to the ground, the ground is a streamline.

Now we have to take into account the influence of the reflected images of all the singularities on the velocities at the original airfoils. This results into an extension of the system of equations (12):

$$\sum_{j=1}^{I}\left(\mathfrak{a}^{(kj)} - \mathfrak{a}'^{(kj)}\right)\bar{\gamma}^{(j)} = \bar{r}^{(k)} + \bar{r}'^{(k)} \ , \quad k = 1,\dots,I \tag{32}$$

with the elements of the matrices $\mathfrak{a}^{(kj)}$ being

$$A'^{(kj)}_{\mu\nu} = \frac{1}{M_j} \frac{\dot{y}_{k\mu}(x_{k\mu} - x_{j\nu}) - \dot{x}_{k\mu}(y_{k\mu} - y'_{j\nu})}{(x_{k\mu} - x_{j\nu})^2 + (y_{k\mu} - y'_{j\nu})^2}$$

for all k, j, μ and ν.

$$y'_{j\nu} = -(2h + y_{j\nu}) \tag{33}$$

is the ordinate of the image of the surface point $P_{j\nu}$.

The negative sign in (32) results from the fact that the image of the elementary vortex $\gamma_\nu^{(j)}$ must have the same quantity but opposite sign.

The additional vector on the right hand side has to express the influence of the images of the elementary sources $q_\nu^{(i)}$. The components of this vector are

$$r'^{(k)}_{\mu} = \kappa'^{(ki)}_{\mu} \tag{34}$$

with $\kappa'^{(ki)}_{\mu}$ from equations (22) and (23), but $y_{i\nu}$ being replaced by $y'_{i\nu}$ in equation (23).

5. SUPERPOSITION OF THE BASIC FLOWS

By superpostion of the basic flows (a_1), (a_2), (b), (d) with proper weight factors a_1, a_2, b, d we want to construct a resulting flow, which satisfies the following conditions:

(1) Parallel flow at infinity with velocity V_∞ and the given angle of attack α.

(2) Kinematic flow condition at the surfaces of all airfoils, except at airfoil No. i between points S and T.

(3) Kutta condition at all airfoils, except for airfoil No. i.

(4) An outflow region shall exist starting from airfoil No. i with the pressure at point U on the upper separating streamline above the trailing edge being equal to the pressure at the starting points S and T at the upper and lower surface of airfoil No. i:

$$c_{pU} = c_{pS} = c_{pT} \quad .$$

Condition (1) is satisfied by calculating the weight factors for the basic flows (a_1) and (a_2) from

$$a_1 = \cos\alpha \quad \text{and} \quad a_2 = \sin\alpha \quad . \tag{35}$$

All other basic flows give no contribution to the flow at infinity.

Condition (2) and (3) are satisfied a priori by each of the basic flows.

The only remaining problem now is to satisfy condition (4).

After the weight factors a_1 and a_2 have been fixed by equations (35), the pressure coefficients c_p can be considered as functions of the remaining weight factors b and d.

So condition (4) can be written

$$\begin{aligned} c_{pU}(b,d) - c_{pS}(b,d) &= f_1(b,d) = 0 \\ c_{pS}(b,d) - c_{pT}(b,d) &= f_2(b,d) = 0 \quad . \end{aligned} \tag{36}$$

The system of two equations can be solved by a two-dimensional Newton iteration, with the partial derivatives of $f_1(b,d)$ and $f_2(b,d)$ being calculated by discrete approximation, for example

$$\frac{\partial f_1(b,d)}{\partial b} \approx \frac{f_1(b+\Delta b, d) - f_1(b,d)}{\Delta b} \quad . \tag{37}$$

To calculate $f_1(b,d)$ for a given pair b, d we need point U on the upper separating streamline, which has the same value of the stream function Ψ as the surface in front of point S. Point U can be found by iteration.

For further details see Ref. 5.

6. BOUNDARY LAYER CALCULATION

For the calculation of the boundary layer we use a program of J. Rotta (Ref. 8) which is based on the simultaneous integration of the momentum and the energy equations of the boundary layer. In our special case case of incompressible flow we have

$$\frac{d\delta_2}{ds} + \delta_2 \frac{H_{12} + 2}{v_t} \frac{dv_t}{ds} = \frac{1}{2} c_f$$

and

$$\frac{d\delta_3}{ds} + \delta_3 \cdot \frac{3}{v_t} \frac{dv_t}{ds} = c_d \quad .$$

For the shape parameter $H_{12} = \delta_1/\delta_2$, the local skin friction coefficient c_f, and the dissipation coefficient c_d for the laminar boundary layer, relations are used which are based on Hartee-velocity-profiles.

For the turbulent boundary layer the velocity-profiles are described by power laws. For the friction coefficient the formula of Ludwieg - Tillmann is used and for the dissipation coefficient the formula of E. Truckenbrodt. For more details see Refs. 8 and 10.

As criterion for separation we take

$H_{32} = \delta_3/\delta_2 = 1.5$ for the laminar boundary layer

$H_{12} = \delta_1/\delta_2 = 4.0$ for the turbulent boundary layer .

As input to the program not only $c_p(s)$ is needed, but also the Reynolds number $Re = V_\infty \cdot c/\nu$ and initial values for the momentum thickness δ_2 and the energy thickness δ_3 of the boundary layer at the first point behind the stagnation point. Rotta recommended

$$\delta_2 = 0.292 \sqrt{\frac{\nu}{(dv_t/ds)_{St}}} \quad \text{and} \quad \delta_3 = 1.64\,\delta_2 \quad .$$

7. NUMERICAL RESULTS

Our method has been programmed in FORTRAN and applied to some typical airfoil combinations. The results have been compared with experiments.

The program so far is applicable to systems of up to 3 airfoils with up to $\Sigma M_k = 140$ given surface points. It needs about 200 K bytes of main storage and about 2 minutes CPU-time on an IBM 360-65 computer for calculating one separated flow, that is the pressure distribution and lift coefficient for one data-set (α, Re), or one point of a $c_L(\alpha)$-curve.

For our examples we used 100 surface points on the main airfoils and 40 points on the auxiliary airfoils. With $Re > 10^6$ we always assumed transition at the calculated laminar separation point and considered only turbulent separation as real.

Our first example is a modified NACA 64-210 airfoil with a dropped nose and a leading edge slat (see Fig. 8). For this configuration experiments of W. Baumert (Ref. 11) are available for comparison. Figure 8 shows the pressure distributions for a flow with moderate rear separation at the main airfoil. Though wind tunnel and finite span corrections were applied to the angle of attack, the measured pressure distribution may still correspond to a somewhat lower α than the one used for the calculation. That would explain the slight deviations of the pressure distributions at the upper surfaces. Figure 9 compares the $c_L(\alpha)$-curves with and without the slat. At about $\alpha = 10^\circ$ the separation point starts to move forward at the main airfoil, and at $\alpha \approx 26.5^\circ$ our calculation indicated additional separation at the slat. Because treating multiple separation is not yet included in our method, we had to stop here, but can assume that from here on the lift breaks down rapidly and we are beyond $c_{L\,max}$. All in all there is rather good agreement of our theoretical results with the experiments, and the positive effect of the slat is well predicted.

Our second example is a modified RAE 2815 airfoil with a slightly dropped nose and a slotted flap (Fig. 10). Comparing the calculated $c_L(\alpha)$-curve with experiments from reference 12, using the experimental Reynolds number $Re \approx 3.8 \times 10^6$ for our calculations we see some slight disagreement. With $Re = 5 \times 10^6$ agreement gets better. In any case there is a remarkable improvement compared to ideal flow theory. With the flap deflection of about 20° there is some separation at the flap already for $\alpha = 0^\circ$. Near $\alpha = 14^\circ$ our boundary layer calculation indicated separation at the main airfoil, too. Fig. 11 shows the maximum lift and the lift for $\alpha = 0^\circ$ in dependance of the overlap s_x of the flap. The lift coefficient c_L for $\alpha = 0^\circ$ has a rather flat maximum at about 3 % overlap, and $c_{L\,max}$ a more distinct maximum at about 4 % overlap.

Our third example is a NACA NACA 23012 airfoil with a slotted flap (Fig. 12). Here also the ground effect was included. Figure 12 shows $c_L(\alpha)$-curves calculated for two different flap angles with and without ground effect. Because no experiments are available for this case we offer in Fig. 13 a qualitative comparison with three-dimensional experiments for a sweptback wing with flaps (Ref. 13). We can see that all the typical features are in good agreement: With the flaps neutral the ground causes an increasing lift for all positive angles of attack. Also the maximum lift is raised. With the flaps deflected there is a slight increase of c_L for the lower angles of attack but a distinct decrease for the higher angles and a reduced maximum lift near the ground.

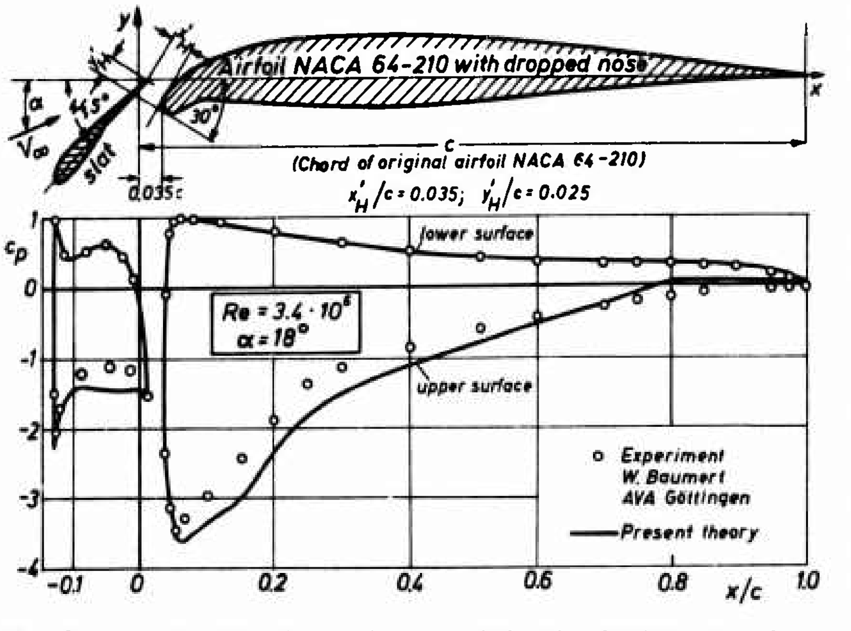

Fig. 8 Pressure distribution for an airfoil with a leading edge slat

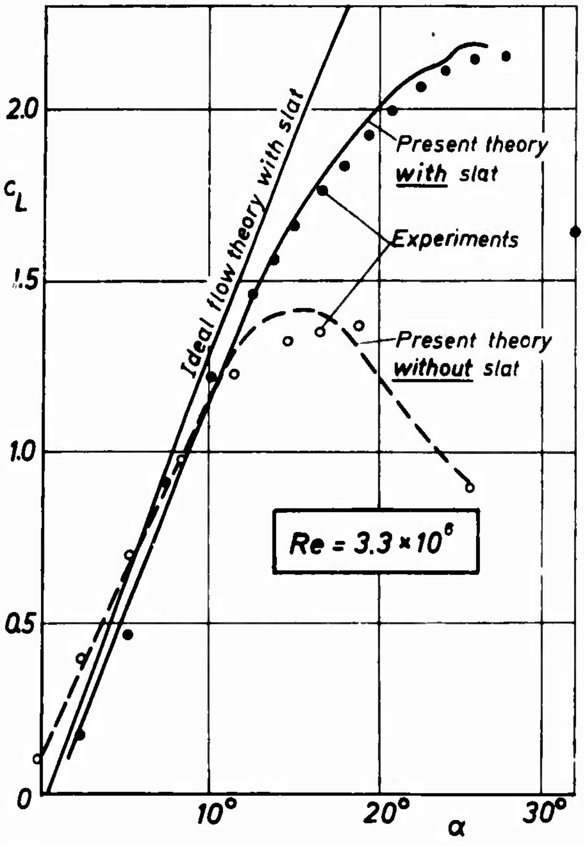

Fig. 9 Lift coefficient versus angle of attack from theory and experiment for the airfoil of Fig. 8 with and without slat

8. CLOSING REMARKS

A numerical method has been developed for prediction of pressure distributions and lift coefficients, including maximum lift, for multi-element airfoil systems in incompressible flow. In addition to the displacement effect of a separated wake, also the effects of boundary layer displacement and ground can be accounted for. The method, though rather complicated and extensive, once programmed for a computer, can easily be applied to almost arbitrary airfoil combinations. Good agreement with experiments was obtained for several slat and flap arrangements and the ground effect was qualitatively well predicted.

Nevertheless the method is far from being perfect, and several extensions seem desirable:

For rather thin airfoil elements and moderate Reynolds numbers the possibility of long bubble separation should be included.

If the high lift devices are very close to the main airfoil it can become important to account for merging and interacting boundary layers. The wake of a forward element merging with the boundary layer of the following element may influence transition and separation.

Sometimes even multiple separation can be important. At some slotted flap configurations there can be a bubble at the lower rear part of the main body and a separated wake at the flap. Also to follow up the $c_L(\alpha)$-curve beyond maximum lift, separation at more than one surface must be taken into account.

Drag prediction is another important task. The pressure drag is much more sensitive to the dead air pressure than the lift. So far our dead air pressure prediction seems good enough to predict the lift with an accuracy of few precent, but for drag prediction the dead air pressure prediction needs improvement.

Finally an extension of the method to compressible and/or three-dimensional flow would certainly be of practical importance. So there is still a wide field to work on.

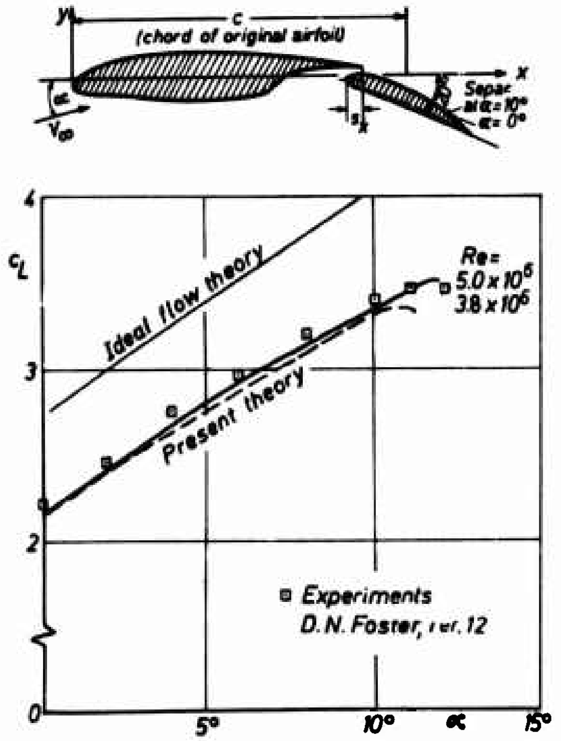

Fig. 10 Airfoil with a slotted flap from Ref. 12 (gap = 0.023·c, overlap s_x = 0.043 c). Lift versus angle of attack

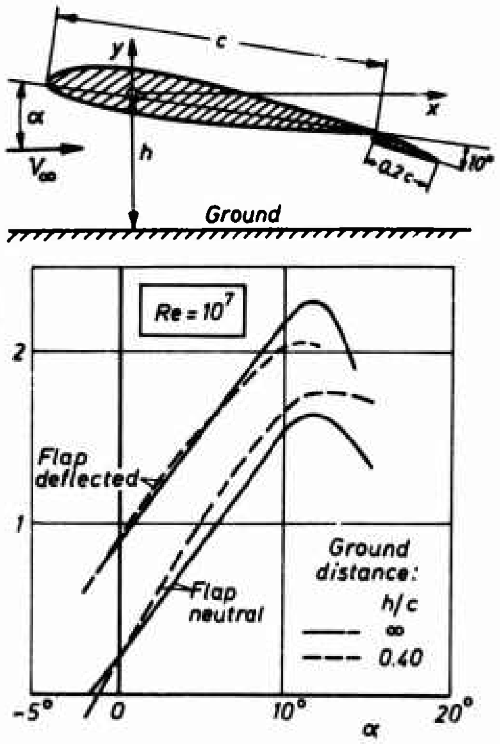

Fig. 12 Lift versus angle of attack, calculated for a NACA 23012 airfoil with a NACA 23012 slotted flap with and without ground effect

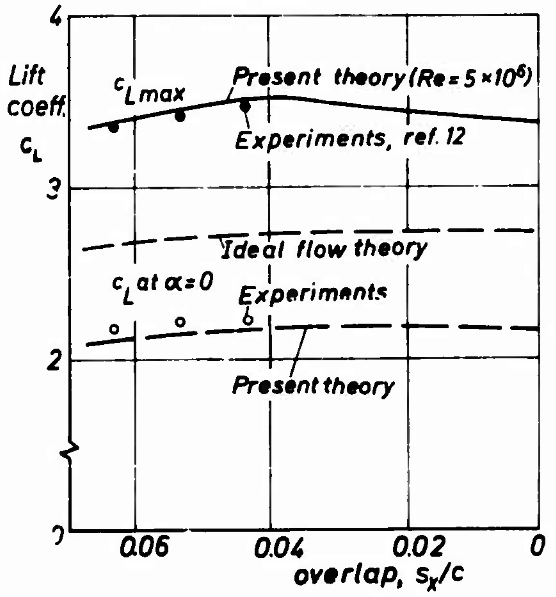

Fig. 11 Lift coefficients versus overlap s_x for the airfoil with a slotted flap of Fig. 10

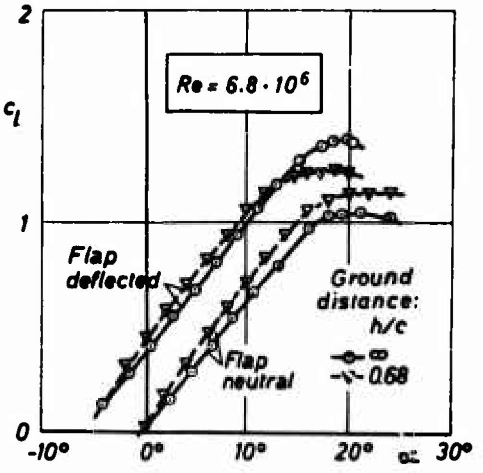

Fig. 13 Lift versus angle of attack, measured for a wing with flap with and without ground effect (Ref. 13)

Wing: airfoil section NACA 64_1-112, aspect ratio 4, 42° sweep back

Flap: 0.2c trailing edge split flap, deflection 60°

REFERENCES

1.	G. V. Lachmann	Boundary Layer and Flow Control, Vol. 1, Pergamon Press, Oxford-London-New York-Paris 1961
2.	D. Schlichting, E. Truckenbrodt	Aerodynamik des Flugzeuges, 2. Band Springer Verlag Berlin-Heidelberg-New-York 1969
3.	AGARD	Fluid Dynamics of Aircraft Stalling AGARD CP 102 (1972), Lisbon
4.	K. Jacob	Berechnung der abgelösten inkompressiblen Strömung um Tragflügelprofile und Bestimmung des maximalen Auftriebs Zeitschr. f. Flugwiss. 17, S. 221-230 (1969)
5.	K. Jacob	Berechnung der inkompressiblern Strömung mit Ablösung für Profilsysteme DFVLR-AVA IB 065-72 A 34 (1973)
6.	A. Walz	Berechnung der Druckverteilung an Klappenprofilen mit Totwasser Jahrbuch dtsch. Luftfahrtforschung 1940 I, S. 265-277 (1940)
7.	E. Martensen, K. v. Sengbusch	Ueber die Randkomponenten ebener harmonischer Vektorfelder Arch. f. Rat. Mechanics a. Analysis, Vol. 5, No. 1, pp. 46-75 (1960)
8.	J. Rotta	Rechenprogramm für Grenzschichten bei kompressiblen ebenen und achsensymmetrischen Strömungen DLR-FB 71-51 (1971)
9.	F. W. Riegels K. Jacob	Berechnung der Druckverteilung endlich dicker Profile ohne und mit Klappen und Vorflügeln Zeitschr. f. Flugwiss. 11, S. 357-367 (1963)
10.	J. Rotta	Turbulent boundary layer calculation with the integral dissipation method Airforce Office of Scientific Research - Industrial Sponsors of Internal Flow Program (AFOSR-IFP) Stanford Conference Proceedings Vol. 1, pp. 177-181 (1968)
11.	W. Baumert, K. Enghardt	Dreikomponenten-Messungen an einem Rechteckflügel mit Vorflügel und abgesenkter Nase DFVLR-AVA-Bericht 71 C 29 (1971)
12.	D. N. Foster H. P. A. H. Irwin B. R. Williams	The two-dimensional flow around a slotted flap RAE Tech. Rep. No. 70164 (1970)
13.	C. Furlong T. v. Bollech	Effect of ground interference on the aerodynamic and flow characteristics of a 42° swept back wing at Reynolds numbers up to $6.8 \cdot 10^{6}$ NACA Rep. 1218 (1955)

EXPERIMENTAL HIGH LIFT OPTIMIZATION OF MULTIPLE ELEMENT AIRFOILS *

by

Björn L.G. Ljungström

FFA, Box 1121, S-161 11 BROMMA

SWEDEN

SUMMARY

High lift optimization is first discussed in a general sense. High lift performance is just one of a number of parameters that have to be assessed in order to evaluate the impact of a particular flap system on the over-all cost efficiency of an aircraft project. The experiments discussed below are concerned with the static performance of flap systems and are therefore optimizations in a more limited sense.

The general usefulness of 2-D testing and the 2-D wind tunnel techniques used for experimental high lift work at the FFA are discussed.

Results are shown from extensive geometrical variations of double- and triple-slotted mechanical flaps. An interesting correlation between optimum slat gap and optimum slat angle is shown. Boundary layer measurements have been carried out in order to gain som further understanding of these slat trends. It is shown that an optimum slat position corresponds to a flow with relatively little interaction between the slat wake and the main wing and flap boundary layers. Similar results are also obtained for the trailing edge, where it is found that the different viscous layers should be kept essentially separated from each other. This is achieved with a large first flap gap and decreasing gaps closer to the trailing edge.

It is clearly shown that the slats or trailing edge flaps cannot be treated separately. The slat position has a substantial effect on the viscous flow over the flaps and is therefore of importance for both leading edge and trailing edge limited cases.

Two different calculation methods have been used. One potential flow method and one method with boundary layer effects including interactions. The use of state of the art calculation techniques for optimization purposes is discussed with these results as a background.

The role of 2-D experiments in high lift development is discussed.

NOTATION

U_∞	free-stream velocity
C_w	wall suction reference pressure coefficient = $\frac{p_w - p_{ref}}{q_\infty}$
p_w	wall suction reference pressure
α	angle of attack
L	lift
L/D	lift to drag ratio
C_L	$\frac{L}{\frac{1}{2}\rho U_\infty^2 \cdot S}$ = lift coefficient
$C_{L\,max}$	maximum lift coefficient
C_D	drag coefficient
Re	$\frac{U \cdot C}{\nu}$ = Reynolds number, based on model chord

C	model unextended chord
S	model reference area
δ_s	slat angle
h_s	slat gap
O_s	slat overlap
h_{f_1}	first flap gap
h_{f_2}	second " "
h_{f_3}	third " "
δ_{f_1}	first flap angle
δ_{f_2}	second " "
δ_{f_3}	third " "

1. INTRODUCTION

The design of high lift systems for coming generations of aircraft is a complex optimization problem involving a large number of parameters.

The primary effects are of course the improvements in airfield and/or payload performance due to the high lift system.

There are however a number of significant secondary effects that have to be evaluated in order to assess the overall improvements due to a particular system development.

The most important of these are:

- Power requirements
- Control and stability requirements
- Cruise performance penalties
- Maintenance requirements
- Structural efficiency, weight
- Noise characteristics
- Ride comfort

---

* Research sponsored by the Swedish Board for Technical Development, the Defence Materiel Administration of Sweden and FFA.

It has consequently become more and more evident that improvement of lift and drag coefficients is just one of several possible ways to improve a high lift system, but one that has certainly dominated the development efforts during the last decades.

The optimization criteria for a high lift system can be expressed as:

a) • **Maximum total benefits for a specified cost**

or

b) • **Minimum costs for a specified mission**

The latter criterion probably represents the most common approach in aircraft design.

These criteria can be applied on many different levels. Fig no. 1 is an example where the costs and primary merits of the high lift system itself are plotted. The trends should represent the envelope of present state of the art systems. The two criteria discussed will result in goals as indicated in the figures (arrows a and b).

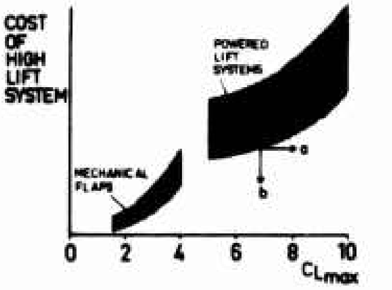

Fig. 1 High lift hardware cost.

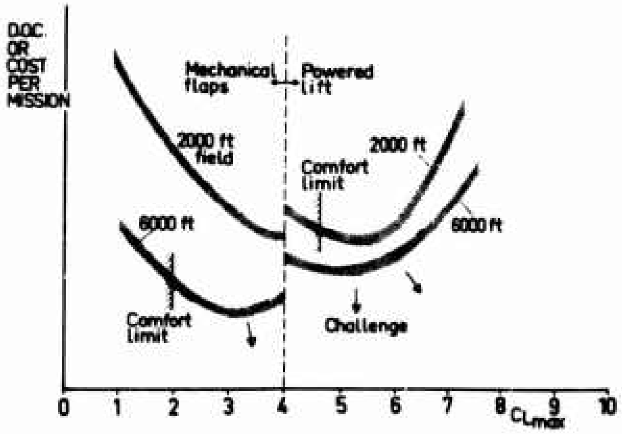

Fig. 2 Operating costs v.s. $C_{L\,max}$.

A much more complete approach is shown in Fig 2 where direct operating cost (per ton km) or cost per mission for a fixed payload, range and cruising speed is plotted against $C_{L\,max}$ of the high lift system. (Similar plots can of course be made for any parameter).

Two different field length requirements are plotted. 6000 ft represents todays short-to medium-range aircraft. The trend for mechanical systems for this case is one way to explain the historical development of such systems. The cost of fairly complicated mechanical flap systems has been small compared to the gains in payload and cruise performance. There are of course practical limits in wing loading which comes out as C_L-limits in Fig 2. These may however be shifted substantially if gust alleviation is used.

There should always exist one optimum $C_{L\,max}$. This optimum increases with decreasing field length. One basic assumption in the diagram is that a powered lift system will give higher costs than a mechanical one at the same C_L. This is reflected by the step change at the limit of mechanical lift. For any given combination of payload-range requirements and state of the art data of high lift systems there should exist one specific field length for which powered lift systems become more economical than mechanical ones. The illustrated case shows this to be close to 2000 ft, which may be true for some combination of payload, range and cruise speed.

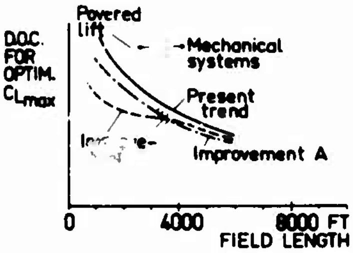

Fig. 3 D.O.C. v.s. field length.

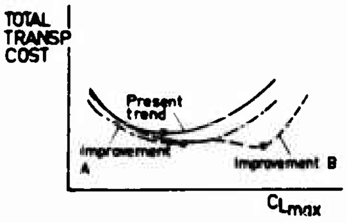

Fig. 4 Transportation cost v.s. $C_{L\,max}$.

Fig 3 shows that the DOC for each optimum $C_{L\,max}$ decreases steadily for increasing field length.

The justification for shorter field lengths is reflected by the total transportation costs plotted in Fig 4, where the facility costs and effects on other transportation modes are incorporated. The interesting question now is, what is the present optimum $C_{L\,max}$ for a specified mission and how will a certain improvement of high lift technology affect the trends? Two examples of possible improvements are plotted in Fig 3. A assumes that there is fairly equal improvement of mechanical and powered lift systems. B assumes that powered lift systems have dramatically improved and mechanical ones only marginally. This will probably have a substantial impact on the potential applications of air-transportation. The question is, how much must the present systems be improved before a certain type of operation becomes economical and are these improvements within reach of R & D efforts? The answers to these questions would be a great help to the aerodynamicist who does not really know where his efforts are most likely to contribute to the development of air-transportation.

One illustration of this is the case of powered lift systems compared to mechanical ones. It is obvious that the field lengths of todays airports cannot economically justify powered lift systems. The question whether they can be used economically will depend on mainly two factors: 1) the potential benefits of short field operation, 2) the development of powered lift systems and their impact on the operating cost of the aircraft.

All these possible implications of high lift system development represent a challenge to the aerodynamicist (and others) which extends from improvements of simple mechanical flaps to development of sophisticated powered lift systems. Mechanical flaps have dominated the air-transportation scene up to now. They will probably continue to do so for quite some time. It is the author's belief that substantial improvement of powered lift systems is required if they are going to be competitive with mechanical ones even for fairly short field lengths. A recent study by the Boeing Company has shown mechanical flap systems to be superior in cost, weight and noise for field lengths down to 2000 ft if gust alleviation is employed (Ref 1).

There is still room for improvements in lift and drag efficiency and may be even more important in stability and control characteristics of sophisticated mechanical flap systems.

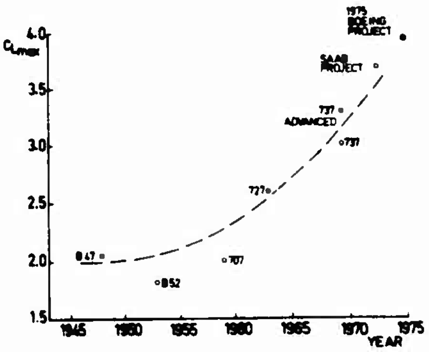

Fig. 5 Maximum lift history of mechanical high lift devices.

Fig 5 shows a time history of $C_{L\ max}$ of mechanical flaps.

There is no evident stagnation of the trend, there has on the contrary been a marked improvement the last ten years partly due to a revived interest for mechanical flap development. The work reported here is one contribution to this effort. Its objectives are to

- **increase our knowledge of the flow around mechanical flap systems,**
- **improve present optimization procedures.**

2. 2-D WIND TUNNEL TESTING

2.1 General

2-D wind tunnel tests have been widely used during the history of aviation for development of both high speed wings and low speed flap systems. They have also been used for more fundamental studies of wing flow problems such as boundary layer growth and separation, boundary layer control, jet flaps, etc.

The obvious advantages of 2-D tests are:

- A higher Reynolds number is achieved for a given wind tunnel size.
- Less complication and cost in model design and adjustments.
- A more generalized flow situation is obtained being well-suited for fundamental studies of boundary layer, etc.
- The complexity and quantity of pressure distributions and boundary layer measurements are significantly reduced.

The main problems are:

- How should the 2-D test be interpreted in the 3-dimensional world and what are the limits for their applicability.
- The difficulty of obtaining truly 2-dimensional flow up to and beyond the stall.

The important question now is to what extent and for what applications will 2-dimensional tests be justified. There is no general answer to this. Extensive comparisons of 2-D tests with 3-D ones should give some guidance, which does however depend on the 2- and 3-dimensional testing techniques used. It could for instance be quite misleading to draw general conclusions about this from 2-D tests with inadequate wall boundary layer control.

The most important applications of 2-D tests with present testing techniques and knowledge are according to the author's belief:

1) Fundamental studies of viscous and inviscous wing flow including experiments to support the development of calculation methods.

2) Studies of high lift performance trends for variations of geometric parameters such as flap shapes, flap angles and gaps in order to improve our ability to optimize high lift system geometries both 2- and 3-dimensionally.

3) Optimization of high lift section geometries for wings of moderate sweep and reasonable aspect ratio, primarily for mechanical flap systems. (The limits in AR and sweep depend on a number of other factors and cannot be given generally). Half-model tests may however for some of these cases be more cost effective, especially for cases where engine-wing interaction is significant.

4) Reynolds number effects on the results for a fixed configuration and may be more important, on the optimum geometry. This knowledge will be helpful in the extrapolation of optimum geometry and performance of both 2-D and 3-D cases from model to full-scale Re.

2-D Optimization problem

The general 2-dimensional high lift optimization problem which is a significant simplification of a real 3-dimensional case, nevertheless has such a large number of variables that it becomes impossible to cover all possible variations experimentally. The variables are: size and shape of flap elements, plus three degrees of freedom for each flap element.

A common situation is that one or a few sets of flap shapes are selected from experience, possibly aided by calculations. The remaining experimental problem is then that of optimizing the positions of the flap elements for each alternative configuration. The experiments in the present report are primarily concerned with this latter problem.

The remaining number of parameters is still substantial for a configuration of given airfoil and flap shapes. The geometry of a wing with a leading edge slat and a triple slotted flap is defined by 12 independent parameters. The problem is then to choose a parameter variation program that will converge towards a well-optimized configuration within reasonable time. A good understanding of the physical background to the performance trends for different geometrical parameters will be very helpful in determining such a program. This includes an understanding of the balance between viscous and inviscous effects that govern the trends for different flap gaps and flap angles, interrelationships between different parameters and interaction between leading edge and trailing edge devices.

Optimization criteria

The criteria that should be applied are first of all determined by the operational requirements being associated with take off, landing and manoeuvring performance. These requirements can be formulated in terms of lift, drag and pitching moment. The criterion for static performance must then be some function of these three parameters. The most simple case has been landing where maximum lift coefficient has been a very dominating requirement. This has been changed lately due to noise requirements, implicating a need for low drag - low power setting approaches.

It is however impossible to give a general function of these parameters which can be used for two-dimensional testing, and it is questionable whether 2-D results give meaningful trends for all three parameters. C_L-results and $C_{L\,max}$ trends are by far the ones that can most easily be interpreted 3-dimensionally. The 2-D drag results are less accurate and represent only a small fraction of the 3-dimensional drag (2-D lift to drag ratios are approx. = 100). The C_L-results are therefore considered to be the most important ones in 2-D testing. Significant differences in 2-D drag are however useful for comparison of configurations with small lift differences, and do also give an indication of the amount of separation.

A comparison of $C_{L\,max}$ and drag trends for different geometrical variables reveals that they can be surprisingly similar for some variables such as third and second flap gap. This means that the geometry for the highest $C_{L\,max}$ in this case has the most efficient flap flow resulting in minimum drag at least for high angles of attack. There are many other parameters where $C_{L\,max}$ and drag trends are quite different such as flap angle and slat angles. A slat position that gives good $C_{L\,max}$ results may have high drag due to separations on the lower side at lower angles of attack.

The "optimization" trends discussed in the following are limited mainly to C_L and $C_{L\,max}$ results.

2.2 2-D Wind tunnel facility

The high lift test results reported below are mainly from 2-dimensional tests in the FFA 3.6 m low speed wind tunnel. The tunnel is equipped with a 2-D insert section as shown in Fig 6.

The vertical walls are equipped with boundary layer bleed and boundary layer suction through a perforated area as shown in Fig 6. The perforated suction boxes are connected to the FFA vacuum rock chamber, which means that very large suction quantities can be obtained.

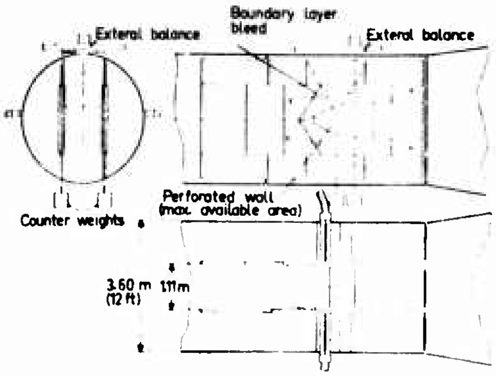

Fig. 6 FFA two-dimensional insert test section.

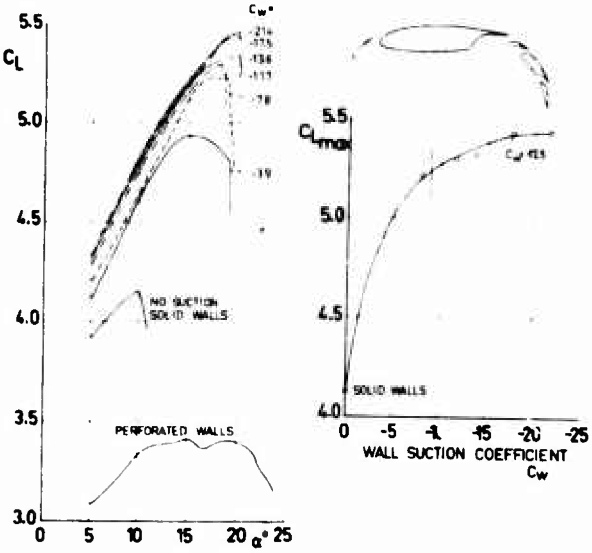

Fig. 7 Effect of wall boundary layer suction for triple slotted flap configuration.

2.3 Wall boundary layer control

Wind tunnel wall boundary layer control is considered to be of paramount importance for the kind of 2-dimensional high lift development work discussed in this paper. The combined boundary layers at the model wall junction will cause local separations that spread and distort the entire flow on the model well before the 2-dimensional $C_{L\ max}$. This effect increases with increasing high lift potential of the model. The use of centre-line pressure measurements will give somewhat better results than balance measurements for the case without boundary layer control, but the flow is still very 3-dimensional with wall induced premature separation. The importance of boundary layer control is illustrated in Fig 7 which shows the effect of wall suction on results for a 2-dimensional triple-slotted wing.

$C_{L\ max}$ increases from 4.2 for solid walls up to 5.45 for the nearly 2-dimensional case.

The steep part of the curve on the right-hand side corresponds to a case where separation is prematurely spread from the walls covering a substantial part of the wing surface. The flattened part of the $C_{L\ max}$-trend corresponds to a flow with small separated regions close to the side walls which decrease in size with increasing suction and do not spread spanwise. The stall is no longer premature as shown in Fig 7, but the flap efficiency at high angles of attack is still somewhat degraded resulting in a slightly too low $C_{L\ max}$.

The suction quantity for the tests is chosen slightly higher than that for which the curve levels-off in Fig 7. It is considered better to have too much suction than too little. The governing criterion for the suction for these tests is to get 2-dimensional conditions at the stall. This means that the suction quantity which is held constant for practical reasons, will be too high for all angles below the stall. This is not considered to be any problem since the effects are fairly small, and the interest of the tests is concentrated around $C_{L\ max}$ optimization and drag measurements around $C_L = 0.69 \cdot C_{L\ max}$. The drag is measured with a wake pressure rake at a spanwise station well away from the wall and should therefore not be too much affected by excessive suction (contrary to the case for too little suction).

2.4 Measurements

Lift and pitching moment is measured with an external mechanical balance, except for the cases where pressure measurements are used.

Drag is measured with a total head rake at a spanwise station which is undisturbed by walls and model brackets.

Balance-measured drag is inadequate for several reasons; It requires a very accurate knowledge of the mean flow direction in the tunnel, due to the very high 2-dimensional L/D ratios (~ 100). The balance results are also strongly affected by local anomalities in the vicinity of side walls and flap brackets.

Pressure distributions are measured on one of the models (Ref 3).

Total head boundary layer traverses are carried out with a motorized, flattened boundary layer probe in order to study the developments and interactions of the viscous layers (see Ref 3).

Wind tunnel corrections. Classical lift and blockage corrections are applied. It is not considered very important for the present purposes to obtain very accurate absolute values of the balance results. The main objective is to study the relative effects due to the configuration changes and these are not affected to any significant extent by the correction method used. One exception to this is the blockage effect due to separations on the model (as introduced by Maskell, Ref 4). There may be significant changes of the amount of separation due to an incremental model change which will effect the blockage term. This can affect the optimization trends through over-estimation of high flap angles with relatively large separated regions.

This blockage correction term has however not been included due to the practical difficulties. It requires an estimation of the drag increment due to separations. This estimation becomes particularly difficult when the model exhibits some separated regions for the whole angle of attack range, which is often the case for the high lift configurations in the present study. This is certainly an area where further development is required.

3. THE LEADING EDGE SLAT

The classical idea about the effect of a slat is illustrated in Fig 8. It is conventionally seen as a way to delay the stall by a modification of the pressure distribution. The flap efficiency is not affected in this case.

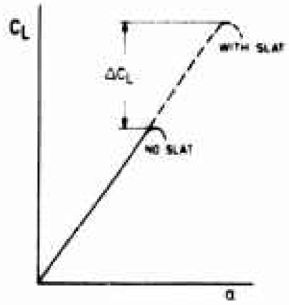

Fig. 8 Classical slat effect.

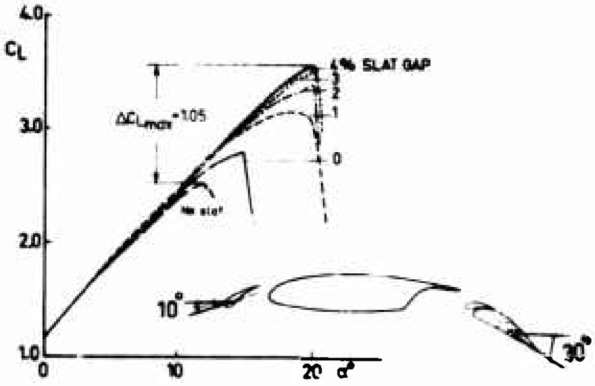

Fig. 9 Slat gap effects for a 10° slat.

Fig 9 shows some experimental results from Ref 7 where the slat gap is varied for a 10° slat and a 20° single-slotted trailing edge flap. The deflection of the slat without any gap gives a small improvement due to the modified pressure distribution. The major part of the over-all slat effect is in this case due to the slat gap which gives a ΔC_{L} max of 1.05 for a 4 % slat gap. The improvement from 1 % gap to 4 % gap is not due to a delay of the stall (the angle of attack of the final stall is the same for these slat gaps) but mainly due to the slat gap effects on the viscous flow over the flap.

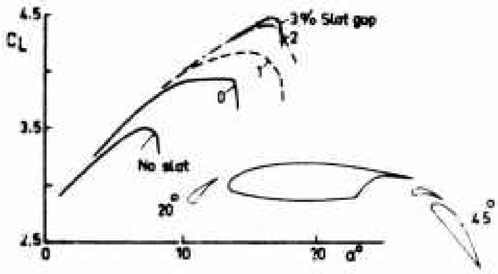

Fig. 10 Gap effects for a 20° slat.

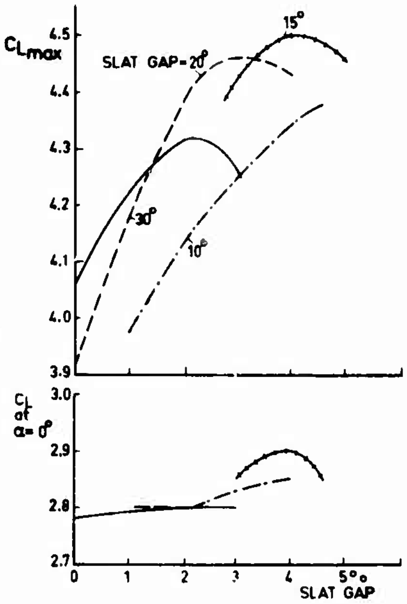

Fig. 11

Slat gap effect for different slat angles.

Fig 10 shows results for a 20° slat. The effects of slat gap are similar but the optimum gap is here about 3 %.

Fig 11 shows $C_{L\,max}$ and C_L at $\alpha = 0$ results for three different slat angles as a function of slat gap. The optimum slat gap increases with a decreasing slat angle. The trends for $\alpha = 0$ reveals that the potential flow effects are comparatively small. The distinctive trends for $C_{L\,max}$ are mainly related to the separation phenomenon.

The slat effect on $C_{L\,max}$ can be divided into two main parts,

1) Delaying the onset of leading edge separation which is governed by the local pressure distribution.

2) The effect on the flap flow including local trailing edge separation which is governed mainly by the slat gap size.

The slat overlap is considered to be of secondary importance. This assumption has been verified in 3-D tests. The overlap is kept approximately constant at a small value with adjustments to ensure a slot flow that is basically aligned to the main wing leading edge surface.

Fig 12 gives an example of the slat effect for a triple - slotted configuration with relatively high C_L values. This is a case where the slat has a visible effect on the flap efficiency for an extended angle of attack range.

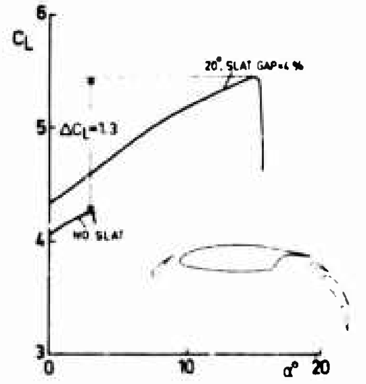

Fig. 12 Slat effect for a triple slotted configuration.

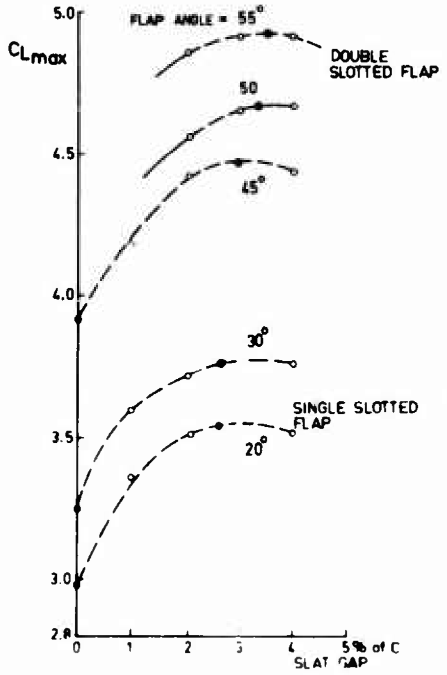

Fig. 13

20° slat trends for different T.E. flaps.

Fig 13 shows the gap trends for a 20° slat for different trailing edge flaps (single- and double-slotted). The similarity is evident but there is a slight increase in the optimum slat gap for higher C_L levels. This should not be surprising since the required gap size should be related to the thickness of the viscous layers involved.

The trends for slat angle and slat gap discussed above are a result of a combination of viscous and inviscous effects. In order to get a better understanding of these effects and their relative importance a series of boundary layer measurements were performed with a model according to Fig 14.

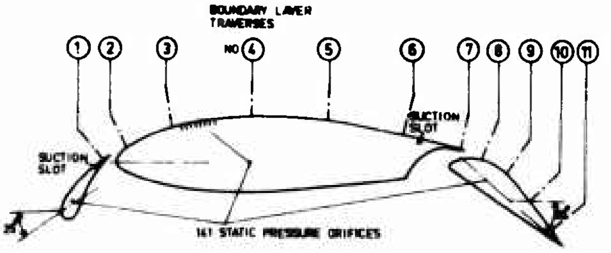

Fig. 14

2-D model for boundary layer experiments.

Slot suction is introduced on this model, not for conventional b.l.c. purposes but as a way to reduce the thickness of the wake leaving the slat. This will make it possible to study the importance of the viscous interaction between slat wake and main wing-flap boundary layers. The position of the slot and the suction quantities are such that the sink effects are an order of magnitude smaller than the C_L differences of interest.

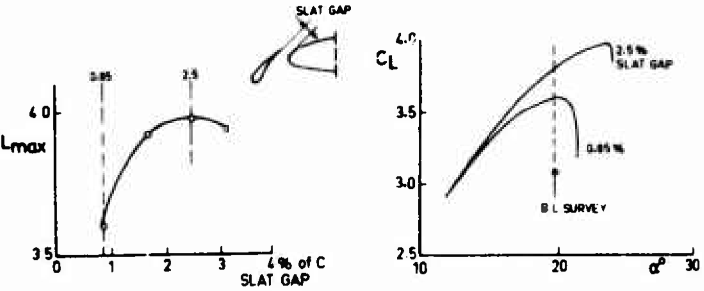

Fig. 15

Slat gap effect for 25° slat.

The model was first tested for a number of slat gaps and a fixed slat angle (25°) without any suction. The results as shown in Fig 15 exhibit the familiar slat gap trend with an optimum gap at 2.5 %. This gap and a smaller 0.85 % gap were selected for further studies. Boundary layer total head measurements were performed at eleven stations along the upper surface of the model at an angle of attack which is 1.5° below the stall. Fig 16 shows the total head profiles over the main wing and flap for the two different slat gaps. The optimum 2.5 % gap corresponds to a viscous layer at the main wing trailing edge where the slat wake is still essentially separated from the main wing boundary layer. It results in a more efficient flow over the flap as shown by the pressure distribution measurement and also by the streamlines from the main wing trailing edge. The slat gap obviously also has a significant effect on the state of the boundary layer close to the surface at the main wing trailing edge. The profile for the small gap is very close to separation and in fact there may be a local separation on the remaining part of the main wing. It is however difficult to determine to what extent the flap flow improvement depends on decreased local separation on the main wing trailing edge and what the contribution is from the redistributed total head losses over the flap.

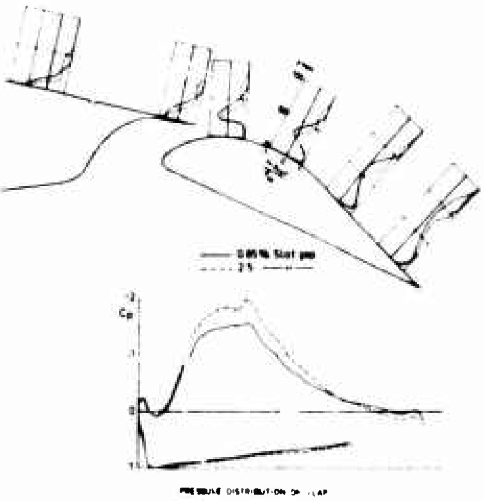

Fig. 16 Slat gap effect on total head profiles and pressure distribution for T.E. flap.

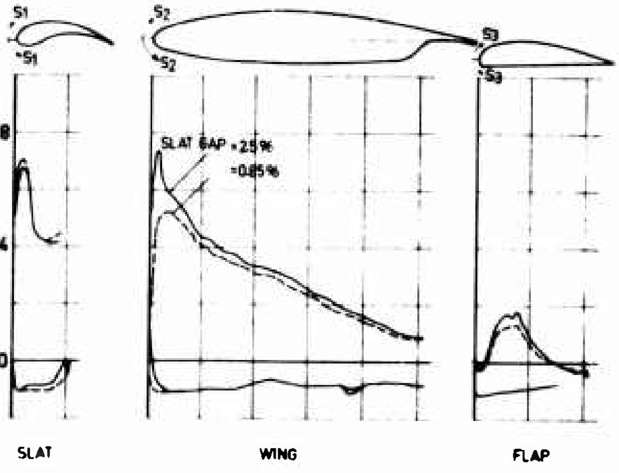

Fig. 17 Slat gap effect on pressure distribution. α= 19.6°.

The pressure distributions on the leading edges are shown in Fig 17. The problem here is how much of the pressure difference is due to the changed local geometry at the leading edge and what is the contribution from the improved flap flow?

In attempt to answer some of these questions, suction was applied on the slat as indicated in Fig 14, in the case of the smaller slat gap (0.85 % of c).

The boundary layer at the trailing edge of the slat was measured for different amounts of suction as shown in Fig 18.

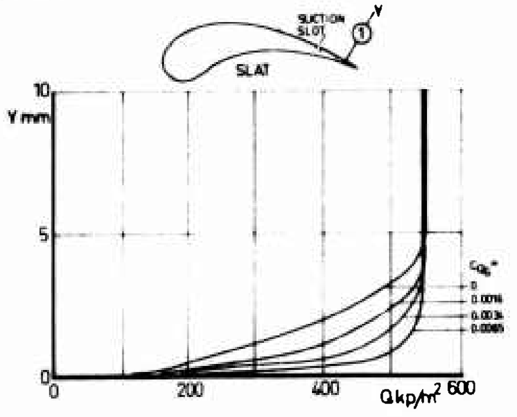

Fig. 18

Effect of suction on slat T.E. boundary layer.

The C_L results with and without suction are shown in Fig 19.

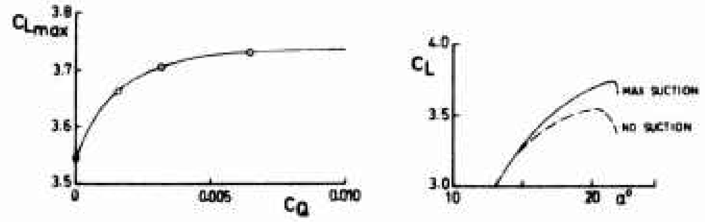

Fig. 19

Effect of reduced slat wake on $C_{L\,max}$ and C_L.

The curve for $C_{L\,max}$ levels-off for the highest amounts of suction, indicating that the part of the slat wake caused by the upper surface boundary layer has been effectively removed. Only a small fraction of the slat wake remains. The C_L curves behave very similarly to the case for different slat gaps except for the final stall which is at roughly the same angle of attack. The leading edge pressure distribution has in this case not been changed by geometrical differences. Boundary layer measurements and pressure distributions for this case are shown in Fig 20.

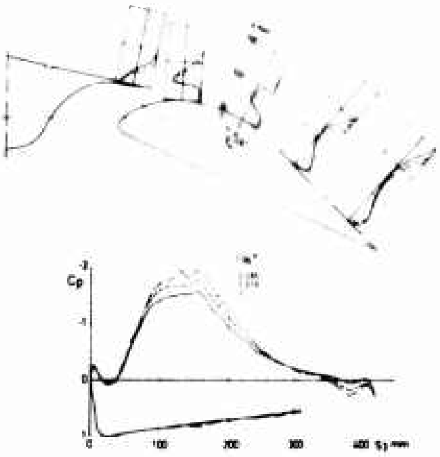

Fig. 20 Effect of reduced slat wake on total head profiles and pressure distribution of T.E. flap. α= 19.6°.

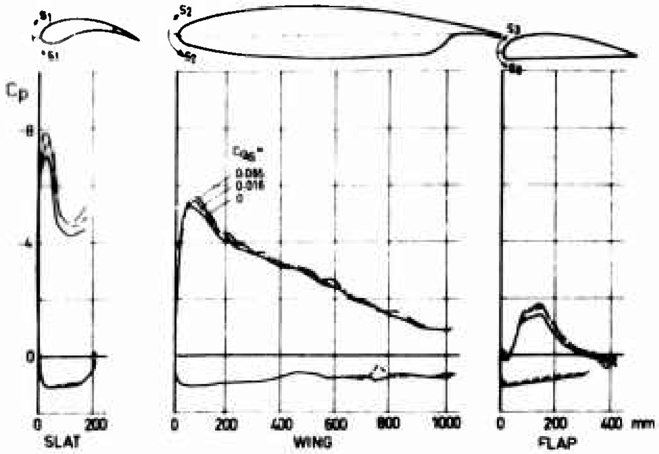

Fig. 21 Effect of reduced slat wake on complete pressure distribution.

The effect on the boundary layer at the main wing trailing edge and the flap pressure distribution are very similar to those for the increased slat gap discussed above. The wake region over the flap is somewhat reduced resulting in improved flap efficiency. This is further reflected in the pressure distribution at the leading edge in Fig 21.

One conclusion that can be drawn from this is that the viscous flow effects of increasing the slat gap are essentially similar elimination of a major part of the slat wake. This is achieved when the slat wake is separated from the main wing boundary layer along most of the main wing upper surface.

The optimum slat gap corresponds to an optimum amount of mixing between the slat wake and the main wing boundary layer. These conditions are however strongly dependent on the slat angle, as illustrated by the trends discussed in Fig 11 above. A bigger slat angle corresponds to a smaller slat wake resulting in a reduced optimum slat gap. It is also probable that more mixing between slat wake and main wing boundary layer is optimum in this case since the viscous effects are generally less for the smaller slat wake. The criteria for optimum mixing conditions do also depend on the over-all C_L level since viscous effects become generally more important for increasing C_L.

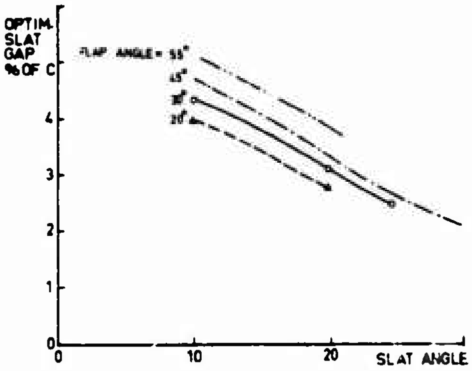

Fig. 22 Correlation between optimum slat gap and slat angle for different T.E. flaps.

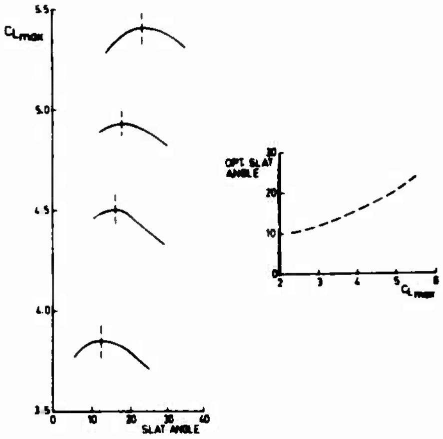

Fig. 23 $C_{L\ max}$ v.s. slat angle.

This is illustrated in Fig 22 where optimum slat gap is plotted versus slat angle for different trailing edge flaps. The trends are very similar for all flap angles but the over-all gap level increases steadily for a fixed slat angle. There is however also a change in optimum slat angle as shown in Fig 23. It increases with increasing C_L level. Higher and higher slat angles are required to give a certain optimum relation between the pressure peaks on the slat and the main wing leading edges. Fig 24 shows the flow over a fairly well optimized two-dimensional configuration with a $C_{L\ max} = 5.5$. (slat angle = 20°). The slat wake is here quite distinguishable at the trailing edge of the third flap. There is consequently even less mixing for this case compared with the cases illustrated above. The size of the slat wake is of the same order of magnitude as the main wing wake.

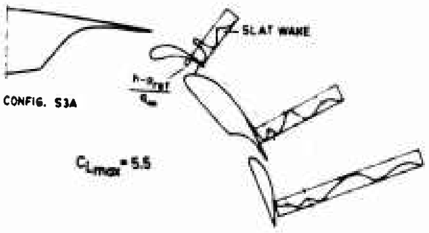

Fig. 24 Total head profiles on optimized triple slotted flap.
$\alpha = \alpha_{STALL} - 1.5°$.

Foster et al (Ref 8) has found that the optimum slat gap corresponds to a case with quite some mixing between the slat wake and the main wing boundary layer. These experiments are however for one fixed slat angle, which is greater than the ones used in the present investigation, and with a 30° single-slotted trailing edge flap. This means that the relative size and importance of the slat wake is much less, resulting in relatively more mixing being present for the optimum balance between viscous and inviscous effects.

4. THE TRAILING EDGE FLAP

4.1 Slat effect on T.E. flap optimization

The merits of a trailing edge flap is often described in terms of flap efficiency expressed as ΔC_L for $\alpha = 0$.

A particular flap configuration is said to have a certain ΔC_L or $\Delta C_{L\ max}$. It may thus be tempting to treat the trailing edge problem separately, trying to establish generalized data about flap efficiencies for different configurations. Experimental results have shown however that the flap optimization can hardly be treated separately from the leading edge problem. The results discussed in Chapter 3 have shown that the conditions for the flap are significantly affected by the slat position. Fig 25 is a good illustration of this.

A double-slotted trailing edge flap was optimized for a fixed leading edge slat (slat angle = 30°, slat gap = 1 %). The result as shown by the solid line was a $C_{L\,max}$ of 4.3 for a 45° flap. The slat was then optimized for the best trailing edge configuration resulting in the improvement according to the dashed line. The trailing edge flap was now optimized again and a further improvement resulted in a $C_{L\,max}$ of 5.0. The optimum flap angle was now 55°. The improved slat position changed the viscous conditions for the trailing edge flow so that a higher flap angle could be used.

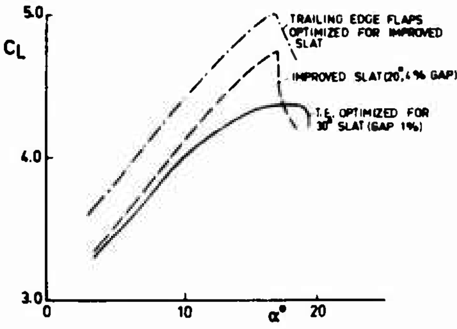

Fig. 25 Interaction between leading edge and trailing edge.

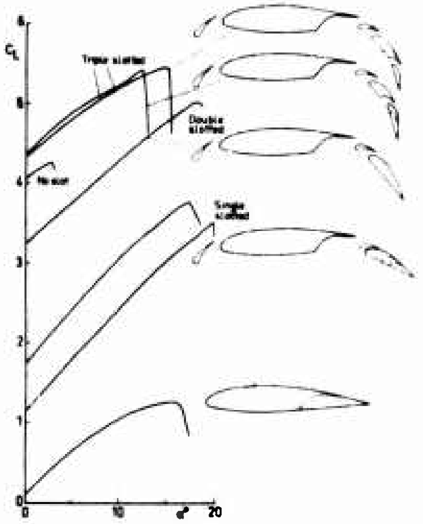

Fig. 26 Summary of C_L results for different T.E. flaps.

A summary of the best lift results for some investigated trailing edge flaps are shown in Fig 26.

A large number of parameter variations have been carried out including individual flap angles, combinations of flap angles, gap sizes and overlaps.

4.2 Flap gap effects

The significance of the flap gap has been investigated by Foster in Ref 8 where the optimum flap gap is explained in terms of a balance between viscous and inviscous effects. The optimum gap corresponds to a flow where the interaction between the main wing wake and the flap boundary layer is marginal. The results from the present work agree very well with Foster's findings for both single; double- and triple-slotted flaps.

Fig 27 shows $C_{L\,max}$ as a function of the two gaps of a double-slotted flap. The trends for C_L at α = 5° is totally different. This is explained in Fig 28. The flap efficiency at low angles of attack is gradually reduced with increasing gap size, mainly due to potential flow effects. The flow at high angles of attack is however improved due to reduced interaction between the main wing wake and the flap boundary layers which, in its turn, reduces the amount of local separation at the trailing edge.

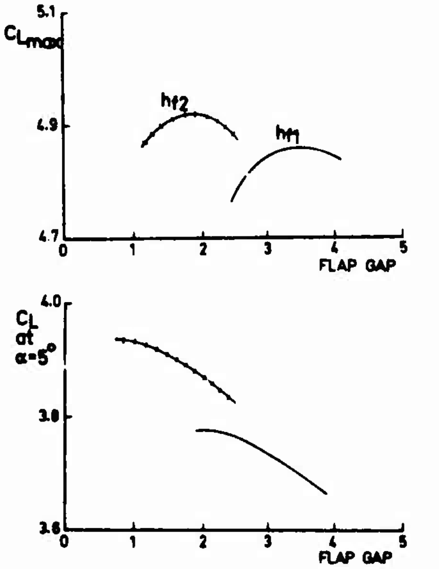

Fig. 27 Flap gap effect on $C_{L\,max}$ and C_L at α= 5°.

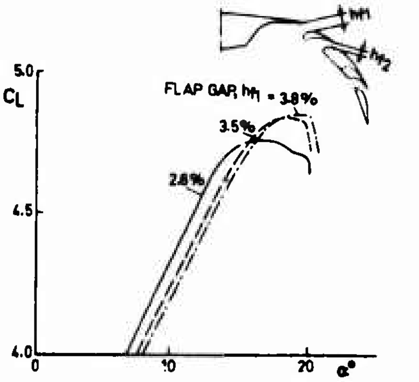

Fig. 28 Flap gap effect on C_L-curves.

Fig 27 also shows that the first flap gap should be larger than the second one. Some explanation of these results are given by the total head profiles measured on a double-slotted flap with optimum gaps shown in Fig 29.

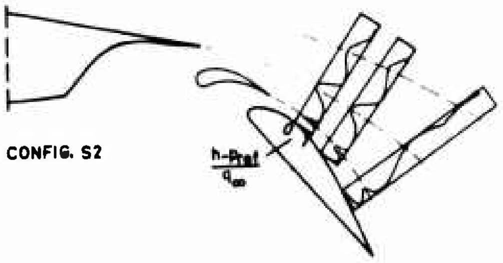

Fig. 29 Total head profiles on optimized double slotted flap.
$\alpha = \alpha_{STALL} - 1.5^{\circ}$.

The measurements are taken at an angle of attack only 1.5° below the stall. All the viscous layers over the flap are still essentially separated by potential flow cores. They are just beginning to merge at the trailing edge of the second flap. A rather big gap is required to separate the large main wing wake from the following shear layers. A smaller second flap gap is needed to separate the small first flap wake from the second flap boundary layer.

The results for triple-slotted flaps are very consistent with this.

Fig 30 shows flap gap trends and total head profiles for the best flap gaps of such a configuration. The different viscous layers are still quite distinguishable at the trailing edge of the third flap.

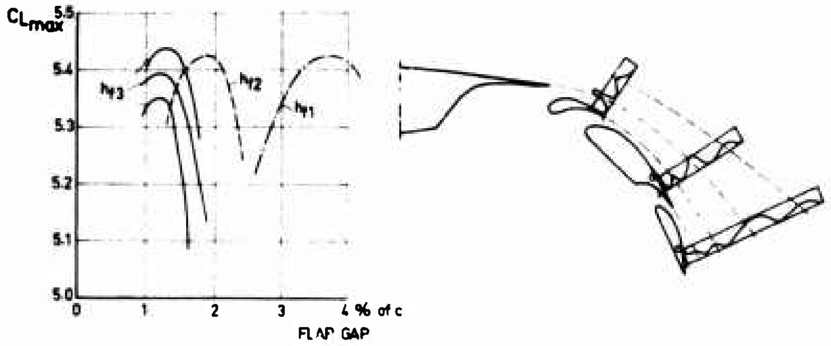

Fig. 30 Flap gap trends for triple slotted flap.

The optimum flap gap appears to be a function of the following parameters:

- The size (displacement thickness) of the viscous layer leaving the trailing edge immediately ahead of the gap.
- The boundary layer thickness on the nearest airfoil element.
- The remaining distance to the trailing edge of the configuration.

It should be noted that the very large flap gaps in the present tests are obtained with an idealized shape of the main wing cut-out. This means that sound contraction ratios in the slot could be maintained up to fairly large flap gaps. More practical wing cut-out shapes may seriously limit the usefulness of such large flap gaps.

It may not be possible to obtain efficient slot flow for the large flap gaps due to local separations in the cut-out causing poor or negative slot contractions.

4.3 Flap angles

It is more difficult to draw any general conclusions about flap angles. The present experiments did however indicate that the first flap angle should account for the largest flow-turning angle, the second flap the second largest, and the third flap the smallest turning angle. A streamline analysis derived from the boundary layer measurements gave the following flow-turning angles (close to the surface) for the three flap elements of the optimized triple-slotted flap:

First flap	30°
Second flap	21°
Third flap	13°

There is also a correlation between flap angle and flap gap. The flap angle affects the viscous layer developments which in its turn affects the required flap gap. Fig 31 is an illustration of this correlation. It shows optimum first flap gap as a function of $C_{L\ max}$ level. The diagram contains points for both single-, double- and triple-slotted cases.

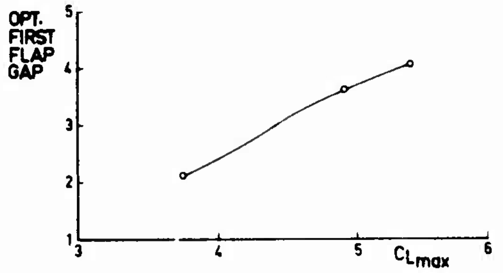

Fig. 31 Optimum flap gap for different $C_{L\ max}$-levels.

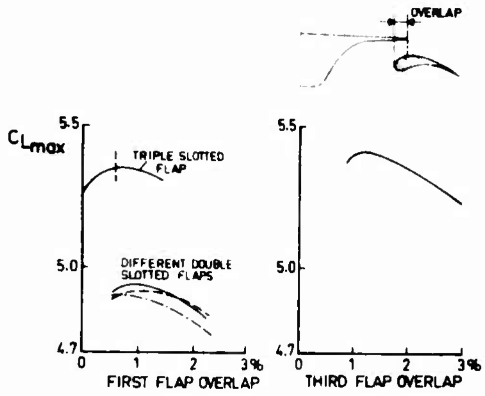

Fig. 32 Effect of overlap on $C_{L\ max}$.

4.4 Flap overlap

Overlap effects on lift are shown in Fig 32 for the first flap of several different flap configurations and for the third flap of a triple-slotted flap. The trends are generally less dramatic than the gap effects discussed above. Three curves are shown for double-slotted configurations with different combinations of flap and slat angles. The optimum overlap is essentially unchanged. The overlap is probably more independent of other parameters than gaps and angles. A variation of the flap overlap and flap angle for a constant flap gap corresponds to

- changed contraction ratio of the slot
- changed conditions for the 'coanda' effect

A high contraction ratio is desired for good slot effectiveness. The 'coanda' effect depends on the inclination of the trailing edge ahead of the gap and the curvature of the flap. The balance of these factors and the general potential flow effects has resulted in overlap sizes between 0.5% 1.1 %. It is however uncertain whether these results can be used for any general conclusions. A different curvature for the main wing under cut-out and the flap leading edge may give different results.

4.5 Relative sizes of flap elements

A comparison has been made between two different alternative triple-slotted configurations, (as shown in Fig 26). The results from these are compared in Fig 33. The lift results are slightly better for the small third flap. The drag is dramatically different. This is due to a larger local separation on the bigger third flap.

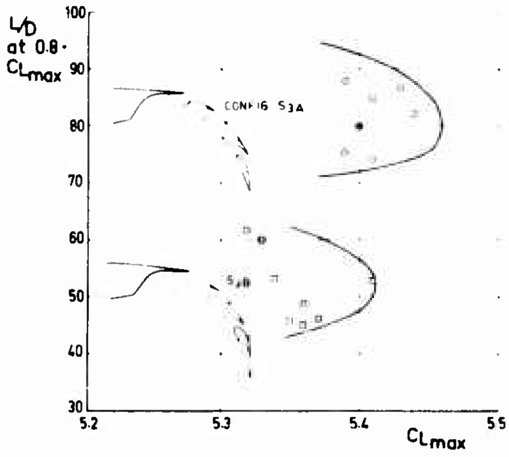

Fig. 33 Comparison of two alternative triple slotted flaps.

This is one example of a case where 2-D drag measurements can be quite useful. Differences of this magnitude should certainly be significant for the three-dimensional case as well.

These results together with the findings about the flap gap effects discussed above do, according to the author's belief, indicate that the best flap configuration is obtained when the sizes of the elements are gradually reduced towards the trailing edge. A triple-slotted flap, with a first element being the largest and the third the smallest, would probably give better results than the present configurations, both in terms of lift and drag.

5. CALCULATIONS

5.1 Potential flow calculations

The Douglas-Neumann potential flow method (Ref 5) has been used in connection with the experiments for the following purposes:

1) As a reference to the experimental results giving an indication of the order of magnitude of the viscous effects.
2) To increase our understanding of the experimental results, particularly the trends for certain geometrical variations.
3) To assess the usefulness of such calculation methods for high lift optimization purposes.

Fig 34 shows potential flow calculations for an optimized triple-slotted configuration at two angles of attack. There are unfortunately no experimental pressure distributions available for this case. The potential flow C_L is compared in the right-hand diagram with the experimental C_L-curve which gives an indication of the magnitude of the viscous effects involved.

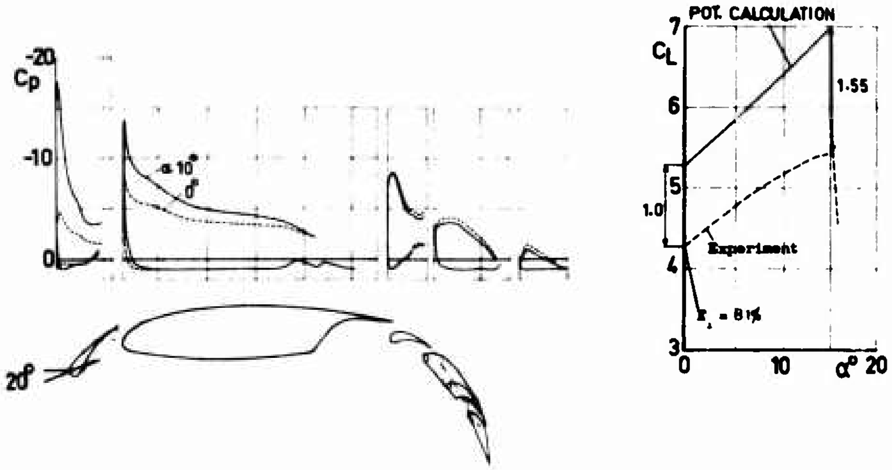

Fig. 34 Potential flow calculation of triple slotted configuration with small third flap element.

The flow efficiency at $\alpha = 0$ is 81 %.

Calculations for the triple-slotted configuration with a larger third flap are shown in Fig 35. The third flap pressure distribution is quite different for this case which may be the explanation to the poor drag results shown in Fig 33.

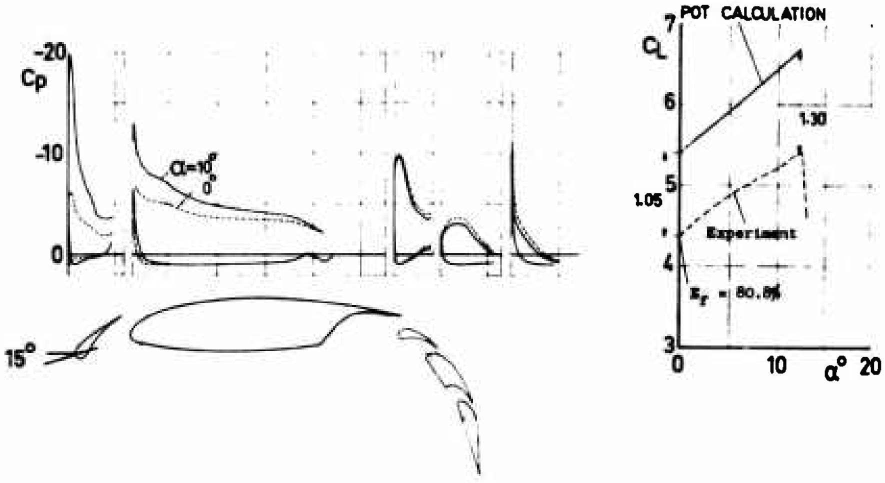

Fig. 35 Potential flow calculation fo triple slotted configuration with big third flap element.

5.2 Calculations with viscous effects

A method developed by Stephens and Goradia at Lockheed, (Ref 6), has been used for the single-slotted flap configuration shown in Fig 14. This method assumes attached flow and accounts for the displacement effect of interacting viscous layers over the main wing element.

The purpose of these calculations was to see whether the method could predict the experimental trends for slat gap. Calculated and experimental pressure distributions for two different slat gaps are compared in Fig 36 (Ref 10).

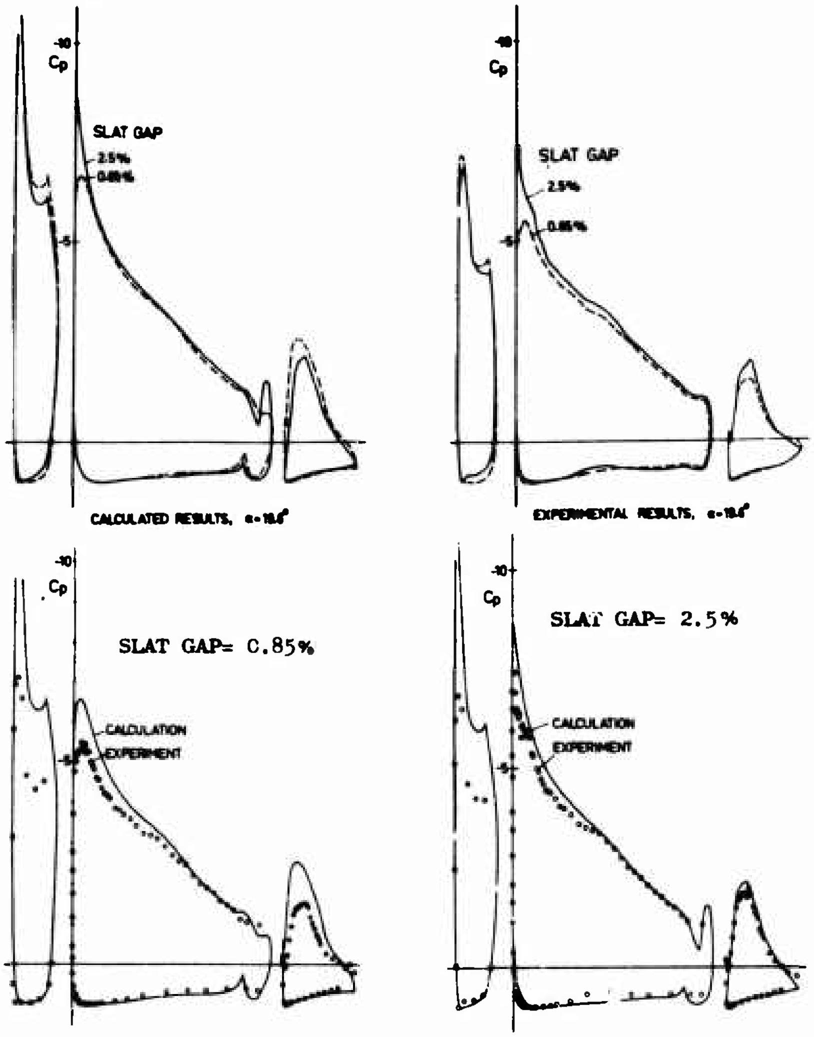

Fig. 36 Pressure distributions calculated with Stevens, Goradia method (Ref 6) for two different slat gaps.

The experimental results show an improved pressure distribution on the flap for the bigger slat gap. The calculation result shows the opposite effect, a reduced flap pressure for the bigger slat gap.

The reason for this is probably that the calculation model for the flow over the flap does not account for a separate wake layer above the flap. The layers are instead combined to one displacement thickness that is added to the flap shape. The calculations show correctly that the increased slat gap causes increased pressure peak at the main wing leading edge. This causes a thicker boundary layer on the main wing which is later added to the flap boundary layer resulting in reduced lift on the flap instead of the improvement obtained for the experiments.

Some of the differences may also be explained by local separations for the experiments which cannot be predicted by the calculations.

These comparisons are made for a constant angle of attack which is a simple case to predict compared to the effects on $C_{L\ max}$.

5.3 General usefulness of calculation methods for optimization purposes

The ultimate calculation method would be one which can be used to predict $C_{L\ max}$ and $C_{L\ max}$ trends for geometrical variations making it possible to optimize a high lift configuration theoretically. Such a method must be able to predict separation and the continuous growth of local separations up to the $C_{L\ max}$. In order to do this it is necessary to include relevant models of the viscous interactions above the main wing and the flaps. There is still a long way to go before this goal is reached.

The best presently available methods can be used for a fairly accurate prediction of pressure distributions on multiple element airfoils with small to moderate flap angles and attached flow. They cannot be used for prediction of $C_{L\ max}$ or the $C_{L\ max}$ trends due to geometrical variations. There are however many other possible ways we can use state of the art calculation methods within the framework of a high lift development program.

Potential flow calculations can be used to improve the shapes of different airfoil elements. They can also be used in the selection of flap configurations for experimental optimization. The calculated pressure distributions will give a good indication of the high lift potential of a particular configuration. The most promising configurations can be selected from a large number of possible alternatives leading to a substantial reduction in the required number of wind tunnel tests.

Calculations should be used parallel to experiments as a reference which will show the magnitude of the viscous effects. They will contribute to the understanding of the experimental results.

Calculations with viscous effects

These methods are in a relatively early stage of development. It is therefore rather uncertain what their use could be at present. Detailed experimental results similar to the ones in Ref 3 are needed to support the further development of these methods.

Some results have been published (Ref 8), where existing methods could predict the trend for flap gap at a constant angle of attack for a single-slotted flap with a small flap angle. This is certainly an important step towards the ultimate goal. It is however uncertain whether the gap trends can also be predicted for high flap angles where the viscous effects become more important.

6. THE ROLE OF 2-D TESTS

There are two main aspects of the role of 2-D tests in aircraft development. The first and probably most widely accepted, is the indirect role of knowledge-oriented applied research which will improve our ability to develop efficient 3-dimensional wings. This kind of work is not connected to any particular well-defined project. Most of the work discussed above should be seen in this perspective.

The other possible aspect is the direct usefulness of 2-D testing in an aircraft development program. Could 2-D tests actually contribute to the efficiency of a particular development program? It is the author's belief that this may be the case for some projects with high aspect ratio wings and small sweep angles.

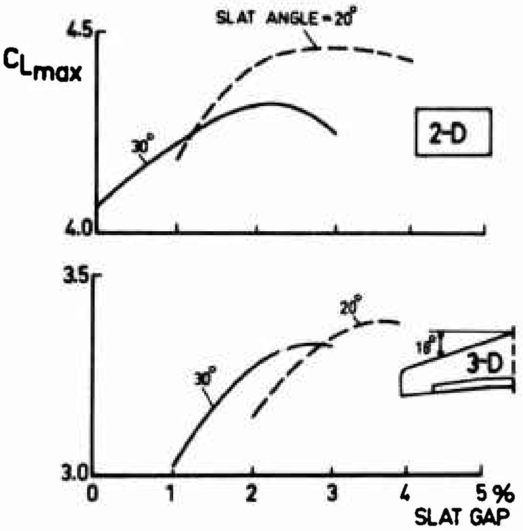

Fig. 37

Comparison of 2-D slat trends with corresponding trends for 3-D full model tests.

Fig 37 shows a comparison between slat position trends for 2-dimensional tests and full model tests. The full model is a SAAB project with an aspect ratio of 7 and a leading edge sweep of 18°. The 2-D section corresponds to the root section of the aircraft wing. The 3-D wing section thickness ratio varies from 15 % at the root to 12 % at the tip. The trends for slat angle and slat gap in Fig 37 are very similar for the two cases. This should indicate that the number of full model variations in this case could have been substantially reduced if 2-D tests were used in advance. A large number of 2-D variations can be made at only a fraction of the cost of similar variations of full model parameters at the same Reynolds number.

Another important problem in aircraft development testing is the extrapolation to full-scale Reynolds number.

Wind tunnel tests are used to develop the best possible geometry and to predict the full-scale performance of this geometry.

There are two different Reynolds number problems involved.

1) What are the Re-effects on the performance of a certain fixed geometry?

2) What are the Re effects on the optimization of the geometry?

2-D tests can probably contribute to the answer of both these questions. Fundamental studies of Reynolds number effects on boundary layer growth, boundary layer interaction and separation phenomena are well suited for 2-D testing.

Another example is the Re-effects on optimization trends for som important geometrical parameters. How are optimum slat gaps, flap gaps and flap angles affected by Reynolds number? This is a case where 2-D results could be quite useful for the extrapolation of 3-dimensional geometries.

7. CONCLUSIONS

7.1 Viscous flow over an optimized configuration

Boundary layer measurements have shown that the best 2-D geometry corresponds to a flow (close to the stall) where there is only marginal interaction between all the different viscous layers involved. The amount of interaction that can be accepted depends on the relative size of the viscous layers.

7.2 Leading edge parameters

The two dominating parameters are slat gap and slat angle. The optimum slat gap has been found to increase rapidly with decreasing slat angle. It also increases slowly with increasing trailing edge flap angle. The angle of an optimum slat gap - slat angle combination increases slowly with increasing over-all C_L level.

7.3 Trailing edge parameters

The optimum trailing edge flap gap is a function of:

- The size of the viscous layer immediately ahead of the gap
- The boundary layer thickness on the nearest airfoil element
- The remaining distance to the trailing edge of the configuration

This results in flap gaps that are larger for the forward flap element and smaller closer to the trailing edge.

The optimum gaps should generally increase with increasing C_L-level.

7.4 2-D optimization methods

The results for slat and flap variations have shown the importance of interaction between leading and trailing edge devices. The leading edge has significant effects on the viscous flow over the flap and therefore changes the conditions for the flap optimization. The trailing edge effect on the leading edge is primarily inviscous.

An efficient optimization program should therefore start with slat optimization for a fixed trailing edge with a flap angle in the vicinity of the expected final geometry. The trailing edge should then be optimized with the best leading edge slat. The slat position must now be varied to check whether the first slat optimization is still valid. If it is not and the new slat position is significantly different, it will be necessary to optimize the trailing edge once again.

REFERENCES

1. Morris, Hanke, Pasley, Rohling — The influence of wing loading on turbofan powered STOL transports with and without externally blown flaps
NASA CR 2320 (Nov 73)

2. Cross, E.J. — STOL Aircraft Technology
VKI Short Course (Sept 73)

3. Ljungström, B.L.G. — Boundary layer studies on a two-dimensional high lift wing
FFA Report AU-862 (Oct 72)

4. Maskell, E.C. — A theory of the blockage effects on bluff bodies and stalled wings in a closed wind tunnel
ARC R & M 3400 (1965)

5. Giesing, J.P. — Solutions of the flow field about one or more airfoils of arbitrary shape in uniform or non uniform flows by the Douglas-Neumann method
Douglas Aircr. Co. Report LB 31946 (Dec 1965)

6. Stevens, Goradia, Braden — Mathematical model for two dimensional multi-component airfoils in viscous flow
NASA CR-1843 (1971)

7. Ljungström, B.L.G. — Wind tunnel high lift optimization of a multiple element airfoil
FFA Report AU-778

8. Foster, Irwin, Williams — The twodimensional flow around a slotted flap
R & M 3681 (1971)

9. Ljungström, B.L.G. — 2-D Wind tunnel experiments with double and triple slotted flaps
FFA Technical Note AU-993 (Nov 73)

10. Weibust, E. — Beräkning av tryckfördelning på 2-D höglyftanordning i anliggande viskös strömning
FFA 1973

THE AERODYNAMICS OF TWO-DIMENSIONAL AIRFOILS WITH SPOILERS

by

G.V. Parkinson[*], G.P. Brown[+], T. Jandali[†]

The University of British Columbia

SUMMARY

Three incompressible potential flow methods have been developed for two-dimensional airfoils with upper surface spoilers. A linearized free-streamline theory is used to predict the steady and transient lift on thin, single-element airfoils of arbitrary incidence, camber, and thickness, with spoilers of arbitrary position, height, and inclination. Two theories for pressure distribution on thick airfoils have been developed. The first, a conformal transformation theory related to Theodorsen's method, and to Parkinson's wake source model for bluff bodies, applies to general single-element airfoils with normal spoilers. The second, adapting the wake source model to Smith's surface source method, applies also to general multi-element airfoils with inclined spoilers. Wind tunnel measurements of steady and transient lift and pressure distribution have been made, using two different airfoil profiles with several different spoiler sizes, positions, and inclinations, and good agreement has been found with the theoretical predictions.

NOTATION

c	airfoil chord
b	spoiler position
h	spoiler height
δ	spoiler angle
ℓ	length of airfoil + cavity
α	airfoil incidence
α_{L0}	airfoil zero lift angle
η	flap angle
U	free stream velocity
ρ	air density
p	air pressure
p_∞	free stream pressure
$C_p = \dfrac{p - p_\infty}{\rho/2\, U^2}$	pressure coefficient
C_{p_b}	base pressure coefficient
L, D	lift, drag
$C_L = \dfrac{L}{\rho/2\, U^2 c}$	lift coefficient
$C_D = \dfrac{D}{\rho/2\, U^2 c}$	drag coefficient

$z = x + iy$	complex airfoil plane
$f(z,t) = \phi + i\psi$	complex acceleration potential
ϕ, ψ	acceleration potential and stream function
$a_x = \dfrac{\partial\phi}{\partial x} = \dfrac{\partial\psi}{\partial y}$	x-component of acceleration
$a_y = \dfrac{\partial\phi}{\partial y} = -\dfrac{\partial\psi}{\partial x}$	y-component of acceleration
v	y-component of velocity
ζ	complex transform plane
$W(s)$	transient lift decrement function
s	airfoil distance travelled in chords
$\bar{s}$	effective response time (Figure 3)
z_n, $n=1$-6	complex planes
z_2'	pseudo-circle complex plane
Γ	airfoil circulation
Q_U, Q_L	discrete source strengths
δ_U, δ_L	discrete source angular positions
$F(z)$	complex velocity potential
$w(z) = \dfrac{dF}{dz}$	complex velocity

---

[*] Professor of Mechanical Engineering.

[+] Graduate Student, now Director of Engineering, dba Silencing, Vancouver, B.C.

[†] Graduate Student, now Research Scientist, Boundary Layer Wind Tunnel, University of Western Ontario, London, Ontario.

1. INTRODUCTION

Wing upper surface spoilers are of great value as control devices for STOL and VTOL aircraft. Deployed symmetrically, they reduce aircraft lift and increase drag. Deployed asymmetrically, they provide roll control. Nevertheless, there has been a lack of general information on their aerodynamic characteristics. Experiments have mostly been ad hoc wind tunnel tests on configurations for particular aircraft, and the only existing significant theory was that of Woods[1], a linearized two-dimensional steady potential flow theory. Subsequently Barnes[2] devised empirical modifications to Woods' theory for the case of normal spoilers. No theory existed for the transient loading following spoiler actuation, although such a theory would be particularly useful in giving designers estimates of response times. For the past six years there has been a research program, in the mechanical engineering department at The University of British Columbia, on the incompressible aerodynamics of two-dimensional airfoils with spoilers. So far in this program, three new theoretical potential flow methods have been developed for the prediction of aerodynamic characteristics, and suitable wind tunnel experiments have been conducted to correlate with the theoretical predictions.

2. THIN AIRFOIL THEORY

Linearized theories have usually been successful in the prediction of lift and moment on airfoils, and a new linearized theory has been developed for this purpose, applicable to thin, single-element airfoils of arbitrary incidence, camber, and thickness, with a spoiler of arbitrary position, height, and inclination. Calculations can be made both for the steady state, with spoiler erect, and for the transient loading following spoiler actuation. The spoiler base pressure cannot be predicted theoretically by any method yet available, and its empirical value is required in the steady-state theory. Free stream pressure is assumed for the spoiler wake in the transient theory. The analytical method is summarized below. Complete details can be found in a recent paper[3]

2.1 Analytical method

An airfoil of chord c is at angle of attack α to a uniform incident flow. An upper surface spoiler of height h and inclination [illegible] to the surface is at distance b from the airfoil leading edge. The flow separates on the bottom at the airfoil trailing edge, and on the top at the spoiler tip, forming a wake which is modelled here as a finite constant pressure cavity, so that the airfoil plus cavity has total length ℓ. The theory gives a relationship between ℓ and the empirically-given cavity pressure, and ℓ becomes infinite for free-stream cavity pressure.

In the linearized physical z-plane representing the airfoil, cavity, and surrounding flow field, the wetted airfoil surface and the cavity boundary become the edges of a slit of length ℓ along the positive real axis. A sequence of simple conformal transformations maps the field outside the slit onto the upper half ζ-plane exterior to the unit semi-circle. The semi-circle represents the airfoil wetted surface from upper surface spoiler tip to lower surface trailing edge, and the positive and negative branches of the real axis exterior to the semi-circle represent the upper and lower cavity boundaries.

The flow field model follows Biot[4] in using the complex acceleration potential

$$f(z,t) = \phi + i\psi, \qquad \frac{df}{dz} = a_x - i\,a_y$$

as the basic flow function for steady and unsteady airfoil problems, and Parkin[5] in adapting the method to foil-cavity problems. In the above, a_x and a_y are the cartesian fluid acceleration components. The real part of f(z,t) is related to pressure coefficient C_p, referred to free-stream pressure, by

$$C_p = -2\phi + C_{p_b}$$

where C_{p_b} is the constant cavity pressure coefficient, and the imaginary part is simply related to the y-components of fluid acceleration and velocity a_y and v, for unsteady flow, while for steady flow, the relation becomes

$$v = -\psi$$

With these relations, the boundary conditions of the problem can be simply expressed in terms of ϕ or ψ, so that analytic functions f(z,t) can be sought to meet the conditions.

2.2 Steady state theory

The flow, uniform at infinity, passes over the stationary airfoil, with spoiler erect, and its fixed trailing cavity. The boundary conditions at the airfoil-cavity system are tangent flow on the airfoil wetted surface, constant pressure on the cavity boundary, and Kutta conditions at the spoiler tip and airfoil trailing edge. In addition, a requirement of zero drag on the total system gives a relation linking ℓ and C_{p_b}.

The analytic functions meeting these conditions are found in the ζ-plane, with complex acceleration potentials matched at corresponding points in the ζ- and z-planes. Since the flow functions are linearized, and all airfoil-cavity boundary conditions are satisfied on the slit real axis between z=0 and ℓ, different geometric characteristics of the airfoil can be treated separately, and the results superimposed. In this way, simple closed form solutions as functions of ℓ are found for the effects of the airfoil angle of attack α and of the spoiler. (A similar solution to that for the spoiler gives the additional effect of a simple trailing-edge flap.)

For the general thin airfoil, with arbitrary chordwise distribution of camber and thickness, the solutions for these effects are found as infinite series in inverse powers of ζ. Unlike the theory for thin airfoils without separation, the present theory predicts an effect of the airfoil thickness distribution on lift and moment, because the asymmetric separation of the flow from the spoiler tip on the upper surface and airfoil trailing edge on the lower surface makes the thickness distribution effectively asymmetric also.

The complete complex acceleration potential f(z) is then the sum of the potentials giving the effects of angle of attack, spoiler (and flap), camber, and thickness, and the airfoil lift coefficient C_L is obtained using the Blasius equation in the form

$$C_D - i\,C_L = \frac{2i}{c}\oint f(z)\,dz \qquad (2.1)$$

2.3 Transient theory

The flow is again uniform at infinity, and the airfoil is stationary, but the spoiler is in motion, with a consequent effect on the cavity. To avoid the complications of C_{p_b} and ℓ varying with time, it is assumed that $C_{p_b} = 0$, so that $\ell = \infty$. There is now an additional normal acceleration boundary condition on the spoiler, but the condition linking C_{p_b} and ℓ is no longer needed.

The problem of interest is the loading arising from constant-rate erection of the spoiler. As in earlier work on transient airfoil aerodynamics (see, for example, Bisplinghoff, Ashley, and Halfman[6]), it is convenient to solve two other problems before this one. First the small-amplitude harmonic oscillation of the spoiler about a mean angle is considered. Then the problem of unit-step actuation of the spoiler is solved by an integral transform of the harmonic oscillation solution. The boundary conditions apply to the geometry corresponding to the spoiler problem of the steady-state theory. Only this geometry is needed for the time-dependent problems. The complete airfoil loading is obtained by adding the steady-state solutions (for the case $C_{p_b} = 0$) for the effects of angle of attack, camber, thickness, (and flap) to the time-dependent spoiler solution.

For the oscillating-spoiler problem, chordwise integration of the acceleration boundary condition gives an expression for ψ on the airfoil and spoiler, and a complex potential is found as a function of ζ by methods like those of the steady-state theory. Constants of the spatial integration (which are harmonic function of time) are found using the tangent flow boundary condition. With the complex potential known, the lift coefficient can be found using Equation (2.1).

The corresponding lift coefficient for the unit-step problem can now be found by an integral transform of the oscillating-spoiler lift coefficient, and finally the lift coefficient for constant-rate spoiler actuation is obtained by a superposition of unit-step solutions, in which it is assumed that the spoiler is erected to angle δ in a finite sequence of incremental angular steps.

2.4 Comparisons with experimental results

Predictions of the steady-state lift were compared with the results of wind tunnel experiments on a 14% thick Clark Y airfoil of 14 in. chord c which could be fitted at several chordwise positions b/c with fixed spoilers of different heights h/c and inclinations δ. The airfoil was mounted vertically on a force balance, and conditions were made as two-dimensional as possible. The test Reynolds number was $4(10)^5$. Figure 1 shows a typical comparison, where the theory is seen to predict accurately the variation of C_L with α. The nonlinear increase of experimental C_L at high α is caused by the growth of the separation bubble at the upstream spoiler base. The transient lift solution is presented in terms of the function W(s), the ratio of the lift decrement after s chords travel of the wing, following spoiler actuation, to the steady-state lift decrement. To determine this function experimentally, another 14% thick Clark Y airfoil of 14 in. chord was built of steel with a mid-span section containing 24 surface pressure taps, each of which could be connected in turn to a cavity containing a condenser microphone. A spoiler ($h/c = .084$ at $\delta = 90^\circ$, $b/c = .70$) could be actuated by a motor at different constant rates to any angle δ up to 90°.

For a given combination of α, δ, wind speed, and spoiler actuation rate, the spoiler was actuated repeatedly with each pressure tap connected in turn to the microphone cavity. Each transient pressure trace was obtained as a photograph of the microphone output on an oscilloscope screen. The instantaneous pressure distribution for the airfoil at any time after the actuation was determined from the ordinate of the trace at that time, and the area of pressure distribution was measured to determine the instantaneous lift. Figure 2 shows a comparison of theoretical and experimental variation of W(s) for three different values of spoiler erection time, expressed in airfoil chords travelled. The agreement is good qualitatively, and fair quantitatively. The experimental values start to rise more slowly than the theoretical and then rise more rapidly towards the steady state. The differences may be partly due to the acceleration characteristics of the actuating motor, which have not been investigated, and partly due to small difference in the meaning of W(s) for the theoretical and experimental results, arising from the method of super-position used in the theoretical linearized solution. Figure 2 is difficult to interpret quantitatively, and Figure 3 gives a different presentation of 7 experimental transient cases in comparison with the theoretical model. Here an effective response time $\bar{s}$, defined in the figure, is given as a function of spoiler erection time. In the experiments, the wind speed, α, δ, and the actuation rate were varied. Agreement with the theory is seen to be quite good.

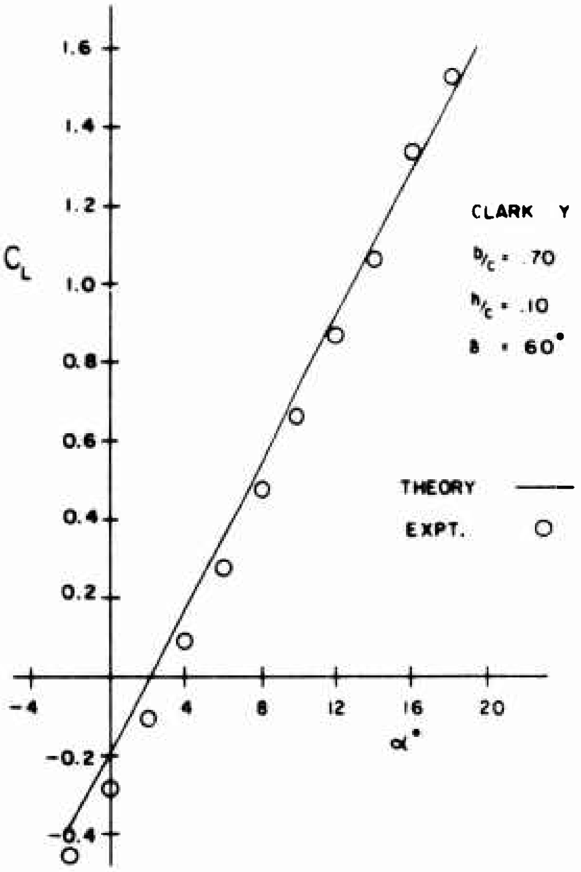

FIGURE 1. STEADY-STATE LIFT VS INCIDENCE BY THIN AIRFOIL THEORY.

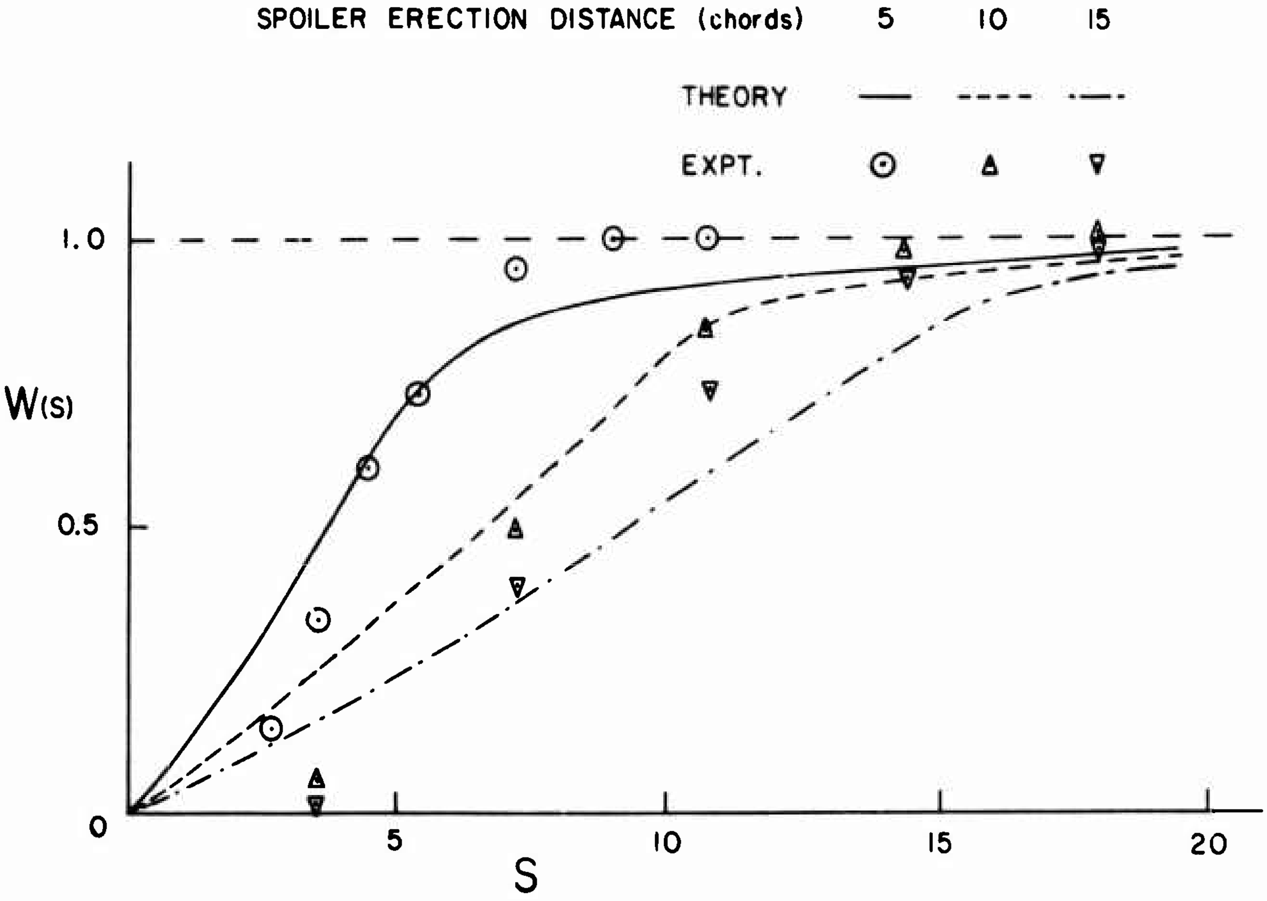

FIGURE 2. TRANSIENT LIFT DECREMENT FOR 8.4% SPOILER AT 70% CHORD.

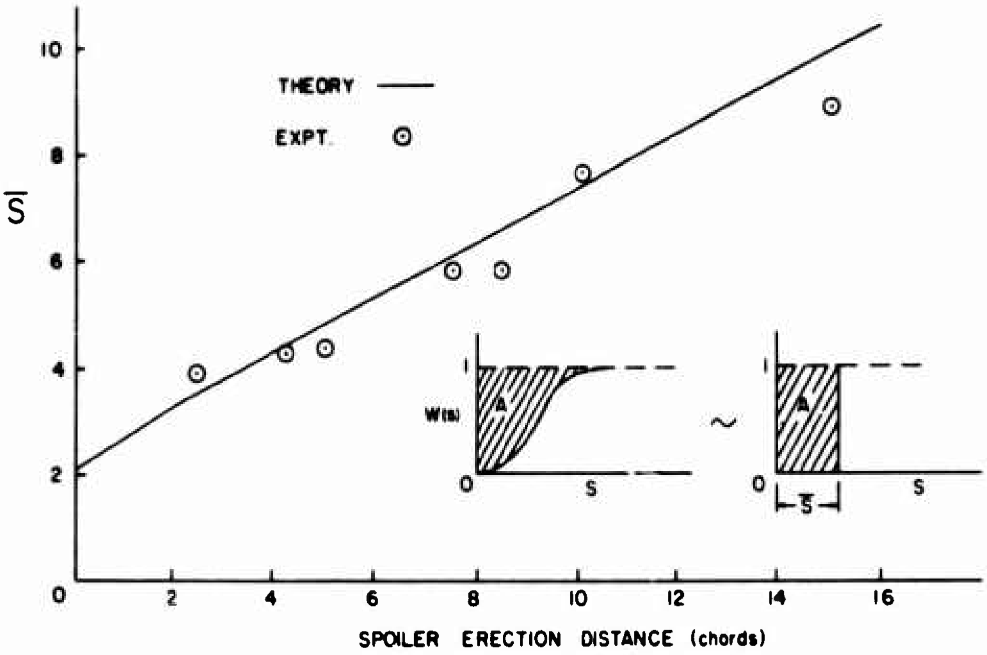

FIGURE 3. EFFECTIVE RESPONSE TIME FOR SPOILER ACTUATION.

3. ANALYTICAL THICK AIRFOIL THEORY

When an accurate airfoil pressure distribution is required, linearized theory is inadequate, and a thick airfoil potential flow theory is needed, often in combination with boundary layer theory. The simplest mathematically-generated thick airfoil shape for which angle of attack, camber, and thickness can be varied is the Joukowsky airfoil, so a useful first step in developing a theory for thick airfoils with spoilers was to work with the Joukowsky profile.

3.1 Theory for Joukowsky airfoils with normal spoilers

A circle in the z_2-plane, passing through $z_2 = 1$ and with centre in the second quadrant is mapped onto a cambered thick airfoil profile with trailing edge at $z_1 = 2$ by the Joukowsky transformation

$$z_1 = z_2 + \frac{1}{z_2} \tag{3.1}$$

If a radial fence is added to the circle in the first quadrant, it will appear on the airfoil as a normal spoiler, very slightly convex forward, as an actual spoiler would be. The circle with radial fence is now translated, rotated, and contracted so that it becomes a unit circle centred at the origin of the z_3-plane, with the fence lying along the positive real axis. A further application of the Joukowsky transformation

$$z_4 = z_3 + \frac{1}{z_3} \tag{3.2}$$

then maps the circle with fence onto a slit along the real axis in the z_4-plane, and this slit is now centred and contracted to 4 units length in the z_5-plane, whereupon a final use of the Joukowsky transformation

$$z_5 = z_6 + \frac{1}{z_6} \tag{3.3}$$

produces a unit circle without fence in the z_6-plane.

The flow model is created in the z_6-plane using Jandali's adaptation of Parkinson's wake source model[7]. The combination of uniform flow with a doublet and a vortex at the origin gives unseparated flow with circulation past the circular cylinder, and this would solve the flow problem for the basic Joukowsky airfoil without spoiler, if the circulation Γ was chosen to satisfy the usual trailing-edge Kutta condition. To simulate the additional effect of the broad wake of the spoiler, in the z_6-plane double sources of strengths $2Q_U$, $2Q_L$ are added on that part of the cylinder surface corresponding to the spoiler and airfoil surface exposed to the wake, and the surface tangent-flow boundary condition is satisfied by adding a sink of strength $(Q_U + Q_L)$ at the origin. These surface sources cause two additional stagnation points to appear on the cylinder surface, and they are made to occur at the points corresponding to the spoiler tip and airfoil trailing edge in the z_1-plane.

These two points are critical points of the overall conformal transformation between the z_1- and z_6-planes, and angles there in the z_6-plane are doubled in the z_1-plane, so that the stagnation streamlines in z_6 become smooth separation streamlines at the spoiler tip and airfoil trailing edge in z_1. The above uses up 2 of the 5 undetermined parameters Γ, Q_U, Q_L, and the angular positions of the sources, δ_U

and δ_L. Two more are determined by specifying that the flow separates at both points at the empirically-given base pressure coefficient C_{p_b}. The flow field in the 'wake' region generated by the mathematical model is ignored, and the loading on the airfoil surface exposed to the wake is assumed to be constant, with coefficient C_{p_b}. The lift coefficient C_L for the airfoil is given by an integration of the pressure coefficient C_p over the airfoil surface, and the $C_L - \alpha$ curve obtained in this way is used to determine the remaining parameter (taken to be the angular position δ_L of the lower source) by requiring this curve to have the zero lift angle α_{L0} predicted by the linearized theory of §2. In this way, the only empirical data needed in the theory is the value of C_{pb} for a given airfoil configuration.

With the flow field determined in z_6, the flow in the physical z_1-plane is found by matching complex velocity potential $F(z)$ at corresponding points in the two planes, and complex velocity $w(z)$ in the airfoil plane is therefore given by

$$w(z_1) = \frac{dF}{dz_1} = \frac{dF}{dz_6}\frac{dz_6}{dz_1} = \frac{w(z_6)}{dz_1/dz_6} \tag{3.4}$$

where (dz_1/dz_6) is the overall transformation derivative. The pressure coefficient C_p is given, using Bernoulli's equation, by

$$C_p = 1 - \frac{|w(z_1)|^2}{U^2} \tag{3.5}$$

where U is the free-stream velocity.

The above is called the 2-source theory. A simpler version eliminates the lower source Q_L at δ_L, and drops the requirement that separation from the airfoil trailing edge must be at C_{p_b}, thus creating a pressure discontinuity at the trailing edge, but removing the need for matching α_{L0}. This is called the 1-source theory. An earlier version of these two theories has been published[8].

3.2 Theory for general single-element airfoils with normal spoilers

Since Theodorsen's theory[9] for unseparated flow past a thick airfoil of arbitrary profile in the z_1-plane is based on the Joukowsky transformation

$$z_1 = z_2' + \frac{1}{z_2'} \tag{3.6}$$

the present theory can easily be adapted to the same airfoil with a normal spoiler. In the Theodorsen theory, since the airfoil is not a Joukowsky profile, the transform contour in z_2' is not a circle. However, since the given profile has coordinates not greatly different from those of some Joukowsky airfoil, the transform contour has coordinates not greatly different from those of a circle.

Accordingly, Theodorsen develops an analytic function to map the pseudo-circle in z_2' onto a true circle in z_2. The present theory merely adds a radial fence to the true circle in z_2, as in §3.1, and the airfoil in z_1 correspondingly acquires a normal spoiler. The transformations for z_2 to z_6, where the contour becomes a circle without fence, and the flow modelling, are unchanged from §3.1. Again, either the 2-source or the 1-source theory can be used.

If, as is usual, the profile has a finite trailing-edge angle, this must be artificially altered to a cusp in order to produce the smooth separation condition at the trailing edge. Only the upper surface is altered to create the cusp, and this is exposed to the wake, so the airfoil properties that affect the flow are not changed. A more complete account of this theory is given in Jandali's doctoral thesis[10].

3.3 Comparisons with experimental results

To test the theory, first a Joukowsky airfoil of 12 in. chord, 11% thickness, and 2.4% camber was built of wood with a mid-span section containing 37 pressure taps. Normal spoilers of h/c = .05 and .10 could be fitted at several chordwise stations. Pressure distributions were measured at a Reynolds number of $4.4(10)^5$. Figure 4 shows a comparison of the predictions of the 1-source and 2-source theories with the measured distribution of C_p. Agreement is seen to be excellent, except for the obvious constant pressure separation bubble upstream of the spoiler, not accounted for in the theory. The simpler 1-source theory is seen to be adequate here, even though it produces a pressure discontinuity at the trailing edge.

As an example of an application of the theory to an airfoil of arbitrary profile, Figure 5 shows a comparison of the 2-source theory and experiment for the 14% thick Clark Y airfoil. The measurements were made at a Reynolds number of $5.3(10)^5$ on the steel airfoil used in the transient experiments, with the pressure taps now connected to a multitube manometer. Agreement is quite good, with the usual exception of the separation bubble in front of the spoiler. The agreement would have been improved if the theoretical and experimental base pressures had been matched exactly.

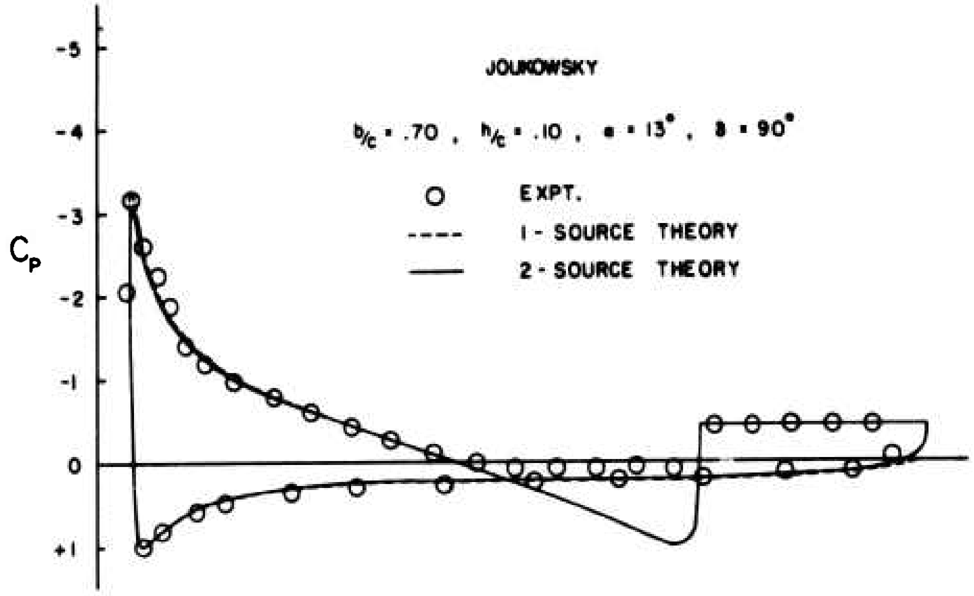

FIGURE 4. PRESSURE DISTRIBUTION FOR JOUKOWSKY AIRFOIL WITH NORMAL SPOILER.

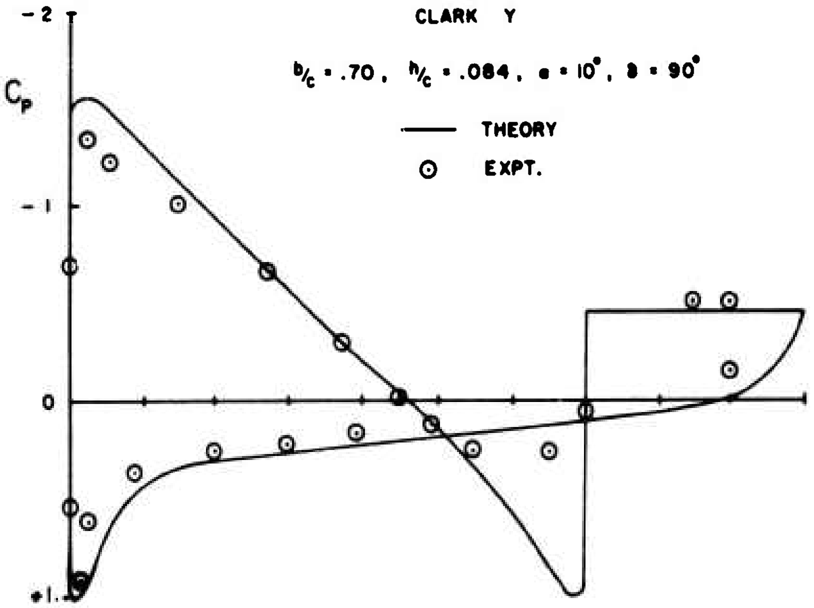

FIGURE 5. PRESSURE DISTRIBUTION FOR CLARK Y AIRFOIL WITH NORMAL SPOILER.

4. NUMERICAL THICK AIRFOIL THEORY

The above analytical thick airfoil theory is applicable only to single-element airfoils with normal spoilers. To develop a theory for multi-element airfoils with inclined spoilers, A.M.O. Smith's surface source distribution method[11] was adapted to the spoiler problem.

4.1 Theoretical method

The basic surface source method of Reference 11 is well known, and will not be described here. In the present application, the discrete wake sources of §3 are used again, and now become onset flows for Smith's method, directly in the airfoil plane. (Smith's method can be combined with conformal transformations, but this has not been done in the present theory.)

Again, both 1-source and 2-source theories are developed. The application of the 1-source method to a single-element airfoil with inclined spoiler is considered first. Unlike the previous analytical method, Smith's method will not handle a two-sided surface, or slit, so the spoiler is given a large circular-arc fillet on its back face, where it doesn't affect the airfoil characteristics that determine the flow. Also, it will be recalled that in Smith's method Kutta conditions are satisfied by matching tangential velocities at the two control points on either side of the flow detachment point.

Accordingly, the discrete source is tentatively located on the surface between spoiler tip and airfoil trailing edge, and a solution is found using the undetermined circulation and discrete source strength to satisfy the Kutta condition and specified C_{p_b} at the spoiler tip. The trailing edge flow is then examined to see if the Kutta condition is satisfied there. If it isn't, the discrete source is moved to a new location, and the process is repeated. This iterative process continues until the trailing-edge Kutta condition is satisfied.

In applying the 2-source method to the same airfoil, it would not be easy to make use of the α_{L0} criterion of §3, but it was observed with the analytical method that the 2-source results approached the 1-source results monotonically as the second source approached the airfoil trailing edge, when its strength vanished. Therefore, since the 1-source method seems to give generally good results except for the trailing-edge pressure discontinuity, the numerical 2-source method arbitrarily locates the second source close to the trailing edge, so that the resulting loading is close to the 1-source loading, but with the correct C_{p_b} at the trailing edge achieved by using the undetermined strength of the second source.

Next, the application of the 2-source method to an airfoil with spoiler and slotted flap is considered. For this configuration the spoiler is on the main foil, and the 1-source model is unsatisfactory because the pressure discontinuity at the main foil trailing edge has a large influence on the flap pressure distribution. The method proceeds as before, with the addition of another unknown, the flap circulation, and another condition to determine it, the Kutta condition at the flap trailing edge.

In this method, the guidelines given in Reference 11 for choosing the number of distributed source elements and grading their size are generally satisfactory. It was found necessary to reduce element size on the underside of the airfoil in the region opposite the discrete sources on the upper surface. For the single-element airfoil 110 elements were found to give good accuracy, while for the airfoil with slotted flap 100 elements on the main foil and 80 on the flap proved satisfactory. Computing time on an I.B.M. 360/67 computer for either 1-source or 2-source models was about 1 minute for the single-element airfoil and about 4 minutes for the airfoil with slotted flap. In each case the time included 6 iterations of the first source position, as described above. Complete details of the method are given in Brown's doctoral thesis[12].

4.2 Results of theory

For single-element airfoils with normal spoilers, the numerical method of §4.1 gives nearly identical results to those of the analytical method of §3.2, except that the numerical method does not give a close approach to the stagnation point in a concave corner. This is not in fact undesirable, since the real flow has a separation bubble there.

Some experiments on the airfoil used for the transient measurements of §2.4 were carried out recently to obtain pressure distributions with the spoiler inclined at different fixed angles, so that further comparisons could be made with predictions of the numerical theory, but the calculations had not been completed at the time of writing. No experimental data is available to test the accuracy of the slotted-flap theory, but the predicted effect of the spoiler in reducing the lift is shown in Figure 6 by a comparison of the C_p-distribution with spoiler retracted and erect. The figure shows the application of the 2-source method to an NACA 23012 airfoil at $\alpha = 8^0$ with slotted flap deflected to angle $\eta = 20^0$, and with a spoiler of $h/c = .10$ at $b/c = .60$ both retracted and erect at $\delta = 90^0$. The large lift reduction on the main foil caused by the spoiler is evident, as is the smaller increase in lift on the flap. (Such an increase is also observed in experiments, although no experiments on this profile were carried out in the present investigation.)

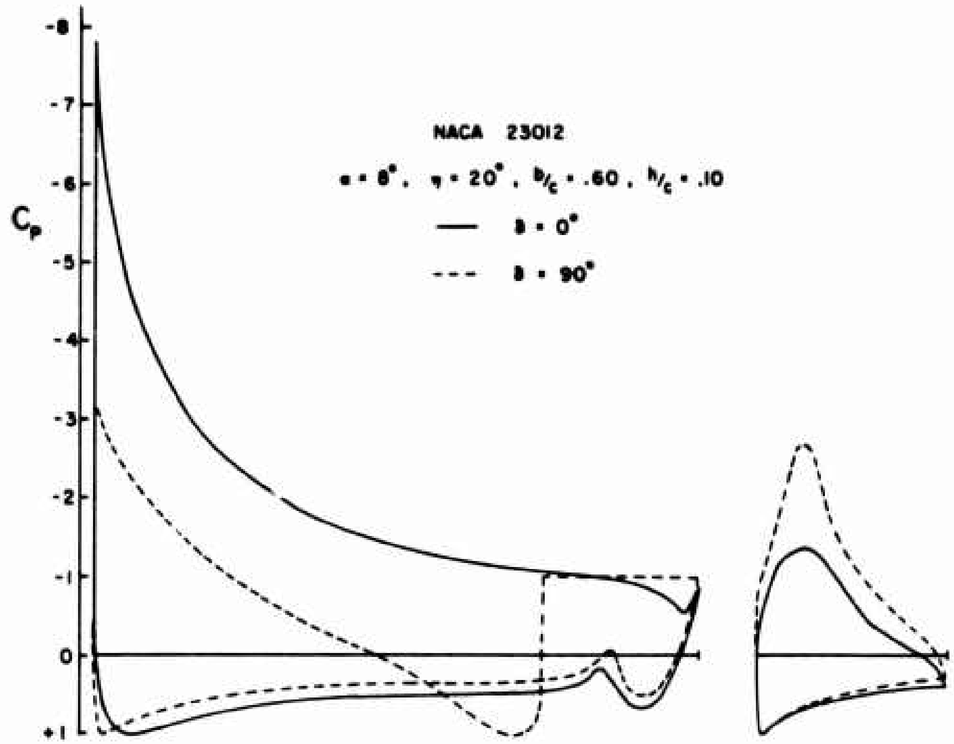

FIGURE 6. PRESSURE DISTRIBUTIONS FOR AIRFOIL WITH SLOTTED FLAP AND SPOILER RETRACTED AND ERECT.

5. DISCUSSION

The three theories described in the preceding sections have been shown to give good estimates of loadings on two-dimensional airfoils with spoilers. The only empirical data needed for their use, in addition to the specification of the airfoil and spoiler geometry, is the value of base pressure coefficient C_{p_b} for each configuration. At least this much empirical information is needed for any useful potential flow theory with flow separation.

The linearized theory gives accurate predictions of steady-state lift for general single-element airfoils with spoilers. The prediction of transient lift is also seen to be quite good, so that the assumption of free-stream pressure in the cavity does not appear to have introduced much error. Although this has not yet been done, the linearized theory could easily be extended to give steady-state and transient pitching moment.

The analytical and numerical thick-airfoil theories give accurate predictions of pressure distribution on general single-element airfoils with normal spoilers. There is every reason to expect that the numerical theory will also give accurate results for single-element airfoils with inclined spoilers, and for multi-element airfoils with normal or inclined spoilers. For single-element airfoils, the 1-source theory may be adequate, but the 2-source theory is needed for multi-element airfoils.

In the above theories, the flows are all two-dimensional and the spoilers are impervious, whereas actual spoilers are of finite span and are usually vented at the base. Current research in the continuing program at the University of British Columbia deals with the experimentally observed effects of spoiler base venting and finite span. Results of these studies will clarify the role of the two-dimensional theories, but it is hoped that the theories will already be useful to designers.

ACKNOWLEDGEMENT

The work described here was supported by Grant 9551-13 of the Defence Research Board of Canada.

REFERENCES

1. Woods, L.C.; 'Theory of aerofoil spoilers', Aero. Res. Counc. R. & M. 2969, 1953.
2. Barnes, C.S.; 'A developed theory of spoilers on aerofoils', Aero. Res. Counc. Current Paper 887, 1965.
3. Brown, G.P., and Parkinson, G.V.; 'A linearized potential flow theory for airfoils with spoilers', Jour. Fluid Mech., 57, 4, 1973, pp. 695-719.
4. Biot, M.A.; 'Some simplified methods in airfoil theory', Jour. Aero. Sci., 9, 1942, p. 185.
5. Parkin, B.R.; 'Linearized theory of cavity flow in two dimensions', RAND Rep. P-1745, 1959.
6. Bisplinghoff, R.L., Ashley, H., and Halfman, R.L.; 'Aeroelasticity', Addison-Wesley, 1955.
7. Parkinson, G.V., and Jandali, T.; 'A wake source model for bluff body potential flow', Jour. Fluid Mech., 40, 3, 1970, p. 577.

8. Jandali, T., and Parkinson, G.V.; 'A potential flow theory for airfoil spoilers', Trans. C.A.S.I., 3, 1, March, 1970, pp. 1-7.
9. Theodorsen, T.; 'Theory of wing sections of arbitrary shape', N.A.C.A. Rep. 411, 1931.
10. Jandali, T.; 'A potential flow theory for airfoil spoilers', Ph.D. thesis, University of British Columbia, 1970.
11. Hess, J.L., and Smith, A.M.O.; 'Calculation of potential flow about arbitrary bodies', Prog. in Aero. Sci., 8, Pergamon, 1966.
12. Brown, G.P.; 'Steady and nonsteady potential flow methods for airfoils with spoilers', Ph.D. thesis, University of British Columbia, 1971.

THE EFFECT OF VORTEX GENERATORS ON THE DEVELOPMENT OF A BOUNDARY LAYER

Sergio De Ponte, Arturo Baron
Politecnico di Milano – Istituto di ingegneria aerospaziale

SUMMARY

Although vortex generators are widely applied on wings and tailplanes, to prevent boundary layer separation, we are not able to predict the aerodynamic characteristics of an airfoil in the presence of vortex generators with the aid of recent computer techniques.

Vortices are introducing mixing and additional turbulence into the boundary layer and we must take into account both effects.

For the understanding of these effects, we carried on an experimental program in order to investigate the turbulent structure of the vortex. Our most significant result is that the vorticity profiles are very similar to those characterizing the viscous case, although the vortex was turbulent. From this result and other theoretical and experimental observations, we build up a model of vortex-boundary layer interaction. This model is the basis of many conclusions about the application of vortex generators as a means of boundary layer control.

We try also to outline the remaining open questions to arrive at a reliable method of calculation.

Notation

r	vortex radius	ω	angular velocity
t	time	ν	kinematic viscosity
V	mainstream velocity	η	eddy viscosity
x	distance along the vortex axis	Γ	circulation
z	vorticity		

1. INTRODUCTION

The application of vortex generators as means of boundary layer control is not new in the aeronautical technique.

We may distinguish two main applications: one in the low speed range and the other in the transonic regime, to prevent shock induced separation. A lot of research was carried on in this second application and it is very well summarized by Pearcey[1]. But we are now interested in high lift conditions. The application of forced mixing to a boundary layer was investigated and described by many Authors. The paper of Schubauer and Spangenberg[2] gives an idea of obtainable results and a good list of references. In the low speed regime, the most important applications of vortex generators are those which try to improve the effectiveness of control surfaces. We will see later that vortex generators fit very well to this application.

The problem of designing a reliable aircraft for low speed flight is not only the one of obtaining very high lift coefficients, but also sufficient control moments. We must notice that, as we decrease the flight speed, we cannot decrease in the same ratio the winds and the atmospheric turbulence. Again, we cannot restrict the planning of future V/STOL airports to wide, obstacle free areas. We may therefore expect larger turbulence than on present airports. This shows that the control problems are very important for a V/STOL aircraft: even more important than in a conventional one.

Of course, a VTOL aircraft has some powered system of producing control moments, and sometimes also a STOL aircraft has similar systems. They may be as effective as desired, depending on the power we give to them. Compared to them, vortex generators are not very effective, but they are simple and safe in the case of an engine failure.

With the use of vortex generators, we may avoid boundary layer separation, but for this purpose we shall first know where separation will take place. And for being able to take the maximum advantage from their presence, by a proper aircraft design, we must be able to calculate the influence of vortices on a boundary layer. We are going to present the first results of a research carried on for this aim.

2. VISCOUS AND TURBULENT VORTICES

Let us consider a straight line vortex after its formation. At the initial time it is a singular line in the field of motion, but it grows with time. Vorticity is spread in space by viscous stresses. An incompressible solution of the Navier Stokes equations, axisymmetric by assumption, is given by the following equation.

$$z = \frac{\Gamma}{8\pi\nu t} e^{-\left(\frac{r^2}{4\nu t}\right)} \qquad (1)$$

In it z is the vorticity, Γ the vortex strength or circulation, ν the kinematic viscosity and r the radius. This is a viscous vortex, because of the simplifications introduced in integrating the equations of motion. But we know from observations that also turbulent vortices exist. A turbulent vortex is often a quite complicated phenomenon. It consists in a non turbulent core, which moves almost alike a solid body and is surrounded by fluid in turbulent motion. Its exact mathematical description is not easy and we will later simplify this model.

But we are not even in the presence of an infinite, one dimensional vortex. We are in the presence of a vortex sheet originating from the trailing edge of a thin wing. The first assumption is that we consider only the tip vortex, made by the rolling up of this sheet.

Wherever the vortex is surrounded by potential flow, its strength Γ remains constant, although its angular momentum may change. Vorticity is spread in the direction normal to the axis, while a vortex element is transported in the mainstream direction. The second assumption is that the diffusion in the normal direction is not affected by the transport motion. This is true when the vortex growth in the normal direction is not large. Looking either to the orders of magnitude of tip vortices or to the experimental results, this condition is very well verified. Both assumptions allow us to use the results obtained for the one-dimensional vortex of Equation (1) to the case of a trailing vortex.

3. THE INTERACTION MODEL

Let us suppose that the tip of the vortex generator comes out of the boundary layer. There is a first part of the vortex which does not merge into the boundary layer and is surrounded by potential flow. To this part we can apply the former considerations. This is true if the vortices of the row do not interact among themselves. When an interaction (with the boundary layer or with another vortex) takes place, the circulation is reduced. This means that also the effectiveness in mixing is reduced. This first part, which we call the non-interacting part, is the most useful for the boundary layer control.

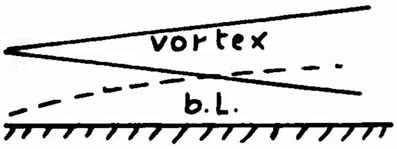

Fig. 1 Interaction

Knowing the size of the generator, its angle of attack and the boundary layer properties upstream the row, we are able to calculate the circulation. We may assume a horseshoe vortex. For calculating the correct induced angle of attack, we may subtract the displacement thickness from the generator height.

Where the circulation is constant, and knowing its initial value, we may calculate the path of the vortex centerline and the induced velocity elsewhere. This is true until the starting of an interaction. We may also notice that an interaction among vortices is a waste of circulation, so that the first design criterion is to obtain that the vortices interact first with the inner, strongly retarded part of the boundary layer.

In order to know where interaction takes place, we have studied the vortex growth. Before describing such a study, two more important things have to be emphasized. The first is the injection of turbulence into the boundary layer. This is favourable, although the amount of turbulent energy introduced is not very large. We must consider that the initial vortex energy is equal to the energy dissipated by the induced drag. Part of this energy is then dissipated into heat by viscosity during the vortex growth.

The second, unfavourable effect is the injection into the outer part of the boundary layer of the vortex core, which has low transport energy.

If we cannot avoid separation, another favourable effect of vortices is the ventilation of the separated wake, with a certain recovery of lift.

4. EXPERIMENTS ON VORTICES

Angular velocity was measured in the vortices by means of a small windmill. (Two windmills of different diameter, 11 and 7 mm, were used to check if the results were the same, to avoid instrument size effects.) Measurements were taken in the non interacting part of the vortex, but being careful not to approach too much the generator, in order to have vortex diameters large enough, compared to the windmill size. A row of counter-rotating generators (48 mm height) was fixed either to a flat plate[3] or to a flapped body sketched in the figure. Both flat plate and body were placed in our wind tunnel and tested at a wind velocity of about 30 m/s.

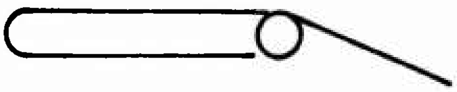

Fig.2 Flapped body

Although bursting of vortices was never observed in the non-interacting part, it does not mean that bursting does not occur.

Minimum, average and maximum of about 30 (from 20 to 60 according to the test) angular velocity measurements for each point is plotted in the figure in dimensionless form (Fig.3). Data are plotted in dimensionless form by dividing angular velocity by its maximum, setting the axis in the center of the points as mean vortex radius, and dividing radii by one half of this radius. This procedure was repeated for the minimum, average and maximum curve, for each measuring station. After finding the vortex axis, the probe was displaced in the radial direction parallel to the surface. In two cases it was displaced in the direction normal to the surface, for checking if the vortex was axisymmetrical, obtaining a positive answer. At the right side of Figure 3 we notice a rather constant vorticity, not tending to zero. It is possible to explain the presence of this vorticity by two reasons. One is the scooping of the boundary layer, the second is the effect of the remaining vortex sheet, not rolled up to build the tip vortex. This result can give us an idea of the accuracy of the approximation of a single horseshoe vortex.

The solid line plotted in the figure is the solution of viscous vortex, given by Equation (1). A viscous vortex is a constant viscosity phenomenon; the comparison leads to the result that we may consider also constant the eddy viscosity in our turbulent vortices. (It was not a viscous vortex, which should have a diameter thousand times less.) Of course, eddy viscosity must be zero in the non turbulent core. But the rate of strain tends to zero as we approach the axis and an error in evaluating the strain-stress relationship does not affect very much the results.

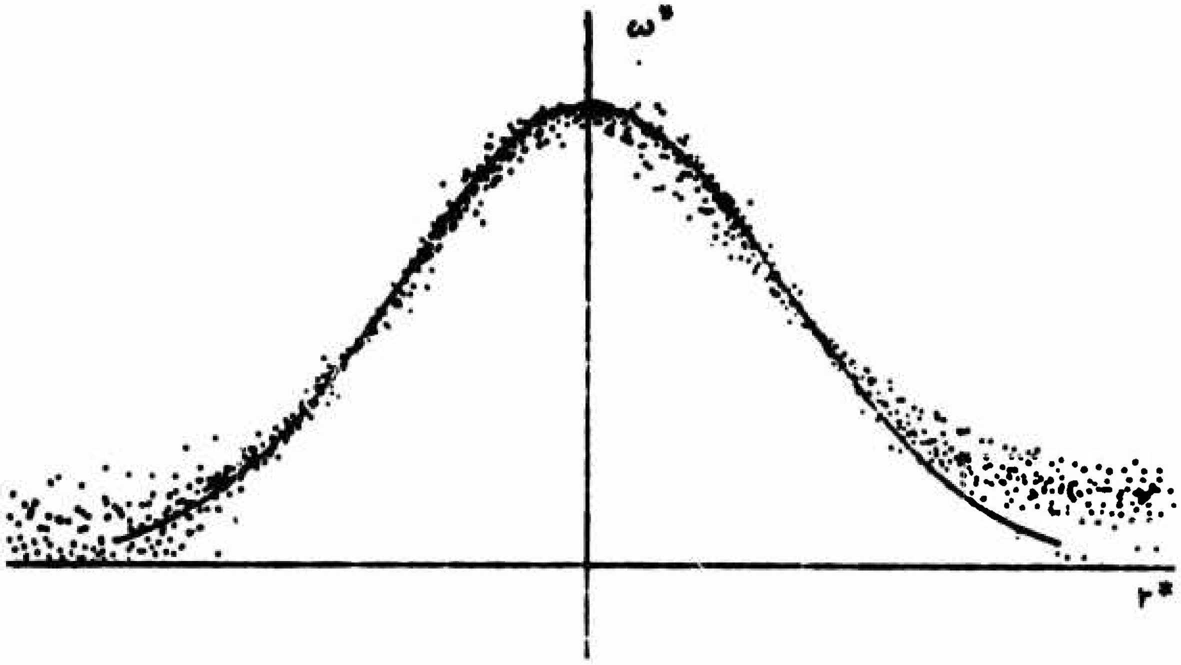

Fig.3 Angular velocity versus radius

In the experiments on the flat plate, where the transport velocity is constant, the maximum of angular velocity, ω_m along the vortex axis fits rather well a law of the type:

$$\omega_m = \frac{\text{const}}{x - x_0} \tag{2}$$

and $x - x_0$ is a coordinate along the axis, starting from a "virtual origin" of the vortex, which lies very close to the generator. This distance is affected by the magnitude of the separation bubble which is formed by the sharp leading edge of the generator. This bubble is ventilated by the tip vortex. We did not investigate carefully this effect, because, in the order of our approximation, it is possible to assume without large errors that this origin is the generator leading edge (it is really a bit upstream). Detailed experiments will give accurate results, but everything depends upon the generator thickness.

Let us consider Equation (1). If we consider a constant transport velocity, the distance x along the axis is function of the time, and we may easily introduce x in Equation (1).

$$t = \frac{x}{V} \tag{3}$$

and, for $r = 0$ we get:

$$z = \frac{\Gamma V}{8 x \pi \nu} \tag{4}$$

which is similar to Equation (2) and means that the eddy viscosity is rather constant also along the vortex. This last assumption is less accurate than the one of constant eddy viscosity across the vortex, and the error may be some 15%, but gives a great simplification: the vortex growth depends only upon one constant, the ratio η/ν. If this ratio is a constant of the vortex, it must be a function only of the vortex Reynolds number R_v

$$R_v = \frac{\Gamma}{\nu}$$

and the eddy viscosity η is a function only of the vortex strength Γ.

We have not yet investigated this relationship in detail: it remains still an open question.

5. STRETCHING OF VORTICES

Let us study a typical application of vortex generators to a control surface. Generators are placed somewhere upstream the hingeline. As we deflect the control surface, we have a velocity peak near the hingeline. During the tests, we noticed that, as we deflect the flap, the angular velocity on the axis was increasing with flap deflection, at a given station downstream the hingeline. This means that the diffusion of vorticity either decreases or increases less than the mainstream velocity. This means also that the length of the non-interacting part of the vortex is increased as we increase the peak by control surface deflection. This effect explains the large number of successful applications of vortex generators to control surfaces and some failure in other applications.

But we shall consider also that, if we place the generators in the velocity peak, instead of placing them upstream, we get a vortex strength increasing with deflection. (This strength is proportional to the mainstream velocity at the generator station.)

We need to be very careful in the choice of the generator station; the knowledge of potential flow and not only of the boundary layer properties is then required.

6. BURSTING OF VORTICES

The inner part of the vortex has dissipated part of its kinetic energy into heat. On the other hand, the pressure along the axis is increasing with vortex diameter: it is increasing with distance along the axis. Pressure tries to push upstream the air around the vortex axis. If the shearing stresses are not large enough, we may have a reversed flow inside the vortex, like in a boundary layer separation.

Of course, adverse pressure gradients are unfavourable and may cause vortex bursting. But another reason for bursting is that the vortex may suck air from a separated region, because of its low pressure. In this case, the vortex core is large and has very low transport energy: the danger of bursting is great.

For this reason, we must avoid high angles of attack, which may produce a large leading edge separation bubble on the generator. This angle does not depend only upon the geometrical value, but also upon the sideslip, which may be very large on a swept wing in high lift conditions.

Although this is verv important, in our earlier velocity profile measurements[4] we observed that, on a flat plate, with vortex generators of low aspect ratio (close to 1) and high angle of attack (45°), the defect of velocity near the axis did not exceed 10%, but a strong pressure gradient will probably change this observation.

In some tests we could not measure the angular velocity in the interacting part of the vortex, because it was too small; extrapolating parameters from the interaction free part, we should have angular velocities at least ten times larger than the minimum measurable. We feel that, in the interacting part, bursting of vortices was occurring, even on a flat plate. If occurring, bursting could be produced either by interaction or by the probe itself. In any case, bursting has to be investigated, but such an investigation requires a very accurate technique and very good instrumentation (laser anemometer?). This is not in the philosophy of this preliminary research.

7. CALCULATIONS OF THE EFFECTS ON A BOUNDARY LAYER

As well known, there exist a large number of available calculation methods for a turbulent boundary layer. We will now suggest only some ideas and will not try to apply our assumptions and results to any one of existing methods.

Vortices are introducing three-dimensional effects: the first question which arises is the possibility of treating only average quantities. Visualizations on separating stream[5] has shown that the separation line is wavy, but the amplitude of the wave is not large. If we want to predict separation, we may assume that it is possible to treat only average quantities.

The effect of forced mixing, emphasized by Schubauer and Spangenberg[2] recalls us the idea of an entrainement method. A way to relate the increased entrainement rate to the vortex properties, is to calculate the waviness of the edge of the boundary layer, as increased entraining area. This is possible knowing vortex location and strength.

Another approach, more complex but probably suitable for the interacting part, is the modification of the velocity profile, adding a new law to the law of the wall and the law of the wake. It will probably require a skin friction investigation.

8. CONCLUSIONS

Up to now we have discussed the various assumptions for simplifying the calculations of the vortex development and of its induced velocity. Further, quantitative experiments are required. We need to investigate the relationship between vortex Reynolds number and eddy viscosity.

Our interaction model confirms the essential importance of spacing, pointed out by Pearcey[1]; the observations on the vortex stretching explain why vortex generators are an effective means of boundary layer control in the presence of velocity peaks, as near hingelines.

REFERENCES

1.	Lachmann	*Boundary Layer and Flow Control.* Oxford, Pergamon Press, Vol.2, pp.1277–1314, 1961.
2.	Schubauer Spangenberg	*Forced Mixing in Boundary Layers.* Journal of Fluid Mechanics, Vol.8, Part 1, pp.10–31, 1960.
3.	Baron	*Uno studio teorico e sperimentale sull'influenza di generatori di vortici sullo strato limite turbolento.* Thesis, Milano, pp.51–114, 1973.
4.	Moltrasio	*Indagine preliminare sugli effetti del generatore di vortici.* Thesis, Milano, 1970.
5.	Celoria	*Aspetti qualitativi e quantitativi dell'effetto di una schiera di generatori di vortici su una corrente con separazione.* Thesis, Milano, 1972.

JET LIFT PROBLEMS OF V/STOL AIRCRAFT

by

J. Barche +)

Vereinigte Flugtechnische Werke-Fokker GmbH
2800 Bremen 1, Hünefeldstraße 1-5, Germany

SUMMARY

Jet lift interference is of paramount importance for the design of jet-supported V/STOL aircraft. The paper summarizes basic flow problems which are assumed to be valid for all different types of said category of aircraft.

1. INTRODUCTION

The development of V/STOL military aircraft has been an attractive goal for many aircraft companies all over the world, and especially in Europe.

Most of the aircraft are designed as jet-supported vehicles, i.e. that

- light-weight lift engines in addition to one or more cruise engines as well as
- cruise engines with a swivelling nozzle system or
- any combination of both types of engines

have been installed either in the airframe or in wing pods.

Due to the lack of natural stability and controlability in hovering and transition flight the engines have to be used for aircraftstabilization too. This is usually done by

- compressor bleed air or
- thrust modulation systems or
- a combination of both.

During the last ten years many types of jet-lifted aircraft have been designed, and some of them manufactured and the flight performance successfully tested.

One example of an early designed and successfully tested aircraft was the

EWR VJ 101 C,

the first VTOL-fighter type aircraft in supersonic range, shown in fig. 1. The VJ 101 C was equipped with three sets of two lift engines. One set was fitted behind the cockpit and used as lift engine only. The two other sets are installed in swivelling wing tip pods, thus acting as lift and cruise engines. The VTOL stability and control were achieved by thrust modulation of all the engines.

Another example of jet supported aircraft, the

Dornier Do 31,

was the first VTOL transport aircraft. The Do 31, shown in fig. 2, was equipped with tip-mounted pods of lift engines, and two lift/cruise engines with the well-known swivelling nozzle system. VTOL stability and control were achieved by thrust modulation and bleed air.

The most popular V/STOL aircraft, the

HSA Harrier

is shown in fig. 3. That aircraft - the only one in military service up to now - is equipped with one lift/cruise engine of the swivelling nozzle type [1]. In V/STOL modes the aircraft is stabilised and controlled by bleed air.

The newest and most modern V/STOL aircraft, the

VFW-F VAK 191 B

is shown in fig. 4. The aircraft, - originally designed for CAS and RECCE missions - uses two lift engines and one lift/cruise engine of the swivelling nozzle type installed in the fuselage [2,3,4]. The lift engines are installed in the front and rear part of the fuselage. They are symmetric with respect to the center of gravity, whilst the main engine was located directly in the center of gravity. Thus thrust increases of each type of engine can be used without shifting the center of thrust. In V/STOL modes aircraft is stabilised and controlled by a bleed air system in all three axes, together with thrust modulation in pitch.

+) Dr.-Ing.
Chief, Flight Physics

In spite of their different design missions and different lay-outs all of these exemplary aircraft have some common basic problems which are directly connected with the installation of engines for lifting the aircraft at small or zero forward speed.

The paper is concentrated on basic

Jet Lift Problems,

and mainly based on the experience with the VAK 191 B which seems to be valid for V/STOL aircraft in general.

2. BASIC PROBLEMS IN V/STOL MODES

If it is assumed that all V/STOL aircraft designers have to solve the same basic problems for their different projects, it is certainly useful to summarize these problems und their physical background.

This can be done best by following a typical take-off- or landing-procedure of an arbitrary V/STOL aircraft as sketched in fig. 5.

2.1 Engine Starting

The take-off-procedure obviously starts with ENGINE INGNITION, system and control check (fig. 5 a). This is done with engines on idle, and if possible with backward deflected jets in order to avoid or reduce the problems of

- GROUND EROSION and
- RECIRCULATION

Hereby GROUND EROSION is understood to be the destructive effect of jets. The magnitude of the erosion depends on jet exit temperature, dynamic head and duration of impact as well as the properties of the ground.

In addition to deflecting the jets backwards ground erosion is also minimized by using specially prepared small sites or at least by using propulsive systems with smaller energy density, such as ejector driven thrust augmentation.

RECIRCULATION is a generalized expresssion for the jet-induced temperature distribution around the aircraft, usually split up in so-called

- farfield effects,
  - caused by heating of the ambient air,
  - resulting in thrust losses,
  - depending on time, wind strength and direction

and

- near field or fountain effects,
  - caused by an upward self-deflection of two jets at minimum on the ground,
  - therefore resulting in local jet fountains, which
  - may heat up parts of the airframe, and
  - may even produce an engine surge, if parts of the fountains are sucked in into the intakes.

The fountain effects are broadly discussed in the following chapters.

2.2 VTO and Hovering

After having cleared the aircraft for take-off the engines are to be set at full power and the jets are deflected in vertical or near vertical position, if a TRUE VERTICAL TAKE-OFF and HOVERING are required (fig. 5 b). In those few seconds time the already defined

- GROUND EROSION and
- RECIRCULATION PROBLEMS

are highly magnified. In addition new problems occur, namely

- NOISE and
- GROUND SUCTION.

NOISE problems are familiar to all aircraft designers. But additionally at small ground clearances a feed-back between sound waves reflected from the ground and anular vortices on the jet boundary may be set in, thus magnifying the noise level [5].

Nevertheless the problems of GROUND SUCTION are for military aircraft of major importance. This is because of the fact that a rather small loss in predicted lift-off potential is equivalent to a considerable decrease in range.

As it is wellknown now - see e.g. [6] - the problems of GROUND SUCTION are the combination of two effects, i.e. the

- suck-down of a jet due to turbulent mixing,
  - as a free jet or
  - as a wall jet, and

- the fountain effect of two jets at minimum
  - which are closely connected with the near field recirculation problems.

Both effects are sketched in fig. 6.

The sucking effect of jets, especially of wall jets always result in effective lift loss, because the entrainment of air into a jet reduces the pressure especially at the lower side of a wing or fuselage. Even if the pressure change remains rather small the wetted surface is large enough to give a negative lift force at the order of a few percent of installed thrust. This is again shown in the left diagram of fig.7a for an aircraft B, which has four nozzles very close to each other. Hence, the flow field resembles a single jet and therefore purely suck-down forces act on the airframe. Thus, as a simple

- design rule
  - the distance between nozzles and wing should be as large as possible,
  - the distance between nozzles and ground should also be as large as possible, and
  - the jet decay which is responsible for the entrainment of air should be as low as possible with respect to engine exhaust flow and nozzle design.

However, modern V/STOL aircraft usually have more than one engine or one engine with multiple nozzles. If for such a system the jets meet the ground independently, each free jet developes its own wall jet. As shown by the jet footprint in fig. 6 and 8, the individual wall jets are separated from each other by so-called stagnation lines. Along these lines a strong outflow or inflow exist, and in the local symmetry plane parts of the wall jets deflect each other upwards. Basically this is an unstable process. However, the upward flow is self-stabilized by a vortex similar to the well-known intake vortex.

Due to that upward fountain flow the jet momentum is partly regained, giving an additional lift force. This is shown in the left diagram of fig.7a for an aircraft A, having six well-spaced nozzles and therefore a rather strong fountain flow between the nozzles in addition to suck-down flow outside.

Hence the above mentioned design rule can be completed and stated as follows:

- the distance between the nozzles should be as large as necessary to obtain individual wall jets, and to avoid a jet cluster.

These positive effects are, however, associated with increased problems in the near field recirculation, leading to the thumb rule,

- the larger the fountain lift is to be achieved, the more attention has to be paid in recirculation.

But fortunately the fountain flow is a rather compact flow and may be located and guided to uncritical parts of the aircraft, thus allowing the designer for most aircraft to ignore the above rule.+)

2.3 Rolling VTO and STO

In order to avoid recirculation problems and/or to use the overload potential of the aircraft a ROLLING VTO or STO technique is often recommended (fig. 5 c). The prediction of take-off performances has to take into account, however, that the effect of forward speed in ground proximity may complicate that procedure [7]. This is mainly an influence on

- free jets as well as on wall jets,
- on rudder effectivness, and
- on lift and cruise engines intakes
- together with crosswind effects.

It can easily be understood that effects of strong cross wind may dictate the performance of the stabilization system, since the natural stability is to be neglected at small forward speeds, and engine intakes can produce remarkable rolling and yawing moments.

But in addition to the above mentioned near and far field recirculation a third type of recirculation, called

- VORTEX RECIRCULATION

may limit the take-off performance.

That type of recirculation is caused by rolling up the wall jet field in a stable vortex sheet under front or crosswind conditions, as shown in fig. 9. The vortex sheet may be sucked in into the intakes, even if the aircraft has just left the ground.

Thus the theoretical improvements of RTO or STO techniques may be limited by typical jet problems, which are not to be considered on a classical aircraft.

+) On the VAK 191 B the rear landing gear doors are used as guide vanes.

2.4 Transition

After a true, rolling or short take-off the pilot opens the so-called

TRANSITION PHASE,

defined as that period in which the wing lift is not yet sufficiently developed, and the aircraft needs jet lift support (fig. 5 d).

During transition the increasing forward speed acts on the jets. This leads to

- an air entrainment, which is distorted by
- jet displacement/wake effects and
- jet bending,

interfering again with the airframe.

The reaction of the jets on the airframe in transition flight may be split into wing-body and tail-body interference.

The

- WING/BODY-JET INTERFERENCE
  is mainly an effect of
  - air entrainment and
  - jet displacement/wake producing a
  - jet-induced down wash field, and
  - local dynamic pressure changes.

If the distance between wing and nozzles is large enough the main interference of the jets consists of an additional

- down wash field, which is equivalent to a
  - jet-induced negative wing camber, which is
  - proportional to the free stream/jet-exit velocity ratio.

Thus the jet-induced lift loss increases with forward speed and may lead to losses in the order of 30 to 40 percent of installed thrust for downward deflected jets at transition end speed.

On the other hand the

- TAIL/BODY-JET INTERFERENCE
  is mainly an effect of
  - jet displacement/wake and
  - jet bending due to forward speed, producing again a
  - jet-induced downwash, and
  - dynamic pressure loss.

Tail-body effects are mainly stability and trim effects, leading to

- reduced stability or even pitch-up, and
- large positive trim angles, not occuring for conventional aircraft.

The entrainment, displacement and wake effects are of course combined, and hard to separate. This complicates the theoretical approach as well as the experimental work with small scale models and cold jet simulation. Nevertheless it seems that the wing effects are proportional to the freestream/jet-exit velocity ratio, and the tail effects proportional to the dynamic pressure ratio.

An example of lift loss in transition for fixed angle of attack and jet exit conditions is sketched in the center diagram of fig. 7 b. Here the aircraft A with six nozzles is compared with an aircraft B with four well-spaced nozzles. For the same total thrust the aircraft A shows slightly reduced lift losses in transition. This is a consequence of the thrust splitting which confirms the above mentioned design rule, that

- the distance between nozzles and wing should be as large as possible.

Nevertheless for both aircraft the lift loss at the end of the transition would be of the order of 30 to 60 percent of the total thrust if the jet exit conditions remain unchanged. But as wing lift increases with speed the jet lift needed for constant level flight decreases. Lift engine thrust may therefore be reduced, and swivelling nozzles turned to cruise conditions.

Due to interference effects, however, which increase with flight speed and decrease with smaller nozzle deflection angles the total jet-induced lift loss reaches its maximum at about the middle of the transition period. This is sketched in the left diagram of fig. 10, where - for a swivelling nozzle engine - a normal force break-down is plotted against flight speed: At zero forward speed the total weight has to be completely jet-balanced. As already mentioned, this needs even out of ground effects a thrust/weight ratio somewhat above unity to compensate the suction losses. As speed increases the difference between actual jet lift from exit momentum components and effective jet lift including the jet interference increases as long as the unfavourable speed effects dominate over the favourable effects of reduced nozzle deflection angles.

This feature is much more important for

PITCH CONTROL and STABILITY

than for lift/thrust/weight balance. As sketched on the right hand side of fig. 10 a fixed positive tail setting produces a nose-down moment increasing with speed. The jet interference effects, however, induce

- strong nose-up moments and
- reduce the aircraft stability.

As the nozzle angle is fixed from the lift/thrust/weight balance the speed-dependent trim change - shown by the dotted line in fig. 10 - is more or less automatically given. This means, that a maximum jet-induced trim change around the middle of the transition period must be expected. Because of the fact that the trim change can only partly be compensated by aerodynamic controls the complete compensation must be achieved by the bleed air or thrust modulation system. Hence the normal transition procedure can define the maximum control power of the longitudinal stabilization and control system.

Jet interaction problems are evidently not restricted to longitudinal motion only. In fact both cross wind or side slip and moderate rolling manoeuvres are normal during transition. Thus jet effects on

LATERAL/DIRECTIONAL CONTROL and STABILITY

have to be included in an analysis.

A typical example of jet-induced rolling and yawing moments of aircraft A are shown on the right hand side of fig. 7 c. The diagram is valid for fixed thrust, nozzle position, angle of attack and yaw. As it can be seen from the plot

- the rolling moment increases with forward speed,
  - i.e. the aircraft is destabilised in roll, and
  - must be artificially controlled since
  - the ailerons are hardly effective at that speed.

But as it can also be seen,

- the weather-cock stability is considerably improved,
  - i.e. the aircraft tends to reduce side slip and
  - to reduce the unfavourable jet-induced rolling moments.

Nevertheless the amount of required control power in roll may be defined by side slip effects during transition [8] , and it may be further assumed that some accidents of VTO aircraft are due to insufficient bleed air control.

Thus the transition performance of a V/STOL aircraft can be severely limited in longitudinal as well as in lateral/directional motion by limited power to control and stabilize the aircraft.

To complete the design rules it may be stated, therefore, that

- the tail setting angle should be increased to rather large positive values,
- the tail plane should be positioned as far away from the jets as possible for stall characteristics mainly,
- the artifical pitch and roll control capacity should be suffiently large to avoid severe restrictions in the transition corridor.

2.5 Wing-borne flight

If the aircraft has accelerated to wing-borne flight speed, the transition phase has ended (fig. 5 e). The swivelling nozzles are in cruise position, and the lift engines - if they exist - are to be shut down. Lift engines intake and exit doors have still to be open for a while, however, in order to ventilate the engines. After the ventilation the doors are closed, and the aircraft has its cruise configuration.

For rearward transition lift engines - if they exist - have to be started again in wing-borne flight. Lift engine starting is usually done either by

- a pressure drop across the engine,
- by bleed air assistance or
- by combination of both.

The simplest means is an engine starting owing to the pressure drop between intake and exit only. To restart the engines a pressure drop must be obtained such as to accelerate the engines to between 7 and 15 percent of the maximum rpm. Hence the intake pressure recovery - at speeds at which the intake flow is partly separated -, the exit pressure and the aircraft's angle of attack and side slip have to be carefully adapted.

After lift engine ignition the pilot starts the rearward transition. The problems associated with the rearward transition are similar ro those of the already discussed forward transition.

3. OPEN PROBLEMS ON JET INTERACTIONS

Successfully developed V/STOL aircraft prove that the flow phenomena associated with jet interactions are well understood in principle. Up to now there are still some gaps of knowledge, however, which are filled mainly by large experimental work either in model or flight tests. Hence, for the next generation of V/STOL aircraft improved methods are required.

3.1 Jet problems in cross flow

One of the still existing key problems in V/STOL aircraft design consists of a proper description of the

FLOW FIELD PAST JETS IN A CROSS FLOW,

dealing with the already mentioned problems of - see e.g. fig. 11 -

- air entrainment,
- jet displacement and wake,
- jet bending as well as
- interference of multiple jets and
- nozzle design.

This is of course a laborious task, since the basic questions of turbulent mixing even in stationary jet flow are not yet completely solved. Thus the main work still to be done will certainly be based on highly sophisticated experimental work. This work should enable to improve the former prediction approaches established in the pioneer days of V/STOL design, and from which some are summarized in the reference list [9,10,11,12,13,14,15,7].

Future methods will be most probably based on potential-theoretical dummys of the real jet flow. Such models - if properly established - would allow better use of the wellknown surface singularity methods for rather complex transition flight problems as well as in simplified form of the prediction of basic problems in an early stage of aircraft design.

Hence each contribution to the said flow phenomena giving a better understanding or prediction method as - e.g. - SNEL's paper [16] on flow field calculation or DFVLR reports on recent years jet flow tests [17] , soon to be published, should be welcomed.

3.2 Jet problems in hovering

Jet problems in hovering or at small forward speeds seem to be less difficult to solve, since the effect of the free-stream velocity vanishes or may be neglected. But near the ground the influence of

- wall jets and especially the
- fountain flow

complicates the prediction again. Hence most work have been and will further be done experimentally. Theoretical studies are mostly limited to single jets or to clustered jets acting as single jets, see e.g. [12] .

Experimental work on recirculation, however, has led to a better understanding of fountain flow phenomena [18] . A theoretical paper on prediction methods of such a flow, describing

- the footprint pattern for almost arbitrary nozzle positions,
- the fountain momentum, its
- relative position and direction

is to be published soon [19] . Thus a theoretical model of a more complex jet flow can be developed.

The calculation of the wing-body pressures, forces and moments can again be done using the panel methods. The ground effect will be simulated by the method of imaging the wing-body, free jet and wall-jet.

The calculation can be simplified, however, using the fact that - see e.g. fig. 12 -

- the pressures on the upper side of a wing are almost unaffected from the jet flow, excepting small perturbations on the leading and trailing edge.

Neglecting the perburbations, from that boundary condition the vortex distribution, cancelling the jet-induced normal velocity components is automatically given. Hence the solution of an integral equation can be avoided and only the knowledge of the tangential jet-induced velocities is needed.+)

+) The boundary condition is also valid in cruise flight for engines mounted above or below the wing, and jet exis nearly parallel to freestream direction.

3.3 Recirculation

As discussed above recirculation problems are usually divided into

- farfield effects,
- nearfield or fountain effects, and
- vortex recirculation in RTO or STO.

The most important and complicated problems are given by the nearfield recirculation, owing to the difficult prediction of the fountain location, direction and strength. As mentioned above, however, the prediction of fountain flow is beeing studied intensively.

As recirculation is associated with temperature effects the temperature field from each jet exit up to the ground, and from the ground via fountain flow to critical parts of the airframe must be known. This temperature field is usually measured in model tests, and one of the most delicate question is the scaling procedure from model to full scale. During the recent years the similarity rules even for complex recirculation flow have been successfully studied [18] . Checks during flight tests confirm the validity of the procedure for the mean temperature levels on engine intakes as well as on the ground or on the aircraft wheels.

As a jet flow field is highly unsteady, calculations or tests based on the assumption of steady flow may not give the correct answer to special problems. Recirculation on engine intakes is one of those problems not to be solved with steady methods as far as engine surge problems are to be analysed. In order to describe the random flow behaviour an application of the well-established statistical methods seems to be useful. This needs, however, a better understanding of the admissible engine distortion parameters, and a close collaboration between airframe and engine designer.

3.4 New jet lift generators

The problems discussed so far are mainly based on jet-lift production with

- lift engines and/or lift/cruise engines.

Other concepts as

- fan-in-wing and/or fuselage
- tilted rotors or
- tilted wings and rotors

have also been studied and partly flight-tested.

In addition each aircraft designer has most probably studied the concept of

- thrust augmenting ejectors,

mainly to avoid the problems of ground erosion and recirculation.

The concept was abandoned, because of

- disappointing low thrust augmentation connected with
- mechanical and structural complications.

During the last years the Aerospace Research Laboratories at Wright-Patterson AFB developed the concept of

- hypermixing nozzles,

which will be presented in the paper of Brown and Murphy [20] . This concept allows an increase in mixing efficiency due to the generation of "free" mixing vortices together with a reduction in mixing length. Hence a new jet lift generator of practical dimensions and augmentation ratios between 1.5 and 2 can be designed.

The practical application, however, the mechanical and structural problems, the problems of jet interference in transition are considered to be still somewhat open, until the results of flight tests of an experimental aircraft are known.

4. CONCLUSION

Successfully tested V/STOL aircraft have demonstrated, that the basic flow phenomena on jet lift generation are well understood. In addition knowledge about the still open gaps has been gained. As long as the V/STOL technique is regarded to be of military or civil interest as long a concentrated research has to be done to fill these gaps. Some of the problems which are assumed to be of major interest for the V/STOL designer have been discussed.+)

+) In order to illustrate the development of V/STOL aircraft a ten minutes film on the VAK 191 B has been prepared.

REFERENCES

Remark: The list contains only a limited number of references. More detailled references are given in the papers of the individual authors.

[1] "Hawker Siddeley Harrier G R. Mk 1"
Aircraft Engineering, Dec. 1969

[2] Riccius, R.; Wolf, B. "Design Optimization Procedure of the VAK 191 B and its Evaluation based on Results from the Hardware Realisation and Test Data"
AGARD-Meeting on Aircraft Design Integration and Optimization, Florence, Italy, Oct. 1973

[3] Wieland, K. "The Development and Flight Testing of the Propulsion System of the VAK 191 B V/STOL Strike and Reconnaissance Aircraft"
AGARD - PP - Meeting, Bad Schliersee, Germany, Sept. 1970

[4] Barche, J. "VAK 191 B - Aerodynamic Design"
Aircraft Engineering, July 1973

[5] Neuwerth, G. "Akustische Rückkopplungserscheinungen am Unter- und Überschall-Freistrahl, der auf einen Störkörper trifft"
DGLR-Tagung, Berlin, 1972

[6] Barche, J. "Offene Probleme der Flugzeug-Aerodynamik"
DGLR-Jahrestagung, Baden-Baden, 1971

[7] Barche, J.; Krenz, G. "Strahleinfluß an V/STOL-Flugzeugen im Übergangs- und Hochgeschwindigkeitsflug"
Luftfahrttechnik/Raumfahrttechnik 15, Nr. 5 (1969); improved German edition of "Jet Influence on V/STOL Aircraft in the Transitional and High Speed Flight Regime"
AGARD - FMP - Meeting; Göttingen, Germany, 1967

[8] Ewald, B. "Sideslip in VTOL-Transition Flight"
Paper to be presented at AGARD - FDP - Meeting on V/STOL Aerodynamics, 24-26 April 74, Delft, the Netherlands

[9] Spreemann, U.P.; Shermann, I.R. "Effects of Ground Proximity on Thrust of a Simple Downward-directed Jet Beneath a Flat Surface"
NACA TN 4407 (1958)

[10] Williams, J.; Wood, M.V. "Aerodynamic Interference Effects with Jet-Lift V/STOL Aircraft under Static and Forward-Speed Conditions"
Z.F W. July 1967 and RAE-TR 66403

[11] Wooler, P.T. "On the Flow Parts a Circular Jet Exhausting at Right Angles from a Flate Plate or Wing"
J.R.A.S. (March 1967)

[12] Seibold, W. "Untersuchungen über die von Hubstrahlen an Senkrechtstartern erzeugten Sekundärkräften"
Jb. WGL (1962)

[13] Ziegler, H.; Wooler, P.T. "An Analytical Model for the Flow of Multiple Jets into an Arbitrary Directed Crossflow in Ground Effect"
AIAA-Paper No. 70-545

[14] Skifstad, J.G. "Aerodynamics of Jets Pertinent to VTOL Aircraft"
J. of Aircraft, May-June 1970

[15] Vogler, R.D. "Interference Effects of Single and Multiple Round or Slotted Jets on a VTOL Model in Transition"
NASA TN D-2380 (1964)

[16] Snel, H. "A Method for the Calculation of the Flow Field Induced By a Jet Exhausting Perpendicularly Into a Cross Flow"
Paper to be presented at AGARD - FDP - Meeting on V/STOL Aerodynamics, 24-26 April 1974, Delft, the Netherlands

[17] Schulz, G. (editor) "Praktische Probleme bei Freistrahlen mit Längs- oder Queranblasung/Triebwerksstrahlsimulation in Windkanälen"
DGLR-Kolloquium, 6. Dec. 1973, DFVLR-Porz-Wahn
(to be published later)

[18] Behnert, R. "Bodeneffekte bei strahlgestützten Senkrechtstartern"
ZTL-Bericht FAG 4, VFW-F 4.10 (1970,71,72)

[19] Behnert, R. "Fontänen-Kopplung im V/STOL-Bodenfeld"
(to be published soon)

[20] Brown, S.L.
Murphy, R.D. "Design and Test of Ejector Thrust Augmentation Configuration"
Paper to be presented at AGARD - FDP - Meeting on V/STOL Aerodynamics, 24-26 April 74,
Delft, the Netherlands

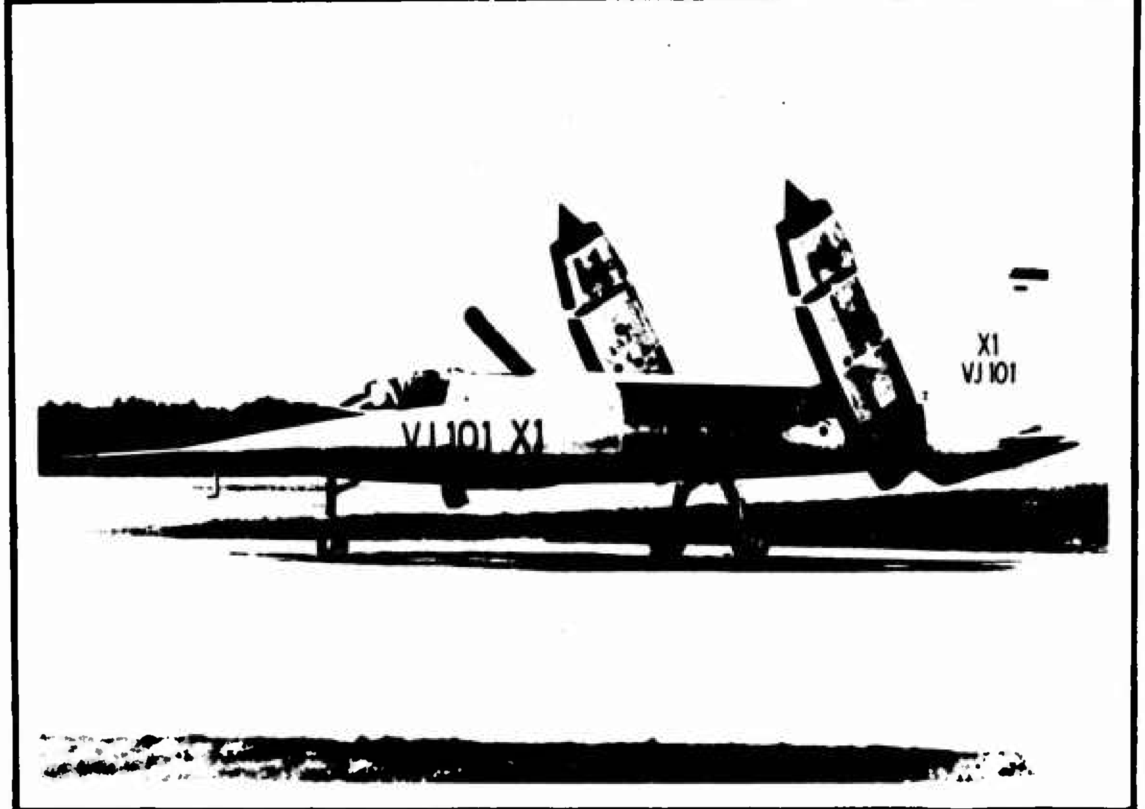
X1
VJ 101
VJ 101 X1

EWR VJ 101 C

VFW-FOKKER

FIG.: 1
Ex 1-74/17

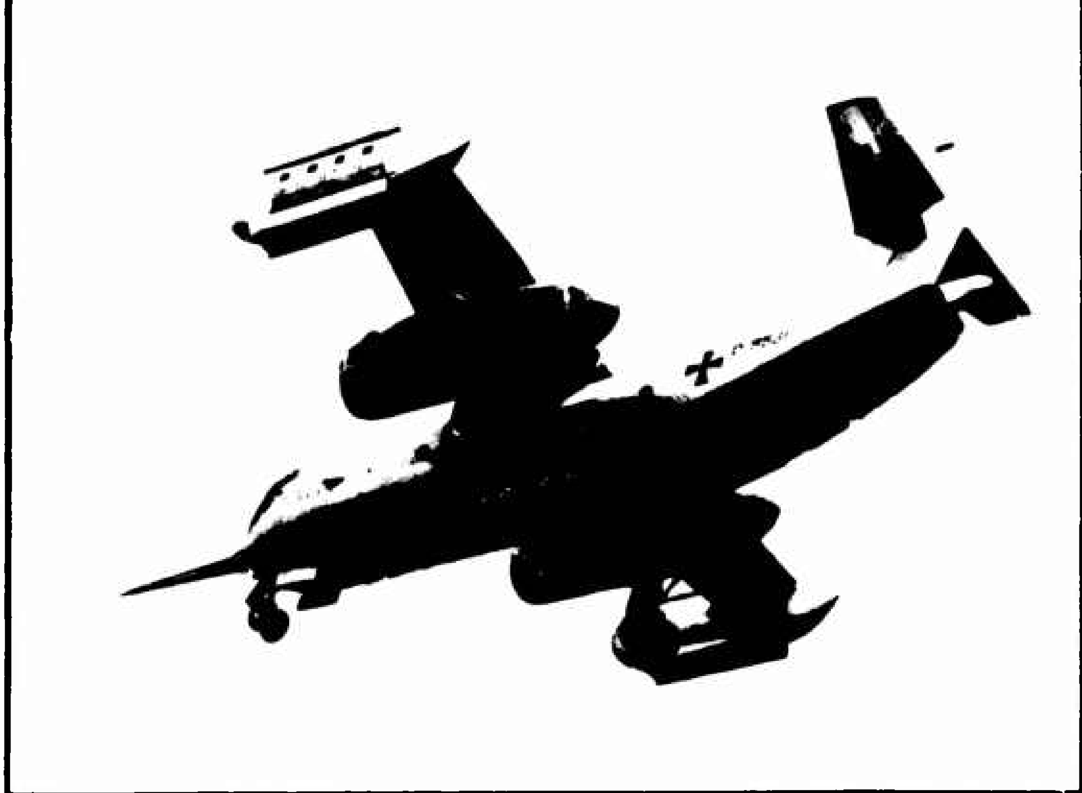

DORNIER DO 31

VFW-FOKKER

FIG.: 2
Ex 1-74/18

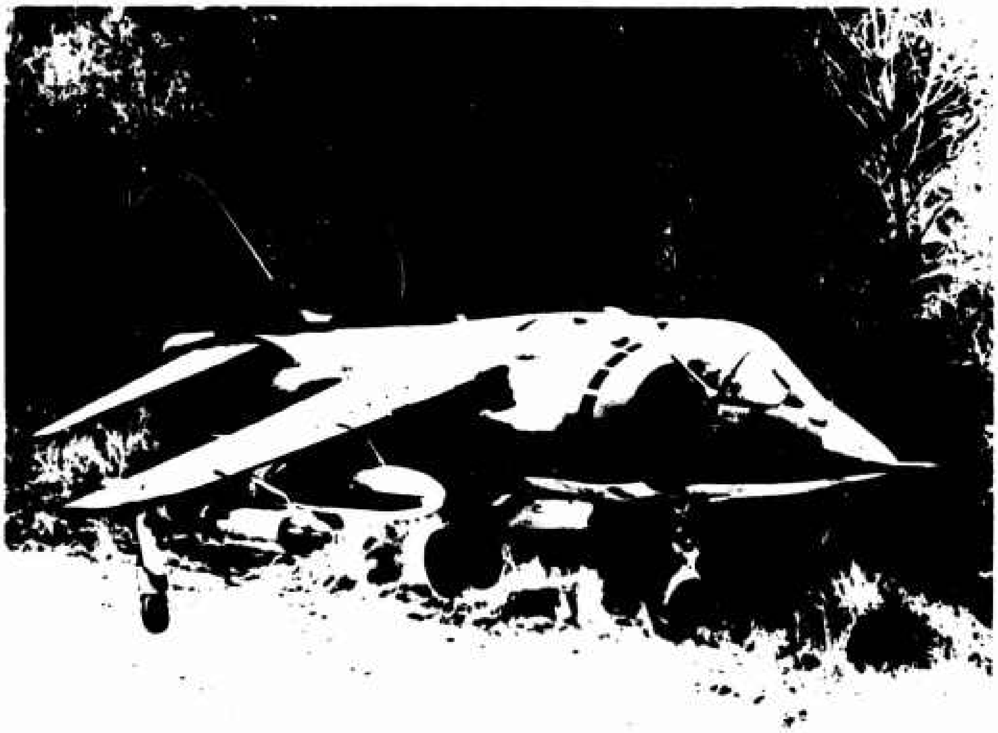

HSA HARRIER

VFW-FOKKER

FIG 3
Ex 1 - 74 / 19

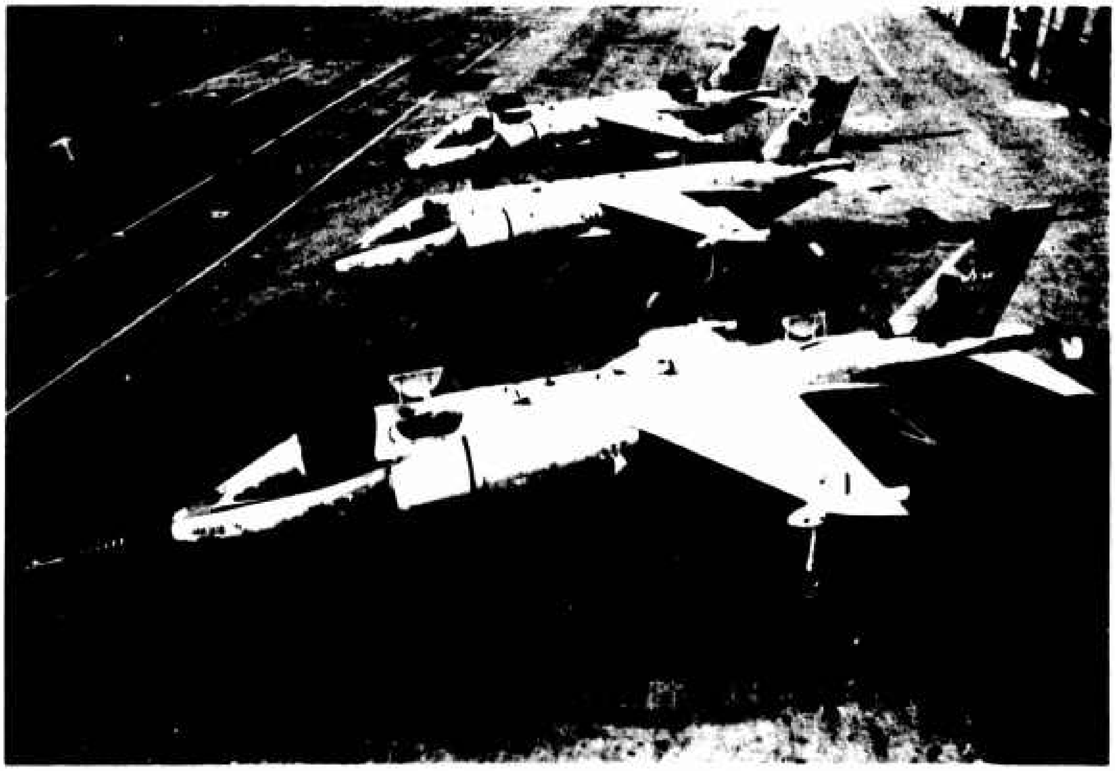

VFW-F VAK 191 B

VFW-FOKKER

FIG 4
Ex 1 - 74/ 20

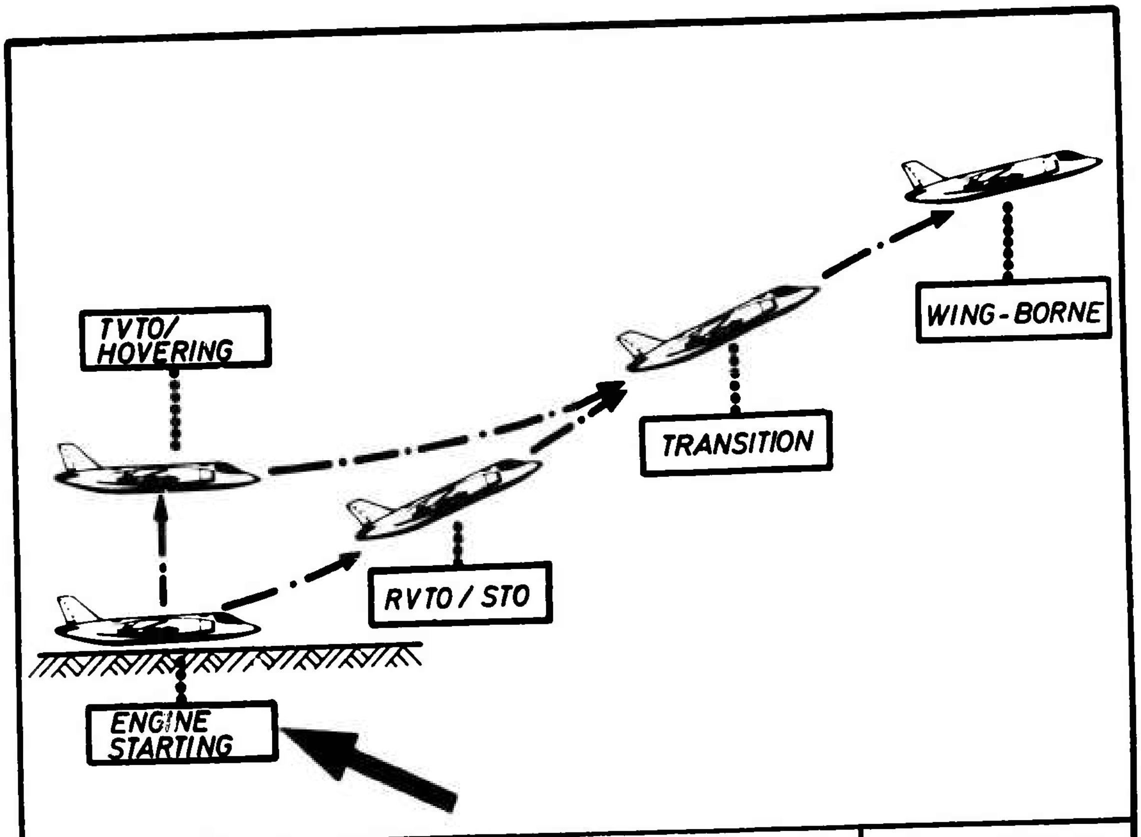
TVTO/
HOVERING
WING-BORNE
TRANSITION
RVTO / STO
ENGINE
STARTING

VFW-FOKKER

V/STOL - AIRCRAFT
TAKE - OFF

FIG.: 5a
Ex 1 - 74 / 21a

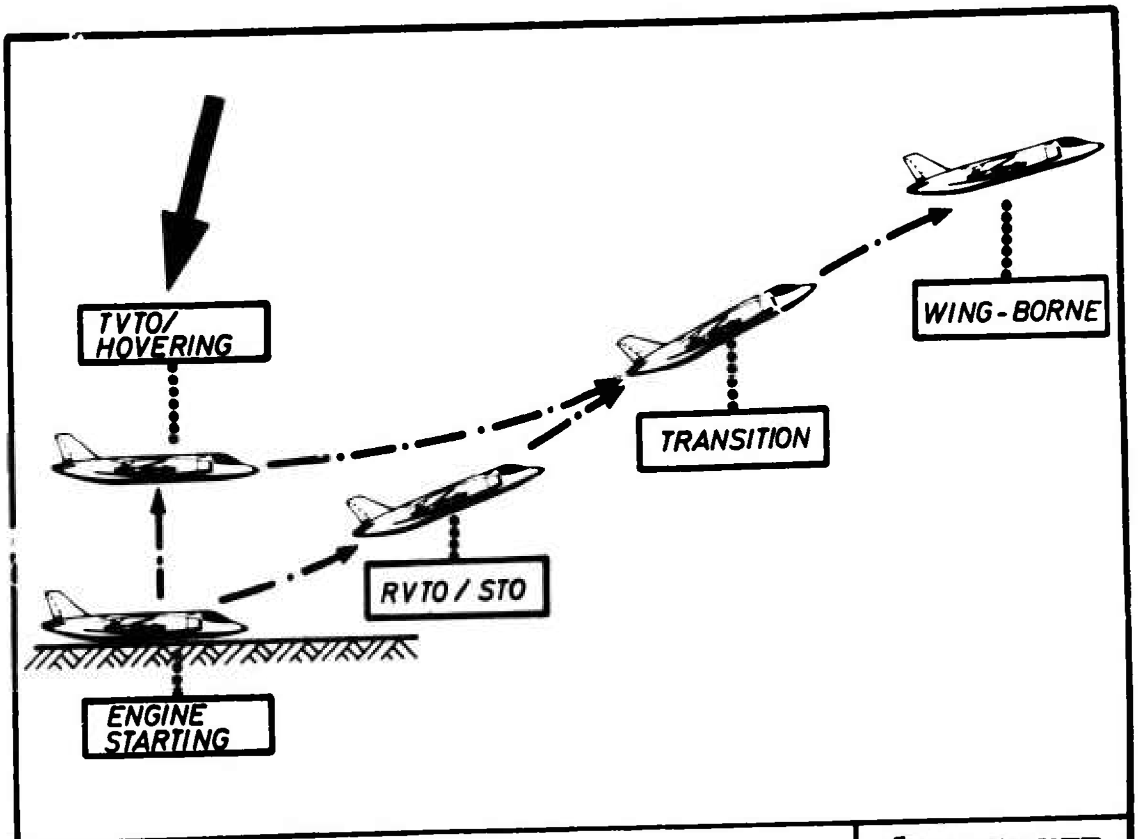
TVTO/
HOVERING
WING-BORNE
TRANSITION
RVTO / STO
ENGINE
STARTING

VFW-FOKKER

V/STOL - AIRCRAFT
TAKE - OFF

FIG.: 5b
Ex 1 - 74 / 21b

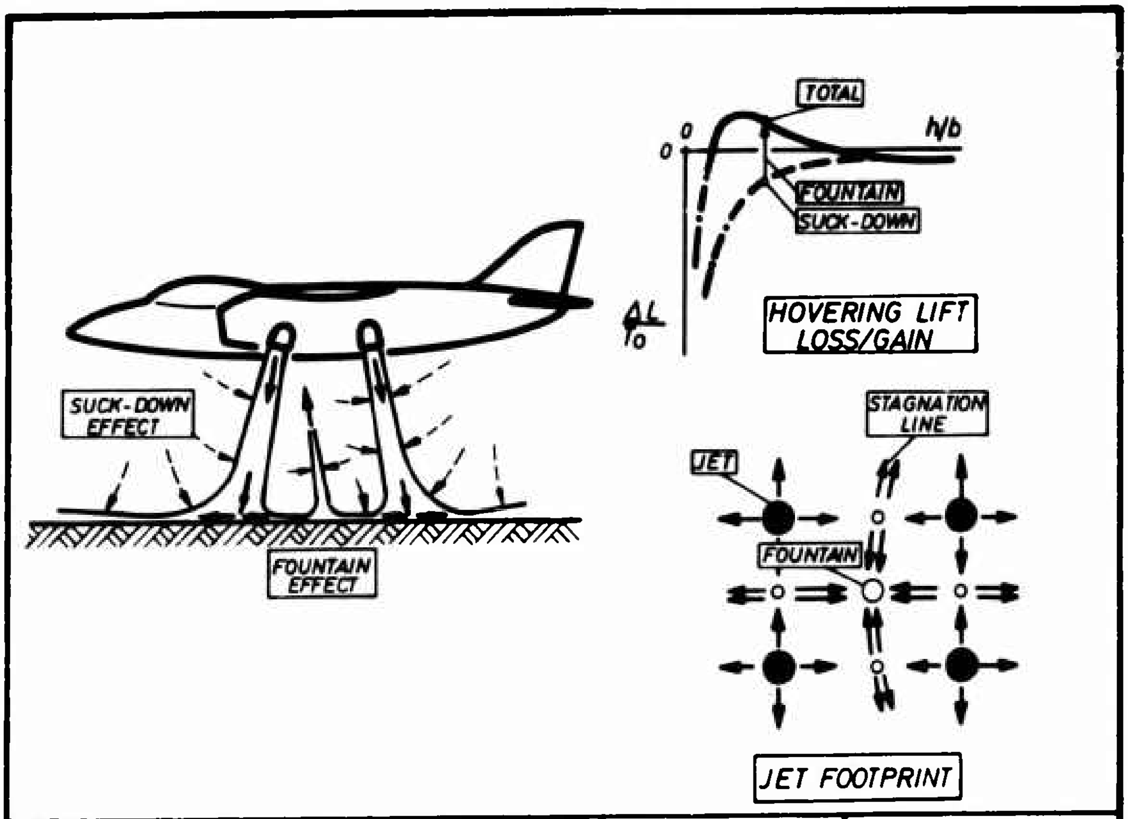
TOTAL
0
0
h/b
FOUNTAIN
SUCK-DOWN
$\frac{\Delta L}{T_o}$
SUCK-DOWN EFFECT
FOUNTAIN EFFECT
STAGNATION LINE
JET
FOUNTAIN

HOVERING LIFT LOSS/GAIN

JET FOOTPRINT

GROUND SUCTION

VFW-FOKKER

FIG.: 6
Ex 1 - 74/22

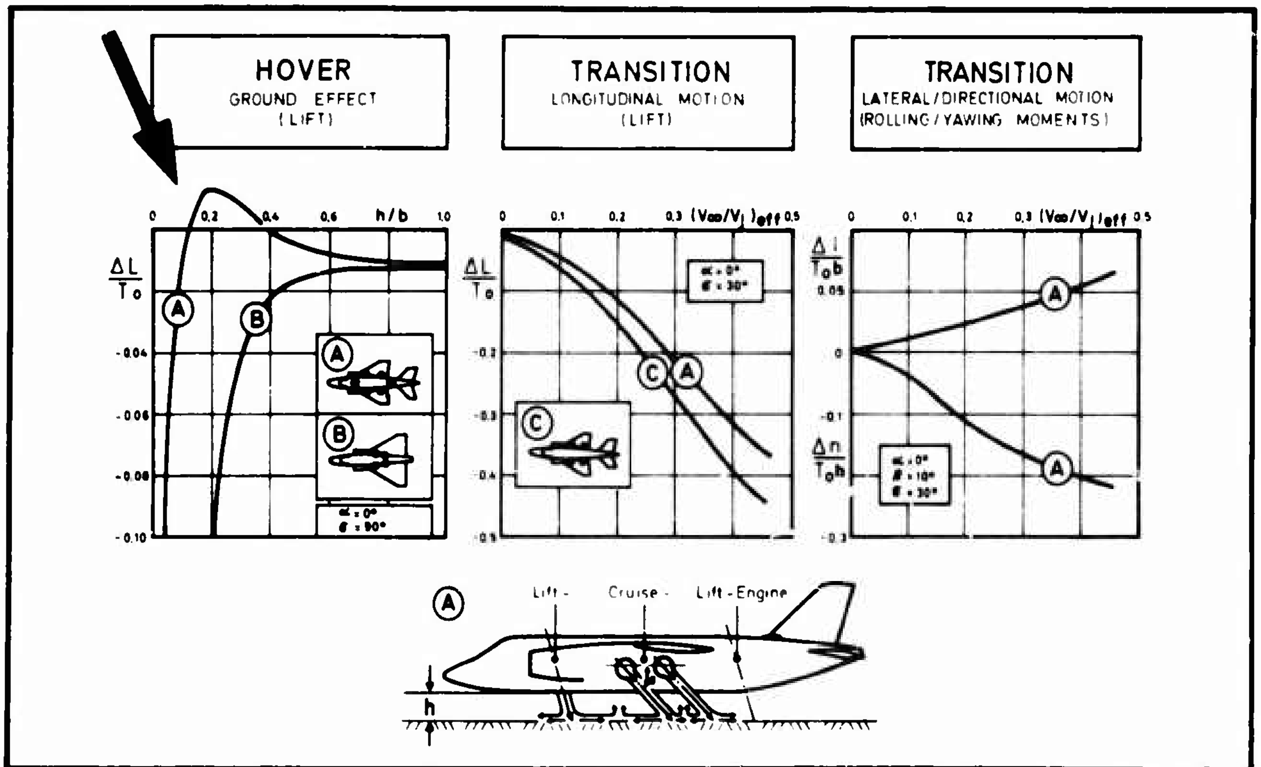

HOVER
GROUND EFFECT
(LIFT)

TRANSITION
LONGITUDINAL MOTION
(LIFT)

TRANSITION
LATERAL/DIRECTIONAL MOTION
(ROLLING/YAWING MOMENTS)

VFW-FOKKER

JET INFLUENCE
aerodynamic effects

FIG 7 a

Ex1-74 /23 a

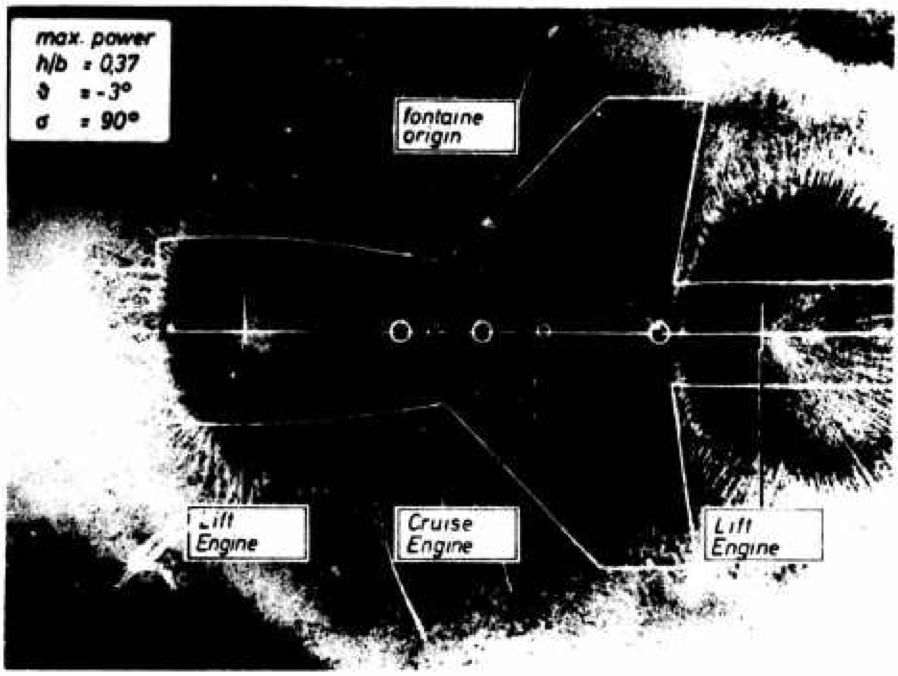
max. power
h/b = 0,37
ϑ = -3°
σ = 90°
fontaine origin
Lift Engine
Cruise Engine
Lift Engine

VFW-FOKKER

JET FOOTPRINT

FIG.: 8

Ex1-74/24

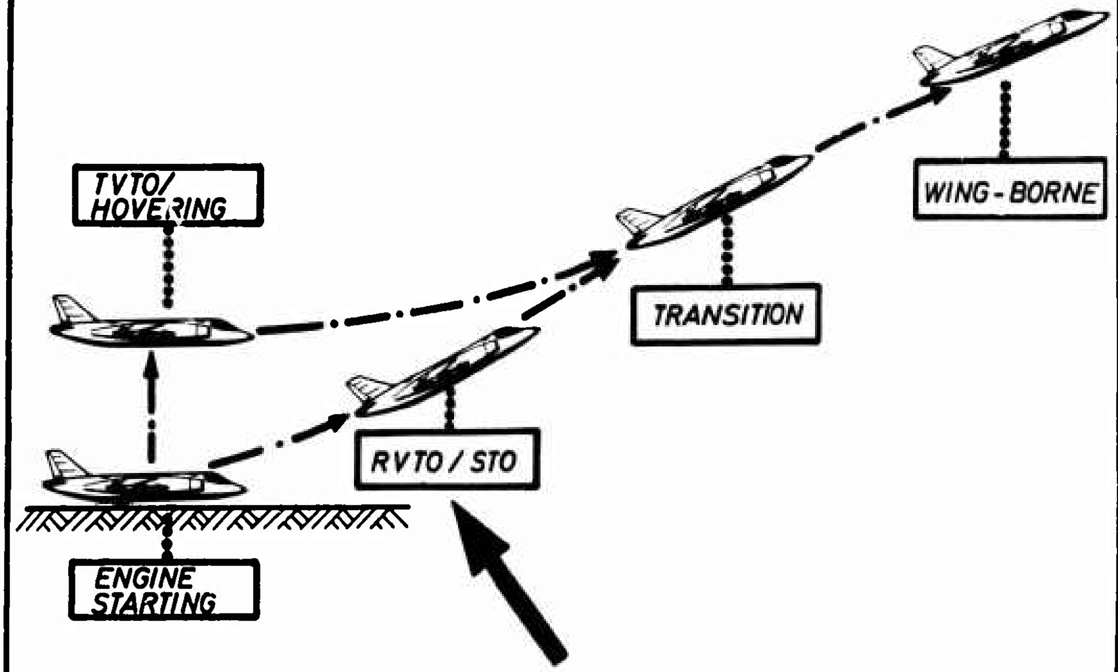
TVTO/ HOVERING
TRANSITION
WING-BORNE
RVTO / STO
ENGINE STARTING

V/STOL-AIRCRAFT TAKE-OFF

VFW-FOKKER

FIG.: 5c
Ex 1-74 / 21c

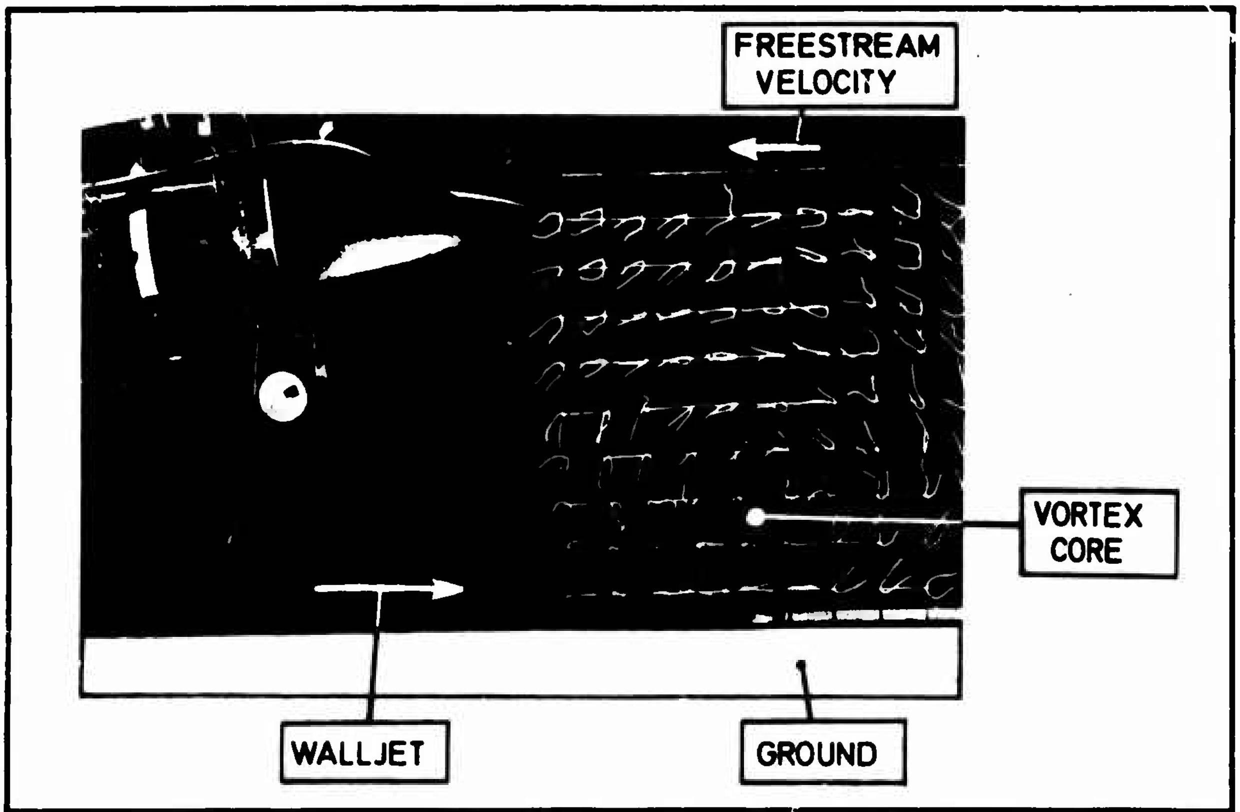
FREESTREAM VELOCITY
VORTEX CORE
WALLJET
GROUND

VORTEX RECIRCULATION
Model Test

VFW-FOKKER

FIG.9
Ex1-74/25

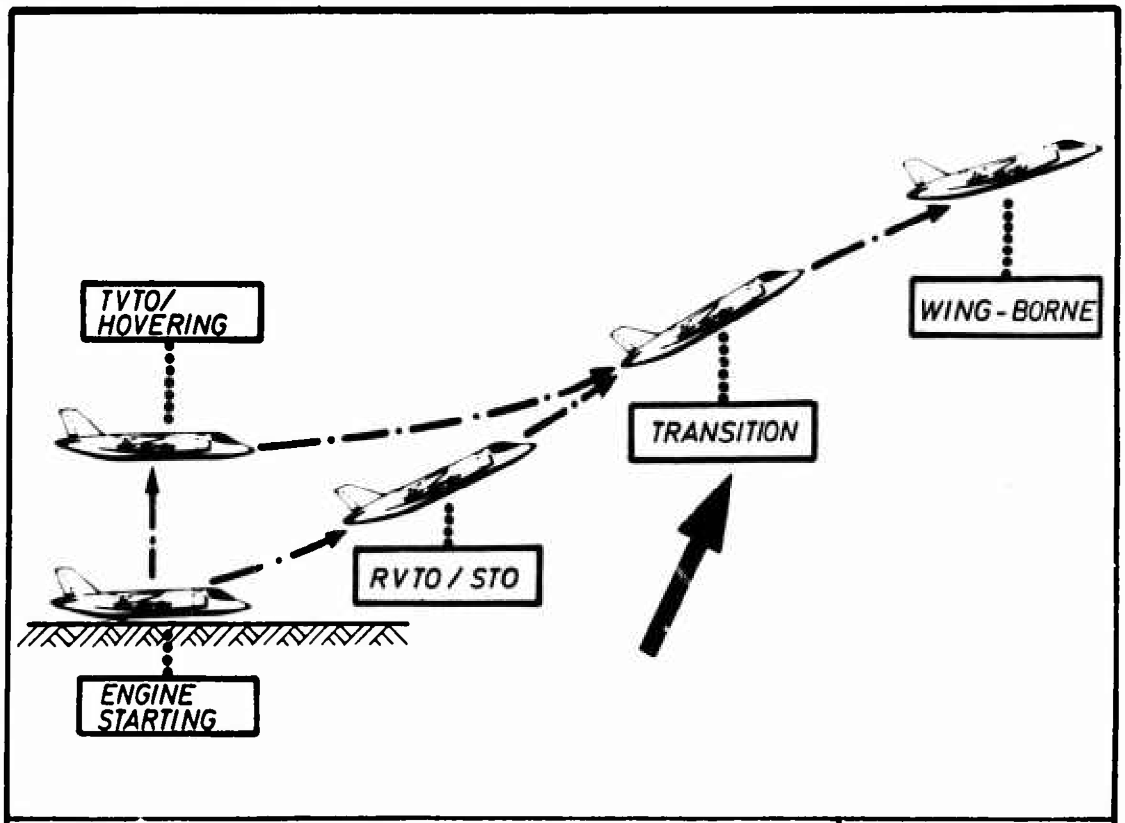
TVTO/ HOVERING
WING-BORNE
TRANSITION
RVTO / STO
ENGINE STARTING

V/STOL - AIRCRAFT
TAKE-OFF

VFW-FOKKER

FIG 5d
Ex 1 - 74 / 21d

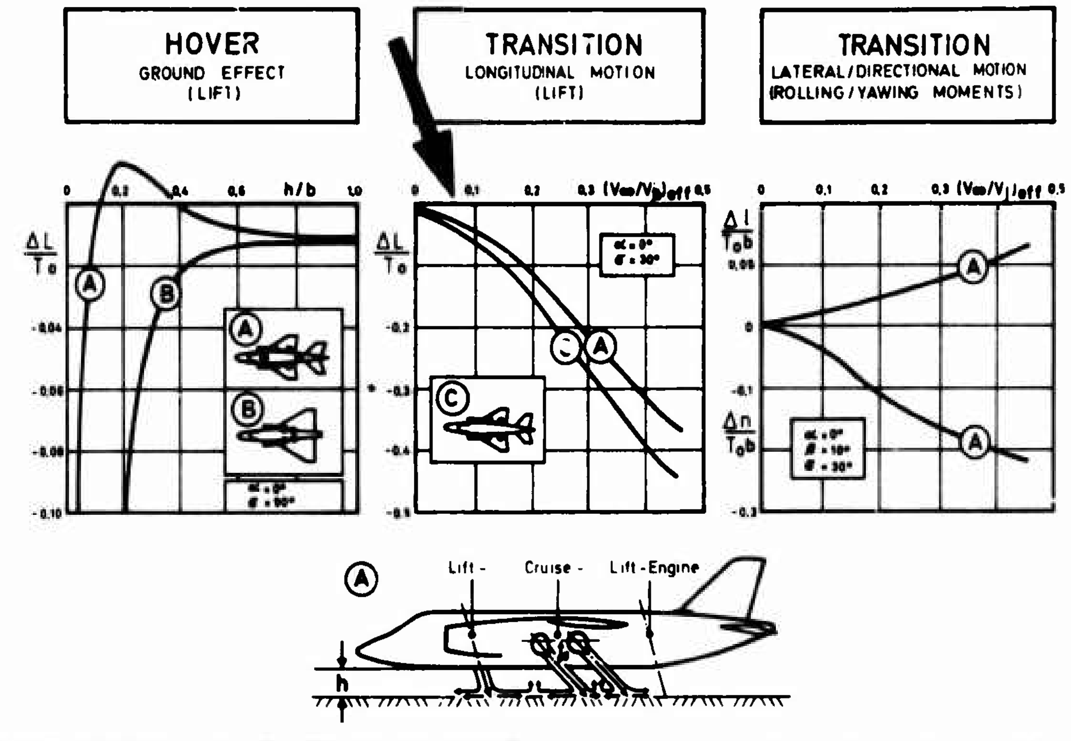

VFW-FOKKER

JET INFLUENCE

aerodynamic effects

FIG 7 b

Ex1-74/23 b

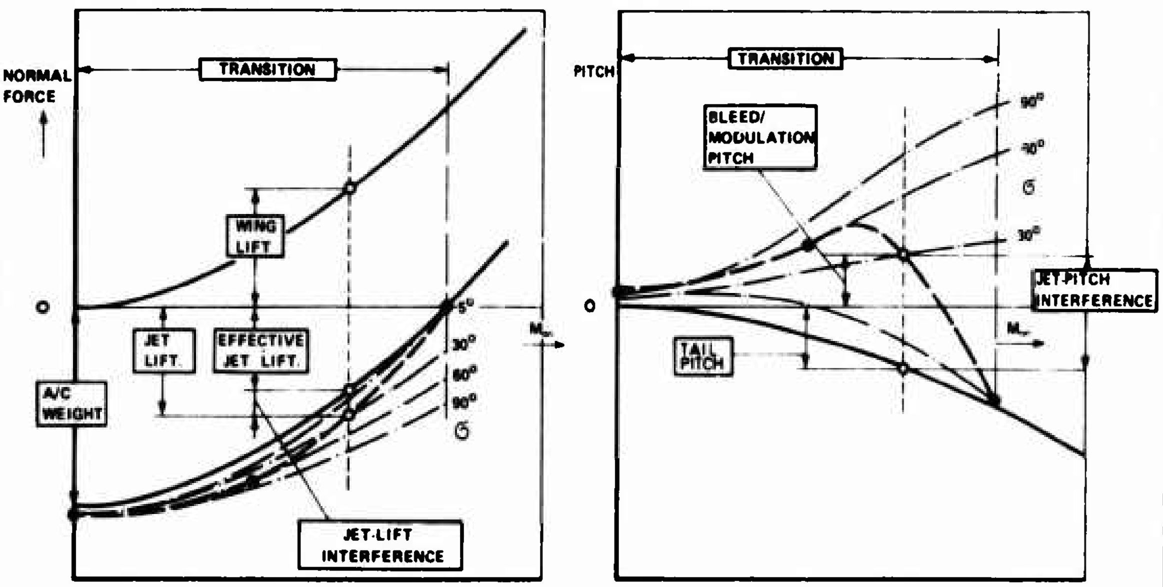

VAK 191 B
JET INTERFERENCE LIFT-PITCHING MOMENT

VFW-FOKKER

FIG : 10
Ex 1-74/26

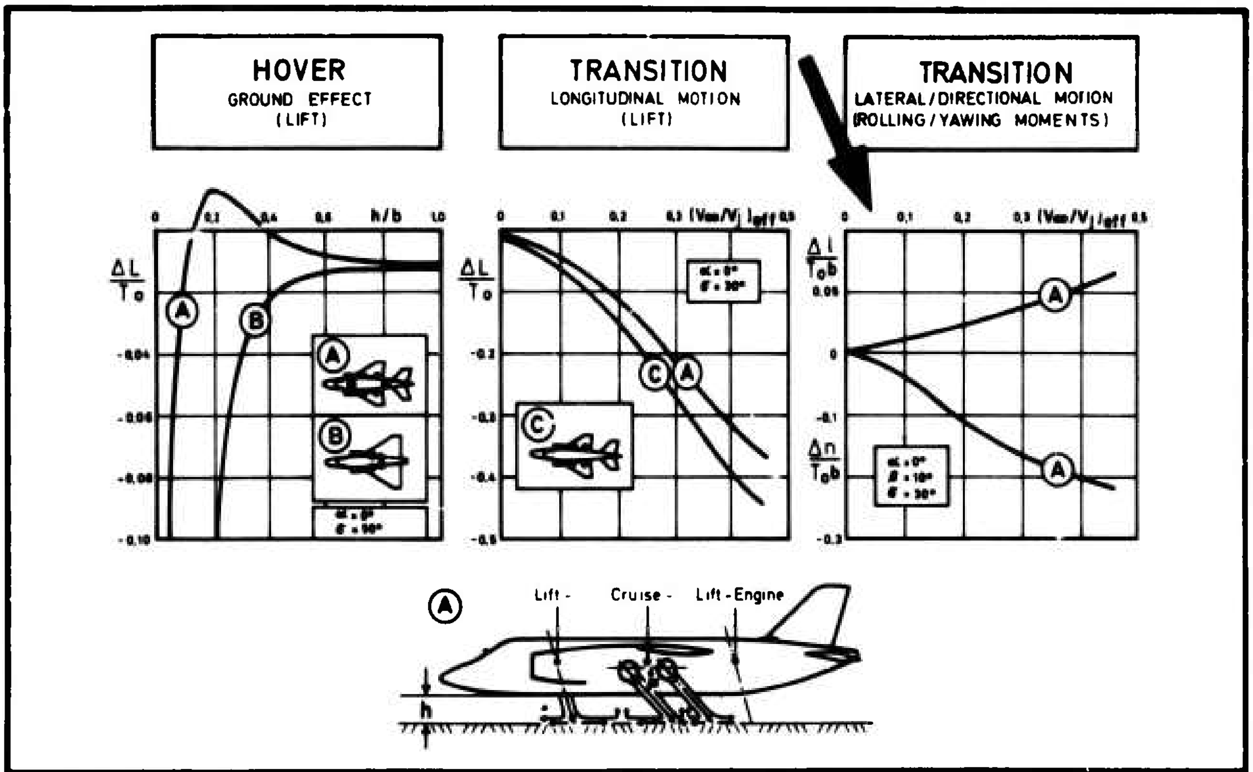

VFW-FOKKER

JET INFLUENCE
aerodynamic effects

FIG 7c
Ex1-74/23c

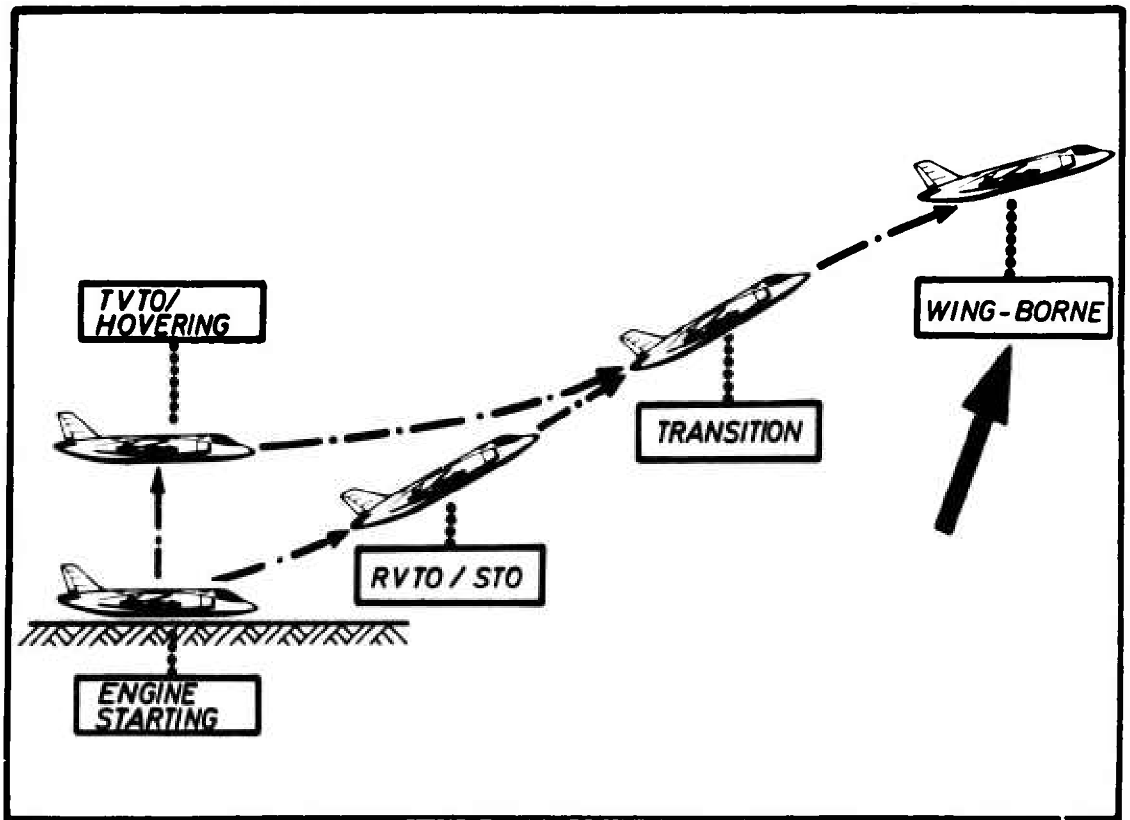
TVTO/ HOVERING
RVTO / STO
TRANSITION
WING-BORNE
ENGINE STARTING

V/STOL-AIRCRAFT
TAKE-OFF

VFW-FOKKER

FIG.: 5e
Ex 1-74/21e

JET INTERFERENCE
SMOKE TUNNEL TEST

VFW-FOKKER

FIG.: 11
Ex1-74/27

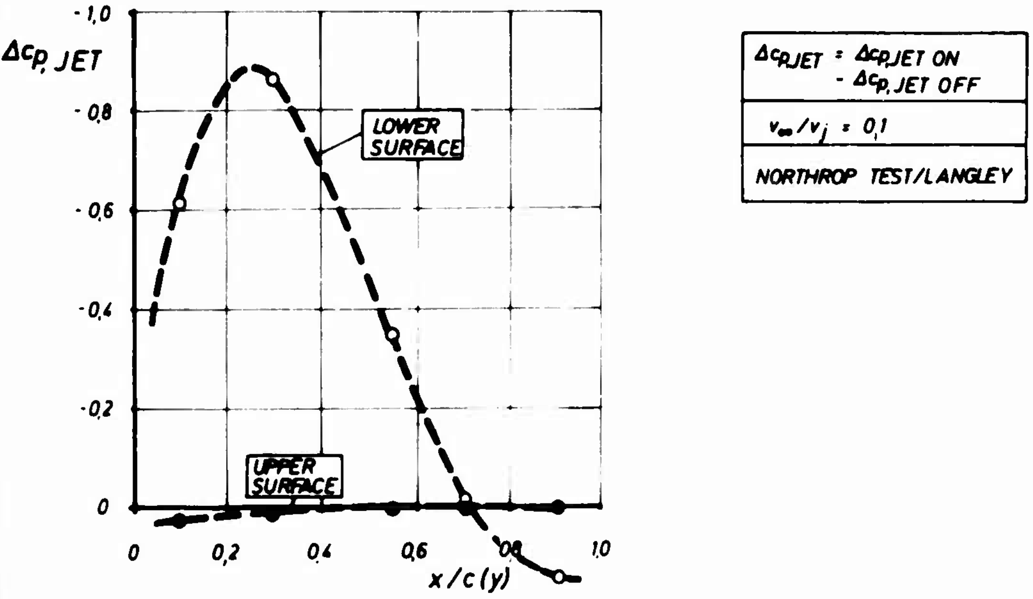

JET EFFECT
WING PRESSURE

VFW-FOKKER

FIG.: 12
Ex1-74/28

SIDESLIP IN VTOL-TRANSITION FLIGHT
A CRITICAL FLIGHT CONDITION AND ITS PREDICTION IN SIMPLE WIND TUNNEL TESTS

B.Ewald
Chief of Experimental Aerodynamics
Vereinigte Flugtechnische Werke-Fokker GmbH
2800 Bremen 1, Hünefeldstrasse 1–5
Germany

SUMMARY

During transition flight a VTOL-aircraft is partly supported by aerodynamic lift and partly by the thrust of the engines, which is vectored near vertically upwards. In sideslip heavy rolling moments may be created by the interference of the jets with the general flow field.

During flight tests of the VAK 191 B VTOL-Fighter large sideslip angles were observed in the transition flight region and resulting rolling moments were investigated up to the boundaries of the aircraft control power in roll.

These flight test results are compared with early low speed wind tunnel results.

A special wind tunnel technique was developed for these tests. Through a three chamber tube compressed air was fed to nozzles representing the lift engines and the lift-cruise engine of the VAK 191 B. The hull of the model was connected to this nozzle-sting arrangement by a six component strain gage balance.

So in this balance only the aerodynamic forces affecting the model hull were measured. As a result of wind tunnel tests with and without engine flow the jet interaction was found.

In the paper the flight test results and the wind tunnel results are compared for a critical sideslip condition. It is shown, that a prediction of critical flight conditions by a low cost wind tunnel technique is possible.

1. INTRODUCTION

During transition flight a VTOL-aircraft is partly supported by the wing lift and partly by the thrust of the engines, which is vectored more or less vertically upwards. In this condition the jets interfere with the flow field due to forward speed of the aircraft and induce additional downwash and sidewash effects. In sideslip thus heavy rolling moments may be created which are normally not controllable with ailerons alone. So this critical flight condition needs careful treatment during wind tunnel tests of VTOL aircraft.

The evaluation of jet effects of VTOL aircraft in the transition flight mode by wind tunnel tests has not yet become a standard wind tunnel technique. A wide variety of experimental procedures has been used with more or less success and most of these techniques are complicated and expensive.

2. VAK 191 B DEVELOPMENT AT VFW-FOKKER

The development of the VTOL Close Air Support Fighter VAK 191 B caused the search for a suitable method to get such wind tunnel results at VFW-Fokker. A relatively cheap test arrangement was found and it should be very instructive to compare the wind tunnel tests with flight test results.

The VAK 191 B is a true VTOL aircraft with a small highly loaded shoulder wing and a mixed propulsion system. A lift-cruise fan-engine (Rolls-Royce RB 193) with swiveling nozzles is installed in the fuselage near the center of gravity. Two lift engines (Rolls-Royce RB 162) are installed nearly vertical in the fuselage in front of and behind the lift-cruise engine. More details on this aircraft may be found in Reference 5 and in Barche's paper given at this meeting. A three-view drawing is given in Figure 1.

Figure 2 shows the airplane in transition flight with gear down and lift engine doors open. Position of the lift-cruise engine nozzles is nearly horizontal.

3. YAW IN TRANSITION, FLIGHT TEST RESULTS

On one of the first transition flights a sideslip condition was reached, that clearly demonstrated the boundaries of the flight region. Figure 3 shows a part of the original "Quick Look" telemetry record of this flight (operation number 2067). The speed varies between 75 and 100 knots, the angle of attack between 5 and 15 degrees.

The aircraft yaws at first for a short time to the right and then to the left with yawing angles between 5 and 15 degrees.

According to the fifth diagram in this figure the aircraft banks to the lee side. The pilot tried to maintain a horizontal bank attitude and the fourth diagram on Figure 3 shows the answer of the aircraft attitude control system.

During the first part of the right yaw condition (Seconds 1758 to 1776) the reaction control system was able to maintain a nearly horizontal bank attitude with about 70% of the maximum available roll control thrust.

During the time period 1778–1792 in spite of the slightly reduced yaw angle several seconds of maximum roll control thrust were necessary to maintain the bank attitude. It is clearly indicated that these critical rolling moments are caused by the increased speed of the airplane. A reduction of speed and angle of yaw stopped this dangerous condition.

The Figures 4 and 5 show the important flight test results of this period after calibration and omission of noise. According to the VAK 191 B VTOL flight control system aileron deflection and reaction control thrust are working in parallel.

It should be noted that the roll acceleration sensor was faulty during this test and the roll acceleration was evaluated by twofold differentiation of bank angle, which is not very accurate.

Figure 6 shows the average engine conditions during the test period. The reaction control roll thrust is generated by downward nozzles inboard of the wing tip pods, which are fed by engine bleed air. So the maximum available control thrust depends on the engine conditions.

The main forces resp. moments about the roll axis are:

- Aerodynamic Moment. This includes all aerodynamic forces acting on the aircraft hull due to the external flow field.
- Rolling moments due to the lift engines inlet flow, acting at the intake contour and adjacent fuselage surface.
- Moments of inertia due to roll accelerations.
- Rolling moment due to Bleed Control Thrust.

(See also Figure 7.)

From the flight test data (Figures 4 and 5) the aerodynamic rolling moment was evaluated, its time history is shown in Figure 8. It indicates a heavy negative rolling moment during the whole period with exception of two seconds at 1782, where a rather small yaw angle coincides with full opposite aileron deflection.

In order to give an impression of the magnitude of the different rolling moment contributions, for some points a rolling moment breakup is given in Figure 9. The maximum available reaction control rolling moment is set equal to 100 in this figure.

4. WIND TUNNEL TESTS

The wind tunnel model, which was used to study these jet effects several years before the flight tests, is shown in Figure 10. It is mounted in the open test section of the DFVLR Low Speed Tunnel at Porz-Wahn (3,28 x 2,33 m^2 test section size). The model scale is 1:10.

Figure 11 shows the design principle of this model. A three channel support sting was mounted in the wind tunnel test section by a wire suspension. Compressed air was fed through this sting to the engine nozzles, which were mounted at the front end of the sting. The upper channel led the air to the lift cruise engine nozzles, while the two lower channels feed the lift engine nozzles.

The complete hull of the model is put around this sting-nozzle arrangement without touching it. The hull is connected to the sting via a six component strain gauge balance. The gaps between hull and nozzles are sealed by a very thin rubber foil.

In this arrangement the strain gauge balance measures the aerodynamic forces acting on the model hull while the sting directly carries the thrust load of the jets. So it is possible to study the influence of the jets on the external flow around the model without interaction of the jet momentum force.

Figures 12 and 13 show the model in the wind tunnel test section. Visualisation of the lift engine jets is obtained by injection of water into the air supply tube.

Due to the wind tunnel equipment and the simple model design the use of full size jet temperatures was not possible. In fact all tests were done simply with cold compressed air. So some thoughts on the correct scaling of the nozzle exit velocities resp. the nozzle pressure ratios were necessary.

Theoretical considerations and preliminary wind tunnel tests with extensive variation of tunnel speed and jet speed showed that the ratio of jet momentum and free stream momentum is the most important scaling parameter for the influence of the jet on the external flow field. This momentum ratio was defined as

$$\Phi = \frac{\rho_E \cdot V_E^2}{\rho_\infty \cdot V_\infty^2} = \left(\frac{V_E}{V_\infty}\right)^2_e$$

where E indicates the nozzle exit flow and ∞ the free stream. In the case of supercritical nozzle pressure ratio a pressure term must be added to the exit momentum.

A typical test result of this model is shown in Figure 14. The rolling moment coefficient is plotted against the angle of yaw for different momentum ratios. The momentum ratios refer to the cold nozzle of the lift-cruise engine; the other nozzles are adjusted analogous to normal relative engine conditions in flight.

The highest momentum ratio of 433 refers to a flight speed of 38 knots, the lowest value (15) to about 190 knots

The rolling moment due to sideslip increases rapidly with increasing jet momentum up to a momentum ratio of 57,7, i.e. down to a flight speed of about 110 knots. With momentum ratios beyond this value the rolling moment coefficient again decreases. This clearly indicates a critical flight region in the vicinity of 100 knots and slightly below. At higher speeds the aileron is strong enough to control the effects and at much lower speeds the rolling moment is easily controlled by the reaction control system.

This model and the associated test technique proved highly successful. About 10 test programs with a total of about 1500 wind tunnel hours were performed. The results of this wind tunnel programme were used as a basis for the development of the aircraft automatic attitude control system and for pilot training in the VAK 191 B-Simulator.

5. COMPARISON FLIGHT TEST – WIND TUNNEL TEST

From the wind tunnel test results the aerodynamic rolling moment coefficient was extracted for the flight and engine conditions occurring during the discussed period of Flight Test Operation 2067. In Figure 15 the aerodynamic rolling moment is plotted against time; the wind tunnel test results are represented by the crosses and the continuous line. The circles indicate the results evaluated from the flight test, which were already shown in Figure 8.

Flight test and wind tunnel results compare very pleasantly over the greater part of the observed period but a few flight test points are very far away from the wind tunnel results. A glance at the bank angle time history shows that these moments coincide with large bank angle accelerations. Under such conditions minor errors in the synchronisation or inaccuracies in the evaluation of roll acceleration (twofold differentiation of bank angle) can produce very large errors in the evaluation of the aerodynamic rolling moment. So one should better forget these parts of the time history and believe in the wind tunnel results.

With the combined results of wind tunnel tests and flight tests a simulation programme was run on the computer to fix flight boundaries for yaw angle in transition flight. These boundaries are plotted in Figure 16. It was assumed that 50% of the available reaction control thrust are allowable for compensation of the roll moment. So a sufficient margin of control thrust is available for manoeuvres.

6. CONCLUSION

The evaluation of the transition flight corridor during the VAK 191 B flight tests demonstrated the restriction of this flight corridor by yaw induced rolling moments, which were predicted of a similar magnitude by early wind tunnel tests. The technique used for this extensive wind tunnel programme proved very successful and not too expensive. The results are in good conformity with the flight test results.

The sensitivity of jet supported VTOL aircraft against yaw angles during their transition flight may lead to the use of a "pedal pusher" analogous to the stall avoiding stick pusher in conventional aircraft.

REFERENCES

1. **Ewald, B.** *VSTOL Wind Tunnel Technique.* AGARD Conference Proceedings No.22, 1967.
2. **Ewald, B.** *VSTOL Windkanal-Messtechnik.* Luftfahrttechnik – Raumfahrttechnik No.3, 1969.
3. Riccius, R. *Erprobung des VSTOL-Experimentalflugzeuges VAK 191 B.* Vortrag Jahrestagung DGLR-ÖGFT, Innsbruck, September 1973.
4. Barche, J.; Krenz, G. *Strahleinfluss an VSTOL-Flugzeugen im Übergangs- und Hochgeschwindigkeitsflug.* Luftfahrttechnik – Raumfahrttechnik No.5, 1969.
5. Barche, J. *VAK 191 B Aerodynamic Design.* Aircraft Engineering, July 1973.
6. – Unpublished VFW-Fokker Development Reports.

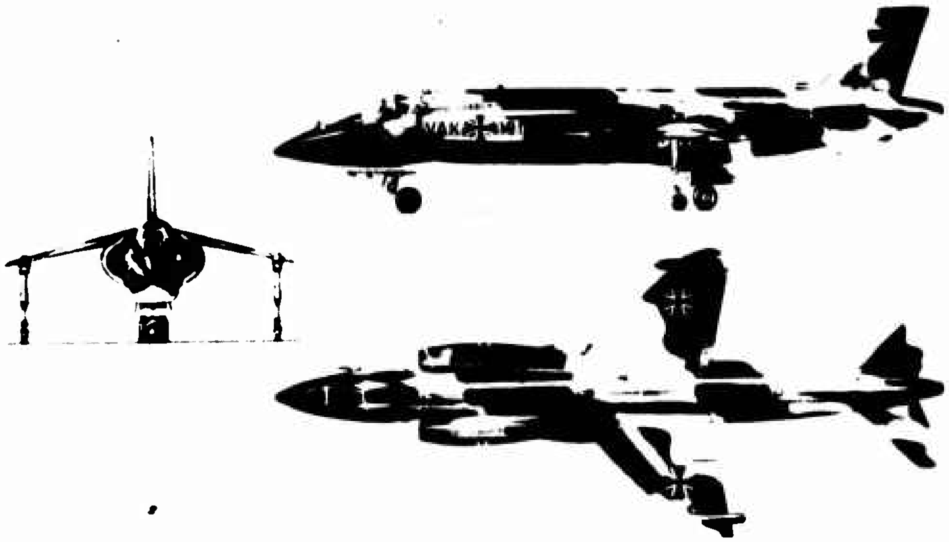

VAK 191 B
VTOL Close Air Support Fighter

VFW-FOKKER

Figure 1
Ex 1 - 74/1

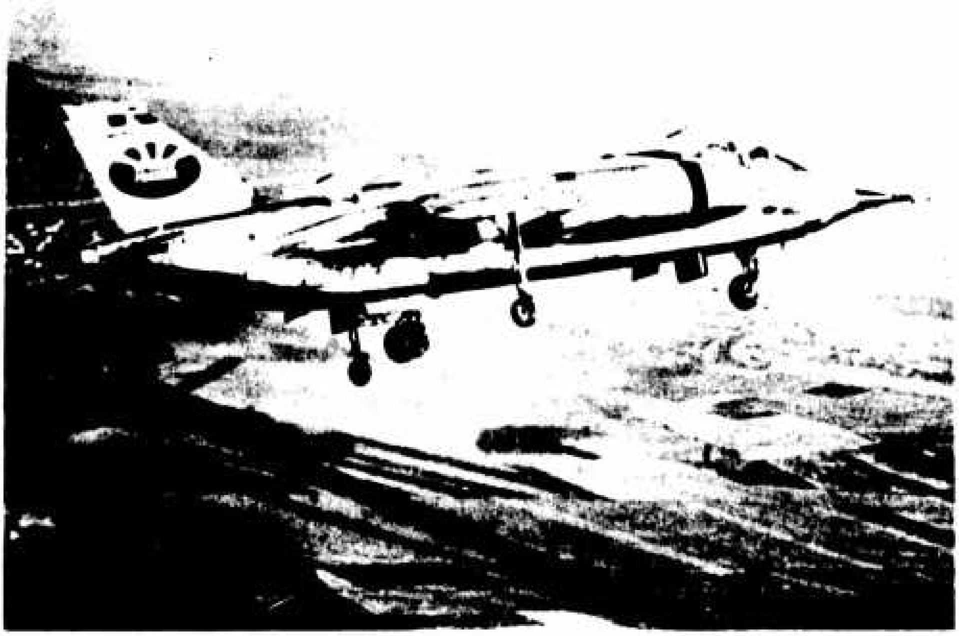

VAK 191 B in Transition Flight

VFW-FOKKER

Figure 2
Ex 1 - 74/2

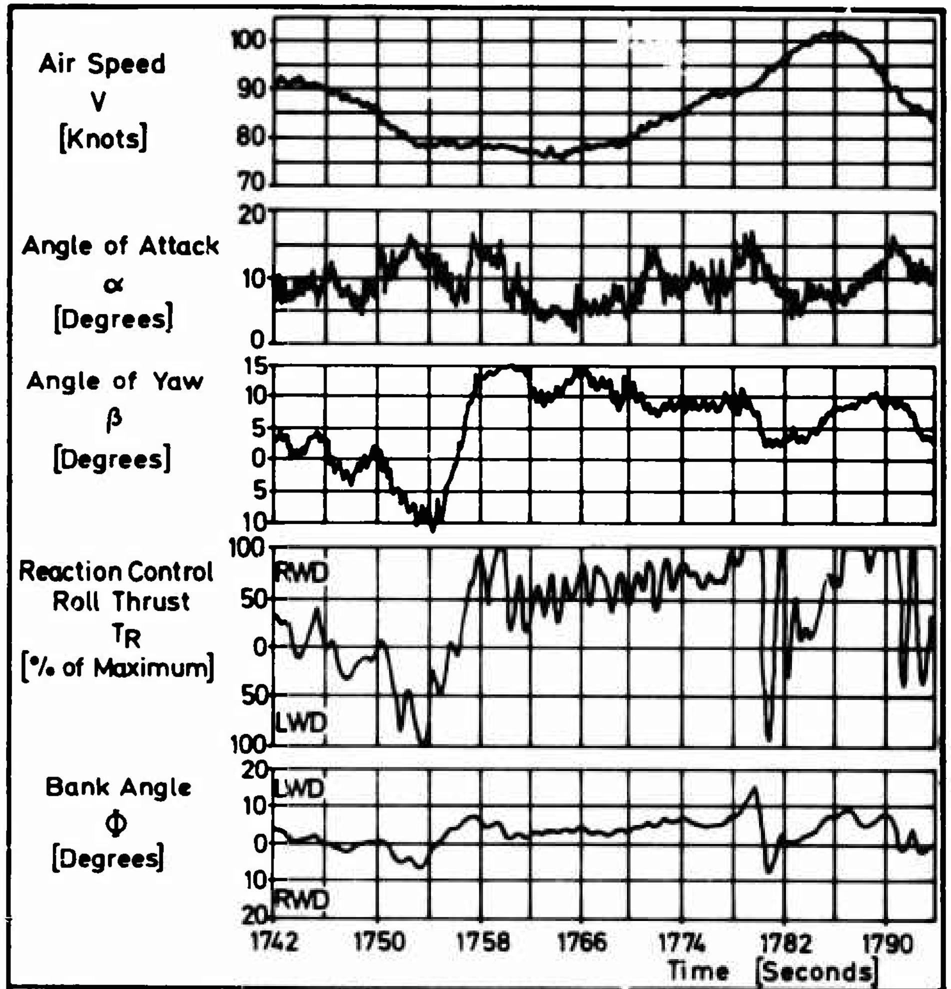

VAK 191 B Flight Test 2067

Quick Look Telemetry Record

VFW-FOKKER

Figure 3
Ex1 - 74/3

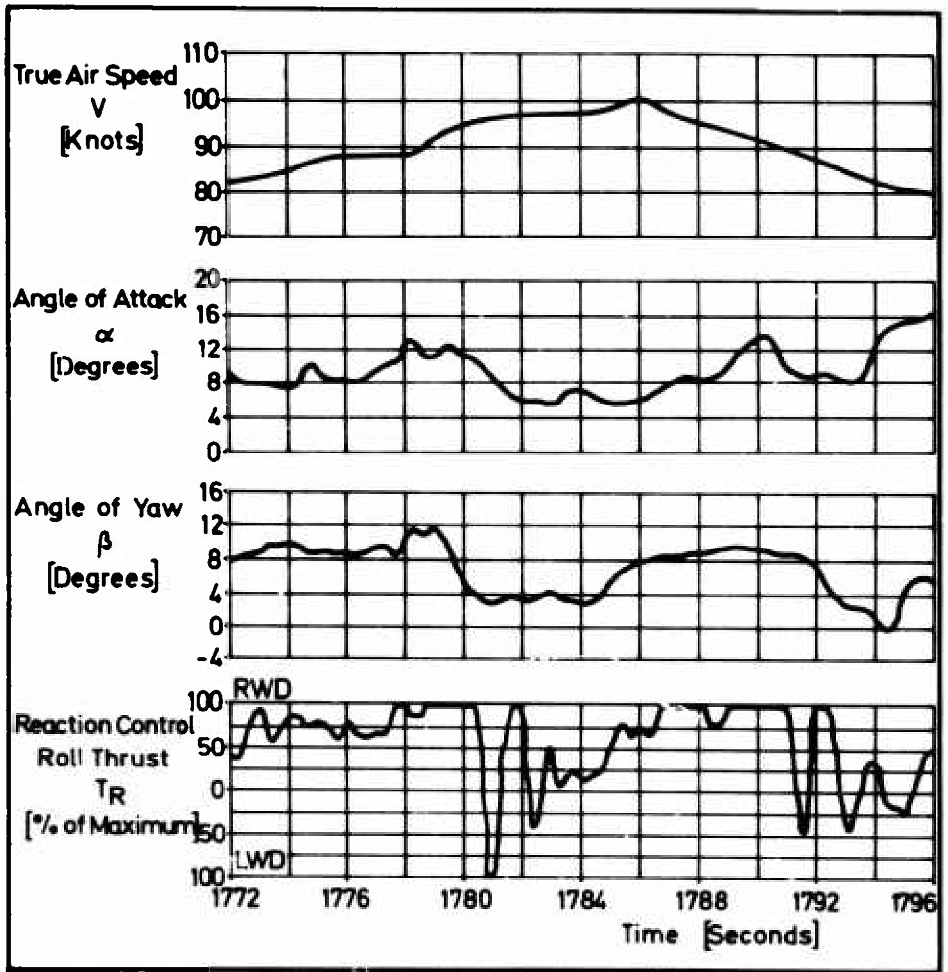

VAK 191B Flight Test 2067

Calibrated Flight Test Results

VFW-FOKKER

Figure 4
Ex1 - 74/4

100214

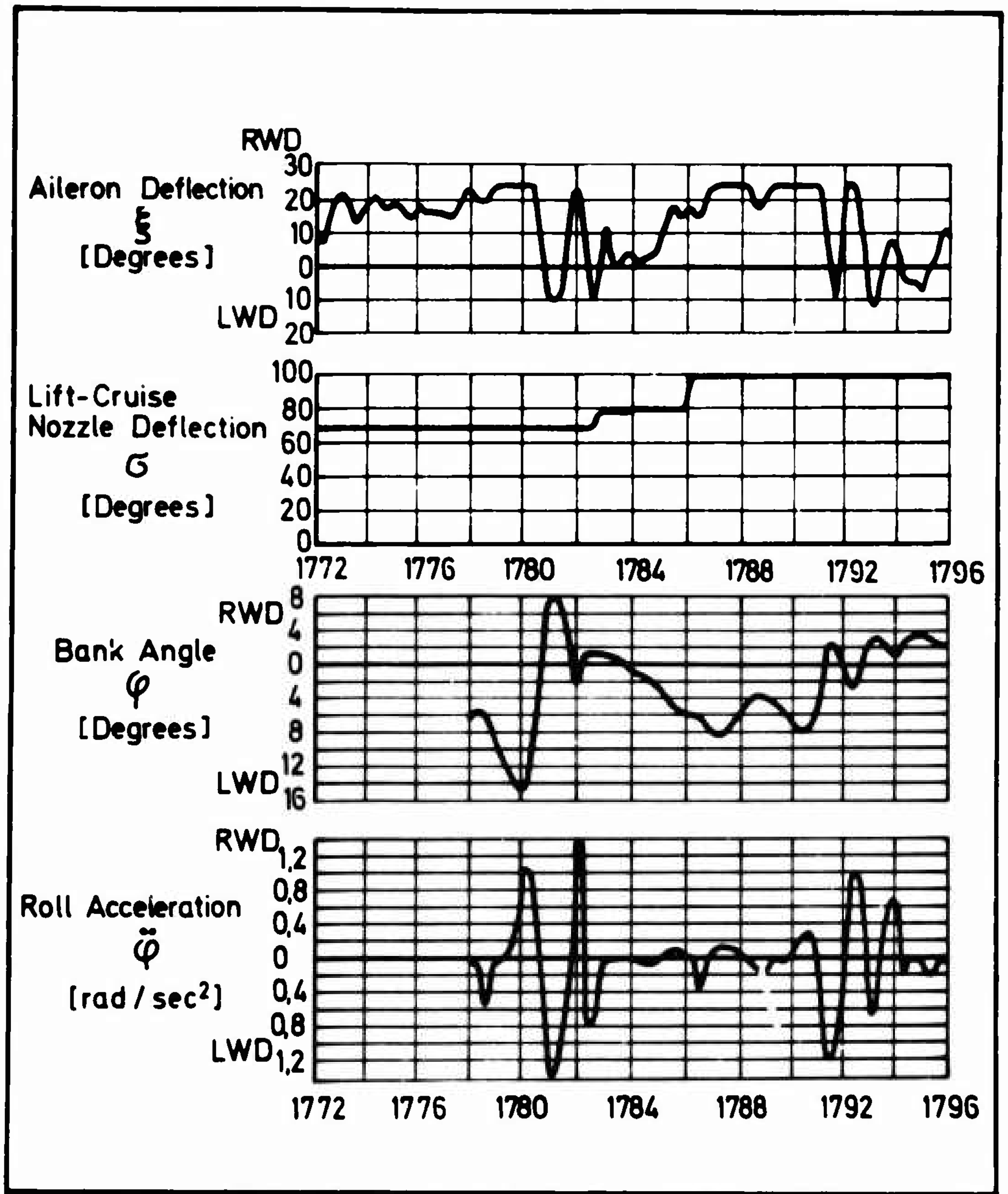

VAK 191 B Flight Test 2067
Calibrated Flight Test Results

VFW-FOKKER

Figure 5
Ex 1 - 74/5

Lift-Cruise Engine (RB 193)

Average Thrust Cold Nozzle	1825	kp
" " Hot Nozzle	2075	kp
" Mass Flow	86	kg/sec

Lift Engines (RB 162)

Average Thrust	1950	kp
Average Mass Flow	38	kg/sec

Maximum Available Reaction Control Roll Moment	480	mkp

VAK 191 B Flight Test 2067
Engine Conditions

VFW-FOKKER

Figure 6
Ex1-74/6

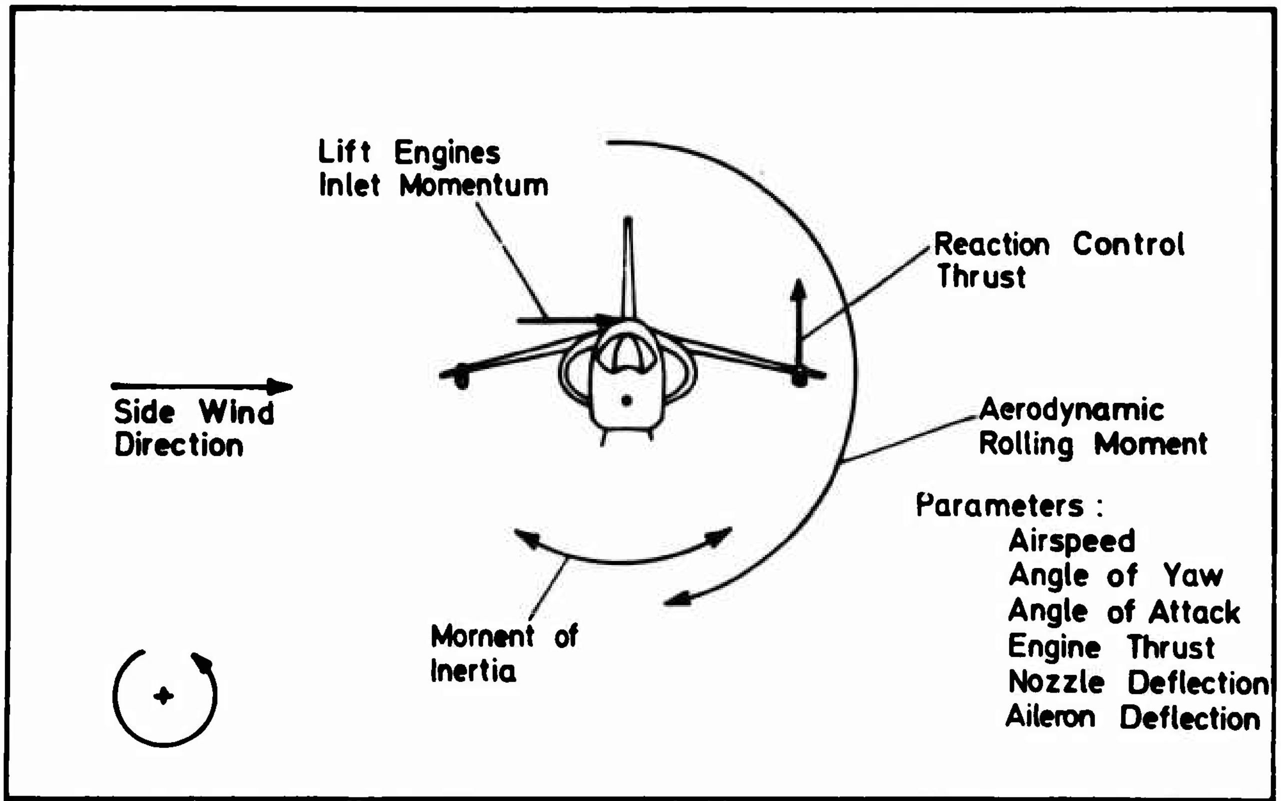

Lift Engines
Inlet Momentum
Reaction Control
Thrust
Side Wind
Direction
Aerodynamic
Rolling Moment
Parameters :
Airspeed
Angle of Yaw
Angle of Attack
Engine Thrust
Nozzle Deflection
Aileron Deflection
Moment of
Inertia
+

Rolling Forces due to Sideslip in Transition

VFW-FOKKER

Figure 7
Ex1-74/7

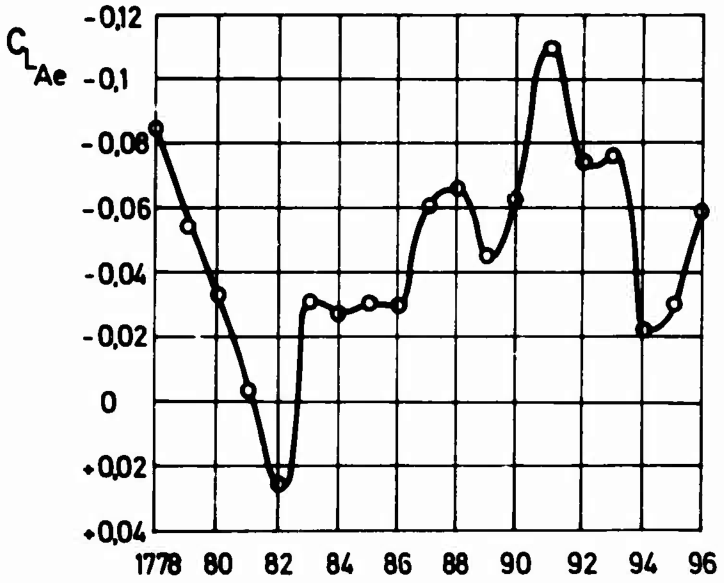

Aerodynamic Rolling Moment
Flight Test Evaluation

VFW-FOKKER

Figure 8
Ex1-74/8

Bleed Control Rolling Moment: ≙ 100
(Maximum available)

Time	Rolling Moment due to:			
	Bleed Control	Lift Egines Intake Momentum	Inertia	Aerodynamic Moment
1761	- 100	- 8	+ 110	- 2
1782	+ 100	- 10	- 120	+ 30
1783	+ 44	- 11	0	- 33
1786	+ 57	- 23	0	- 34
1788	+ 100	- 24	- 5	- 71

Breakup of Rolling Moment

VFW-FOKKER

Figure 9
Ex1 - 74/9

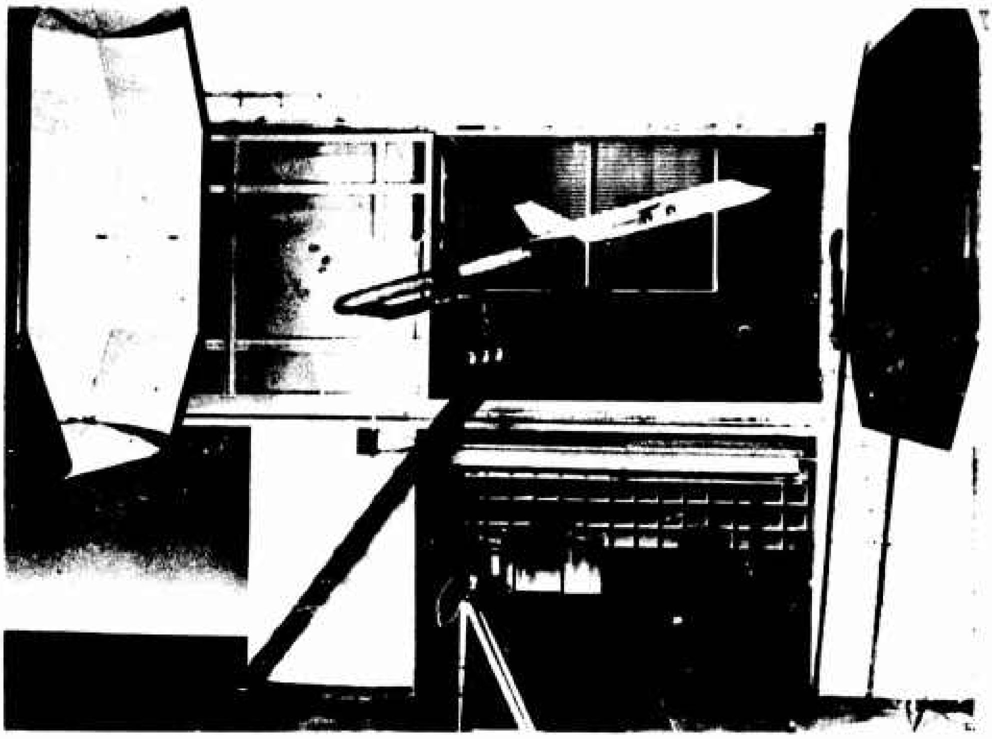

Jet Induced Downwash Wind Tunnel Model
DFVLR Low Speed Tunnel (2,3 x 3,3 m^2)

VFW-FOKKER

Figure 10
Ex1-74/10

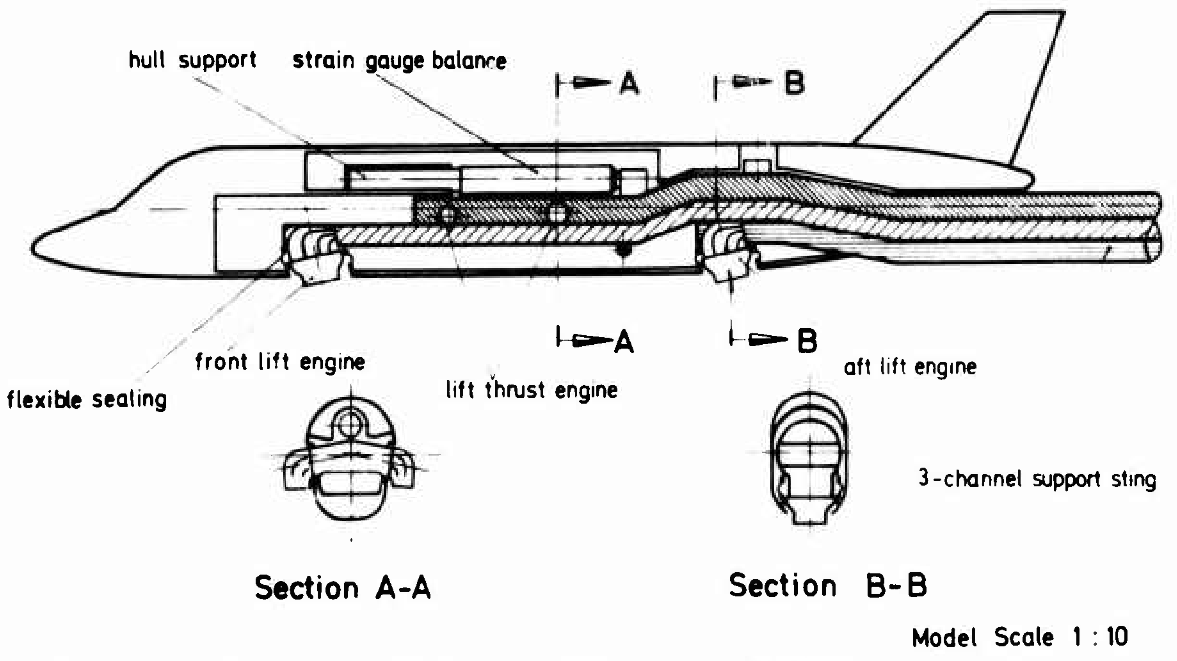
hull support
strain gauge balance
A
B
A
B
front lift engine
flexible sealing
lift thrust engine
aft lift engine
3-channel support sting
Section A-A
Section B-B
Model Scale 1 : 10

Wind Tunnel Model for Jet Induced Downwash Effects

VFW-FOKKER

Figure 11
Ex1-74/11

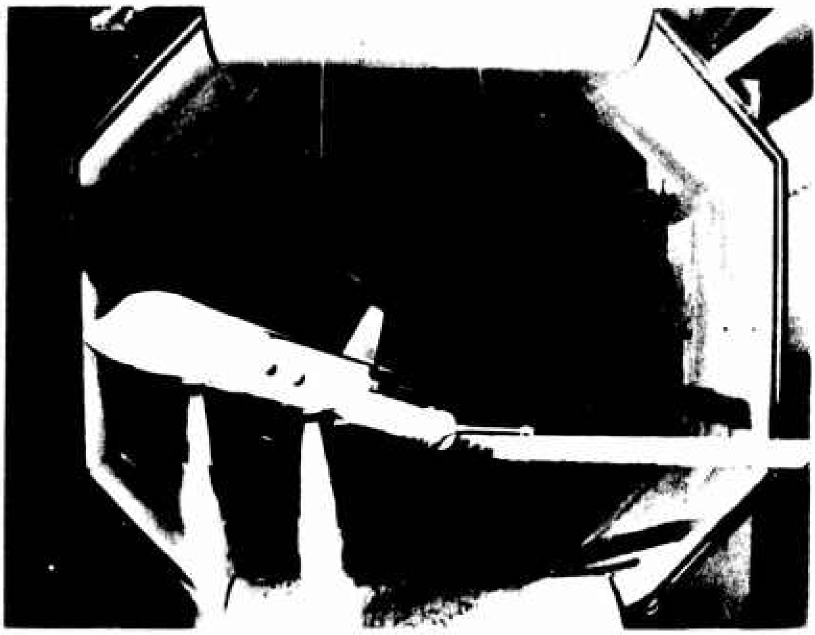

Model in the DFVLR - Porz - Wahn Tunnel
(2,3 x 3,3 m^2 Open Test Section)

VFW-FOKKER

Figure 12
Ex 1 - 74/12

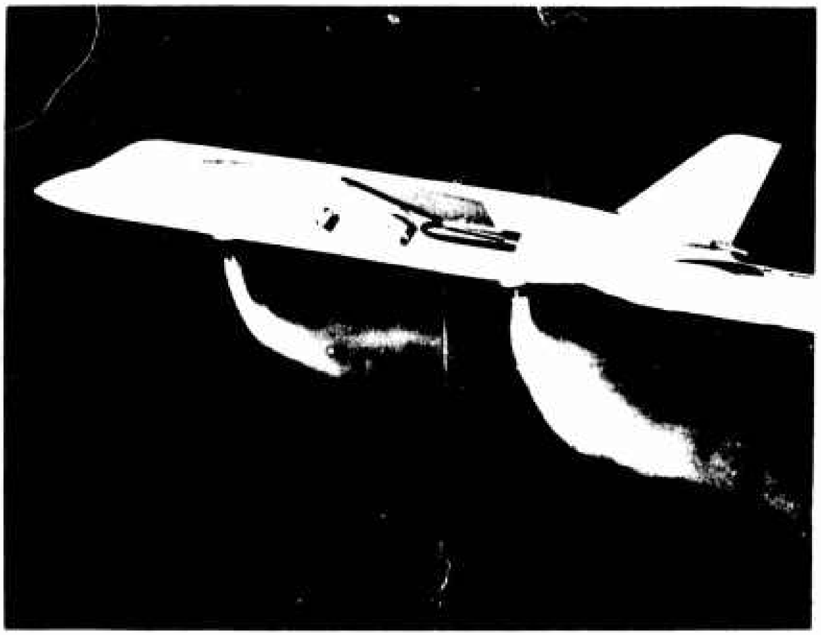

Flow Visualisation of Lift Engine Jets

VFW-FOKKER

Figure 13
Ex 1 - 74/13

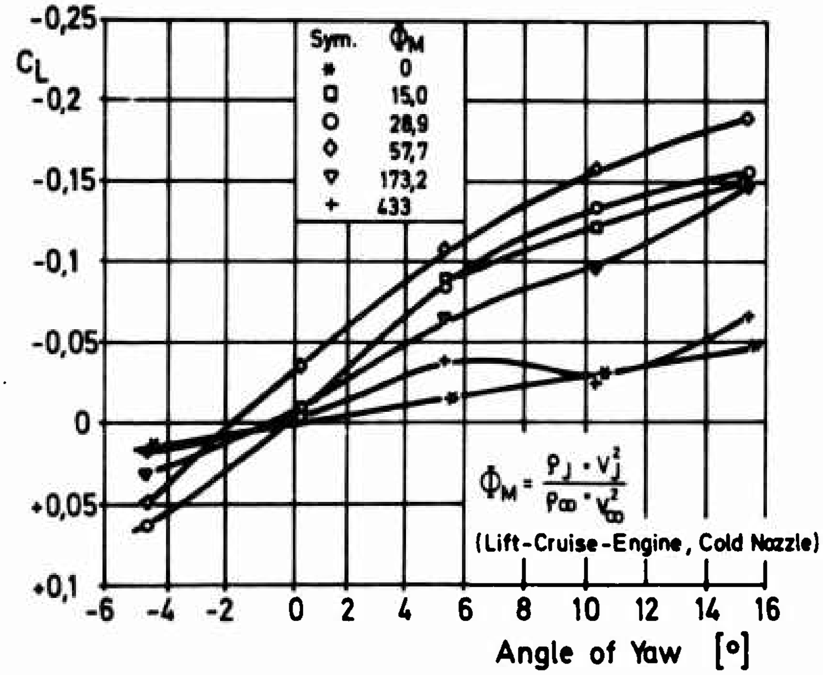

Typical Wind Tunnel Test Result
Rolling Moment (σ = 90°, α = 12°)

VFW-FOKKER

Figure 14
Ex1 - 74/14

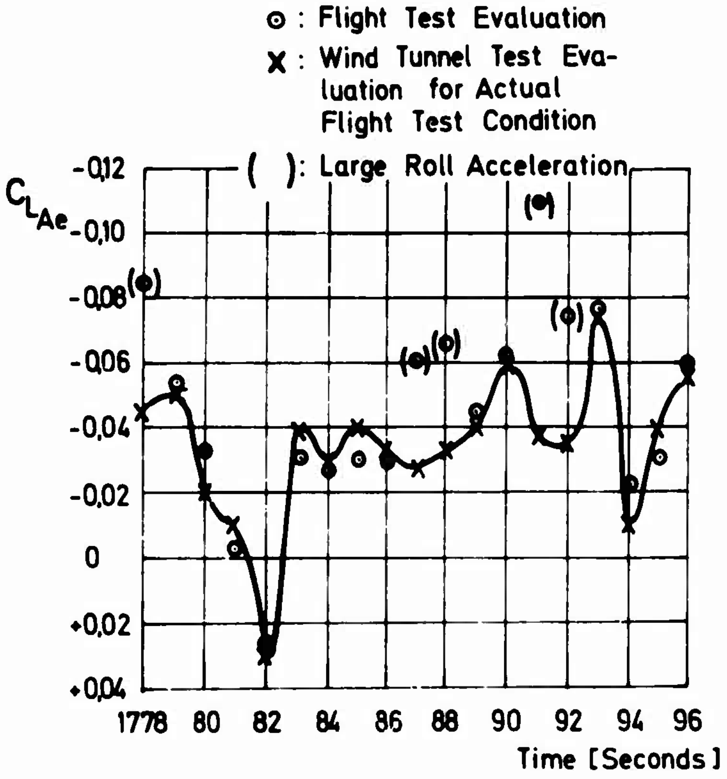

Comparison between Flight Test Results and Wind Tunnel Tests

VFW-FOKKER

Figure 15
Ex 1 - 74/15

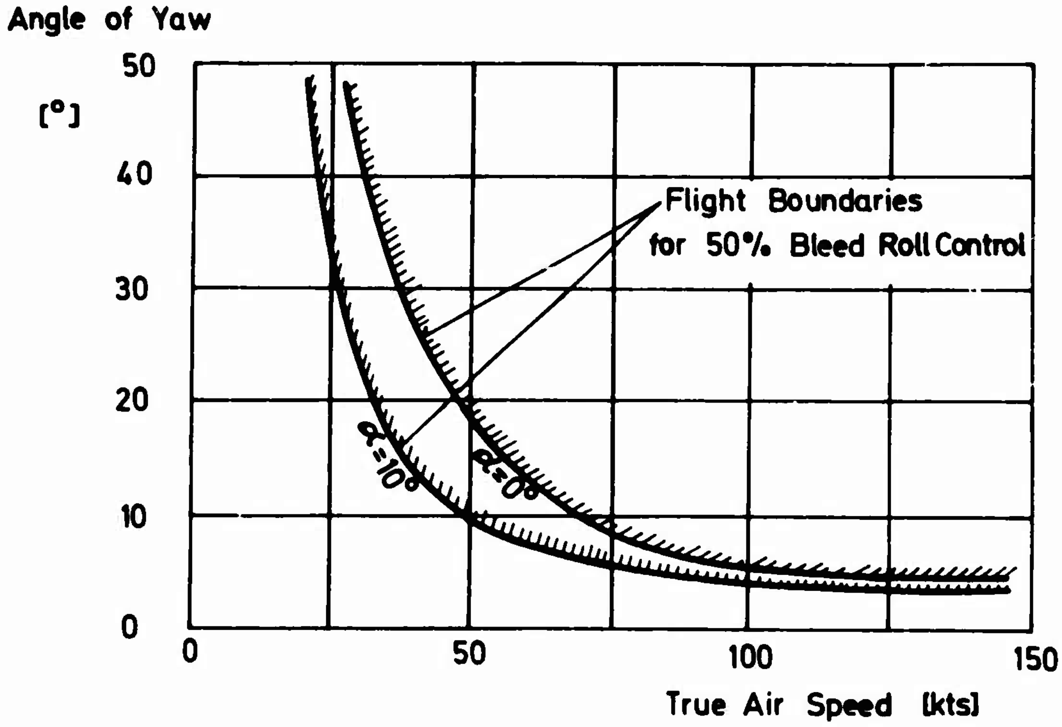

Flight Boundaries for Yaw Angle in Transition

VFW-FOKKER

Figure 16
Ex 1-74/16

A METHOD FOR THE CALCULATION OF THE FLOW FIELD INDUCED BY A JET EXHAUSTING PERPENDICULARLY INTO A CROSS FLOW

by

H. Smel

National Aerospace Laboratory NLR

Anthony Fokkerweg 2, Amsterdam 1017, Netherlands

SUMMARY

A description is given of a method for the calculation of the potential flow field arising from the interaction of a turbulent jet with an uniform free stream. The method is applied to the case of a jet perpendicularly into a cross flow.

The basis of the method is a semi-empirical model for the jet development. The model assumes the jet to entrain free stream mass together with its free stream momentum. The decay of axial velocity in the jet is used as empirical input. The geometry of the jet surface and jet entrainment follow from the model.

The velocity potential outside the jet is represented in terms of a distribution of constant strength source panels on the jet surface. A set of quadratic equations, describing mass and momentum transfer from the exterior flow to the jet, consistent with equations used for the jet model, yields the normal velocity distribution and the source strengths of the surface panels. Pressure distributions on a flat plate from which the jet exhausts are calculated.

LIST OF SYMBOLS

A	jet cross sectional area
$a(s)$	Fourier coefficient of u_n
AN, AX, AY, AZ	influence coefficients
AP	panel area
B_j	Fourier coefficient of u_n
$\bar{B}_1, \bar{B}_2$	discretized Fourier coefficients
C	vortex entrainment constant
$C(s)$	circumference of jet cross section
c	distance along cross-sectional circumference
c'	$2\pi c/C(s)$
C_D	drag coefficient
C_p	pressure coefficient
D	drag force
d_e	diameter of jet orifice
E	entrainment function
E_k	entrainment coefficient from ref.2
$\underline{e}_x, \underline{e}_y, \underline{e}_z$	unit vectors in x,y,z directions
$F_1 \quad F_2$	form factors related to velocity distribution
$q(s,c')$	linearizing factor of s on S
M	jet momentum flux
$\underline{n}$	unit vector normal to S
p	static pressure
Q	jet mass flux
δQ	mass flux through panel
ΔQ	mass flux through panel strip

R	U_j/U_∞
S	jet surface
s, ξ, η	curvilinear orth. co-ordinates, s along jet axis
U	s component if velocity in jet region
U_j	jet exhaust velocity
U_m	max. of U in cross section
U_∞	cross flow velocity
$\hat{U}$	$(U_m - U_\infty)/U_\infty$
$\underline{u}$	velocity vector outside S
$\tilde{\underline{u}}$	$\underline{u} - U_\infty \underline{e}_x$
$u_n, u_x, u_y\ u_z$	n,x,y and z components of $\underline{u}$
x, y, z	cartesian co-ordinates
α	$\ln F_{2c}/\ln F_{1c}$
θ	angle between s and z axes
ρ	distance between field point and point on S
σ	source density
Φ	velocity potential
φ	$\Phi - U_\infty x$
ψ	angle with neg. x direction on plate

Indices

R	refers to end of potential core
e	refers to $s = 0$
o	refers to $U_\infty = 0$

1. INTRODUCTION

Interaction effects between turbulent jets and free streams may contribute significantly to the pressure distributions on aircraft structures from which the jets are blown. The objective of the present paper is the construction of a method for the calculation of the flow fields arising from jet to free stream interaction.

The jet properties, i.e. the jet trajectory, growth of the cross sectional area and the entrainment, are calculated from a semi-empirical jet model, outlined in section 2. The flow outside the jet boundary is assumed to be potential flow, linked to the turbulent jet flow by the normal velocity distribution on the jet boundary. The velocity potential is expressed in terms of a distribution of constant strength source panels on the jet surface. A set of quadratic equations for the normal velocity distribution is derived, describing mass and momentum transfer from the exterior flow to the jet. The equations are consistent with those used in the jet model. The normal velocity distribution is written as a set of truncated Fourier series, discretized with respect to the surface panels. The equations are solved for the Fourier coefficients of the normal velocity distribution, and the source strengths of the surface panels follow from a system of linear algebraic expressions.

The method will be derived for the case of a round turbulent jet, exhausting perpendicularly from a plate into a uniform cross flow. This particular configuration was chosen for the reason that it has been used in nearly all of the published experimental work on the subject. The measured jet development, as well as measured pressure distributions on the flat plate from which the jet exhausts, have been published in numerous papers and may be compared with theoretical results. The flow field resembles that occuring in the transition flight of V/STOL configurations with lift jets, blowing from the wings.

2. THE JET MODEL

2.1. Physical description of a jet in a cross flow

Consider a jet exhausting with uniform velocity U_j from a circular orifice with diameter d_e into a uniform cross flow of velocity U_∞, perpendicular to U_j. The jet orifice is coplanar with an infinitely large plate in the x,y plane. The co-ordinate systems and the geometry of the configuration are defined in figure 1.

Immediately downstream of the orifice, a turbulent mixing region develops at the jet circumference. This region spreads inward and outward, and at some distance from the orifice, the entire jet cross section becomes part of the turbulent mixing region. At distances from the orifice smaller than where turbulent eddies of opposite sides meet, a part of the cross section has not yet experienced turbulent mixing. The more or less cone shaped region composed by these parts is usually called the potential core region. The velocity here equals the jet efflux velocity U_j, if the jet to cross flow velocity ratio $R = U_j/U_\infty$ is not too small. Let length along the jet axis be measured by s, and the length of the potential core region be denoted by s_R. The jet flow region with $s > s_R$ will be called the fully developed region. The maximum velocity U_m in the cross sections in this region decreases with increasing s.

The jet, exhausting perpendicularly to the cross flow, is deflected in cross flow direction. This means that the cross flow exerts a force on the jet, or in other words, that momentum is transferred from the cross flow to the jet. The cross flow also deforms the cross sectional shape of the jet into a kidney like shape, as indicated in figure 1. In the downstream ends of this shape, a contra rotating vortex pair develops, visualized with smoke by Hacket and Miller (ref.1). The vortex pair enhances the entrainment, by turning back a part of the cross flow passing by the sides of the jet, to be entrained at the downstream side of the jet.

Keffer and Baines (ref.2) observed that the deformation of the cross section is completed at the end of the potential core, the shape being preserved in the fully developed region of the jet flow. They introduced a natural system of co-ordinate axes in the cross section, defined as follows. The ξ-axis is the locus of points of maximum velocity along lines of constant y in the cross sectional plane. The η axis is also defined in the cross sectional plane, such that s, ξ and η form a curvilinear orthogonal system of axes.

Let U be the s-component of velocity in the jet flow region, and $U_m(s)$ its maximum in a cross section at s. Measurements of Keffer and Baines (ref.2) show that the value of $(U-U_\infty)/(U_m-U_\infty)$ on the ξ axis is a function of $\xi/\xi_{1/2}$ only, independent of $s (\geqslant s_R)$ and R. $\xi_{1/2}$ is the value of ξ where $(U-U_\infty)/(U_m-U_\infty)$ equals 1/2, and the differences $U-U_\infty$ are algebraic differences. Figure 2 shows the measured velocity distribution, taken from ref.2. The distribution co-incides with the velocity distribution in a jet exhausting into a stagnant medium.

2.2. Main assumptions

The measured velocity similarity along the ξ-axis

$$\frac{U-U_\infty}{U_m-U_\infty} = f\left(\frac{\xi}{\xi_{1/2}}\right)$$

is generalized to

$$\left.\begin{aligned} &\frac{U-U_\infty}{U_m-U_\infty} = f\left(\frac{\xi}{\xi_{1/2}}, \frac{\eta}{\eta_{1/2}}\right) \\ &\text{for all } R,\ s \geqslant s_R \end{aligned}\right\} \tag{1}$$

i.e. it is assumed that velocity similarity also exist with respect to the η-axis. If the cross sectional shape is preserved for $s > s_R$, (1) can be transformed into

$$\frac{U-U_\infty}{U_m-U_\infty} = f_1\left(\frac{\xi}{\sqrt{A}}, \frac{\eta}{\sqrt{A}}\right) \tag{2}$$

if A is the cross-sectional area. The function f_1 may still depend on R, since the cross sectional shape depends on R. In fact, the shape remains circular for $R = \infty$

The mass flux Q and the momentum flux M through the jet cross sections can be expressed in terms of A and $U_m - U_\infty$ as follows

$$Q = \iint_A U\,dA = A\left[(U_m-U_\infty)F_1 + U_\infty\right] \tag{3}$$

$$M = \iint_A U^2\,dA = A\left[(U_m-U_\infty)^2 F_2 + 2(U_m-U_\infty)F_1 + U_\infty\right] \tag{4}$$

with

$$F_1 = \iint_A f_1\left(\frac{\xi}{\sqrt{A}}, \frac{\eta}{\sqrt{A}}\right) d\frac{\xi}{\sqrt{A}}\, d\frac{\eta}{\sqrt{A}} \tag{5}$$

$$F_2 = \iint_A f_1^2\left(\frac{\xi}{\sqrt{A}}, \frac{\eta}{\sqrt{A}}\right) d\frac{\xi}{\sqrt{A}}\, d\frac{\eta}{\sqrt{A}} \tag{6}$$

The values of the form factors F_1 and F_2 are independent of s for $s \geqslant s_R$. It will now be assumed that those values do not depend on R either, and consequently may be computed from free jet data.

In the potential core region, the expressions (3) and (4) may still be used, but F_1 and F_2 must change with s, from their initial value of 1 (uniform outflow) to their respective values at the end of the potential core. Let the constant values of F_1 and F_2 in the fully developed region be denoted by F_{1c} and F_{2c}. In the potential core a relation $F_2 = f(F_1)$ must exist, satisfying $F_2 = 1$ for $F_1 = 1$ and $F_2 = F_{2c}$ for $F_1 = F_{1c}$. From (2), (5) and (6) it follows that also must be satisfied $F_1 \geqslant F_2 \geqslant F_1^2$.
We will prescribe for $s \leqslant s_R$

$$F_2 = F_1^{\alpha} \quad , \quad \alpha = \ln F_{2c} / \ln F_{1c} \tag{7}$$

which satisfies all conditions if $1 < \alpha < 2$. In ref.3 the numerical values of F_{1c} and F_{2c} were calculated, using Tollmien's (ref.4) velocity profile, to be :

$$F_{1c} = 0.196 \, , \qquad F_{2c} = 0.093$$

so that

$$\alpha = 1.46$$

Assumptions are also necessary with regard to the mechanism which deflects the jet axis. Let the jet axis be defined to be everywhere parallel to the direction of the jet momentum flux. The deflection of this flux is assumed to be due to both entrainment of free stream mass with its associated free stream momentum (in x-direction) and the action of a drag force perpendicular to the jet axis. This is the most general formulation of the deflection mechanisms used by other authors. It is argued in ref.3 that the dragforce is associated with a wake region behind the jet, resulting from flow separation. Separation will, however, be much less severe than in the case of flow past a solid obstacle, due to the sink action of entrainment and the action of the contra-rotating vortex pair.

In the following chapter, equations will be derived for the jet properties using the general formulation for the deflection mechanism. Under the assumption that the influence of the drag force is restricted to a region of the jet with length of the order of the potential core length (where separation may be significant), it will be shown that the drag force term in the equations may be neglected for larger values of R.

2.3. The jet equations

The basic relations governing the jet flow are the equations of conservation of mass and momentum. Since the complete equations describing turbulent flow cannot be solved in detail, use will be made of the integrated form of the equations, the integrals extending over the jet cross sections. The equation of conservation of mass express the fact that the jet surface is not a streamtube. In fact, this equation may be regarded as a definition of entrainment, stating that the rate of increase in mass flux equals the local entrainment. Using (3) one obtains

$$\frac{dQ}{ds} = U_\infty \frac{d}{ds}\left[A(F_1 \tilde{U} + 1) \right] \tag{8}$$

if

$$\tilde{U} = \frac{U_m - U_\infty}{U_\infty} \tag{9}$$

The integrated momentum flux changes due to momentum entrainment and the action of the drag force D. With the jet angle θ as defined in figure 1, we have

$$\frac{d}{ds}(M \sin\theta) = U_\infty \frac{dQ}{ds} + D \cos\theta \tag{10}$$

$$\frac{d}{ds}(M \cos\theta) = - D \sin\theta \tag{11}$$

D is expressed in the conventional way in terms of a drag coefficient C_D and the cross flow component $U_\infty \cos\theta$ normal to the jet. $\sqrt{A}$ is taken as a measure for the width of the jet

$$D = C_D \tfrac{1}{2} U_\infty^2 \cos^2\theta \sqrt{A} \tag{12}$$

For M in (10) and (11) the expression from (4) can be substituted. The equations can be written in non-dimensional form. A and Q are divided by their respective initial values A_e and $Q_e = U_j A_e$, s is divided by d_e. Relation (8) is used both in its differential form as in integrated form. One arrives at the following set of equations

$$\frac{A}{A_e} \cos\theta \left(F_2 \tilde{U}^2 + 2F_1 \tilde{U} + 1 \right) = R^2 - \int_0^{s/d_e} \frac{C_D}{\sqrt{\pi}} \sqrt{\frac{A}{A_e}} \cos^2\theta \sin\theta \, d(s/d_e) \tag{13}$$

$$\begin{aligned} \frac{A}{A_e} \sin\theta \left(F_2 \tilde{U}^2 + 2F_1 \tilde{U} + 1 \right) = {} & \frac{A}{A_e} (F_1 \tilde{U} + 1) - R \; + \\ & + \int_0^{s/d_e} \frac{C_D}{\sqrt{\pi}} \sqrt{\frac{A}{A_e}} \cos^3\theta \, d(s/d_e) \end{aligned} \tag{14}$$

$$E = \frac{1}{Q_e} \frac{dQ}{d(s/d_e)} = \frac{1}{R} \frac{d}{d(s/d_e)} \left[\frac{A}{A_e} (F_1 \tilde{U} + 1) \right] \tag{15}$$

$$\frac{Q}{Q_e} = \frac{1}{R}\left(F_1\,\mathcal{U} + 1\right) \qquad (16)$$

The relative magnitude of the C_D terms will now be analysed for the potential core region. For equation (13) one should compare the change in z-momentum relative to its initial value, or

$$\frac{\Delta M_z}{(M_z)_e} = \left[\int_0^{s_R/d_e} \frac{C_D}{\sqrt{\pi}}\sqrt{\frac{A}{A_e}}\,\cos^2\theta\,\sin\theta\,d(s/d_e)\right]\Big/R^2$$

In ref.3 an asymptotic solution for large R is constructed for the potential flow region. It is shown that $\sin\theta_R = O(1/R)$, $s_R/d_e = O(1)$, $A_R/A_e = O(1)$ and $Q_R/Q_e = O(1)$

$$\Delta M_z/(M_z)_e = O(1/R^3) \qquad (17)$$

For equation (14) the magnitude of the C_D term has to be compared to the magnitude of the entrainment term. One obtains, using (16)

$$\frac{C_D\ \text{term}}{\text{entr. term}} = \left[\int_0^{s_R/d_e} \frac{C_D}{\sqrt{\pi}}\cos^3\theta\sqrt{\frac{A}{A_e}}\,d(s/d_e)\right]\Big/R\left(\frac{Q_R}{Q_e}-1\right) = O(1/R) \qquad (18)$$

The more detailed asymptotic analysis in ref.3 shows that the C_D term has its most important influence on θ_R , where C_D appears in the $O(1/R^2)$ term. For A_R/A_e , Q_R/Q_e and s_R/d_e , C_D appears first in the $O(1/R^3)$ term. Beyond the potential core it was assumed that C_D loses it significance. For those reasons C_D has been neglected in this study. Comparison of calculated and measured jet properties will show that this yields good results for R larger than about 6. With $C_D = 0$, equations (13) and (14) reduce to algebraic equations.

2.4. Empirical input

Counting the number of unknowns and the number of available equations reveals that both in the potential core region as in the fully developed region, the set of equations is not complete. In the potential core region, F_1 , F_2 , A/A_e, Q/Q_e and θ are unknown functions of s ,while $\mathcal{U} = R-1$ is known. Equations for this region are (7), (13), (14) and (16). In the fully developed region A/A_e , Q/Q_e , θ and $\mathcal{U}$ are to be determined as functions of s , from equations (13), (14) and (16) with $F_1 = F_{1_c}$ and $F_2 = F_{2_c}$. Only at $s = s_R$, where $F_1 = F_{1_c}$, $F_2 = F_{2_c}$ and $\mathcal{U} = R-1$, equations (13), (14) and (16) form a closed set of three equations for A_R/A_e , Q_R/Q_e and θ_R. However, the value of s_R/d_e is another unknown.

The missing equation is basically an expression for the entrainment E as a function of s/d_e . If $E(s/d_e)$ is known for all s/d_e the equations can be solved in both regions, using (15) as an extra equation. The length of the potential core can also be calculated, by equating $Q(s_R/d_e)/Q_e$ from integration of (15) with Q_R/Q_e from (13), (14) and (16).

For the potential core region an expression for $E(s/d_e)$ will be derived using physical arguments. It is assumed that the entrainment in this region can be written as the entrainment E_o in the potential core region of a free jet ($R = \infty$) plus a contribution of the contra-rotating vortex pair. This last contribution will be shown to behave like 1/R . Mathematically, the resulting formula can be interpreted as the first two terms of an expansion of E for large R. The $R = \infty$ contribution is assumed to be a function of integer powers of the s/d_e only, and to satisfy the following requirements. i) E_o increases with increasing s/d_e , ii) $E_o(0) = 0.128$ (see ref.5), iii) $E_o(s_R/d_e) = 0.32$ (see ref.6) and iv) $\int_0^{s_R/d_e} E_o(s/d_e)\,d(s/d_e) = \frac{F_{1_c}}{F_{2_c}} - 1$ since for $R \rightarrow \infty$ $Q_R/Q_e = F_{1_c}/F_{2_c}$ follows from (13), (14) and (16). In ref.3 it is shown that $E_o(s/d_e)$ is uniquely determined by these requirements if only two powers of s/d_e are used. The resulting expression reads :

$$E_o(s/d_e) = 0.128 + 10^{-3}\left[1.176\,(s/d_e)^2 + 0.616\,(s/d_e)^3\right] \qquad (19)$$

The vortex contribution to the entrainment is assumed to be proportional to the vorticity in s-direction produced by the cross flow interaction with the jet. The vorticity produced per unit of length equals the component in the cross sectional plane of the velocity difference between jet and cross flow. Let $(dQ/ds)_v$ be the vorticity contribution to the entrainment, then

$$\left(\frac{dQ}{ds}\right)_v = \text{constant}\,.\,d_e\int_0^{s/d_e} U_\infty\cos\theta$$

or

$$\left(\frac{1}{Q_e}\frac{dQ}{d(s/d_e)}\right)_v = \frac{C}{R}\,\frac{z}{d_e} \approx \frac{C}{R}\,\frac{s}{d_e} \qquad (20)$$

since $\cos\theta \approx 1$ in the potential core region. The entrainment formula for the potential core region then reads

$$E(s/d_e) = \frac{1}{Q_e}\frac{dQ}{d(s/d_e)} = 0.128 + 10^{-3}\left[1.176(s/d_e)^2 + 0.616(s/d_e)^3\right] + \frac{C}{R}\,\frac{s}{d_e} \qquad (21)$$

Taking the constant of proportionality C in (21) equal to 1.273, calculated values of s_R/d_e match well with measurements, as is demonstrated in figure 3.

For the fully developed region the foregoing arguments do not apply. The functional behaviour of the entrainment cannot be described with any degree of certainty in this region. Many different entrainment functions have been postulated by different authors, but none have been directly compared with measured mass fluxes. Usually, some parameters in the entrainment functions are determined by matching calculated and measured jet trajectories. This is basically not correct, due to a different definition of calculated and measured trajectories.

If entrainment is to be used in the calculation of the induced flow field, as is the case in this study, it seems preferable to use different empirical input. The (measured) decay of axial velocity along the jet axis will be used here. There are sufficient velocity decay data available in the literature to make this feasible. For R values not covered by measurements, decay curves can be constructed by interpolation. For numerical reasons, an analytical fit to the measurements is used of the form

$$\frac{U_m - U_\infty}{U_j - U_\infty} = \left(\frac{s_R}{s}\right)^{f(s/d_e)} , \quad s \geqslant s_R \tag{22}$$

2.5. Solution of the jet equations

Equations (7), (13), (14), (16) and (22) are to be solved for the potential core region. Integration of (22) yields Q/Q_e :

$$\left.\begin{aligned} &\frac{Q(s/d_e)}{Q_e} = 0.128\,\frac{s}{d_e} + 10^{-3}\left[\frac{1.176}{3}\left(\frac{s}{d_e}\right)^3 + \frac{0.616}{4}\left(\frac{s}{d_e}\right)^4\right] + \frac{C}{2R}\left(\frac{s}{d_e}\right)^2 \\ &\text{for} \quad s/d_e \leqslant s_R/d_e \end{aligned}\right\} \tag{23}$$

The potential core length can be calculated next. (13), (14) (with $C_D = 0$) and (16) are solved at $s = s_R$ ($U_m = U_j$, $F_1 = F_{1_c}$, $F_2 = F_{2_c}$) for A_R/A_e , θ_R and Q_R/Q_e yielding for Q_R/Q_e

$$\frac{Q_R}{Q_e} = \frac{P_R\left(R\sqrt{R^2+1-P_R^2} - P_R\right)}{R^2 - P_R^2} , \text{ if } P_R = \frac{R\left[(R-1)F_{1_c} + 1\right]}{(R-1)^2 F_{2_c} + 2(R-1)F_{1_c} + 1} \tag{24}$$

Combination of (23) for $s = s_R$ and (24) gives a relation for s_R , which is solved numerically. For $s \leqslant s_R$, the trajectory angle θ follows after dividing (14) through by (13) :

$$\theta = \arctan\left[\frac{1}{R}\left(\frac{Q}{Q_e} - 1\right)\right] \tag{25}$$

while the jet spread as measured by A/A_e follows numerically from

$$\frac{A}{A_e}\left[(R-1)^{2-\alpha}\left(\frac{R}{A/A_e}\,\frac{Q}{Q_e} - 1\right)^{\alpha} - 1\right] = R\left[\sqrt{R^2 + \left(\frac{Q}{Q_e} - 1\right)^2} - 2\,\frac{Q}{Q_e}\right] \tag{26}$$

, which results from combination of (7), (13), (16) and (25).

For the fully developed region, equations (13), (14), (16) and (22) have to be solved, with $C_D = 0$, $F_1 = F_{1_c}$, $F_2 = F_{2_c}$. One obtains

$$\frac{Q}{Q_e} = \frac{P\left(R\sqrt{R^2+1-P^2} - P\right)}{R^2 - P^2} \qquad \text{if} \quad P = \frac{R\left(\hat{U}F_{1_c} + 1\right)}{\hat{U}^2 F_{2_c} + 2\hat{U}F_{1_c} + 1} \tag{27}$$

$$\frac{A}{A_e} = \frac{R\,Q/Q_e}{\hat{U}F_{1_c} + 1} \tag{28}$$

$$\theta = \arctan\left[\frac{1}{R}\left(\frac{Q}{Q_e} - 1\right)\right] \tag{29}$$

while $$\tilde{\mathcal{U}} = (R-1)\,\frac{\mathcal{U}_m-\mathcal{U}_\infty}{\mathcal{U}_j-\mathcal{U}_\infty} = (R-1)\left(\frac{s_R}{s}\right)^{f(s/d_e)}$$

is known from (22). The entrainment follows from its definition (15) after differentiation of (27)

$$\left.\begin{aligned} E &= \frac{1}{Q_e}\frac{dQ}{d(s/d_e)} = \frac{R^2\left[P-R\sqrt{R^2+1-P^2}\right]^2}{\sqrt{R^2+1-P^2}\,(R^2-P^2)^2}\,\frac{dP}{d(s/d_e)} \\ \frac{dP}{d(s/d_e)} &= -\,\frac{R\left(F_{1_c}F_{2_c}\tilde{\mathcal{U}}^2+2F_{2_c}\tilde{\mathcal{U}}+F_{1_c}\right)}{F_{2_c}\tilde{\mathcal{U}}^2+2F_{1_c}\tilde{\mathcal{U}}+1}\,\frac{d\tilde{\mathcal{U}}}{d(s/d_e)} \end{aligned}\right\}\qquad(30)$$

The jet trajectory finally follows by numerical integration (Simpson's rule)

of $$\frac{d(z/d_e)}{d(s/d_e)} = \cos\theta\ ,\qquad \frac{d(x/d_e)}{d(s/d_e)} = \sin\theta \qquad(31)$$

with $\theta(s/d_e)$ from (25) and (23) for $s \leq s_R$, from (29), (27) and (22) for $s > s_R$.

2.6. Comparison with measurements

In figure 3, calculated values of s_R/d_e are compared with measured values, for a wide range of R values. Agreement is satisfactory. Figure 5 compares calculated and measured jet trajectories for some values of R. These trajectories cannot be compared straightforwardly, since they are given by different definitions. The calculated trajectory is defined as the locus of momentum centroids in the subsequent cross sections, while the measured trajectory is the locus of points of maximum velocity in the cross sections. Those points do not coincide due to the deformation of the cross section. If the shape of the cross sections and the velocity distribution are known, the distance between the two trajectories can be calculated. To estimate this distance, the cross sectional shape given in figure 4 has been used. It is an ellipse in an elliptical coordinate system, resembling the shape of the high speed region of the jet, measured by Endo and Nakamura (ref.7). An axes ratio of 3.5 has been chosen, such that the ratio of circumferential length and the square root of the cross sectional area equals 4.6, a value measured by Platten and Keffer (ref.8). A Tollmien velocity distribution has been assumed for both the ξ and the η axis. The resulting expression for the distance between the two axes is (see ref.3)

$$\frac{X_c}{d_e} = \frac{\sqrt{\pi}}{2}\left[\frac{\tilde{\mathcal{U}}^2+8.3\,\tilde{\mathcal{U}}+52}{25\,\tilde{\mathcal{U}}^2+110\,\tilde{\mathcal{U}}+310}\right] \qquad(32)$$

This formula is used to correct the calculated trajectory; the corrected trajectory is also given in figure 5. Although (32) is only a crude estimate, the corrected trajectories compare very well with the measured ones,especially for higher values of R.

In figure 6 calculated and measured jet spread are compared. The measured values are taken from refs.2 and 7, where $\xi_{1/2}/d_e$ values are given. Calculated values of $\sqrt{A/A_e}$ for $s \geq s_R$ should be proportional to $\xi_{1/2}/d_e$; the measured values have been multiplied by a constant to match $\sqrt{A/A_e}$ at s_R . Agreement is satisfactory.

Keffer and Baines (ref.2) give measured values of an entrainment coefficient, which will be denoted here by E_K , defined as

$$E_K = \frac{dQ}{ds}\,\frac{1}{Q/A-\mathcal{U}_\infty}\,\frac{1}{Sh}\,\frac{1}{\sqrt{A}}$$

where Sh equals the ratio of the circumference of the cross section and $\sqrt{A}$. To determine Q and A from measurements, the velocity profiles were cut off in ref.2 where $(\mathcal{U}-\mathcal{U}_\infty)/(\mathcal{U}_m-\mathcal{U}_\infty) = 0.1$. Using $Sh = 4.6$, as reported by Platten and Keffer (ref.8) , $E(s/d_e)$ can be expressed in terms of E_K by

$$E(s/d_e) = \frac{1}{Q_e}\frac{dQ}{d(s/d_e)} = \frac{9.2}{\sqrt{\pi}}\sqrt{\frac{A}{A_e}}\left[\frac{Q/Q_e}{A/A_e}-\frac{1}{R}\right]E_K$$

In figure 7, calculated values of $E(s/d_e)$ for R = 6 and 8 are compared to values following from the above formula with E_K from ref.2 for R = 6 and 8. Q/Q_e and A/A_e have been taken from the calculations. The agreement in form of calculated and measured entrainment curves is satisfactory although an appreciable difference in level exists. This can probably be attributed to the cut of the measured velocity profile, as mentioned above.

A more direct check on the increase of the mass flow can be obtained by comparing calculated values of Q/Q_e with measured values from Kamotani and Greber (ref.9). Kamorani and Greber use the same cut off condition for the velocity profile as Keffer and Baines. Assuming a Tollmien velocity profile, it can be shown that if $(\mathcal{U}-\mathcal{U}_\infty)/(\mathcal{U}_m-\mathcal{U}_\infty)$ is cut off at its 0.1 value, the mass flux relation (16) should, in the fully developed region, be replaced by

$$\frac{Q}{Q_e} = \frac{A}{A_e}\cdot\frac{1}{R}\left[(R-1)\,\tilde{F}_1\left(\frac{\mathcal{U}_m-\mathcal{U}_\infty}{\mathcal{U}_j-\mathcal{U}_\infty}\right)+0.5\right]$$

where $\tilde{F}_1 = 0.183$, and A/A_e is the cross sectional area based on Tollmien's distribution, cut off at $(U - U_\infty)/(U_m - U_\infty) = 0.0$. In figure 8, mass flow values calculated from this formula are compared to the measured values of ref.19, for R = 6 and 8. In contrast to figure 7, the calculated entrainment values now appear to be lower than the measured values of Kamotani and Greber. The flattening of the calculated mass flux curve for R = 6 at higher values of s/d_e can be due to errors in the velocity decay curve used in the jet model, which was extrapolated from the measurements of ref.2.

3. THE POTENTIAL FLOW FIELD INDUCED BY THE JET

3.1. General viewpoints concerning the modeling of the potential flow field

The flow arising from jet to free stream interactions is assumed to consist of two parts, viz. the turbulent jet flow region analysed in the preceeding section, and a potential flow field surrounding the jet. This potential flow field extends to infinity, where it satisfies undisturbed free stream conditions. Let the velocity potential pertaining to this field be Φ, and the disturbance potential $\varphi = \Phi - U_\infty x$. φ satisfies the Laplace equation

$$\left.\begin{aligned} &\nabla^2\varphi = 0 \\ \text{and} \quad &\varphi \to 0 \quad \text{if} \quad |x|, |y|, z \longrightarrow \infty \end{aligned}\right\} \tag{33}$$

φ is then uniquely determined (except for an additive constant) by a given distribution of its normal derivative $\partial\varphi/\partial n$ on a surface surrounding the turbulent jet flow region. This approach is more general than using line distributions of singular solutions of (33) along the jet axis in an attempt to model physically discernable effects of the jet (entrainment, blockage, vortex pair) as is done by many authors (e.g. refs.9 through 11).

The problems arising using the general approach are the choice of the surface S on which to prescribe $\partial\varphi/\partial n$ and the specification of $\partial\varphi/\partial n$. In this study use will be made of the jet boundary surface, following from section 2. It will be shown that equations (13) and (14) for the jet deflection, and the entrainment relations (21) and (30) yield information concerning $\partial\varphi/\partial n$ on this surface.

Some remarks should be made about the assumption that the flow everywhere outside the jet region is potential flow. This excludes the existence of a wake region downstream of the jet, which would result from flow separation. There is experimental evidence of flow separation on the plate, at the edge of the jet, where the plate boundary layer separates due to an adverse pressure gradient. The ensuing wake region is not modeled. There is no conclusive evidence that separation occurs at some distance from the plate. In fact, flow measurements by Mehmel (ref.12) suggest that the flow does not separate. It is indeed concievable that entrainment and the action of the jet vortex pair are sufficient to prevent separation.

3.2. Formulation of the equation for the normal velocity on S

Let position on the jet boundary S be described by coordinates s and c, such that c measures linear distance along the circumference of a jet cross section at distance s along the jet axis. Let the length of the circumference be given by

$$C(s) = \oint dc \qquad \text{at constant s} \tag{34}$$

A normalized coordinate c' will be defined by

$$c' = 2\pi c/C(s) \quad , \quad \oint dc' = 2\pi \tag{35}$$

Let $g(s,c')$ be the linearizing factor of the s coordinate on S, such that $\int g(s,c')ds$ measures linear distance along lines of constant c'. For the entrainment of mass one then obtains the following relation

$$\frac{2}{\pi^2}\frac{C(s)}{d_e}\frac{1}{R}\int_0^{2\pi}\left[-\frac{u_n(s,c')}{U_\infty}g(s,c')dc'\right] = \frac{1}{Q_e}\frac{dQ}{d(s/d_e)} \tag{36}$$

where u_n is the normal velocity component on S, directed into the potential flow region. The transfer of momentum in x and z directions must obey the following relations :

$$\left.\begin{aligned} &\frac{2}{\pi^2}\frac{C(s)}{d_e}\frac{1}{R}\int_0^{2\pi}\left\{\left[-\frac{u_n(s,c')}{U_\infty}\cdot\frac{u_x(s,c')}{U_\infty} - \frac{p(s,c')}{U_\infty^2}n_x(s,c')\right]g(s,c')dc'\right\} = \\ &= \frac{1}{U_\infty Q_e}\frac{dM_x}{d(s/d_e)} = \frac{1}{Q_e}\frac{dQ}{d(s/d_e)} \end{aligned}\right\} \tag{37}$$

$$\left.\begin{aligned} &\frac{2}{\pi^2}\frac{C(s)}{d_e}\frac{1}{R}\int_0^{2\pi}\left\{\left[-\frac{u_n(s,c')}{U_\infty}\cdot\frac{u_z(s,c')}{U_\infty} - \frac{p(s,c')}{U_\infty^2}n_z(s,c')\right]g(s,c')dc'\right\} = \\ &= \frac{1}{U_\infty Q_e}\frac{dM_z}{d(s/d_e)} = 0 \end{aligned}\right\} \tag{38}$$

For the right hand sides of (37) and (38), use has been made of (13) and (14). The entrainment, appearing in the right hand sides of (36) and (37) is known from the jet model. The value of the pressure p is related to the local velocities by Bernouilli's law :

$$p = \text{constant} - (u_x^2 + u_y^2 + u_z^2)/2 \tag{39}$$

The normal velocity u_n on S is directly related to $\partial\varphi/\partial n$ through

$$\frac{1}{U_\infty}\frac{\partial\varphi}{\partial n}(s,c') = \frac{u_n(s,c')}{U_\infty} - n_x(s,c') \tag{40}$$

From potential flow theory it is known that u_x, u_y and u_z on S are linear functionals of the distribution of $\partial\varphi/\partial n$ on S. Hence equations (36), (37) and (38) form three equations (for every value of s) for $u_n(s,c')$

Let the line $c'=0$ be the intersection of S with the plane $y=0$, facing the cross flow. It is evident that both jet geometry and the u_n distribution are symmetric with regard to $c'=0$ and $c'=\pi$ for every cross section. The quantity $u_n(s,c')q(s,c')$ may then be written as a Fourier cosine series in c'

$$\frac{u_n(s,c')}{U_\infty}q(s,c') = a(s) + \sum_{j=1}^{\infty} B_j(s)\cos(jc') \tag{41}$$

a(s) follows immediately from (36)

$$a(s) = -\frac{\pi}{4}\frac{d_e}{C(s)}R\frac{1}{\varphi_e}\frac{dQ}{d(s/d_e)} \tag{42}$$

while (37) and (38) form a system of two equations for the remaining Fourier coefficients $B_j(s)$.

It will be assumed that instead of (41) a truncated Fourier series may be used for a sufficiently accurate description of the normal velocity distribution :

$$\frac{u_n(s,c')}{U_\infty}q(s,c') = a(s) + B_1(s)\cos c' + B_2(s)\cos 2c' \tag{43}$$

This expression gives the most important features of the distribution; the cos (c') term differentiates between upstream and downstream parts of the circumferences, while the cos(2c') term differentiates between up- and downstream parts and the sides of the circumference. Another argument for using (43) is that the higher harmonics have less influence on the induced flow field, since their effects decrease more rapidly with distance. Finally, the use of higher harmonics would necessitate the use of smaller surface panels in the approximate solution of the problem, described in section 3.3. Using (43), equations (37) and (38) form two equations for $B_1(s)$ and $B_2(s)$.

3.3. Discretization of the equations

The Neumann problem to be solved for the potential flow field reads

$$\begin{aligned} &\nabla^2\varphi = 0 && \text{outside S} \\ &\varphi \to 0 && \text{at infinity} \\ &\frac{\partial\varphi}{\partial n} = f(s,c') && \text{on S} \end{aligned} \tag{44}$$

where $f(s,c')$ has to be obtained from (37), (38), (40) and (43). The solution of (44) may be expressed as the integral over a distribution of simple sources on S. According to ref.13

$$\varphi_P = \frac{1}{4\pi}\iint_S \frac{\sigma(\xi)}{\rho}d\xi \tag{45}$$

if φ_P denotes the velocity potential in a field point P, $\sigma(\xi)$ the local density of the source distribution in point ξ on S and ρ the distance between P and ξ. The presence of the plate is accounted for by using a mirror image with respect to z = 0 of the jet surface. Application of the boundary condition on S gives an integral equation for $\sigma(\xi)$:

$$\left(\frac{\partial\varphi}{\partial n}\right)_S = f(s,c') = \frac{1}{4\pi}\underline{n}\cdot\underline{\nabla}\iint_S \frac{\sigma(\xi)}{\rho}d\xi \tag{46}$$

For known $f(s,c')$, an approximate solution of (46) can be constructed by the method of influence coefficients or panel method, originally formulated by Hess and Smith (ref.14). The method approximates the surface by a finite number of small quadrilateral panels, on each of which the source density σ_j (the index denotes the panel number) is taken to be constant. Boundary conditions are imposed in one point on each panel, the collocation point. The problem is then reduced to the determination of the unknowns σ_j. Equation (46) can be written as

$$\left(\frac{\partial\varphi}{\partial n}\right)_i = \frac{1}{4\pi}\underline{n}_i\cdot\sum_{j=1}^{N}\left(\underline{\nabla}\iint_{AP_j}\frac{dAP_j}{\rho_{ij}}\right)\sigma_j = f_i \tag{47}$$

where AP_j denotes the j^{th} panel, f_i the value of $\partial\varphi/\partial n$ in the i^{th} collocation point.

Let $\underline{e}_x$, $\underline{e}_y$ and $\underline{e}_z$ be unit vectors in x,y and z direction respectively, and let influence coefficients AX_{ij}, AY_{ij} and AZ_{ij} be defined by

$$\underline{e}_x AX_{ij} + \underline{e}_y AY_{ij} + \underline{e}_z AZ_{ij} = \frac{1}{4\pi}\underline{\nabla}\iint_{AP_j}\frac{dAP_j}{\rho_{ij}} \tag{48}$$

It is clear from this definition that the influence coefficients give the velocity components in the i^{th} collocation point, induced by a source distribution of strength one on the j^{th} panel. The total induced velocity $\underline{u}_i$ in the i^{th} collocation point reads :

$$\underline{u}_i = \underline{e}_x \sum_{j=1}^{N} AX_{ij}\sigma_j + \underline{e}_y \sum_{j=1}^{N} AY_{ij}\sigma_j + \underline{e}_z \sum_{j=1}^{N} AZ_{ij}\sigma_j \tag{49}$$

The influence coefficient AN_{ij} for the normal velocity can be written as

$$AN_{ij} = \frac{1}{4\pi}\, \underline{n}_i \cdot \underline{\nabla} \iint \frac{dAP_j}{\rho_{ij}} = n_{x_i} AX_{ij} + n_{y_i} AY_{ij} + n_{z_i} AZ_{ij} \tag{50}$$

The values of the elements of AN_{ij} can be calculated by evaluating the defining integrals numerically, and (47) becomes a set of linear equations for σ_j

$$\sum_{j=1}^{N} AN_{ij}\sigma_j = f_i \tag{51}$$

We will proceed with the determination of the boundary conditions f_i . First the Fourier series (43) will be discretised with respect to the surface panels. The jet surface is panelled stripwise. Lower and upper boundaries of the i^{th} panel strip lie in cross-sectional planes at $s = s_i$ and $s = s_{i+1}$ respectively. Each panel in the strips replaces a part of S bounded in lateral direction by lines of constant c'. Only half of the jet $(y > 0)$ is paneled , the other half is taken into account by symmetry conditions. Consider the mass flux $\delta Q(j,i)$ through a surface element bounded by s_i and s_{i+1}, c'_j and c'_{j+1}, to be replaced by the j^{th} panel of the i^{th} ring. One has

$$\left.\begin{aligned} \frac{\delta Q(j,i)}{U_\infty} &= \int_{s_i}^{s_{i+1}} \left\{ \int_{c'_j}^{c'_{j+1}} -\frac{u_n(s,c')}{U_\infty}\, q(s,c')\,dc' \right\} \frac{C(s)}{2\pi}\, ds = \\ &= \frac{c'_{j+1} - c'_j}{\pi} \int_{s_i}^{s_{i+1}} -\frac{a(s)\,C(s)}{2}\, ds + \frac{\sin c'_{j+1} - \sin c'_j}{\pi} \int_{s_i}^{s_{i+1}} -\frac{B_1(s)\,C(s)}{2}\, ds + \\ &+ \frac{\sin 2c'_{j+1} - \sin 2c'_j}{2\pi} \int_{s_i}^{s_{i+1}} -\frac{B_2(s)\,C(s)}{2}\, ds \end{aligned}\right\} \tag{52}$$

The normal velocity in the collocation point of the relevant panel will be taken as a mass flux conserving average :

$$\frac{u_n(j,i)}{U_\infty} = -\frac{\delta Q(j,i)}{U_\infty\, AP(j,i)} = \frac{\pi R}{4}\, \frac{\delta Q(j,i)}{Q_e}\, \frac{d_e^2}{AP(j,i)} \tag{53}$$

The first integral in the right hand side of (52) is known from (42). In fact :

$$\int_{s_i}^{s_{i+1}} -\frac{a(s)C(s)}{2} = \frac{1}{2} \int_{s_i}^{s_{i+1}} \frac{dQ}{ds} = \frac{\Delta Q(i)}{2} \tag{54}$$

The integrals involving $B_1(s)$ and $B_2(s)$ are unknown. Let the non-dimensional quantities $\overline{B}_1(i)$ and $\overline{B}_2(i)$, pertaining to the i^{th} ring be defined by

$$\overline{B}_1(i) = \frac{\int_{s_i}^{s_{i+1}} B_1(s)C(s)ds}{\int_{s_i}^{s_{i+1}} a(s)\,C(s)ds} \quad , \quad \overline{B}_2(i) = \frac{\int_{s_i}^{s_{i+1}} B_2(s)C(s)\,ds}{\int_{s_i}^{s_{i+1}} a(s)\,C(s)\,ds} \tag{55}$$

Using (54) and (55), (52) can be written as :

$$\left.\begin{aligned} \frac{u_n(j,i)}{U_\infty} &= -\frac{\pi R}{8}\, \frac{d_e^2}{AP(j,i)}\, \frac{\Delta Q(i)}{Q_e} \left[\frac{c'_{j+1} - c'_j}{\pi} + \right. \\ &\left. + \frac{\sin c'_{j+1} - \sin c'_j}{\pi}\, \overline{B}_1(i) + \frac{\sin 2c'_{j+1} - \sin 2c'_j}{2\pi}\, \overline{B}_2(i) \right] \\ \text{or} \qquad \frac{u_n(j,i)}{U_\infty} &= \overline{a}(j,i) + \overline{B}_1(i)\,\overline{b}(j,i) + \overline{B}_2(i)\,\overline{d}(j,i) \end{aligned}\right\} \tag{56}$$

the definition of $\overline{a}$, $\overline{b}$ and $\overline{d}$ of j, i following from (56). For the value of $\partial\varphi/\partial n = f$ in the collocation point of the j^{th} panel of the i^{th} strip we have, according to (40)

$$\frac{1}{U_\infty}\frac{\partial\varphi}{\partial n}(j,i) = \frac{f(j,i)}{U_\infty} = \frac{u_n(j,i)}{U_\infty} - n_x(j,i) = \overline{a}(j,i) - n_x(j,i) + \overline{B}_1(i)\,\overline{b}(j,i) + \overline{B}_2(i)\,\overline{d}(j,i) \tag{57}$$

The values of $\overline{a}$, $\overline{b}$ and $\overline{d}$ can be determined from the known jet geometry and entrainment.

Equations(37) and (38) will now be approximated by a system of quadratic algebraic equations for the quantities $\overline{B}_1(i)$ and $\overline{B}_2(i)$, making use of (51) and (57). It will be convenient to return to the subscript notation of (51). The subscript k then indicates the k^{th} panel, which is identical to the j^{th} panel of the i^{th} strip if $k = (i-1)J + j$, where J is the number of panels per strip. h_k is then a different notation for h (j,i).

Since the elements of the f_k vector in the right hand side of (51) are linear combinations in $\overline{B}_1(i)$ and $\overline{B}_2(i)$ according to (57), the elements of the σ_j vector must also be linear combinations in $\overline{B}_1(i)$ and $\overline{B}_2(i)$. In fact, one can write

$$\frac{\sigma_j}{U_\infty} = m_j + \sum_{i=1}^{I} \overline{B}_1(i)\, m_{1j}(i) + \sum_{i=1}^{I} \overline{B}_2(i)\, m_{2j}(i) \tag{58}$$

where I equals the total numbers of strips used to approximate the surface. From (51) and (57) it follows that the vectors m_j, m_{1j} and m_{2j} are the solutions of the following sets of linear equations

$$\left.\begin{aligned}&\sum_{j=1}^{N} AN_{ij}\, m_j = \bar{a}_i - n_{x_i}\\ &\sum_{j=1}^{N} AN_{ij}\, m_{1j}(k) = \frac{\partial(f_i/\mathcal{U}_\infty)}{\partial \bar{B}_1(k)} \quad , \quad \sum_{j=1}^{N} AN_{ij}\, m_{2j}(k) = \frac{\partial(f_i/\mathcal{U}_\infty)}{\partial \bar{B}_2(k)}\end{aligned}\right\} \quad (59)$$

The column vectors in the right hand sides of the last two equations of (59) have non-zero entries only for the elements corresponding to the kth panel strip. The induced velocity components in x, y and z direction in the collocation points follow from (49) after substitution of σ_i from (58). To obtain the total velocity, $\mathcal{U}_\infty$ should be added to the x component of $\underline{\tilde{u}}$. The resulting expressions read

$$\frac{u_{x_i}}{\mathcal{U}_\infty} = X_{1_i} + \sum_{k=1}^{I} X_{2_i}(k)\bar{B}_1(k) + \sum_{k=1}^{I} X_{3_i}(k)\bar{B}_2(k)$$

$$\frac{u_{y_i}}{\mathcal{U}_\infty} = Y_{1_i} + \sum_{k=1}^{I} Y_{2_i}(k)\bar{B}_1(k) + \sum_{k=1}^{I} Y_{3_i}(k)\bar{B}_2(k)$$

$$\frac{u_{z_i}}{\mathcal{U}_\infty} = Z_{1_i} + \sum_{k=1}^{I} Z_{2_i}(k)\bar{B}_1(k) + \sum_{k=1}^{I} Z_{3_i}(k)\bar{B}_2(k) \qquad (60)$$

with

$$X_{1_i} = 1 + \sum_{j=1}^{N} AX_{ij}\, m_j \quad , \quad X_{2_i}(k) = \sum_{j=1}^{N} AX_{ij}\, m_{1j}(k)$$

$$X_{3_i}(k) = \sum_{j=1}^{N} AX_{ij}\, m_{2j}(k) \qquad \text{and similar expressions}$$

for Y_{1_i} etc.

Equations (37) and (38) are integrated with respect to s, between s_i and s_{i+1} for the ith panel strip. The c' integration is divided in intervals between c'_j and c'_{j+1}, corresponding to the surface panels. A typical integral

$$\int_{s_i}^{s_{i+1}} \int_{c'_j}^{c'_{j+1}} - u_n(s,c')\, u_x(s,c')\, q(s,c')\, dc'\, ds$$

is then approximated by $-u_n(j,i)\, u_x(j,i)\, AP(j,i)$. Difficulties are encountered with respect to the surface integrals involving the pressure p. Applying (37) and (38) or their discretised form to a typical panel strip (see figure 9) in a virtual field of constant pressure, one finds that both x and z components of the jet momentum change due to pressure contributions. In reality, pressure forces on the upper and lower cross sections bounding the strip will balance this change, but in the jet model this cannot be accounted for. Thus the constant in (39) will unduly enter into equations (37) and (38). This problem is overcome using a modified jet surface for the pressure forces. This modified surface is cylindrical, with axis along the tangent to the jet axis at $s_{av} = \frac{1}{2}(s_i + s_{i+1})$. Cross sectional shape and area of the cylinder equal the shape and are of the jet cross section at s_{av}. The modified panel strip is bounded by planes perpendical to the cylinder axis at s_i and s_{i+1}. Lateral panel boundaries are lines of constant c', at the same c' values as used in the original panel network. Thus the collocation points of corresponding original and modified panels are very close. The total pressure force on the panel strip acts perpendicularly to the direction of the jet axis at s_{av}, and the constant in (39) can be omitted.

Let $\widetilde{AP}(j,i)$ denote the area of the modified panel, $\underline{\tilde{n}}(j,i)$ the normal unit vector on the panel and $\tilde{\theta}_i$ the angle between the jet axis at s_{av} and the z-axis. The discretised forms of (37) and (38) then read for the ith strip

$$\left.\begin{aligned}&\sum_{j=1}^{J} -\left[\frac{u_n(j,i)}{\mathcal{U}_\infty}\,\frac{u_x(j,i)}{\mathcal{U}_\infty}\,\frac{AP(j,i)}{d_e^2}\right] + \cos\tilde{\theta}_i \sum_{j=1}^{J}\left[\frac{u_x^2(j,i) + u_y^2(j,i) + u_z^2(j,i)}{\mathcal{U}_\infty^2}\,\frac{\widetilde{AP}(j,i)}{d_e^2}\,\tilde{n}_p(j,i)\right] =\\ &= \frac{\Delta Q(i)}{Q_e}\,\frac{\pi R}{8}\\ &\sum_{j=1}^{J} -\left[\frac{u_n(j,i)}{\mathcal{U}_\infty}\,\frac{u_x(j,i)}{\mathcal{U}_\infty}\,\frac{AP(j,i)}{d_e^2}\right] + \sin\tilde{\theta}_i \sum_{j=1}^{J}\left[\frac{u_x^2(j,i) + u_y^2(j,i) + u_z^2(j,i)}{\mathcal{U}_\infty^2}\,\frac{\widetilde{AP}(j,i)}{d_e^2}\,\tilde{n}_p(j,i)\right] = 0\end{aligned}\right\} (61)$$

where $\tilde{n}_p$ is the component of $\underline{\tilde{n}}$ in the plane parallel to $y = 0$. With u_n known from (56) and u_x, u_y and u_z from (60), the equations (61) for i = 1, . . . , I form a set of 2I quadratic algebraic equations for the 2I unknowns $\bar{B}_1(i)$ and $\bar{B}_2(i)$. When these quantities are solved from (61), σ_j can be calculated from (58) for all panels, and the induced flow field can be calculated from the discretised form of (45).

3.4. Solution of the equations for the Fourier coefficients

Let the vector C_j, with $j = 1, \ldots, 2I$ be defined by

$$C_j = \overline{B}_1(j)\,,\quad C_{I+j} = \overline{B}_2(j)\,,\quad j = 1, \ldots, I \tag{62}$$

The system of equations (61) will be denoted by

$$\left.\begin{aligned} F_i(C_j) &= \sum_{j=1}^{2I}\sum_{k=1}^{2I} A_{jk}^{(i)} C_j C_k + \sum_{j=1}^{2I} B_j^{(i)} C_j + D^{(i)} \\ &\text{for } i = 1, \ldots, 2I \end{aligned}\right\} \tag{63}$$

Due to the non linearity of the system, a real solution does not necessarily exist. For this reason, a procedure was used to find a generalized (least squares) solution. Let

$$F = \sum_{i=1}^{2I} F_i^2(C_j) \tag{64}$$

The generalized solution is defined as the real vector $\widehat{C}_j$ that minimizes the functional F. $F(\widehat{C}_j)$ will not necessarily equal zero. The vector $\widehat{C}_j$ is determined with an iterative procedure. Let $C_{j,k}$ be the k^th^ iterate, the k+1^st^ will be of the form

$$C_{j,k+1} = C_{j,k} + \lambda_k \Delta_j \tag{63}$$

where Δ_j is a search or direction vector, and λ_k determines the steplength along Δ_j.
At $\widehat{C}_j$ the derivatives of F with respect to the C_j equal zero, i.e.

$$G_i(\widehat{C}_j) = \frac{1}{2}\frac{\partial F}{\partial C_i} = \sum_{l=1}^{2I} F_l \frac{\partial F_l}{\partial C_i} = 0\,,\quad i = 1, \ldots, 2I \tag{65}$$

The search vector Δ_j is the Newton Raphson correction vector for the iterative solution of (65)

$$\sum_{j=1}^{2I} \frac{\partial G_i}{\partial C_{j,k}} \Delta_j = -G_i(C_{j,k}) \tag{66}$$

The scalar λ_k is taken such that $F(C_{j,k} + \lambda\Delta_j)$ is minimized for $\lambda = \lambda_k$. Due to the fact that the expressions $F_i(C_j)$ are quadratic in C_j, the value of λ_k can be computed straightforwardly, In fact, using (65) and (66) one can write

$$\left.\begin{aligned} F(C_{j,k} + \lambda\Delta_j) &= F(C_{j,k}) + (2\lambda - \lambda^2)\sum_i G_i\Delta_i + \\ &\quad + 2\lambda^3 \sum_i \Big[A^{(i)} \sum_j \frac{\partial F_i}{\partial C_j}\Delta_j\Big] + \lambda^4 \sum_i \big[A^{(i)}\big]^2 \\ \text{with}\quad \sum_i\sum_j \frac{\partial^2 F_l}{\partial C_i \partial C_j}\Delta_i\Delta_j &= \sum_i\sum_j A_{ij}^{(l)}\Delta_i\Delta_j = A^{(l)} \end{aligned}\right\} \tag{67}$$

At λ_k, $dF/d\lambda = 0$, hence

$$2(1-\lambda_k)\sum_i G_i\Delta_i + 6\lambda_k^2 \sum_i\Big[A^{(i)}\sum_j \frac{\partial F_i}{\partial C_j}\Delta_j\Big] + 4\lambda_k^3 \sum_i \big[A^{(i)}\big]^2 \tag{68}$$

from which λ_k is solved in the computer program using an exact method. If (68) has one real root, $F(\lambda)$ has a minimum for that root. If there are three real roots $\lambda_1 < \lambda_2 < \lambda_3$, $F(\lambda)$ has minima at λ_1 and λ_3, and the λ with the lowest value of $F(\lambda)$ is chosen. In ref.15 it is shown that if $F(\widehat{C}_j) = 0$, the search vector Δ_j from (66) approaches the Newton Raphson correction vector $\overline{\Delta}_j$ for the iterative solution of (63), for C_j approaching $\widehat{C}_j$. In the numerical procedure, efficient use has been made of the quadratic character of $F_i(C_j)$ for the updating of all required coefficients and function values after each iteration.

A remaining problem is that minimization of (64) will not yield a unique solution in general. For instance, (63) may have several real solutions, which will all be minima of F. If (63) has no real solutions there still may be several "lowest" minima of (64). Moreover, the solution procedure described above leads to a local minimum, but unless F = 0 at the obtained "solution" $\widehat{C}_j$, one does not know whether the local minimum is an absolute minimum, if not all minima of (64) are evaluated. In such a situation one would like to formulate constraints on the values of the $\widehat{C}_j$ components, to limit the space in which physically interpretable solutions can be expected. Such constraints can indeed be formulated by requiring inflow across the entire jet boundary S, i.e. $u_n(s, c') \leq 0$ for all s and c'. Using (43), (55) and (62), this requirement imposes the following condition on $\widehat{C}_j$

$$\begin{aligned} &1 + \widehat{C}_j \cos c' + \widehat{C}_{I+j}\cos 2c' \geq 0 \\ &\text{for } 0 \leq c' \leq \pi \text{ and } j = 1, \ldots, I \end{aligned} \tag{69}$$

This inequality can be rewritten as

$$\begin{aligned} |\widehat{C}_j| &\leq \sqrt{8\widehat{C}_{I+j} - 8\widehat{C}_{I+j}^2} && \text{for } \tfrac{1}{3} \leq \widehat{C}_{I+j} \leq 1 \\ |\widehat{C}_j| &\leq 1 + \widehat{C}_{I+j} && \text{for } -1 \leq \widehat{C}_{I+j} \leq \tfrac{1}{3} \end{aligned} \tag{70}$$

Thus $\widehat{C}_j$ and $\widehat{C}_{I+j}$ must be inside the contour defined by (70) to ensure inflow through all panels.

For the calculations, the results of which are discussed in section 3.5, (70) was used to help establish a "best" solution $\tilde{C}_j$ in the following way. From an initial estimate $C_{j,o}$ a local minimum at $\tilde{C}_j$ was obtained. If $\tilde{C}_j$ did not comply with (70) for every j, a new estimate$'_{j,o}$ was formed by multiplying the relevant components with a scalar so that they just fall inside the region defined by (70). This process was repeated until the solution $\tilde{C}_j$ of the new initial estimate equals that of the preceeding one. The solutions $\hat{C}_j$ obtained in this manner satisfied (70) for the panel strips close to the plate, but not for a number of panel strips far away. This is probably due to the fact that the jet surface is truncated and beyond the last panel strip, the jet is not represented in any way. This should be acceptable for the calculation of the pressure distribution on the plate.

An alternative way of defining a "best" solution is by rigidly imposing (70), i.e. by finding the minimum of F in the region of C_j space defined by (70). Judging from the performed calculations, this would probably result in a minimum on the border of the constraints. The choice of the "best" solution in the present calculation is based on the idea that satisfying the momentum equations in the best possible way is more important than satisfying the inflow requirements. It is felt however that this problem should be studied more thoroughly to arrive at a more satisfying choice of a best solution.

3.5. Discussion of calculated results and comparison with measurements

Plate pressure distributions have been calculated for three values of the jet to free stream velocity ratio, viz. R = 6, 7 and 8. In all cases the jet surface was defined by the jet model and using the cross sectional shape of figure 4. The surface was approximated by 17 panel strips, each containing 10 panels for half of the jet surface $(0 \leq c' \leq \pi)$. The longitudinal dimensions of panel strips are small close to the plate, increasing with distance away from the plate, according to the dimensions chosen in ref.16.

The static pressure coefficient c_p, defined by

$$c_p = \frac{p - p_\infty}{\frac{1}{2} U_\infty^2} = 1 - \frac{V^2}{U_\infty^2}$$

can be calculated in the entire potential flow field. In figure 10, calculated values of c_p for R = 6, 7 and 8, along rays on the plate at angles $\psi = 0^\circ, 30^\circ, \ldots, 180^\circ$ to the negative x-direction, are compared with measured c_p values for R = 5 and 6, from refs. 17 and 18 respectively. It is evident that the calculated negative c_p values are much larger in magnitude than the corresponding measured values. This discrepancy can partly be attributed to the behaviour of the boundary layer on the plate. In reference 18, the influence of the momentum thickness of the boundary layer on the c_p distribution is shown. The negative c_p values increase with decreasing momentum thickness, especially close to the jet orifice. We can conclude that the differences between calculations and measurements have the expected character. However, the magnitude of the differences in c_p values far from the jet orifice are larger than should be expected.

There is a qualitative agreement between measured and calculated c_p values in the sense that changes with R occur in the same direction for $\psi = 0^\circ, 30^\circ, \ldots, 120^\circ$. This is especially evident for $\psi = 0^\circ$ and 30°, where c_p varies strongly with R. At $\psi = 60^\circ, 90^\circ$ and 120° measurements show little variation of c_p with R, and this is also obtained from calculations. On the ray $\psi = 180^\circ$, there is no resemblence at all between measured and calculated c_p behaviour. This is accounted to the wake like flow behind the jet close to the plate, resulting from plate boundary layer separation. This cannot be modeled in a potential flow calculation. On the ray $\psi = 150^\circ$, measured and calculated c_p values are of comparable magnitude.

Calculated and measured pressures are compared in a different way in figure 11, where isobars for R = 6 (compared to measured isobars for R = 5, since measurements for R = 6 seem to be lacking) and R = 8 are shown. The calculated isobars are shown for $0^\circ \leq \psi \leq 150^\circ$, since the potential flow pressure distribution in the wake has no resemblence to what actually happens on the plate. It is clear from figure 9 that the calculated regions of negative pressure are much larger than the corresponding measured regions.There is only qualative agreement in the sense that the shapes of the isobars with lobes extending in downstream direction, are fairly well represented, as are the decreasing size and increasing downward shift of the isobars with decreasing R.

4. CONCLUSIONS

A model for the development of a jet in a cross flow and the induced potential flow field has been presented. The model is self consistent to the respect that momentum transfer assumptions used in the jet model are also enforced for the boundary conditions of the induced flow field, yielding a set of equations for the normal velocity distribution on the jet surface. The velocity potential of the induced flow field is calculated using a panel method.

The results of the jet model compare well with measurements. Only qualitative agreement could be established between calculated and measured pressure distributions on the flat plate from which the jet exhausts. The quantitative differences can in part be ascribed to the interaction of the plate boundary layer with the exhausting jet.

Acknowledgements

The present work was performed under contract with the Netherlands Agency for Aerospace Programs (NIVR). The author expresses his gratitude to Dr. B.M. Spee for many helpful discussions and to Mr. I. van de Veer, who composed most of the necessary computer programs.

REFERENCES

1. Hacket, J.E. and Miller, H.R.
"The aerodynamics of the lifting jet in a cross flowing stream". In "Analysis of a jet in a subsonic cross wind", NASA SP-218 (1969) pp. 37-48.

2. Keffer, J.F. and Baines, W.D.
"The round turbulent jet in a cross-wind". Journal of Fluid Mechanics Vol.15 (1963) pp. 481-497.

3. Snel, H.
"A semi-empirical model for the development of a round turbulent jet in a cross flow.
NLR TR 71107 U(1971).

4. Tollmien, W.
"Calculation of turbulent expansion processes" NACA TM.1085 (1945). (Reprint of ZAMM, vol 6, 1926).

5. Wygnanski, I.
"The flow induced by two-dimensional and axisymmetric turbulent jets issuing normally from an infinite plane surface". The Aeron. Quarterly (Nov. 1964) pp. 378-380.

6. Ricou, F.P. and Spalding, D.B.
"Measurements of entrainment by axisymmetric turbulent jets. JFM Vol 11 (1961).

7. Endo, H. and Nakamura, M.
"Bending and development of three dimensional turbulent jets in a cross-wind". National Aerospace Lab. (Japan) TR-216.

8. Platten, J.L. and Keffer, J.F.
"Entrainment in deflected axisymmetric jets at various angles to the stream. UTME-TP 6808, June 1968.

9. Taganov, G.I.
"On an interaction effect of a spatial turbulent jet with a transversal flow". Fluid Dynamics Transactions, Vol 4 (1968) pp. 783-791.

10. Wooler, P.T., Burghart, G.H. and Gallagher, J.T.
"Pressure distribution on a rectangular wing with a jet exhausting normally into an airstream".
Journal of Aircraft, Vol 4, No 6 (Nov.-Dec. 1967) pp.537-543.

11. Wooler, P.T.
"On the flow past a circular jet exhausting at right angles from a flat plate or wing".
Journal of the Aeronautical Society, Vol 71 (March 1967) pp. 216-218.

12. Mehmel, D.
"Untersuchungen über das Strömungsfeld eines schräg angeblasenen Strahles". Teil I, AVA (Göttingen) Bericht 67 A 53 (1967).

13. Lamb, H.
"Hydrodynamics", Dover Publishing Company, New York (1945).

14. Hess, J.L. and Smith, A.M.O.
"Calculation of potential flow about arbitrary three-dimensional bodies" Douglas Aircraft Corp.
Rep. Es. 40622 (1962).

15. Snel, H.
"A potential flow model for the flow field induced by a jet exhausting into a uniform cross flow".
NLR TR 73048 U (1973).

16. Snel, H.
"A method for the calculation of the flow field induced by a free jet". NLR TR 72040 U (1972).

17. Vogler, R.D.
"Surface pressure distributions induced on a flat plate by a cold airjet issuing perpendicularly to a low-speed free-stream flow". NASA TN-1629 (March 1963).

18. Bradbury, L.J.S. and Wood, W.N.
"The static pressure distribution around a circular jet exhausting normally from a plane wall into an airstream. RAE Techn. Note No. Aero 2978 (August 1964).

19. Kamotani, Y. and Greber, I.
"Experiments on a turbulent jet in a cross flow". NASA CR-72893 (June 1971).

20. Jordinson, R.
"Flow in a jet directed normal to the wind". British Aeronautical Research Council, R & M 3074 (1958).

21. Patrick, M.A.
"Experimental investigation of the mixing and penetration of a round turbulent jet injected perpendicularly into a transverse stream". Trans. Instn. Chem. Engrs. Vol.45 (1967) p.T16-T31.

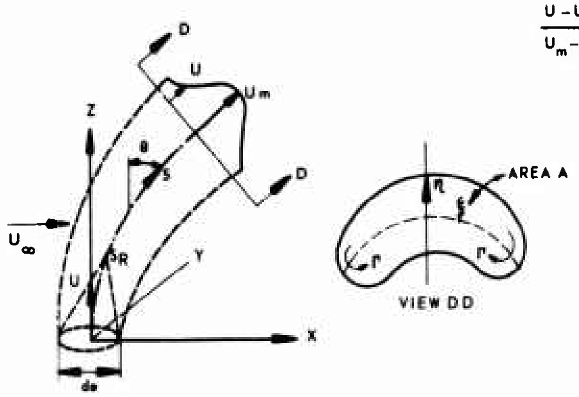

FIG. 1 DEFINITION OF CO- ORDINATES

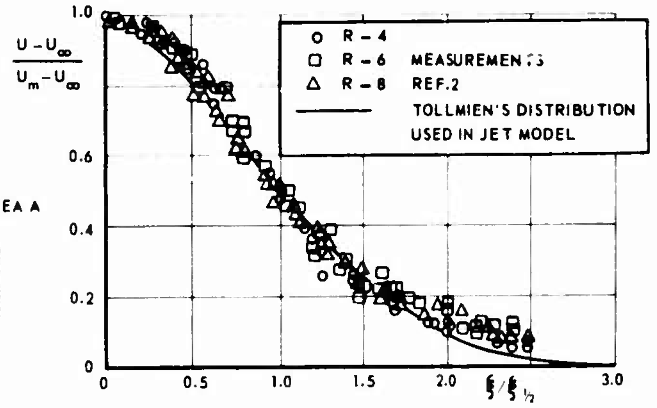

FIG. 2 VELOCITY SIMILARITY IN THE JET FROM (1), COMPARED TO TOLLMIEN'S DISTRIBUTION

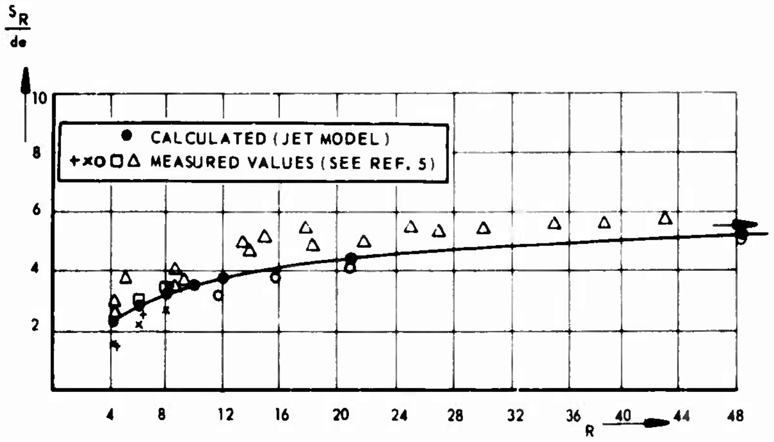

FIG. 3 COMPARISON OF CALCULATED AND MEASURED VALUES OF THE POTENTIAL CORE LENGTH s_R/d_e

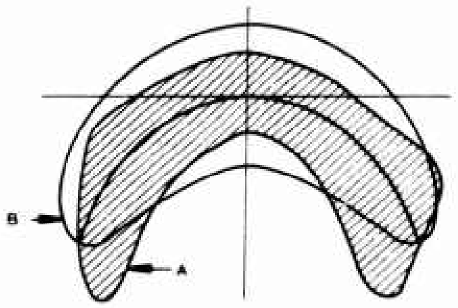

FIG. 4 CROSS SECTIONAL SHAPE (B) USED IN JET MODEL AND MEASURED SHAPE OF HIGH SPEED REGION (A) FROM REF. 7

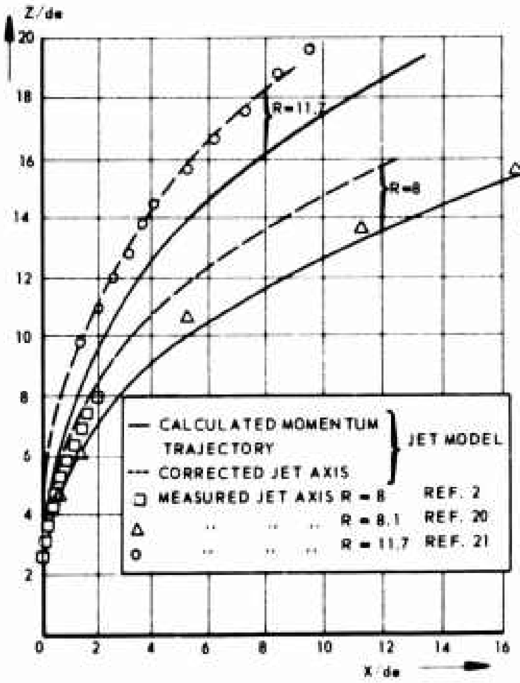

FIG. 5 COMPARISON OF MEASURED AND CALCULATED JET AXES

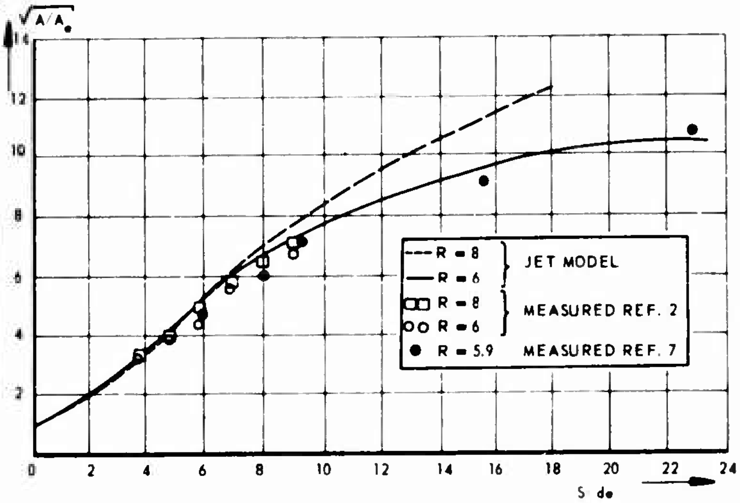

FIG. 6 COMPARISON OF CALCULATED AND MEASURED JET SPREAD

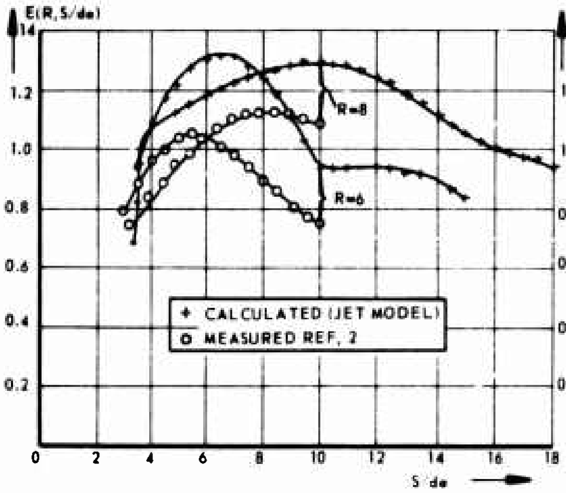

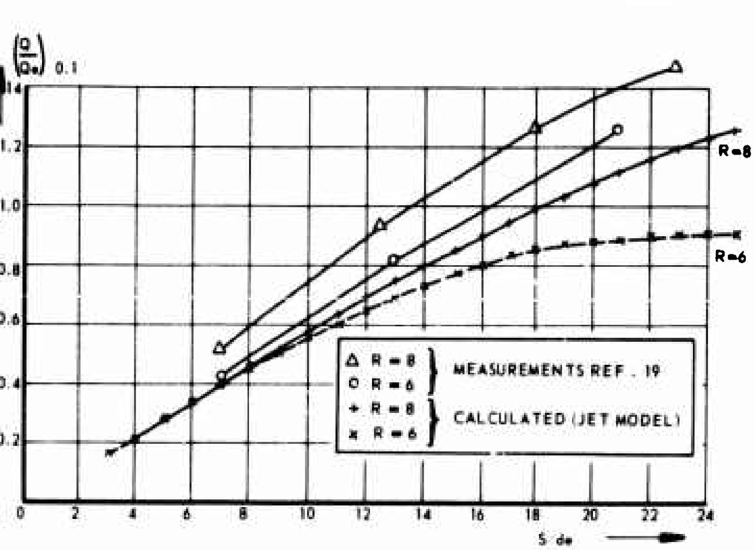

FIG. 7 COMPARISON OF CALCULATED AND MEASURED JET ENTRAINMENT

FIG. 8 COMPARISON OF MEASURED AND CALCULATED JET MASS FLUX

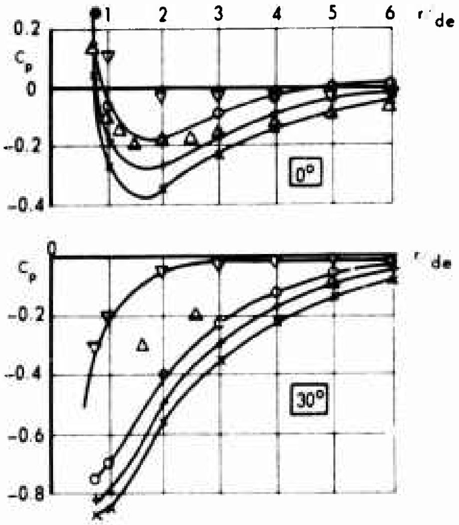

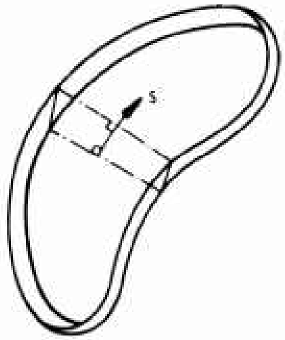

FIG. 9 TYPICAL PANEL STRIP

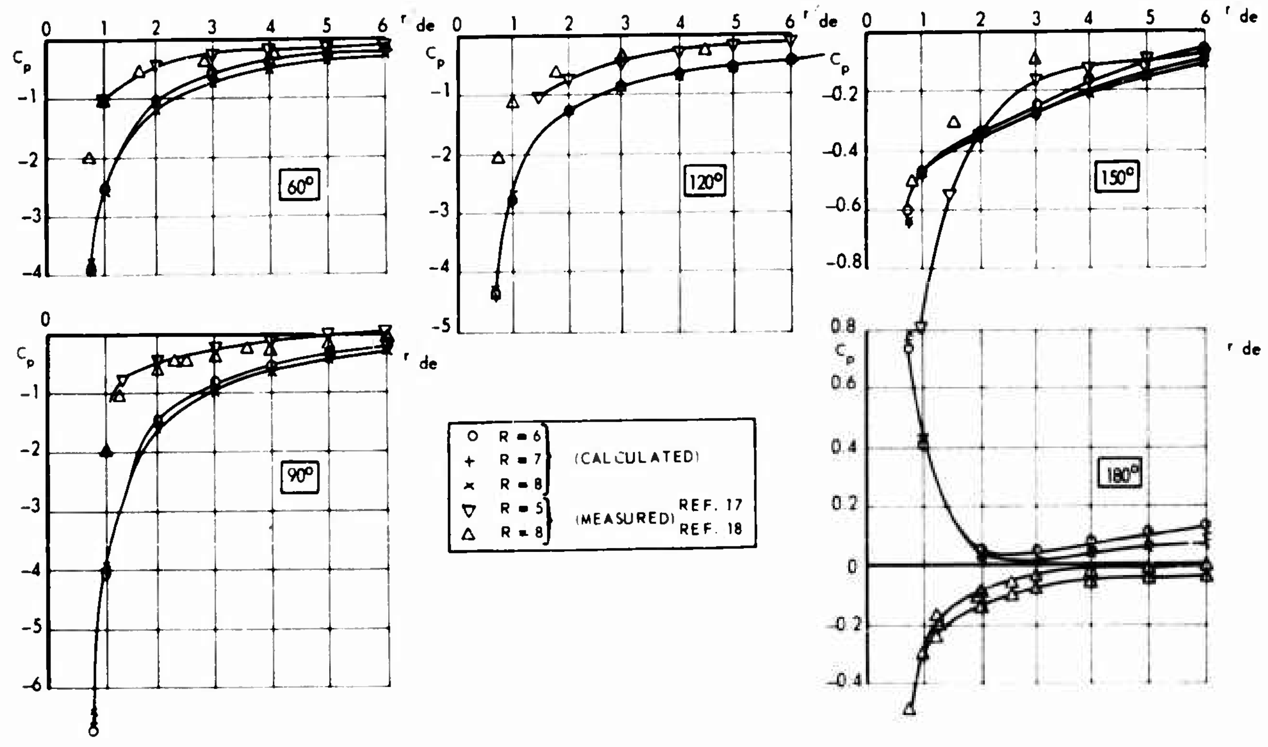

FIG. 10 COMPARISON OF CALCULATED AND MEASURED C_p VALUES ALONG RAYS ON THE PLATE

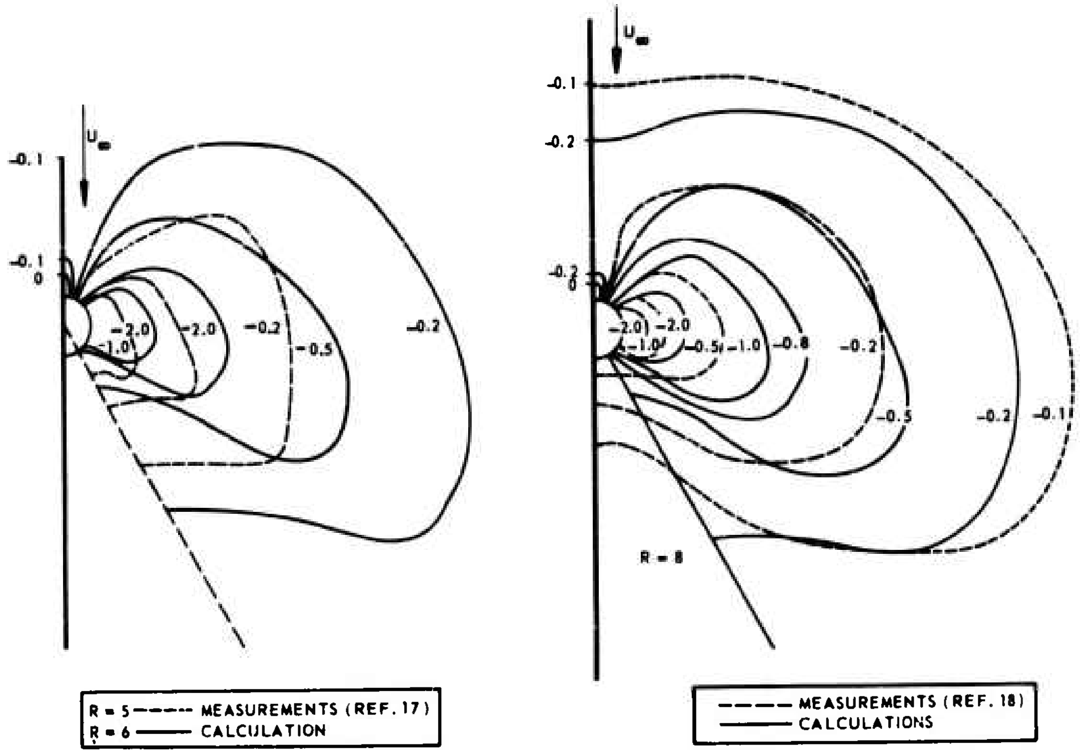

FIG. 11 COMPARISON OF MEASURED AND CALCULATED PRESSURE DISTRIBUTION ON THE FLAT PLATE

DESIGN AND TEST OF EJECTOR THRUST AUGMENTATION CONFIGURATIONS

Dr S L Brown
Mr R D Murphy
Prototype Division
Air Force Flight Dynamics Laboratory
Wright-Patterson AFB, Ohio 45433 USA

SUMMARY

Until recently the application of ejector thrust augmentation (ETA) to VTOL aircraft design has not been practical due to the relatively low augmentation ratios and large volume required for installation. With the development of the hypermixing primary injection nozzle by the USAF Aerospace Research Laboratories, an ETA system has emerged which improved the mixing efficiency and performance over past ejector designs. These encouraging results have prompted the USAF Flight Dynamics Laboratory to investigate the feasibility of incorporating ETA into an operational VTOL aircraft.

Preliminary design studies have been directed towards subsonic and supersonic VTOL close air support fighters. In addition to demonstrating the feasibility of the ETA VTOL aircraft, the studies have served to delineate special problems in the areas of engine cycle characteristics, internal aerodynamics and external aerodynamics.

Two 2-D wind tunnel tests have been conducted to address the external aerodynamic problem areas. The wind tunnel models incorporate a trailing edge ETA system with geometry consistent with current VTOL design schemes. One test investigates the vertical flight mode and the other the transition flight mode. The tests results served to better define the local wing/ejector flow phenomena, build confidence in ejector design and in general validate previously developed design philosophy and methodology.

NOMENCLATURE

A_0 = Primary nozzle exit area (effective)

A_1 = Secondary flow area

A_2 = Throat area

A_3 = Diffuser exit area

C_D = Nozzle discharge coefficient = $\frac{\text{effective area}}{\text{actual area}}$

C_J = Primary blowing coefficient = $\frac{T_J}{q\, S_{Ref}}$

C_L = $L/q\, S_{Ref}$ = Lift coefficient

ΔC_L = $(C_L)_{C_J>0} - (C_L)_{C_J=0}$

$C\mu$ = Gross blowing coefficient = $\frac{T_3}{q\, S_{Ref}}$

D_R = Ejector ram drag

DAR = A_3/A_2 = Diffuser exit area ratio

ETA = Ejector Thrust Augmentation

IAR = A_1/A_0 = Inlet area ratio

L = Diffuser length (distance from A_2 to A_3)

PR = Total pressure ratio (P_{plenum}/P_{amb})

S = Distance between nozzle centerlines

S_{Ref} = Reference Area

T = Thrust

V = Velocity

$\beta = \frac{\int V_3^2\, dA_3}{\bar{V}_3^2 A_3}$ = Mixing parameter

δ_A = Aft diffuser flap angle

δ_F = Forward diffuser flap angle
(VTOL model)

or

Diffuser flap angle (Transition model)

$\bar{\delta}$ = $1/2\ (\delta_F + \delta_A)$ = Mean diffuser angle

η = Nozzle efficiency = $\frac{(V_J)\ \text{Actual}}{(V_J)\ \text{Isen}}$

ϕ = Augmentation ratio

subscripts

$(\ )_3$ - Conditions at the diffuser exit

$(\ )_\infty$ - Free stream conditions

$(\ )_{Isen}$ - Isentropic

$(\ )_J$ - Primary air

1.0 INTRODUCTION

Thrust augmentation has been an appealing, but elusive, concept for many years. The results of a one-dimensional flow analysis as suggested by Von Karman, are enough to encourage any designer of V/STOL aircraft. Unfortunately, when engineers tried to apply the concept, the results were disappointing. The failure to realize the potential could be charged to incomplete mixing between the primary air and secondary air. Efficiencies of these systems were on the order of 25%. There was obviously room for improvement, provided the basic flow phenomenon could be understood and improved.

The Aerospace Research Laboratories (ARL) at Wright-Patterson AFB undertook a program of basic research on thrust augmentation. The results have been significant and are well documented in the open literature (Ref 1-3). The main contribution has been the development of the hypermixing nozzle, which improved the mixing efficiency by an order of magnitude. With the hypermixing primary injection nozzle, an ejector thrust augmentation (ETA) system has emerged yielding higher augmentation ratios with shorter ejector mixing length, thus smaller required volumes. It is now possible to design augmentors of practical dimensions that have an augmentation ratio of 2. These results have prompted a new look at VTOL airplanes with thrust augmentation.

Preliminary design studies incorporating the ARL hypermixing ejector system have been directed to subsonic VTOL close air support fighters. The studies have demonstrated the feasibility of an ETA system and the capability of ETA to compete with other VTOL systems in terms of performance and cost. The combination of the ETA system with a turbojet or turbofan engine is attractive because the ejector effectively increases the bypass ratio, providing increased total gross thrust available for application during the VTOL and STOL mode. The complete synthesis of the engine-ejector system with an airframe can be further utilized to provide favorable aerodynamic effects.

To study the aerodynamic/augmentor interaction, two wind tunnel tests were conducted. A VTOL model was tested to determine lift-off and low speed transition, while a transition model was tested to determine the characteristics of the upper end of the transition envelope.

2.0 WIND TUNNEL MODEL (VTOL)

The VTOL model was designed to assess the lift off and low speed transition phases of flight. The model was configured to emphasize these areas, which included verifying some new design concepts as well as identifying problem areas. The testing was conducted in the 7 x 10 low speed tunnel at NASA Ames.

The wind tunnel model was a two-dimensional, constant chord design with the augmentor assembly extending aft from the 34% chord line. The major components are identified in Figure 1, and the installed model is shown in Figure 2. The span was 30 in., the chord with the flaps up, clean configuration was 44.5 in., and the maximum thickness was 10%. There were ten hypermixing nozzles spaced on 3 in. centers. The large end plates provided a quasi-2D test arrangement.

A fundamental parameter for augmentors is the ratio of secondary area to primary area, denoted by IAR. The secondary area is that area open to the entrained air at the plane of injection of the primary nozzles. For the VTOL model, the geometric measurement is IAR = 21.55. The ten primary nozzles accounted for 83.3% of the internal air, the diffuser wall BLC accounted for 16.7% internal air, while the end wall blowing was variable, with blowing adjusted to insure attached flow.

The hypermixing nozzles were positioned with the thrust vector 90° to the wing chord plane to maximize VTO thrust. Primary high pressure air was supplied to the nozzles and BLC slots from the plenum in the forward wing.

The diffuser was formed by the forward and aft flap doors, which could be moved through the range $45° \le \delta \le 90°$ and $1 \le DAR \le 2.1$. These positions allowed simulation of VTOL and transition operation.

2.1 Nozzle Calibration

A hypermixing nozzle is basically a convergent nozzle with a rectangular exit. The exit is designed to create streamwise vorticity to enhance the mixing in the diffuser. For manufacturing simplicity, the nozzles were two-dimensional, resembling a constant chord wing, with the exit at the trailing edge. The exit was configured to a typical hypermixing design. The external shape of the nozzle conforms to the thickness distribution of a NACA 64 series airfoil. The 2-D design was selected to simplify manufacturing and to provide a passage for air from the plenum in the forward wing to the aft manifold. This arrangement supplied air to the BLC slots on the aft manifold without the requirement of a separate plenum supply.

The new nozzle design required a calibration test to demonstrate adequate efficiency. Efficiencies were determined as a function of plenum pressure ratio. The results are shown in Figure 3, and they indicate an increasing efficiency with PR. The effective area also shows an increase with PR.

2.2 Static Performance

The parameter governing VTOL performance is the static augmentation, defined by

$$\phi = \frac{T_{augmented}}{T_{primary}}$$

The value of T_{aug} and ϕ must be sufficiently large to insure lift-off with an adequate margin for acceleration and control. Of the several parameters that affect static augmentation, this test examined pressure ratio, exit/throat area, diffuser length/nozzle spacing, and mean diffuser angle.

The pressure ratio of an ETA system is an important parameter because it impacts augmentor performance, internal volume, and engine selection. Figure 4 shows the variation of ϕ with PR for several DAR. The open symbols indicate the performance of the basic configuration, which had some surface roughness at the flap hinge, while the solid symbols indicate improved performance after careful smoothing of the flap hinge. The measurements indicated that the maximum augmentation occurs at a moderate PR range of 1.5 to 1.7 with ϕ decreasing significantly at higher PR. This trend is unfavorable, since PR > 2 is desirable to minimize internal volume. The solid symbols indicate the importance of BLC in maintaining high values of ϕ.

Sufficient diffuser length is necessary for the flow to mix and diffuse, but design constraints may limit the actual length allowed. Previous work (Ref 4) has shown that a governing parameter is L/S.

Measurements were made with L/S = 5 and L/S = 10. The differences in diffuser performance are most clearly seen in Figure 5, which shows a comparison of exit velocity profiles.

The diffuser flow can be quantified with the parameter β, defined in Ref 4 as $\beta = \dfrac{\int V_3^2 \, d\, A_3}{\bar{V}_3^2 \, A_3}$

The spanwise velocity distribution was assumed constant, so that β was evaluated only for the chordwise variation in V_3. The L/S = 5 configuration had a maximum value of $\beta = 1.121$, while the L/S = 10 configuration had an improvement to $\beta = 1.072$. The ideal case is $\beta = 1$, while previous work indicates $\beta = 1.03$ is a practical lower limit. These numbers suggest that further improvement is possible.

One dimensional flow theory (Ref 6) indicates a dependence of augmentation on DAR. Fig 6 shows that the model performance at PR = 1.3 reflects this dependence but at a lower level of augmentation than predicted. The theoretical prediction is based on the methodology of Ref 11, which assumes viscous losses based on ARL data. This data shows the impact of the losses indicated by the β parameter.

Although the nozzles were fixed at 90°, the diffuser flaps could be rotated so that the mean diffuser angle $\bar{\delta} < 90°$. This configuration would simulate the low speed phase of transition. The results are shown in Figure 7 for the L/S = 5 case only. The first observation to be made is that ϕ varies linearly from $\bar{\delta} = 90°$ to $\bar{\delta} = 50°$. The second observation is that DAR is still a significant parameter. About any given mean angle, it is possible to vary DAR, which implies diffusion while turning. The set of 3 solid points applies to a configuration with δ_A varied to change DAR. A relative maximum occurred with DAR = 1.2, while DAR = 2.0 resulted in minimal performance. These two observations would suggest that diffusion and augmentation is possible without the primary flow vector aligned with $\bar{\delta}$.

2.3 Forward Speed Performance

The lifting characteristics at forward speed are of prime importance for the transition maneuver and STOL operation. The configuration was tested with short doors, giving an L/S = 5 and hence less than maximum augmentation. This compromise was necessary because of tunnel wall restriction. The test results are shown as a function of the primary blowing coefficient. Most of the testing was conducted at V = 60 kts (q = 12 psf) with a few selected points at higher speeds.

Figure 8 shows typical lifting characteristics for various values of the blowing coefficient. There is no evidence of stall, even at the high angles of attack that may be required for transition. An important feature of an augmentor wing in transition is the supercirculation caused by the jet sheet at the trailing edge. Supercirculation creates a ΔC_L. This parameter is plotted in Figure 9 for various flap settings. There is additional circulation on the ETA wing since ΔC_L is greater than the vectored component of C_J for all cases; however, the augmentor wing did not perform at the level predicted by potential theory for jet flaps (Ref 8). These results indicate improvement should be made in the diffuser flap design for transition. It is possible that ΔC_L might exceed the theoretical level, since C_J may be augmented. However, the value of ϕ at forward speed was not determined, so a true theoretical upper limit was not established. Figure 10 shows a typical streamline pattern, and illustrates the complexity of the flow. Because the stagnation point is inside the inlet, the flow is required to negotiate severe pressure gradients to turn approximately 240°. This problem illustrates the compromise required between designing for VTOL and STOL. The VTOL model had an inlet optimized for the static, lift-off case. To have an ETA wing that will operate effectively from lift-off through transition, the aft inlet and flap may require a redesign, and possibly some BLC to insure adequate performance for transition.

3.0 WIND TUNNEL MODEL (TRANSITION)

The transition model was designed to assess the ejector wing characteristics during the final stages of the transition mode and conversion to conventional flight. Three flight modes were investigated; cruise, flaps down (ejector power off) and full power lift. The wing was tested from static conditions to 165 FPS, through the angle of attack range of -10° to +32° and with a variation in ejector primary pressure ratio from 1.0 to 2.25. The test was conducted in the Lockheed-Georgia low speed wind tunnel and served to determine: (a) the performance of the ejector at static and forward speed conditions; and (b) the aerodynamic characteristics of the wing-ejector combination.

3.1 Model Configuration

The transition model was a large two-dimensional wing with a span of 76.5 inches, a chord of 60 inches and a thickness to chord ratio ($^t/c$) of 15%. The airfoil section was a 747a to 40%C and 0015-34 to the trailing edge with 2.23% camber. It was mounted between two circular metric end plates of 6.5 ft diameter. These end plates had four tangential blowing slots which provide two-dimensional results.

The ejector bay was full span with a 5 in width (Figure 11). The centerline of the ejector bay was inclined 60° to the wing chord plane. There were 30 hypermixing nozzles spaced on 2.5 inch centers. Nozzles at the ends of the ejector bay are placed with their centers 2 inches from the end plates. The straight walled, constant area mixing section extended 2.1 inches below the hypermixing nozzle exit plane. Primary airflow was introduced into the ejector through the hypermixing nozzles and two boundary layer control (BLC) slot nozzles running the full span of the wing. One slot nozzle was at the top of the forward side of the inlet and the other was located at the bottom of the aft side of the mixing section. The nominal inlet area ratio was 18.5 with 77% of the flow going to the hypermixing nozzles and 23% to the BLC slots (8% inlet and 15% diffuser).

The model had three flow systems which were fed from both sides of the model. These flow systems fed the hypermixing nozzles, the inlet BLC and the diffuser BLC independently. All feed ducts were designed such that the duct Mach number never exceeded 0.25.

The flap system was composed of an aft flap, which was similar to a conventional simple flap, and a forward flap which was hinged at the ejector bay exit. The forward flap when closed covered the ejector and when deflected, formed the ejector diffuser wall. The reference flap setting of the system was based only on the aft flap angle for all diffuser exit area ratios. For variation of DAR, the diffuser door was modulated. For this test, the variation of DAR was 1.4 to 2.0. A leading edge slat positioned at 60° to the wing chord was also tested.

To complete the two-dimensional aspects of the test, the wing and end plates were mounted between two large non-metric wall sections built inside the tunnel. Figures 12 and 13 show the model mounted between these false walls. The walls completely span the tunnel from floor to ceiling and were 28 feet long. The model support struts, ducting and instrumentation were all located inside these walls so that no airloads were transmitted to the balance.

3.2 Nozzle Calibration

The hypermixing nozzles used in this test were the same as those used by ARL in past ejector research (references 1-5). The exit areas were increased slightly to produce the inlet area ratio of 18.5. The hypermixing nozzle and the calibration facility are shown in Figures 14 and 15. The hypermixing nozzle calibration plot is shown in Figure 16. The velocity efficiency (η) is shown to vary from .93 to .95. This velocity coefficient compares reasonably well to past hypermixing designs. The discharge coefficient is .905.

The effective exit area of the inlet and diffuser BLC slots was 1.45 sq in and 3.00 sq in respectively. These areas yielded a total effective exit area of 19.57 sq in which produced an inlet area ratio of 18.65.

3.3 Static Performance

The measure of performance for the static tests was the gross augmentation ratio. The augmentation levels for this transition model were obtained by integrating pressures from 14 pressure rakes mounted at the ejector exit and dividing by the product of measured mass flow and isentropic velocity.

$$\phi\text{Gross} = \frac{\text{FORCE (RAKE DATA)}}{\dot{m}_{\text{MEASURED}} \times V_{J_{\text{ISENTROPIC}}}}$$

Seven of these rakes were suspended from the flap while the remainder were mounted from the door as shown in Figure 13.

Figure 17 shows the gross augmentation for a pressure ratio of 1.87, flap settings of 20° and 30° and various diffuser exit area ratios. The predicted augmentation is also shown in this figure. The 5-7% difference in augmentation is attributed to the flow non-uniformity. Predicted augmentations are based on $\beta = 1.03$; the β values for this ejector configuration are 1.28 for the 20° flaps and 1.055 for the 30° flap, as shown in Figures 19 and 20.

The variation of augmentation at a constant diffuser exit area ratio with pressure ratio is depicted in Figure 18. The trend of increasing augmentation ratio with pressure ratio does agree with the predicted trend; however, it is contrary to that observed with the VTOL model.

3.4 Forward Speed Performance

The performance of the augmentor wing with forward velocity is considered from two aspects; ejector performance alone and total wing characteristics. Both of these areas are critical when evaluating the transition characteristics.

Since the ejector acts as both a thrust and lift augmentor, it is important to understand the ejector geometries required to optimize both of these parameters. Consider the following:

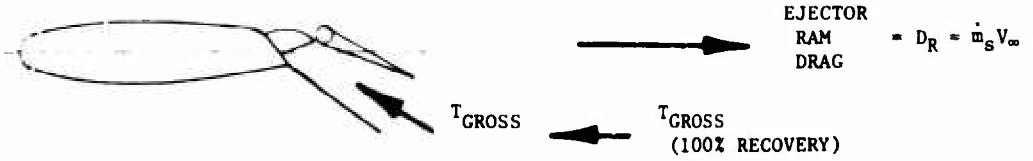

$$\phi\ \text{NET} = \text{NET AUGMENTATION} = \phi\ \text{GROSS} - \frac{D_R}{\dot{m}_{\text{MEASURED}} \times V_{J_{\text{ISENTROPIC}}}}$$

$$C_\mu = \frac{T_{\text{GROSS}}}{q\ S_{\text{Ref}}}$$

Consider first the requirement to optimize lift (i.e., gross augmentation). Figure 21 shows the variation of gross augmentation with diffuser exit area ratio and forward velocity at an angle of attack of 1° and a flap angle of 30°. A cross-plot of figure 21 showing the relationship of (maximum gross augmentation) and gross augmentation at DAR = 1.9 for various velocities is shown in figure 22. Also, shown in this figure is the same relationship for an angle of attack of 10° to 21°. A summary plot of gross augmentation at a velocity of 100 and 150 FPS is shown in figure 23. In all cases, it is clear that a constant diffuser exit area ratio of 1.9 yields essentially the optimum value of gross augmentation.

Consider now the optimization of forward thrust or net augmentation. Figure 24 shows the variation of net augmentation for 30° flaps at various velocities and diffuser exit area ratios. Figures 25 and 26 again show that a diffuser exit area ratio of 1.9 is very close to the condition for maximum net augmentation.

These results show that for this ejector configuration and a flap setting of 30° there will be very little compromise between achieving optimum horizontal thrust (i.e., net augmentation) and lift (i.e., gross augmentation) while holding a constant diffuser exit area ratio. This capability would eliminate the requirement of a complicated mechanical programming of DAR as the aircraft goes through transition geometry and attitude changes.

To show the total wing characteristics, the lift, force and moment polars are shown in Figures 27, 28 and 29 for a constant diffuser exit area ratio of 1.8. The blowing coefficient (C_μ) is equal to the gross thrust (rake data) divided by q S. It should be noted that the C_μ's show on the polars are at $\alpha = 1°$ and vary slightly with α. The nominal jet deflection angle is also slightly different from the flap deflection angle.

4.0 CONCLUSIONS

The results of these tests can be summarized as follows:

1. It is feasible to design a wing with a high performance trailing edge ETA system for a VTOL aircraft. The air supply, nozzles, and diffuser can be contained within the mold lines of a conventional airfoil section.

2. Static augmentation on the order of that achieved by ARL is possible in an aircraft configuration if sufficient BLC is provided. Growth of the boundary layer due to surface roughness decreases augmentation significantly.

3. For the transition flap setting of 30° both the optimum thrust (i.e., net augmentation) and lift (i.e., gross augmentation) can be achieved at a constant diffuser exit area ratio. This affords the potential of developing a system which does not require modulation of the ejector configuration to achieve maximum performance.

4. In both tests, performance decreased from the predicted levels with an increase in forward velocity. This was due to having a fixed inlet optimized for static conditions. A design compromise to obtain an inlet that is satisfactory for $V_\infty > 0$ may result in a loss of static performance.

REFERENCES

1. Quinn, B., "Compact Ejector Thrust Augmentation." Journal of Aircraft, Vol 10, No 8, August 1973, pp 481-486.

2. Fancher, R B., "Low Area Ratio, Thrust Augmenting Ejectors," Journal of Aircraft, Vol 9, No 3, March 1972, pp 243-248.

3. Eastlake, C N., "The Macroscopic Characteristics of Some Subsonic Nozzles and the Three-Dimansional Turbulent Jets They Produce," Rpt. ARL 71-0058, (AD 728-676), 1971, Aerospace Research Lab., Wright-Patterson AFB, Ohio.

4. Quinn, B, "A Simple Estimate of the Effect of Ejector Length on Thrust Augmentation," Journal of Aircraft, Vol 10, No 5, May 1973, pp 313-314.

5. Bevilaqua, P M, "An Evaluation of Hypermixing for V/STOL Aircraft Augmentors," AIAA Paper 73-654.

6. McCormick, B W, Aerodynamics of V/STOL Flight, Academic Press, New York, 1967.

7. NASA SP-320, "STOL Technology."

8. Spence, D A, "The Lift on a Thin Airfoil with a Jet-Augmented Flap," The Aeronautical Quarterly, Aug 1958, pp 287-299.

9. Chan, Y Y, "Lift Induced by Suction Flaps on Augmentor Wings," C.A.S.I. Transactions, Aug 1969.

10. Streiff, H G, Ashby R, Krishnamoorthy, V "A Two Dimensional Test of a Single Bay Cold Thrust Augmentation Ejector Wing," AFFDL-TR-74-4.

11. Nagaraja, K S, Hammond, D L, Graetch, J E, "One-Dimensional Compressible Ejector Flows," AIAA/SAE 9th Propulsion Conference, Nov 1973.

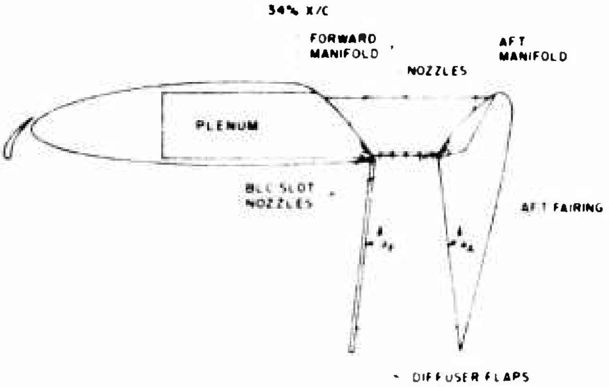
34% X/C
FORWARD MANIFOLD
NOZZLES
AFT MANIFOLD
PLENUM
BLC SLOT NOZZLES
AFT FAIRING
DIFFUSER FLAPS

FIGURE I VTOL AUGMENTOR WING CROSS SECTION

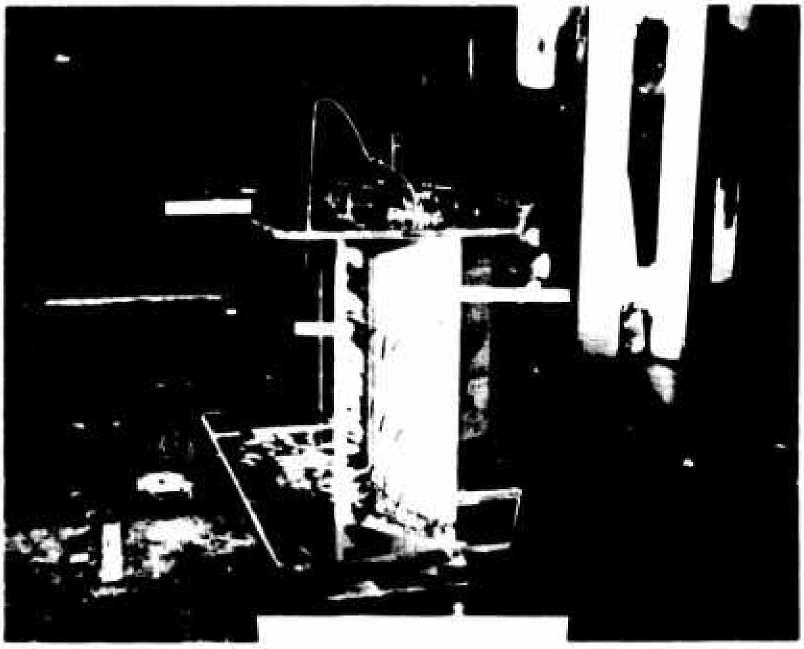

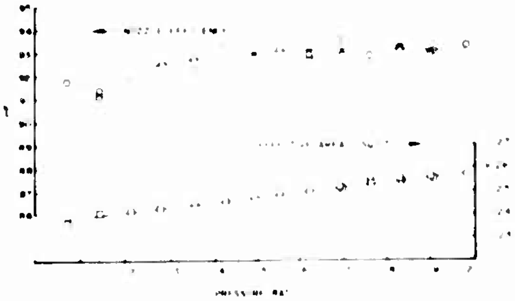

FIGURE 3 NOZZLE CALIBRATION

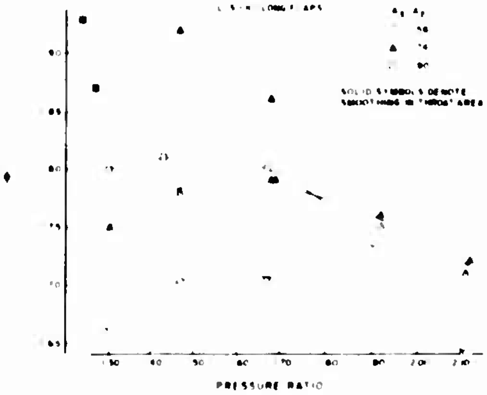

FIGURE 4 STATIC AUGMENTATION

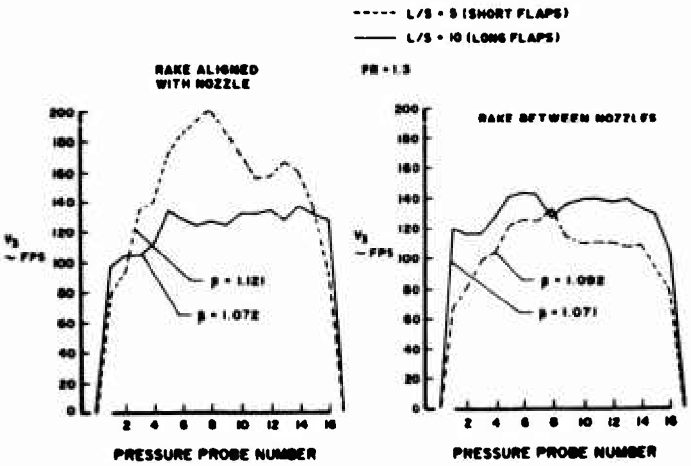

FIGURE 5 VELOCITY PROFILES-DIFFUSER EXIT

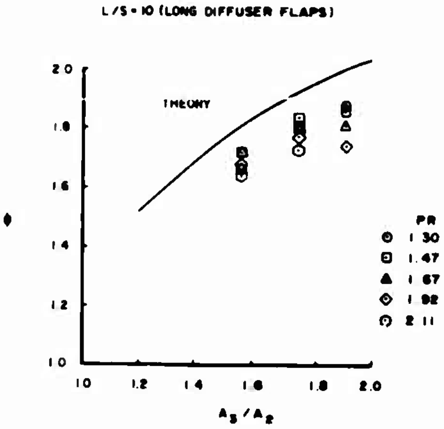

FIGURE 6 STATIC AUGMENTATION

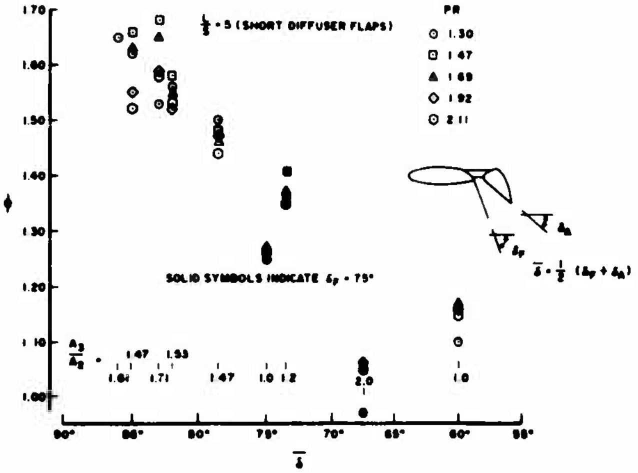

FIGURE 7 OFF-ANGLE STATIC AUGMENTATION

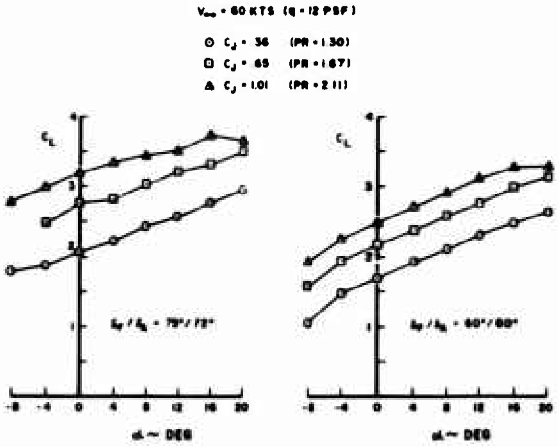

FIGURE 8 CONSTANT SPEED LIFT COEFFICIENTS

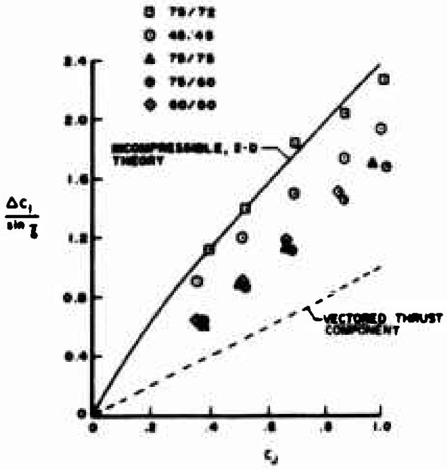

FIGURE 9 LIFT INCREMENT DUE TO BLOWING

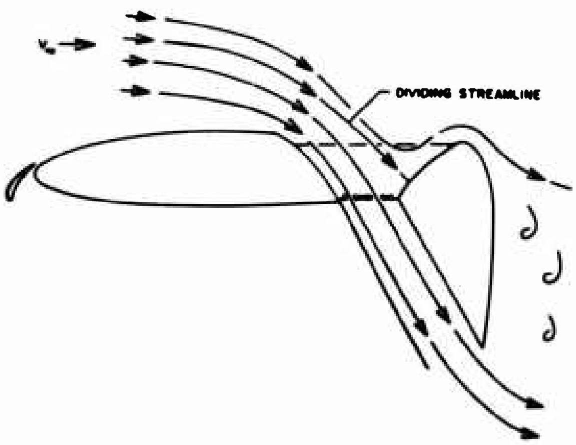
V_∞
DIVIDING STREAMLINE

FIGURE 10 FORWARD SPEED STREAMLINE PATTERN

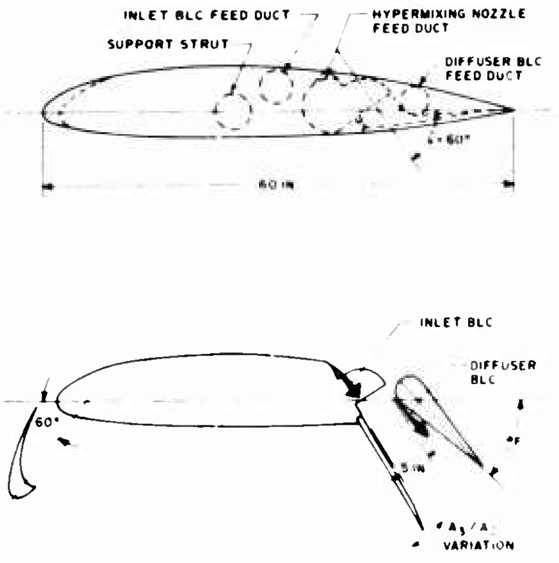
INLET BLC FEED DUCT
HYPERMIXING NOZZLE FEED DUCT
SUPPORT STRUT
DIFFUSER BLC FEED DUCT
δ = 60°
60 IN
INLET BLC
DIFFUSER BLC
60°
δF
5 IN
A_3/A
VARIATION

FIGURE 11 TRANSITION MODEL CONFIGURATION

FIGURE 12 END WALLS

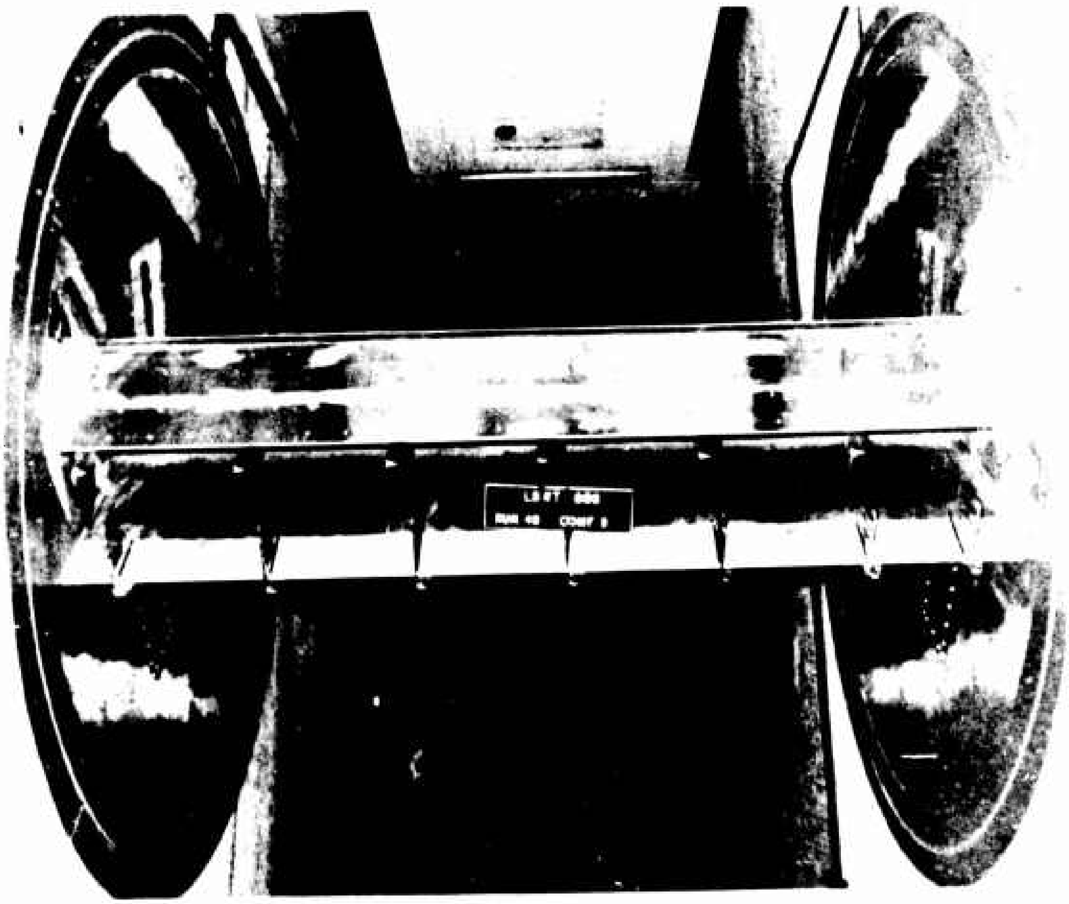

FIGURE 13 DIFFUSER (AFT VIEW)

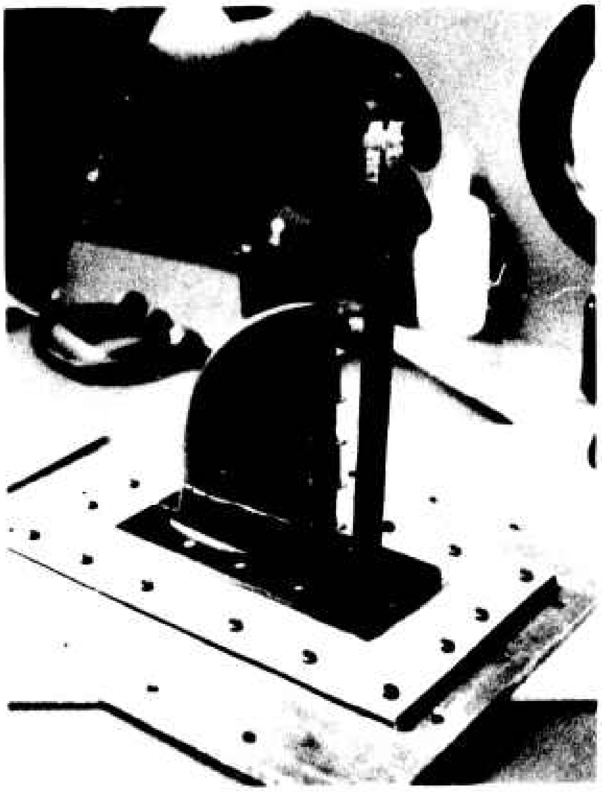

FIGURE 14 HYPERMIXING NOZZLE

FIGURE 15 CALIBRATION RIG

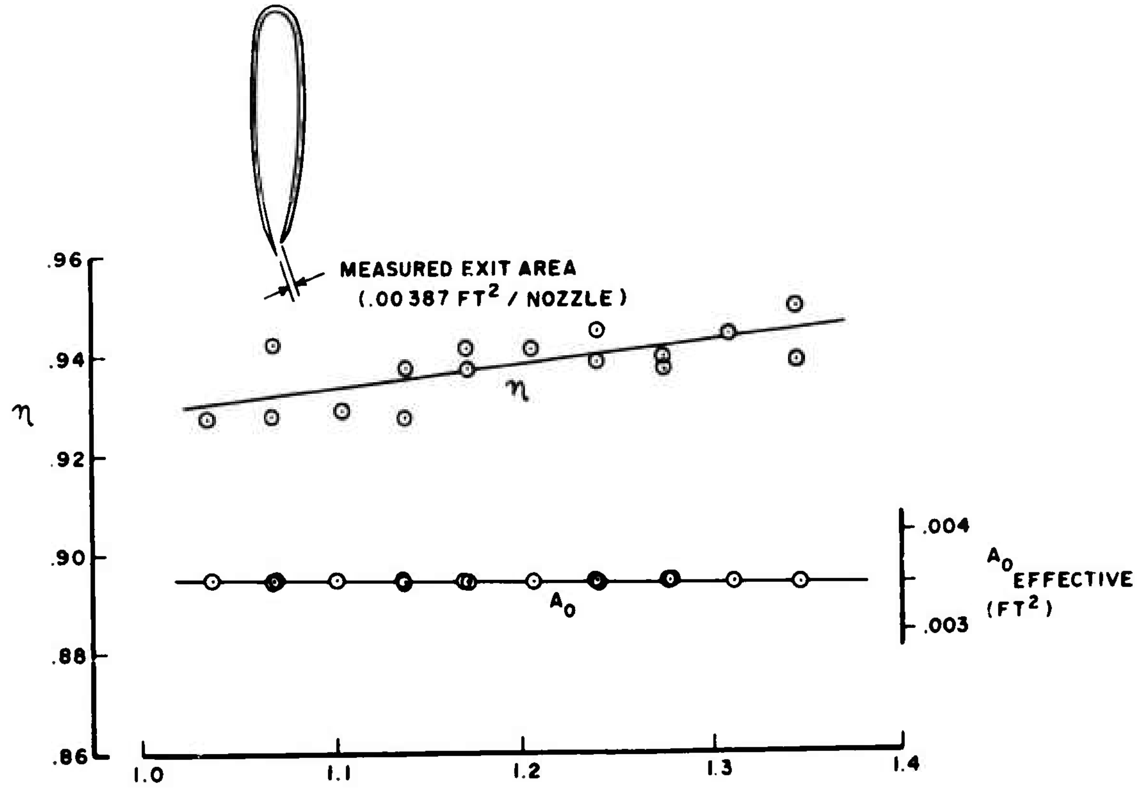

FIGURE 16 NOZZLE CALIBRATION (VELOCITY EFFICIENCY)

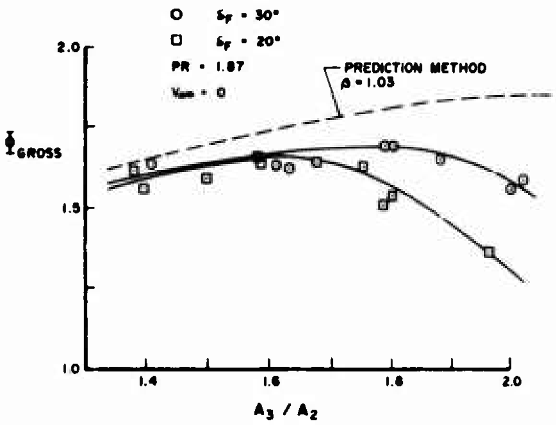

FIGURE 17 VARIATION OF AUGMENTATION WITH DIFFUSER EXIT AREA RATIO

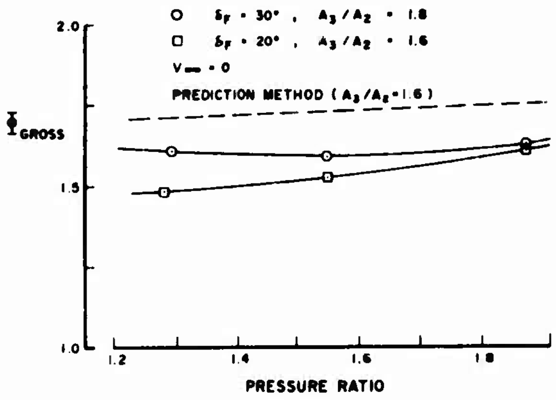

FIGURE 18 VARIATION OF AUGMENTATION WITH PRESSURE RATIO

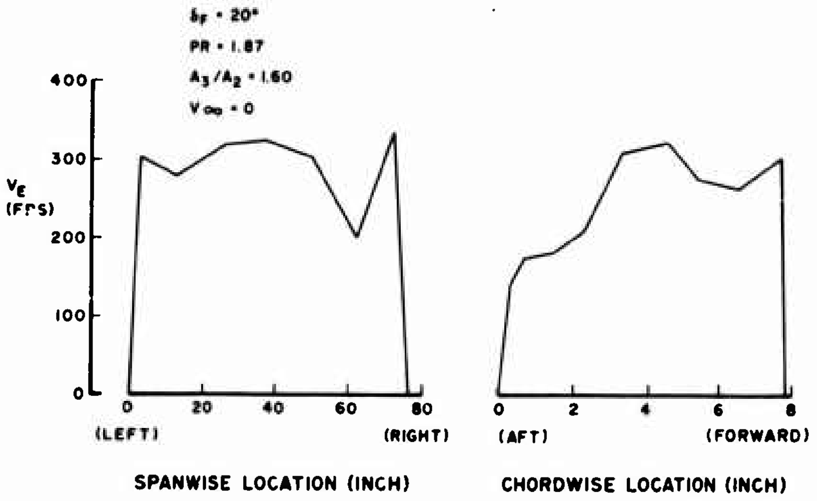

FIGURE 19 DIFFUSER EXIT VELOCITY DISTRIBUTION (δ_F = 20°)

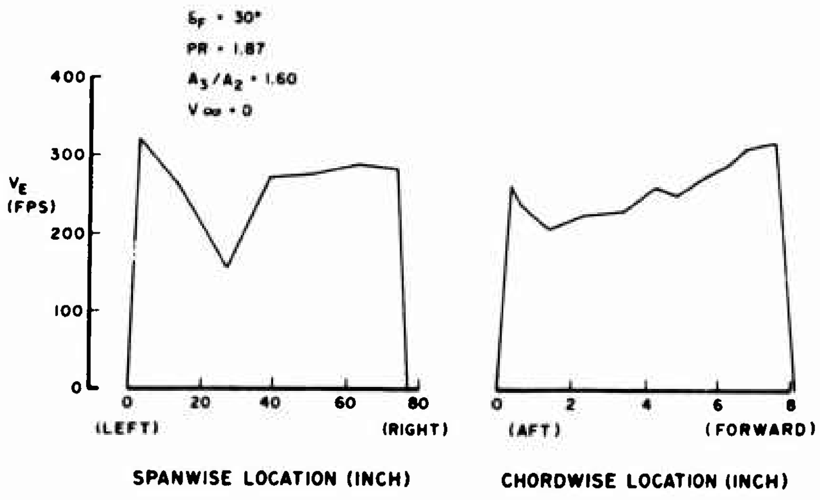

FIGURE 20 DIFFUSER EXIT VELOCITY DISTRIBUTION (δ_F = 30°)

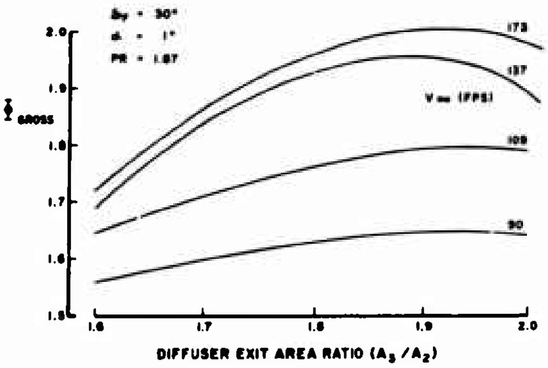

FIGURE 21 EFFECT OF VELOCITY ON GROSS AUGMENTATION

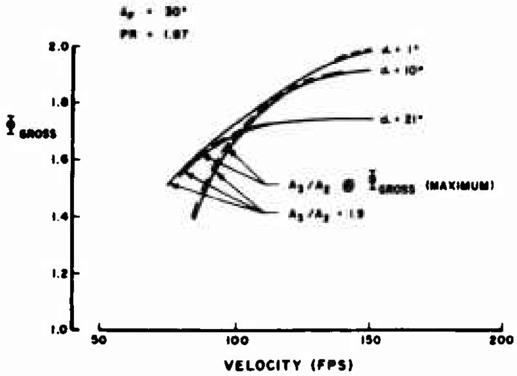

FIGURE 22 OPTIMUM AUGMENTATION

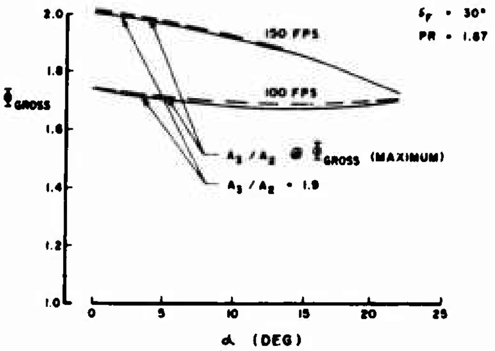

FIGURE 23 EFFECT OF ANGLE OF ATTACK ON AUGMENTATION

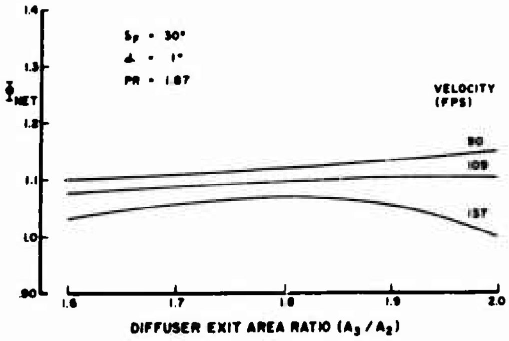

FIGURE 24 EFFECT OF VELOCITY ON NET AUGMENTATION

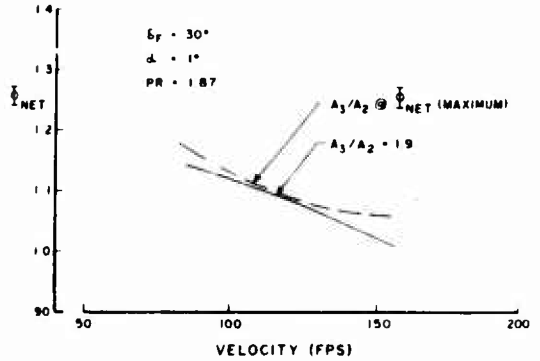

FIGURE 25 OPTIMUM NET AUGMENTATION AT α = 1°

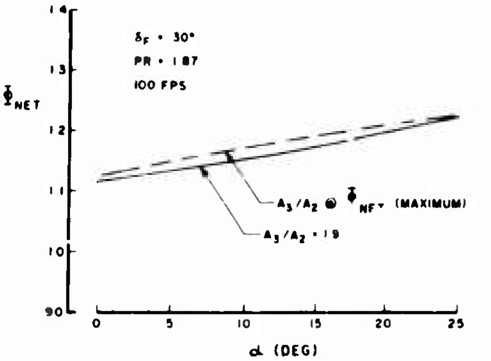

FIGURE 26 EFFECT OF ANGLE OF ATTACK ON NET AUGMENTATION

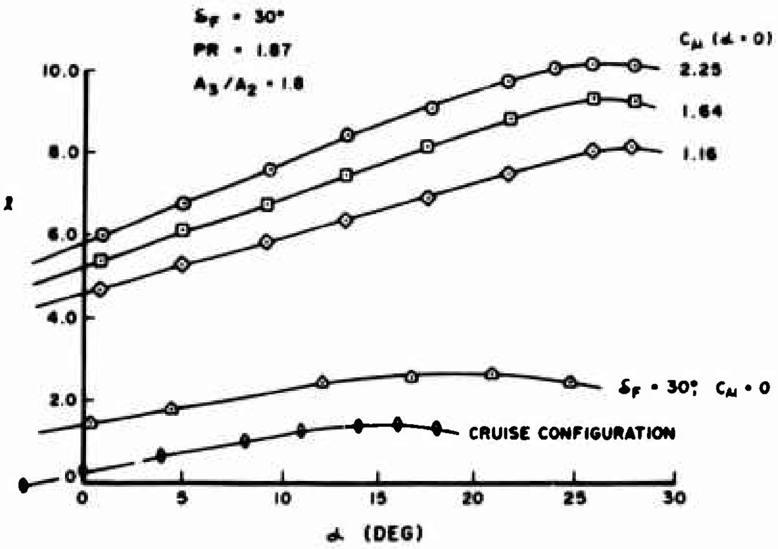

FIGURE 27 LIFT POLAR ($\delta_F = 30°$)

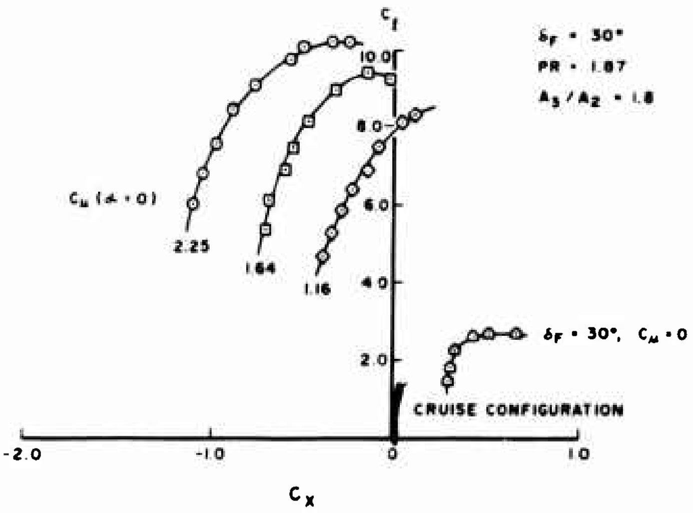

FIGURE 28 FORCE POLAR ($\delta_F = 30°$)

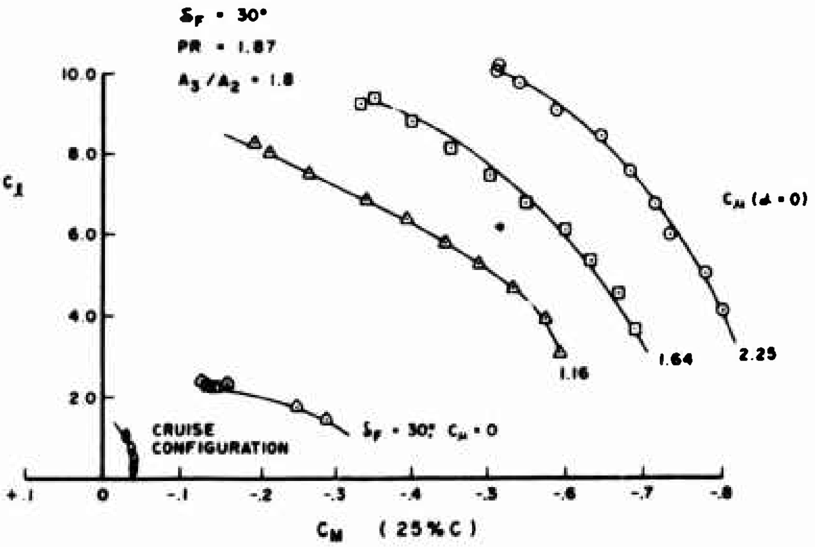

FIGURE 29 MOMENTS ($\delta_F = 30°$)

GROUND EFFECT ON AIRFOILS WITH FLAPS OR JET FLAPS

by

K. Gersten, R. Löhr, E. Beese

Ruhr-Universität Bochum, Germany

SUMMARY

The two-dimensional incompressible flow past airfoils with flaps or jet flaps near ground is investigated. The inviscid flow is calculated by potential theory methods. It is shown, that the nonlinear effects due to larger angles of attack and flap angles become increasingly important for airfoils approaching the ground. In the study these nonlinear effects are therefore emphasized. For the airfoils with jet flaps wind tunnel measurements including ground simulation have been carried out. The theoretical results are compared with the experiments and with linear theory.

RESUME

Des recherches ont été effectuées sur l'écoulement bidimensionnel d'un fluide incompressible autour de profils d'ailes à volet ou à jet au voisinage du sol. L'écoulement non visqueux est calculé par l'application de méthodes déduites de la théorie potentielle. On démontre que les effets nonlinéaires résultant d'angles d'incidence et de volets élevés gagnent en importance pour des ailes s'approchant du sol. En conséquence, cette recherche s'interesse plus particulièrement à ces effets nonlinéaires. Des mesures en soufflerie, sur des profils d'ailes à jet, incluant les effets de sol, ont été effectuées. On compare les résultats théoriques aux résultats expérimentaux et à ceux de la théorie linéaire.

NOTATION

b	wing span
c	wing chord
c_μ	jet momentum coefficient, $c_\mu = 2J/\rho U_\infty^2 cb$
c_L	lift coefficient, $c_L = 2L/\rho U_\infty^2 cb$
c_M	moment coefficient, $c_M = 2M/\rho U_\infty^2 c^2 b$
c_R	rudder moment coefficient, $c_R = 2M_R/\rho U_\infty^2 c^2 b$
$F(\bar{x}), F_n(\bar{x})$	functions in Eq.(13)
f_n	coefficients in Eq.(13)
$G(\bar{x}), G_n(\bar{x})$	functions in Eq.(14)
g_n	coefficients in Eq.(14)
h	ground distance
J	jet momentum
L	lift
M	pitching moment, cf.Figs.4, 5 and 9
M_R	rudder moment, cf. Fig.4
N	number of vortices
N_F	number of vortices located on the flap

U_∞	free-stream velocity
$\bar{u}$	induced velocity component in x-direction
$\bar{v}$	induced velocity component in $\bar{y}$-direction
x	coordinate in airfoil chord direction
$\bar{x}$	nondimensional horizontal coordinate, $\bar{x} = x/c \cos\alpha$, cf. Figs.1 and 7
y	coordinate perpendicular to airfoil chord
$\bar{y}$	nondimensional vertical coordinate cf. Figs.1 and 7
Y, Y_n	functions in Eq.(15)
y_n	coefficients in Eq.(15)
$\bar{y}_j(\bar{x})$	location of the jet, cf. Fig.7
α	angle of attack
Γ	vortex strength
γ	vortex distribution
γ_c	vortex distribution on the airfoil
γ_j	vortex distribution on the jet
η	flap angle, cf. Fig.1
η_j	jet angle, cf. Fig.7
λ	ratio of flap chord to airfoil chord

1. INTRODUCTION

To calculate forces and moments on wings inviscid theory is usually being applied. Very often the further assumption is made that the angle of attack is small. This assumption leads to a strongly simplified vortex model used in potential theory to calculate the flow past wings. For wings with flaps usually the corresponding assumption of small flap angles is being made.

When wings near ground are considered the assumption of small angles of attack and small flap angles is not as good as for wings far from ground. This has the following reason. If the assumption of small angles of attack and flap angles is used the vortex sheet which represents the wing is usually located in a plane parallel to the ground. For larger angles this simplified vortex model is not any more sufficient and the vortices have to be located at the wing itself and on the flap. Due to this more complicated vortex model in which the vortices are not located in one plane nonlinear effects will result. It can be easily understood, that the exact location of the vortices becomes more important when the wing is approaching the ground.

The purpose of this investigation is to study the nonlinear effects due to large angles of attack and large flap angles for airfoils with flaps or jet-flaps near ground. To simplify the problem only two-dimensional flows around airfoils are considered. Thickness and camber of the airfoils are assumed to be zero. Two different problems are investigated:

1. The flat plate with flaps. In this case the following geometrical parameters are studied: The flap chord ratio λ, defined as the ratio of the flap chord to the main chord, the angle of attack α, the flap angle η, and the relative ground distance h/c.
2. The flat plate with jet flap at the trailing edge. In this case the following parameters are considered: The jet angle η_j, the angle of attack α, the jet momentum coefficient c_μ and the relative ground distance h/c.

The two problems are considered separately because in both cases different methods of potential theory are being used to calculate forces and moments on the airfoils. The aim is, to find out what the nonlinear effects due to large angles of attack and flap angles will be, if the airfoil approaches the ground.

2. AIRFOILS WITH FLAPS NEAR GROUND

2.1. The vortex lattice model

The forces and moments on the airfoils with flaps near ground have been calculated by using the vortex lattice method. This method is quite commonly used for calculating the three-dimensional flow past wings of finite span, [1] - [5], or more complicated three-dimensional wing - body combinations, [6]. In this method the airfoil is represented by a number of discret single vortices which are properly distributed along the chord of the wing (see Fig. 1). This proper distribution of the vortices is chosen on the basis of the so-called Pistolesi theorem. After this theorem the whole chord is broken into N subintervals and in the one-quarter-points of the intervals single vortices are located. The three-quarter-points of all subintervals are then used as sensing points in which the kinematic flow condition has to be satisfied. In other words, in these sensing points the flow velocity induced by all vortices combined with the free-stream velocity U_∞ has to be parallel to the airfoil or flap surface.

It is well known that for this particular choice of vortex and sensing points the coefficients for lift and pitching moment of a flat plate at angle of attack is given correctly by this vortex lattice model independently of the number of vortices N. In Fig. 2 it is shown that for increasing number of vortices the exact solution for the flat plate vortex distribution is well approached. In the same figure another vortex distribution is shown for a flat plate near ground. This case, which corresponds to an angle of attack of 90° and ground distance equal to zero, can be solved analytically. Comparison between vortex lattice method and exact analytical solution is quite satisfactory. The lift coefficients given in the table of the figure show the tendency towards the exact values for increasing number of vortices.

2.2. The vortex lattice method for airfoils with flaps

For airfoils with flaps the question arises how to choose the location of the vortex points and sensing points. In this study the flap and the rest of the airfoil have been considered as two different systems to which the usual vortex lattice method is applied separately. In other words the flap is broken into $N_f = 0{,}5\ N$ equal subintervals and for each of them the Pistolesi theorem is applied. In the same way the rest of the airfoil is broken into $N - N_f = 0{,}5\ N$ equal subintervals and the Pistolesi theorem is applied again. N is always an even number. In order to check this particular choice of vortex points and sensing points the vortex distribution of an airfoil with flaps but without ground has been calculated by the vortex lattice method and compared with the analytical solution found by conformal mapping, [7], [8], see Fig. 3. Although there is a systematic deviation from the exact solution even for a very large number of vortices, the total lift is determined very accurately as can be seen from the table in the figure.

In the following calculations the particular arrangement of vortex and sensing points in the vortex lattice method described above has been used. The coefficients for the total lift, the pitching moment and the rudder moment have been calculated for different flap configurations and flap angles, and in Fig. 4 these values are compared with the analytical solutions found by Keune [7], [8]. The figure shows very good agreement for all lift coefficients. The pitching moment is sufficiently well represented for flap angles less than $\eta = 30^\circ$. For larger flap angles deviations in the moment coefficient appear. Good agreement are found again for the rudder moment coefficients. In general, this particular application of the Pistolesi theorem to airfoils with flaps is working sufficiently well for most practical purposes.

2.3. Ground effect for airfoils with flaps

By using the nomenclature given in Fig. 1 for an airfoil with a flap the following system of N linear equations for N vortices can be derived:

$$\frac{\bar{v}}{U_\infty + \bar{u}} = -\tan\alpha \qquad \text{at sensing points } i = 1, \ldots N - N_F \tag{1}$$

$$\frac{\bar{v}}{U_\infty + \bar{u}} = -\tan(\alpha + \eta) \qquad \text{at sensing points } i = N - N_F + 1, \ldots N \tag{2}$$

The location of the sensing points are given by

$$\left.\begin{aligned} \bar{\xi}_i &= \frac{1-\lambda}{N - N_F}\left(i - \frac{1}{4}\right) \\ \bar{\eta}_i &= (1 - \lambda - \bar{\xi}_i)\tan\alpha \end{aligned}\right\} \qquad i = 1, \ldots N - N_F \tag{3}$$

$$\left.\begin{aligned} \bar{\xi}_i &= 1 - \lambda + \frac{\lambda}{N_F}\left(i - \frac{1}{4} - N + N_F\right)\frac{\cos(\eta+\alpha)}{\cos\alpha} \\ \bar{\eta}_i &= -(\bar{\xi}_i - 1 + \lambda)\tan(\alpha + \eta) \end{aligned}\right\} \qquad i = N - N_F + 1, \ldots N \tag{4}$$

Here $\bar{u}$ and $\bar{v}$ are the components in $\bar{x}$- and $\bar{y}$-direction, respectively, of the velocity induced by all vortices $\Gamma_i (i = 1, \ldots N)$.

The location of the vortex points are given by

$$\left.\begin{aligned} \bar{x}_i &= \frac{1-\lambda}{N - N_F}\left(i - \frac{3}{4}\right) \\ \bar{y}_i &= (1 - \lambda - \bar{x}_i)\tan\alpha \end{aligned}\right\} \qquad i = 1, \ldots N - N_F \tag{5}$$

$$\left.\begin{aligned} \bar{x}_i &= 1 - \lambda + \frac{\lambda}{N_F}\left(i - \frac{3}{4} - N + N_F\right)\frac{\cos(\eta+\alpha)}{\cos\alpha} \\ \bar{y}_i &= -(\bar{x}_i - 1 + \lambda)\tan(\alpha + \eta) \end{aligned}\right\} \qquad i = N - N_F + 1, \ldots N \tag{6}$$

From the N values $\Gamma_i (i = 1, 2, 3, \ldots N)$ the coefficients for lift, moment and rudder-moment are given by the following formulae:

$$c_L = \frac{2L}{\rho U_\infty^2 cb} = \frac{2}{c\,U_\infty^2}\sum_{i=1}^{N}\Gamma_i(U_\infty + \bar{u}_i(\bar{x}_i)) \tag{7}$$

$$c_M = \frac{2M}{\rho U_\infty^2 c^2 b} = \frac{2\cos\alpha}{c\,U_\infty^2}\sum_{i=1}^{N}\Gamma_i\left[(U_\infty + \bar{u}_i(\bar{x}_i))\,\bar{x}_i + \bar{v}_i(\bar{x}_i)\,\bar{y}_i\right] \tag{8}$$

$$c_R = \frac{2M_R}{\rho U_\infty^2 c^2 b} = \frac{2\cos\alpha}{c\,U_\infty^2}\sum_{i=N-N_f}^{N}\Gamma_i\left[\bar{u}_i(\bar{x}_i)(\bar{x}_i - 1 + \lambda) + \bar{v}_i(\bar{x}_i)\,\bar{y}_i\right] \tag{9}$$

where $\bar{u}_i$ is the horizontal, and $\bar{v}_i$ the vertical component of the velocity at the location of the vortex Γ_i induced by all vortices except Γ_i.

In Fig. 5 typical results of a series of calculations for airfoils with flaps near ground are shown. It can easily be seen that the curves become more nonlinear when the airfoil is approaching the ground. In other words, for airfoils near ground linear theory is restricted to very small flap angles and nonlinear theory has to be applied when larger flap angles are being used. In general one can conclude from these results that for flap angles smaller than about $\eta = 15^\circ$ lift and pitching moment coefficients increase for decreasing the ground distance. This tendency at least is also predicted by linear theory. For flap angles larger than $\eta = 15^\circ$ the tendency is reversed, i.e. the coefficients for lift and pitching moments decrease when the airfoil is approaching the ground.

Fig. 6 shows as a typical example for the influence of the angle of attack on the lift coefficient for an airfoil with flap near ground. The nonlinearity due to larger angles of attack is not very much pronounced so that linear approximation might be sufficient for most practical cases. The strong depence of lift curve slope $\partial c_L/\partial\alpha$ on flap angle and ground distance is again demonstrated by this figure. The decrease of c_L due to ground approximity is a typical nonlinear effect and cannot be described by linear theory.

3. AIRFOILS WITH JET FLAPS NEAR GROUND

3.1. Nonlinear jet flap theory

The inviscid two-dimensional flow past a flat plate with a jet flap at the trailing edge is being considered. The entrainment due to the jet is neglected. The jet is assumed to be very thin so that it can be represented by a vortex sheet. The form of the jet is not known a priori and has to be found by the calculation procedure. The jet flap near ground is therefore represented by a vortex model shown in Fig. 7. The flat plate is represented by distribution of vortices with the intensity γ_c and the jet is represented by a curved vortex sheet with the intensity γ_j. The ground is simulated by the "mirror" technique. In the linear theory both vortex distributions would be located on a straight line parallel to the ground. In the vortex configuration shown in this figure and used in this investigation nonlinear effects come into the analysis due to large angles of attack α and large jet angles η_j. There are three unknown functions: the vortex distribution $\gamma_c(\bar{x})$ on the airfoil, the vortex distribution $\gamma_j(\bar{x})$ on the jet and the jet location $\bar{y}_j(\bar{x})$. There are three conditions available for calculating these three functions. 1. The kinematic flow condition at the airfoil. 2. The kinematic flow condition on the jet, where the resulting flow velocity has to be parallel to the jet. 3. The condition which relates the strength of the vortex distribution on the jet with the jet curvature. This condition results from the equilibrium of centrifugal force and pressure difference within the curved jet. The three conditions are given in the following equations:

$$\frac{\bar{v}}{U_\infty} + \frac{\bar{u}}{U_\infty} \tan\alpha = -\tan\alpha \qquad (10)$$

$$\frac{\bar{v}}{U_\infty} - \bar{y}_j' \frac{\bar{u}}{U_\infty} = \bar{y}_j' \qquad (11)$$

$$c_\mu \cdot 1 \cdot \bar{y}_j'' = -\frac{\gamma_j(\bar{x})}{U_\infty} 2\left(1 + \frac{\bar{u}}{U_\infty}\right)\left(1 + \bar{y}_j'^2\right)^2 \cos\alpha \qquad (12)$$

Here $\bar{u}$ and $\bar{v}$ are the components of the velocity induced by all vortices of the vortex model and are usually given by lengthy integrals some of which are singular. Details of these integrals can be found in Reference [9]. These three equations are a system of coupled nonlinear singular integral equations. Typical vortex distribution $\gamma_c(\bar{x})$ and $\gamma_j(\bar{x})$ are shown in Fig. 8 for the two cases $\eta_j \neq 0$, $\alpha = 0$ and $\alpha \neq 0$, $\eta_j = 0$.

For the unknown functions $\gamma_c(\bar{x})$ and $\gamma_j(\bar{x})$ and $\bar{y}_j(\bar{x})$ the following series of functions have been assumed:

$$\frac{\gamma_c(\bar{x})}{U_\infty} = F(\ln(\bar{x})) + \sum_{n=0}^{N} f_n F_n(\bar{x}) \qquad (13)$$

$$\frac{\gamma_j(\bar{x})}{U_\infty} = G(\ln(\bar{x})) + \sum_{n=0}^{N} g_n G_n(\bar{x}) \qquad (14)$$

$$\bar{y}_j'(\bar{x}) = Y(\ln(\bar{x})) + \sum_{n=0}^{N} y_n Y_n(\bar{x}) \qquad (15)$$

These series have been chosen in analogy to an equivalent system of series used by Spence [10] in his linear jet flap theory. By using this series the system of coupled integral equations is reduced to a system of algebraic equations for the unknown coefficients f_n, g_n and y_n in the equations. The resulting system is a system of nonlinear algebraic equations. This has been solved by an iteration process starting with results found by linear theory. The system was solved by a method of Gauss-Banachiewicz using the electronic computer Telefunken TR 440 of the computer-center of the Ruhr-University Bochum. The coefficients of the forces and moments can be found by an integration of the vortex distribution.

3.2. Results of the theory and comparison with experiments

In the following a few typical results of the method described will be shown. In Fig. 9 the lift curves $c_L(\alpha)$ (upper side) and the pitching moment $c_M(\alpha)$ (lower side) are given for two cases. On the left side the jet angle is $\eta_j = 0^o$, on the right hand side the jet angle is $\eta_j = 28{,}6^o$. There are curves shown for different ground distances h/c and a comparison between the general nonlinear theory and the linear theory is made. In all cases one important result can be found: Linear theory shows an increase of the force coefficients for an airfoil approaching the ground. The nonlinear theory, however. leads to the opposite tendency for larger angles of attack. In other words, for α larger than about 10^o the coefficients of lift and moment are decreasing for an airfoil approaching to the ground. Another important result, found from these calculations is the fact, that the range in which linear theory can be applied is strongly reduced to very small angles of attack for an airfoil closer to the ground. This again shows the importance of nonlinear effects for airfoils close to the ground.

In Fig. 10 theoretical results are compared with experiments which have been carried out in the wind tunnel of the Institute of Fluid Mechanics of the Technical University in Braunschweig. For zero jet angle ($\eta_j = 0^o$) linear as well as nonlinear theory agree very well with experiments for the airfoils without ground and near ground. This is different for higher jet angles. For $\eta_j = 30^o$ and more pronounced for $\eta_j = 60^o$ there is a large difference between the results of linear and nonlinear theory. It can be easily seen that nonlinear theory gives much better agreement with experiments than linear theory.

CONCLUSION

1. The vortex lattice method can be applied to airfoils with flaps near ground. Nonlinear effects due to large angles of attack and large flap angles can be easily included.
2. A theory for airfoils with jet flaps near ground has been developed which leads to a nonlinear dependence of the lift and moment coefficients on angle of attack and jet angle.
3. Nonlinear effects due to large angles of attack as well as large angles of flaps or jet flaps become essential for airfoils close to the ground.
4. The forces increase due to ground for small angles of attack and, in contrast to linear theory, decrease for large angles of attack. For airfoils with zero angle of attack the forces increase due to ground for small flap angles or jet angles and decrease due to ground for large flap angles.
5. Comparison with experimental results show very good agreement for jet flap airfoils. Linear theory is valid only for small angles of attack and small jet angles and the regime in which it is applicable is reduced to smaller angles for airfoils approaching the ground.

REFERENCES

1. Wieghardt, K.: Über die Auftriebsverteilung des einfachen Rechteckflügels über die Tiefe. ZAMM 19 (1939), 5, 257-270.
2. Scholz, N.: Beiträge zur Theorie der tragenden Fläche. Ing.-Archiv. 18 (1950), 84-105.
3. Schlichting, H. and Kahlert, W.: Calculation of lift distribution of swept wings. RAE Rep. Aero 2297 (1948).
4. Hedman, S.G.: Vortex lattice method for calculating of quasi steady state loadings on thin elastic wings in subsonic flow. FFA Rep. 105 (1966).
5. Belotserkovskij: Calculation of the flow around wings of arbitrary planform in a wide range of angles of attack. NASA-TT-F-12291 (1969).
6. Körner, H.: Berechnung der potentialtheoretischen Strömung um Flügel-Rumpf-Kombinationen und Vergleich mit Messungen. Z. Flugwiss. 20 (1972), 9, 351-368.
7. Keune, F.: Auftrieb einer geknickten Platte. Luftfahrtforschung 13 (1936), 85-87.
8. Keune, F.: Momente und Ruderauftrieb einer geknickten ebenen Platte. Luftfahrtforschung 14 (1937), 558-563.
9. Löhr, R.: Der Strahlklappenflügel in Bodennähe unter besonderer Berücksichtigung großer Anstell- und Strahlklappenwinkel. Ph.D. Thesis, Ruhr-University Bochum, 1973.
10. Spence, D. A.: The lift coefficient of a thin jet-flapped wing. Proc. Roy. Soc. (A) 238 (1956), 43-68.

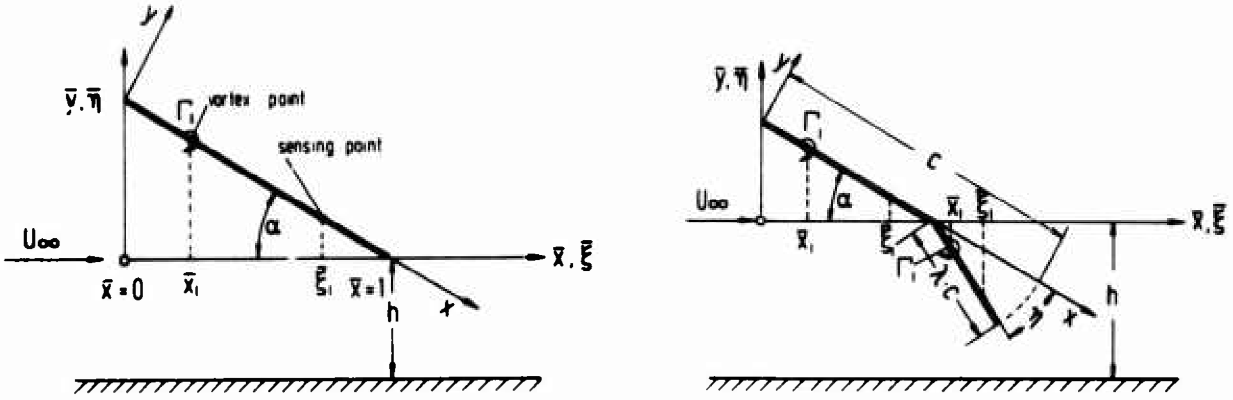
$\bar{y},\bar{\eta}$
y
Γ_1
vortex point
sensing point
α
U_∞
$\bar{x},\bar{\xi}$
$\bar{x}=0$
$\bar{x}_1$
$\bar{\xi}_1$
$\bar{x}=1$
h
x
$\bar{y},\bar{\eta}$
y
Γ_1
c
α
U_∞
$\bar{x}_1$
$\bar{\xi}_1$
$\bar{\xi}_1$
$\bar{x}_1$
Γ_1
λc
λ
x
h
$\bar{x},\bar{\xi}$

Fig. 1 Nomenclature

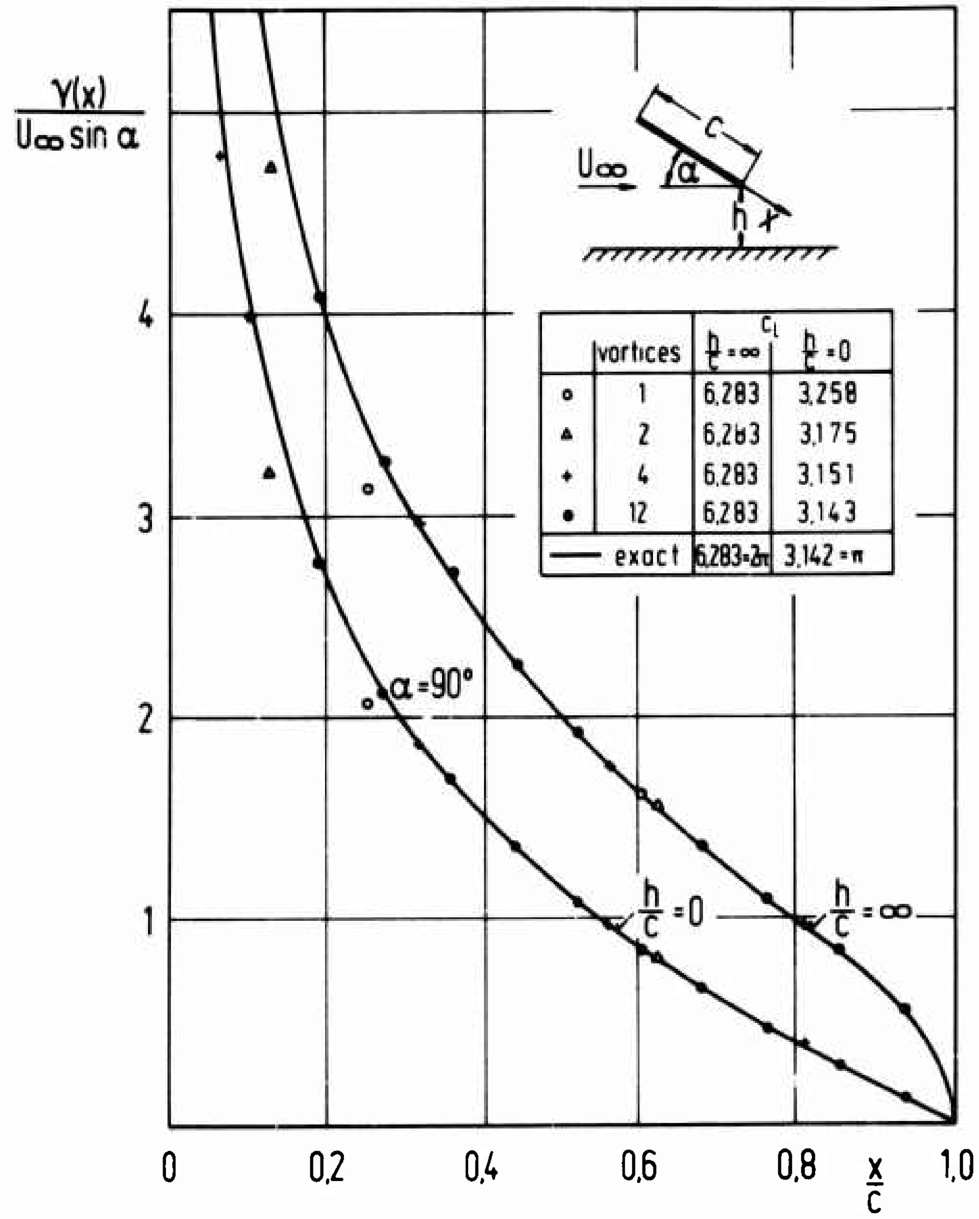

	vortices	c_L $\frac{h}{c}=\infty$	$\frac{h}{c}=0$
○	1	6,283	3,258
▲	2	6,283	3,175
+	4	6,283	3,151
●	12	6,283	3,143
—	exact	6,283=2π	3,142=π

Fig. 2 Vortex distribution for a flat plate with and without ground. Comparison of vortex lattice method with exact analytical solutions.

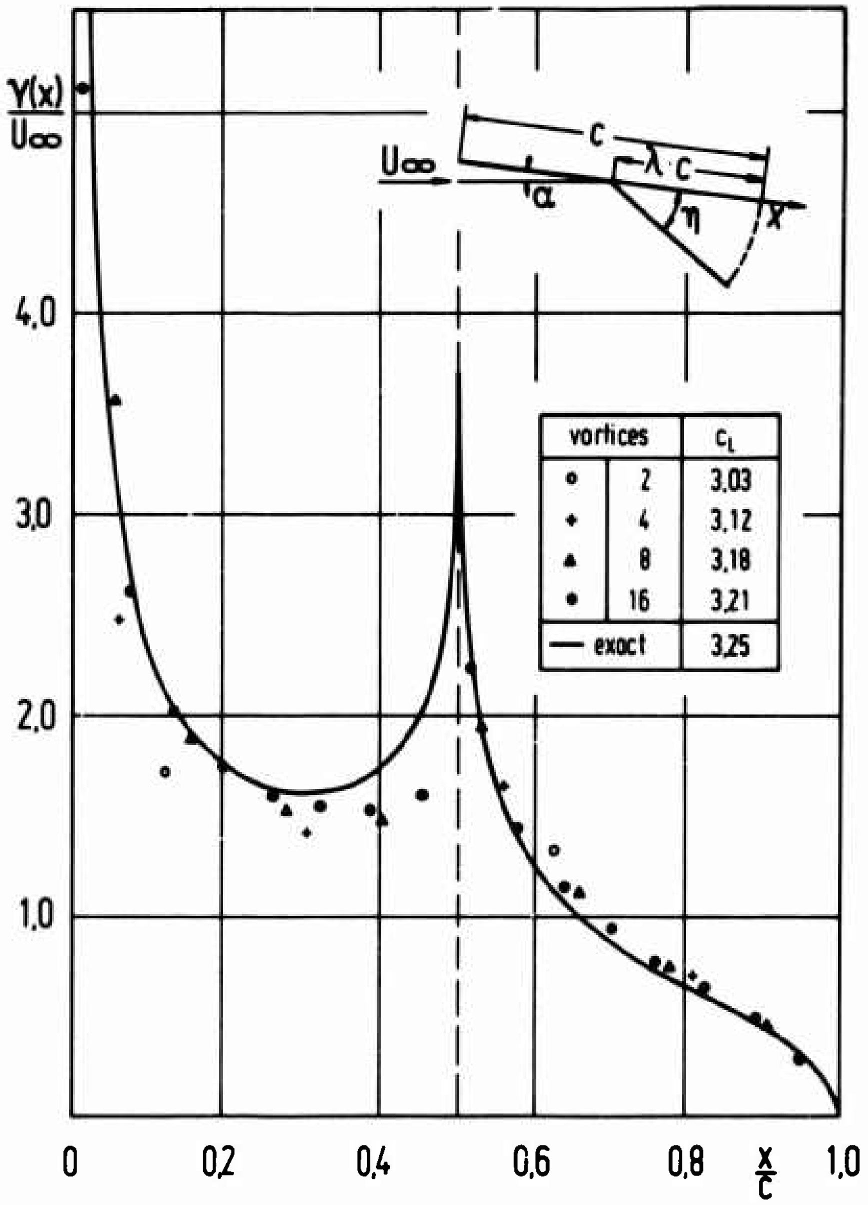

Fig. 3 Vortex distribution for a flat plate with flap. Comparison of vortex lattice method with exact analytical solution after Keune [7], [8]
$\lambda = 0{,}5;\ \alpha = 7^{o};\ \eta = 30^{o}$

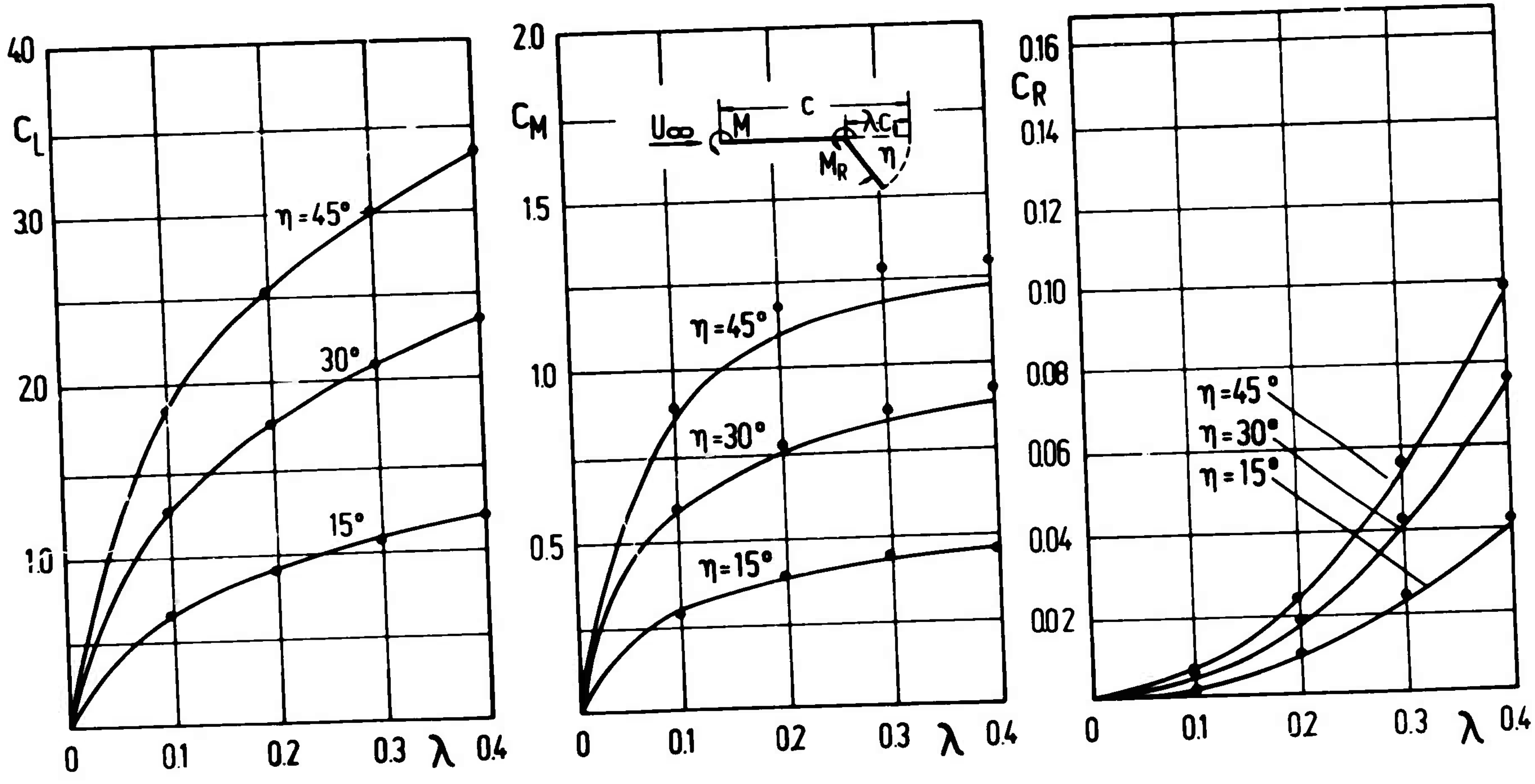

Fig. 4 Coefficients of lift, moment, and rudder moment as functions of flap chord ratio λ and flap angle η for a flat plate with flap ($\alpha = 0^o$).

(Comparisons · Vortex lattice method
——— Exact solution after Keune [7], [8])

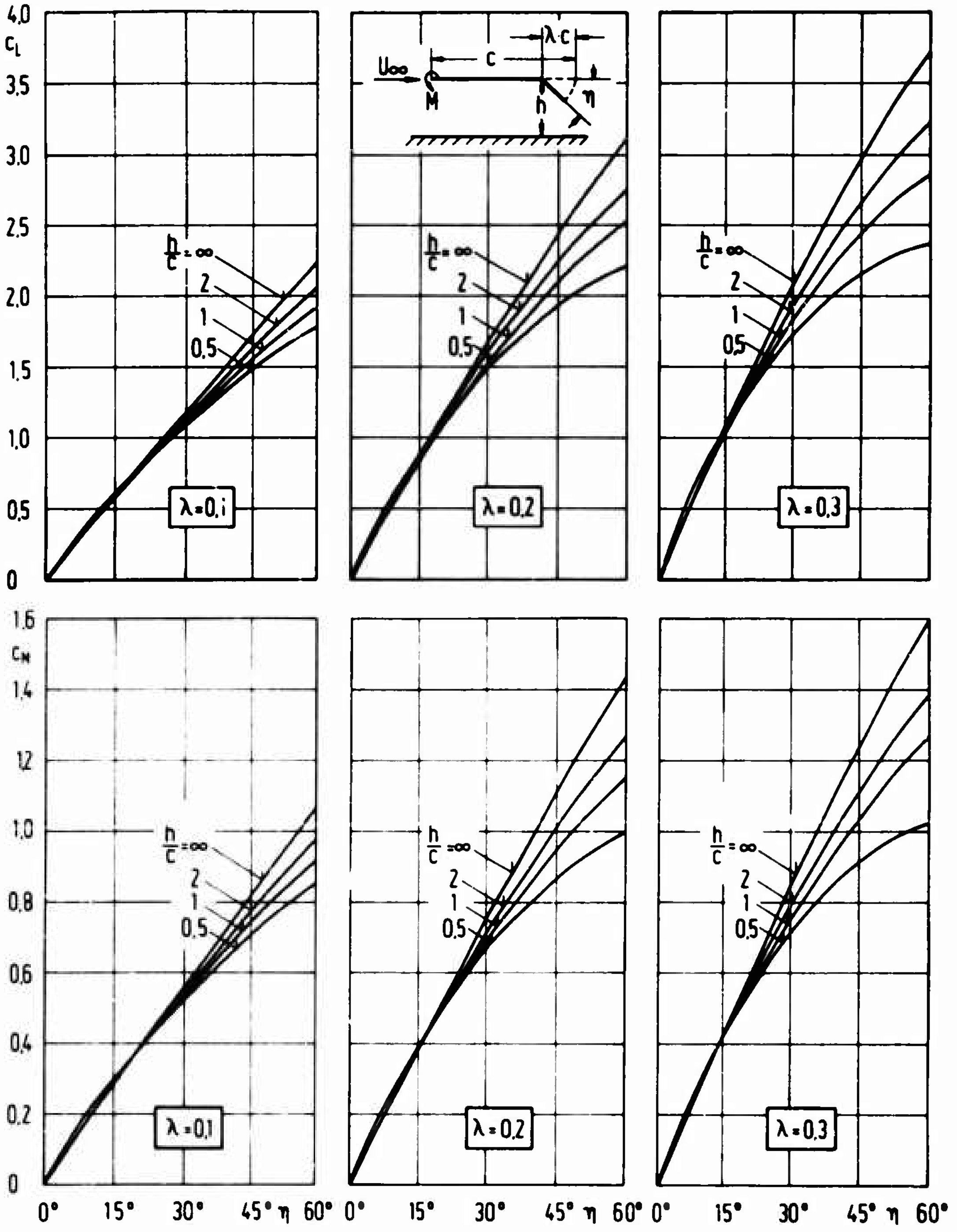

Fig. 5 Coefficients of lift and moment as functions of flap chord ratio λ and relative ground distance h/c. ($\alpha = 0^\circ$)

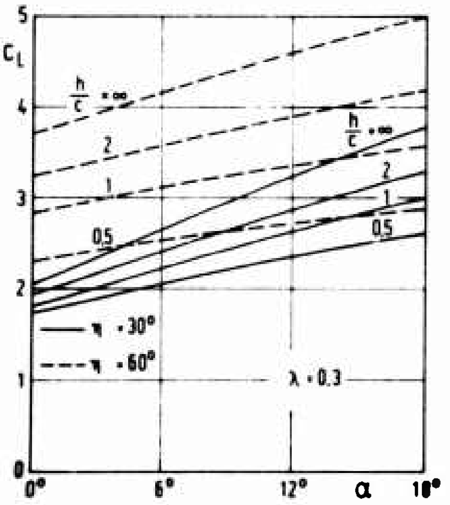

Fig. 6 Lift coefficient as function of angle of attack α, flap angle η, and relative ground distance h/c.

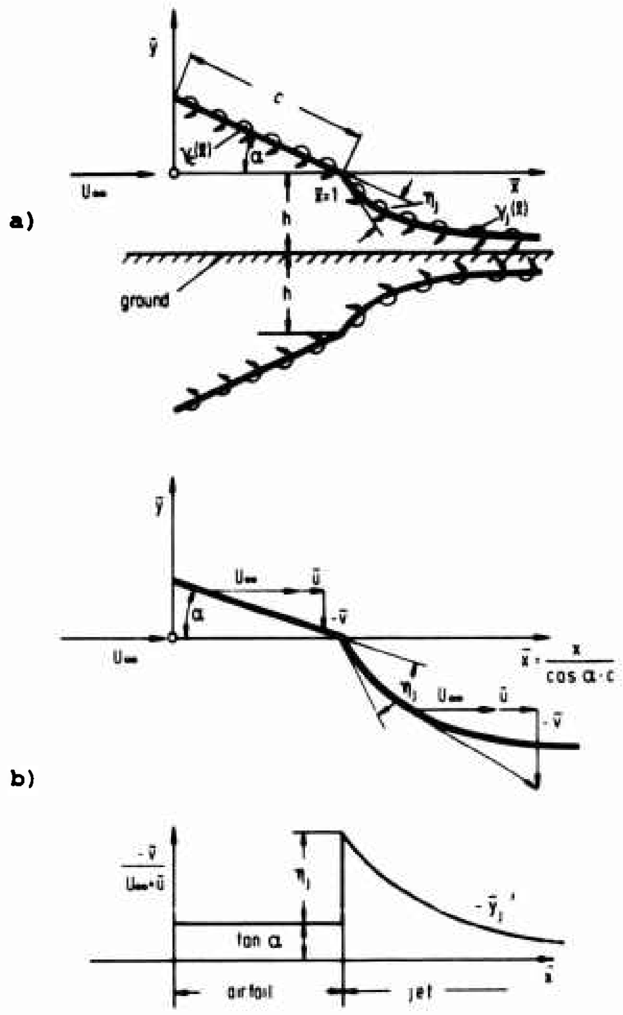
a)
$\bar{y}$
c
$\gamma_c(\bar{x})$
α
U_∞
$\bar{x}=1$
η_j
$\gamma_j(\bar{x})$
$\bar{x}$
h
h
ground
b)
$\bar{y}$
U_∞
$\bar{u}$
$-\bar{v}$
α
U_∞
$\bar{x} = \frac{x}{\cos\alpha \cdot c}$
η_j
U_∞
$\bar{u}$
$-\bar{v}$
$\frac{-\bar{v}}{U_\infty+\bar{u}}$
η_j
$-\bar{y}_j'$
tan α
$\bar{x}$
airfoil
jet

Fig. 7 Nomenclature for an airfoil with jet flap near ground.
a) Vortex model
b) Kinematic flow condition

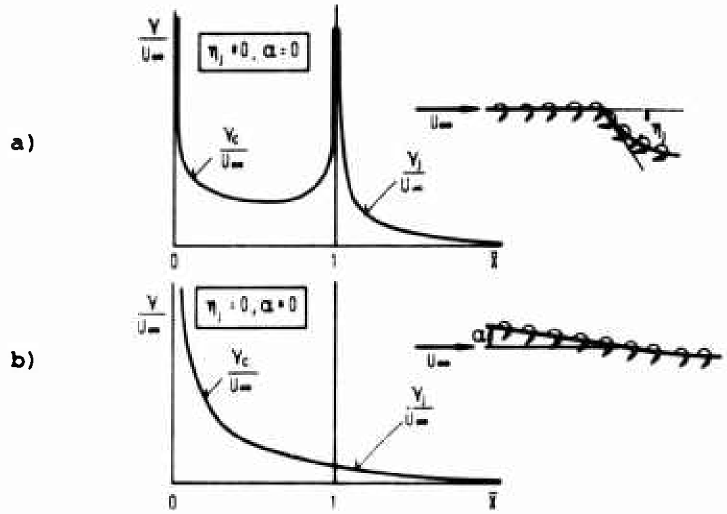

Fig. 8 Vortex distribution for an airfoil with jet flap.
a) $\eta_j \neq 0$, $\alpha = 0$
b) $\eta_j = 0$, $\alpha \neq 0$

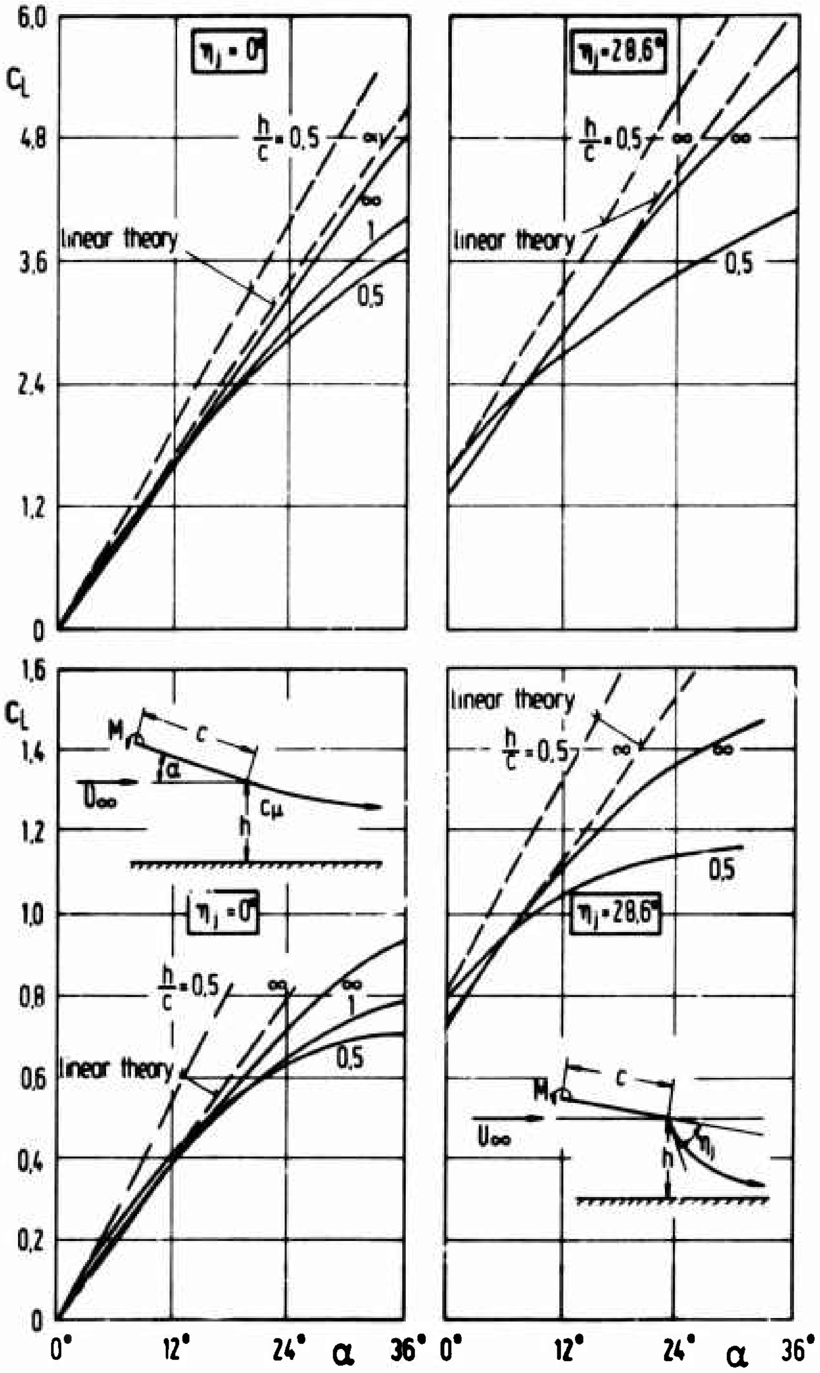

Fig. 9 Coefficients of lift and moment as functions of angle of attack α and relative ground distance h/c, jet momentum coefficient $c_\mu = 0{,}5$.

Comparison of linear and nonlinear theory.

Left: $\eta_j = 0^\circ$ Right: $\eta_j = 28{,}6^\circ$

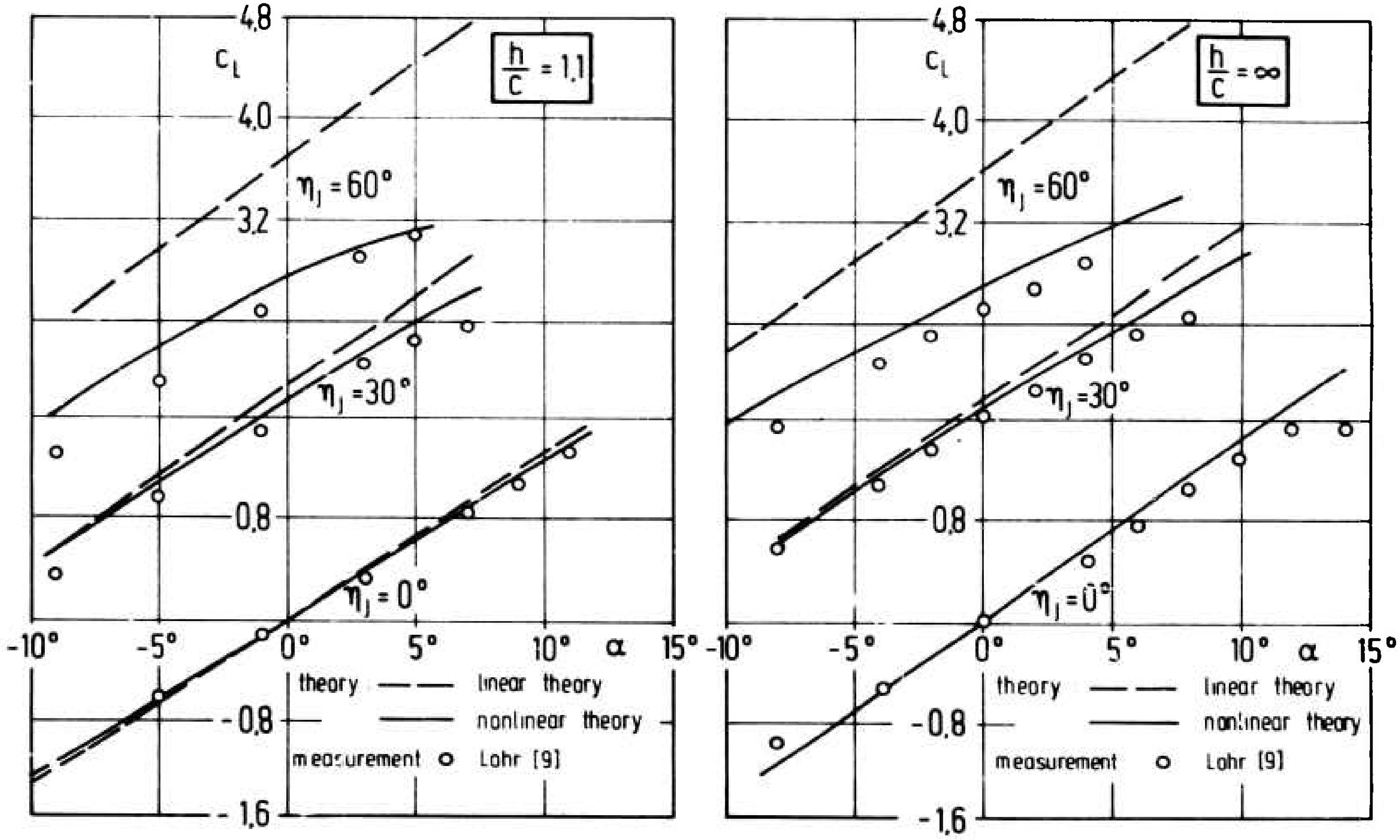

Fig. 10 Lift coefficient as function of angle of attack α for a flat plate with jet flap. Jet momentum coefficient c_μ = 0,8.

Comparison of theory and measurements

Left: h/c = 1,1 Right: h/c = ∞

MEASUREMENT OF TILT ROTOR VTOL ROTOR WAKE-AIRFRAME GROUND AERODYNAMIC INTERFERENCE FOR APPLICATION TO REAL TIME FLIGHT SIMULATION

by

Troy M. Gaffey
Bell Helicopter Company
P. O. Box 482
Fort Worth, Texas 76101
U.S.A.

and

Martin D. Maisel
U.S. Army Air Mobility R&D Laboratory
Ames Directorate
Ames Research Center
Moffett Field, California 94035
U.S.A.

SUMMARY

The hover and low speed rotor wake-airframe-ground aerodynamic interference characteristics of the XV-15 Tilt Rotor Research Aircraft, now under construction in a joint U.S. Army-NASA program, have been measured in wind tunnel tests of a scale model and applied to real time flight simulation.

The principal findings of the tests are: (1) A static instability in roll occurs during hover in ground effect. The instability vanishes at airspeeds greater than 20 knots and at height-diameter ratios greater than 1.5. (2) In forward flight, rolled-up rotor wake vortices lie just above the horizontal stabilizer and produce the effect of a net upwash on it. (3) When the aircraft sideslips, it reduces the upwash effect at the horizontal stabilizer and causes nose-up pitching with yaw. (4) Interference between the rotors wakes and the vertical fins reduces directional stability, and makes the aircraft directionally unstable for sideslip angles less than 4 degrees at speeds less than 40 knots.

Semi-free flight scale model tests and real time flight simulation evaluated the effect of aerodynamic interference on handling qualities. These showed a significant influence in hover and at low speeds, with the influence more pronounced in ground effect than out of it. At airspeeds above 60 knots, interference does not have a significant effect on handling characteristics. In hover and low speed flight, the XV-15's stability augmentation system minimizes the influence of aerodynamic interference and makes the handling characteristics satisfactory.

LIST OF SYMBOLS

a_H - Lift curve slope of horizontal stabilizer

α_F - Fuselage angle of attack

α_H - Horizontal stabilizer angle of attack

C_{m_H} - Contribution of horizontal stabilizer to aircraft pitching moment coefficient

$C_{m_{iH}}$ - Variation in aircraft pitching moment coefficient with incidence of horizontal stabilizer

C_{n_V} - Contribution of vertical fins to aircraft yawing moment coefficient

ϵ_H - Downwash angle at horizontal stabilizer

h/D - Height of rotor plane above ground divided by rotor diameter

i_H - Horizontal stabilizer incidence angle

i_N - Nacelle incidence angle (90° means rotor shaft is vertical, 0° means rotor shaft is horizontal).

η_H - Dynamic pressure ratio at horizontal stabilizer

η_V - Dynamic pressure ratio at vertical fins

$\bar{V}_H$ - Horizontal stabilizer volume

V_∞ - Velocity along flight path

$\partial\sigma/\partial\beta$ - Sidewash factor at fins

SUBSCRIPTS

W - Contribution of wing-body

R - Contribution of rotor wake

T - Total (contribution of rotor wake plus wing-body)

1. INTRODUCTION

For more than twenty years the tilt rotor concept has appeared to be a promising way to obtain a VTOL aircraft having the hover and low speed flight characteristics of the helicopter and the high-speed cruise characteristics of the fixed wing aircraft.[1,2] The XV-3, an early effort to demonstrate the feasibility of the tilt rotor concept, was successfully flown in both the helicopter and airplane modes of flight and showed that it was easy to convert from one flight mode to the other.[3,4] While the XV-3 verified the principles of the concept, it revealed several technical problems in the airplane mode of flight. These problems, which had to be solved before development could proceed,[3,5] were light damping of the aircraft flight modes, excessive flapping of the rotor blades in maneuvers, and aeroelastic instability of the rotor-nacelle-wing dynamic system. Industry and government agencies have over the past ten years come to understand these problems and have found practical design solutions, thus permitting development of the concept to proceed.[6,7,8]

The XV-15 Tilt Rotor Research Aircraft, (Figure 1), is the next step in the development of the Tilt Rotor VTOL concept. Under development in a joint U.S. Army/NASA program, the XV-15 will perform proof-of-concept flight research and generate technical data for the design of tilt rotor aircraft for military and civil application. Two XV-15's are being built by Bell Helicopter Company, the prime contractor. Rollout of the first aircraft is scheduled for September 1975, with first flight in July 1976. Some of the characteristics of the aircraft are given in Table I.

Part of the XV-15 flight readiness program is real-time, pilot in the loop, flight simulation which is investigating handling qualities, furnishing design data for the cockpit layout and the automatic flight control systems, and aiding in the development of normal and emergency procedures. The simulation's mathematical model includes representation of aerodynamic interference between the rotor wakes, the airframe, and the ground because the XV-3 flight test program encountered several handling problems in hover and low speed flight that were attributed to this interference. (These included a tendency to dart laterally when hovering IGE, a longitudinal stick position reversal at low forward speeds, and an unacceptable pitch oscillation at speeds below 25 knots. At speeds below 35 knots, there was a divergent, long-period directional oscillation that induced nose-up pitching if allowed to reach large amplitude.[3] These characteristics appear to be inherent to the tilt rotor concept because of the combination of laterally disposed rotors and a conventional wing and empennage.) It was essential to include an accurate representation of these aerodynamic interference characteristics in the math model for XV-15 simulation to allow the handling qualities in hover and low speed helicopter flight to be evaluated and to make the simulation useful for the design of the stability and control augmentation system.

This paper discusses tests of a one-fifth scale model which measured rotor wake, airframe, ground interference. The tests were conducted under NASA contract and monitored by the U.S. Army AMRDL/NASA Tilt Rotor Project Office at NASA-Ames. Complete results of the tests are available in Reference 9.

2. TEST APPARATUS AND PROCEDURES

The approach was somewhat novel in that a dynamically scaled, powered, flutter model was used. Because the model was Froude scaled it could fly in semi-free flight to establish trim flight parameters and demonstrate handling characteristics. The dynamically-scaled model also furnished data on rotor loads and airframe vibration.

2.1 Model and Instrumentation

The model is a one-fifth scale model of the Bell Helicopter Company Model 300, and is aerodynamically and dynamically similar to it. (The XV-15 and Model 300 designs differ primarily in powerplant and landing gear installations; therefore the results of the model tests are directly applicable to the XV-15.) The model had been used earlier to investigate the coupled rotor-nacelle-wing aeroelastic stability and flight mode stability in airplane mode.[10]

In construction the model is typical of flutter models in that the mass and stiffness distribution of the major structural components including rotors are scaled to preserve natural frequency ratios and the mass ratio (Lock number). Fairings of fiberglass, balsa, and aluminum provide the correct aerodynamic contour. The rotors are interconnected and powered by two 3.4 horsepower Task motors. They are controlled by a servo feedback system that gives proportional control of the rotor collective and cyclic pitch (including differential collective for roll control and differential cyclic for yaw control). The elevator and ailerons are controlled by "beep" type controls and the incidence of the flaps and empennage is ground adjustable.

One blade on the right-hand rotor is strain gaged for bending moments and torsion. The right-hand mast is strain gaged for torque, and potentiometers measure rotor control positions. The wing, fuselage and empennage are strain gaged to measure bending and torsion, and there are accelerometers on the nacelles, at the pilot's station and aircraft c.g., and on the vertical fins. The position of the model with respect to its mount is measured in terms of pitch, roll, yaw, and vertical translation. The empennage is mounted to the fuselage through a two-component strain gage balance which measures empennage lift and rolling moment.

2.2 Description of Tests

Hover tests measured static roll stability, wing download, and the influence of ground effect on rotor performance and investigated controllability. To minimize recirculation the hover tests were conducted outdoors, with the model attached to a vertical rod by a sliding gimbal as shown in Figure 2. For the static tests, the rod was fixed in the vertical position and the model restrained in pitch and yaw. Roll static stability was determined from the measurement of rolling moment required to hold a given roll angle. The wing download was determined from a comparison of net lift of the aircraft at a given blade collective pitch setting and various settings of the flaps and ailerons and with the wing aerodynamic fairings removed (as shown in Figure 2). Rotor performance was measured at various height-diameter ratios (h/D) to establish the influence of ground effect on performance.

Hover controllability tests were conducted with the lower end of the vertical rod unrestrained, thus allowing the model to translate laterally and longitudinally as well as vertically and with the model free to pitch, roll, and yaw. Three model operators "piloted" the model, with one operator controlling each axis.

Wind tunnel tests measured control positions, aircraft attitude, and power required in trimmed forward, rearward and sideward flight. Controllability was investigated in semi-freeflight tests. These tests took place in the LTV low-speed wind tunnel, which has a V/STOL test section 15 feet by 20 feet in cross section. For the XV-15 scale model the tunnel has a maximum speed equivalent to 100 knots, full-scale. A moving belt ground plane was used for IGE tests. The model was mounted on a vertical rod mount, as shown in Figure 3, and was free to translate vertically and to pitch, roll, and yaw. Model operators used the remote proportional control system to fly the model.

Control position, aircraft attitude, and power required for a range of flight conditions were obtained by flying the model to the desired condition. Data were taken at several h/D ratios and for four nacelle incidence angles (90°, 75°, 60° and 30°). Figures 4, 5, and 6 show examples of the trim data obtained from the semi-freeflight test.

Stick position and power required for helicopter mode level flight are shown in Figure 4. The stick gradient is shallow for OGE flight up to an airspeed of 60 knots and there is a stick reversal indicated for IGE flight. Figure 5 shows the variation of stick position and power with pitch attitude (representing climb and descent conditions). The stick position gradient with angle of attack was stable over the range of airspeeds tested. Figure 6 shows the variation in trim stick position with sideslip angle. Note that it takes forward stick to trim pitch with either direction of sideslip.

In order to isolate the aerodynamic interference between the rotor wakes and the airframe, the model was mounted on a sting with a six-component, internal, strain gage balance located close to the model center of gravity. Trim parameters established during the semi-freeflight test were used to obtain a trimmed condition on the sting. Pitch, yaw, and control position sweeps were made about the trim point. Sweeps were repeated for the model with the rotors, the wing aerodynamic fairings, the empennage and combinations of these components removed to isolate aerodynamic interference effects. Figure 7 is an example of the data from the force and moment test.

A tufted grid was set up behind the empennage, as shown in Figure 8, to display the flow in the vicinity of the empennage. Smoke was also injected upstream of the model for flow visualization.

3. DISCUSSION OF RESULTS

3.1 Hover

Static roll stability in hover was examined at rotor height/diameter (h/D) ratios from 0.5 (wheels on ground) to 1.0. Figure 9 shows that an instability exists above an h/D = 0.54. The roll instability was found to be linear with roll angle over the ±6 degree roll range tested. Interpolation of the data indicates that the maximum instability occurs at $h/D = 0.85$. Previous tests[3,11] have shown that the instability vanishes at height/diameter ratios of 1.5 and above. Semi-freeflight wind tunnel tests showed that the roll instability vanishes at airspeeds above approximately 20 knots.

When the model was tested with the wing fairings removed, there was almost no roll instability. Although the mechanism causing the roll instability was not established, it appears that cross flow induced by the rotor downwash causes a reduction in pressure on the underside of the low wing. The strength of the cross flow varies with h/D, causing the roll stability to vary.

The full-scale control input required for trimming the measured instability was found to be 0.051 inches of lateral stick per degree of roll at an equivalent full-scale gross weight of 8,250 pounds. The lateral control requirement is expected to increase linearly with the rotor downwash dynamic pressure. Thus at the maximum VTOL gross weight of the XV-15 (15,000 pounds) the maximum lateral control requirement is predicted to be 0.093 inch of stick per degree of roll. For a ten-degree wing drop in ground effect, the lateral stick for trim would be 0.93 inch. Maximum lateral stick travel available is ±4.8 inches.

Wing download was measured by comparing data taken with the wing fairings on and off. At a thrust representing the XV-15 aircraft at 10,600 pounds, the wing download was 11.4 percent of thrust at $h/D = 1.0$, as shown in Figure 10. This is higher than the 7 percent predicted by extrapolating XV-3 model data, and it appears that a Reynolds number effect causes the difference. Hoerner[12] shows that the drag of cross-sectional shapes with rounded edges and flat sides is strongly dependent on Reynolds number (see Figure 11). These shapes are comparable to a wing with flaps deflected, at an angle of attack of -90 degrees. The drag coefficient drops by approximately 50 percent as Reynolds number increases from that of the model (2×10^5) to full-scale (2×10^6). Thus the model download, 11.4 percent thrust (at $h/D = 1.0$), is predicted to be 5 to 7 percent of thrust for the full-scale aircraft. This level is verified by comparing another small scale model test[11] conducted at Reynolds numbers around 4×10^5 with a full-scale rotor-and-wing download test[13] (see Figure 10).

Figure 10 shows that the download diminishes and becomes an upload when the rotor-and-wing system approaches the ground. This effect is due to a positive pressure developed under the wing much as the base pressure is developed on a peripheral jet air cushion vehicle.

The flap setting to minimize wing download was investigated at $h/D = 1.0$. As shown in Figure 12, flaps/aileron settings of 45°/25°, 60°/45° and 75°/45° each increased the net thrust over the baseline case (0°/0°) by six percent. A setting of 75°/75° increased the net thrust over the baseline by only 4.7 percent. While Reynolds number effects make the download data questionable, the trend suggests that the optimum setting may be in the range of 45 degrees. Additional data is needed to establish the flap/aileron setting for minimum download.

The influence of ground proximity on rotor performance was evaluated by testing the model with the wing panels on and off at h/D ratios ranging from 0.5 to 1.0. The measured increase in rotor thrust due to ground effect is shown in Figure 13. At constant power, thrust increased nearly 20 percent as the rotor descended from a height of one diameter to 0.5 diameter (wheels on ground). The presence or absence of the wing panels did not make a significant difference (see Figure 13). At $h/D = 0.5$ the power required to hover was reduced from that required at $h/D = 1.0$ by 12 percent at a high gross weight and 20 percent at low gross weight.

3.2 Forward Flight

Aerodynamic interference in forward flight was investigated by the observation of flow in the vicinity of the wing and empennage and the measurement of the effect of interference on the empennage.

Smoke injected upstream of the left-hand rotor showed the nature of rotor-wing aerodynamic interference. Tests of a 1/10-scale model had previously shown that the wing download in hover changes to an upload in forward flight.[11] As shown in Figure 14, the wing begins to contribute lift at an airspeed of 35 knots, whereas linearized wake theory would predict the wing to be immersed in the rotor wake at that low an airspeed. Observation of the flow showed that at speeds as low as 20 knots the rotor induced a strong upwash at the wing leading edge and that the rotor wake was completely off the wing at speeds over 30 knots. The nonuniformed induced velocity of the rotor appears responsible for the wake moving off the wing at low airspeeds.

The flow patterns in the vicinity of the empennage were studied using photographs of the tufted grid and smoke visualization. Figure 15 shows flow patterns sketched from photographs. At 16 and 20 knots, the patterns suggest a net downwash at the horizontal stabilizer, but empennage balance data indicates a net upload even at those airspeeds. At 30 and 40 knots, the flow patterns are distinct and show that rolled up rotor wake vortices are located directly above the horizontal stabilizer. At these speeds, the wake from each rotor has the appearance of the wake of a highly loaded low-aspect-ratio wing. The effect is to produce upload on the horizontal stabilizer, probably due more to vortex-induced lift than to an actual upwash.

The tufted grid was not used at airspeeds higher than 40 knots. Smoke patterns at higher speeds showed that the rolled-up vortices move downward and outward as airspeed increased. A net upwash over the span of the horizontal stabilizer was visible at airspeeds between 60 and 100 knots.

When the model was yawed, the vortex cores shift laterally with respect to the fuselage centerline. As will be shown later, this has two effects: (1) it reduces the strength of the rotor-wake-induced lift on the horizontal stabilizer, reducing the upload and causing nose-up pitching, and (2) for yaw angles between 0 and 12 degrees, it reduces directional stability, apparently due to the vortices moving laterally with respect to the fins. At yaw angles greater than 12 degrees, the rotor wakes were found to increase the effectiveness of the fins and thereby increase the directional stability of the aircraft.

The interference between the rotor wakes and the empennage was extracted from the test data using the assumption that the aerodynamic interference is superimposed on the aerodynamic characteristics of the basic airframe. The downwash at the horizontal stabilizer is assumed to be caused by the wing and the rotors, with each acting separately, and with the total downwash being the sum of the respective downwashes. (It is recognized that representing the effect of the rotor wake on the horizontal stabilizer in terms of a net upwash or downwash is a gross simplification, but this approach makes the problem tractable for application to real time simulation. To represent the actual flow field in the vicinity of the empennage with a rigorous math model is not presently feasible. Additional data on pressure distributions, local flow velocities, etc. would be required to develop a more rigorous model.)

The mathematical manipulations used to extract interference effects from the test data were as follows: For example knowing, that

$$C_{m_H} = C_{m_{\text{Tail on}}} - C_{m_{\text{Tail off}}} = -a_H \eta_H \bar{V}_H \alpha_H \qquad (1)$$

and

$$C_{m_{iH}} = \left(C_{m_{iH = 4°}} - C_{m_{iH = 0°}}\right) \Big/ 4° = -a_H \eta_H \bar{V}_H \qquad (2)$$

hence,

$$\alpha_H = C_{m_H} / C_{m_{iH}} = \alpha_F - \epsilon_{H_W} \qquad (3)$$

giving,

$$\epsilon_{H_W} = \alpha_F - \alpha_H = \alpha_F - C_{m_H} / C_{m_{iH}} \qquad (4)$$

The horizontal stabilizer lift curve slope was estimated by the method given in Reference 14, and the dynamic pressure ratio was calculated from

$$\eta_{H_W} = C_{m_{iH}} / a_H \bar{V}_H \qquad (5)$$

The downwash and dynamic pressure ratio due to the rotor's wakes was determined by using Equations (1) through (5) to determine first the total (wing + rotor) downwash and dynamic pressure ratio, ϵ_{H_T} and η_{H_T}. The downwash and dynamic pressure ratio due to the rotors were than determined from

$$\epsilon_{H_R} = \epsilon_{H_T} - \epsilon_{H_W} \qquad (6)$$

and

$$\eta_{H_R} = \eta_{H_T} - \eta_{H_W} \qquad (7)$$

Figure 16 compares the effective net downwash angle and dynamic pressure ratio at the horizontal stabilizer with those due to the wing/nacelle/fuselage (rotors off). The effect of the rotors is to produce a net upwash and an increase in dynamic pressure ratio. The contribution due to the rotors is shown in Figure 17 in terms of downwash velocity ($V_{H_R} = V_\infty \tan \epsilon_{H_R}$) and dynamic pressure ratio η_{H_R}.

Sideslip was found to reduce the magnitude of the upwash at the horizontal stabilizer, as shown in Figure 18. The downwash velocity was determined by assuming the total dynamic pressure ratio to be constant (equal to its value at zero sideslip). The reduction in upwash velocity causes nose-up pitching when the aircraft is sideslipped.

The effect of the rotor wake on directional stability was determined by taking the ratio between the rotors-on and rotors-off yawing moment coefficients. Knowing

$$C_{n_V} = C_{n_{\text{Tail on}}} - C_{n_{\text{Tail off}}} \qquad (8)$$

and defining

$$K_\beta = \frac{C_{n_V}\ \text{Rotors On}}{C_{n_V}\ \text{Rotors Off}} \qquad (9)$$

K_β is then effectively the ratio of the product of the fin efficiency factor and the fin sidewash factor:

$$K_\beta = \frac{\eta_{V_T}(1-\partial\sigma/\partial\beta)\ \text{Rotors On}}{\eta_{V_W}\ (1-\partial\sigma/\partial\beta)\ \text{Rotors Off}}$$

The measured variation of K_β with sideslip angle and airspeed is shown in Figure 19. Note that at low airspeeds the aircraft is directionally unstable for sideslip angles between ±4 degrees.

Data such as shown in Figures 16 through 19 were also obtained for nacelle incidence angles of 75°, 60°, and 30°. There was a significant reduction in aerodynamic interference as the nacelles were tilted forward. For example, as shown in Figure 20, the downwash and dynamic pressure ratio at the horizontal stabilizer induced by the rotor wakes is very similar at 75° and 90° nacelle incidence, while at 60° and 30° there is substantially less interference.

4. EVALUATION OF THE EFFECT OF AERODYNAMIC INTERFERENCE ON HANDLING QUALITIES

The effect of rotor-wake-airframe-ground aerodynamic interference on the XV-15's handling qualities was evaluated by observing model flying characteristics during the semi-freeflight tests and from pilot comments during real time, pilot in the loop, flight simulation.

4.1 Semi-Freeflight Tests

During hover controllability tests, the model pilots were assigned the task of lifting off to a hover and maintaining position over the takeoff point. Controlling the model proved to be exceedingly difficult, and most of the test time was spent developing pilot skill. (It should be noted that the model time scale is 2.24 times real time.) Hover could generally be maintained over a spot until a wind gust or control input disturbed the model in roll. The model would then translate laterally to the translational limits. Attempts to regain control generally resulted in overcontrolling. It soon became evident that it would take too long to develop the necessary pilot proficiency to obtain useful data and the investigation was discontinued.

In the wind tunnel semi-freeflight tests, the model could be trimmed at the lowest speed achievable in the tunnel (approximately 16 knots full scale). In the 16 to 30 knots range, control was difficult but manageable. Above 35 knots, the model became very easy to trim and control and above 50 knots the model would maintain a trimmed condition "hands off." The model was also flown in sideward and rearward flight at speeds up to 35 knots. In both cases, roll control was difficult but manageable while pitch and yaw control were fairly easy (even in rearward flight). The model was noticeably more stable in descents, including autorotation, than in level flight and climbs. A brief investigation of controllability at nacelle incidence angles of 60° and 30° showed the model to be easy to control about all axes. In general, the model's handling characteristics in hover and at low speed were similar to those observed in the XV-3 flight tests (as discussed in Section 2).

4.2 Real Time Flight Simulation

Real time pilot in the loop simulation was conducted on the NASA-Ames Flight Simulator for Advanced Aircraft (FSAA)[15] in December 1973. The math model included the static instability in roll in hover, the effect of IGE operation on rotor performance, the wing download variation with airspeed, and the effect of the rotor's wakes on the horizontal stabilizer and fin.[16]

Although the effects of the interference were not evaluated directly, their influence was noted during the evaluation. Observed effects included: (1) Increased workload to control roll when operating IGE. This effect of the static instability in roll was most apparent when taking off or landing. (2) Stick position reversal, directional instability, and pitch coupling with sideslip during transition from hover to forward flight. (3) Nose down pitching when increasing collective pitch at speeds between 20 and 60 knots. All of these characteristics were similar to those observed in the scale model semi-freeflight tests.

The XV-15 has a dual, three axis stability and control augmentation system (SCAS) that increases the aircraft's damping and provides control quickening. Evaluation included operation with the SCAS off, and with one channel per axis failed. With the SCAS off, the adverse effect of interference on handling characteristics was very apparent and in the 20 to 50 knot speed range made the simulator difficult to fly. The pitch coupling with sideslip was the most disturbing characteristic and the pilot had to be careful to coordinate turns. With the SCAS on, the effects of interference are not as apparent and the simulator was easy to fly. Even with one channel per axis failed, the SCAS provides acceptable handling characteristics.

5. CONCLUDING REMARKS

The use of a Froude scaled flutter model proved to be a practical means of measuring rotor wake-airframe-ground aerodynamic interference. The capability to establish trimmed flight conditions and to demonstrate handling characteristics with semi-freeflight tests provides data not obtainable with a more conventional force and moment model.

The fact that handling characteristics observed during real time, pilot-in-the-loop, flight simulation were similar to those observed in semi-freeflight tests of the model gives credence to the mathematical representation of the measured aerodynamic interference. Further confidence is provided by the similarity between SCAS off hover and low speed handling characteristics on the simulator and those observed in the XV-3 flight tests (the XV-3 did not have a SCAS).

This program has increased confidence that the XV-15's stability and control augmentation system will minimize the adverse effects of aerodynamic interference and provide satisfactory hover and low speed handling characteristics.

6. REFERENCES

1. Hafner, R., The Case for the Convertible Rotor, Tenth Cierva Memorial Lecture, The Aeronautical Journal of the Royal Aeronautical Society, Vol. 75, August 1971.

2. Lichten, R. L., et al, A Survey of Low-Disc-Loading VTOL Aircraft Designs, AIAA Paper No. 65-756, Aircraft Design and Technology Meeting, November 1965.

3. Deckert, W. H. and Ferry, R. G., Limited Flight Evaluation of the XV-3 Aircraft, Air Force Flight Test Center TR-60-4, May 1960.

4. Davis, C. E. and Lichten, R. L., Flight Test Experience With the XV-3 Low-Disc-Loading V/STOL Aircraft, IAS Paper No. 61-63, presented at 29th Annual Meeting, January 1961.

5. Hall, W. E. Jr., Proprotor Stability at High Advance Ratios, Journal of the American Helicopter Society, June 1966.

6. Edenborough, H. K., Investigation of Tilt-Rotor VTOL Rotor-Pylon Stability, Journal of Aircraft, Vol. 5, No. 6, March April 1968.

7. Wernicke, K. G., Tilt-Proprotor Composite Aircraft, Design State of the Art, Presented at the 24th Annual National Forum of the American Helicopter Society, May 1968.

8. Edenborough, H. K., Gaffey, T. M., and Weiberg, J. A., Analyses and Tests Confirm Design of Proprotor Aircraft, AIAA Paper 72-803, Aircraft Design, Flight Test and Operations Meeting, August 1972.

9. Marr, R. L., Sambell, K. W., and Neal, G. T., V/STOL Tilt Rotor Study - Volume VI - Hover, Low Speed and Conversion Tests of a Tilt-Rotor Aeroelastic Model, NASA CR 114615, May 1973.

10. Marr, R. L. and Neal, G. T., Assessment of Model Testing of a Tilt Rotor VTOL Aircraft, presented at AHS Symposium on Status of Testing and Modeling Techniques for V/STOL Aircraft, October 1972.

11. Wilson, J. C., Powered-Force Wind Tunnel Test of Bell Helicopter C100-F1B Tilt Rotor Aircraft, NASA Langley V/STOL Report 31.

12. Hoerner, S. F., Fluid-Dynamic Drag, published by the author, 1958.

13. Gillmore, K. B., Survey of Tilt Rotor Technology Development, presented at AGARD Flight Mechanics Panel, September 1971.

14. Anon, USAF Stability and Control DATCOM, Air Force Flight Dynamics Laboratory, Wright-Patterson Air Force Base, October 1960 (Revised September 1970).

15. Rathert, G. A. Jr., NASA Ames Simulation Sciences Division Simulator Facilities Description Sheets, April 1970.

16. Harendra, P. B., et al, V/STOL Tilt Rotor Study - Volume V - A Mathematical Model for Real Time Flight Simulation of the Bell Model 301 Tilt Rotor Research Aircraft, NASA CR 114614, April 1973.

TABLE I XV-15 CHARACTERISTICS

Weights		
Weight Empty	lb	8,400
Design GW	lb	13,000
Maximum VTOL GW	lb	15,000
Powerplant (2)		
Manufacturer & Model	Avco Lycoming	LTC1K-4K
Max Continuous Power	SHP	1,250
Contingency Power (2 min)	SHP	1,760
Rotor (2)		
Diameter	ft	25
Solidity	ND	.089
Tip Speed		
Helicopter Mode	ft/sec	740
Airplane Mode	ft/sec	600
Wing		
Span	ft	32.17
Area	sq ft	181
MAC	ft	5.225
Empennage ("H" Tail)		
Horizontal Tail Area	sq ft	50.25
Total Vertical Tail Area	sq ft	50.5
Design Limit Airspeeds		
Helicopter	kts (EAS)	156
Conversion	kts (EAS)	189
Airplane	kts (EAS)	300

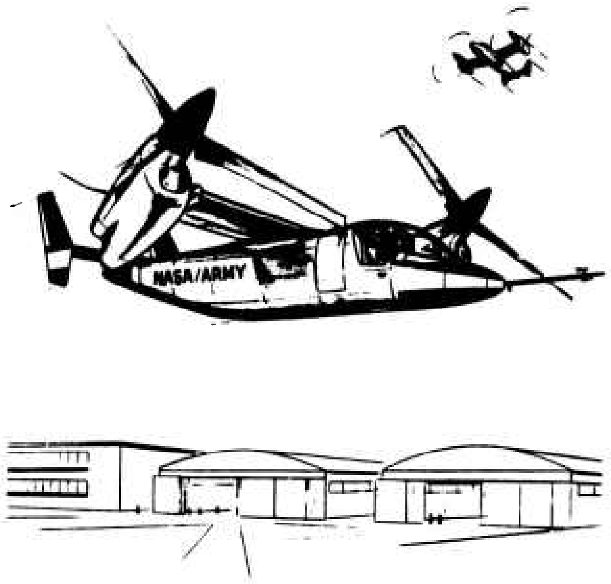

Figure 1. XV-15 Tilt Rotor Research Aircraft.

Figure 2. Hover Test (Wing Aerodynamic Fairing Removed).

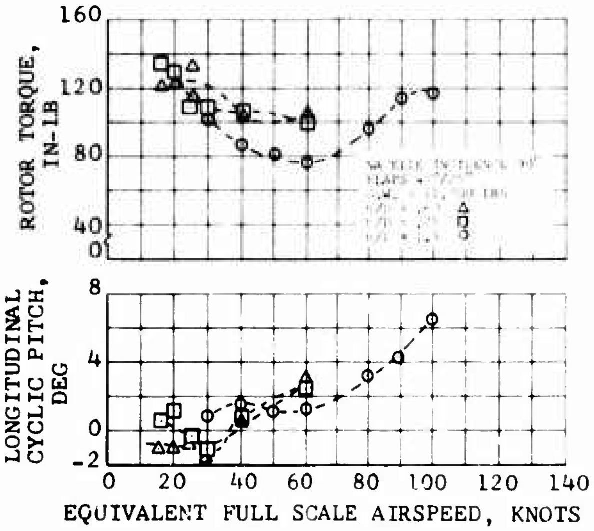

Figure 4. Level Flight Trim Parameters, Semi-free Flight Test.

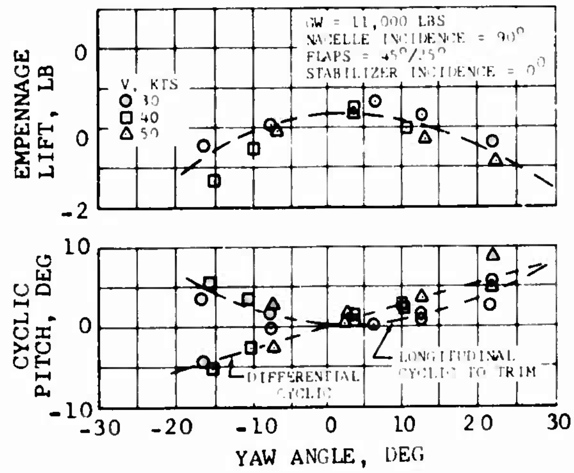

Figure 6. Variation of Trim Parameters With Sideslip, Semi-free Flight Test.

Figure 3. Semi-free Flight Wind Tunnel Test.

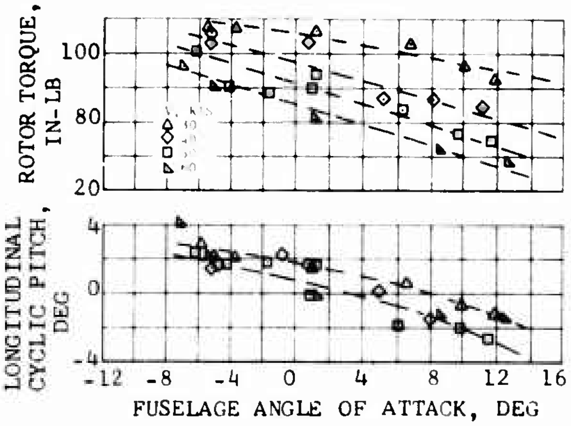

Figure 5. Variation of Trim Parameters With Angle of Attack, Semi-free Flight Test.

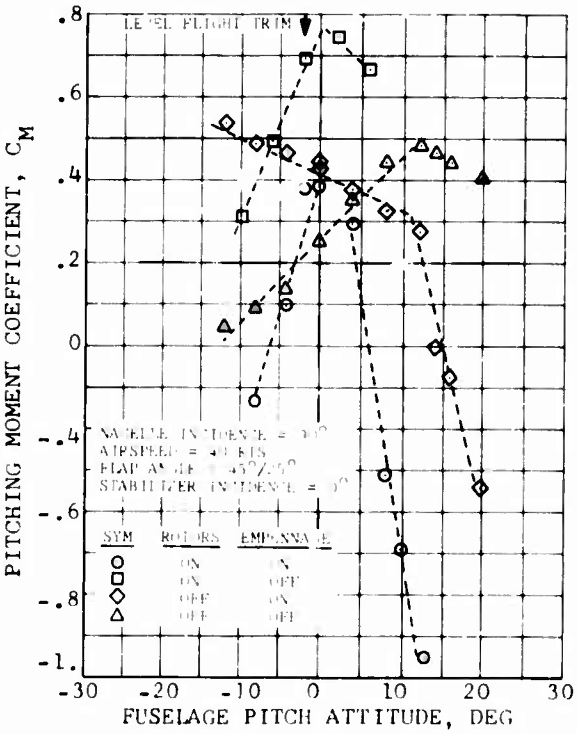

Figure 7. Example of Sting Mount Data Showing Effect of Rotors and Horizontal Stabilizer on Pitching Moment.

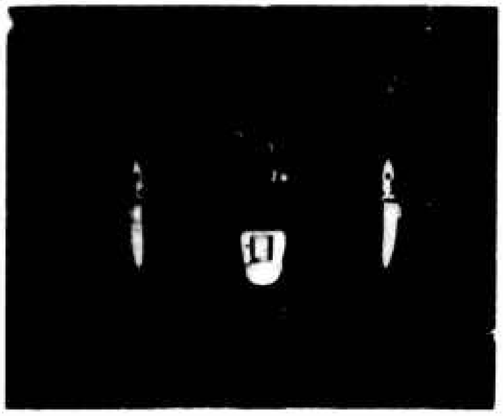

Figure 8. Sting Mount Test With Internal Six Component, Strain Gage Balance.

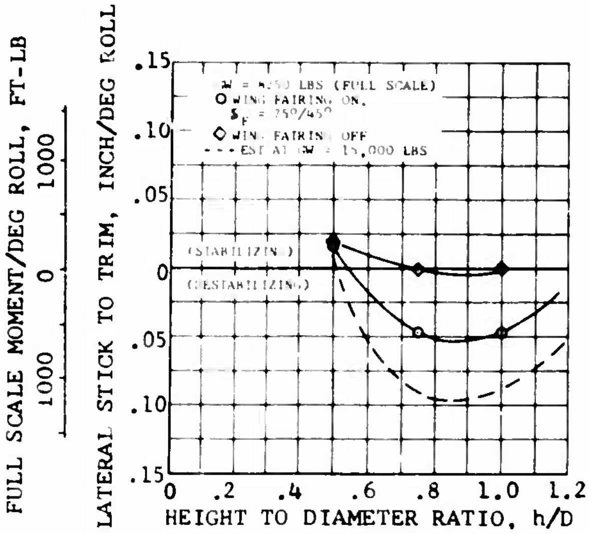

Figure 9. Static Roll Instability in Hover.

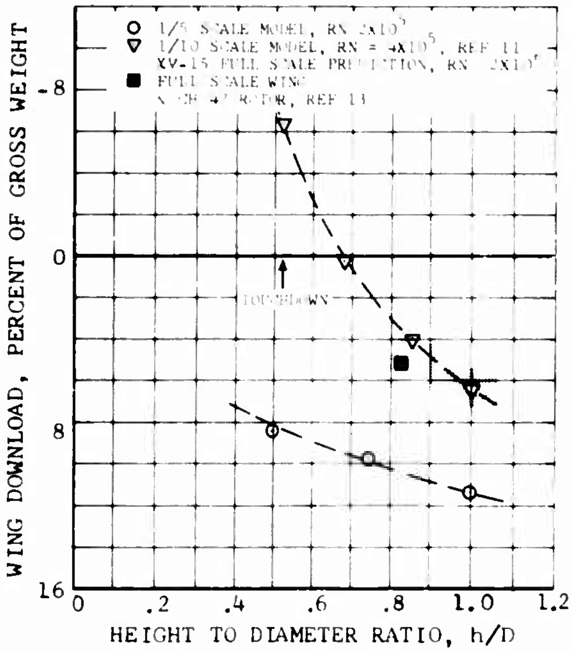

Figure 10. Wing Download in Hover.

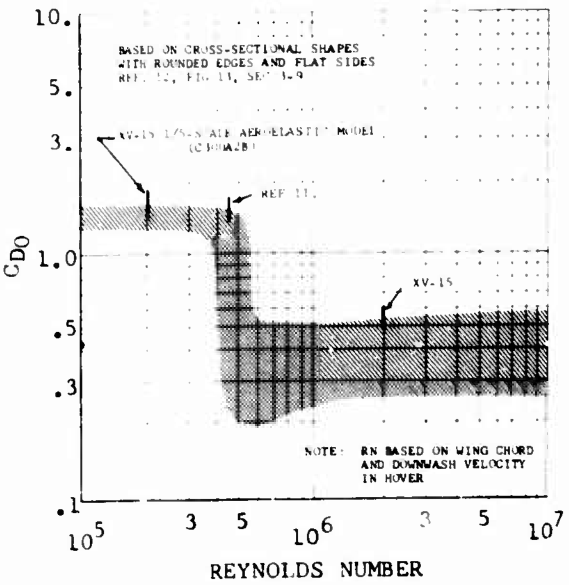

Figure 11. Drag Coefficient of Wing at α_w = -90° Versus Reynolds Number.

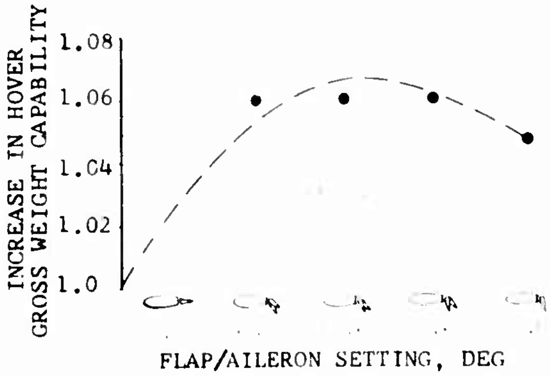

Figure 12. Effect of Flap/Aileron Setting on Wing Download.

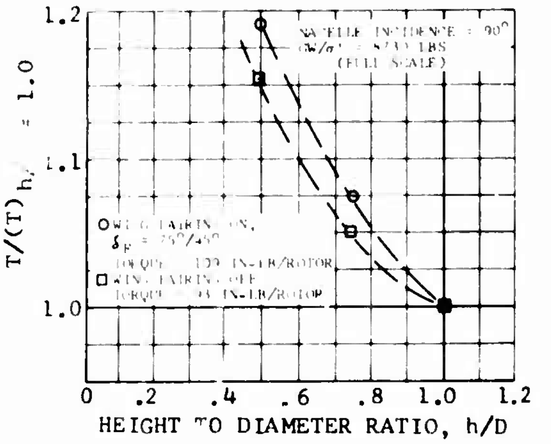

Figure 13. Vertical "Spring" in Ground Effect.

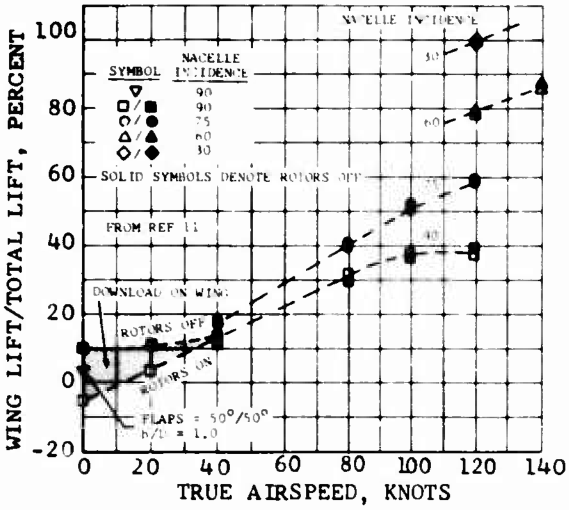

Figure 14. Rotor Airframe Interference in Forward Flight.

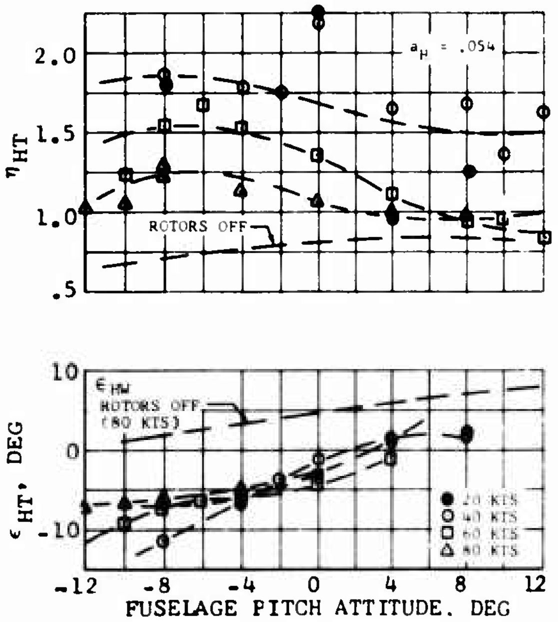

Figure 16. Horizontal Stabilizer Net Aerodynamic Characteristics, Nacelle Incidence 90°.

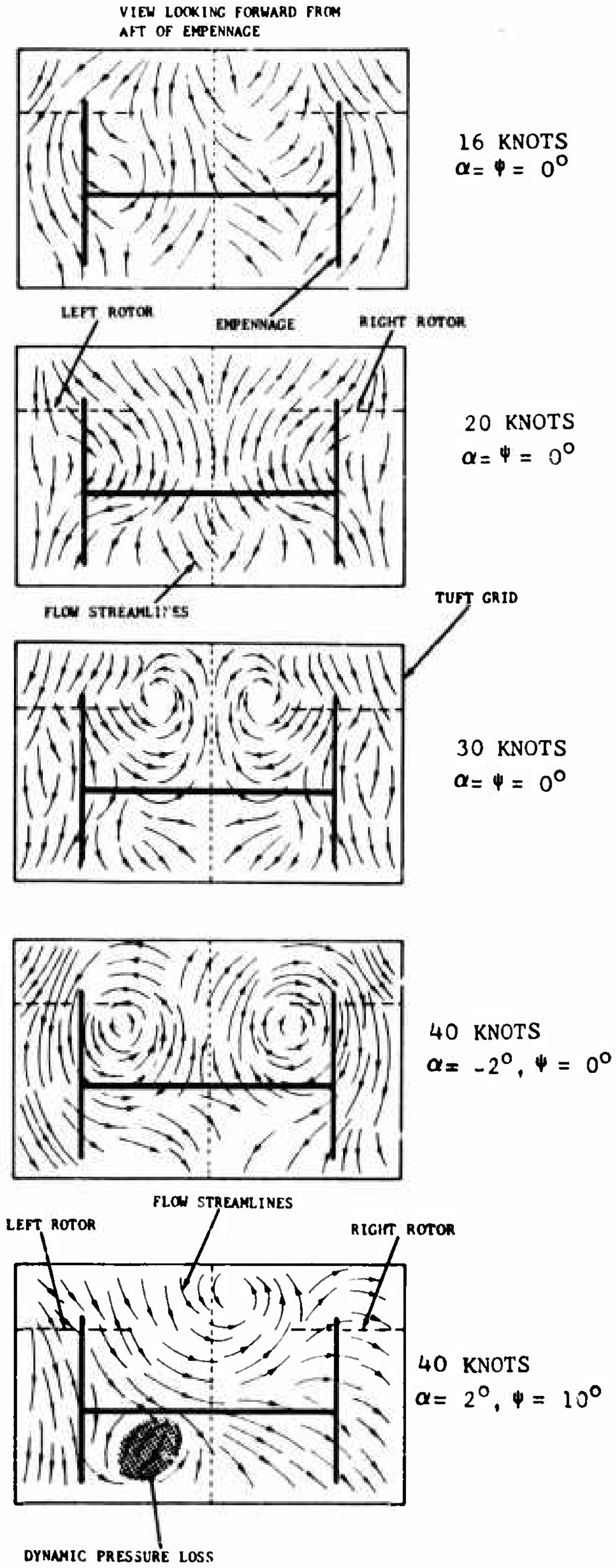
VIEW LOOKING FORWARD FROM AFT OF EMPENNAGE
16 KNOTS
α = ψ = 0°
LEFT ROTOR
EMPENNAGE
RIGHT ROTOR
20 KNOTS
α = ψ = 0°
FLOW STREAMLINES
TUFT GRID
30 KNOTS
α = ψ = 0°
40 KNOTS
α = -2°, ψ = 0°
FLOW STREAMLINES
LEFT ROTOR
RIGHT ROTOR
40 KNOTS
α = 2°, ψ = 10°
DYNAMIC PRESSURE LOSS

Figure 15. Flow Patterns in the Vicinity of the Empennage in Level Flight, Nacelle Incidence 90°.

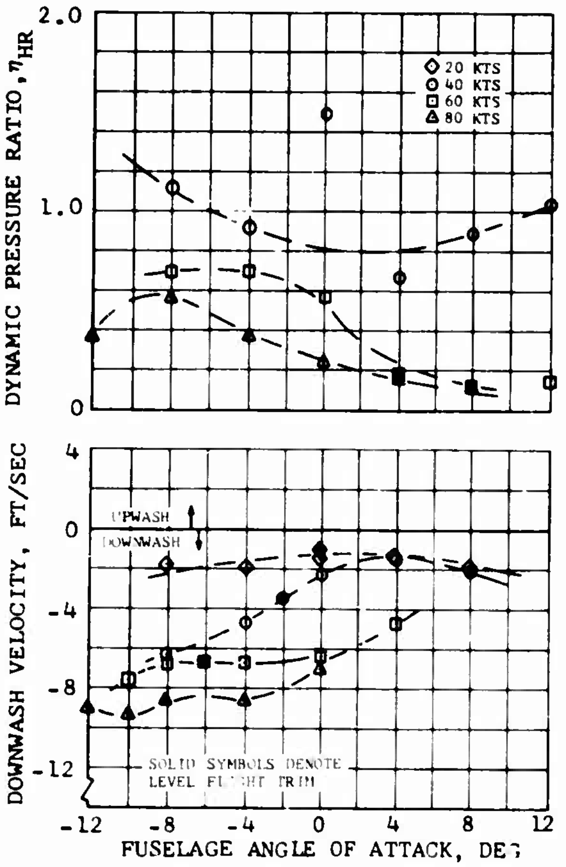

Figure 17. Downwash and Dynamic Pressure Ratio at Horizontal Stabilizer Due to Rotor Wake, Nacelle Incidence 90°.

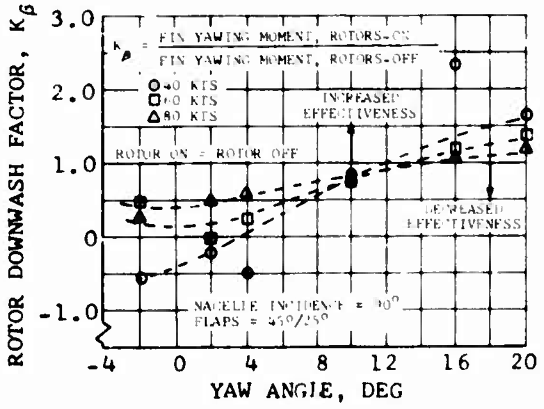

Figure 19. Effect of Rotor Wake on Directional Stability, Nacelle Incidence 90°.

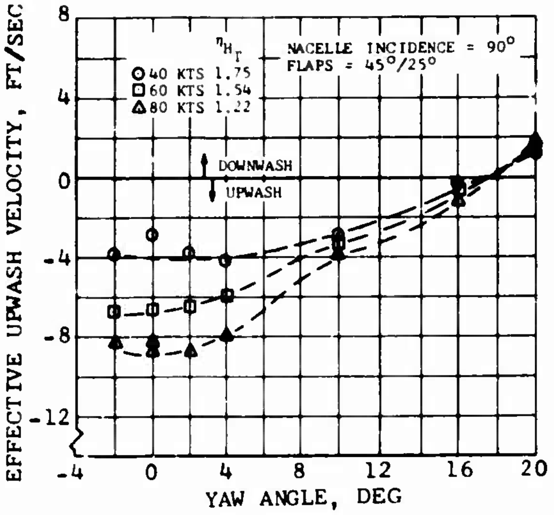

Figure 18. Effect of Yaw Angle on Rotor Wake Upwash at Horizontal Stabilizer, Nacelle Incidence 90°.

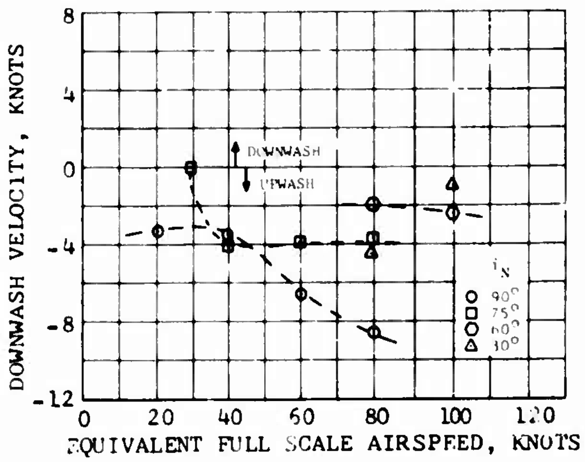

Figure 20. Comparison of Measured Downwash Velocity at Horizontal Stabilizer Contributed by Rotor For Several Nacelle Incidence Angles.

U. S. AIR FORCE V/STOL AIRCRAFT AERODYNAMIC PREDICTION METHODS

Henry W. Woolard
Flight Control Division, Control Criteria Branch (FGC)
U. S. Air Force Flight Dynamics Laboratory
Wright-Patterson AFB, Ohio 45433, USA

SUMMARY

Three U. S. Air Force sponsored programs dealing with the development of analytical methods for the prediction of the aerodynamic characteristics of V/STOL aircraft are reviewed in part. Two of the programs are concerned with the aerodynamics of STOL aircraft exclusively, with emphasis on high-lift systems utilizing internally-blown flaps, under-the-wing externally-blown flaps, and mechanical flaps combined with thrust vectoring. A third program is concerned with the power-induced aerodynamics of lift-jet, lift-fan, and vectored-thrust V/STOL aircraft operating in the hover and transition flight regimes. In this paper principal emphasis is placed upon describing selected methods that employ rational analytical modeling of the real aerodynamics in conjunction with empirical modifications as required. Little attention is given to pure empirical methods. Some comparisons with experiment are given, but the main emphasis is on the description of methodology.

NOTATION

A	aspect ratio or cross-sectional area
c_ℓ, C_L	section and finite-wing jet-flapped wing-lift coefficients respectively. Includes the circulation and reaction lift contributions of the "captured" fraction (see Fig. 2) of the blowing jet that produces supercirculation.
$c_{\ell_{sp}}$, $C_{L_{sp}}$	section and finite-wing lift coefficients respectively due to the "spilled" fraction (see Fig. 2) of the blowing jet.
$\hat{c}_\ell$, $\hat{C}_L$	total section and finite-wing jet-blown wing lift coefficients respectively $\hat{c}_\ell = c_\ell + c_{\ell_{sp}}$; $\hat{C}_L = C_L + C_{L_{sp}}$.
c_{ℓ_α}, C_{L_α}	$\partial c_\ell/\partial\alpha$ and $\partial C_L/\partial\alpha$ respectively.
c_μ, C_μ	section and finite-wing blowing-momentum coefficients respectively.
k_π, K_π	$[(c_{\ell_\alpha})_\pi/(c_{\ell_\alpha})_o]_{theo}$ and $[(C_{L_\alpha})_\pi/(C_{L_\alpha})_o]_{theo}$ respectively, where the subscript "theo" denotes idealized theoretical values.
S_w, S'_w	projected wing areas respectively for flaps retracted and extended.
q	dynamic pressure, $\rho U^2/2$.
$\tilde{\alpha}$, α	two- and three-dimensional angles of attack respectively.
α_i	induced angle of attack.
δ_f	flap deflection angle.
$(\ )_c$	denotes the captured fraction of the engine jet exhaust impinging on the flap system (see Fig. 2).
$(\ )_s$	denotes the stall state.
$(\ )_{sp}$	spilled fraction of the engine exhaust jet impinging on the flap system (see Fig. 2).
$(\ )_{ZL}$	denotes the $c_\ell = C_L = 0$ state, not $\hat{c}_\ell = \hat{C}_L = 0$ (see definitions for c_ℓ, C_L, $\hat{c}_\ell$, and $\hat{C}_L$).
$(\ )_\pi$, $(\ )_o$	denotes power-on and power-off states respectively.
$(\ )'$	denotes a coefficient (except as applied to c' and S'_w) based on the extended chord length, c', or the projected wing area, S'_w, resulting from the Fowler action of a flap, e.g., $a' = (S_w/S'_w)a$, $b' = (c/c')b$, etc.
$(\ )^*$	denotes a hypothetical flapped wing for which the flow over the flap segments is always attached, but for which leading-edge separation may occur.
$\Delta_x y$, $(\Delta_x y)_z$	denotes respectively a change in y due to x and a change in y due to x at the state condition z, where x, y, and z may be any variable or parameter.
K_Γ	empirical correction (Convair) to the induced-drag aerodynamic efficiency factor, e_π (See page 22-5 and Fig. 5).

1. INTRODUCTION

During the past several years, the U.S. Air Force Flight Dynamics Laboratory has sponsored a number of programs concerned with the development of analytical methods for the prediction of the aerodynamic characteristics of STOL and V/STOL aircraft. This paper reviews some of the methods evolving from three of these programs. Two of the programs are concerned with the aerodynamics of STOL type aircraft exclusively, with emphasis on high-lift systems utilizing internally-blown flaps, under-the-wing externally-blown flaps, and mechanical flaps combined with thrust vectoring. One of the two STOL programs, known as the STOL Tactical Aircraft Investigation (STAI), is a broad-based effort dealing with many facets of STOL Tactical Aircraft Technology of which the aerodynamic prediction methodology is only a part. The background and scope of this program is outlined by Osborn and Oates[1] in the fourth paper of this Symposium. The Tactical Aircraft Investigation program involved separate efforts by the Convair Division of General Dynamics, the Los Angeles Aircraft Division of Rockwell International Corporation, and the Boeing Company. The other STOL program was performed by the Douglas Aircraft Company of the McDonnell Douglas Corporation. A third program, conducted by the Aircraft Division of the Northrop Corporation, is concerned with the power induced aerodynamics of lift-jet, lift-fan, and vectored-thrust V/STOL aircraft operating in the hover and transition flight regimes.

As originally conceived by the Air Force Flight Dynamics Laboratory, the aerodynamic prediction methods developed under the STOL Tactical Aircraft Investigation were to be of the handbook preliminary design and evaluation type; that is, relatively simple in form, easy to apply, and conforming generally to the spirit of the U.S. Air Force Stability and Control DATCOM[2] and the British Royal Aeronautical Society Aerodynamics Data Sheets[3]. Whenever possible, the methods developed were to be based upon fundamental flow principles with appropriate empirical modification as opposed to a total reliance upon empiricism. To aid in the establishment of some of the empirical constants, as well as to provide an aerodynamic data base for the other facets of the investigation, extensive wind-tunnel tests[1] were conducted as a part of the program. In contrast to the STOL Tactical Aircraft Investigation, the Douglas program deals primarily with relatively complicated prediction methods and secondarily with simple handbook-type methods. The Douglas program did not include an experimental investigation, but some comparisons of the methods with the wind-tunnel data of the STOL Tactical Aircraft Investigation are made. The Northrop program utilizes methodologies that vary from moderate complexity to the simpler handbook type. In their program, Northrop conducted wind-tunnel tests on transverse jets and on a vectored-thrust fighter-aircraft configuration.

Due to space limitations, it is impossible to review the subject methods and their validation in any great depth. Principal emphasis is placed, therefore, upon describing selected methods that employ rational analytical modeling of the real aerodynamics in conjunction with empirical modifications as required. Little attention is given to pure empirical methods. Some comparisons with experiment are given, but the principal emphasis is on methodology. Further details regarding the methods may be found in the cited references.

2. STOL TACTICAL AIRCRAFT INVESTIGATION PROGRAM

This section reviews the aerodynamic prediction methods[4,5,6] developed by the three contractors participating in the STOL Tactical Aircraft Investigation. The high-lift systems considered are wings with internally-blown flaps (IBF), wings with under-the-wing externally-blown flaps (EBF), and wings with mechanical flaps and engine-nacelle installations having a thrust vectoring capability (MF/VT). These systems are illustrated in Fig. 1. Note that the internally-blown flap system consists of two subdivisions: (1) a pure jet-flap system; and (2) a jet-augmented flap system. The pure jet-flap system involves blowing at the extreme trailing edge whereas the jet-augmented flap system involves a blowing from a location upstream of the trailing edge, usually near the flap leading edge. High-lift systems utilizing ejector flaps (augmentor wing) or upper-surface blowing are not treated in this investigation. Each contractor was responsible for specific high-lift systems. Convair studied internally-blown flaps, externally-blown flaps, and mechanical flaps with thrust vectoring; Rockwell studied externally-blown flaps; while Boeing investigated mechanical flaps with thrust vectoring. The Boeing Company was responsible also for a low level experimental effort on internally-blown flaps. Although there was no Air Force requirement for Boeing to develop IBF analytical prediction methods, nevertheless an analysis was performed and is reported upon in Ref. 7.

The approach employed by all the contractors is to develop methods for the power-on effects incremental to the power-off aerodynamics. For the power-off base, Convair utilizes the methods of DATCOM[2] with some modifications of its own for multi-slotted flaps, Rockwell International utilizes DATCOM, while Boeing uses its own methods in combination with those of DATCOM.

This review is concerned with the methods for predicting the incremental power effects. Consideration is not given directly to the power-off aerodynamics, although the subject is indirectly alluded to.

Prediction of the incremental power effects for internally- and externally-blown flap systems is accomplished by relating the actual systems to the two- and three-dimensional potential-flow aerodynamics of pure jet-flapped wings by means of flow-model analogies and appropriate correction factors.

2.1 Potential Flow Theories for Jet-Flapped Wings

In the Convair and Rockwell methodologies, the incremental power effect on wings with internally- or externally-blown flaps is based upon heuristic and/or empirical modifications to two- and three-dimensional potential-flow theories for pure jet-flapped wings. For two-dimensional flows, both contractors use the well-known thin-airfoil jet-flap wing-section theory of Spence[8,9]. Although there are a number of alternative methods available for the two-dimensional case, they appear to offer little advantage over the Spence method. The methods available for three-dimensional jet-flap wing flows fall into the two categories of either a lifting-surface theory or a lifting-line theory. Generally, the lifting-surface theories were considered to be too complicated for the handbook type methods to be developed in the STOL Tactical

Aircraft Investigation. Convair, however, did employ the Das[10] lifting-surface theory to establish some universal parameters for one of their approximate procedures. Basically, the requirement in this program is for relatively simple analytical expressions. A lifting-line analysis of a "jet-flapped elliptic wing" satisfies this need.

A jet-flapped elliptic wing, or alternately a blown elliptic wing, is defined herein as a wing having an elliptic planform, an elliptic span loading, and an elliptic spanwise distribution of blowing momentum. Analogous to an unblown elliptic wing, the blown elliptic wing has the properties that the section lift coefficient, c_ℓ, section blowing momentum coefficient, c_μ, and the downwash angle are constant distributed spanwise. Additionally, the section and total lift coefficients, c_ℓ and C_L, are equal and the section and total blowing momentum coefficients, c_μ and C_μ, are equal.

Lifting-line theories for jet-flapped elliptic wings have been developed principally by Maskell and Spence[11], Hartunian[12], Kerney[13], and Tokuda[14]. In general, these theories yield the result that the power-on to power-off lift-curve slope ratio, K_π, is a function of the Spence[8] two-dimensional lift-curve slope ratio, k_π, the three-dimensional momentum coefficient, C_μ, and the wing aspect ratio, A; that is, $K_\pi = f(k_\pi, C_\mu, A)$. The specific form of the function f depends upon which of the aforementioned theoretical methods is employed. All of the theoretical methods, except Kerney's, yield lift-curve slopes that are almost identical. Kerney's method yields slope values that are approximately 5% higher than the other methods.

On the basis of favorable comparison with experiment, Convair utilizes Kerney's theoretical results, while Rockwell employs the well-known results of Maskell and Spence.

2.2 Convair Methodology

For the three powered-lift systems, Convair[4] develops methodologies for the wing-lift curve, including the maximum lift coefficient, the induced drag, thrust recovery, flap pitching-moment increments, downwash, and the lateral-directional stability derivatives.

Convair assumes that the power-on total lift curve is given by

$$\hat{C}_{L_\pi} = (S_w'/S_w)\left[(C'_{L_\alpha})_{ZL,\pi}\sin(\alpha-\alpha_{ZL,\pi}) + C'_{\mu_{sp}}\sin(\alpha+\delta_{SP})\right] \quad (1)$$

There are four basic assumptions associated with the foregoing equation. These are:

1. The lift curve is represented by a sine curve.

2. The zero-lift power-on jet-flap lift-curve slope is essentially independent of the spanwise details of the blowing.

3. The incremental lift coefficient due to blowing with flaps deflected is dependent upon the spanwise distribution of blowing.

4. The spilled portion (subscript sp in Eq. 1) of the jet momentum, that is, the portion not captured by the trailing-edge flap system, is treated as a vectored thrust term.

The second assumption suggests that for internally- and externally-blown flaps, the zero-lift power-on jet-flap lift-curve slope can be predicted by means of blown elliptic-wing theory. This leads to

$$(C'_{L_\alpha})_{ZL,\pi} = (C'_{L_\alpha})_{ZL,0}\,K'_\pi \quad (2)$$

where the power-off lift-curve slope is predicted by the best available methodology taking into account wing geometry and viscous effects.

The incremental lift coefficient referred to in the third assumption determines the power-on angle of zero lift in Eq. 1. For the purpose of estimating this increment, Convair generated a series of partial-span lift factors for internally-blown flapped wings using the Das[10] jet-flapped wing lifting-surface theory. These factors were found to correspond so closely to those for mechanical flaps[15,16] that is was considered adequate to use the mechanical flap factors for both purposes.

The lift-curve slope ratio, K'_π, in Eq (2) is to be taken from jet-flapped elliptic-wing theory (Kerney's[13] in this case) and involves the section blowing-momentum coefficient c_μ, which is the same as the total coefficient, C_μ, for the blown elliptic wing. In applying blown elliptic-wing theory to the prediction of the lift-curve slope for actual systems, consideration must be given to the determination of the proper blowing momentum coefficient to be used in the theoretical relations. For this purpose, it is convenient to define a circulation-effective blowing momentum coefficient and an apparent blowing momentum coefficient. The circulation-effective blowing momentum coefficient, C_{μ_c}, is the momentum coefficient based on that fraction of the jet momentum flux that increases the wing circulation by means of a jet-flap effect, that is, by means of a relatively strong trailing jet sheet. This definition is a convenient artifice for delineating a momentum coefficient that may be used in the theoretical blown elliptic wing relations. It should not be construed from this terminology that the remaining fraction of the jet does not induce circulation on the wing by means of such effects as entrainment, blockage, and vorticity. A vectored jet near a wing, but not impinging upon it, for example, induces wing circulation by the aforementioned means. The apparent blowing momentum coefficient is the momentum coefficient at the nozzle exit of the blowing device: for an internally-blown flap, the slot exit; for an externally-blown flap, the engine-exhaust plane. For a jet-augmented flap, the circulation effective momentum coefficient is of a smaller magnitude than the apparent momentum coefficient due to surface friction (scrubbing) losses experienced by the blown stream in flowing from the exit slot downstream along the flap surface to the trailing egge. For an externally-blown flap, there is also a scrubbing loss. In addition, only that portion of the jet exhaust intercepted (captured) by the flap (see Fig. 2) contributes to the circulation effective momentum coefficient. The spilled portion of the engine jet exhaust contributes a jet reaction force primarily and an interference force secondarily. One of the deficiencies of the Convair method is that it does not account for the interference force of the spilled fraction of the jet which becomes the vectored jet in a MF/VT system.

Finally, consideration must be given to the trailing-edge jet-deflection angle. For a jet-augmentedflap, it reasonably may be assumed that the jet stream leaves the trailing edge tangent to the affected surface. For an externally-blown flap, it may be assumed also that the captured portion of the jet exhaust stream leaves the trailing edge parallel to the affected surface. The determination of the flow direction for the spilled portion is somewhat more difficult; as an approximation, Convair assumes a flow direction parallel to the engine exit-nozzle axis.

It is of interest to note at this point that Rockwell handles the effective momentum coefficient and trailing-edge jet-deflection angle in a different manner. The Rockwell method will be discussed subsequently.

Estimation of the three-dimensional circulation-effective blowing-momentum coefficient, C'_{μ_c}, and the spilled momentum coefficient, $C'_{\mu_{sp}}$, is made on the basis of a highly simplified flow concept involving the geometric considerations illustrated in Fig. 2. The respective momentum coefficients are given by

$$C'_{\mu_c} = C'_{\mu_{XTE}}(A_c/A_j), \qquad C'_{\mu_{sp}} = C'_{\mu_{XTE}} - C'_{\mu_c} \qquad (3),\ (4)$$

where the areas are defined in the figure. The area ratio (A_c/A_j) is unity for internally-blown flaps, zero for mechanical-flap vectored-thrust systems, and ranges from zero to unity for externally-blown flaps. The parameter, $C'_{\mu_{XTE}}$, is the momentum coefficient at the extended trailing-edge location shown in Figure 2 and includes scrubbing losses for which Convair gives a methodology. For internally- and externally-blown systems, the section circulation-effective momentum coefficient, c'_{μ_c}, employed depends upon the property being calculated in accordance with assumptions (2) and (3) from Eq (1). For the calculation of the lift-curve slope, c'_{μ_c} is taken equal to $\bar{c}'_{\mu_c}$, where $\bar{c}'_{\mu_c} = C'_{\mu_c}$ for both blowing systems.

For the calculation of the partial-span effects, the section circulation-effective momentum coefficients are given by

$$c'_{\mu_c} = (S'_w/S'_j)C'_{\mu_c} \quad \text{(IBF)}, \qquad (c'_{\mu_c})_n = (S'_w/S'_j)_n\ (C'_{\mu_c}/N) \quad \text{(EBF)} \qquad (5),\ (6)$$

where N is the total number of engines, each assumed to be producing the same thrust, n is the n^{th} engine, and S'_j is defined in Fig. 2.

For a finite-span wing, Convair has developed a theoretical relation for the maximum lift coefficient increment due to blown trailing-edge flaps. The relation derived is based on the assumption that the blown and unblown wings are geometrically and aerodynamically elliptic in the sense described earlier. It is also assumed that stall occurs on the upper surface near the leading edge or at or behind the knee of a leading-edge device when present and at a value of a stall parameter, $(C_p x^{1/2})_s$, that is independent of the application of power. In the stall parameter, C_p is the pressure coefficient, x the distance from the leading edge as a fraction of the chord, and s denotes the stalled state. A similar criterion for the stall of two-dimensional jet-flapped wings has been previously employed by Foster[17] and Moorhouse[16,18]. In the calculation of the stall parameter, Foster, Moorhouse, and Convair all employ Spence's[9] relation for the pressure distribution on a jet-augmented flapped wing section. The Convair analysis, however, accounts for the finite wing by replacing α by the wing-section angle of attack $(\alpha-\alpha_i)$.

On the aforementioned bases, Convair obtains the following relation for the maximum lift coefficient increment

$$\Delta_\pi C_{L_{max}} \approx (3/4)(\Delta_\pi C_L)_{\alpha_{s,\pi}} + (3/4)(2\pi)(\alpha_{i_\pi} - \alpha^*_{i_o})_{\alpha=\alpha_{s,\pi}} \qquad (7)$$

where a geometric interpretation of the terms in the equation appears in Fig. 3. For very high aspect ratio wings, the second term in Eq. (7) vanishes and Eq. (7) reduces to the following result having the same form as obtained by Moorhouse[18]

$$\Delta_\pi c_{\ell_{max}} = (3/4)(\Delta_\pi c_\ell)_{\tilde{\alpha}_{s,\pi}} \qquad (8)$$

where the tilde denotes the two-dimensional angle of attack and the subscript s denotes the stalled state. A geometric interpretation of the terms in Eq. (8) appears in Fig. 3. Equation (7) is the basic relation used in deriving the maximum lift coefficient relation. However, since the power-on stall angle is unknown and the lift methodology of Eq (1) is nonlinear, Eq (7) needs further manipulation and interpretation to predict the maximum lift. Equation (7) has been displayed in lieu of the more complicated maximum lift relation because of its simpler geometric interpretation on the lift-curve plots (Fig. 3).

It is very important to note that the lift increments in Eqs. (7) and (8) are to be added to a hypothetical power-off wing for which the flow is assumed to always remain attached on the flap segments, a condition denoted by the asterisks on Fig. 3. This situation is designated by Convair[4] as full boundary-layer control (BLC), meaning for the trailing-edge flaps, or as the "BLC effect." Separation on this hypothetical wing therefore must occur near the leading edge which is in accordance with the assumption of the theoretical analysis. Trailing-edge blowing does, of course, promote flow attachment on the flap segments, as assumed. Convair has developed a method for determining the lift curve, including the maximum lift, for the hypothetical power-off wing with full boundary-layer control. This methodology involves the determination of the incremental maximum lift coefficient due to flap deflection, established on the basis of the stall parameter analysis previously described. In the analysis, the theoretical flap effectiveness (corresponding to no separated flow over the flap elements) is employed in conjunction with the experimental maximum lift coefficient for an unflapped wing section. Ultimately, then, the experimental basis for the Convair power-on maximum lift methodology is the power-off stall of the unflapped wing. This differs from Moorhouse's[16,18] analysis which is referenced to the flapped wing power-off stall.

The thrust-recovery factor and the induced-drag coefficient are two power-affected quantities required for the prediction of the drag coefficient. Convair's methodology for the thrust-recovery factor is principally empirical and will not be discussed. The induced-drag coefficient is given by $C_L^2/\pi A e_\pi$, where e_π is a power-on aerodynamic efficiency factor. The aerodynamic efficiency factor is determined from considerations of conservation of global momentum and assumptions regarding the affected mass flows and their vectored change in direction. For the wing, the affected mass flow is that enclosed by a circle with a diameter equal to the wing span; for the jet exhaust, the affected mass flows are the captured and spilled flows. Conservation of momentum and the definition of induced drag yields

$$\hat{C}_L = (\pi A/2)\varepsilon_\infty + C_\mu \overline{\delta}_j , \qquad C_{D_i} = (\pi A/4)\varepsilon_\infty^2 + (C_\mu/2)\,\overline{\delta}_j^2 \tag{9), (10}$$

where ε_∞ is the downwash angle at infinity and $\overline{\delta}_j$ is an effective jet-turning angle given by

$$\overline{\delta}_j = (A_c/A_j)\varepsilon_\infty + (A_{sp}/A_j)\,(\delta_T+\alpha) \tag{11}$$

where δ_T is the inclination of the engine jet exhaust axis relative to the wing reference line. For IBF systems, Eqs (9) and (10) reduce to the well-known relations given by Maskell and Spence[11]. The downwash angle ε_∞ is given by the Maskell and Spence relation, corrected for the power-off efficiency factor e_o, and using lift and momentum coefficients given respectively by $C_L = \hat{C}_L - C_{L_{sp}}$ and C_{μ_c}. Sufficient relations are now available to determine the power-on efficiency factor e_π which is given in Ref. 4. Sample comparisons of theoretically predicted lift curves and power-on aerodynamic efficiency factors are shown in Figs. 4 and 5 respectively. The agreement between analysis and experiment shown for the lift curves should not be considered as typical. Reference 4 presents a large number of comparisons for all three high-lift systems and for a variety of parametric combinations of wing sweepback, aspect ratio, and flap systems. Some of these yield better agreement than shown in Fig. 4, others worse.

From an examination of all the comparisons given in Ref. 4, the following may be concluded. For all the high-lift systems, the analytic and experimental drag polars, $C_D(C_L)$, generally agree reasonably well for values of C_μ below 2.0. For values of C_μ between 2.0 and 4.0, the agreement is somewhat random. For the IBF and EBF systems, the predicted lift curves, $C_L(\alpha)$, agree reasonably well with experiment. For MF/VT systems, the lift curve agreement is poorer, with the characteristic that the predicted slopes are less than the experimental ones. This may be due to neglect of the interference effect of the spilled fraction of the jet exhaust in the methodology.

For IBF systems, Convair determines the incremental pitching-moment coefficient due to power for blown multiple-element flaps through the use of Spence's derivatives for jet-augmented flaps, but abandons the usual linear superposition principle for a very unusual psuedo-superposition scheme. The two-dimensional values are then modified for three dimensions by factors involving the flap-span ratio, ratio of the flap-affected area to total wing area, and the squared cosine of the sweep-back angle. The rationale for the methodology is not entirely clear, but in a large number of comparisons with experimental data from Ref. 19, the average of the absolute percentage error was found to be 3%.

For the pitching-moment methodology for EBF systems, a heuristic model is employed in which the flap elements are replaced by downward facing semi-circular cylindrical scoops. The lift on the scoops is estimated by means of an analogy to ring airfoils. The scoop list is then used to estimate the pitching moment due to the flaps. In a large number of comparisons with experimental data from Ref. 19, the average of the absolute percentage error was found to be 11%.

The Convair downwash methodology assumes that the distances involved are reasonably far downstream from the wing, say, of the order of the horizontal tail location. The method determines a basic downwash angle to which empirically determined increments in downwash are added. The empirical increments account for the effects of sweepback, aspect ratio, and type of high lift system employed. The basic downwash distribution is determined by assuming that the longitudinal distribution is equivalent to that along the longitudinal axis of a single horseshoe vortex having a span equal to the span of a pair of rolled-up vortices, and the vertical distribution corresponds to that along the vertical axis in the Trefftz plane of an elliptically-loaded lifting line with the Trefftz plane origin translated vertically to the empirically determined location of the wing wake.

The incremental lateral-directional-stability derivatives due to power are handled by a method analogous to Ref. 2.

2.3 Rockwell International Methodology

Rockwell's[5] studies are devoted exclusively to the externally-blown flap system. Rockwell develops methods for the lift curve, including the maximum lift coefficient, the induced drag, thrust recovery, downwash, asymmetric engine operation, and the static longitudinal and lateral-directional-stability derivatives.

Rockwell employs the Maskell and Spence[11] aspect-ratio correction factor, F, where $C_{L_\pi} = c_{\ell_\pi} F(A, C_\mu)$, and the specific form of the function F is given by Maskell and Spence. In determining a momentum coefficient and jet-deflection angle for use in the blown-elliptic wing relations, Rockwell does not divide the exhaust jet into distinct captured and spilled regions, as done by Convair, but instead employs an overall effective jet-deflection angle and overall effective momentum coefficient, both of which are determined empirically. The effective momentum coefficient is given by ηC_μ, where η is a turning-efficiency factor accounting for the jet-turning losses. Both the turning-efficiency factor, η, and the effective jet-deflection angle, $\bar{\tau}$, are determined from static tests and assumed to be applicable at forward speed. From correlations with the Rockwell wind-tunnel tests, the jet-turning efficiency was found to be a linear function of the jet-turning angle, with the slope determined by the type of flap system and the wing sweepback angle. Rockwell uses the captured-jet fraction concept to establish a correlation for the effective jet-deflection angle and finds that two generalized curves of the turning-angle ratio, $\bar{\tau}/\delta_{tf}$, as a function of the impingement parameter, Z_f/R_f, (see Fig. 2) adequately establish the jet-deflection angles for the double and triple-slotted flap systems tested by Rockwell. In the turning-angle ratio, δ_{tf} is the deflection angle of the trailing-edge flap segment. In estimating R_f, Rockwell assumes a 12.5 degree expansion angle instead of the 6 degree angle shown in Fig. 2. Curves of the turning-angle ratio are presented by Osborn and Oates[1] (see their Fig. 12).

In the Rockwell methodology, the incremental lift coefficient due to power for an externally-blown flap system is given by

$$\Delta_\pi C_L = (1+t/c)F(A.\eta c_\mu'')\ [\lambda(\partial c_\ell/\partial\delta_f)\sin\bar{\tau} + \nu(\partial c_\ell/\partial\alpha)\alpha] \tag{12}$$

where $F(A,\eta c_\mu'')$ is the Maskell and Spence aspect ratio correction, t/c is the thickness ratio of the mean aerodynamic chord of the flapped portion of the wing, the partial derivatives are from Spence's[9] two-dimensional jet-augmented flap theory, and λ and ν are partial-span correction factors employed by Williams, Butler, and Wood[20]. The momentum coefficient, c_μ'', is given by $c_\mu'' = (S_w/S'')C_\mu$, where S'' is defined in Fig. 6. The partial-span factors are given by $\lambda = S''/S_w$ and $\nu = (S''/S_w, \eta c_\mu'')$, and the partial derivatives are functions of the momentum coefficient, $\eta c_\mu''$. Equation (12) directly accounts for the aspect ratio and partial-span effects, but only indirectly accounts for sweepback effects through the jet-turning efficiency, η.

Correlations of the incremental lift coefficient due to power at zero angle of attack $(\Delta_\pi C_L)_{\alpha=0}$ and the power-on finite-wing lift-curve slope $(\partial C_L/\partial\alpha)_\pi$ appear in Figs. 7 and 8 respectively. These quantities are given respectively by the first and second terms on the right-hand side of Eq. (12). Most of the test points shown are for an aspect ratio of 7, a quarter-chord sweep angle of 24 degrees, and full-span leading and trailing-edge flaps. There are several test points for zero sweepback and a number of points for moderate deviations from the aforementioned values of aspect ratio, sweep, and flap span.

Rockwell develops a methodology for the incremental maximum lift coefficient due to power based on a three-dimensional modification to the two-dimensional relation given by Eq. (8). The rationale for the method is not entirely clear. In any case, Rockwell presents a simpler alternate relation which is completely empirical and compares more favorably with experiment.

Rockwell develops a methodology for the wing incremental pitching moment due to power on the following basis. The jet-reaction vector is assumed to pass through the trailing edge of the flap and to be located spanwise at the average location of the engines. The spanwise location of the circulation lift is assumed to be located at the power-off mean aerodynamic chord. The power-on chordwise center-of-pressure locations due to circulation lift at zero angle of attack and circulation lift at angle of attack are assumed to be equal to the power-off values. Since the two-dimensional power-on center-of-pressure locations are easily calculated theoretically, it is not clear why this capability was not included in the methodology. A comparison of the calculated incremental pitching moment with experiment is shown in Fig. 9.

Rockwell's test data for the power-on induced drag coefficient failed to agree with the induced drag coefficient calculated by the Maskell and Spence[11] relation. Rather good agreement was obtained, however, by using the power-off induced drag relation based on the power-on circulation lift.

2.4 Boeing Methodology

In the STOL Tactical Aircraft Investigation, Boeing was responsible for aerodynamic prediction methods for high-lift systems employing mechanical flaps in combination with vectored thrust. Since Boeing's methods for the power-induced interference are completely empirical, they are not discussed. It is worth noting, however, that on the basis of the studies made, Boeing found that the equivalent jet-velocity ratio $(q_\infty/q_{jet})^{1/2}$, which is proportional to $C_J^{-1/2}$, provided a useful similarity parameter for the power-induced incremental lift, moment, and drag coefficients. For the range of jet-thrust coefficients investigated $(0 \le C_J \le 2.0)$, it was found that the aforementioned aerodynamic coefficients were directly proportional to $C_J^{1/2}$. This property served to reduce the number of parametric design curves required.

The Boeing methodology is incorporated in a digital-computer program written in Fortran IV language for use on CDC 6000/7000 series computers. A users' manual and program listing is given in Ref. 6.

Although there was no Air Force requirement for Boeing to develop IBF analytical prediction methods, Davenport[7] nevertheless conducted a jet-flapped wing lifting-line analysis which is concerned principally with the influence of non-planar trailing vortices on the wing aerodynamics. In the Davenport analytic model, the wing is represented by a finite number of horseshoe vortices distributed spanwise and originating from local quarter chord positions. For each horseshoe vortex, the trailing vortex system is divided into two inclined longitudinal segments as shown in Fig. 10. On the basis of this model, Davenport develops a computer program for calculating the wing aerodynamic characteristics. In limited comparisons with other experiments and other theories, Davenport's method appears to predict the drag polar, $C_D(C_L)$, better than other methods at high momentum coefficients and jet angles. The method does not, however, predict the pitching-momentum coefficient as well as does the Lopez-Shen[21] method.

3. THE DOUGLAS AIRCRAFT COMPANY PROGRAM

Douglas was responsible for developing new methodologies and adapting or modifying existing methodologies to the prediction of the aerodynamic characteristics for each of the three high-lift systems employing internally-blown flaps, externally-blown flaps, and mechanical flaps combined with thrust vectoring. These methodologies were to be incorporated into a comprehensive digital computer program. Sophisticated analytical techniques were to be employed as opposed to essentially handbook-type methods.

The nucleus of the Douglas methods for internally-blown and externally-blown flap systems is a linearized theoretical lifting-surface type jet-flapped wing analysis which Douglas identifies as the Elementary Vortex Distribution (EVD) method[21,22]. This method is implemented by means of a relatively large size digital computer program. For wings of zero thickness, the method is capable of handling arbitrary wing planforms with arbitrary spanwise distribution of twist, flap chord, jet-blowing momentum and jet-deflection angle. Within the framework of a linearized model, the EVD method represents one of the most general and most exact solutions available for jet-flapped finite-span wings. As such, the method not only serves as a useful analysis and design tool, but provides also a convenient basis of comparison for other approximate methods of analysis.

Initial development of the EVD method was sponsored by the Douglas Aircraft Company and the U. S. Office of Naval Research. The Air Force sponsored improvements to the original digital computer program and extensions of the methodology to the determination of rotary derivatives, flow-field details, wing-body aerodynamics, horizontal tail aerodynamics, and ground effects[23,24,25].

Conceptually, the EVD method is directly applicable to IBF systems. In application, however, small empirical corrections are applied to account for such items as airfoil thickness and boundary-layer displacement effects on the lift-curve slope, flap effectiveness, and other factors.

The EVD method is, of course, not directly applicable to externally-blown flap systems and an analogy is developed for this application.

For vectored-thrust interference effects on MF/VT systems, Douglas employs, with some minor modifications, the Northrop[26] methodology, which is to be described subsequently.

The mathematical modeling for the Douglas jet-flapped wing methodology is illustrated in Fig. 11, where it is seen that the vorticity $\gamma(x,y)$ over the wing and jet sheet is represented by elementary horseshoe vortices (e.g., abcd) distributed over these regions. The governing equation is the classical linearized lifting-surface downwash integral equation for distributed elementary horseshoe vortices, subject to the boundary conditions on the wing and jet sheet and appropriate enforcement of the Kutta condition. The usual approach in solving lifting-surface boundary value problems is to employ a finite element method in which the total vortex sheet is replaced by a large but finite number of small rectangular elements over which the bound vorticity distribution may be taken as discrete and of unknown magnitude or as distributed with the distribution characterized by a single unknown parameter indicative of the gross vortex strength; and the boundary conditions are satisfied at discrete points on each element instead of continuously. In this formulation, the integral equation and boundary conditions are converted into a set of simultaneous linear algebraic equations for the unknown vortex strengths. For unblown wings, a variety of finite-element schemes have been employed. In the vortex-lattice method, for example, the bound vorticity distribution is represented by a discrete vortex. Another approach is to represent the bound vorticity by a stepwise distribution wherein the vorticity is constant over each element. Both of these schemes possess the disadvantage that the vortex-induced downwash is singular in certain regions, thereby requiring careful selection of the control point location for satisfying the boundary condition. If, however, the bound vorticity distribution is taken to consist of piecewise distributions of linear and appropriate special continuous forms as shown in Fig. 11c, the induced downwash is everywhere finite and closely satisfies the boundary condition at all points on the vortex surfaces rather than at a discrete number of points only. Additionally, in this scheme, the control point does not have to be carefully selected in some particular way. Because of these important properties, the piecewise distributed vorticity scheme has been applied by Douglas to the three-dimensional jet-flapped wing problem.

In the Douglas methodology, the piecewise vorticity distribution is taken to be the sum of the overlapping special elementary vortex distributions (EVDs) shown in Figs. 11d, e, and f. These special EVDs are: (1) a triangular distribution identified as a regular EVD; (2) a leading-edge EVD which is the classical leading-edge inverse square-root vorticity variation minus a linear variation; (3) a distribution for a discontinuity in slope, i.e., a hinge EVD, which is a logarithmic vorticity variation minus a linear variation; and (4) an asymptotic EVD which properly accounts for the decay in vorticity along the jet sheet far downstream and additionally satisfies the Kutta condition at infinity.

Some comparisons of the lift and spanwise load distributions calculated by the EVD method with those obtained by the theoretical methods of Maskell and Spence[11] and Das[10] for jet-flapped wings and with some experimental results of Das for jet-flapped wings are made in Refs. 22 and 23. These comparisons generally are inconclusive regarding the accuracy of the EVD method for jet-flapped wings since neither of the theoretical methods to which the comparisons are being made is exact and the experimental results are of uncertain accuracy.

With the EVD jet-flapped wing method as a nucleus, Douglas developed a comprehensive computer program identified by the code name STAMP for STOL Transport Aerodynamic Methods Program. The STAMP program is intended to aid in the preliminary design and analysis of STOL transport aircraft employing internally-blown jet flaps, externally-blown jet flaps, and mechanical flap systems combined with vectored thrust. It is written in the Fortran IV language and can be readily adapted for use on many large computer systems. Versions are currently in operation on the CDC 6000 series and the IBM 370 series computers.

The STAMP computer program package is a collection of computer programs, each of which is designed to analyze a particular aircraft component, plus interference methods to account for the influence of one component on another. Although intended for the analysis of complete aircraft configurations, the program has been structured so that components can be analyzed separately or in any desired combination. Within the limitations of each theoretical method, the program calculates aerodynamic and stability and control data for arbitrary jet wings (internally blown and externally blown), for vectored jets, and for arbitrary fuselage and empennage arrangements. These data can be calculated both in free air and in proximity to the ground.

The bases for some of the methods incorporated in the STAMP computer program will now be described.

The methodology for ground effects is a linear one employing an image wing to achieve the ground-plane simulation. Caution is required in applying the ground-effects solution at small wing heights since ground impingement of the jet and/or other nonlinear flow phenomena which invalidate the small perturbation assumption of linear theory may be present. Some guidelines regarding the limitations of the ground effects method may be gained from the comparisons between theory and experiment shown in Fig. 12. The experimental data shown is from wind tunnel tests[28] on a semispan rectangular wing model with full span jet-augmented flaps deflected to 55 degrees. It is seen here that the discrepancy between theory and experiment is a function of the relative ground height and the momentum coefficient; as the momentum coefficient is lowered, the ground height at which reasonable agreement is obtained is lowered, with the reverse effect occurring as the momentum coefficient is increased.

The methodology for predicting jet-flapped wing yawing and rolling moments due to sideslip employs the vortex system associated with the asymmetric arrangement shown in Fig. 13. The yawing moment is made up of contributions from asymmetric distributions of the chordwise loading, leading-edge suction, and the horizontal component of the jet reaction. Without dihedral, the wing rolling moment is due to the flow asymmetry illustrated. A $\cos \beta$ correction is also applied to obtain the effective blowing-momentum coefficient. The effect of dihedral is accounted for by an equivalent wing twist and an appropriate correction to the jet-deflection angle. No comparisons with experiment have been made for these lateral-directional derivatives.

The method for estimating the rotary derivatives of jet-flapped wings is based on the assumptions of quasi-steady motion for the wing and the jet-deflection angle at the wing trailing edge and neglect of the jet-sheet rotary motion aft of the trailing edge. Although this latter assumption is subject to question, its validity cannot be presently resolved since there is no appropriate jet-flap experimental data with which to compare.

In the Douglas flow-field method, for the jet-flapped wing under consideration, the vorticity distributions on the wing and jet sheet and the jet-sheet shape are first determined by the EVD method. For the purpose of determining the flow field, the elementary vortex distributions are replaced by discrete horseshoe vortices, with the jet-sheet vortices located on the displaced sheet as calculated by the EVD method. In order to account for the trailing vortices behind the unblown portions of the wing a highly simplified scheme is adopted. In this scheme the trailing vortex sheet at each spanwise segment is assumed to be planar and to extend to infinity downstream inclined at an angle midway between the freestream direction and a tangent to the camber line at the trailing edge. Although there is no theoretical basis for this scheme, comparisons of the simplified wake shape calculated by this method to those predicted by more exact roll-up methods verify that the approximation is reasonable. It is apparent that the foregoing analytical model should not be applied to points closer to the wing or jet-sheet than about one local element length.

Comparisons of the downwash angle as calculated by theory with the experiments[28] conducted on the same wing model as employed in Fig. 12 are shown in Fig. 14. It is seen in the figure that generally good agreement is obtained except in those regions near the jet sheet. Additional comparisons also show comparable agreement.

Douglas develops methods for determining the aerodynamics of the horizontal tail and the fuselage in the jet-wing flow field, neglecting interference of the tail and body upon the wing and jet sheet. The horizontal-tail interference is treated by considering the jet-wing flow to be an equivalent induced camber. The fuselage interference is handled by considering the fuselage to be a slender body in a nonuniform flow. The slender-body assumption greatly simplifies the analysis and allows the treatment of non-axisymmetric bodies. The analysis is limited to bodies without vortex shedding and therefore for which there is no lift but only a moment due to the jet-wing interference.

4. THE NORTHROP AIRCRAFT DIVISION PROGRAM

The purpose of this program was to develop engineering analytic methods for predicting the aerodynamic and stability and control characteristics of high-disk loaded V/STOL aircraft of the lift jet, lift fan, and vectored thrust types in the hover and transition flight regimes. The methods developed were to be applicable to aircraft configurations having a conventional wing, fuselage, and empennage. High angles of attack were to be considered. In general, the methodology was to represent a compromise between handbook methods and methods utilizing complicated computer programs. The results of the program are documented in Refs. 26 and 27.

In the development of the theoretical methods of this study, it is assumed that the incremental power-induced aerodynamics can be determined independently of the unpowered aerodynamics and the resulting effects added together to obtain the total aerodynamics. It is assumed also that the aerodynamics of the aircraft components can be treated individually and added together to obtain total aircraft aerodynamics.

The basic flow problems that have been solved for use as building blocks in the methodology of this program are: (1) the flow field for single and multiple jets exhausting from a flat plate transversely to a free stream; (2) the interference aerodynamics of a jet exhausting transversely from a wing or body; (3) forces and moments on an air intake transverse to the free stream; (4) nonlinear wing and body aerodynamics for high angle of attack.

Since the aerodynamics of transverse jets is an important element of the problem, a significant portion of the investigation is concerned with this flow case.

The final prediction methods obtained are based upon theoretical and theoretical-empirical methods. The empirical information required for the basic transverse-jet flow behavior is obtained from wind-tunnel tests on a circular flat plate model with transversely exhausting jets. The results of these tests are documented in Ref. 27. For the purpose of validating the final methods as applied to an aircraft, wind-tunnel tests were conducted on a complete aircraft model.

The flow model for the transverse jet flow-field theory is shown in Fig. 15. In this model, entrainment into the jet due to viscous mixing is taken into account. The jet internal flow is treated in a global sense; that is, the velocity and other properties within the jet are taken to be uniform over a cross section. In formulating the equations of motion, the forces applied to the jet are assumed to consist of tangential and normal components due to viscous entrainment, and a normal component due to an equivalent solid-body section drag. In order to make the problem determinant, knowledge regarding the entrainment rate and the section drag coefficient is required. A relation of logical form, containing three empirical parameters, is assumed for the entrainment rate. One of the parameters is determined by the condition that the theory agree with known results for a jet exhausting into quiescent air. The remaining two parameters are selected to give good correlation of the theoretical jet centerlines and surface pressures with the experimental data taken in this program. In order to determine the equivalent solid-body section drag coefficient, information regarding the jet cross-sectional shape is required. In this regard, it is observed experimentally that in the initial jet expansion region, called the developing region, the jet progressively deforms from an initial circular cross section into a kidney-shaped one such as shown on the figure. Once the kidney shape is attained, the jet cross sections remain relatively similar in shape as the jet develops downstream. The region of similar cross sections is called the developed region. It has been determined experimentally that the boundary between the developing and developed region occurs at a normal distance from the wall approximately equal to three tenths of the product of the initial jet diameter and the ratio of the jet efflux velocity to the free-stream velocity.

Since it is rather difficult to treat the exact jet cross sectional shape, a simplified shape of elliptical form is assumed. Observations show that, for a kidney-shaped cross section, the best fitting ellipse is one having a minor to major axis ratio of 1/4. Experimental data further indicate that, in the developing region, the minor to major axis ratio decreases linearly with distance from the jet orifice. With this information on the jet cross section at hand, it is possible to determine the jet local section drag coefficient from known data on section drag coefficients for circular and elliptical cylinders.

The system of governing equations is now determinant. Since the system is nonlinear, however, recourse to a digital computer solution is required.

Having solved the governing equations, the variations of the entrainment and the cross sectional shape along the jet centerline are known. The induced flow field due to the jet is then determined by representing the entrainment by an appropriate sink distribution and the cross sectional shape by an appropriate doublet distribution along the jet centerline.

A comparison of theoretically predicted jet centerline trajectories with experiment is shown in Fig. 16 for initial jet angles from 60 to 120 degrees. As may be seen, the agreement is rather good.

A representative example of the agreement between theory and experiment for surface pressure distributions is shown in Fig. 17. As may be seen, the agreement at lateral positions is generally good. Directly ahead and directly behind the agreement is poorer, although for some tests the agreement forward of the jet is better than shown here. In general, the poorest agreement is obtained in the wake region behind the jet. This is to be expected, since there is no provision in the theory to properly handle this region.

The single-jet mathematical model is utilized to develop an analytical model for the flow fields of double and triple exhausting jets. In this extension, the multiple-jet configuration is treated as an arrangement of discrete jets, each having its own singularity distribution. The interference of the singularities upon each other is not taken into account; instead, the upstream jets are assumed to develop independently of the downstream ones and the downstream jets are assumed to exhaust into a stream of reduced velocity resulting from the blockage of the upstream jets.

Once the trajectories of the multiple jets have become merged, the merged jet is considered to be a single one and is analyzed by single-jet theory with the initial condition associated with the merging appropriately taken into account. Some empirical relations are required for the aforementioned model. These have been determined from Ref. 27 for an arbitrary arrangement of double jets and for tandemly aligned arrangements of triple jets.

Conformal mapping techniques are used to analyze the interference effects of jets on bodies and wings for regions not too close to the jet itself. The velocities induced on the bodies by the jet are first determined using the jet cross-flow theory. The problem is then treated in a slender-body sense, i.e., the flow about body sections normal to the long axis is treated in a two-dimensional sense and the boundary-value problem associated with the interference velocities is solved by mapping the body cross section onto the circle plane. A modification is then made for the three-dimensional effect.

The nonlinear body aerodynamic analysis is similar to that used successfully for high angle of attack missile aerodynamics. The linear effects are accounted for by classical slender-body theory with the nonlinear behavior accounted for through the use of a viscous cross-flow drag coefficient.

The nonlinear wing aerodynamics is analyzed by a double lifting-line theory with the boundary condition satisfied at the three-quarters chord position. The chordwise positions of the lifting lines are determined in a manner such that the theoretical section pitching moments are in agreement with experimental values. The circulation strengths of the lifting lines are then determined to give the required section normal force throughout a large angle of attack range.

surface

Several handbook-type methods are devised for quickly estimating the/interference effects of a single jet. These methods assume that the interference aerodynamics for a given flow situation is approximately equivalent to that for a single jet exhausting from a flat plate. In Vol. I of Ref. 26, universal non-dimensional curves are presented for rapid estimation of the interference lift and moment based on the aforementioned assumption.

The methodologies developed in the Northrop Program are incorporated into a comprehensive computer program which allows selection of options for calculating: (1) the flow field for one or more jets exhausting from a flat surface transversely to a free stream; (2) interference aerodynamics for a jet in a wing or body; (3) nonlinear wing or body aerodynamics; (4) a conformal mapping routine; (5) wing aerodynamics by a lifting-surface theory. The last option is a previous capability and was not developed under the present program. The computer program is written in Fortran IV language for a CDC 6600 computer system. A users' manual and program listings are given in Vol. III of Ref. 26.

Wind-tunnel tests were conducted on a twin-engine (wing mounted) hypothetical fighter aircraft configuration model with a fuselage lift fan and a 90 degree thrust vectoring capability for the two propulsion engines. In addition, the deflected propulsion engine exhausts could be positioned at several longitudinal locations. The model and tests are described in Vol. II of Ref. 26. The purpose of the test program was to acquire aircraft configured data for use in validating and improving the analytical prediction techniques. In addition to providing for obtaining six component forces and moments in the tests, the model was equipped also with extensive surface-pressure instrumentation.

The experimental data taken and the correlations made on the configuration model are too extensive for presentation here. Detailed information is available, however, in Vol. II of Ref. 26. Regarding the total induced lift, reasonable agreement between theory and experiment generally is obtained. For the detailed pressure distributions, good agreement is obtained for wing regions outboard of the nacelles, but not for the inboard regions. Theoretical pressure distributions for regions behind the jet lift on the body failed to agree favorably with experiment. It is concluded that some judgment must be exercised in applying the methods developed to actual aircraft configurations. Guidelines for doing so are available in Vol. II of Ref. 26.

5. CONCLUDING REMARKS

It is believed that there is a need for both handbook- and complicated computer-program-type methods in V/STOL aerodynamic prediction methodology. In particular, there is a need for handbook methods based upon fundamental flow principles with appropriate empirical modification as opposed to total reliance upon empiricism, since the former has more growth potential than the latter. Examination of the handbook-type methods developed under the STOL Tactical Aircraft Investigation reveals a tendency to seek early recourse to empiricism; a notable exception is in the lift and induced drag methodology developed by Convair. For those STAI methods having a substantial empirical base, judgment should be exercised in applying the methods to aircraft of significantly different configuration. Despite the foregoing comments, the STOL Tactical Aircraft Investigation Design Compendiums[4,5,6] contain considerable information useful to the preliminary designer.

Regarding powered-lift methodologies of the handbook type requiring further improvement or development, there is a need for rational methods for predicting the interference effects of vectored jets, and the pitching moment, the lateral-directional stability derivatives, the rotary derivatives, and ground effects for all the subject powered-lift systems.

The methods derived under the Douglas program generally represent a high state of technological development. Consequently, their application requires considerable indoctrination on the part of the user. The Douglas investigation has served to delineate some of the difficulties involved in the prediction of ground effects and emphasizes the need for further development in this area. Validation of the Douglas method for the rotary derivatives awaits the availability of appropriate experimental data.

The outstanding achievement of the Northrop program is the transverse jet flow-field prediction methodology. This methodology[26] has been available for over two years and has been received favorably by the U. S. Aerospace industry. An area requiring improvement is the prediction of the wall pressures immediately downstream of the jet.

6. REFERENCES

1. Osborn, R.F. and Oates, G.S.: Wind-Tunnel Investigation of Three Powered Lift STOL Concepts. AGARD Symposium on V/STOL Aerodynamics, Paper No. 4, Delft, Netherlands, 24-26 April 1974.

2. Anonymous: USAF Stability and Control DATCOM, Air Force Flight Dynamics Laboratory, Feb., 1972.

3. Anonymous: Royal Aeronautical Society Aerodynamics Data Sheets.

4. Hebert, J., Levinsky, E.S., Ramsey, J.C., Laudeman, E.C., Altman, H.G., and Barbee, L.G.: STOL Tactical Aircraft Investigation. Vol. II, Design Compendium, Convair Aerospace Division of General Dynamics. AFFDL TR 73-21, Vol. II, May 1973. (AD 766 941)

5. Roe, M.H., Renselaer, D.J., Quam, R.A., et al: STOL Tactical Aircraft Investigation - Externally Blown Flap, Vol. II. Design Compendium. Los Angeles Aircraft Division, Rockwell International AFFDL TR 73-20, Vol. II, April 1973.

6. Runciman, W.J., Letsinger, G.R., Ray, B.F., and May, F.W.: STOL Tactical Aircraft Investigation, Vol. II, Part I, Aerodynamic Technology: Design Compendium, Vectored Thrust/Mechanical Flaps. The Boeing Company, AFFDL TR 73-19, Vol. II, Part I, May 1973. (AD 766 639)

7. Davenport, Franklyn J.: STOL Tactical Aircraft Investigation, Vol. II, Part II, A Lifting Line Analysis Method for Jet-Flapped Wings. The Boeing Co., AFFDL TR 73-19, Vol. II, Part II, June 1973.

8. Spence, D.A.: The Lift Coefficient of a Thin, Jet-Flapped Wing. Proc. of the Royal Society of London, Series A, Vol. 238, No. 1212, Dec. 1956, pp. 46-68.

9. Spence, D.A.: The Lift on a Thin Aerofoil with a Jet-Augmented Flap. The Aeronautical Quarterly, Vol. IX, Pt 3, Aug. 1958, pp. 287-299

10. Das, H.: Tragflachentheorie fur Tragflugel mit Strahlklappen (Lifting Surface Theory for Wings with Jet Flaps). Gesellschaft fur Luftfahrt, 1960, pp. 112-133. Translated in National Research Council of Canada Report NRC 77-1122, 1964.

11. Maskell, E.C. and Spence, D.A.: A Theory of the Jet Flap in Three Dimensions. Proc. of the Royal Society of London, Series A, Vol. 251, 1959, pp. 407-425.

12. Hartunian, R.A.: The Finite Aspect Ratio Jet Flap. Cornell Aeronautical Laboratory Report AI-1190-A-3, Oct. 1959.

13. Kerney, K.P.: A Theory of the High-Aspect-Ratio Jet Flap. AIAA Journal, Vol. 9, No. 3, March 1971, pp. 432-435.

14. Tokuda, N.: An Asymptotic Theory of the Jet Flap in Three Dimensions. Journal of Fluid Mechanics, Vol. 46, Part 4, April 27, 1971, pp. 705-726.

15. Lowry, John G. and Polhamus, Edward C.: A Method for Predicting Lift Increments Due to Flap Deflection at Low Angles of Attack in Incompressible Flow. NACA TN 3911, January 1957.

16. Moorhouse, David J.: Predicting the Maximum Lift of Jet-Flapped Wings. AGARD Symposium on V/STOL Aerodynamics, Paper No. 3, Delft, Netherlands, 24-26 April 1974.

17. Perry, D.H.: A Review of Some Published Data on the External-Flow Jet-Augmented Flap (with an Appendix by D.N. Foster), British ARC C.P. No. 1194, 1972.

18. Moorhouse, D.J.: A Practical Look at the Stall and High Lift Operation of Externally Blown Flap STOL Transport Configurations, Paper No. 16, Fluid Dynamics of Aircraft Stalling. AGARD Conference Proceedings No. 102, Nov. 1972. (AD 753 441)

19. Hebert, J., Ramsey, J.C., Laudeman, E.C., Ponomareff, N.A., and Altman, H.C.: STOL Tactical Aircraft Investigation, Wind Tunnel Data Analysis. Convair Aerospace Div. of General Dynamics. AFFDL TR 73-21, Vol. IV, May 1973.

20. Williams, J., Butler, S.F.J., and Wood, M.N.: The Aerodynamics of Jet Flaps. British ARC R&M 3304, Jan. 1961.

21. Lopez, M.L. and Shen, C.C.: Recent Developments in Jet Flap Theory and Its Application to STOL Aerodynamic Analysis. AIAA Paper No. 71-578, June 1971.

22. Shen, C.C., Lopez, M.L., and Wasson, N.F.: A Jet-Wing Lifting-Surface Theory Using Elementary Vortex Distribution. AIAA Paper 73-652, July 1973.

23. Goldhammer, M.I., Lopez, M.L., and Shen, C.C.: Methods for Predicting the Aerodynamic and Stability and Control Characteristics of STOL Aircraft; Basic Theoretical Methods, Air Force Flight Dynamics Laboratory, Technical Report AFFDL TR 73-146, Vol. I, 1973.

24. Goldhammer, M.I. and Wasson, N.F.: Methods for Predicting the Aerodynamic and Stability and Control Characteristics of STOL Aircraft; STOL Aerodynamic Methods Computer Program, Air Force Flight Dynamics Laboratory, Technical Report AFFDL TR 73-146, Vol. II, 1973.

25. Goldhammer, M.I. and Lopez, M.L.: Methods for Predicting the Aerodynamic and Stability and Control Characteristics of STOL Aircraft; Engineering Methods. Air Force Flight Dynamics Laboratory, Technical Report AFFDL TR 73-146, Vol. III, 1973.

26. Wooler, P.T., Kao, H.C., Schwendemann, M.F., Wasson, H.R., and Ziegler, H.: V/STOL Aerodynamic Prediction Methods Investigation. Air Force Flight Dynamics Laboratory, Technical Report AFFDL TR 72-26, Jan. 1972. Vol. I, Theoretical Development of Prediction Methods (AD 752 557): Vol. II, Application of Prediction Methods (AD 752 558); Vol. III, Manual for Computer Programs (AD 752 559); Vol. IV, Literature Survey (AD 752 563)

27. Fricke, L.B., Wooler, P.T., and Ziegler, H.: A Wind Tunnel Investigation of Jets Exhausting into a Crossflow. Air Force Flight Dynamics Laboratory, Technical Report AFFDL TR 70-154, Dec. 1970. Vol. I, Test Description and Data Analysis (AD 718 122); Vol. II, Additional Data for the One-Jet Configuration; Vol. III Additional Data for Two-Jet Configurations; Vol. IV, Additional Data for the Three-Jet Configuration (AD 718 123).

28. Vogler, R.D. and Turner, T.R.,: Wind-Tunnel Investigation at Low Speeds to Determine Flow-Field Characteristics and Ground Influence on a Model with Jet-Augmented Flaps. NACA TN 4116, 1957.

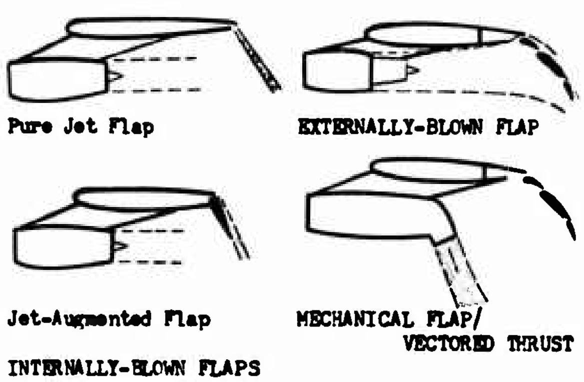
Pure Jet Flap
EXTERNALLY-BLOWN FLAP
Jet-Augmented Flap
INTERNALLY-BLOWN FLAPS
MECHANICAL FLAP/
VECTORED THRUST

Fig. 1 Illustration of Powered High-Lift Systems Studied

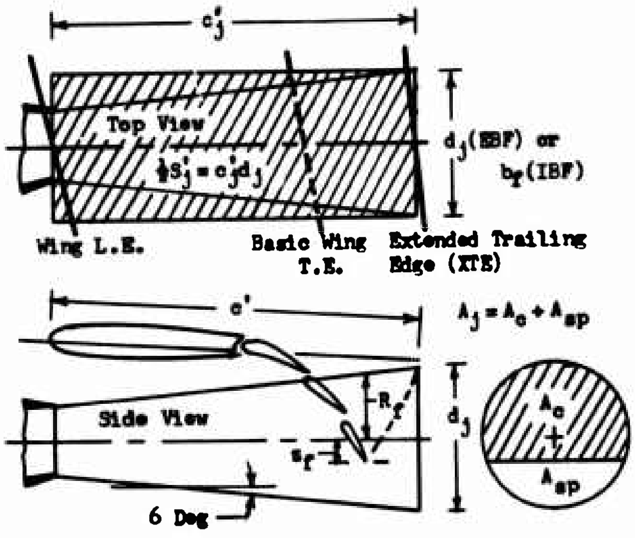
c_j'
Top View
$S_j' = c_j'd_j$
d_j(EBF) or
b_f(IBF)
Wing L.E.
Basic Wing T.E.
Extended Trailing Edge (XTE)
c'
$A_j = A_c + A_{sp}$
Side View
R_f
d_j
δ_f
6 Deg
A_c
A_{sp}

Fig. 2 Illustration Defining Jet-Exhaust Parameters.

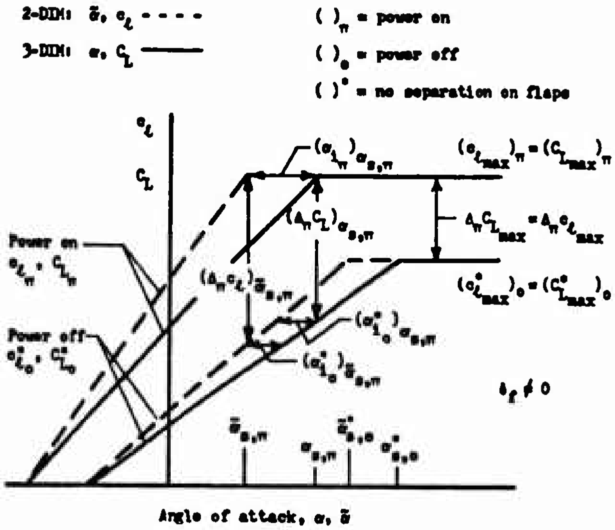
2-DIM: $\tilde{\alpha}$, c_ℓ - - - -
3-DIM: α, C_L ———
$(\ )_\pi$ = power on
$(\ )_o$ = power off
$(\ )^\circ$ = no separation on flaps
c_ℓ
C_L
$(\alpha_{L_\pi})_{\alpha_{s,\pi}}$
$(c_{\ell_{max}})_\pi = (C_{L_{max}})_\pi$
$(\Delta_\pi C_L)_{\alpha_{s,\pi}}$
$\Delta_\pi C_{L_{max}} = \Delta_\pi c_{\ell_{max}}$
Power on
c_{ℓ_π}, C_{L_π}
$(\Delta_\pi c_\ell)_{\tilde{\alpha}_{s,\pi}}$
$(c^\circ_{\ell_{max}})_o = (C^\circ_{L_{max}})_o$
Power off
$c^\circ_{\ell_o}$, $C^\circ_{L_o}$
$(\alpha^\circ_{L_o})_{\alpha_{s,\pi}}$
$(\alpha^\circ_{L_o})_{\tilde{\alpha}_{s,\pi}}$
$\delta_f \neq 0$
$\tilde{\alpha}_{s,\pi}$
$\alpha_{s,\pi}$
$\tilde{\alpha}^\circ_{s,o}$
$\alpha^\circ_{s,o}$
Angle of attack, α, $\tilde{\alpha}$

Fig. 3 Illustration of the Elements of the Maximum-Lift Prediction Methodology.

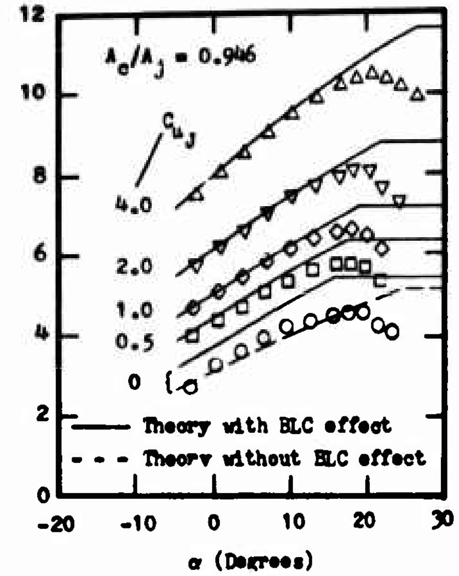

Fig. 4 Correlation of Convair Maximum-Lift Methodology with EBF Test Data, $A = 8.0$, $\Lambda_{c/4} = 12.5^\circ$, Triple-Slotted Flap, $\delta_f = 60^\circ$ (From Fig. 5-38, Ref. 4).

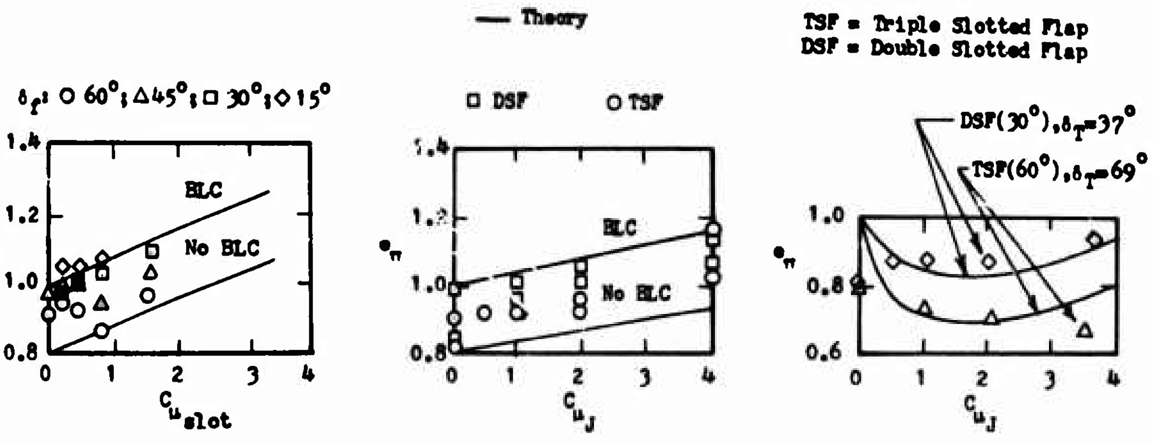

(a) IBF ($K_\Gamma = 2.0$)

(b) EBF ($K_\Gamma = 1.0$)

(c) MF/VT ($K_\Gamma = 2.0$)

Fig. 5 Correlation of Convair Induced-Drag Methodology for IBF (Plain Flap), EBF, and MF/VT Systems, $A = 8.0$, $\Lambda_{c/4} = 25^\circ$ (From Fig. 6-2, Ref. 4).

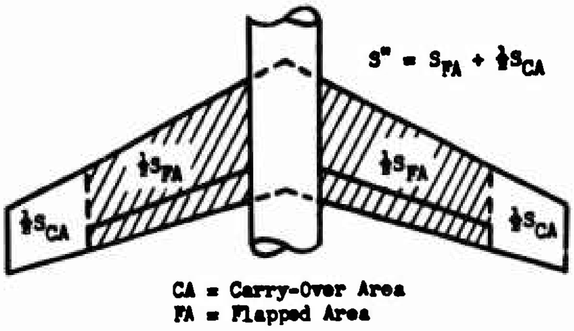
S" = S_FA + ½S_CA
½S_FA
½S_FA
½S_CA
½S_CA
CA = Carry-Over Area
FA = Flapped Area

Fig. 6 Definitions of Wing Areas used in Rockwell Methodology.

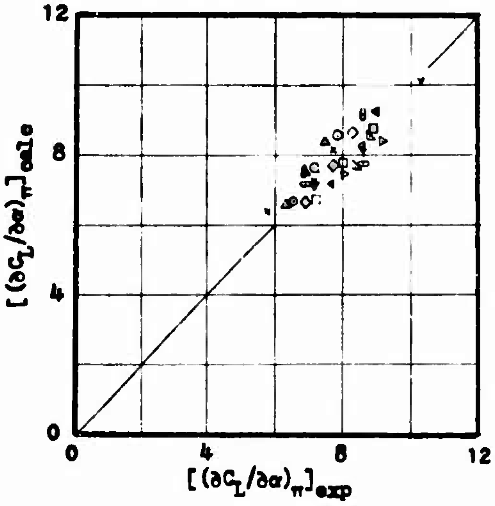

Fig. 8 Rockwell Correlation of Calculated and Experimental Power-on Finite-Wing Lift-Curve Slope (From Fig. 19, Ref. 5).

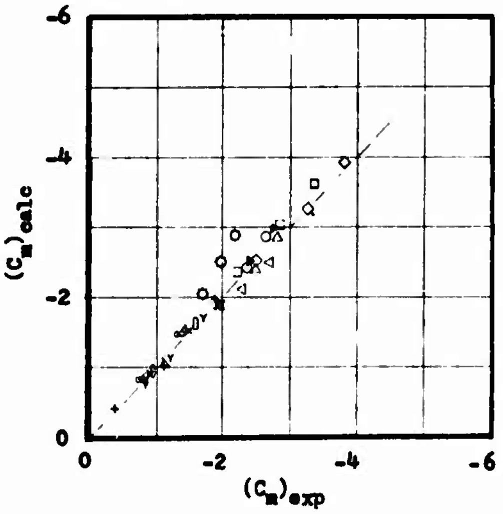

Fig. 9 Rockwell Correlation of Pitching-Moment Coefficient Methodology (From Fig. 46, Ref. 5).

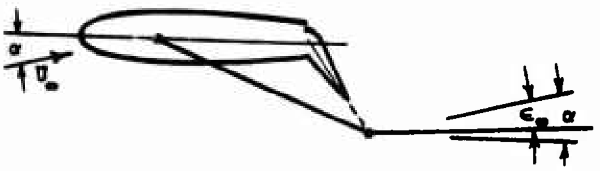

Fig. 10 Side View of Non-Planar Trailing Vortex System Used in Davenport Methodology.

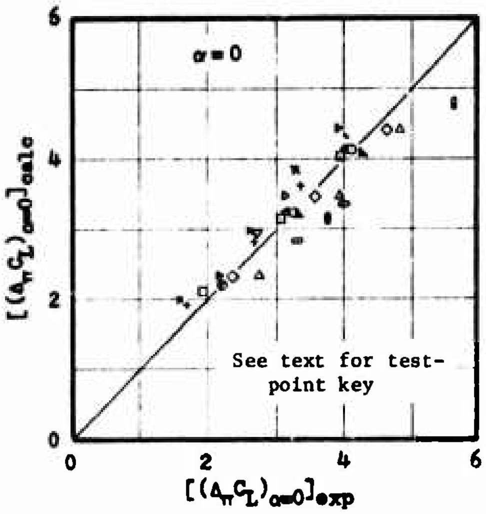

Fig. 7 Rockwell Correlation of Calculated and Experimental Incremental Lift Coefficient Due to Power at Zero Angle of Attack (From Fig. 17, Ref. 5).

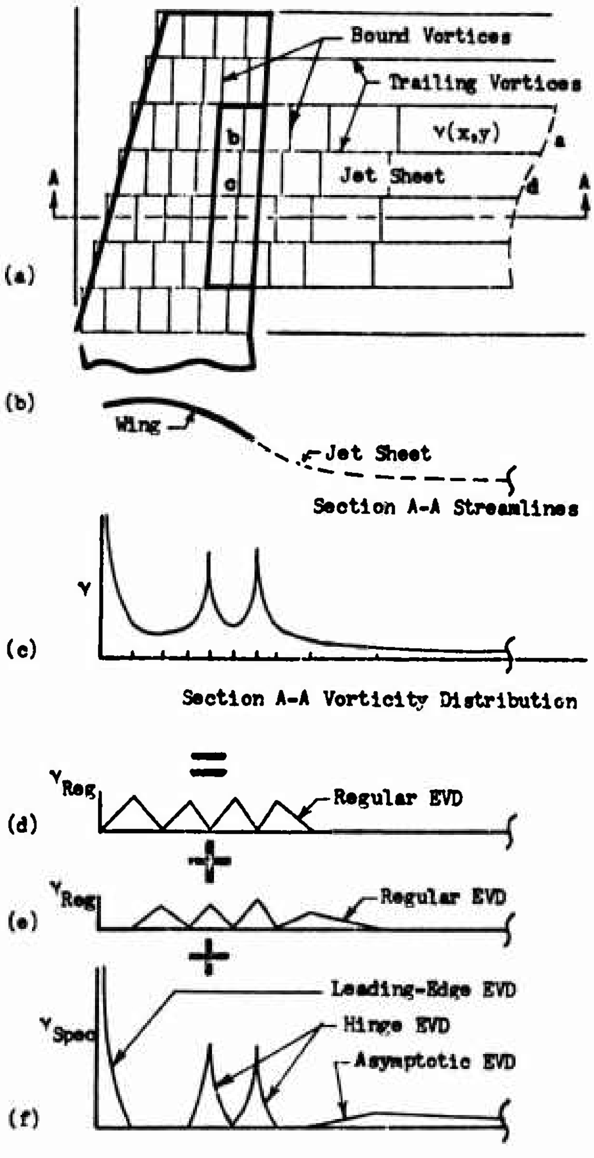
Bound Vortices
Trailing Vortices
b
c
a
d
γ(x,y)
Jet Sheet
A
A
(a)
(b)
Wing
Jet Sheet
Section A-A Streamlines
γ
(c)
Section A-A Vorticity Distribution
γ_Reg
Regular EVD
(d)
γ_Reg
Regular EVD
(e)
γ_Spec
Leading-Edge EVD
Hinge EVD
Asymptotic EVD
(f)

Fig. 11 Illustration of Essential Features of Douglas EVD Method

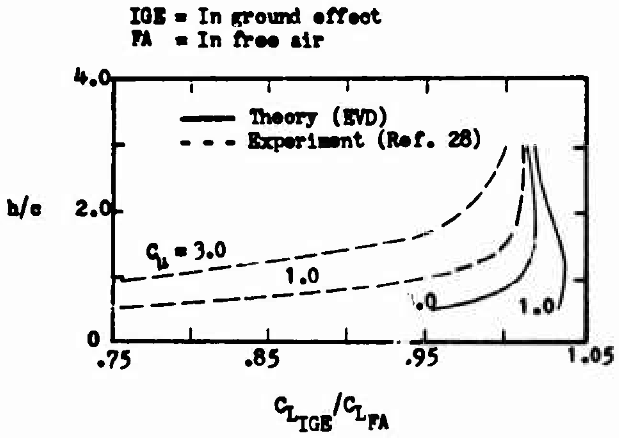

Fig. 12 Comparison Between Douglas EVD Theory and Experiment for the Effect of Height, h, Above Ground on the Lift of a Rectangular Jet-Augmented Flapped Wing, $c_f/c = 0.125$, $\delta_f = 55^\circ$, $A = 8.3$ (From Fig. 2.39, Ref. 23).

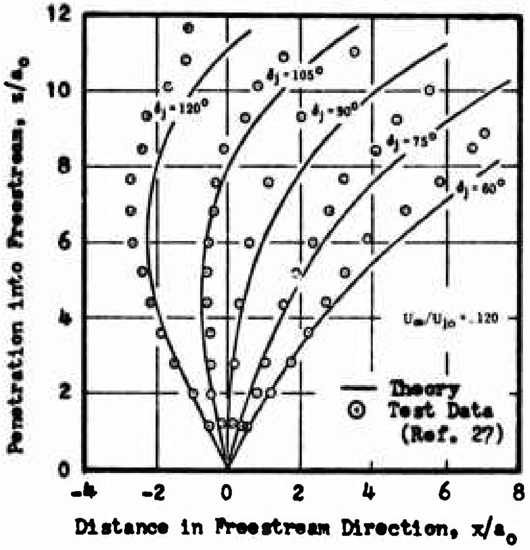

Fig. 16 Comparison of Theoretical and Experimental Transverse-Jet Center-Line Trajectories (From Fig. 9, Ref. 26).

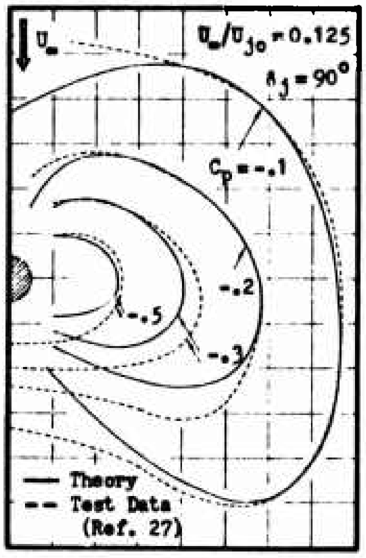

Fig. 17 Comparison of Theoretical and Experimental Wall Pressures for a Single Jet Exhausting Normally to the Freestream (From Fig. 15, Ref. 26).

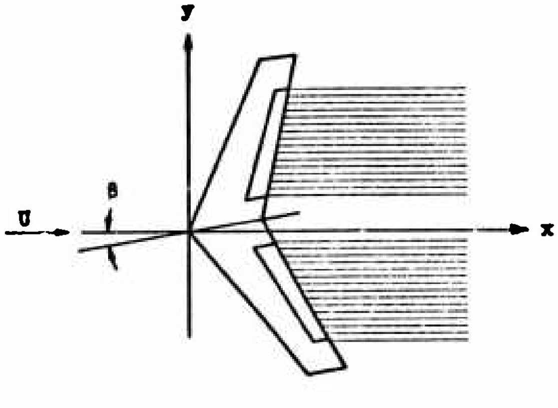

Fig. 13 Treatment of a Yawed Jet-Flapped Wing by the Douglas EVD Method.

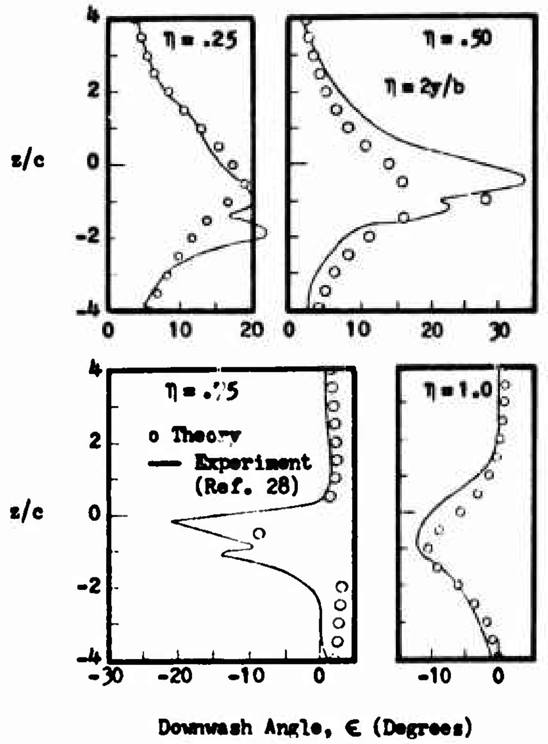

Fig. 14 Comparison Between Douglas Theory and Experiment for the Vertical Variation in Downwash Angle at Downstream Station $x/c = 3.0$ for a Rectangular Jet-Augmented Flapped Wing, $c_f/c = 0.125$, $\delta_f = 55^\circ$, $A = 8.3$, $C_\mu = 1.67$, $C_L = 5.3$ (From Fig. 2.44, Ref. 23).

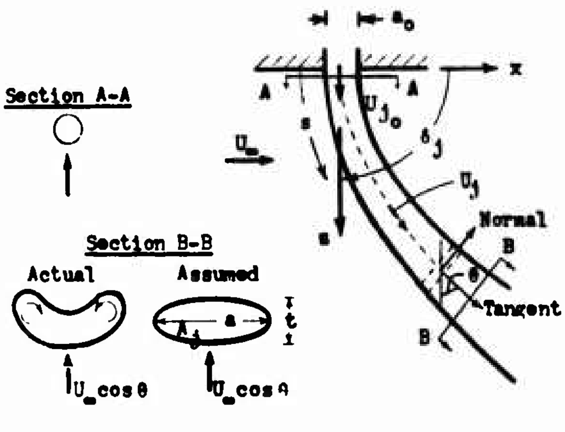
a_o
x
A
A
U_{j_o}
δ_j
U_j
U_∞
s
z
Normal
B
θ
Tangent
B
Section A-A
Section B-B
Actual
Assumed
A_j
a
t
$U_\infty \cos\theta$
$U_\infty \cos\theta$

Fig. 15 Illustration Defining the Essential Elements of the Northrop Transverse-Jet Flow-Field Analysis.

PREDICTION OF AERODYNAMIC INTERFERENCE EFFECTS WITH JET-LIFT AND FAN-LIFT VTOL AIRCRAFT*

by

Dieter Welte

Dornier GmbH
799 Friedrichshafen, Germany
Postfach 317

SUMMARY

The paper gives a guide-line to the project engineer for a rough estimation of the jet induced lift losses of VTOL aircraft configurations with jet-lift and fan-lift engines hovering in and out of ground effect. The nature and magnitude of the aerodynamic jet interference effects is found empirically by dimensional analysis of the flow field and by measurements. Jet induced lift losses and pitching moments with forward speeds are shortly discussed on the basis of wind tunnel measurements.

The discussions and illustrations are based mainly on the theoretical and experimental work done by Dornier in the field of VTOL aerodynamics.

NOTATIONS

c	wing chord
c_p	pressure coefficient $(p-p_\infty)/\frac{1}{2}\rho_j w_j^2$
d	diameter of jet exit
de	equivalent diameter of all jet exits of the aircraft
$\bar{D}$	angular mean diameter $\frac{1}{\pi}\int_0^{2\pi}[r(\theta)-d/2]d\theta$
F	jet thrust
h	height of jet exit above ground
H	height of fuselage above ground
K_j	impact pressure decay parameter
ΔL	Lift increment
p	static pressure
p_t	plenum total pressure
p_∞	ambient static pressure
q_j	impact pressure at jet exit
q_x	maximum jet impact pressure at x
r	radial coordinate
S	planform area of the aircraft
S_j	jet exit area
v_∞	free stream velocity
w_j	jet velocity at exit
X	distance normal to jet exit, in Paragraph 3 chordwise direction
X_i	point of maximum rate of impact pressure decay
θ	angular coordinate
ρ_i	density at jet exit

1. INTRODUCTION

One of the most important data of a new aircraft project, especially a VTOL aircraft, is the installed thrust. After deduction of the losses remains the net thrust which fixes the performances and the control of a VTOL aircraft. For this the project engineer must know in the early stage of the definition of the project the jet induced lift losses in and out of ground effect and with forward speeds.

Due to the complicated flow conditions it is not possible by now to determine the jet induced forces and moments of any VTOL aircraft theoretically. Workable calculation methods exist only for simple cases, as e.g. for the plate with centrally located jet with and without ground effect; the same is valid for approaches to solve this problem with forward speeds. There is a great number of measurements of most different aircraft configurations and of simplified principle models also.

---

* The studies have been sponsored by the Ministry of Defense of the Federal Republic of Germany.

With a view to future VTOL aircraft the following pages try to indicate the most important parameters and to offer the project engineer criteria for the estimation of the jet interference effects. The basis for these criteria is the experience Dornier gained on developping and testing the VTOL jet transport aircraft Do 31 and on developping it further to the Do 131, on wind tunnel testing the VTOL light aircraft Do LSK with lift/cruise fans and by evaluating the literature.

2. POWER EFFECTS IN HOVER OUT OF GROUND EFFECT

A number of experimental, empirical, and theoretical investigations have been devoted to the problem of determining the forces exerted on a stationary body from which a jet exhausts. Particular attention has been paid to thrust losses of lifting jet configurations, both in and out of ground effect. The most pertinent results to date are contained in an empirical relation for lift loss out of ground effect

$$-\frac{\Delta L}{F} = \sqrt{\frac{S}{S_j}} \cdot K_j \cdot \left(\frac{p_t}{p_\infty}\right)^{-0,64} \cdot C \qquad (1)$$

with $$K_j = \sqrt{\frac{\partial[q_x/(p_t-p_\infty)/\partial(x/d)]_{max}}{x_i/d}}$$

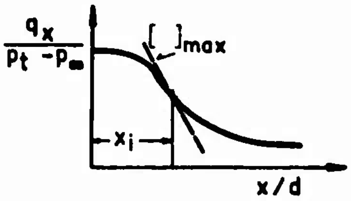

from References [1] and [2]. In Eq. (1) the first term means the ratio of the airframe planform area to the jet exit area, and the second term means the parameter of the jet impact pressure decay. The third term takes into account the well known change of jet impact pressure decay with the pressure ratio. From model tests with fighter configurations with centrally located jets and jet exit velocity near the speed of the sound, Ref. [1] found for the expression $(p_t/p_\infty)^{-0,64} \cdot C = 0,009$. Obviously the factor C depends on the location of the jet within the planform of the aircraft. A centrally located jet will induce higher lift losses than a peripherically located one. For example, from model tests with the VTOL transporter Do 31 the podded lift engines installed at the wing tips induced a lift loss of 2,2 % compared with 3,6 % of the cruise/lift engine installed below the inner wing.

Postulating that the factor C is a universal constant the influence of jet location within the planform will be taken into account by the following considerations. If p is the local pressure on the lower surface of the wing or fuselage the downward directed force is $\Delta L/F = \int_s (p-p_\infty)\,dS/S_j \rho_j w_j^2$

or

$$\frac{\Delta L}{F} = \frac{1}{2} \int_s c_p \, dS/S_j \qquad (2)$$

with cp as the local pressure coefficient. It is now assumed that cp is inversely proportional to the radial distance from the jet axis: $c_p \sim 1/(r/d)$. From this expression and with Eq. (2) thelift loss comes out as $-\Delta L/F \sim \int_s 1/(r/d)\,dS/S_j$

or

$$\frac{-\Delta L}{F} \sim \frac{4}{\pi d} \int_0^{2\pi} [r(\theta)-d/2]\,d\theta \qquad (3)$$

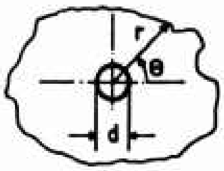

with $dS = r\,dr\,d\theta$. The integral of Eq. (3) signifies the angular mean diameter $\bar{D} = \frac{1}{\pi} \int_0^{2\pi} [r(\theta)-d/2]\,d\theta$ of the planform area without the jet area. Hence follows the lift loss

$$\frac{-\Delta L}{F} \sim \frac{\bar{D}}{d} \qquad (4)$$

In the special case of a circular plate of outer diameter D with centrally located jet the angular mean diameter is $\bar{D} = D$, and the lift loss comes out as $\Delta L/F \sim (S/S_j)^{1/2}$. This last formula results in the same relation between the lift loss and the area ratio as Eq. (1) and thus confirms that the assumption for c_p leading to Eq. (2) is valid. By replacing the square root of the area ratio from Eq. (1) by the diameter ratio of Eq. (4) and with the parameter K_j of the jet impact pressure decay we obtain the new formula for the lift loss

$$\frac{-\Delta L}{F} = \frac{\bar{D}}{d} \cdot K_j \cdot \left(\frac{p_t}{p_\infty}\right)^{-0,64} \cdot C \qquad (5)$$

As postulated in Eq. (5) the factor C is constant for any planform. A simple example will show the difference in lift loss between Eqs. (1) and (5). The circle with radius R and the quarter circle with radius 2R have the same area $S = \pi R^2$ but the angular mean diameter of the circle is $\bar{D} = 2\pi R$ and that of the quarter circle is $\bar{D} = \pi R$. Using Eq. (1) the same lift loss would be obtained for both cases, whereas with Eq. (5) the lift loss of the circle is twice that of the quarter circle, which seems reasonable.

The two different methods, i.e. Eq. (1) and Eq. (5), for calculating the lift loss will now be proved by comparing them with the results of wind tunnel tests with a model of the Do 31. Two configurations will be investigated: separately blowing lift jets and separately blowing lift/cruise jets. Since the jet exit velocity is near the speed of the sound we take from Ref. [1] that $C \cdot (p_t/p_\infty)^{-0,64} = 0{,}009$. In the case of a multiple nozzle one can choose three different flow models concerning the impact pressure decay on the jet axis:

flow model	analytical model	lift loss $-\Delta L/F$	K_j	$-\Delta L/F$
I	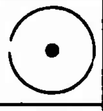	$0.009\sqrt{\frac{S}{4S_j}}\,K_j$	0.2125	0.02
II	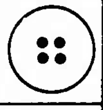	$0.009\sqrt{\frac{S}{4S_j}}\,K_j$	0.425	0.04
III	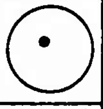	$0.009\sqrt{\frac{S}{S_j}}\,K_j$	0.2125	0.04
I	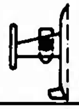	$0.009\,\frac{\bar{D}}{2d}\,K_j$	0.2125	0.017
II	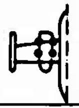	$0.009\,\frac{\bar{D}}{2d}\,K_j$	0.425	0.034
III	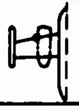	$0.009\,\frac{\bar{D}}{d}\,K_j$	0.2125	0.034
Do 31 : area ratio $\frac{S}{S_j} = 425$, diameter ratio $\frac{\bar{D}}{d} = 16.6$				

Fig.1 Alternative analytical and flow models for the calculation of the lift losses due to the lift/cruise engines of the Do 31

Model I: The four single nozzles are represented by one nozzle with equivalent diameter and the pressure decay of a normal jet.

Model II: The four single nozzles are represented by a fourfold mixing nozzle with equivalent diameter and a pressure decay of a mixing nozzle.

Model III: Each of the nozzles will be treated separately with a pressure decay of a normal jet.

The impact pressure decay parameter for a normal jet is $K_j = 0{,}2125$ whereas the jets of four nozzles arranged at the edge of a quarter have the value $K_j = 0{,}425$ according to measurements of Ref. [2]. Fig. 1 summarizes the principle of the calculation with the three flow models combined with the two analytical methods of Eq. (1) and Eq. (5) for the lift/cruise engine configuration of the Do 31. The results of the calculations for separately blowing lift engines and lift/cruise engines are shown in Table 1.

Table 1
Lift loss $-\Delta L/F$ of the Do 31 hovering out of ground effect

Do 31	engine config.	analytical model	flow model I	II	III	test
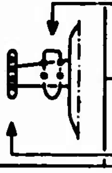	lift/cruise engine	Eq. (1)	0.02	0.04	0.04	0.036
		Eq. (5)	0.017	0.034	0.034	
	lift engines	Eq. (1)	0.02	0.04	0.04	0.022
		Eq. (5)	0.012	0.024	0.024	

Because, in this special case, the factor K_j for the mixing nozzle is twice that of the normal jet the lift loss is the same for flow model II and III and half the value for model I. In case of lift/cruise engines there is a good agreement between tests and theory according to Eq.(1) as well as Eq. (5) if flow model II or III is used. In case of the peripherically located lift engines, only Eq. (5) agrees with the tests. This confirms the validity of the considerations which led to Eq. (5). It is obvious that lift losses of flow model I are too low since the pressure decay of the equivalent single jet is quite different from the real value in our case. For calculating lift losses for VTOL aircraft with multiple jets it is recommended to use Eq. (5) and to calculate the impact pressure decay of the jet with a mixing nozzle according to flow model II or with separate treatment of each nozzle according to flow model III, depending on which of the two is available.

3. GROUND EFFECT IN HOVERING

During hovering near the ground the aircraft is subject to additional induced forces. A single jet which is vertically or obliquely directed to the ground, after deflection, flows radially parallel to the ground like a wall jet. Like the free jet the wall jet entrains with the ambient air. If a pair of jets or jet rows are directed to the ground there exists a strong up flow between them. For a given VTOL configuration hovering near the ground both effects, entrainment and upflow, will exist and influence each other. The following tries to interpret and elaborate the existing empirical relations. The flow field of a VTOL aircraft hovering near ground may be split into four basic types shown in Fig. 2.

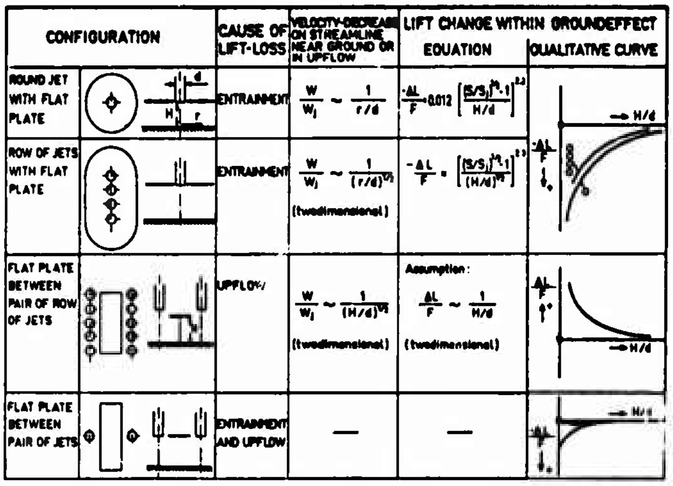

CONFIGURATION	CAUSE OF LIFT-LOSS	VELOCITY-DECREASE ON STREAMLINE NEAR GROUND OR IN UPFLOW	LIFT CHANGE WITHIN GROUNDEFFECT EQUATION	QUALITATIVE CURVE
ROUND JET WITH FLAT PLATE	ENTRAINMENT	$\frac{W}{W_j} \sim \frac{1}{r/d}$	$\frac{-\Delta L}{F} = 0.012\left[\frac{(S/S_j)^{1/2}-1}{H/d}\right]^{2.3}$	
ROW OF JETS WITH FLAT PLATE	ENTRAINMENT	$\frac{W}{W_j} \sim \frac{1}{(r/d)^{1/2}}$ (twodimensional)	$\frac{-\Delta L}{F} = \left[\frac{(S/S_j)^{1/2}-1}{(H/d)^{1/2}}\right]^{2.3}$	
FLAT PLATE BETWEEN PAIR OF ROW OF JETS	UPFLOW	$\frac{W}{W_j} \sim \frac{1}{(H/d)^{1/2}}$ (twodimensional)	Assumption: $\frac{\Delta L}{F} \sim \frac{1}{H/d}$ (twodimensional)	
FLAT PLATE BETWEEN PAIR OF JETS	ENTRAINMENT AND UPFLOW	—	—	

Fig.2 Basic types of ground effect

3.1 Round Jet Centrally Located in a Flat Plate

There are well known empirical relations for the velocity decay of a free jet and a walljet. Any characteristic velocity within the free jet and the walljet is inversely proportional to the distance from the jet exit and the radial distance r from the stagnation point respectively

$$\frac{w}{w_j} \sim \frac{1}{r/d} \qquad (6)$$

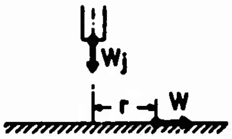

The velocity induced by the walljet at a height H above the ground is inversely proportional to the height

$$\frac{w'}{w} \sim \frac{r}{H} \qquad (7)$$

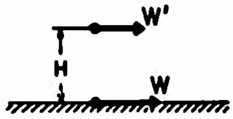

Equations (6) and (7) show a relation between the jet exit conditions and the flow condition at any point above the ground

$$\frac{w'}{w_j} \sim \frac{1}{H/d} \qquad (8)$$

If it is assumed that the suction forces on the lower side of the plate are proportional to the second power of the induced velocity the lift loss comes out as:

$$\frac{\Delta L}{F} \sim \int_s \frac{w'^2 ds}{F} \sim \frac{1}{(H/d)^2} \cdot \frac{(S-S_j)}{S_j} \qquad (9)$$

Eq. (9) is nearly the same as Ref. [3] found in his empirical investigations for the lift loss:

$$\frac{-\Delta L}{F} = 0{,}012 \left[\frac{(S/S_j)^{1/2}-1}{H/d}\right]^{2{,}3} \qquad (10)$$

Fig. 3 shows a comparison of Eq. (10) with measurements of Ref. [4] and [5]. Further simplification of Eq. (9) leads to $-\Delta L/F \sim (D-d/H)^2$ which is nearly the same equation as Ref. [4] obtains from his empirical investigations for the lift loss

$$\frac{-\Delta L}{F} = 0{,}012 \left(\frac{D-d}{H}\right)^{2{,}3} \qquad (11)$$

Eq. (11) shows that the lift loss depends only on the net area surrounding the jet and on the ground distance. As will be seen below, this is only valid for the round jet.
If the jet exit is not centrally located within the planform of the aircraft it is suggested to use Eq. (11) by replacing the equivalent planform diameter D by the mean angular diameter $\bar{D}$ as defined in Paragraph 2. This procedure has not been proved by measurements but seems physically reasonable.

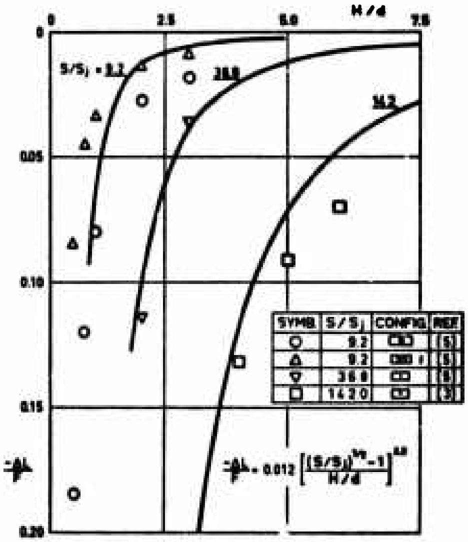

Fig.3 Lift-loss near ground, comparison of theory and test, entrainment effect dominant

3.2 Row of Jets in the Middle of a Place

Fig. (3) shows test results with a narrow rectangular jet exit. The curve is more flat than for the round jet. The reason is that the entrainment of a quasi two-dimensional jet is slower than for a round one. Compared with the inverse linear relation of Eqs. (6) und (7) the velocity decay in the two-dimensional case is proportional to the square root of the distances.

The dimensional analysis then results in the lift loss:

$$\frac{-\Delta L}{F} \sim \frac{S/S_j}{H/d} \qquad (12)$$

Since for the axisymmetric case Eq. (9) corresponds to Eq. (10) one may derive from Eq. (12) the following relation for the lift loss for the two-dimensional case:

$$\frac{-\Delta L}{F} = C\left[\frac{(S/S_j)^{1/2}-1}{(H/d)^{1/2}}\right]^{2,3} \qquad (13)$$

In this case the lift loss depends on the three parameters: plate area, jet exit area, and ground distance. This means, that C is not a universal constant but depends on the ratio of these parameters. This relation must be found by experiment.

3.3 Flat Plate between a Pair of Rows of Jets

In the plane of symmetry of a pair of rows of jets directed vertical to the ground there is a strong upflow which hits the body located between the jets. The lift force produced in this way depends strongly on the planform of the body between the jets. As an example Fig. 4 shows the lift induced by the two rows of lift engine jets of the VTOL aircraft Do 31 and Do 131 over the ground distance.

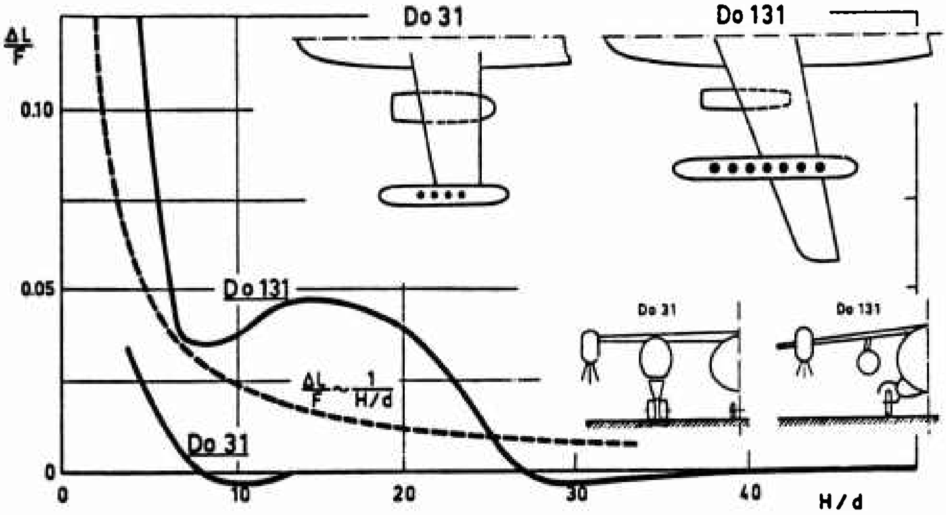

Fig.4 Jet-induced lift near ground, measurements, upflow-effect dominant

The differences between the two curves primarily result from the different shapes and the arrangement of the fuselages and undercarriage doors. This example shows, on the other hand, that it is not difficult to influence the jet interference in a reasonable manner by means of flaps or strakes at the sides of the fuselage.

The momentum of the upflowing jet and consequently the force on the lower side of the fuselage is proportional to the square of the velocity in the upflow. As a rough approximation the velocity slows down in the two-dimensional case inversely with the square root of the ground distance. Then the momentum of the upflow which hits the body is proportional to

$$\frac{\Delta L}{F} \sim \frac{1}{H/d} \cdot f\,(S/S_j) \qquad (14)$$

Fig. 4 shows that the relation of Eq. (14) gives a clue of the influence of the ground distance on the induced force.

3.4 Flat Plate between a Pair of Jets

Since in this case the character of the flow field is a mixture between the first case and the third case it is more difficult to give an idea of the magnitude of the interference effects. The upflow between the jets causes lift gain, whereas outside this area the entrainment of the jets produces lift loss.

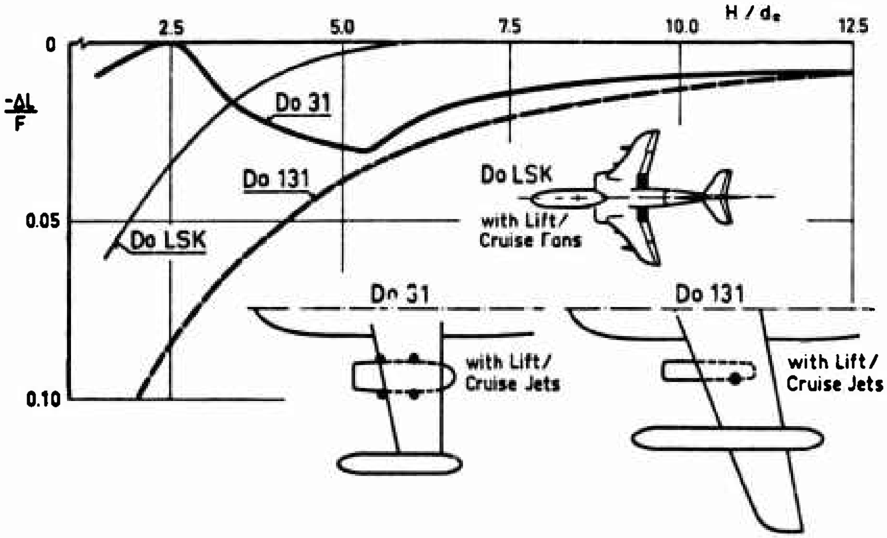

Fig.5 Lift-loss near ground, measurements entrainment effect dominant on Do 131 and Do LSK, entrainment- and upflow-effect on Do 31

As an example, Fig. 5 shows the induced lift loss of different VTOL aircraft models tested by Dornier. In the case of the Do LSK and Do 131 the entrainment effect dominates, whereas in the case of the Do 31 with the fourfold lift/cruise engine jet the upflow and entrainment effects have nearly the same magnitude of opposite sign.

4. FORWARD SPEED INTERFERENCE EFFECTS

In addition to the entrainment effect in hovering flight, at forward speeds the lifting jet efflux imposes a blockage effect on the external airflow along the airframe surface. On the other hand, the jet when leaving the nozzle exit is deflected downstream, and its transverse cross section rapidly distorts from a round to a horseshoe shape. These characteristics modify the main stream flow field about the airframe, promoting suction and pressure regions.

In the static case, as shown in the second chapter, the mainly influencing parameters for jet interference are the square root of the area ratio and the jet decay parameter. In addition thereto, the most important parameters with forward speeds are the chordwise location of the jet exit within the wing planform and the ratio of free stream velocity to jet exit velocity. In Fig. 6 the jet-induced lift and pitching moment is plotted against the chordwise location of the jet with the velocity ratio as parameter. The plots result from measurement of Ref. [6] with a rectangular wing of aspect ratio 5 and a jet blowing vertically downwards in the plane of symmetry. The ratio of wing planform area to jet exit area is 145. If the nozzle blows downwards in the front half of the wing chord the induced lift loss and pitching moment increases with forward speed resulting from suction regions to the rear and the side of jet exit. It is clear that the induced pitching moment changes the sign when the nozzle crosses the reference quarter chord point. If the nozzle is shifted aft from mid-chord to the trailing edge the lift loss decreases more and more with increasing free stream velocity. For the highest free stream velocity the jet induces positive lift and a pitch-down moment. These effects stem from the well known jet flap effect, i.e. a jet which blows downwards from the trailing edge of a wing, like a real flap, produces lift and a pitch-down moment.

In spite of the limited character of the results it seems that the most important parameters were shown. As in the hovering case of Paragraphs 2 and 3 it is assumed that the aerodynamic forces induced by the jet decrease proportional to the radial distance from the jet exit and it is suggested, according to the considerations of Paragraphs 2 and 3, to use the following relation for estimating the jet interference effects for other configurations:

$$\frac{\Delta L}{F} = \left(\frac{\Delta L}{F}\right)_{\text{Fig. 6}} \cdot \frac{\bar{D}/d}{(\bar{D}/d)_{\text{Fig.6}}} \qquad (15)$$

with the diameter ratio of the configuration of Fig. 6 $\bar{D}/d$ = 9,2 and 6,9 for the jet exit location X_j/c = 0,5 and 0 or 1 respectively. From static tests we know the influence of the jet decay parameter on the jet entrainment. We do not know the influence of the jet decay parameter with forward speeds on the jet deflection, on the blockage effect, and on the jet flap effect. Further experimental research work is necessary.

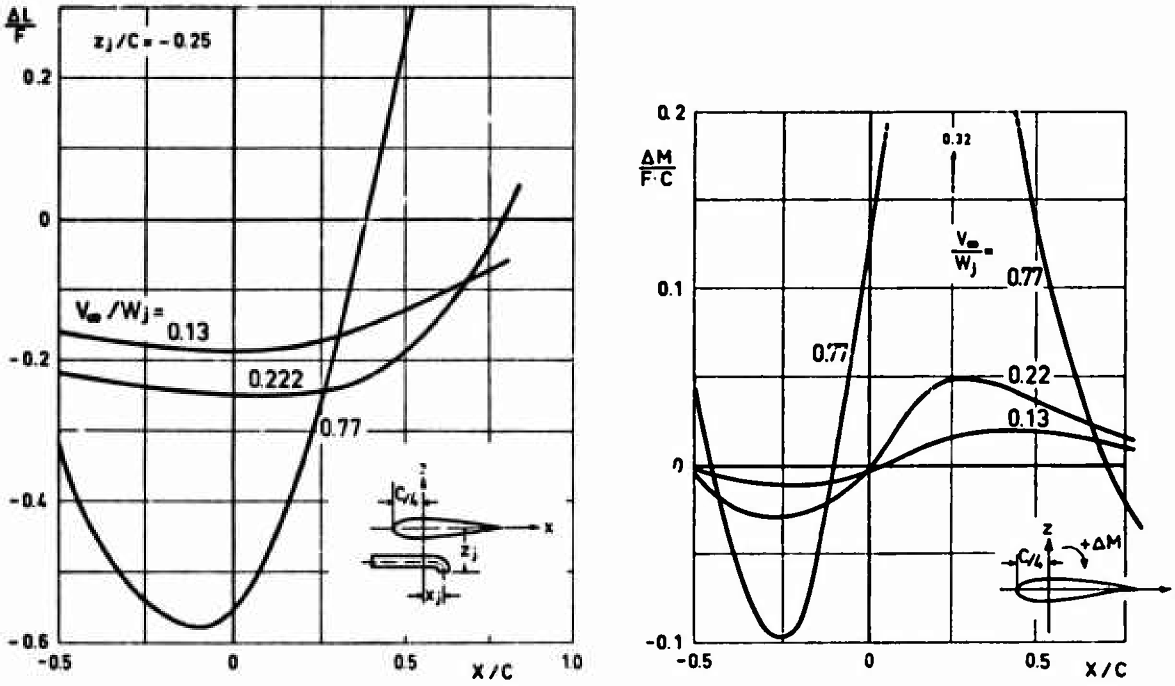

Fig.6 Influence of chordwise position of jet exit and of velocity ratio on lift loss and pitching moment change of a wing

The last Fig. 7 shows a compilation of the measured lift losses from Ref. [7] and from Dornier of most different VTOL aircraft configurations plotted against the velocity ratio. The curves confirm qualitatively the above statements. The centrally located jets in lifting surfaces produce heavy lift losses, whereas the jet blowing from the trailing edge like on the Do LSK produces positive lift due to the jet flap effect. Unfortunately there was not enough time to prove Eq. (15) by the measurements of Fig. 7 quantitatively.

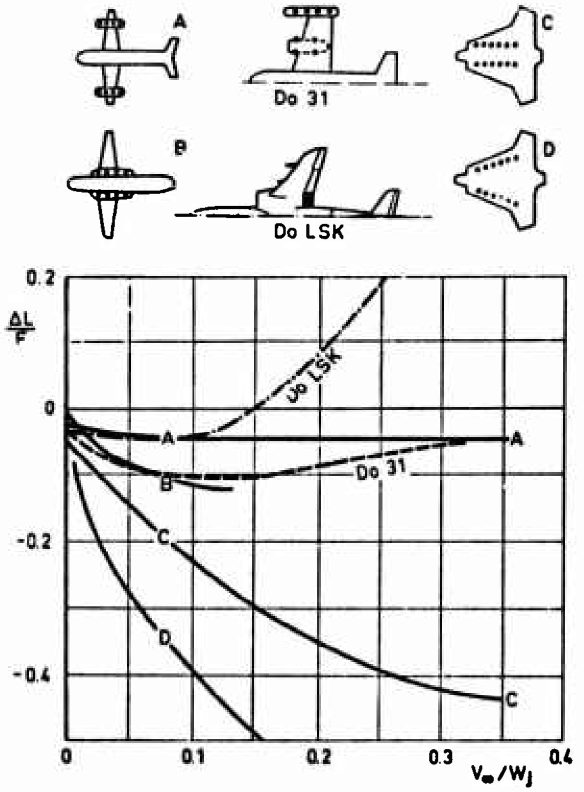

Fig.7 Jet-induced lift with forward speed for different VTOL configurations

5. CONCLUDING REMARKS

The paper gives a help to the designer to estimate the jet interference effects on VTOL configurations. Hovering out of ground the lift loss can be calculated within a scatter of one percent. Within ground effect, by analysing the jet flow field, it is possible do decide whether there is lift gain or lift loss. In the case of lift loss it is possible to reduce it by simple means. With forward speeds the lift- and pitching moment-change is suggested to estimate with the help of a simple, empirically derived formula. The parameters are the velocity ratio, the diameter ratio and the chordwise position of the jet exit.

6. REFERENCES

[1] Gentry, G.L., Margason, R.J. — Jet-Induced Lift Losses on VTOL Configurations Hovering In and Out of Ground Effect. NASA TN D-3166, 1966

[2] Shumpert, P.K., Tibbetts, J.G. — Model Tests of Jet-Induced Lift Effects on a VTOL Aircraft in Hover. NASA CR-1297, March 1969

[3] Hall, G.R. — Scaling of VTOL Aerodynamic Suckdown Forces. J. Aircraft, Vol. 4, No. 4 (1967)

[4] Wyatt, L.A. — Static Tests of Ground Effect on Planforms Fitted with Centrally Located Round Lifting Jet. ARC CP No. 749 (1964)

[5] Vogler, R.D. — Interference Effects of Single and Multiple Round or Slotted Jets on a VTOL Model in Transition. NASA TN-D 2380 (1964)

[6] Baumert, W., Harms, L — Einfluß eines Düsenstrahls auf die aerodynamischen Beiwerte von über der Strahldüse angeordneten Flügeln. DGLR Mitt. 70-28.

[7] Williams, J. — The Aerodynamics of V/STOL Aircraft. v. Karman Institut for Fluid Dynamics, Brussuls, Lecture Series 9, May 13-17 1968.

A REVIEW OF THE LIFTING CHARACTERISTICS OF SOME JET LIFT V/STOL CONFIGURATIONS

*P.G. KNOTT and +J.J. HARGREAVES
Military Aircraft Division, British Aircraft Corporation

SUMMARY

One of the important factors in the design of jet lift aircraft concerns the changes to the wing lift that occur as a result of the interaction between the lifting jet efflux and the free stream. These interactive effects can be large, depending on the configuration.

It is the object of this paper to present a small selection of the more interesting results and to review the attempts that have been made to develop empirical methods of prediction.

The data correlation attempts discussed include the use of Bradbury's similarity laws, a curve fitting exercise using data from tests on a finite wing with jet size and position as variables, and a method which approximates the lift to thrust coefficient relationship linearly. It is intended to apply this latter method to the study of configuration effects on multi-jet arrangements in particular.

When considering the choice of configuration, the location of the lift jets is one of the most fundamental parameters and test results are presented to show some of the lift trends. Finally some results from tests conducted in ground effect in both hover and forward speed are discussed.

In conclusion it is apparent that although a broad understanding of the subject has been achieved, little real progress has been made towards quantifying the effect of variables for design purposes.

SOMMAIRE

L'un des plus importants facteurs rencontré au cours de la création d'un avion à sustentation motorisée, concerne les variations auxquelles est sujet la portance alaire dûes aux interactions entre l'efflux du plan de sustentation et de l'écoulement non perturbé. Ces effets d'interaction peuvent être importants en fonction de la configuration.

Ce traité a pour but de présenter un petit nombre de résultats intéressants et d'un sommaire des essais effectués afin de développer les méthodes empiriques de la prédiction.

Les essais discutés ici pour la corrélation des renseignements comprennent les lois de similarité de Bradbury, les adaptations à une courbe en servant des informations obtenues suite aux essais effectués sur une aile finite, les dimensions et la position du réacteur étant variables, et d'une méthode entraînant l'approximation linéaire du coefficient de rapport de la portance à la poussée. On envisage l'application de cette dernière méthode, en particulier, aux études des effets de configurations sur les dispositions multi-réacteurs.

Pour la configuration, la position des réacteurs est l'un des paramètres les plus importants, et l'on a fait la présentation des résultats des essais dans le but de montrer quelques tendances de portance. Enfin, l'on discute de quelques résultats des essais effectués au sujet de l'effet de sol sur la vitesse en vol stationnaire et en vol vers l'avant.

En conclusion, il est évident que malgré une large connaissance du sujet, aucun progrès concrets n'ont été faits sur la quantification des effets de variables pour les projets d'études.

NOTATION

A_j - geometric jet nozzle area
b - wing span
C_L - airframe lift coefficient (excludes direct jet thrust)
C_{L_A} - power off C_L
C_{L_I} - jet induced C_L ($= C_L - C_{L_A}$)
Co - root chord
Cs - suction coefficient
$C_{\mu j}$ - gross jet momentum coefficient
D - diameter of circle whose area is wing area S
$\bar{D}$ - angular mean diameter $= \frac{1}{\pi}\int_0^{2\pi} r \, d\theta$
dj - jet nozzle diameter
e - base of natural logarithm
h - model height above ground
L - airframe lift
L_I - jet induced lift
L_{Io} - jet induced lift in hover
$L_{I\infty}$ - jet induced lift in hover away from ground effect
Mj - jet Mach number
Mo - freestream Mach number
Pj - jet static pressure
Po - freestream static pressure
r - radial distance from jet centre
S - gross wing area
Tj - gross momentum thrust
Vj - jet velocity
Vo - freestream velocity
x_j - distance of jet centre from leading edge
α - angle of attack
γ_j - ratio of specific heats of jet flow
γ_o - ratio of specific heats of freestream flow
Δ - increment of
δ_F - flap deflection
δ_N - nozzle deflection
ρ_j - jet density
ρ_o - freestream density
θ - angular displacement

---

* Principal Engineer, Wind Tunnel Department
+ Senior Engineer, Wind Tunnel Department

1. INTRODUCTION

One of the considerations in the design and operation of jet lift aircraft concerns the way in which the efflux from the lifting jets interacts with the airframe lifting surfaces and the freestream to alter the forces and moments on the aircraft. These jet interaction effects are by no means trivial, and need to be taken into account when estimating the performance of the aircraft in VTOL, transition and STOL flight.

The N.A.T.O. countries have been interested in jet lift aircraft for the last 20 years at least and many companies and research establishments have concerned themselves with the design, research and development of such aircraft during this period. B.A.C., amongst others, studied the N.A.T.O. specifications N.B.M.R.3 and 4 (Military V/STOL strike and transport aircraft) in the late 1950's and early 1960's. Much of the effort was directed to small scale wind tunnel tests in which the direct jet and airframe forces were separately measured. These experiments highlighted the jet lift interaction effects, showed the trends and order of magnitude and set the stage for the construction of a larger facility (fig. 1) and the start of a programme of research.

FIG. 1

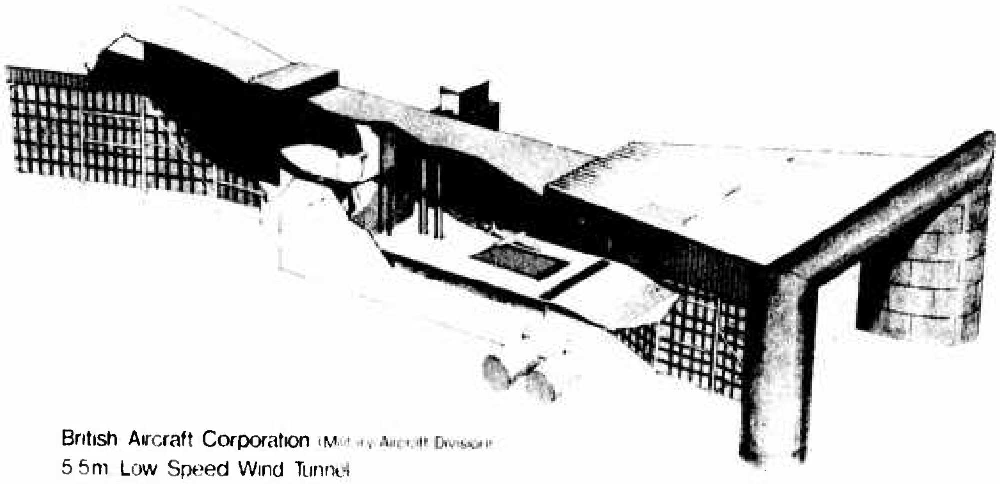

British Aircraft Corporation (Military Aircraft Division)
5.5m Low Speed Wind Tunnel

Like many establishments the early research started with the investigation of the pressure field on an infinite surface from which the jet emerges[1,2,3,4]. Recently this type of investigation has been repeated and extended[5,6] and it is extracts from this work that form the starting point for this review.

Most of the material reviewed in this paper has been taken from low speed wind tunnel tests on complete aircraft models with lifting jets, with the model located sufficiently far away from the floor and walls to be out of ground effect and not significantly constrained by the walls. The purpose of reviewing some of this work is partly to promote discussion on these characteristics and partly to examine the possibilities for correlation of the data. The correlation motive stems from the requirement to produce relatively simple expressions which can be used in computer aided parametric studies associated with the preliminary design process.

After assessing the infinite wall data, results from a simple finite wing with single lifting jet are examined before the characteristics of practical wing/body/multi-jet arrangements are presented. Some results which show the effect of ground proximity both in hover (VTOL) and at forward speed (STOL) are included for the sake of completeness.

Considering the time scale over which this work has been carried out, one cannot help the feeling that real progress in understanding and the development of analytical methods has been depressingly slow. It should be noted however that a considerable amount of the effort that has been applied, has been, and still is being directed towards test technique development, e.g. engine simulation. It is also worth noting that the characteristics are non-linear which, combined with a multiplicity of configuration and jet parameters, has made analysis very difficult. Understanding has been influenced, sometimes wrongly, by the method of presentation adopted. This point is discussed in the following text. In this context it should be noted that a linear assumption is implicit in the definition of the jet lift interaction term L_I when applied to finite wings, and this may also be a possible source of misunderstanding when examining the effect of variables.

2. SOME SIMPLE CONFIGURATIONS

2.1 The infinite wall correlation

A study by Thompson[5] includes a correlation by the similarity law developed by Bradbury[6].

This correlation shows that the path of the jet, defined as the trajectory of the maximum total pressure at any section, is a function of the effective velocity ratio

$$(Vo/Vj)_e = (\rho o Vo^2/\rho j Vj^2)^{\frac{1}{2}} = Mo/Mj \text{ only.}$$

Furthermore, the integration of the pressure field, Cs, to any given radius, r, is shown to collapse well as a function of the effective velocity ratio and the area of integration. It is this feature that is pleasantly surprising and of possible practical interest.

Thompson also tested non-circular jets and showed that the same form of correlation could be substantiated but that the constants change significantly for different shaped jets. It seems likely that the correlation could also be influenced by the jet structure e.g. velocity profile and centre-line decay rate. One may expect to see increased scatter due to these effects when other sources of data are included. Data scatter is also likely to result from a degree of unsteady behaviour in the region behind the jet. The correlation is therefore not as good (fig. 2) when data from three other different sources[1,2,4] is compared. In the presentation of figure 2 the range of the parameters is limited to that of particular interest i.e. the lower values of r/dj and Vo/Vj.

2.2 Comparison with results from a simple finite wing model

A simple 60° delta wing model with a single lifting jet was tested under U.K. Government research contract by B.A.C. in 1967. The tests performed covered two wing to jet area ratios, S/Aj, and three chordwise locations of the jets $\chi j/Co$. These results are presented on figure 4, and have been reduced to the infinite wall correlation form on Figure 3. On figure 3 the expressions have been changed into the finite wing equivalents:-

$$Cs(Vo/Vj)_e \equiv 2\, L_I/Tj \qquad \text{and} \qquad r/dj \equiv \frac{1}{2}\,(S/Aj)^{\frac{1}{2}}$$

The original correlation curve for round jets from Thompson is again reproduced for comparison.

In relating the infinite plane wall to the finite wing a linearised assumption is made, in that L_I is an incremental force defined as the difference between the airframe lift with power on to that with power off. This can only be considered an approximation to the infinite wall equivalent, which has zero lift, power off, because of the non-linear terms arising from the thickness and camber interaction with the jet induced effects.

The finite wing to infinite wall comparison is disappointing in that it does not even show good correlation with area ratio for the central jet positions (2 and 4) which one might have expected. The infinite wall correlation cannot cater for any edge effects of course. This is shown in particular by position 3, the rear jet case.

This comparison suggests that the infinite wall similarity approach should be abandoned in favour of an empirical analysis which combines both area ratio and chordwise location. Such an approach has been recently made and is discussed in the following section. The characteristics of these finite wing results and their implications to aircraft design are also discussed in the following section.

FIG. 2

INFINITE PLANE WALL SUCTION COEFFICIENT FOR ROUND JETS.

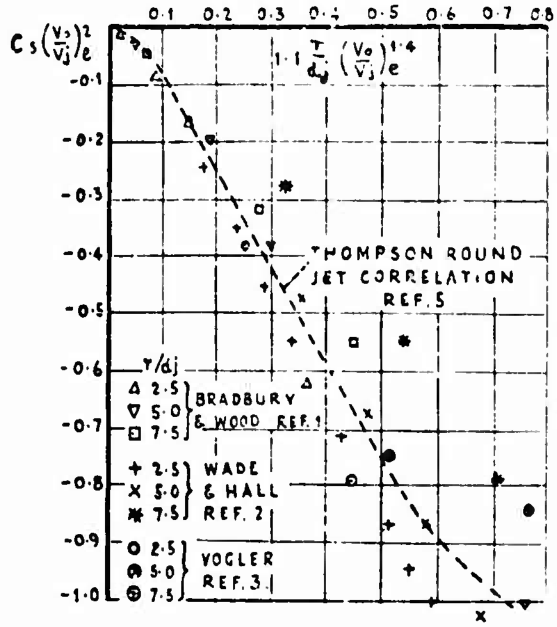

FIG. 3.

COMPARISON OF A SIMPLE FINITE WING WITH INFINITE WALL CORRELATION.

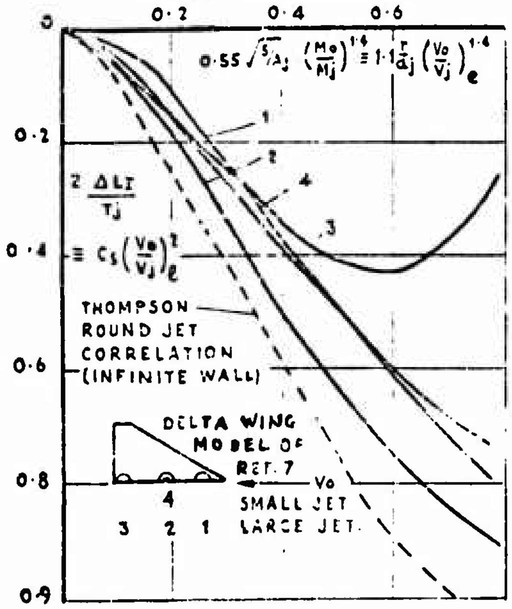

2.3 Jet chordwise location effects

Referring still to the delta wing model results[7], an empirical expression has been derived by trial and error to fit this data, (Figure 4). In the interest of simplicity, a good fit to the smaller jet data has been sacrificed since the larger jet case is of more practical interest. Even so

SINGLE JET DELTA WING MODEL OF REF. 7

OUT OF GROUND EFFECT $\delta_N = 90°$

FIG. 4

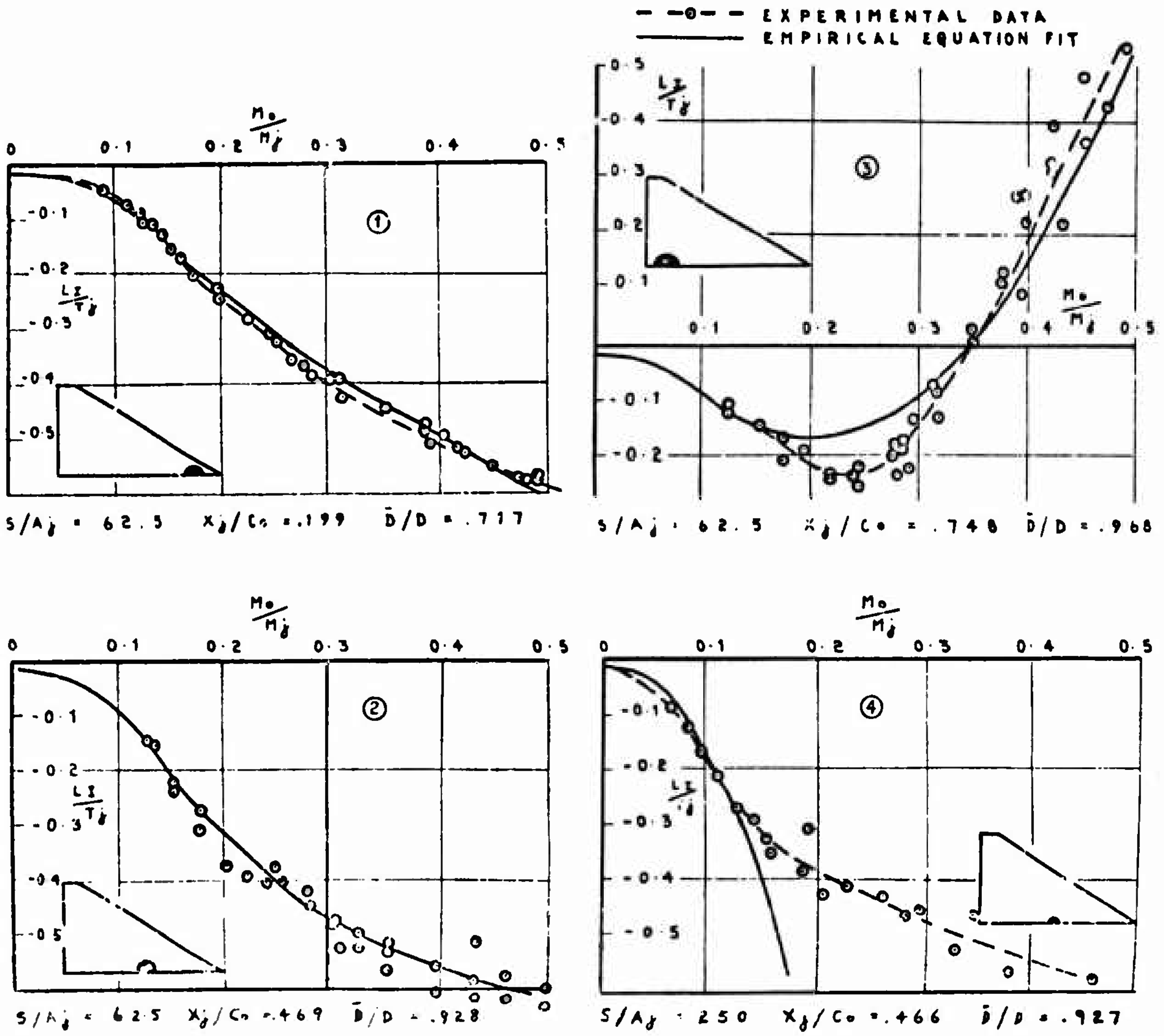

the fit to the rear jet position case is not particularly good but the resulting expression is relatively simple and does merit some further discussion.

The expression is:- $L_I/T_j = L_{I_O}/T_j - (1 - e^{-50(M_o/M_j)^2})(K_1 M_o/M_j + K_2 (M_o/M_j)^2)$

where L_{I_O} is the zero forward speed, or hover value, not derived in this expression.

The exponential term gives the correct shape to the curve at the important low speed end. K_1 and K_2 are functions of area ratio and jet location and for this case are:-

$$K_1 = 0.30\ (S/A_j)^{\frac{1}{2}} (\bar{D}/D)^2 \qquad K_2 = -6.4\ (x_j/C_o)^{2.75}\ (S/A_j)^{0.224}\ (\bar{D}/D)^2$$

Points of interest are that an $(S/A_j)^{\frac{1}{2}}$ term arises as in the infinite wall correlation; and that it was impossible to derive an expression anything like the characteristics without introducing a weak area ratio dependence with the position effect in K_2. This latter point is one that demonstrates the non-linear relationships between the variables.

This form of expression might be applicable to other configurations with K_1 and K_2 re-calculated, and, given a good set of suitable data, it might be possible to extend the expression to another variable, but it looks as though the best that one can hope for is a series of such expressions each covering a limited range of variables.

This expression is presented in graphical form on figure 5 to show the area ratio and chordwise location trends that one might expect from practical configurations. Some of the interesting features are the arresting of the lift loss that occurs as the jet is moved rearward on the lifting surface, as Mo/Mj increases; and to a lesser extent as the ratio of the wing area S to total jet area Aj reduces. These jet position trends are confirmed on practical configurations as will be shown in subsequent sections.

FIG. 5

EMPIRICAL EXPRESSION FOR L_I/T_j OUT OF GROUND EFFECT

$\alpha_N = 90°$

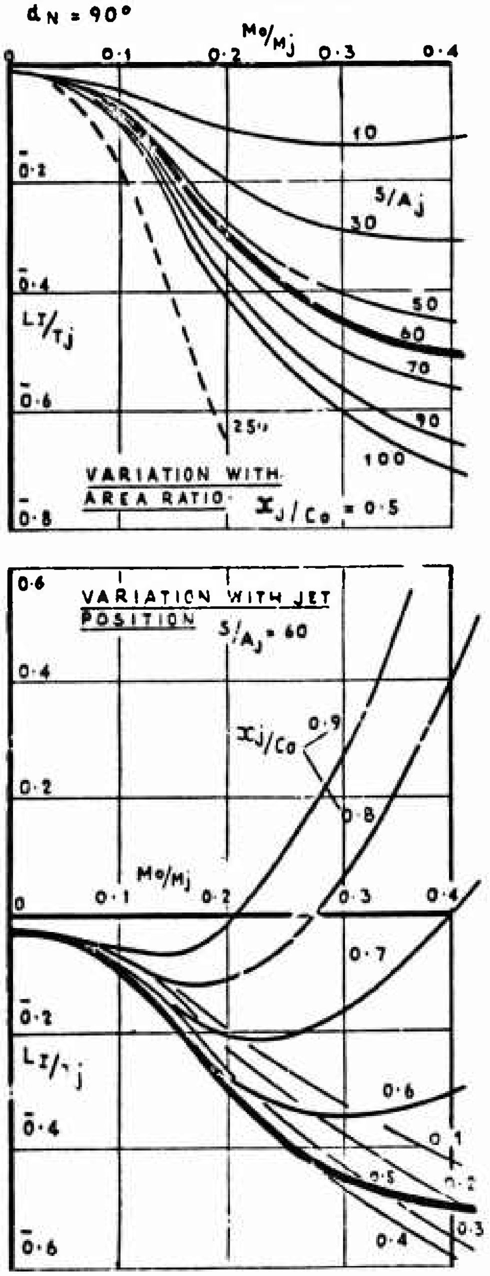

It should be noted, and this is further discussed in the next section, that this particular form of presentation i.e. L_I/Tj v Mo/Mj can be misleading at the higher speed end of the plot since although L_I/Tj can be numerically large positive or negative the changes in total wing lift, C_{L_I}, are only small, and at these higher speeds the total airframe lift is influenced increasingly more by the power off characteristics i.e. small changes in incidence will swamp quite large values of L_I/Tj.

3. MULTI-JET WING/BODY CONFIGURATIONS

3.1 Presentation of results

From the earliest days at B.A.C. tests were carried out with the direct thrust Tj and airframe forces separately measured. Since the 'power off' data point was always measured, but in general did not form an essential part of the investigation, except as a datum condition, it became practice to subtract this 'power off' value from the 'power on' data. The resulting jet interaction increment e.g. L_I, was then non-dimensionalised by the direct jet thrust (gross thrust). In order to include the hover condition, the interaction term was plotted against the reciprocal of the thrust coefficient, $1/C_{\mu j}$, which gives a forward speed squared scale. This presentation is particularly useful when considering the initial part of transition from a VTO. Also, the use of the thrust coefficient rather than the Mach no. ratio is more convenient for project design work since the gross thrust is usually readily obtainable from engine brochures. In the study of the more basic situations, such as discussed in section 2 of this paper $(Vo/Vj)_e$ or Mach no. ratio Mo/Mj has been used as the base parameter. The relationship can be expressed as:-

$$1/C_{\mu j} = \frac{1}{2}\,\gamma o/\gamma j.\rho o/\rho j.S/Aj.(Mo/Mj)^2 = \frac{1}{2}\,S/Aj.(Mo/Mj)^2$$

In these presentations the hover and low speed lift is emphasised i.e. the regime where the vehicle is largely jet thrust supported and subsequently to be termed the 'low speed regime'. At the 'high speed' end of the powered lift flight regime, where wing lift progressively takes over, the lift loss presented as a proportion of thrust may be misleading and the lift term is better presented as a lift coefficient. In recent years attention has been focussed not only on VTO and transition but also on the use of vectored thrust and/or lift engines for very short take-off and land performance. Given this emphasis, the hover condition is no longer of much interest and attention is focussed on the wing lifting capability from typical lift off speeds to fully wing borne flight.

The model shown on figure 6 is one of a number recently tested in the study of V/STOL combat aircraft using vectored propulsion and/or lift engines. This configuration is an example of the, so called, 'lift + lift/cruise' concept The results from one test run on this model are shown plotted in a form suitable for very STOL assessment. The total wing/body lift coefficient C_L is plotted against the thrust coefficient $C_{\mu j}$. The origin is now the power-off lift (zero $C_{\mu j}$ value) and the scale is one of decreasing forward speed. This particular example is at a height above that which is influenced by the ground (out of ground effect) and at zero incidence but with wing flaps down to produce increased 'power off' lift. The results for a number of test runs were plotted in this way, covering height, incidence and thrust vector angle variables and it was noticed that it was possible to obtain a good approximation to the data by two straight lines as shown in fig. 6. The lift could thus be expressed as:-

$$C_L = C_{L_A} + K_1\,C_{\mu j},$$ below $C_{\mu j}'$, termed the 'high speed' region

and

$$C_L = C_{L_A} + K_1\,C_{\mu j}' + K_2\,(C_{\mu j}-C_{\mu j}'),$$ above $C_{\mu j}'$ and termed the 'low speed' region

Transforming to L/Tj terms:-

$$\frac{L_I}{Tj} = \frac{C_L - C_{L_A}}{C_{\mu j}} = K_1$$ in the 'high speed' region, i.e. constant lift loss,

and

$$\frac{L_I}{Tj} = \frac{C_L - C_{L_A}}{C_{\mu j}} = K_2 + (K_1-K_2)\,\frac{C_{\mu j}'}{C_{\mu j}}$$ in the low speed region.

When $1/C_{\mu j} = 0$ i.e. $Mo = 0$; $L_{I_O}/Tj = K_2$. K_2 is thus the zero forward speed hover lift loss which therefore re-asserts itself as a feature of the presentation.

FIG. 6

VECTORED CRUISE + LIFT ENGINE MODEL

$S/A_j = 30$ $\alpha = 0°$ $\delta_F = 30°$ $\delta_N = 60°$

OUT OF GROUND EFFECT

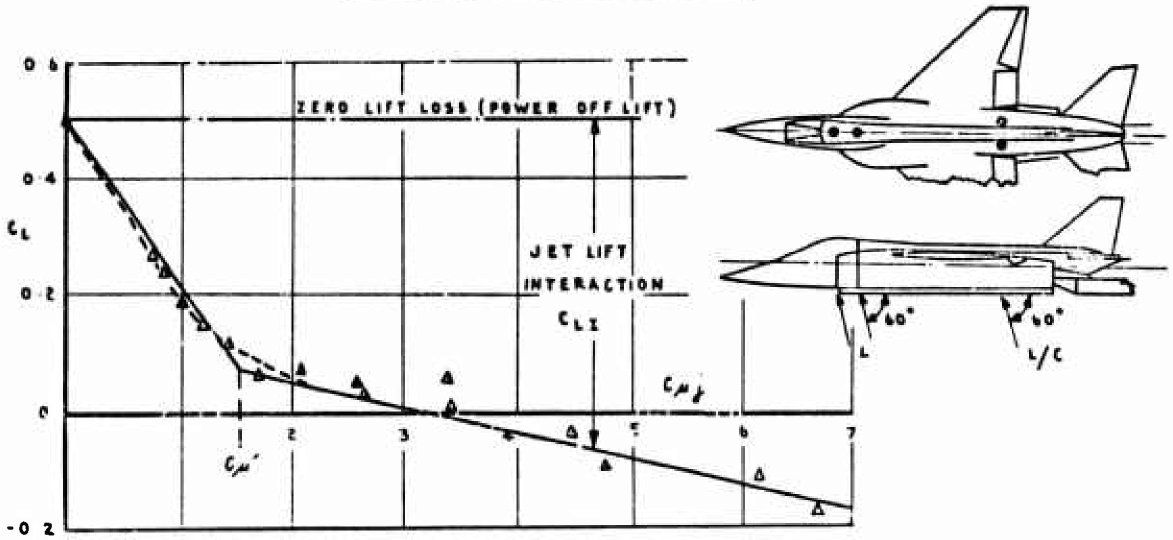

Fig. 7 shows the L_I/Tj form and the definition of K and K . Referring again to Fig. 6, there does not appear in general to be a very sharp change in slope^{1}of the ^2C_L v $C_{\mu j}$ graphs at $C_{\mu j} = C_{\mu j}'$, such that there could be said to exist a critical thrust coefficient, but the concept of $C_{\mu j}'$ may well be useful as the basis of a data correlation method which relates $C_{\mu j}'$ and K_1 to the configuration variables. $L_{Io}/Tj = K_2$ and C_{LA} could be predicted from other sources.

Figure 7 shows the same run data plotted in interference terms as L_I/Tj and C_{LI} against $1/C_{\mu j}$, with the data fitted by the same equation of fig. 6. Inspecting the 'high speed' end in terms of L_I/Tj it appears that the linear fit giving a constant value of L_I/Tj is not particularly good. In general, from the inspection of a wider range of data, it is clear that L_I/Tj is not constant above $C_{\mu j}'$. However inspection in terms of C_{LI}, which is more meaningful, reveals that this is not an unreasonable approximation. The L_I/Tj presentation magnifies what is really only a relatively small variation in C_{LI}.

The significance of lift loss for this case is shown in the presentation of the lower part of fig. 7 where the total lift is plotted with and without the jet interaction term. Note the non-zero origin of this graph. The $1/C_{\mu j}$ scale is also marked in full scale speed in knots assuming an approximately sonic jet efflux velocity and a relatively high wing loading (500 kg/m² or 100 lb/ft²). It is interesting to note that without lift losses, the total lift equals the thrust at about 90 kts whereas with the lift loss this does not occur until about 160 kts. In the application of such data to performance studies such as S.T.O. capability, one needs to look at tunnel results covering all relevant variables such as height above ground, aircraft attitude, jet vector angle, wing configuration and the influence of local geometry such as nozzle toe angle, nozzle exit shape, fuselage strakes, external stores etc. A discussion on the effect of all these variables is beyond the scope of this paper but some of the major effects of jet locations are discussed in subsequent sections.

In further considering the value of the linear C_L v $C_{\mu j}$ fit as a correlation basis, it is necessary

VECTORED CRUISE + LIFT ENGINE MODEL

CONFIGURATION AS FIGURE 6.

FIG. 7.

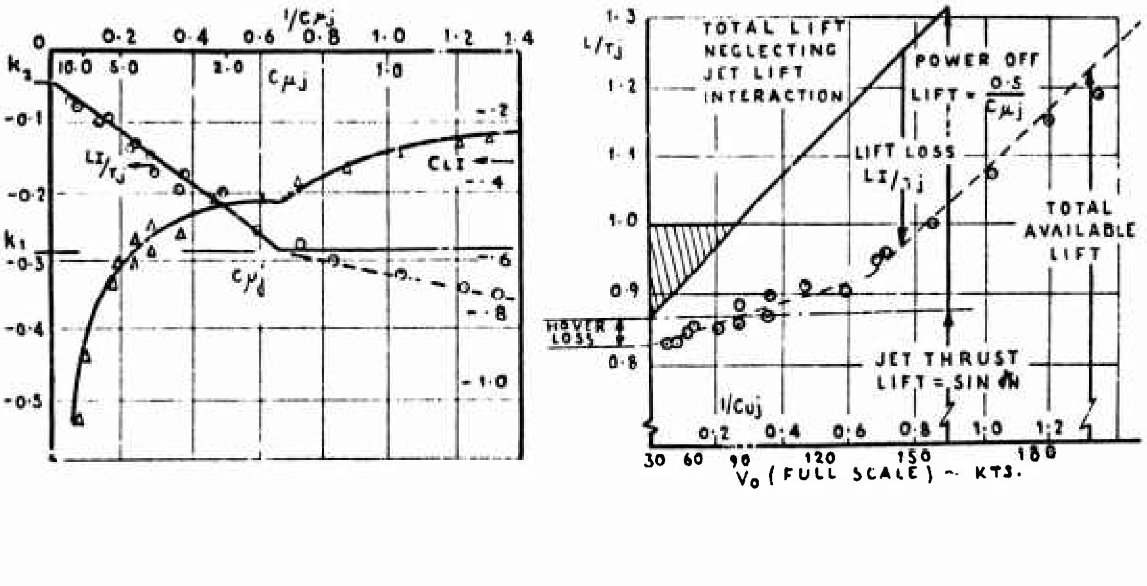

to test the quality of fit against a range of other configurations. Figure 8 is an example of one other configuration, a N.A.S.A. investigation of a model of the Kestrel (Harrier prototype)[8]. This example has been chosen because the tests cover jet vector angles from 0° to 90° (propulsion to hover) and some of the testing was carried out at higher velocity ratios, up to Mo/Mj = 1.0, appropriate to cruise rather than transition flight.

Figure 8 shows a plot of C_L v $C_{\mu j}$ for the condition:- out of ground effect, $\alpha = 0°$, $\delta_T = 0°$, tail on, for a range of nozzle angles, δ_N, of 0°, 65° and 95°. The full range of $C_{\mu j}$ is shown on the main plot and the high speed end of the range is shown to a larger scale on the inset plot. A linear fit has been imposed to all the variables of this presentation i.e. C_L v $C_{\mu j}$ in both the 'high speed' and 'low speed' regimes, the variation of C_L with δ_N, and the variation of $C_{\mu j}{}'$ with δ_N. It appears that the linear fits are quite reasonable.

These results also reveal a number of other interesting features:- firstly it is noticed that there is a loss of lift at $\delta_N = 0$, i.e. in the propulsive mode, relative to the power off condition. The B.A.C. model of figure 13 also has these characteristics, which appear to be typical of arrangements which have nozzles close up under the wing. The loss of lift arises from the accelerated flow on the lower surface of the wing near the wing root, which in turn is thought to be associated with jet entrainment and blockage effects. This loss of lift occurs at all speeds.

The slopes of the 'low speed' lines, K , give the hover lift loss values. From Fig. 8 these are 8.9%, 4.2% and 4.5% at δ_N = 95°, 65° and 0° respectively. The value at 95° is the only one of significance and seems to be quite typical. It is interesting to note that the $\delta_N = 0$ case gives the highest value, but this does not seem to have any practical significance.

Looking at the inset graph the 'high speed' losses can be inspected in greater detail. Since the experimental data has been carried out up to Mo/Mj = 1.0 there is a good cover of data in this regime. A shallow curve would be a better fit but a straight line is quite good after only a very small change to the 'power off' value. Quite apart from the data correlation consideration, this 'high speed' regime data is of practical interest in the context of thrust vectoring for manoeuvre at high subsonic speeds. In the application of this data to the high speed condition it should be noted that the tests were performed in a low speed tunnel, such that at Mo/Mj = 1.0, Mo and Mj were of the order of 0.3, hence no compressibility effects are included. In the application of the data in both high and low speed regimes it must be remembered that area ratio S/Aj is an important parameter in determining the magnitude of the losses (see figure 5). This model has a value of 16.7 which seems very low. The data may not, for example, be too representative of operational Harrier.

Since there are lift losses at $\delta_N = 0°$ relative to the power off condition, it could be argued that in the context of lift available for manoeuvre by thrust vectoring the datum should be the power on $\delta_N = 0°$ condition, not the 'power off' condition. Clearly lift losses cannot be ignored in either the low or high speed applications.

LIFT LOSSES IN TRANSITION AND CRUISE FLIGHT FIG. 8

N.A.S.A. KESTREL MODEL OF REFERENCE 8

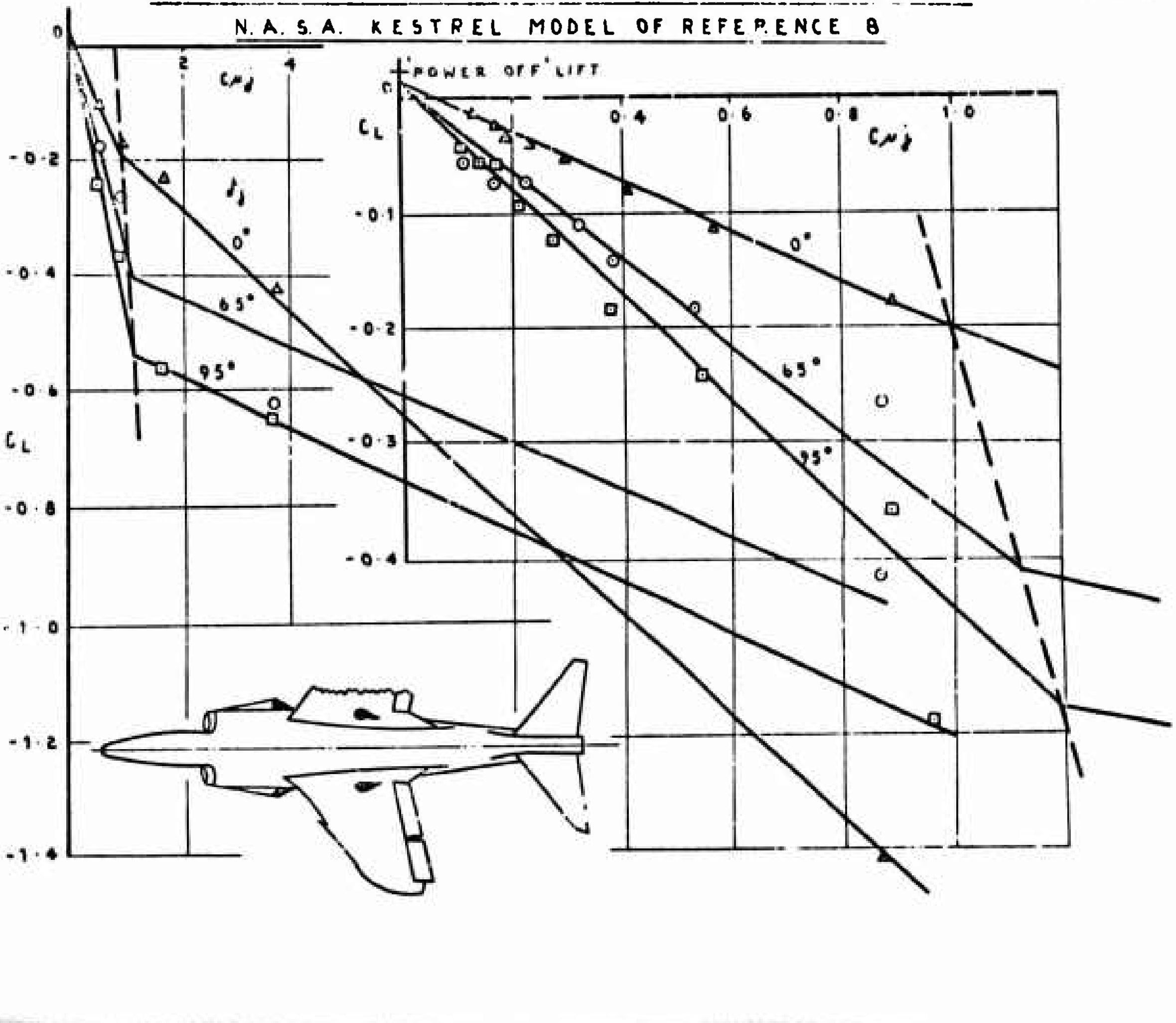

FIG 9

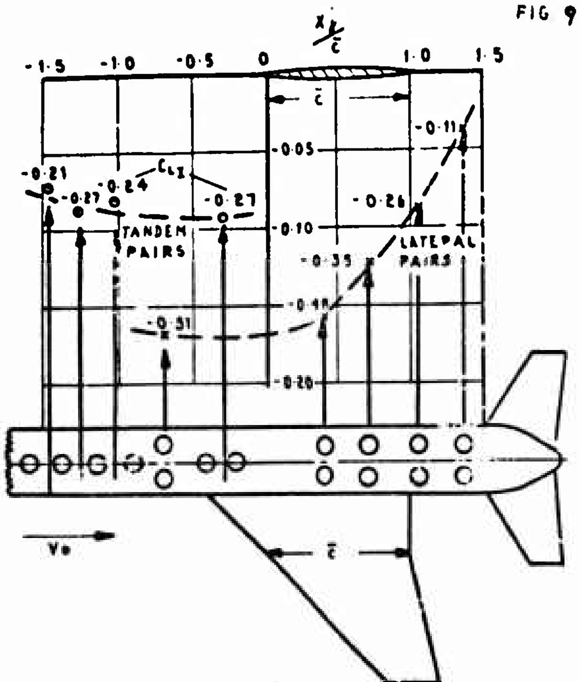

LIFT + LIFT/CRUISE STUDY
EFFECT OF JET LOCATION
OUT OF GROUND EFFECT
JET EFFLUX NORMAL TO FREE-STREAM
$M_o/M_j = 0.15$

FIG 10

EFFECT OF NOZZLE LOCATION
LIFT-CRUISE & LIFT + LIFT-CRUISE CONCEPTS
OUT OF GROUND EFFECT JET
EFFLUX NORMAL TO FREE-STREAM

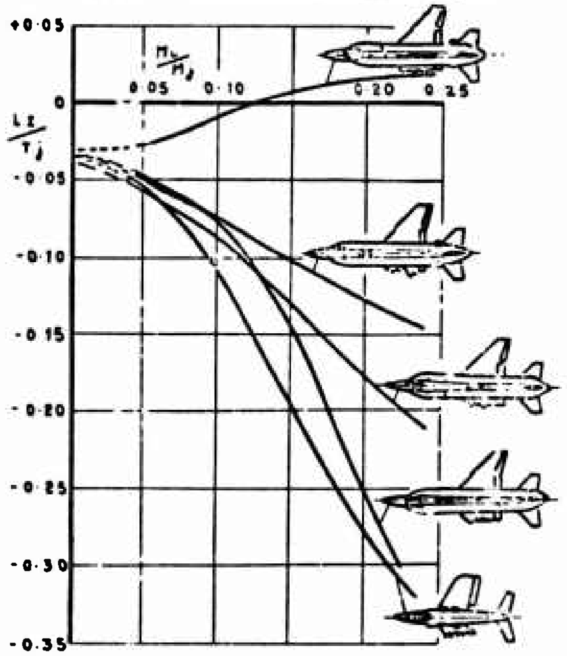

3.2 Configuration effects at forward speed

Returning again to jet fore and aft location effects, the results shown on figure 9 have been taken from part of the study of the aerodynamics of the 'lift plus lift/cruise' concept. This figure looks at pairs of jet nozzles and illustrates well the idea that the 'further aft the better', from the lift interaction point of view. It has to be remembered of course that there are many other considerations and also that this is constant incidence data, i.e. does not consider the lift capability from changing wing camber and incidence. In this study the forward lift jets are in tandem and these give lower lift losses away from ground effect than the side-by-side case. The rear pairs (vectored cruise nozzles) are placed side by side in the belief that as the jet location moves rearward the interaction will eventually become favourable and that when this occurs the effect will be amplified by a lateral spread of the jets. Figure 10 shows this latter point rather better. The top curve is for a rear pair only and some small amount of lift augmentation does occur above Mo/Mj = 0.1. This is rather better than the example of Fig. 9, due to the fuselage side, rather than fuselage base,

LIFT ENGINE LOCATION EFFECTS

FIG. 11

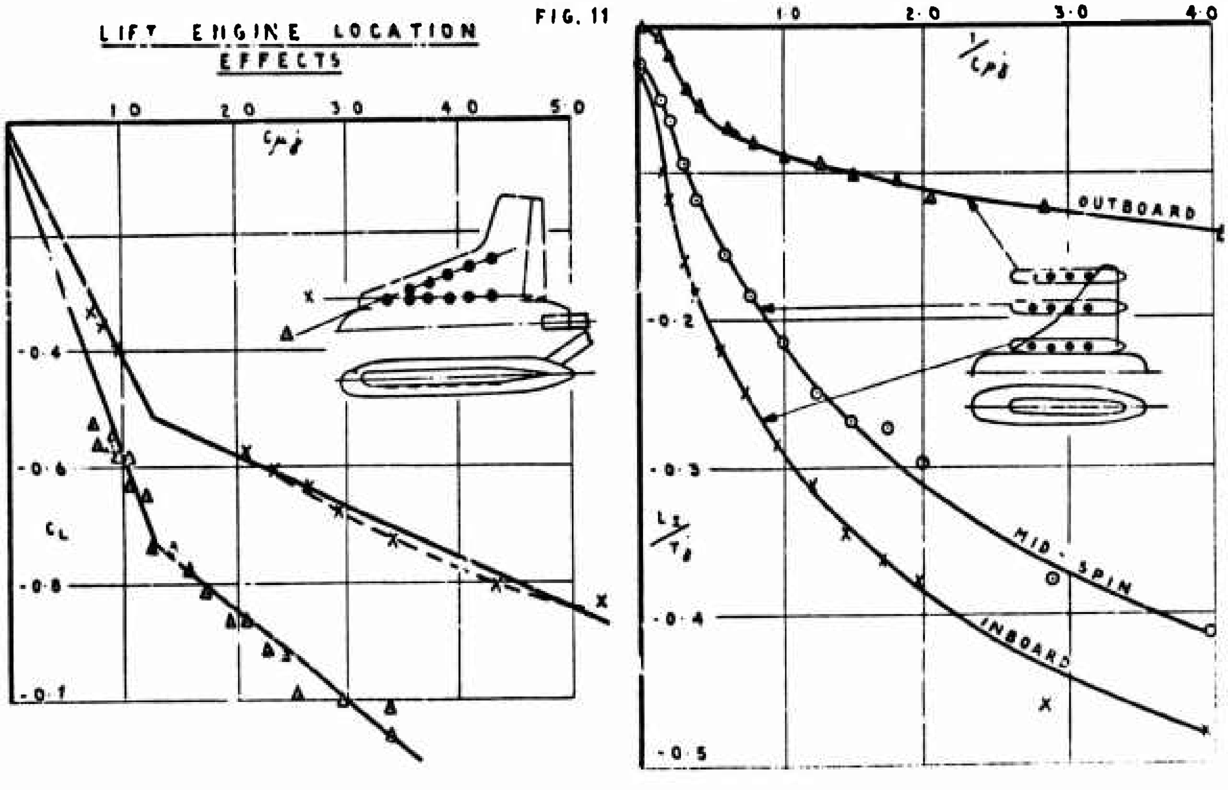

location of the jets. Putting both lift and lift/cruise pairs onto the aircraft, as one has to, to trim, the relative merits of various combinations can be seen. Jet efflux angle and ground effect can change the lift losses considerably and a very much broader view would have to be taken in choosing a layout than is conveyed by this one example, but it does show that there is some scope for optimisation. The bottom curve of this figure has been taken from tests on a B.A.C. model with four vectoring nozzles in the style of the Pegasus/Harrier but not similar in any detailed respect.

The following figures (11, 12) are taken from V/STOL tunnel tests on models built as part of a jet lift transport study carried out in the 1960-1966 period. They have been selected because they show some interesting jet location effects in addition to the fore and aft location considerations already discussed. The first of these, Fig. 11, shows the difference between locating the lift jets along the swept leading edge compared with a tandem layout, on a low aspect ratio swept wing transport. The increased lift loss in the former case is quite significant. Again this data is for the out of ground effect condition, with lift jets normal to the freestream (configuration typical of the start of transition from VTO). This data is presented here in the C_L v $C_{\mu j}$ form to test again the dual linear approximation idea. Fig. 11 also shows results from another model in this low aspect ratio transport study family, where it is clear that the dual linear fit approximation would be poor. On this model it was possible to move the lift engine pods spanwise and the result of so doing is quite appreciable, such that with the pods near the wing tip the losses are approaching insignificant proportions. Finally, Fig. 12 is drawn from a more conventional high aspect ratio transport configuration, and the lift losses out of ground effect are almost negligible. These latter results are shown as a function of height above ground as well as thrust coefficient. At $1\frac{1}{2}$ spans above ground the model is clearly outside the ground influence.

FIG. 12

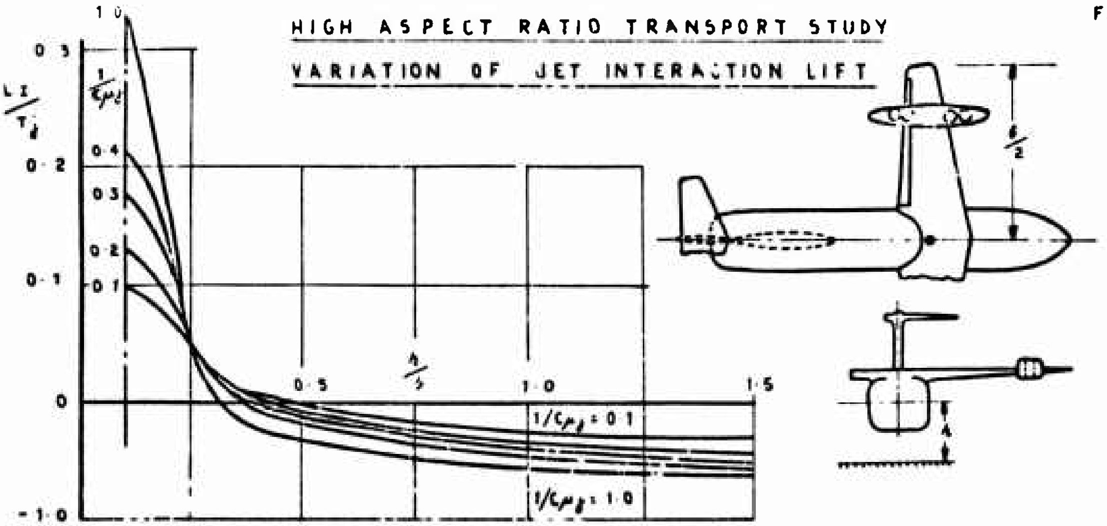

HIGH ASPECT RATIO TRANSPORT STUDY

VARIATION OF JET INTERACTION LIFT

3.3 Ground effect in hover and at forward speed

Remaining with Fig. 12, ground effect is seen to be favourable in this case, but it is interesting to note how rapidly the effects will fall off with the initial rise away from undercarriage height. Ground effects are not always favourable but they always fall off rapidly with the initial increase in height.

Fig. 13 shows some ground effect results for the four vector nozzle configuration of Fig. 10. In hover ($Mo/Mj = 0$) the lift losses are larger in ground effect than away from ground but as the forward speed increases the trend is the other way. Cross plotting against Mo/Mj at $h/b = 1.5$ (out of ground effect) and $h/b = 0.3$ (in ground effect) a larger lift loss at low speeds and a smaller dependency on forward speed is evident. These characteristics are found to be quite common amongst the fuselage mounted engine arrangements, but quite different from the pod type of Fig. 12. In general ground effects at forward speed are the most difficult to understand and have also been the cause of many re-appraisals of ground simulation technique, following unrepeatable or inconsistent trends in test data. There is however some hope that knowing or being able to predict the zero forward speed ground effect, it will be possible to correlate the forward speed effects.

The zero forward speed condition appropriate to VTOL could be described as two separate studies, viz:- the 'out of ground', and the ground effects. Away from ground the lift interaction is negative without exception but usually small, of the order of 5%. In ground effect the interaction can be relatively large negative or positive depending on configuration. This is well illustrated by Fig. 14 taken from a hover study on a proposed 8 lift jet VTOL combat aircraft. These trends are to-day quite well known if not fully understood, yet in 1961 when they were obtained they were sufficiently novel and interesting to provide some of the impetus for further study. Recently attempts have been made to produce an empirical relationship which will approach the trends of such data. The method is based on the single jet correlation of Wyatt[9] which gives increasing lift loss with reducing height and predicts only those cases with closely spaced jets which approach the single jet condition. An additional term to account for the lift augmentation effect of multiple jets which have some surface area between them is required. This term is analogous to a partial peripheral jet condition i.e. a weak ground cushion; but still requires much further study. The complete expression proposed would take the form:- $L_{I_0}/Tj = L_{I_\infty}/Tj + (\Delta L_I/Tj)_{\text{SUCK DOWN}} + (\Delta L_I/Tj)_{\text{AUGMENTATION}}$

where L_{I_∞}/Tj is the out of ground value.

GROUND EFFECTS AT FWD. SPEED
VECTORED LIFT / CRUISE CONFIGURATION
JETS NORMAL TO FREE STREAM
30° TOE OUT

FIG. 13

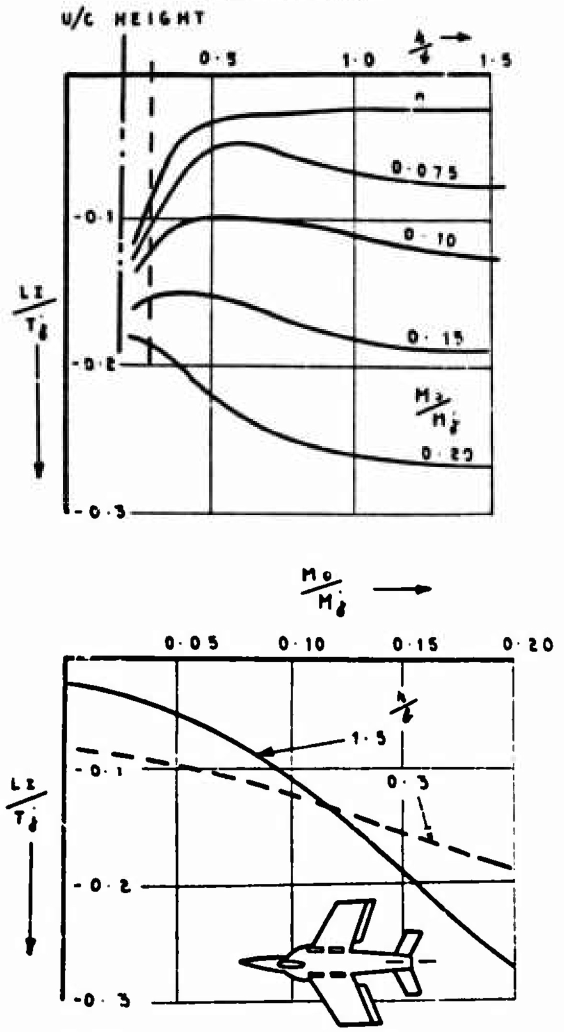

$(\Delta L_I/T_j)_{\text{SUCK DOWN}} = A\left(\frac{S-d_j}{h}\right)^B$ as per Wyatt (Reference 9)

and $(\Delta L_I/T_j)_{\text{AUGMENTATION}} = C(d_j/h)^D$

A and B are evaluated by Wyatt[9], D has been chosen = 2 and C is defined as the product of a number of terms collectively called the 'Augmentation Function'. All these terms are functions of the spacing of the jets or the area or perimeter encompassed by them.

Development along these lines has not so far revealed a worthwhile formulation. The reasons for this might be partly explained if the augmentation effect is not entirely a cushion formed by the outward turning of the jets, as in the Air Cushion Vehicle case, but also comprises pressures from the inward turning part of the jets being deflected upwards from the ground and impacting on the lower surface.

In ground effect in particular the characteristics are very sensitive to local geometry in the region of the nozzle exits. An example of this is shown in Figure 15 which depicts some zero forward speed results from another model in the low aspect ratio transport study. This model had 12 lift engines represented by compressed air ejector units giving both jet and intake flow. In this example it is the effect of jet flows at zero cross flow that are being studied. Vertical strakes were added either side of the two rows of exit nozzles on the lower fuselage running the full length of the nozzle row. It was hoped that these would improve the ground cushion effect in hover and possibly also at low forward speed. Two strake depths were used, half and full jet diameter. The effect is not entirely what was expected. A larger ground effect cushion is achieved but there is an unexpected and serious increase in the lift loss out of ground. This was not understood and led to some fundamental experiments being carried out to determine whether or not the improvement of ground effect characteristics was necessarily associated with a deterioration in the out of ground effect losses. The second part of Fig. 15 shows that it is not necessarily the case, and

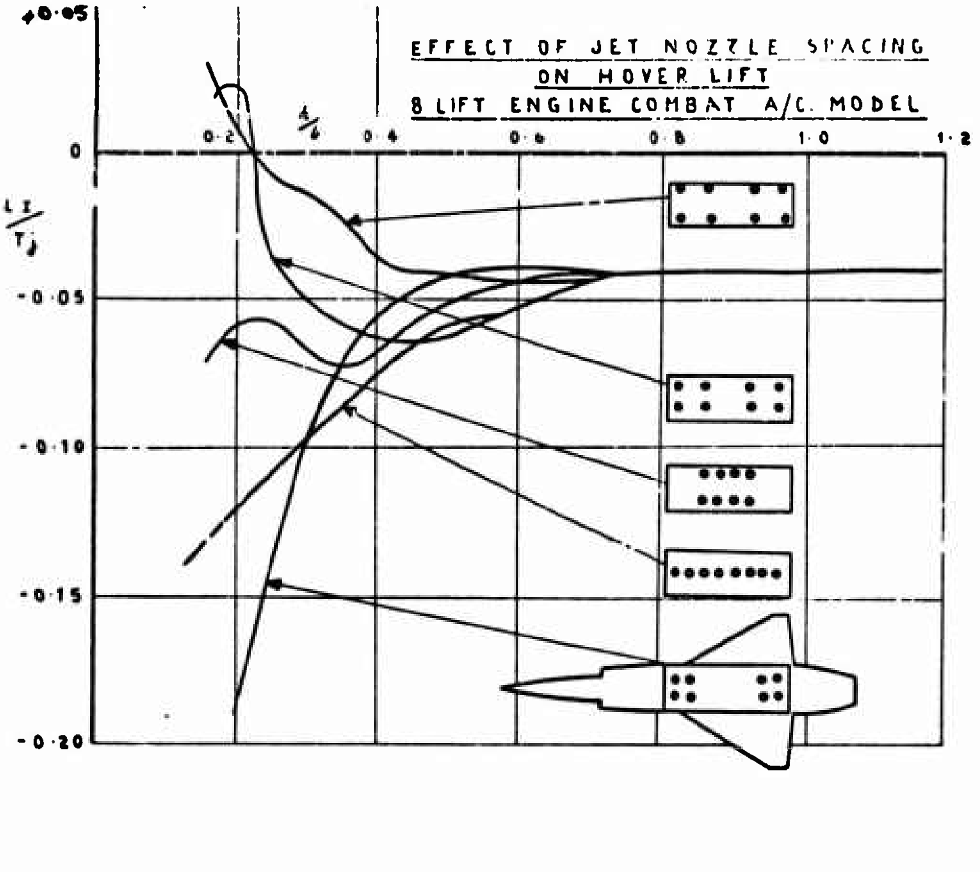

EFFECT OF JET NOZZLE SPACING ON HOVER LIFT
8 LIFT ENGINE COMBAT A/C. MODEL

FIG. 14

FIG. 15

THE EFFECT OF STRAKES ON HOVER LIFT IN AND OUT OF GROUND EFFECT

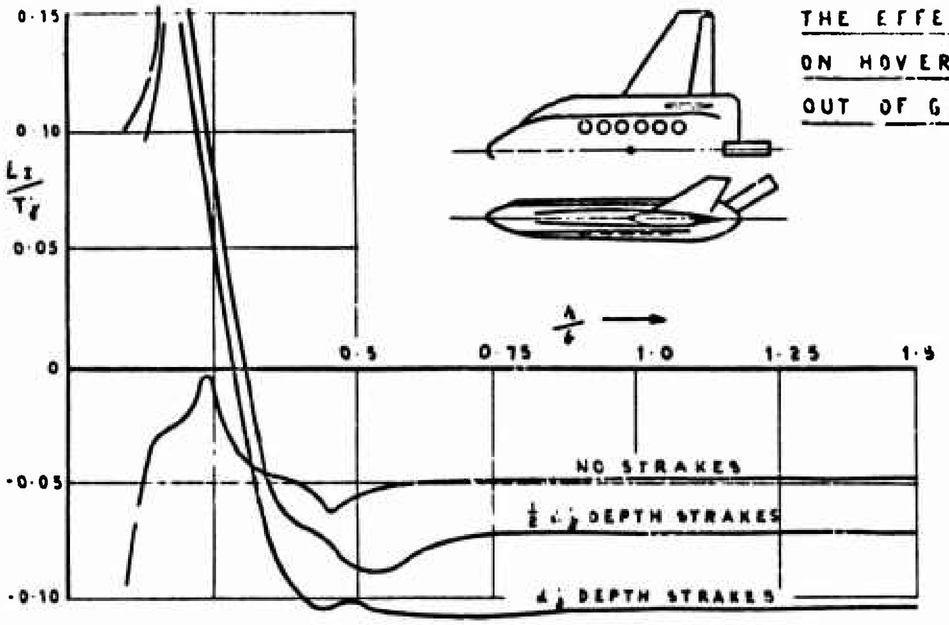

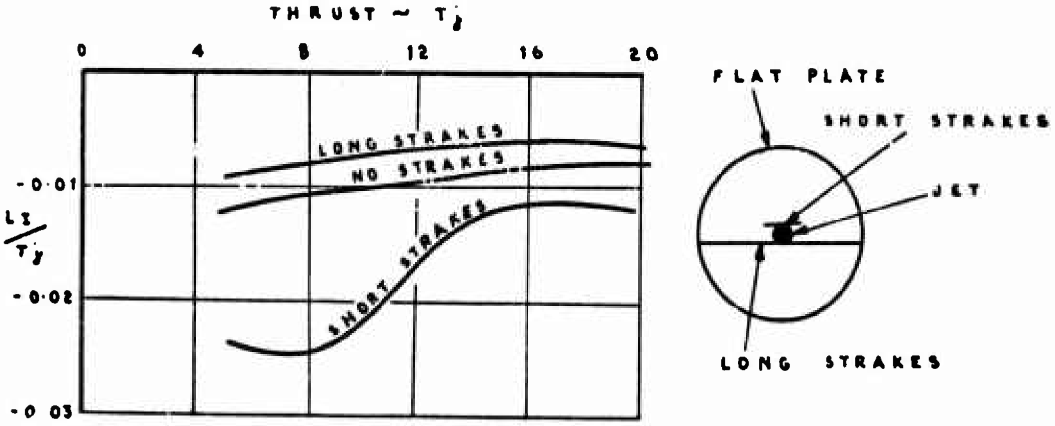

indicates that extending the strakes well beyond the jet could be the way to improve the situation.

These results also show another feature of the out of ground effect hover lift loss which merits attention. It is often assumed that the lift loss is linear with the thrust i.e. L_{I_O}/T_j = constant. This is shown here not to be quite true, and a small reduction in proportional lift loss occurs as the thrust is increased. This behaviour is in some way associated with the changing properties of the jet and hence its entrainment characteristic. A more detailed discussion of this feature can be found in reference 10.

4. CONCLUSIONS

A glimpse at the lifting characteristics of jet lift aircraft has been given, sufficient to indicate the many variables involved which have some bearing on the behaviour and choice of configuration.

Since there is much scope for loss of lift and very little for gain or augmentation, the merits of jet lift when compared with alternative methods which have greater augmentation potential are not obvious but it seems that volume, weight and simplicity are points which may favour a jet lift solution.

Accepting that direct lift solutions will continue to be studied for certain specifications it is important that, having learned something about the jet and wing interactive effects, the task of quantifying the knowledge should be pursued so that it can be used to improve the design of future aircraft. If the data can be expressed in a relatively simple form, yet give a reasonably broad coverage, it will become another important package in the overall aircraft synthesis process, used in the optimisation and performance prediction of future projects.

This paper has attempted to show that a modest start to this task has been made. Progress has been slow because of the complexity of the problem which results from the non-linear relationships between the many variables involved. Also it must be remembered that much of the effort that has been devoted to the subject over the last decade has been channelled into wind tunnel technique development of a complex and specialised nature. This technique work still occupies a large proportion of Wind Tunnel effort and it has increasing application to propulsion studies on conventional aircraft in the context of engine external flow simulation.

REFERENCES

1. L.J.S. Bradbury and M.N. Wood — The Static Pressure Distribution around a Circular Jet exhausting normally from a Plane Wall into an airstream. R.A.E. Tech. Note Aero.2978 August 1964

2. J.M. Wade and K. Hall — Preliminary results from Tests on a Jet issuing from a plane wall in the 18 ft V/STOL Facility. B.A.C. Warton Wind Tunnel Report AXR.1 November 1963

3. G.H. Gelb and W.A. Martin — An experimental investigation of the flow field about a subsonic jet exhausting into a quiescent and low velocity airstream. Canadian Aeronautics and Space Journal Vol. 12 No. 8 October 1966

4. R.D. Vogler — Surface pressure distributions induced on a flat plate by a cold air jet issuing perpendicularly from the plate and normal to a low speed freestream flow. N.A.S.A. TN.D-1629 March 1963

5. A.M. Thompson — The flow induced by jets exhausting normally from a plane wall into an airstream. Ph.D. Thesis. Imperial College September 1971

6. L.J.S. Bradbury — Unpublished note on the 'Similarity Law' 1968

7. J.J. Hargreaves and D.C. Womersley — An experimental investigation of the aerodynamic forces on wings with lifting jets. Force model tests at R.A.E. Farnborough. B.A.C. Warton Wind Tunnel Report AXR.13 1966

8. R.J. Margason, R.D. Vogler and M.M. Winston — Wind Tunnel Investigation at Low Speeds of a Model of the Kestrel (XV-6A) Vectored - Thrust V/STOL Airplane. NASA TN.D 6826 July 1972

9. L.A. Wyatt — Static tests of ground effect on planforms fitted with a centrally located round lifting jet. RAE Aero. Tech. Note 2826 June 1962

10. A.D. Hammond — Thrust Losses in Hovering for Jet VTOL Aircraft. Paper 12 NASA SP 116 April 1966

REQUIREMENT FOR SIMULATION IN V/STOL RESEARCH AIRCRAFT PROGRAMS

Hervey C. Quigley and Curt A. Holzhauser
Ames Research Center, NASA
Moffett Field, California 94035

SUMMARY

Because piloted simulation has proven to be effective in establishing needed criteria throughout most of the stages of research aircraft development, simulation has become an integral part of NASA research-aircraft programs. The general stages of program development are; conceptual design studies, preliminary design, detailed design, manufacturing and ground test, preflight planning, and research flight test.

Two current V/STOL programs in which simulation is playing an essential role are (1) the development and flight research of the Augmented Jet-Flap STOL-Research Aircraft and (2) design studies of advanced VTOL research aircraft. For VTOL aircraft, periods of simulation were scheduled during the conceptual design phase only; for STOL aircraft, periods were scheduled throughout the program. The simulation studies proved significant in helping establish criteria for the aircraft design and in facilitating the study of problems associated with new flight profiles, new methods of control, and special emergency conditions.

1. INTRODUCTION

The aviation industry has long recognized the essential role that simulation plays in the development of aircraft, from conceptual design studies to the training of operational pilots. Many aspects of aircraft simulation were covered in a general discussion at the 1970 AGARD Symposium on Simulation (ref. 1).

Although NASA has used a flight simulator in aircraft research for many years, only recently did simulation become an integral part of NASA research-aircraft programs. This paper discusses the role of simulation in two current V/STOL programs: (1) the development and flight research of the Augmented Jet-Flap STOL-Research Aircraft and (2) design studies of advanced VTOL-research aircraft. Included is a discussion of the simulators that were used, the timing of simulation in the programs, the development of the mathematical models, and the significant results obtained.

The many definitions of aircraft simulation require that we specify our use of the term in this paper. By "simulation," we mean the computer simulation of the response and operational characteristics of an aircraft, with the computer under the control of a pilot who uses aircraft-type controls in a flight simulator.

The unavailability of design criteria and operational experience in V/STOL-research aircraft requires the use of a flight simulator in most phases of V/STOL research and development programs. Simulation has: (1) provided design criteria, (2) greatly reduced the risk in flight testing, (3) enabled project pilots to participate in establishing the required criteria and defining the scope of flight-test missions at earlier stages of the program than would otherwise have been possible, (4) greatly reduced the time-to-completion of the project, and (5) significantly reduced overall program costs.

2. SIMULATION REQUIREMENTS

2.1 Purpose of simulation

Table 1 lists the program phases and simulation purposes of each phase. This type of development plan assumes, of course, that there is an adequate data base to initiate the program.

Table 1. Purpose of Simulation

Program phase	Purpose
Conceptual design studies	– Determine feasibility of concept for normal and emergency operation – Establish requirements – Define possible configurations
Preliminary design	– Define basic configuration – Establish design criteria – Conduct trade studies to minimize cost and complexity
Detail design	– Optimize subsystem – Study failure modes – Obtain pilots preliminary evaluation
Preflight planning	– Obtain pilots evaluation of: (1) Complete design (2) Possible failure conditions – Establish emergency procedures – Assist in planning initial flight-test program
Research flight tests	– Assist in flight-test planning – Supplement flight-test results – Define modifications to improve research capabilities

2.2 Simulator

At Ames Research Center, we have several excellent motion-flight simulators for use in V/STOL research-aircraft programs. Figure 1 shows the Flight Simulator for Advanced Aircraft (FSAA), which was used for most of the simulations discussed in this paper. The FSAA is an advanced 6-degree-of-freedom motion simulator with a large transport-aircraft cockpit. In particular, the large rotational and translational displacements, ±15.2 m (50 ft) for lateral motion, provided realistic motion cues. The cockpit flight deck can be equipped with instruments and control levers to match the aircraft to be simulated. Realistic pilot flight-control forces and gearing are generated by the control force-feel analog-computer system. A color-television display provides the pilot with a 3-D scale-model landscape. The landscape model includes an airport with a conventional runway and a 457.2-m (1500 ft) STOL runway. An aircraft-engine noise generator can be used to give proper aural cues.

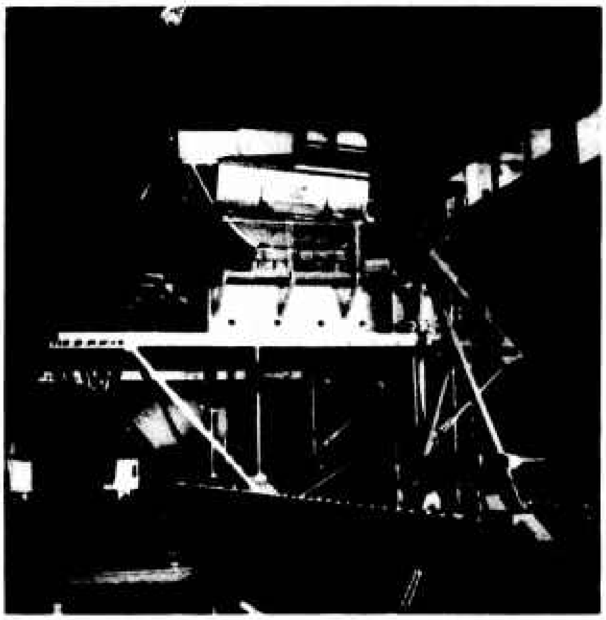

Fig. 1 Flight Simulator for Advanced Aircraft (FSAA).

Figure 2 is a schematic diagram of the FSAA simulation system. The central computing unit of the simulation system is a large-capacity digital computer that processes the programmed mathematical model of the airplane. In response to control commands from the cockpit and to simulated atmospheric disturbances, this central computing unit calculates the instantaneous aircraft state and communicates this information to the motion and visual drive units. Analog computers perform the interfacing between the signal conditioning functions on the incoming control signals and the signals sent by the digital unit to the cockpit instrumentation and motion and visual drive systems. The control-feel loader computer is a separate analog system that interfaces with the central digital computer to provide control-force tailoring to a range of flight conditions. A more detailed description and a discussion of the use of the FSAA is presented in references 2 and 3, respectively.

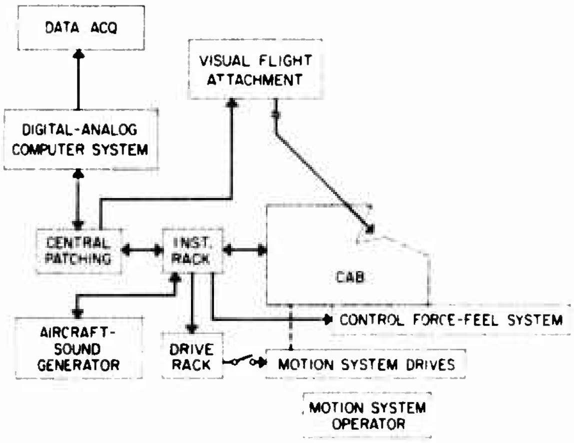

Fig. 2 Schematic diagram at FSAA simulation system.

2.3 Mathematical model

The mathematical model defines the specific aircraft for the simulation. Therefore, the mathematical model will be changing constantly throughout the development stages. The simulation mathematical model requirements for V/STOL research aircraft are similar to those presented in reference 4. Table 2 indicates the requirements for the mathematical model in each stage of the NASA V/STOL research-aircraft programs. In all cases, the FSAA simulation has been preceded by considerable mathematical analysis of the aircraft response and stability characteristics, and, in most cases, some simpler simulator studies were also performed, either fixed base or with limited motion. The mathematical analysis that is required to define in detail the propulsion, aerodynamic, and control characteristics of the aircraft for simulation permits an initial estimate of the aircraft response and stability to determine if there may be a need for various aircraft modifications, such as stabilization systems, failure compensation systems, and control modifications. In addition, these computations provided a valuable independent check of the simulation, since they were from a completely separate computer program. The mathematical model continues to grow in detail, complexity, and accuracy as the aircraft program grows. With each increasingly complex stage of aircraft development, the mathematical modeling and presimulation analyses are used to bracket variables and filter out unneeded simulation tests. The simulation, in turn, supplies information needed for the ongoing testing and analysis.

Table 2. Mathematical Model Requirements

Program Phase	Requirements
Conceptual design studies	– Estimation of aerodynamics based on theoretical estimates and preliminary wind-tunnel data – Simplified control concepts – Estimation of proposed engine characteristics
Preliminary design	– Best predicted aerodynamic data – Preliminary control-system characteristics – Estimation of engine characteristics
Detail design	– Best prediction of all basic systems – Preliminary subsystems characteristics
Preflight planning	– All systems updated to best prediction
Research flight tests	– Basic aircraft model corrected to correlate with flight-measured data – Best prediction of research equipment

3. SIMULATION OF THE AUGMENTED JET–FLAP STOL–RESEARCH AIRCRAFT

3.1 Objectives

The Augmented Jet-Flap STOL-Research Aircraft, which first flew in May 1972, is a modified deHavilland C-8A, Buffalo (fig. 3). The objectives of the research aircraft program are to: (1) determine in-flight aerodynamic performance, stability, and control, as well as the handling qualities of a jet-STOL aircraft that incorporates an augmented jet-flap propulsive-lift concept; (2) contribute to the development of criteria for the design and operation of jet-STOL transport aircraft; and (3) provide a jet-STOL transport aircraft for STOL systems research and development. The development of the augmented jet-flap concept and the modification of the Buffalo is a cooperative research program with the Canadian Government (refs. 5 and 6).

Fig. 3 Photograph of Augmented Jet-STOL Research Aircraft.

3.2 Aircraft modifications

Figure 4 shows some of the dimensions and characteristics of the modified aircraft in a three-view drawing. The major modifications and additions comprise the following: wingspan was reduced to increase the wing loading to 2.39 kN/m^2 (50 psf); an augmented jet-flap system was installed along with drooped boundary layer control ailerons; repositioned and redesigned spoilers were installed in front of the drooped ailerons; a body boundary-layer control system and fixed full-span leading-edge slats were added; the T-64 engines were replaced by Rolls Royce Spey (MK801SF) split-flow turbofan engines; an air distribution duct system was added to supply fan air to the augmented jet flaps; also provided was a lateral-directional stability augmentation system and an extended nose boom for air-data sensors. The lateral control system was entirely new and consisted of ailerons, spoilers, and augmentor choke. The rudder and elevator control surfaces are basic Buffalo. Figure 5 is a diagram of the ducting system which supplies the engine fan air to the dual augmented flap nozzles and boundary-layer control ailerons. Reference 7 includes a discussion of the development and performance of the modified Spey engine for the aircraft. Further description of the aircraft, engine, and systems is included in references 8 and 9.

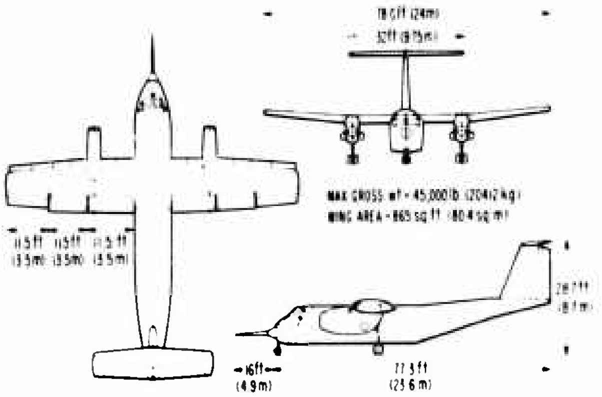

Fig. 4 Three-view drawing of Augmented Jet-STOL Research Aircraft.

3.3 Simulation periods

Figure 6 shows the time schedule for the development and flight research of the aircraft and the periods of simulation. These periods correspond to the simulation periods shown in Table 1. The timing of the simulations during the development cycle were somewhat constrained by the availability of simulation facilities and manpower. It would have been desirable, for example, to have had the conceptual design simulation performed a few months earlier to provide more time for analysis and formal reporting of the results before the requests for proposal for the aircraft modification were issued to prospective contractors. However, preliminary results were available to prospective contractors. Also, because of delays in completing the ground tests and in simulator availability, the preflight planning simulation preceded the first flight by a greater time spread than desired. The pilots did not consider the spread to be intolerable, however.

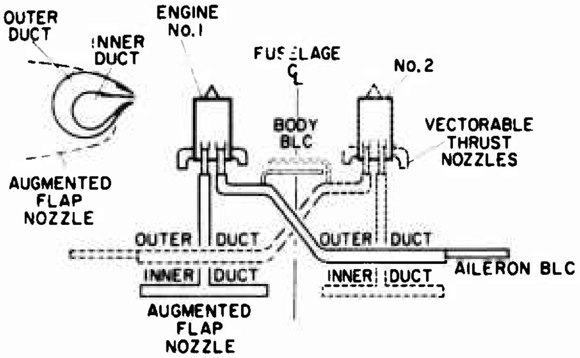

Fig. 5 Engine fan air-distribution system.

Simulation efforts in preparation for the flight experiments started many months before the flight tests of these experiments were scheduled to begin. The dashed line on Fig. 6 implies several studies are being conducted concurrently on different simulators. Early efforts are required because of the need to identify the requirements for research equipment; in some cases, the simulation is a research task in itself, with reports being issued that are independent of the direct application to the aircraft. The discussion of simulation as part of research projects is an interesting subject, but is beyond the scope of this paper.

The FSAA (fig. 1) was used for all phases of simulation, except the conceptual design phase. For this phase, the Ames Limited-Motion Transport Simulator with 3° freedom of motion was used. The simulator system (fig. 2) was about the same for both simulators, the only significant difference being the motion system. The cockpit was configured like the aircraft, with the overhead throttle and vectorable thrust lever as shown in Fig. 7. The cockpit instrumentation was quite standard with the addition of an angle-of-attack and sideslip indicator and a vectorable thrust nozzle-position indicator.

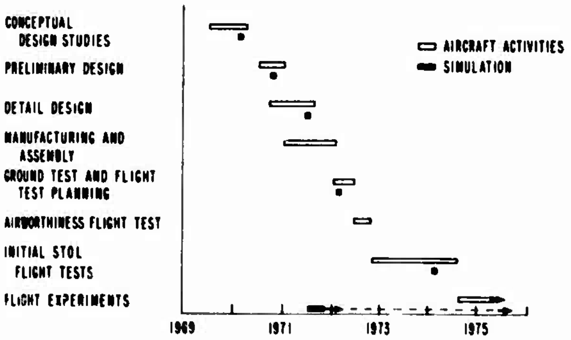

Fig. 6 Aircraft development and simulator periods.

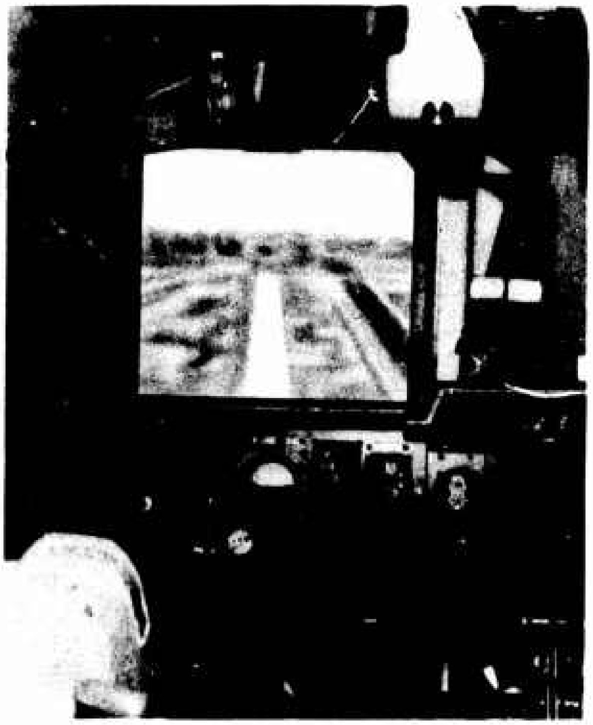

Fig. 7 Cockpit of FSAA with Augmented Jet-Flap Research-Aircraft controls and instruments.

3.4 Mathematical model development phases

The mathematical model for the aircraft was started during the conceptual design studies, and a simplified model of the aircraft was used for this phase of the simulation. Aerodynamic characteristics of the model were based on the results of a large-scale model test in the Ames 40- by 80-Foot Wind Tunnel, using a wing that was similar to the Buffalo wing, but with an augmented jet flap (refs. 10 and 11). In the initial mathematical model, the aerodynamics were simplified and equations written for the lift, drag, and pitching moments characteristics. This representation of the aerodynamic characteristics was quite satisfactory, but was not accurate for large perturbations from the nominal conditions; for example, maximum lift was not programmed. The static and rotary derivatives were calculated, using available wind-tunnel data and theory; many of these derivatives were also programmed as functions of angle-of-attack, momentum coefficients, and flap angles.

In the subsequent preliminary design phase, the mathematical model was updated to be more representative of the proposed aircraft. At this period in the development of the aircraft, initial estimates of weight, moment of inertia, and control-system configuration, etc., had been identified. The model was expanded to include details of the control system, engine characteristics, and revised aerodynamics characteristics. Since there were significant differences between the wind-tunnel model and the proposed aircraft wing, the wind-tunnel aerodynamic data had to be corrected to account for the differences in the flap-chord/wing-chord ratio and aspect ratio. Using basic wind-tunnel data, the lift, drag, and pitching moments, as functions of angles-of-attack, were predicted for five flap deflections and eight values of momentum coefficients. The ground effect was also programmed, based on the large-scale wind-tunnel data. The other characteristics of the aircraft in the model were changed to conform to the preliminary design configuration. This simulation mathematical model had several unique features: the engine characteristics had to be separated into vectored hot thrust (primary flow), inlet mass flow (ram drag and inlet moments), and cold thrust (augmentor and aileron blowing, see fig. 5). The cold thrust was converted to a jet-momentum coefficient and distributed along the span of the wing according to the independent, dual airducting system. The wing aerodynamics were also separated into spanwise segments in order to calculate rolling and yawing moments that were due to asymmetric blowing. Lateral control characteristics were described as a function of jet-momentum coefficient as well as surface deflection. All control surfaces were described separately so that each could be studied separately and system malfunctions, including hydraulic power supply failures, could be simulated. Reference 12 presents the basic mathematical model that was used in the preliminary and detail designs, and reference 13 presents the method of programming that model on the digital computer for both design phases. Of course, more detail and updating was added during the detail design and preflight planning phases.

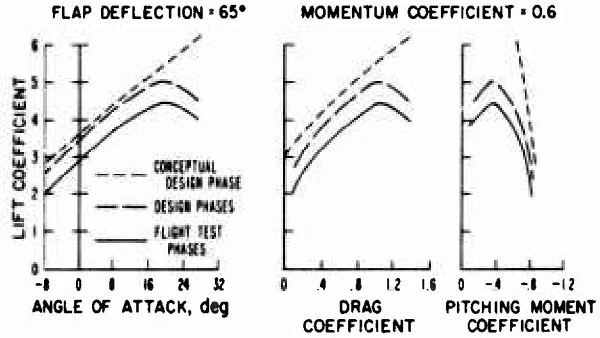

Fig. 8 Comparison of representative aerodynamic characteristics used in updating mathematical model.

Following the initial flight tests, the mathematical model aerodynamics were again changed to match the flight-determined data for the simulation period during the initial STOL flight tests. The changes in lift, drag, and pitching moment for the three changes to date in the aerodynamic characteristics are illustrated for one value of moment coefficient in Fig. 8. Because of the limitation on flight testing at higher values of angle-of-attack, the angle-of-attack values above 16° shown on the lower curve are still the predicted values. The lower pitching-moment curve is also a revised estimate. Other changes are being made to the model as additional analyses of the flight-test data is completed.

The following paragraphs discuss the objectives, items studied, and some of the significant results obtained in each simulation phase.

3.5 Conceptual design phase

During the conceptual design simulation, the main objective was to use the simulator to determine if the modified Spey engine and the Buffalo aircraft could be successfully combined to perform the jet-STOL research-aircraft mission. Table 3 lists the items studied and the results obtained from the simulation during this phase as they applied to the development of the aircraft. Several types of controls were tried on the simulator for the control of the vectored hot thrust. Levers positioned overhead next to the throttles were chosen (fig. 7), because the pilot found that the best method for flight-path control on the landing approach was to keep the throttles fixed and use the vectored thrust for flight-path control. The pilot would, therefore, use the throttle and vector-thrust controls interchangeably with his right hand. For aborted approaches, the throttles and nozzle levers are both advanced forward (thrust vector-angle aft). The simulation showed that a technique for transition from cruise to a steep approach angle by using vectored thrust, throttle, and flap deflection, and from STOL takeoff to climb, would not be difficult.

The control characteristics were found to be satisfactory, but the stability was marginal about all three axes. It was found that lateral-direction stability augmentation would be highly desirable and an automatic speed control would greatly improve the pilot ratings.

Table 3. Conceptual Design Studies Phase: Simulator Results

Item Studied	Results
Vectored thrust control	1. Position overhead adjacent to throttle 2. Position command 3. Forward motion for aft thrust
Stability and control	1. Stability low about all axis 2. Stability augmentation required 3. Airspeed control desirable
STOL operational characteristics	1. Takeoff conventional with high rotation rates 2. Approach flight path control with vector thrust and fixed throttle 3. Flare capability low
Engine failure	1. Takeoff performance marginal 2. Cross-over ducting required to control failure on approach 3. High lift loss with failure on approach requires special procedures.

The engine-out performance characteristics were found to the acceptable on the landing approach, but a special technique for recovery due to lift loss with engine failure would have to be determined. The control required for recovery from an engine failure on approach was very high unless cross ducting was incorporated into the aircraft to reduce the rolling moments due to not only asymmetric jet-flap lift but, also, the vector hot thrust which is at about 90° to the flight path on a steep approach. The engine-out takeoff performance was marginal. The conclusions reached during the conceptual design studies were as follows: (1) the technical risk of building the research aircraft was low, (2) the aircraft could perform a variety of jet-STOL research missions, and (3) development of the aircraft should proceed.

3.6 Preliminary design phase

Some of the significant item studies and results obtained during the preliminary design simulation are listed in Table 4. This simulation was conducted jointly by the contractors and NASA to allow for rapid assimilation of the results into the design effort. The

Table 4. Preliminary Design Phase: Simulator Results

Items Studied	Results
Lateral control system	Criteria established for: – Control power – Sensitivity – Wheel force – Surface rates – Aileron droop
Longitudinal control	1. Buffalo control moment adequate 2. Revised control forces required
Stability	Augmentation required to improve: – Roll damping – Spiral stability – Turn coordination – Dutch-roll damping
STOL operational characteristics	1. Nominal takeoff flap deflection of 30° confirmed 2. Nominal landing flap deflection of 65° confirmed 3. Initial takeoff and landing procedures determined 4. High pilot workload
Engine failure	1. Takeoff - Large change in climb angle – Recovery procedures standard 2. Landing approach – Lift loss requires rapid pilot response to minimize altitude loss – Flap change required for go-around – Cross-duct satisfactorily minimizes control requirements
Augmented flap duct failure	1. Worse failure requires maximum lateral control 2. Affected engine must be shut down to recover 3 Pilot indication required to identify failure

objectives of this simulation were to help define the basic aircraft configuration, to determine design criteria, and to continue the study of operational characteristics. Since the lateral control system was the only completely new flight-control system being designed, much attention was given this subject. As a result of the criteria established on the simulator, the aileron droop could be defined, control wheel gearing determined, and the fuel system revised to reduce the roll moment of inertia and increase available roll-control power at landing gross weights. The basic Buffalo elevator control system was found to be acceptable if the control forces were reduced. Operational characteristics were studied to confirm the nominal takeoff- and landing-approach flap deflections of 30° and 65°, respectively. The engine-out characteristics were studied in detail during this simulation. The three conditions that are associated with an engine failure in a propulsive-lift aircraft are loss of lift, loss of thrust, and asymmetrical lateral and directional control. The simulation determined that the asymmetric control was not a problem with the cross-ducting arrangement shown in Fig. 5. But, the reduction in fan air to the augmented flap system gave a loss in lift. Figure 9 shows the variation of flight-path angle with airspeed for the nominal two-engine takeoff and landing approach conditions and for single-engine performance with emergency power on the remaining engine. In takeoff (flaps 30°), the lift loss was found to be insignificant, but the engine-out climb angle was reduced from 14° to 1.8°. A 1.5° climb was considered minimum with one engine. In the landing approach, the lift loss was quite significant, resulting in a loss of altitude below the approach path and an increase in airspeed. To minimize the altitude loss, a special technique was required. After recovery, the pilot could elect either to continue the approach at a slightly higher airspeed or perform a go-around. A go-around at most-gross weights required a reduction in flap deflection to achieve a positive rate of climb.

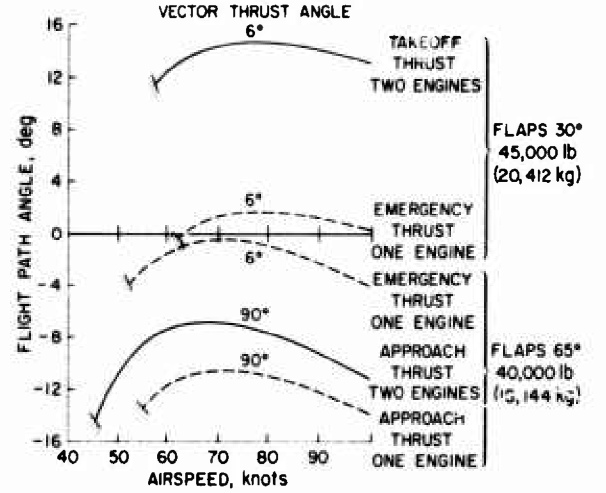

Fig. 9 Variation of flight-path angle with airspeed for takeoff and landing configurations.

Stability augmentation system criteria was also determined for the aircraft, along with criteria for structural and hydraulic system designs. Because some simulated augmented duct failures could result in aircraft motions that were difficult to control, the requirement for conservative duct design was established.

3.7 Detail design phase

The simulation during the detail design phase (Table 5) was essentially a continuation of the previous simulation. Specific attention was given to the augmentor-flap duct failures. The preliminary design simulation had established the requirement for an increased safety margin for the ducts; the detail design phase examined methods for providing indications of duct failure to the pilot so that he could establish a procedure for recovery. There could be very large rolling moments associated with some duct bursts. It was found that, if the pilot were warned which duct had failed, he could shut that engine down and satisfactorily control the airplane with a duct burst. A similar indication was studied for engine-out, but was found not to be required.

Table 5. Detail Design Phase: Simulator Results

Items Studied	Results
Lateral control system	1. Nonlinearities in control system not acceptable 2. Redesign required to make linear
Stability augmentation system	1. Determined optimum gains 2. Determined authority 3. Hardover failures controllable 4. Gain changes required with flap deflection
Augmented flap duct failure	1. Duct failure indication light and pressure gauges for each duct required by pilot 2. With indication, duct failures controllable by shutting down affected engine
Engine failure	1. No indication required 2. Procedures can be developed for control
General	Design considered satisfactory

The final configuration of the lateral and directional Stability Augmentation System (SAS) is shown in Fig. 10. The lateral SAS includes roll-rate feedback to lateral control to improve the roll damping that results from the large increase in roll moment-of-inertia and reduced span. Also, yaw-rate feedback was required to stabilize the spiral mode, and lateral control feed forward was included to quicken the lateral control near zero wheel deflection. In the directional axis, roll angle and yaw rate were fed back to rudder deflection to improve Dutch-roll damping and roll-rate feedback for turn coordination. Satisfactory handling qualities were obtained by changing the gain with flap deflection and by adding an airspeed switch to disconnect both systems at 100 knots. Reference 14 contains a further discussion of the preliminary and detail design simulation phases.

3.8 Preflight planning phase

The items studied and results obtained during the preflight planning simulation are listed in Table 6. The main objectives of this simulator effort were to determine operational and emergency procedures to be used in the early flights of the aircraft, to give pilots the experience on the simulator of "flying" under these conditions, and to identify the limits to be used in the flight-test program. Since the first flights would not be in the STOL mode, specific attention was given to the more conventional mode of flight, as well as to the STOL mode. During this simulation period, all four of the project pilots plus the contractor pilots "flew" under conditions that covered the complete flight operational envelope of the airplane and the following emergency conditions:

- Takeoff and landing engine failures
- Hardover stability augmentation failures
- Vectored thrust nozzle failures
- Augmentor-flap duct failures
- Hydraulic system failures
- Aborted takeoffs and landing
- Minimum speed with a failed engine

Since the ground-effect data used in the mathematical model was of doubtful accuracy, the simulation program also included a range of lift loss with height above the ground. With the highest estimate for lift loss with height, the pilots found that the flare in STOL approaches resulted in poor flares with high sink-rate at touchdown, while the low values were marginally satisfactory. The simulation, therefore, studies a flight-test procedure for progressively increasing the STOL approach angle from −3° up to the desired −7.5° during the initial STOL landings to avoid any high sink-rate landings. All the pilots who participated in this final simulation before the airplane flew concluded that the airplane was operationally airworthy as simulated.

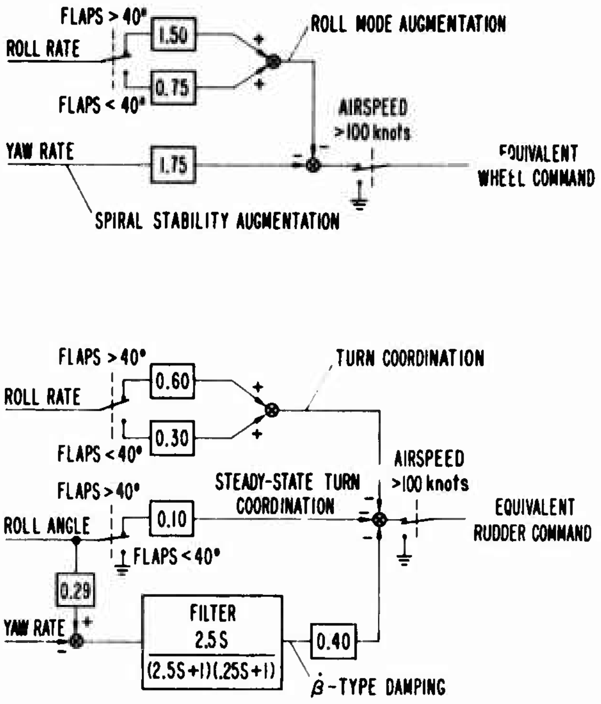

Fig. 10 Lateral and directional stability augmentation system.

Table 6. Preflight Planning Phase: Simulation Results

Items Studied	Results
Conventional takeoff and landing	1. Conventional takeoff and landings to be used on first flights 2. Takeoff flap deflection 25° 3. Landing flap deflection 30° 4. Engine out performance and control satisfactory
STOL operational characteristics	1. Procedures established for – Takeoff – Transition – Approach – Landing – Engine out on takeoff – Engine out on approach – Duct failure – Stability augmentation failure – Hydraulic system failure – Aborted takeoff – Aborted landing 2. Flares difficult with lift loss in ground effect
General	Aircraft ready to start flight tests

3.9 Research flight tests

It was quite gratifying to those on the ground at the first flight of the aircraft on May 1, 1972, at Seattle, Washington, to hear The Boeing Company test pilot state that the airplane flew in a more conventional flight mode, "just like the simulation." Subsequent flights demonstrated that, in most respects, this is also true in the STOL mode.

The lift characteristics determined in flight were somewhat lower than predicted, as shown by the lower curve of Fig. 8. These data are only for a jet momentum coefficient (C_J) of 0.6 and 65° flap deflection. The agreement between flight and predicted lift characteristics was better as C_J was reduced. The effect of this difference is that a 2° to 3° higher angle of attack is required for a given airspeed. It is not known at this time whether the difference is due to performance of the augmented jet flap or the prediction methods for extrapolating the wind-tunnel data to the Buffalo wing. The flare and the longitudinal control are the two areas in which there are significant differences in flight characteristics compared to simulation. The flare characteristics were different because there was an inherent problem in providing pilots the proper cues and because the simulation mathematical model for ground effect was not correct. The lift loss with height above the ground was too large, the reduction in drag too low, and the pitching moment too high. Because the simulation had covered a range of lift losses in ground effects, the only real surprise to the pilots was the tendency to float when full flares were attempted; this effect was due to reduced drag in ground effect. References 15 and 16 present some preliminary results on the initial flight tests.

The longitudinal control was found to be only marginally satisfactory in flight at nominal STOL and conventional flight modes and was unacceptable at very low airspeed and high angles of attack, because of the adverse dynamic force characteristics and the reduced elevator deflection (15° out of a possible 25°) available with low column forces. It was recognized in the early simulation phases that the force characteristics of the elevator control system was only marginally satisfactory, but the magnitude of the problem was not fully realized, because the mechanical characteristics of control system were not completely simulated in the mathematical model. The dynamic force characteristics could not be accurately modeled because of the limitations of the equipment. The large increase in control force at high elevator-deflection angles was not known to exist on the Buffalo until after initial taxi tests had started on the aircraft. The longitudinal control system has now been modified to a fully powered system to eliminate any restriction in flight from that source. It is now possible to accurately model the longitudinal control system on the simulator.

The simulation during the Documentation and Pilot Assessment Phase is primarily to indoctrinate additional pilots who will be flying the airplane to assess its STOL operational characteristics during the latter part of this flight-test period. The simulator test plan is similar to the preflight planning phase, modified by the experience and pilot opinion obtained during the flight tests. The project pilots will also participate in this simulation to train the new pilots and to study revised flare techniques with the model aerodynamics and ground-effect update that will be more representative of the aircraft. All pilots that are to fly the aircraft will be trained in STOL operational and emergency procedures on the simulator. Such simulator experience reduces the flight time that is required to train a new pilot. On a research aircraft with a design service life of only 500 hours, the saving of only a few flight hours is significant.

Simulation is continuing to be used extensively in the flight research programs that are planned for the aircraft. These programs include the research and development of avionics systems for terminal area navigation and automatic and manual guidance systems, as well as STOL aircraft certification and the study of STOL-aircraft handling qualities.

4. SIMULATION OF CANDIDATE V/STOL RESEARCH AIRCRAFT

4.1 Objective

The use of simulation in the development of a STOL research aircraft is discussed in the previous section. This section discusses the use of simulation in evolving conceptual jet, V/STOL aircraft designs into potentially viable candidate research aircraft. An objective pursued in this phase is to evolve designs of aircraft that are capable of very-steep-gradient climbing and descending flight throughout the hover-to-conversion, low-speed flight regime. An advanced V/STOL steep-curved decelerating profile which is used as a goal is compared in Fig. 11 with typical CTOL and STOL approach paths. The V/STOL approach path is for a descent rate of 10 m/s (2000 ft/min) while decelerating at 0.15 g. The capability of making simultaneous decelerating descents along a steep-curved landing-approach path to a vertical landing under either VFR or IFR weather conditions offers advantages in terms of reducing noise footprints, terrain clearance, real-estate requirements, and block time.

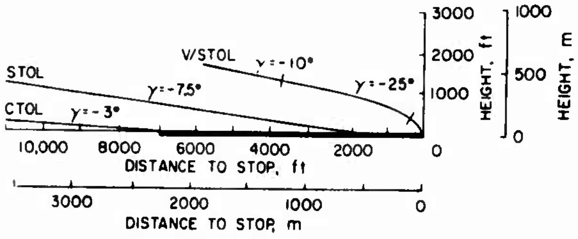

Fig. 11 Typical landing approach profiles for V/STOL, STOL, and CTOL aircraft.

The extent to which such approaches can be utilized operationally has not been established. Consequently, a prerequisite to a viable V/STOL research aircraft is the capability of conducting a near-terminal research-flight investigation along such advanced approach profiles. It has been found that these requirements have been most difficult to achieve, and that significant design tradeoffs are involved in obtaining the large low-speed envelope with good handling under IFR conditions with safety during and after a propulsion- or stabilization-system failure. Simulations for the conceptual design studies of potential V/STOL aircraft and their control systems were more extensive than for the STOL research aircraft, because the V/STOL mathematical model was more complicated by the integration of the propulsion system with the control and stabilization system and by the requirement of satisfactory performance and handling over a larger envelope. This has led to a greater dependence on experienced research pilots for providing detailed assessments of the aircraft characteristics in the early design stages.

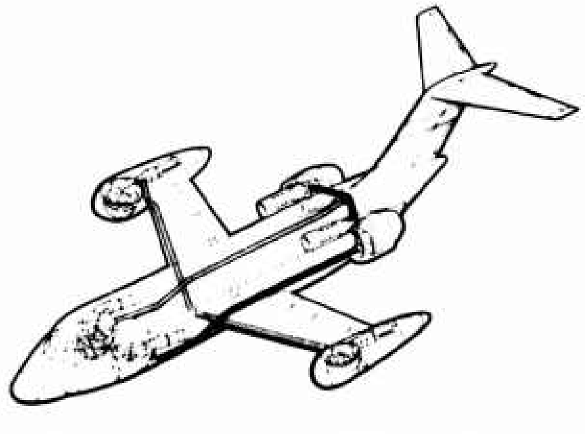

Fig. 12 An example of a candidate V/STOL research transport design.

4.2 Integrated propulsion/control system

Figure 12 shows one of the candidate designs that has been studied. The design features an integrated propulsion/control system that utilizes six gas generators which drive six tip-turbine-driven adjacent fans (generally known as remote fans). Four of the remote lift fans, two in the forward fuselage and one in each wing-tip pod, are used only in the vertical and low-speed flight mode; the two aft lift-cruise fans are used in all flight modes. The engines in the wing tips are interconnected, and opposite forward and aft engines in the fuselage are interconnected; e.g., the left-forward engine is connected to the right-rear engine. The advantage of interconnecting is two-fold. One, no significant moments are produced by a gas-generator failure; and two, it permits modulation of fan thrust over a wider range to satisfy attitude- and translation-control requirements. This integrated propulsion/control system capitalized on the very short duration (fractions of a second up to a few seconds) transient characteristics of the propulsion system. The potential of this integrated system may be seen in Fig. 13 by the significant reduction in gas-generator power required over a noninterconnected system (one gas generator driving one fan). Details of this aircraft design and propulsion/control system, which was developed by McDonnell Aircraft Company, can be found in reference 17. While this novel propulsion/control system showed large potential in meeting the objectives during the initial conceptual studies, it was necessary to verify whether the design guidelines in Table 7 could be satisfied. Of primary concern were the control response, control power, and effect of failures. Before a simulation could be performed, it was necessary to develop an acceptable data base for the propulsion/control system. Consequently, a full-scale investigation was initiated with two gas generators, ducting, and valves to determine steady-state and transient behavior of the propulsion/control system. Reference 18 contains a discussion of the full-scale tests.

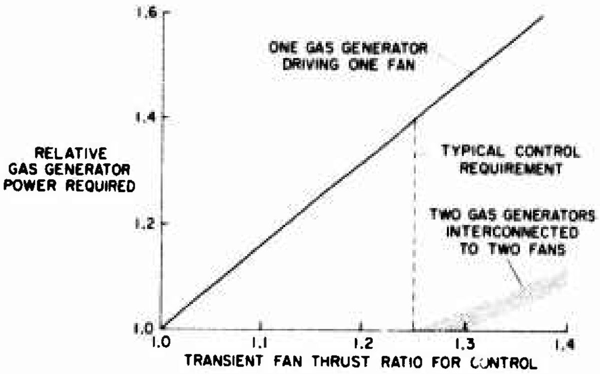

Fig. 13 Design impact of interconnected and noninterconnected engines on gas-generator size.

Table 7. Design Guidelines for V/STOL Research Transport Low-Speed Control Systems

1. Control power. Example control moment/inertia design values for normal operation are 0.75, 0.40 and 0.30 rad/sec^2 for the roll, pitch, and yaw axes, respectively.
2. Control response. Example first-order control moment time constants for normal operation are 0.2 and 0.3 sec for attitude and height control, respectively.
3. Generation of pure attitude control about a given axis without coupling with other axes and without coupling with height control.
4. A system integrated with the propulsion system as required to minimize weight and cost penalties of the combined propulsion and control systems.
5. Control moment force generators, if other than the main propulsive lifting units, that are not the predominant contribution to perceived noise level.
6. A system that maintains symmetric forces and moments about the aircraft during and after failure of the critical gas generator (or remotely powered fan).
7. System simplicity, particularly to minimize maintenance.

The initial simulation was performed on the Ames 6-Degree-of-Freedom Simulator, which has proven to be a particularly good tool for hovering evaluations because considerable motion is available and real-world cues can be used (ref. 19). The lateral control characteristics and pilot ratings for hovering the candidate design with the Stability Augmentation System (SAS) ON, for conditions of no wind, and wind with turbulence are compared in Fig. 14 with a previously reported simulation of an ideal configuration (ref. 19) and from flight evaluation of a VTOL transport, the DO-31 (ref. 20). For no wind, and normal SAS ON operation, the candidate design was rated satisfactory, as would have been expected from other test data. However, crosswinds and turbulent conditions degraded handling characteristics considerably. The degradation was not apparent in flight with the DO-31 aircraft which had a similar gross weight, control power, and frequency. The DO-31 aircraft had satisfactory handling qualities during hovering flight in light-to-moderate turbulence and winds up to 20 knots, which would indicate that the simulation results are somewhat pessimistic. The simulation showed that the new integrated propulsion/control system was generally satisfactory for hovering under normal operating conditions (i.e., no failures), but some improvements should be made.

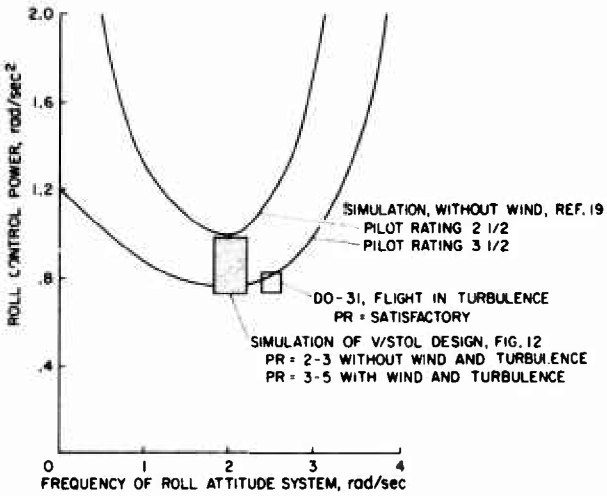

Fig. 14 Evaluation of integrated propulsion/control system; hovering flight, with and without wind, SAS ON.

4.3. Stability Augmentation System (SAS)

A question that impacts the design of the candidate integrated propulsion/control system is whether the design should provide adequate response with SAS failure or whether the SAS system should be redundant with complexity as required to achieve a fail-operational system. Figure 15 is an example of an evaluation of the V/STOL design of Fig. 12. Pilot ratings are shown for a hovering flight task with the SAS OFF and no wind for four different propulsion/control system capabilities; SAS ON is shown for comparison. The desired pilot rating for an emergency is 6.5 or better. With the SAS OFF the basic aircraft is unsafe in hovering flight (pilot rating of 10). Transient fan-thrust modulation could be increased, but that design approach is poor, as illustrated by the very small improvement obtained when the basic control power level was increased by a factor of 1.4. Reducing the value of the control-moment time constant by half improved ratings somewhat, but not enough. The results of the evaluation suggest that serious consideration should be given to a SAS fail-operational design approach for the candidate research aircraft.

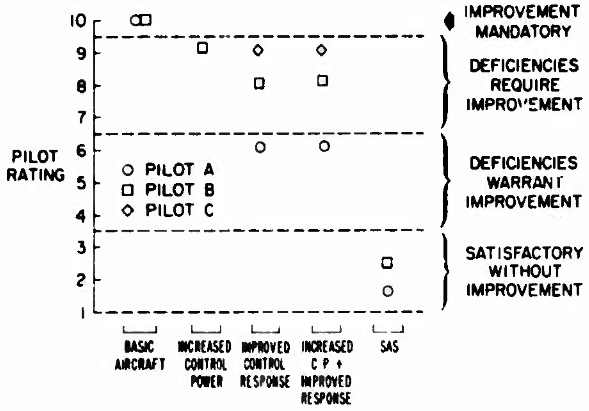

Fig. 15 Pilot ratings from simulation of V/STOL transport design of Fig. 12; hovering flight, no wind.

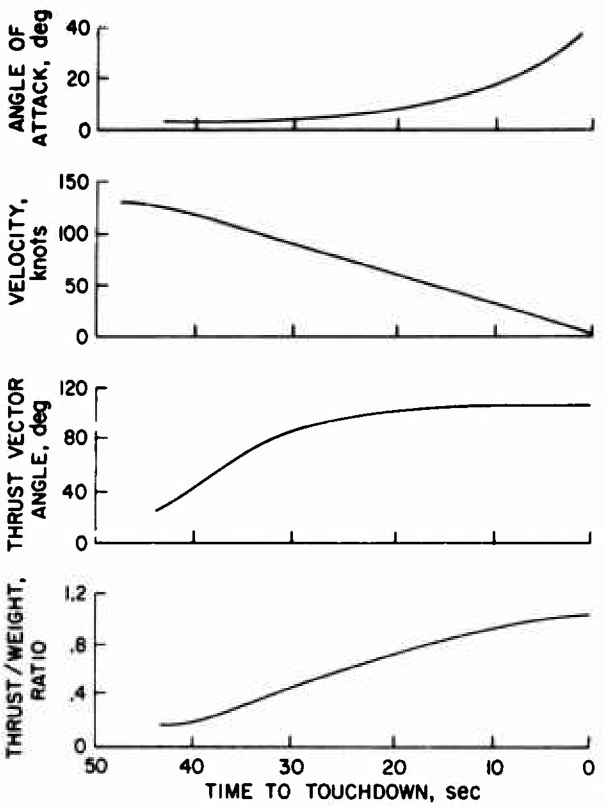

Fig. 16 Variation of controlling parameters for landing approach at a rate-of-descent of 4 m/sec (800 fpm), 0.15-g deceleration, and level fuselage.

4.4 Thrust management system

The previous considerations were for hovering only. The propulsion/control system must also operate satisfactorily over a broad speed and thrust range and be integrated for precise flight-path control so that a pilot can fly demanding VTOL profiles such as shown in Fig. 11. The system demands are indicated by the computed parameters in Fig. 16 for a descent rate of 4 m/sec (800 fpm) and 0.15 g deceleration. Good attitude control and stabilization must be achieved for an effective thrust-vector range of 20° to over 100° while the thrust-weight ratio is increased from 0.2 to over 1.0. After initial piloted simulation investigations, there was little confidence that the candidate V/STOL research-aircraft configuration would in fact be able to operate over such advanced approach paths. The pilot workload levels were high and his tracking performance poor because the parameters that a pilot normally likes to keep constant; i.e., airspeed, angle of attack, and thrust, must be varied in the final phases of landing. In addition, another parameter must be controlled, the angle of the thrust vector. As shown in Fig. 16, these parameters change rapidly as a function of time, and the pilot has very little time to sort things out.

4.5 Subsequent progress

Successive simulations were performed to sort out different forms of thrust-vector controls and to find the extent and form of automation needed to satisfactorily perform complex flight paths. The progress that has been made is indicated in Fig. 17, where a high-performance approach "flown" with acceptable pilot workload on the FSAA simulator is compared with that achieved during NASA flight tests of the DO-31 aircraft and with the goal. The landing approach profiles are presented in terms of the relationship between height above the landing site to horizontal distance to touchdown.

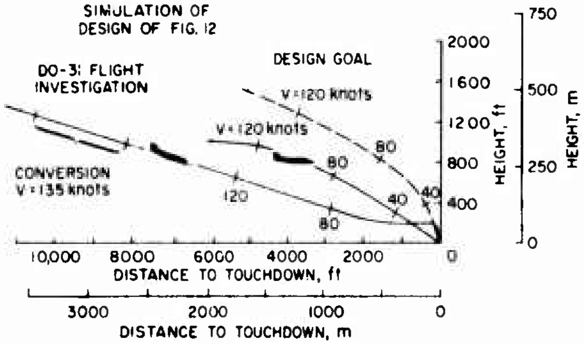

Fig. 17 Comparison of landing approaches flown with design goal in terms of distance-to-touchdown.

The simulation results presented in Fig. 17 illustrate that considerable progress has been made toward realization of the design goals. With the capability of the DO-31 aircraft as a reference, improvements achieved to date have been due to a comprehensive piloted simulation program which attacked simultaneously the interrelated areas of propulsion/control system, stability augmentation system, thrust-management system pilot displays, automation, and aircraft characteristics. Each of these items impacted the design of the aircraft. To further refine this conceptual design study, additional wind-tunnel and control-system testing and periods of simulation are planned.

5. CONCLUDING REMARKS

Flight simulation has become an integral part of NASA V/STOL research aircraft development programs. The main objective of a research aircraft is to provide an aircraft for flight research into new concepts and missions. This implies that design criteria and operational experience and procedures are not available for orderly development and initial flight testing of a new type of aircraft. Simulation provides a means for obtaining some of the required information in a manner in which research pilots can contribute significantly. The requirements for simulation in such programs have been illustrated in two research aircraft programs: (1) the Augmented Jet-Flap Research Aircraft for which the initial development is complete and flight research has started, and (2) an advanced V/STOL research aircraft for which designs are being developed. In both of these programs, periods of simulation were scheduled during the conceptual design phase and, in case of the STOL aircraft, periods were scheduled throughout the program. The simulation studies were significant in establishing design criteria and furthering the study of problems associated with new flight profiles, new methods of control, and special emergency conditions for the aircraft.

REFERENCES

1. Anon.: AGARD Conference Proceedings No. 79 on Simulation. AGARD CP 79, March 1970.

2. Zuccaro, Joseph J.: The Flight Simulator for Advanced Aircraft – A New Aeronautical Research Tool. AIAA Visual and Motion Simulation Technology Conference, March 1970.

3. Bray, R. S.: Initial Operating Experience with an Aircraft Simulator Having Extensive Lateral Motion. NASA TM X-62,155, May 1972.

4. Lee, Alan H.: Flight Simulator Mathematical Models in Aircraft Design. AGARD Conference Proceedings No. 79 on Simulation. AGARD CP 79, March 1970.

5. Wick, B. M.; and Kuhn, R. C.: Turbofan STOL Research at NASA, Astronautics and Aeronautics, Vol. 9, No. 5, May 1971.

6. Whittley, D. C.: The Augmentor Wing Research Program; Past, Present, and Future. AIAA Paper 67-741, Tenth Anglo-American Aeronautical Conference, Los Angeles, CA, Oct. 1967.

7. Conway, John A.: The Development of an Integrated Propulsion System for Jet STOL Flight Research. Paper presented at AGARD Propulsion and Energetics Panel Meeting on V/STOL Propulsion, Sept. 1973.

8. Quigley, H. C.; Sinclair, S. R. M.; Nark, T. C.; and O'Keefe, J. V.: A Progress Report on the Development of an Augmentor Wing Jet STOL Research Aircraft. SAE Paper 710757, National Aeronautic and Space Engineering and Manufacturing Meeting, Los Angeles, CA, Sept. 1971.

9. Ashleman, R. H.; and Skavdahl, H.: The Development of an Augmentor Wing Jet STOL Research Aircraft (Modified C-8A), Summary. NASA CR-114503, Aug. 1972.

10. Koenig, D. G.; and Corsiglia, V. R.: Aerodynamic Characteristics of a Large-Scale Model with an Upswept Wing and Augmented Jet Flap. NASA TN D-4610, June 1968.

11. Cook, A. M.; and Aiken, T. N.: Low-Speed Aerodynamic Characteristics of a Large-Scale STOL Transport Model with an Augmented Jet Flap. NASA TM X-62,017. March 1971.

12. Cleveland, W. B.: The Handling Qualities Simulation Program for Augmentor Wing Jet STOL Research Aircraft. American Federation of Information Processing Societies, Vol. 39, Fall Joint Computer Conference, Nov. 1971.

13. Cleveland, W. B.; Vomaske, R. F.; and Sinclair, S. R. M.: Augmentor Wing Jet STOL Research Aircraft Digital Simulation Model. NASA TM X-62,149, April 1972.

14. Spitzer, R. E., Rumsey, P. C., Quigley, H. C.: Use of the Flight Simulator in the Design of a STOL Research Aircraft. AIAA Paper 72-762, Aug. 1972.

15. Quigley, H. C.; and Vomaske, R. F.: Preliminary Results of Flight Tests of the Augmentor Wing Jet STOL Research Aircraft. NASA SP-320, Paper 20, Oct. 1972.

16. Innis, R. C.; and Anderson, S. B.: Comparison of Simulator and Flight Results on Augmentor Wing Jet STOL Research Aircraft. NASA SP-320, Paper 21, Oct. 1972.

17. Novak, L. R.: A Low Risk Approach to Development of a Quiet V/STOL Transport Aircraft. AIAA 7th Annual Meeting and Technical Display, Houston, Texas, AIAA Paper 70-1409, Oct. 1970.

18. Deckert, W. H.; and Rolls, L. S.: Integrated Propulsion/Energy Transfer Control Systems for Lift-Fan V/STOL Aircraft. Paper IIG presented at AGARD Propulsion and Energetics Panel Meeting on V/STOL Propulsion, Sept. 1973.

19. Grief, R. K.; Fry, E. B.; Gerdes, R. M.; and Gossett, T. D.: Effect of Stabilization on VTOL Aircraft in Hovering Flight. NASA TN D-6900, 1972.

20. Holzhauser, C. A.; Morello, S. A.; Innis, R. C.; and Patton, J. M., Jr.: A Flight Evaluation of a VTOL Jet Transport Under Visual and Simulated Instrument Conditions. NASA TN D-6754, 1972.

A LITERATURE SURVEY ON JETS IN CROSSFLOW

by

E.C.P. Ransom and P.M. Wood

Kingston Polytechnic,
Kingston-upon-Thames,
Surrey, England.

SUMMARY

The salient features of a literature survey on the interference effects of jets in cross flow are outlined. From the large number of reports on this subject a systematic catalogue has been devised and a critical survey compiled, which aims to provide the designer and research worker with a guide to available literature and to future research needs.

The catalogue lists reports reviewed and contains a tabulation of data in terms of the independent variables, dependent variables and test techniques.

The critical review analyses the experimental work to investigate the effect on aerodynamic forces and moments of (a) the fluid and geometrical properties of the jet and cross flow, e.g., jet velocity profile, nozzle cross section shape, (b) the geometrical arrangement of the aerodynamic elements, e.g., multiple jet spacing relative to airframe, nozzle to ground height. The conclusions indicate those parameters which have significant effects but have not been the subject of systematic investigations. Recommendations are made for further research effort.

INTRODUCTION

The flow field created by a jet or jets interacting with the fluid surrounding the jet efflux has received considerable attention from both designers attempting to optimise configurations of jet lift aircraft and research workers seeking a clearer understanding of this type of flow phenomena. There are many reports which are generally available. There are also a significant number that up to now have not been widely published, which describe work carried out by aero-space companies in the United Kingdom.

In order to assess the current situation the more recent reports, available in English, have been catalogued and reviewed. The terms of reference of this exercise restrict the survey to the cases when subsonic or sonic jets discharge at oblique angles to a cross flow having Mach Numbers ranging from $M = 0.6$ to zero.

PROVISION OF A CATALOGUE

A catalogue has been devised in order to assist the designer in his search for relevant information. Only basic data is presented but this will nevertheless greatly assist in the location of reports likely to be useful. In order to present the data in as concise an order as possible, three basic categories have been selected:

(i) Independent variables.
(ii) Measured data.
(iii) Test techniques.

Also included in the tabulation are the ranges of variation of these parameters. A typical example of the information included is given in Table 1.

This type of table, therefore, indicates the quantity of data available in each topic, and also where this data may be readily obtained. It is also valuable in that it highlights areas which require further investigation. Naturally it cannot reveal all the detail contained in a report nor does it provide an assessment of the quality of data. In order to obtain some guide to this latter aspect the writing of a critical review was undertaken.

CRITICAL REVIEW

This has been confined to the general field defined below, together with the associated main areas of interest:

The effect upon aerodynamic interference forces and moments of changes in

(a) the fluid properties and the particular geometric (spatial velocity) flow characteristics of the jet and cross flow,

and (b) the geometry of the aerodynamic element influenced by the nozzle system.

Other related but less major areas are included such as:

Reingestion of exhaust gases into engine intakes.
Surface erosion due to impinging jets.
Wind tunnel test limits.

The review is sub-divided in such a manner that attention is given to each parameter in turn (Table 2). This enables as full an appreciation as possible to be given to the individual pieces of tabulated data.

Since no theories are currently available for viscous fluids, the review does not contain an assessment of the various inviscid theories for predicting pressure distributions over surfaces. Wakes cannot be created in inviscid fluid flows, and since the wake region is of considerable importance in jet interference studies, the inclusion of theories which preclude this would only be misleading.

Presented now, in an abbreviated form, are some of the more significant results of this review:

1.1. JET FLUID PROPERTIES

1.1.1 Velocity Profile

Almost all the fundamental experimental work has been carried out using nozzles producing a jet with a "flat" axial velocity profile at nozzle exit. Often the actual velocity deviates from the mean in a form defined as "profile roughness", which may range from ± 0.5% (Ref. 1) to ± 10% (Ref. 2). It is significant that no comparative studies have yet been undertaken to establish the importance of this.

The effect of gross change in velocity profile has not been investigated although it is suspected that this could be a significant variable. Gentry and Margason (Ref. 3) have studies the effect of a variation in nozzle length on induced forces and have shown that there is a change in interference lift loss. It is suspected that this change in lift loss can be attributed to the alteration in velocity profile caused by the increase in nozzle length. It is surprising but valuable to note that such a significant parameter has largely been ignored, and it is clear that some further work is essential.

The effect of cross flow is interesting. Fig. 1 (after Brown, Ref. 4) shows the constant velocity contours before and after the imposition of cross flow. In still air the axi-symmetric, undeflected jet has the same nominslly flat, axial velocity profile along any diameter.

When subjected to cross flow, the maximum velocity occurs at two stations either side of the diameter, which is in the plane of symmetry of the deflected jet. The largest velocity on this particular diameter occurs on the cross flow downstream side.

1.1.2 Jet Trajectories

These have proved of interest since the very beginning of V/STOL research since they may be used in the calculation of a pressure field. There are at least five ways of defining the jet path:

1. the line of maximum stagnation pressure,
2. the line of maximum dynamic pressure,
3. the line of maximum velocity,
4. the line of maximum stagnation temperature,
5. the line of vortex centres.

Since none of these give precisely the same trajectory, it is therefore necessary to exercise great care when comparing data from different sources.

It is generally assumed that under the same conditions of cross flow, the trajectories of circular jets are unaffected by the geometry of the surface from which they emerge, but a satisfactory correlation has not been achieved as yet. Harding (Ref. 5) presents some evidence which indicates that under certain conditions surface geometry may influence the path taken by the jet.

The trajectory is also affected by the shape of the initial cross section, which is worthy of further investigation, and most of the available data only applies to axisymmetric jets.

1.1.3 Jet Entrainment

The rate of entrainment into a jet is important, particularly in the region close to the jet exit, because it affects the local flow velocities over adjacent surfaces, and hence the local static pressures. Direct measurements are possible only in certain cases, and when used (refs. 6, 7, 8) a good correlation of data was obtained. This information is only of limited use since no information is given concerning the properties of the jet.

An alternative assessment which enables entrainment rates to be compared is given by the decay of dynamic head.

Inside the potential core no entrainment occurs. Thus a study of the length of this core indicates the rate of entrainment. The effect of variation in this is demonstrated in Fig. 2, after Ousterhout (Ref. 9), which shows that with a shorter potential core indicating higher entrainment rates the induced pressure field is generally more extensive.

In the absence of cross flow, Bradbury (Ref. 11) has shown that the presence of tabs in the nozzle reduces the length of the potential core, and also changes the jet decay characteristic.

When cross flow is present, there is evidence that at a velocity ratio of about 5, the behaviour of the flow field changes. This is indicated by an alteration in the jet decay characteristic. Keffer and Baines (Ref. 10) show that this occurs at a velocity ratio of 4. Brown (Ref. 4) shows that the shape of the decay curve changes significantly at a velocity ratio of 5.

Clearly there is a need to establish if separate indentifiable flow regimes exist, and to determine the influencing parameters.

1.1.4 Temperature Effects

Although experimental work with jets at elevated temperature has been carried out, it has so far not been possible to satisfactorily isolate this parameter from other effects. Scatter of results reported by Holdeman (Ref. 12) is thought to be due to different jet and cross flow conditions, but a proportion of this information was for velocity ratios of no interest to V/STOL designers.

1.2 CROSS FLOW PROPERTIES

1.2.1 Velocity Profile

With one exception all the work reported concerned cross flows with nominally flat profiles. Ref. 4 deals with the effects of both a positively and negatively sheared cross flow, and comparisons are made with the uniform flow case. The effects on induced pressure fields are significant but the basis of comparison may lead to difficulties. It is probably safe to assume that out of ground effect, sheared flows are unlikely to be encountered, but in ground effect the chances are very much greater. It is suggested that this would provide a useful area for further work.

1.2.2 Surface Boundary Layers

Thompson (Ref. 13) demonstrates that surface boundary layers may not be a major factor influencing induced forces. In a study of the pressure field due to an axisymmetric jet discharging into a uniform cross flow it is shown that whilst boundary layer thickness changes the distribution of pressure, the effect on overall forces is thought to be minimal.

1.3 NOZZLE GEOMETRY

1.3.1 Nozzle Shape

There is evidence which suggests that the circular nozzle is preferable for V/STOL application. The trajectory of a narrow jet edge on to the cross flow is unstable and can oscillate laterally to the cross flow direction under certain conditions causing the induced pressure field to change in a sympathetically cyclic fashion. The same jets when presenting a broad face to the cross flow create a larger blockage to the flow. The wake width is larger due to the flow "separation" at the edge of the jet and the resulting interference pressure field is more extensive (Refs. 13, 14).

1.3.2 Multiple Nozzle Array

Apart from Ref. 15 the experimental work is mainly concerned with aircraft models. From work carried out by the British Aircraft Corporation and Hawker Siddeley Aviation Ltd. it is clear that the arrangement of jets is important and in general jets which are more evenly distributed give better characteristics than those grouped into clusters. Ref. 16, for example, discusses hovering in ground effect. Under ground effect conditions multiple nozzles can produce jet fountains, which may give rise to the reingestion of hot gases into engine intakes, or impingement of hot gases on to aircraft components.

2.1. GEOMETRY OF THE AERODYNAMIC ELEMENT

Introduction

The existence of surfaces near to the nozzle exit or the jet trajectory undoubtedly has an effect on induced forces and moments. This is due to the influence which these surfaces have on local velocities (both in speed and direction) and as a general rule the effects will be more significant the closer the surface is to the jet.

2.1.1 Flat Surface

The only geometrical variable in the case of the finite surface is the shape of the leading edge, which varies from a sharpened edge to a rounded nose section. Since this is likely to affect only the development of surface boundary layer which has little influence (see 1.2.2), provided the nozzle is set close to the leading edge.

2.1.2 Body of Revolution

Ousterhout (Ref. 9) compares pressure coefficients and pitching moments generated by a jet emerging from a cylinder with its axis parallel to the main stream with those on a flat plate produced under identical flow conditions. All the data is obtained at velocity ratios less than 4, which is below the critical value reported by Brown (Ref. 4) and Keffer and Baines (Ref.10).

2.1.3 Wings

Recent work (Ref. 18) has suggested that there are two patterns of flow behaviour created by a jet emerging from a wing. At velocity ratios less than 6 the interference surface pressure field is different from that induced on a flat plate by identical cross flow conditions. At velocity ratios greater than 6, considerable similarity exists between the two pressure fields when compared at the same velocity ratio.

Further evidence for this change of behaviour is presented in Figs. 6, 7, 8 and 11 of the paper by Knott and Hargreaves which is presented at this Symposium (Ref. 22).

The factors affecting this apparent transition in flow pattern are not known with certainty, but it is possible that there may be some connection with the results reported by Keffer and Baines (Ref.10) and Brown (Ref.4) concerning jet trajectories (see 1.1.2).

2.1.4 Aircraft

Because of the large number of variables and because results may be applicable to only one specific model, it is unsound to draw general conclusions.

Aircraft types may be classified broadly as:

Fuselage mounted jets.
Wing mounted jets.
Podded jets.

Four operating regimes may be recognised:

No cross flow - out of ground effect.
With cross flow - out of ground effect.
No cross flow in ground effect.
With cross flow in ground effect.

A considerable amount of data is available, of which Refs. 3, 16, 19, 20 and 21 are but a small selection, but there appears to be a scarcity of generalised information for aircraft in ground effect with cross flow.

FURTHER WORK

The most significant feature arising from this exercise is the need to establish if there is more than one type of flow pattern, and which parameters are important. Four independent sources suggest that there may be at least two flow regimes, and it is clear that some careful experimental work is required.

To support this work, it appears necessary to ascertain the significant factors affecting jet behaviour both without and with a cross flow. A carefully designed experimental programme is required which will separate out such parameters as velocity profile, profile "roughness", turbulence, jet Reynolds number, boundary layer thickness, jet temperature, jet pressure ratio, and geometrical design of the nozzle and plenum chamber, so that jet decay characteristics may be accurately defined.

ACKNOWLEDGEMENTS

This paper is based upon work supported by the Ministry of Defence. The authors wish to thank the following for advice and assistance during the course of the project:

The Royal Aircraft Establishment, Bedford, in particular Mr. D.N. Foster;

The Military Aircraft Division of the British Aircraft Corporation, in particular Mr. P.G. Knott;

Hawker Siddeley Aviation Ltd., in particular Mr. C. Bore, who also suggested this project.

The paper is reproduced by permission of Her Britannic Majesty's Stationery Office, and is British Crown Copyright.

REFERENCES

1.	Bradbury, L.J.S.	The impact of an axisymmetric jet on to a normal ground. Aeronautical Quarterly, Volume 23, May 1972, pp. 141-147.
2.	Trebble, W.J.G.	Investigation of the effect of tunnel walls on the flow near a model containing a lifting jet. Royal Aircraft Establishment, Farnborough, England. To be published.
3.	Gentry, C.L. and Margason, R.J.	Jet induced lift losses on VTOL configurations hovering in and out of ground effect. NASA TN D-3166, February 1966

4. Brown, D. The circular jet in a uniformly sheared cross flow. Ph.D. Thesis, University of Bristol, 1967.

5. Harding, C. The trajectory of a circular jet of air issuing normally to a subsonic main stream. ARG 32, September 1967, British Aircraft Corporation (Operating) Ltd., Preston.

6. Ricou, F.P. and Spalding, D.B. Measurements of entrainment by axisymmetrical turbulent jets. Journal of Fluid Mechanics, Volume 11, Part 1, 1961, pp. 21-32.

7. Searle, N. Entrainment by axisymmetric jets impinging on a flat plate. M.Sc. Thesis, Cranfield Institute of Technology, June 1964.

8. Arbuckle, J.A. Investigation of density effects on entrainment by impinging jets. M.Sc. Thesis, Cranfield Institute of Technology, May 1965.

9. Ousterhout, D.S. An experimental investigation of a cold jet emitting from a body of revolution into a subsonic free stream. NASA CR-2089 August 1972.

10. Keffer, J.F. and Baines, W.D. The round turbulent jet in a cross-wind. Journal of Fluid Mechanics, Volume 15, Part 4, April 1963, pp. 481-496.

11. Bradbury, L.J.S. Entrainment into an axisymmetric jet. University of Surrey. Unpublished progress report 1972/73, November 1973.

12. Holdeman, J.D. Correlation for temperature profiles in the plane of symmetry downstream of a jet injected normal to a crossflow. Lewis Research Centre, NASA TN D-6966, September 1972.

13. Thompson, A.M. The flow induced by jets exhausting normally from a plane wall into an airstream. Ph.D. Thesis, University of London, September 1971.

14. Wu, J.C., Mosher, D.K and Wright, M.A. Experimental and analytical investigation of jets exhausting into a deflecting stream. AIAA/AHS VTOL Research, Design and Operations Meeting, February 1969. AIAA Paper 69-223.

15. Fricke, L.B., Wooler, P.T. and Ziegler, H. A Wind tunnel investigation of jets exhausting into a crossflow. Volumes 1 - 4. Northrop Corporation. AFFDL-TR-70-154 Volumes 1 - 4, December 1970.

16. Thompson, A.M. On the static lift characteristics of jet lift V/STOL aircraft configurations. British Aircraft Corporation Ltd. ARG.42, May 1968.

17. Leyland, D.C. The significance of jet induced interference lift on V/STOL aircraft take-off performance. British Aircraft Corporation, Preston, PM 167, June 1964.

18. Mikolowsky, W. and McMahon, H. An experimental investigation of a jet issuing from a wing in crossflow. Journal of Aircraft, Volume 10, No. 9, September 1973.

19. Shumpert, P.K. and Tibbetts, J.G. Model tests of jet-induced lift effects on a VTOL aircraft in hover. NASA CR-1297, March 1969.

20. Wade, J.M. and Knott, P.G. 18' low speed tunnel results from V/STOL model R6. A low aspect ratio multi jet lift research model. British Aircraft Corporation Report No. AXR. 15, June 1968.

21. Harris, A.E. et al. P.1127 1/10th scale ground effects model test results. Hawker Siddeley Aviation Ltd. Report IDR 171, August 1962.

22. Knott, P.G. and Hargreaves, J.J. A review of the lifting characteristics of some jet lift V/STOL configurations. AGARD CP 143 V/STOL Aerodynamics April 1974.

TABLE 1

		Symbol	Unit	Ref. 9
1.	**INDEPENDENT VARIABLES**			
1.1	**Nozzle Geometry**			
	Number of nozzles			1
	Array of nozzles			-
	Shape and size of nozzle	d	mm	C 6.4 + 9.5
	Inclination of nozzle axis:			
	θ_{zx}		Degrees	0
	θ_{zy}		Degrees	0
	Plenum chamber			✓
1.2	**Model Geometry**			
	Surface/body type from which jet discharges			F.F.P.,A.B.
	Reingestion guards			No
	Intakes			No
1.3	**Jet Fluid Properties**			
	Composition			Air
	Velocity at nozzle exit	U_{je}	m/s	53-209
	Stagnation temperature	T_{oj}	K	300
	Static pressure	P_j	kN/m^2	Atmos.
1.4	**Cross Flow Fluid Properties**			
	Composition			Air
	Velocity	U_∞	m/s	27-61
	Stagnation temperature	$T_{o\infty}$	K	300
	Static pressure	P_∞		Atmos.
1.5	**Jet/Cross Flow Parameters**			
	Velocity ratio	Ye/U_∞		2-3.3
	Effective velocity ratio			-
1.6	**Secondary Effects**			
	Ground effect			No
2.	**MEASURED DATA**			
	Jet trajectories			
	Entrainment			
	Surface pressure distribution			✓
	Aerodynamic forces and moments			F + M
	Pressure, velocity and temperature profiles			V
	Ground effects			No
	Net thrust			No
3.	**TEST TECHNIQUES**			
3.1	**Experimental**			
	Wind tunnel			✓
	Other			
3.2	**Theoretical**			
	First principles			
	Semi-empirical			

TABLE 2

1.1 JET FLUID PROPERTIES

- 1.1.1 Velocity profile
- 1.1.2 Trajectories
- 1.1.3 Entrainment
- 1.1.4 Temperature effects

1.2 CROSS FLOW PROPERTIES

- 1.2.1 Velocity profile
- 1.2.2 Boundary layer

1.3 NOZZLE GEOMETRY

- 1.3.1 Nozzle shape
- 1.3.2 Multiple nozzle array

2.1 GEOMETRY OF AERODYNAMIC ELEMENT

- 2.1.1 Flat surface
- 2.1.2 Body of revolution
- 2.1.3 Wings
- 2.1.4 Aircraft

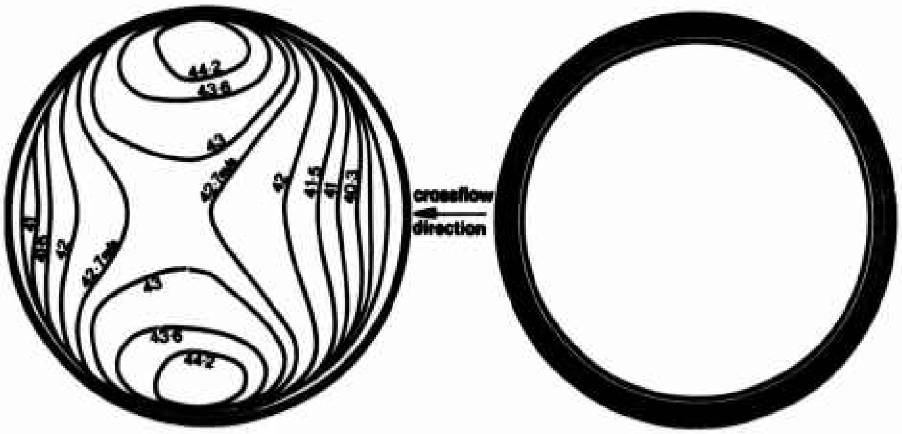

Fig.1 Velocity contours at nozzle exit (Brown Ref.4)

without crossflow

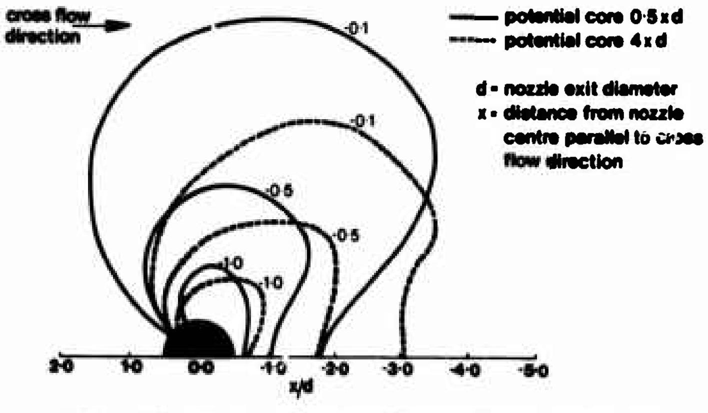

— potential core 0·5 x d
----- potential core 4 x d

d = nozzle exit diameter
x = distance from nozzle centre parallel to cross flow direction

Fig.2 Comparison of flat-plate pressure coefficient contour data for two investigations at the same value of velocity ratio (2.85) (Ousterhout Ref.9)

APPENDIX A

ROUND TABLE DISCUSSION AT THE CONCLUSION OF THE SYMPOSIUM

Mr J.P.HARTZUIKER (Chairman) :	N.L.R. Amsterdam 1017 Netherlands
Mr D.H.HICKEY	Ames Research Center NASA Moffett Field, California 94035 USA
Mr B.EGGLESTON	De Havilland Aircraft of Canada Ltd. Downsview, Ontario Canada
Professor J.H.D.BLOM	Fokker VFW.BV, Schipol-Oost Netherlands
Professor Dr J.BARCHE	VFW – Fokker GmbH 28 Bremen Germany
Professor Dr K.GERSTEN	Ruhr Universitat Bochum Germany
M.P.PERRIER	Avions Marcel Dassault-Breuget Aviation 92214 St Cloud France

ROUND TABLE DISCUSSION

Mr J.P.Hartzuiker, Chairman: We have set up a panel here which will cover most of the topics we discussed during the meeting. They will set the scene for a further discussion, and it is hoped that there will be a large contribution from the audience. I have asked the panel to cover approximately half the time which we have available, and the rest of the time could be used for a discussion from the floor. The outcome of this Round Table Discussion will be added in printed form to the proceedings of this symposium.

I would like now to introduce the panel; if that is still necessary. I have on my left Mr Hickey, who is Assistant Branch Chief of the Large Scale Aerodynamics Branch at NASA – Ames. You know Mr Hickey, of course, from the excellent introductory review he gave, and the subjects of his comments will be the necessary research to improve operating economics and technology of the VSTOL system. On my right-hand side we have Mr Eggleston who is the Advanced Project Manager of DeHavilland, Canada. You have all been there for his introductory paper on powered high lift systems, and in view of the quality of that paper, I am sure we all look forward to hearing the further comments he might have on the subject. Then again, going left, I would like to introduce Professor Blom, who is Chief of Aerodynamics of Fokker VFW in Amsterdam and who is also a lecturer at the Aerodynamics Department where we are guests today. He is prepared to give his point of view on mechanical high-lift systems. In view of the connections of Professor Blom with the F27 and F28 aircraft, I think his comments will be very welcome. Going to my right we have, as you know, the third contributor of an introductory review, Dr Barche, Head of the Flight Physics Department of VFW Fokker in Bremen. As you have heard the clear summary of the problems of jet lifts, I think you will be eager to know his further comments on what should be done on that subject. On my far left, we have Professor Gersten from Ruhr University in Bochum, who presented a lecture this morning. He will give his comments on sessions 4 and 5 of this symposium, i.e., Ground Effects and Aerodynamic Prediction Methods and Simulation Requirements. Finally, I would like to introduce to you another man whom we have also seen this week, M. Perrier, who is Chief of Theoretical Dynamics of AMDBA, which is in short Dassault-Breguet. M. Perrier is eager to give his comments on the application of computational methods to the subject of VSTOL aerodynamics. I would now like to invite Mr Hickey to give his first comments.

Mr Hickey: Thank you Mr Hartzuiker. We have had an interesting two or three days of discussion on V/STOL aerodynamics. My task now is to try to relate this to airplane economics. Before I start, I would like to point out that economics are made up of at least two parts, one being indirect operating costs and the other being direct operating costs. Indirect costs are a function of what it takes to run an airline exclusive of the airplane; the cost of the airport, baggage systems, navigational aids, etc. Whereas, the direct operating cost is more a function of the airplane, and that is what I will discuss; that is, how V/STOL aerodynamics impact on direct operating cost. Mr Ljungstrom in Paper No. 13 made this point. In the broadest sense of the word, when we talk about V/STOL aerodynamics and improving aerodynamics, we are talking about reducing direct operating costs. Even if we consider handling qualities or development of control systems, they all feed back into the airplane efficiency in doing its mission. I have several slides to help illustrate the discussion. Figure 1 shows direct operating cost vs. field length for a number of different STOL concepts. Let us look first at the aircraft equipped with mechanical flaps. You will notice the knee of the curve at about a 4000 ft field length. At a 3000 ft field length we find that they have about the same direct operating costs as the propulsive lift concepts. We have heard some very interesting and excellent work on mechanical flaps during this meeting. M. Perrier, for example, showed prediction methods and also showed data with a maximum lift of 4½. The maximum lift for the data that you see here is more of the order of 3½. Of course, the excellent work that Dr Jacob presented was very interesting as well as that of Mr Ljungström. However, we can't necessarily relate maximum lift to direct operating costs – other factors may be important. For example, the thrust-to-weight ratio may be defined by the engine-out climb rate during take-off. If so, it is necessary to optimize lift-drag ratio at low angles of attack and low flap deflections rather than for $C_{L_{max}}$. The powered lift aircraft results shown on the chart have a knee at about 3000 ft, and all of the three concepts studied have about equal direct operating costs. To make STOL more attractive for short haul we should minimize direct operating costs by lowering the overall level and removing the knee from the curve, if possible. Let us now examine the important factors in direct operating cost. Figure 2 lists these factors. The direct operating cost is the cost per hour of operating the airplane divided by the velocity of the airplane. The velocity is, of course, the distance divided by the cruise time plus manoeuvre time. An increase in cruise velocity or reduction in manoeuvre time will improve direct operating cost. A factor that enters into the cost per hour is the fuel used, and the equation for distance per pound of fuel is on the bottom of the chart. High air speed, low specific fuel consumption, good cruise lift-to-drag ratio and low aircraft weight reduces fuel requirements. The aircraft weight also enters into the cost term. Figure 3 shows a weight breakdown of a typical STOL airplane. We see that the structure amounts to about 44%, the propulsion system about 15%, the fixed equipment 12%, fuel 14% and payload 15%. The only items that can be altered with aerodynamics are the propulsion system and the fuel required. Fixed equipment is a constant weight, payload is a constant weight, and structure is a constant percent of gross weight. Using these factors, the sensitivity of direct operating cost to improvements in aerodynamics has been derived. Figure 4 lists these sensitivities. A 10% increase in $C_{L_{max}}$ results in a weight change of about 3%. This arises from the assumption that an improved $C_{L_{max}}$ means a lower take-off speed, and there is less engine thrust required to accelerate the aircraft. The thrust required is another sensitivity factor, and this assumes that with a more efficient propulsive lift system, engine thrust and weight can be reduced by 10%. This saving reduces aircraft weight by about 3%. The other factors evaluated were specific fuel consumption, cruise L/D, and cruise speed, which reduced aircraft weight by 2.8% each. If we take these as cumulative gains, weight is reduced about 15%. To the first order, direct operating cost and aircraft weight are dependent and a similar reduction in direct operating cost would be expected. It would be very difficult to make 10% improvements in all of these factors, thus the gain that can be realized is probably much less than 15%. Based on this conclusion, more significant gains must be realised before the goal of lowering direct operating cost and removing the knee of the curve in the first slide can be realized. In the first paper the advantage of increasing augmentation ratio from 1.3 to 2 on an augmented jet flap aircraft was discussed. This improvement would reduce direct operating costs approximately 15% and would remove the knee from the direct operating cost curve. However, this low leverage, from aerodynamics means rather large improvements are required. The workers in V/STOL aerodynamics are encouraged to maintain their research efforts and look for significant improvements.

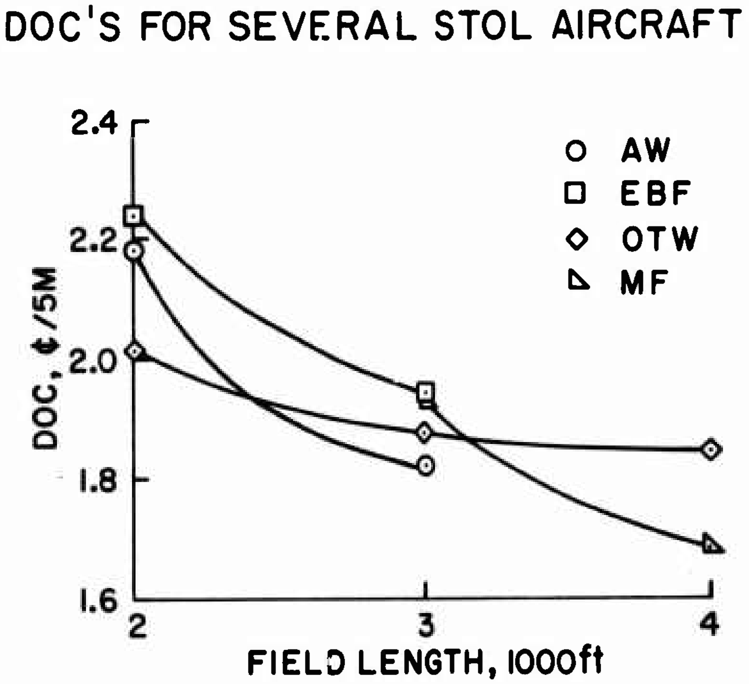

Figure 1

Chairman: Are there any comments or questions from the floor for Mr Hickey?

Dr Rogers: I wondered if Mr Hickey would really comment on and give his own views as to why we need V/STOL transport systems anyway. That seems to be a more fundamental question. Certainly, I think it is questionable whether 2000 ft runways are ever going to be required or indeed will ever be economic. Whilst one can certainly achieve these technically, is it likely that the DOC will be acceptable to airlines in the difficult days ahead, and in addition, is it true that in concentrating on DOC one is doing the wisest thing, because ultimately what matters is the cost of the total system. I am not sure that the simple answer isn't going to be conventional aircraft with some STOL capability when it is needed. That is deliberately controversial, but I would be grateful for your comments.

Mr Hickey: I think, at least in the States, we feel that the short-haul transportation system needs to be improved. This can be done certainly, using existing airports, new runways on large airports, and airplanes of 4000 ft field length. That is well established and can be done right now. It is my view however, that with the current environmental awareness of the public, they are going to object and continue to object to airplanes near them and over them, and that shorter field lengths will help to minimize these objections. These objections will be less because when a new airport is required, it will be a shorter field length. Even if you have a 4000 ft runway, a 2000 ft field length aircraft will have its advantages, because take-offs can be offset to submit the community to less noise because more of the noise is contained on the airport. For landing, again you can offset and land in the last 2000 ft and minimize noise that way. Furthermore, a 2000 ft airplane lands slower, has a higher descent angle and will have less noise. So I think V/STOL aircraft systems will come. I have no idea when that will be.

Dr Rogers: I think I dispute that. Obviously, this is not the time for technical figures, but I am not sure that it is

FACTORS IN V/STOL ECONOMICS

$$\text{DIRECT OPERATING COST} = \frac{\text{COST}}{\text{HOUR}} \cdot \frac{1}{\text{VELOCITY}}$$

$$\text{WHERE VELOCITY} = \frac{1}{\text{CRUISE TIME} + \text{MANEUVER TIME}}$$

$$\frac{\text{DISTANCE}}{\text{lb OF FUEL}} = V \cdot \frac{1}{\text{SFC}} \cdot \frac{L}{D} \cdot \frac{1}{W}$$

Figure 2

WEIGHT BREAKDOWN OF STOL AIRCRAFT

COMPONENT	PERCENT WEIGHT
STRUCTURE	43.9
PROPULSION SYSTEM	14.4
FIXED EQUIPMENT	12.5
FUEL	13.8
PAYLOAD	15.4

Figure 3

EFFECT OF AERODYNAMIC REFINEMENT

10 PERCENT IMPROVEMENT	WEIGHT CHANGE, percent	CUMULATIVE WEIGHT CHANGE, percent
$C_{L_{MAX}}$	3.0	3.0
THRUST REQUIRED	3.0	6.6
SFC	2.8	9.5
CRUISE L/D	2.8	12.0
CRUISE SPEED	2.8	14.4

Figure 4

true that as you decrease the runway length the noise area decreases also. I suspect, and have seen figures which have suggested, that the noise footprint is in fact independent of the actual take-off runway because of increased engine power.

Mr Hickey: The point I was trying to make was that if you had a 4000 ft field you would still use a 2000 ft airplane on that and bias take-off and landing operations, because then some of the noise would be on the airport instead of the surrounding area.

Dr Rogers: I wonder if I could provoke a European view on this because certainly, I have read and I accept your government reports on this. Is it still true that anybody in Europe is interested in 2000 ft?

Mr Hickey: Perhaps you are representing Europe. There were still other parts to the original question. You mentioned that direct operating cost is only a part of the system. I realize that, and I tried to take care of it in the first part of my discussion. It may be that the indirect operating costs are a more important part of the system and could bias results either more in the direction of short field length or in the other direction. In terms of the airplane, I think that direct operating cost is a reasonable thing to discuss.

Prof. Küchemann: I would like to ask a few more general questions which occurred to me listening to all the papers. Therefore, it it not addressed only to Mr Hickey but perhaps also to the other panel members. What struck me was that we have looked at powered lift systems, but one could say that they were all rather peculiar in trying to match up two partners which really do not go well together, namely, an isolated engine nacelle and a wing. It is always most awkward, and many of the schemes seem to be illmatched and require either an awful lot of engineering or produce very awkward lousy flows. So, why this preference for just these few schemes? One thing that I am not at all clear about, having listened to all this, is, which of these practical powered lift schemes can do things which go beyond what one could, for instance, do with boundary layer control? Have they really gone beyond this boundary? I don't think that I, personally, got a clear answer to that. Do these schemes just produce what one would, perhaps, get in an attached flow or in an ideal inviscid flow, or do they go beyond that and are they genuinely powered lift? If they get us near the ideal flow, then one could do the same, presumably, with various schemes of boundary layer control. We did not really hear much about how these schemes compare. A similar question is that many of the schemes involve variable geometry in a very essential way, for instance, by increasing the wing area. Again I wasn't quite clear how much of the benefits that have been claimed are just due to this variable geometry, or, are there any benefits from achieving better aerodynamics and having more efficient flows? Again, that boundary was not very clear to me. Is it, perhaps, that we have concentrated rather on just the lift side of the problem? Very few people have talked about lift-to-drag ratios and what it all costs. That surprised me a little. Isn't that important any more? Why was there so little comment on this particular aspect? I was pleased that at least one speaker said that he could still see a future for mechanical flaps. What we ought to try to do at this Round Table Discussion is to see more clearly what we should do in future. Is there a future for powered lift systems, and if so, in what direction should we go?

Mr Hickey: I am not sure that I understand all of your questions. The first one, perhaps, was do these STOL systems really produce more lift than potential flow. I think that the answer is yes, they do. I do not think there is really any question about that, when you have an efficient propulsive lift system. Whether you need propulsive lift systems or not, may be another question, but they have that capability. As far as better aerodynamics are concerned, I was also disturbed as I mentioned climb-out lift-to-drag ratio is likely to define engine size in a STOL airplane. I am also concerned about cruise aerodynamics.

M. Perrier: What I want to comment on is that we have done work on mechanical flaps exactly as in the conventional manner. That means that extreme extension of the chord is not the origin of the maximum C_L we have obtained. We have the same extended chord as on a Boeing 727. The problem is only the work on the viscous flow around the wing section. We have begun by a study to see what is the shape of the wing section in order to have the separation as far as possible. After that, we have put an iteration in order to have a better compromise between the different slots at different positions. It is a very long job, but I am sure that we have not obtained the maximum that we can obtain. I know that if, for example, we are reducing the sweep angle with the effect of a reduced speed in cruise, we will have a greater C_L for the same sweep angle, for example, as a Boeing DeHavilland augmentor jet wing. We will have a greater C_L. What I hope is that by improving the knowledge of the viscous flow, essentially the knowledge of the turbulent viscous flow, of the mixing of turbulent mixed flow, we can go further in the future. I hope so.

Mr Eggleston: I would like to provide a partial answer to Dr Küchemann's earlier question and also the other one. The origins of civil STOL go back to around 1968, I would suggest, when the major airports in the U.S. suffered from severe congestion. You could spend half an hour circuiting New York in an airplane waiting to let down and a lot of time was lost and a lot of fuel burned going around in circles. About that time DeHavillands got interested in civil STOL, and particularly, downtown STOL. Shortly after that there was a recession in the U.S., the economy slowed down, airlines introduced the wide body jets and congestion temporarily vanished.

Recent statistics we have seen on operations at 8 major hub airports in the U.S. indicate that congestion is coming back again. However, there are limits as to what you can do in terms of aircraft spacing for wake avoidance considerations which govern how quickly you can put airplanes into existing runways . . . so we see civil STOL still as something that could come. As congestion returns, it may be worse than you have seen it before, maybe 10 years from now. It may also be predominantly a U.S. problem for perhaps the rates of growth in Europe are not going to be as rapid as the U.S. and in your time scale maybe VTOL will be the preferred solution. You may be able to leapfrog a generation of airplanes. But we would view VTOL as being so far down the pipeline, that it isn't likely to be available in time to provide relief from congestion in the U.S. and I think that we reasonably believe that civil jet STOL will find its place in North America even if it doesn't in Europe.

Chairman: Thank you, Mr Eggleston. We might come back to these more general questions later on, but I would prefer to give the word now again to Mr Eggleston, who has made a prepared comment on powered high lift systems.

Mr Eggleston: First of all, Mr Hartzuiker, I would like to thank the FDP for this opportunity to be involved in the Round Table Discussion reviewing the subject of the powered lift papers that were presented at this meeting. Secondly, I would like to congratulate the authors of the papers for the very good material which they have presented, although it is still apparent that a lot remains to be done on all the high lift systems which were discussed. I will review each of the high lift systems in turn, trying not to let personal bias influence me and hoping I do not miss out any author's name en route

Augmentor-Wing developments were reviewed in two U.S. papers by Hickey and Quigley, and the ejector powered Aladdin project was reviewed by M. Sagner of France. This work showed the advantages of the lobe-type primary nozzles in terms of increasing augmentation and reduced noise levels and these aspects will be of particular importance in future, when we are looking at large civil STOL airplanes. The scope of the NASA research is so broad that it does not leave me with many openings for suggesting where future research should be done. I will confine myself, therefore, to remarks on the type of configurations which seem to be being adopted, particularly in the propulsion area

Current U.S. studies are directed towards ultra quiet civil STOL aircraft, and to achieve low noise levels they have been directed toward bleed propulsion engines which have 80% of the thrust going into the wing and 20% residual thrust coming from the core. This leads to great problems in integrating the large duct system inside the wing, and there are penalties in cruise fuel consumption because of the very low bypass ratio of the powerplants. If blowing thrust levels were reduced to say 40% of total, using the three stream engines which I discussed in my own talk, this would reduce the installation problem and would allow higher bypass ratio engines to be used and so improve the cruise fuel consumption. These are very important points to think of in future because of the rapidly increasing cost of fuel. Another advantage of the three stream type of engine is that maybe it can be developed from existing engines, whereas, in the case of the 80/20 engine, it would almost certainly have to be a special purpose engine which would only have the one application. It would make it very difficult for the one project to carry the entire cost of such an engine. We saw several films of the Buffalo/Spey Research Aircraft, and I think that these demonstrated that technically, at least, the Augmentor-Wing is furthest advanced of the powered lift systems, and a high degree of confidence can be placed in its performance.

Externally Blown Flaps received the greatest attention at this meeting, and I think our understanding of the relative contributions of jet flap effect, boundary layer control effect and thrust deflection contributions was greatly improved by the presentation of Ashill and Foster. Surprisingly, this work suggested, at least at the thrust coefficient that they tested, that the jet flap component was small, which calls into question the basic assumptions of several of the semi-empirical methods of performance prediction which were presented at the meeting. The very detailed flow surveys that were presented by Wickens of NAE, Canada, showed the extremely complex nature of a flow caused by EBF interaction. It suggests that purely analytical methods of predicting EBF performance are going to be a long way away and as a result, it seems likely that wind tunnels will provide the prime source of data for new EBF configurations. For anything outside the range of current experience, it will be necessary to test models and unfortunately the cost of models is inordinately high. I find this all the time, particularly when you have internal blowing systems and I wonder if the quasi 2-D technique which we have used at DeHavilland and which NAE have used in their experiments, could not provide a very low cost way of looking at more advanced configurations. It might be of interest to do some work on Externally Blown Flaps which use thrust vectoring for we tend to think of the nozzles as always being pointed in one direction, and at best it is only going to be in the right direction at one condition. The EBF's suffer from flap impingement at take-off as a source of thrust loss, noise and a source of flap loads. Our own studies of the take-off performance of EBF's indicate that if the jets were tilted down for take-off you might see some improvement in those three areas so this could be an area where future research is warranted.

The Internally Blown Flap remains of interest and ONERA in France and DeHavilland, Canada, described recent work on two dimensional models, and DeHavilland Canada, also described some three dimensional work. The lift performance of the Internally Blown Flap is equivalent to the most sophisticated of the mechanical flap systems that was shown at this symposium, and it does this without much complexity in terms of mechanical or pneumatic devices. The IBF has a very low bleed requirement which I think should be remembered when we are considering the rapidly increasing cost of fuels. Future research on the IBF could consider blown multi-slotted flaps as a means of further reducing bleed level requirements and also, perhaps eliminating entirely the need for special purpose bleed engines. Further work on vectored thrust Internally Blown Flaps seem warranted, as it is a way to increase the lift available and allow us to go to higher wing loadings and so improve our cruise lift-drag ratios.

The mechanical flap vectored thrust was discussed in papers by Osborne and also by DeHavilland, Canada. Future work on this concept should look at improved flap designs and also develop low loss lightweight thrust deflectors suitable for use in the limited range of deflection angles appropriate to high bypass ratio engines, which were only of the order 70°.

No papers were presented at this meeting on upper surface blowing, and I would suggest that simple modifications to the externally blown flap models which were used in the NAE tests and the RAE tests could provide very useful comparative data on the externally blown flap and the upper surface blown flap. It would be a very simple investigation, and I think it would be very worthwhile.

The extension of model data on maximum lift coefficients to full-scale Reynolds numbers poses many problems. The paper by Moorehouse suggested for full-span jet flaps without leading edge slats that perhaps Stratford's criteria would be adequate. The situation for aircraft with part-span jet flaps or mechanical flaps and unblown leading edge slats is much more complex and research on developing methods of $C_{L_{max}}$ prediction from model data would appear a very worthwhile area for documentation.

Finally, I am impressed at the wide range of useful research which is going on throughout the NATO countries. I guess it is a measure of the maturity of the current work on powered lift aircraft that now, instead of people just talking about obtaining a very high $C_{L_{max}}$, and that my $C_{L_{max}}$ is better than your $C_{L_{max}}$, we find now that even pure aerodynamicists are talking about practical things like engine-failed climb gradients and $C_{L_{max}}$ with an engine failed with the aircraft trimmed longitudinally and laterally. I think this transition is tremendous, and I hope that it is a positive indication that operational jet STOL airplanes are very nearly with us.

Chairman: Thank you Mr Eggleston. I think you have given a very comprehensive and clear picture of how you think it should be. Are there any comments or questions from the floor?

Mr Moorehouse: Just a brief comment on Mr Eggleston's last point about three-engined maximum lift. I think in a gross sense that the maximum lift appears to be just a function of the total $C\mu$, so if you lose 25% of that in general, you are losing 25% of the increment due to the power.

Mr Eggleston: Well, this may be a debatable point. I have an intuitive feeling that it will depend very much on the type of high lift system. I think, for instance, that if you had a twin engined over-the-wing blowing airplane, and it lost an engine on one side that it should be much worse off say, than a four engine EBF airplane with the engines spread out more.

Mr Moorehouse: I will rephrase what I said. I think we have found that when we have looked at the $C_{L_{max}}$ of a four-engined configuration, with three or four engines operating, $C_{L_{max}}$ is a function of total power coefficient rather than a straight factor. It may be a reflection on the accuracy of the data. I agree that a twin-engined configuration is different.

Chairman: Are there any more comments? If not, I would like to call on Professor Blom to give his point of view on mechanical high lift systems.

Prof. Blom: Mr Chairman, you have asked me to comment on mechanical high-lift systems. Under that heading we had 5 papers in this symposium, among which three were devoted to aerodynamics of high-lift devices. One was devoted to the prediction of airfoil characteristics with spoilers and one was on the physical interpretation of the effect of small size vortex generators. When we recall these papers, perhaps it would be interesting to have a short summary of their contents. Jacob and Steinbach of Germany presented their method for prediction of lift from multi-element airfoil systems in which the effect of the boundary layer displacement on the circulation and pressure distribution is included, and in which, on the basis of criteria for real separation on the most aft located element, a model is developed for numerical calculation of lift and maximum lift with rear separation present. The method is, in its present form, restricted to a two-dimensional geometry, non-interacting boundary layers as shed from the multi-elements of the airfoil system, and shapes without slot cavities leading to other forms of separation than the rear separation. Within these restrictions, the calculation method may yield useful lift and pressure distribution data. Ljungström from Sweden presented his results of elaborate experiments in the wind tunnel on multi-element airfoils desgined for high lift. The information was presented against the background of requirements related to transport type of aircraft and is compared to results of calculated lift and pressure distribution using the methods of Stevens and Goradia of Lockheed. Extensive geometrical variation of double and triple slotted mechanical flaps, in most cases in combination with slats as leading edge devices, are explored in two-dimensional testing to achieve optimum high lift. To gain insight in the effect of interaction of wakes from upstream elements with the boundary layer of a more aft located element the wake characteristics have been artificially influenced in the experiment by applying suction to the upper surfaces. On the basis of the experience gained, some general conclusions are drawn on favorable arrangements of the airfoil elements and slot gaps. Perrier and Lavenant from France gave us their views on how they would extend their method for calculation of the pressure distribution of lifting wing body combinations to incorporate the effects of boundary layer. Wind tunnel results obtained on an aircraft model with full span, deep chord, high lift devices indicate the potential of mechanical high lift devices for STOL applications. This model was shaped according to criteria obtained with the developed calculation method.

For further discussion, and in view of the limited time available, further comments are restricted here on my side to the subject of the development of mechanical high-lift devices. From the papers presented in this symposium on V/STOL aerodynamics, it is clear that the emphasis in developing mechanical high-lift devices was on achieving higher max lift to avoid, or at least postpone, the need to adopt mechanically, and otherwise more elaborate systems, using some form of powered lift. However, the economy of transportation as expressed in the Direct Operating Costs of the flying vehicle, to a large extent depends on the total amount of expensive machinery needed in the aircraft, including the propulsion units. The best solution for a particular transport task obviously requires analyses of all cost elements involved. However, in particular for the less ambitious airfield performance requirements where the mechanical high lift devices seem to have their place low thrust levels in relation to aircraft weight still are an important asset to low cost. Consequently, to achieve this, the high-lift devices have to be designed for high lift-to-drag ratios in take-off and balked landing flight conditions, combined with a relatively high maximum lift capability. It may be remembered that Lockheed, in designing the four engined C5A transport aircraft, went to great pains in achieving high lift-to-drag ratios at high maximum lift for the take-off condition.

In relation to a considerable experimental effort over the past years spent in Holland on this subject, it can be stated, that optimizing a high lift system for the more complicated criteria based on a weighted balance between lift-to-drag on one side, and maximum lift on the other side, leads to high lift devices which may considerably differ from the shapes generated in the process of optimizing for maximum lift only. A good point for further consideration, therefore, seems to be the prospective which can be seen in the methods of numerical calculation in the field of drag reduction of high lift systems. This is a point for further discussion perhaps.

In relation to drag aspects of high lift systems, one further observation seems to be relevant here. In many cases the aircraft designer accepts cavities in slots of the multi-element high lift system in the interest of low drag in the condition that all feathers of the wing are retracted to restore the original airfoil shape. In these cavities a trapped vortex may be generated, which often, under conditions of strict two-dimensional flow, show surprisingly small drag effect in comparison with conditions with the vortex removed, using a faired contour surface. In the three-dimensional wing, however, the momentum exchange between the external flow and the trapped vortex may contain a span-wise component, or in other cases, a span-wise flow in the trapped vortex leading to a considerable increase in drag. Likewise, drag measurements with a momentum rake behind one profile section in quasi-two-dimensional wind tunnel arrangements may lead to largely erroneous results because of span-wise transport of boundary layer and wake material that takes place, mostly unobserved and not necessarily due to the presence of a trapped vortex. There are two aspects to this. Two-dimensional test results on drag of high lift devices should be watched with a healthy amount of suspicion and the conversion of two-dimensional data to a three-dimensional wing often produces some unwanted surprises when the actual wing is tested. These effects should be given further consideration in future research.

Chairman: Thank you Professor Blom, for your suggestions.

Mr Ljungström: First, I would like to agree very much with Professor Blom about his comments on the drag problem. I think also that the drag may be the most important problem right now for mechanical high lift devices. I would like to add that in the work that has been presented in my paper here that all the experiments were also carried out with rake drag measurements, so we have an extensive amount of data on the two-dimensional drag taken from wake integrations. We have compared these drag measurements with the corresponding three-dimensional tests at the same Reynolds number. We can see that the optimization trends for drag are, of course, very different from two-dimensional to three-dimensional tests. That, of course, is due to the large amount of induced drag, or vortex drag, in the three-dimensional case. This really made it very hard to see what use you can have of the two-dimensional drag trends for optimization purposes. To study this a bit more closely, we are now performing some half-model tests, where we are carrying out wake surveys of the complete half-model span.

Chairman: Any more questions or comments on this point? Dr Barche.

Dr Barche: I missed a paper on high-lift problems of typical transonic profiles. We found that on wings with typical transonic profiles, because of their increased thickness at the leading edge and reduced sweep, high $C_{L_{max}}$s could be achieved with very simple mechanical flaps. On the other hand, the lift-drag ratio for take-off flap settings seems to be worse than with classical airfoils. So, I would think that on that new profile technique we should have some comments.

Chairman: Thank you Dr Barche. Transonic profiles are not directly V/STOL, but there might be some comments here.

M. Perrier: It seems to me, not as a point of view of a fluid mechanical engineer, but as a point of view of a manufacturer, that a transonic STOL aircraft will not have very simple mechanical flaps, but variable-geometry mechanical flaps, becasue we know quite well that it is already necessary for CTOL when you seek the best compromise between low speed and high speed. I insist that, in fact, the problem of profile drag is not very important at very high C_L because if you make the product of $\frac{1}{\pi A}$ by $(C_L)^2$ you see that it is a very important figure. For example, for the typical aircraft, if you assume that you have a 0.05 k and a value of C_L of 4, that means that you have something like 0.8 in C_D due to vortex drag and you cannot avoid that drag. It is due to the span of the wing; you have generated a certain lift in a certain span, and it costs a certain price. That is, 0.8 in C_D. It is not at all the same in the cruise or CTOL conditions; at C_L less than 1 or 1½, you have exactly the same problem as usual actually, with a profile drag which is not negligible compared with the induced drag.

Prof. Blom: It all depends on the ambition you have in creating short take-off and landing conditions. If we are discussing an aircraft which is capable of day to day operations from 4000 ft, rather than 2000 ft, it is my personal experience that every small decrement in drag contribution, either viscous or due to the vortex drag, pays, and creates a better airplane which can fly with less power. To quote a number, the latest version of the Dutch Fokker F28 twin-engined airplane can perform the low-speed single-engine take-off climb with a lift to drag ratio of approximately 10 in a take-off configuration corresponding with a max. lift coefficient of 2.8. This L/D of 10 is not achieved by considering the viscous drag on the flap insignificant. It is very important to have the utmost from that flap in this respect.

Mr Back: In talking about the drag we have got to be clear whether we are talking about take-off or landing. We are looking for high $C_{L_{max}}$s to get steep approaches, and one of the problems on the steep approach may be of getting adequate drag in order to keep an engine's response characteristics satisfactory. We are, however, very concerned about obtaining low drag during the take-off phase. I think that in the discussions during this week very little has been said about the flap angles for take-off and the associated performance.

Mr Eggleston: There was a slide in my paper which I didn't present on the screen, which did show some engine failed climb gradients for typical 2000 ft STOL airplanes. They will run to very high values, even with the EBF configuration which suffers from flap impingement and by the time you have put enough thrust in to go through a 35 ft screen in 2000 ft, you have a substantial climb gradient available. It may be in the order of 13° or more, all engines operating, and even with engine failed it will be of the order of 6°. When you are talking a new airplane, I do not think you should also get involved in frozen thinking about the powerplant side. Some of the parameters in the powerplant can be changed relatively simply for the expensive bits of an engine are usually the hp compressors, the combusters and the hot end, while fans can be changed without too much difficulty, particularly if you have gear boxes in between the fan and its turbine. With STOL aircraft, if there are problems in having to go to low aspect ratio configurations to get landing gradients that are satisfactory, you can always get back, at least to some degree, to an acceptable climb situation by playing around with the bypass ratio of the engine. All is not lost if you have to tailor the configuration specifically to a landing requirement.

Chairman: I think the time permits us to have one more comment from Mr Ljungström.

Mr Ljungström: I have one short comment about the drag. From our tests, it turned out that the kind of configurations you get when you optimize for $C_{L_{max}}$ is for rather small interactions between the different wake layers. This also means that we get the most efficient flow. If we look at the drag results, we can see that these turn out to have rather low drag values, too, at lower C_L. The difference might be that the gaps are just somewhat smaller, if we optimize for minimum drag at a certain C_L, which should be something like 0.65 $C_{L_{max}}$. We have tried to do that too, and it turns out that the gaps should be somewhat smaller. Then the compromise should be a gap somewhere between the two. This is of course true only for gap optimization for a given set of flap angles which is the only case for which drag measurements give any conclusive trends.

Prof. Blom: Perhaps there is a need to say more about the differences we have found in optimization of high lift devices for combined L/D and maximum lift criteria in comparison with results for maximum lift only.

We found two substantial differences on slat position, the best slat angle with the drag criterium included came out much smaller and also the slat-gap had to be small. The gap of the slat then being much narrower than the one found by Ljungström in his experiments.

Nevertheless, for take-off configurations of the F28 aircraft the increment in $C_{L\,max}$ due to the extension of the slat is 1.2, based on a 1g-stall and as measured in flight.

Dr Barche: If we discuss jet lift, we have to ask for what application – civil or military application? Here, in this meeting, I got the general impression that there will be no near future application of jet-lifted civil airplanes, the main reason being the cost effectiveness, which is lower than for conventional aircraft of equivalent payload and range. Other reasons – we didn't discuss here – are the engine situation, the reliability of civil jet-lifted aircraft, the engine failure situation and the noise. What we discussed here was that the improved STOL systems are working against jet-lifted civil aircraft.

I also got the impression that on the military side, the situation is somewhat different. It might be because the Harrier is already introduced, and in the U.S. discussions are going on the sea control ships. But I feel that military jet-lifted aircraft also have to be more cost effective; they have to be less complicated; they should have better maintenance capability and furthermore improved reliability seems to be needed.

To summarize what was produced here during the meeting, I feel that three different aspects on jet-lifted aircraft have been considered :

(1) How to improve our knowledge of the complex jet-lift interactions:

(2) What about critical flight conditions and their predictions?

(3) What about new jet-lift generators avoiding the typical jet problems we have to live with using lift or lift cruise engines?

I think these three different aspects treated here, give a good picture of what has to be done, is being done or has been done recently.

I also felt that the progress reported here was not so impressive as it was previously. Indeed, jet-lifted aircraft are flying already and on the other hand the general situation seems not to promote civil or even military aircraft as was expected some years ago. I feel that if there is a political or economical saturation we are still far from a saturation of our knowledge. I think we can all agree that there are a lot of gaps in our knowledge to be filled.

But there is a simple question: "Is it really worthwhile to fill those gaps?" My answer is "Yes", because problems which are treated on jet-lifted aircraft are closely connected with modern non-jet lifted aircraft. To illustrate this, the use of high-by-pass engines with large diameters installed close to wings, fuselages or tails, gives us interaction problems similar to those we have to study on jet-lifted aircraft: problems of jet-wing/body interactions are quite independent, whether the jet is more or less vertical or parallel to the free stream. I strongly believe that general jet-research should be continued, but not restricted to steady flows only. More and more, in interaction problems, the random character of jet flows has to be studied.

Chairman: Thank you Dr Barche. One of the main points I got out of this is the question of what is the near future of jet-lift aircraft as we see it at the moment. Any comments on that? That is apparently a very difficult question. Are there any more comments on what Dr Barche has said? If not, then I would like to pass the word to Professor Gersten who will give some comments on Sessions 4 and 5 of this meeting.

Prof. Gersten: Mr Chairman, I would like to split up my comment into two parts: one on ground effect and one on prediction methods. *Ground effect* has again to be split up into mechanical and powered lift systems on one side and the jet lift systems on the other side. From what I have learned here at the meeting on ground effect for mechanical and powered lift systems, there obviously exist cases where the ground effect is positive and other cases where the ground effect is negative. It became quite clear at the meeting, that these effects due to ground can be predicted quite well by potential theory (method of images). If a method is available which can predict the forces at high angles of attack or high jet angles, far from ground, then this method can be extended easily to predict also these forces near ground.

There are of course problems left which have just been touched during the meeting, and I would like to draw attention to one particular aspect mentioned by Mr Hickey, i.e., the dynamic aspect, as he called it, or I would say the unsteady aspect of the ground effect. It may be possible that the height above ground changes so rapidly during take off or landing that unsteady aerodynamic effects have to be taken into account. Therefore, there is a need for more research work on unsteady lifting surface theory near ground.

Much more difficult is the situation for the ground effect of jet-lift systems. We heard from several lectures, Dr Barche and others, that there are two effects close to the ground, i.e., the suck-down and the fountain flow effect, the first one due to entrainment, the second one due to multiple jet arrangement. As far as I can see, we are very far from any kind of reasonable modelling of the flow field. This field is a combination of viscous flow regimes in the jets or at the boundaries of the jets. These viscous flow regimes have to be matched with the outer flow which might be a potential flow. There is still much work to be done to develop a reasonable and simple model which describes the essential features of such a system. Here, I think, theoreticians as well as experimentalists should come together in the future and work together on these problems.

This brings me to the other subject which I wanted to comment on, i.e. the *prediction methods*. I would like to talk only about the more sophisticated prediction methods, not about handbook-type prediction methods. In the more sophisticated prediction methods one has to know quite a bit about the physics of the flow field. As we have seen at the meeting, the flow fields are not simple and not easy to understand.

To answer one of Dr Küchemann's questions about the pecularities of the flow fields, this is perhaps just a matter of getting acquainted with this kind of flow field. Perhaps we feel that these fields, which are very complicated and mixtures of viscous and inviscid flow domains, are peculiar because they cannot be handled easily by classical methods like potential flow theory, lifting surface theory etc. It will be a matter of time, while we work on these more complicated fields, before we feel that they are completely normal and have no peculiarities in them.

As far as prediction methods are concerned, I found particularly the paper by Dr Perrier from Dassault-Breguet very impressive, and also the Douglas "EVD" method which was mentioned by Mr Woolard. Obviously, these two papers give a fairly good picture about the state of the art of the more sophisticated prediction methods.

I got the impression from these two papers, as well as from others, that we may come eventually to an end with those prediction methods which are more or less of the classical type, that means, prediction methods which use the simple concept of classical boundary layer theory. They start with a potential theory, calculate the boundary layer afterwards, perhaps calculate the displacement of the boundary layer, feed this displacement effect back into the potential flow theory, and then by an iteration process, might end up with a picture of the whole flow field. Obviously, there are limits for this kind of method and one good example of these limitations was given in the paper by Mr Ljungström, where it was shown that wakes of slats for example are not necessarily developing in a near wall region, but nevertheless have an important effect on the pressure distribution of the airfoil which in a classical prediction method should be determined by potential flow theory. We are now facing the situation that obviously the simple concept of outer inviscid flow and near wall boundary layer flow is not working, or has to be modified and extended, to take into account situations where the "outer flow" does not have constant total pressure because of wakes or slats or other disturbances upstream.

Therefore, I feel that in the future prediction methods have to be developed by two groups of people who come together from two sides: from potential flow theory and from boundary layer theory. If these two groups could be combined and if the whole concept of outer flow boundary layer interaction is reconsidered for change or modification then, perhaps, we can end up with the method which at least for the two-dimensional case would give a much better picture and could lead to an optimization of the two-dimensional flow past multi-element airfoils.

Of course, there are the problems of three-dimensionality, and they are much more complicated. At least we should try to take as much as we can of the physics into the more sophisticated prediction methods. When we then try to put the most important features of the flow field into the mathematical models, we may come to a better description of these quite complicated flow fields.

Chairman: Thank you Professor Gersten. It might be appropriate here to go directly to M. Perrier and ask for his point of view of the application of computer methods.

M. Perrier: Before my comment on this, I would like to show very quickly three figures. Frame 5 is what the computational method is not. You see it is a conventional correlation type presentation of high lift devices. The point that you see at the curve in the upper part of the slide corresponds to flight results of aircraft of Dassault-Breguet and you see that efficiency is very poor, of the order of 0.3 to 0.4. That is just the sort of thing that you can learn with that sort of computation. In Frame 6 I have given you the reason why you are obliged to make calculations. It is an example of optimization of the position of a slot. You can see a certain number of iterations, and we have indicated good and bad positions. The direction of the arrow is for a better C_L, for example, or a better C_D. What you can see is that when you have to cope with 5 slots, not at all independent of each other, and on each slot you have to take 20 positions for optimization, it is impossible to do that experimentally. To

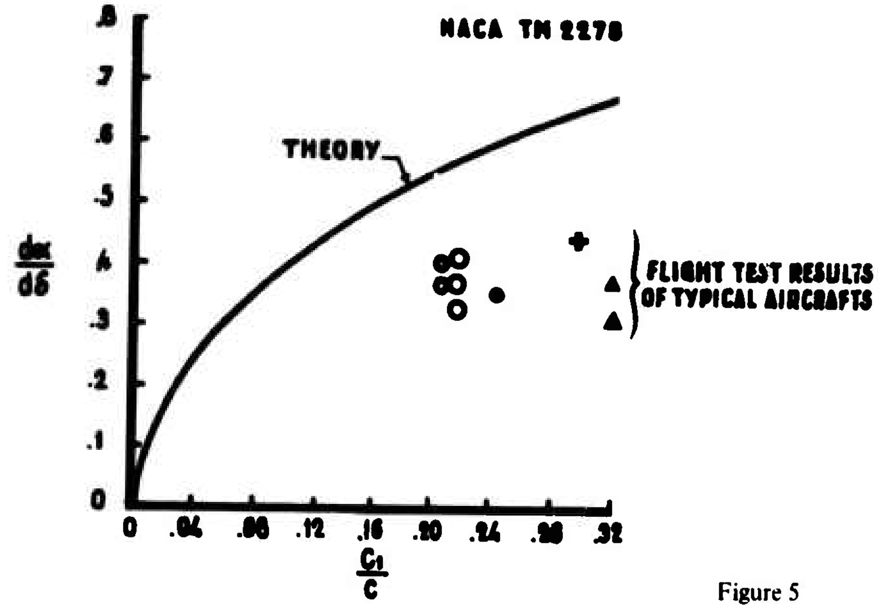

Figure 5

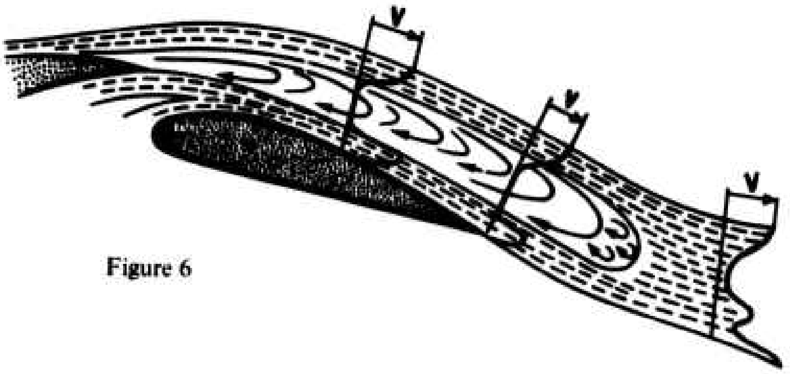

Figure 6

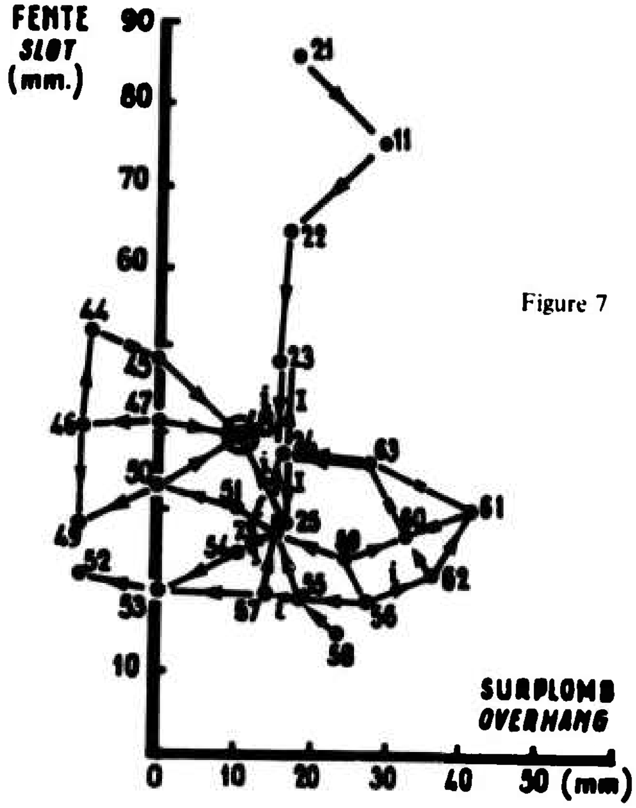

Figure 7

return to what Prof. Gersten has said, and to prove that all the problems of computation are not simple problems, figure 7 shows you some fundamental problems of viscous layers with separated regions (in white) and viscous layers with no separation but a turbulent regime (in blue). What you can see in these slides is that it is very difficult to avoid computation in the future for increasing the flap efficiency There are three levels of computations; the first one is the correlation type, and it seems to me that it is outside the scope of my optimization. The second one is a typical job for people in industry, i.e., how to build a very huge program in order to take into account all the different parts of the flow field. The third one is how to include in the program good bricks in the same way as we do a wall. For that, it is necessary to choose a very good breakdown of the theoretical and physical model, and after that, to improve step-by-step the validity of the total program by improving each brick of the program. If I mention some history, I can say that on the Mirage 3V vertical aircraft we have done very limited calculations in order to have the spanwise lift distribution for prediction of the one-engine-out condition, which is a very annoying problem, and we discover that we have much work to do in that direction. On the last project, we have done all the preliminary work by computing the flow fields, and it seems to me that it will be the case in the future for all the projects of V/STOL. What I would like to comment on regarding what has been said by different people in this discussion is that people have made a great improvement in bricks, but greater improvements are necessary. For example, some Italian people have only determined what vortex generator complete field model to study. In the same way there is the problem of interaction between the jet lift and the external flow for a VTOL. It is a complicated problem, and it is the beginning of computational methods. After that we have to make a schematization and go a long time in order to obtain the pressure.

Chairman: Thank you M. Perrier. I would ask the audience if there are any remarks or comments on what Professor Gersten and M. Perrier have said.

Dr Spee: I agree in general with Professor Gersten's remarks, but he is still talking about calculating boundary layers. The pressure gradient is assumed to be negligible in the direction normal to the boundary layer. Now if you look at high lift systems with a number of airfoil elements with wakes that are coming off the elements and going over the following elements, you are facing the problem where you will have viscous interaction but also large pressure gradients normal to the wakes. My feeling is that the only proper way to solve this problem in a two-dimensional flow is by calculating the whole flow field. The three-dimensional problem is probably far too complicated to describe theoretically. I know that M. Perrier has been working and is working on finite element methods and finite difference methods and we are doing similar things at NLR, and I have the feeling that finally you have to use such a method to come to an optimization of multi-element wings in two-dimensional flow. Of course then you are still far from an optimization of the three-dimensional case. I feel a little bit pessimistic here since I heard people say that it is an impossible task to get an optimization out of the experimental work in the wind tunnel only, since there are so many parameters involved. You also cannot get the final result from calculations. As Professor Blom pointed out, the three-dimensional effects can be very important. So we are still far from where we would like to be. Anyway one of the things we have to start now is trying to develop workable methods for field calculations for the two-dimensional case.

Mr Clark: Is it too early to ask this question? Does the Panel have any opinion as to the strength or relative intensity of the trailing vortices behind V/STOL aircraft in comparison with those observed behind similar commercial aircraft? In other words, will it be more serious for a small aircraft flying behind them or will the vortices be more broken up? You have the wing vortices and, in addition, you have these lifting vortices giving turbulent flows.

Mr Eggleston: The basic relation giving the approximate strengths of the bound and trailing vorticity is

$$\Gamma = \frac{UC_{L}C}{2}$$

from this we see that to a first approximation the strength of the vorticity is proportional to the velocity, lift coefficient and chord and depends on their interchange. If the rate at which lift coefficient increased could be maintained at the rate which velocity reduced, then the vortex strength of a STOL aircraft would be similar to conventional aircraft.

Chairman: Do you believe that? I think we are about at the end of this symposium. There is one more question from Mr Mavriplis.

Mr Mavriplis: This isn't a question really, it is more of a comment. I would like to come back to mechanical high-lift systems and to what Prof. Blom said. I couldn't agree more that there is a requirement for achieving high $C_{L\max}$ and at the same time high lift-to-drag ratios. Until now we have spoken about optimizations of given airfoil shapes, by using slats and multi-slotted flaps. There is another approach to it, and we have not spoken about it at all in this meeting, i.e., to deal with new shapes, to try to produce new airfoils which provide high lift-to-drag ratios at the same time as high $C_{L_{max}}$ figures and to try to actually reduce the number of elements in take-off configurations to achieve simple mechanical high lift devices. There is great need for design methods of this kind.

Chairman: Thank you for your comments. Is there anybody who has a very pressing comment to make before we close this Round Table Discussion? If not, I think that is the end of it.

I would like to start out by thanking all the contributors to this discussion. Firstly, the speakers from this side of the table; then I would like to thank the people from the audience who contributed to the discussion. It might be that from this discussion we have a better idea of where we should go in the future as far as V/STOL aerodynamics is concerned. I hope we will profit from this.

As Chairman of the Programme Committee, I have then to close this symposium, and I would like to thank all those who made it a fruitful one. Firstly, I would like to thank the authors and the contributors to the discussion; I hope that their efforts have been rewarded by the fresh exchange of ideas. As for the Fluid Dynamics Panel, we must thank those who invited us here, the Netherlands National Delegates of AGARD, Professor Gerlach and Mr Marx. It was a pleasure to have this symposuim here in the Netherlands. Of course, at the same time, we are very grateful that the Aeronautical Department of this University made it possible to meet here in this splendid building. For this our thanks go to the Dean of the Department, Professor van Ingen. not forgetting his staff who performed such excellent organizational and supporting work; I mention particularly the projection which was perfectly done. We record our thanks also the Netherlands Coordinator of AGARD and the Panel Executive, together with their staffs, for their excellent work in preparing this meeting and in guiding us through these last three days. Of course one of the main problems we still have in Europe and in NATO is the difference in languages; the interpreters have done an excellent job which has contributed to the success of this meeting. Three days ago the Chairman of the Fluid Dynamics Panel opened this meeting, and perhaps he will want to say something at this point.

Prof. Küchemann: Ladies and Gentlemen, there is just one more job to be done and that is for me, on behalf of you all, to thank Mr Hartzuiker. He did all the hard work in preparing the meeting, and he has been extremely successful. It really matters whether the meeting is well prepared or not, and we have seen that it was. Before closing this symposium, I would like to thank Mr Hartzuiker for all the work he did for us.

AGARD Conference Proceedings No.143
Advisory Group for Aerospace Research and Development, NATO
V/STOL AERODYNAMICS
Published October 1974
368 pages

Proceedings of the Fluid Dynamics Panel Symposium held at Delft, Netherlands, 24–26 April 1974. Twenty six papers and Round Table Discussion dealing with High-Lift Systems (Powered and Mechanical), Jet Lift, Ground Effect, and Aerodynamic Prediction Methods and Simulation Requirements. Helicopters and noise have been dealt with in other recent symposia and are not included.

AGARD-CP-143
533.652.6:533.694:
533.682.

Vertical takeoff aircraft
Short takeoff aircraft
Aerodynamic characteristics
High lift devices
Lift
Jets
Ground effect
Meetings
Test facilities

AGARD Conference Proceedings No.143
Advisory Group for Aerospace Research and Development, NATO
V/STOL AERODYNAMICS
Published October 1974
368 pages

Proceedings of the Fluid Dynamics Panel Symposium held at Delft, Netherlands, 24–26 April 1974. Twenty six papers and Round Table Discussion dealing with High-Lift Systems (Powered and Mechanical), Jet Lift, Ground Effect, and Aerodynamic Prediction Methods and Simulation Requirements. Helicopters and noise have been dealt with in other recent symposia and are not included.

AGARD-CP-143
533.652.6:533.694:
533.682.

Vertical takeoff aircraft
Short takeoff aircraft
Aerodynamic characteristics
High lift devices
Lift
Jets
Ground effect
Meetings
Test facilities

AGARD Conference Proceedings No.143
Advisory Group for Aerospace Research and Development, NATO
V/STOL AERODYNAMICS
Published October 1974
368 pages

Proceedings of the Fluid Dynamics Panel Symposium held at Delft, Netherlands, 24–26 April 1974. Twenty six papers and Round Table Discussion dealing with High-Lift Systems (Powered and Mechanical), Jet Lift, Ground Effect, and Aerodynamic Prediction Methods and Simulation Requirements. Helicopters and noise have been dealt with in other recent symposia and are not included.

AGARD-CP-143
533.652.6:533.694:
533.682.

Vertical takeoff aircraft
Short takeoff aircraft
Aerodynamic characteristics
High lift devices
Lift
Jets
Ground effect
Meetings
Test facilities

AGARD Conference Proceedings No.143
Advisory Group for Aerospace Research and Development, NATO
V/STOL AERODYNAMICS
Published October 1974
368 pages

Proceedings of the Fluid Dynamics Panel Symposium held at Delft, Netherlands, 24–26 April 1974. Twenty six papers and Round Table Discussion dealing with High-Lift Systems (Powered and Mechanical), Jet Lift, Ground Effect, and Aerodynamic Prediction Methods and Simulation Requirements. Helicopters and noise have been dealt with in other recent symposia and are not included.

AGARD-CP-143
533.652.6:533.694:
533.682.

Vertical takeoff aircraft
Short takeoff aircraft
Aerodynamic characteristics
High lift devices
Lift
Jets
Ground effect
Meetings
Test facilities

DISTRIBUTION OF UNCLASSIFIED AGARD PUBLICATIONS

NOTE: Initial distributions of AGARD unclassified publications are made to NATO Member Nations through the following National Distribution Centres. Further copies are sometimes available from these Centres, but if not may be purchased in Microfiche or photocopy form from the Purchase Agencies listed below. THE UNITED STATES NATIONAL DISTRIBUTION CENTRE (NASA) DOES NOT HOLD STOCKS OF AGARD PUBLICATIONS, AND APPLICATIONS FOR FURTHER COPIES SHOULD BE MADE DIRECT TO THE APPROPRIATE PURCHASE AGENCY (NTIS).

NATIONAL DISTRIBUTION CENTRES

BELGIUM
Coordonnateur AGARD – VSL
Etat-Major de la Force Aérienne
Caserne Prince Baudouin
Place Dailly, 1030 Bruxelles

CANADA
Defence Scientific Information Service
Department of National Defence
Ottawa, Ontario K1A 0Z3

DENMARK
Danish Defence Research Board
Østerbrogades Kaserne
Copenhagen Ø

FRANCE
O.N.E.R.A. (Direction)
29, Avenue de la Division Leclerc
92, Châtillon sous Bagneux

GERMANY
Zentralstelle für Luftfahrtdokumentation
und Information
8 München 86
Postfach 860881

GREECE
Hellenic Armed Forces Command
D Branch, Athens

ICELAND
Director of Aviation
c/o Flugrad
Reykjavik

ITALY
Aeronautica Militare
Ufficio del Delegato Nazionale all'AGARD
3, Piazzale Adenauer
Roma/EUR

LUXEMBOURG
See Belgium

NETHERLANDS
Netherlands Delegation to AGARD
National Aerospace Laboratory, NLR
P.O. Box 126
Delft

NORWAY
Norwegian Defence Research Establishment
Main Library
P.O. Box 25
N-2007 Kjeller

PORTUGAL
Direccao do Servico de Material
da Forca Aerea
Rua de Escola Politecnica 42
Lisboa
Attn: AGARD National Delegate

TURKEY
Turkish General Staff (ARGE)
Ankara

UNITED KINGDOM
Defence Research Information Centre
Station Square House
St. Mary Cray
Orpington, Kent BR5 3RE

UNITED STATES
National Aeronautics and Space Administration (NASA)
Langley Field, Virginia 23365
Attn: Report Distribution and Storage Unit
(See Note above)

PURCHASE AGENCIES

Microfiche or Photocopy
National Technical
Information Service (NTIS)
5285 Port Royal Road
Springfield
Virginia 22151, USA

Microfiche
ESRO/ELDO Space
Documentation Service
European Space
Research Organization
114, Avenue Charles de Gaulle
92200 Neuilly sur Seine, France

Microfiche
Technology Reports
Centre (DTI)
Station Square House
St. Mary Cray
Orpington, Kent BR5 3RF
England

Requests for microfiche or photocopies of AGARD documents should include the AGARD serial number, title, author or editor, and publication date. Requests to NTIS should include the NASA accession report number.

* * *

Full bibliographical references and abstracts of AGARD publications are given in the following bi-monthly abstract journals:

Scientific and Technical Aerospace Reports (STAR),
published by NASA,
Scientific and Technical Information Facility
P.O. Box 33, College Park
Maryland 20740, USA

Government Reports Announcements (GRA),
published by the National Technical
Information Services, Springfield
Virginia 22151, USA

Printed by Technical Editing and Reproduction Ltd
Harford House, 7-9 Charlotte St, London, W1P 1HD